

BULGARIAN CHEMICAL COMMUNICATIONS

2015 Volume 47 / Number 2

*Journal of the Chemical Institutes
of the Bulgarian Academy of Sciences
and of the Union of Chemists in Bulgaria*

Prediction model of the effect of light intensity on phenolic contents in *hypericum triquetrifolium turra*

M. S. Odabas^{1*}, J. Radusiene², B. Karpaviciene², N. Camas¹

¹Ondokuz Mayıs University, Bafra Vocational School, Samsun, Turkey

²Nature Research Centre, Institute of Botany, Zaliuju ezeru 49, Vilnius LT-08406, Lithuania

Received February 17, 2014; Revised August 25, 2014

The objective of the present study is to develop a prediction model for the phenolic contents in *Hypericum triquetrifolium* Turra with multiple regression analysis. The best estimating equations for the phenolic compounds (chlorogenic acid, rutin, hyperoside, isoquercetrin, quercitrin and quercetin) contents are formulized as $PC = (a) + (b \times L) + (c \times L^2)$, where PC is the phenolic content, L is light intensity ($\mu\text{mol m}^{-2} \text{s}^{-1}$) and a, b and c are coefficients. Multiple regression analysis was carried out until the least sum of squares (R^2) was obtained. R^2 value was 0.70 for rutin and 0.97 for chlorogenic acid. Standard errors were found to be significant at the $p < 0.001$ level.

Keywords: *Hypericum triquetrifolium*, phenolic compounds, modeling, light intensity.

INTRODUCTION

The genus *Hypericum* L. includes, at the most recent count, 469 species of flowering plants classified into 36 taxonomic sections [1]. The species of this genus have been used as traditional medicinal plants due to their wound-healing, bactericide, anti-inflammatory, diuretic and sedative properties for hundreds of years [2]. Despite the large number of *Hypericum* species, undoubtedly, only *H. perforatum* has been studied in depth as a pharmaceutical important medicinal plant [3]. In particular, extracts of *H. perforatum* are now widely used in Europe as a drug for the treatment of depression [4]. In Turkey, the genus is represented by 89 species, of which 43 are endemic [5].

Hypericum triquetrifolium Turra. is an herbaceous perennial plant, which grows in open, dry stony, sandy ground and cultivated fields in Turkey [6]. It has been traditionally used by Turkish folk in the treatment of bile and intestine ailments [7]. The plant has great pharmaceutical potential with its well-documented antinociceptive, anti-inflammatory, antioxidant, antibacterial, antifungal and cytotoxic activities [8, 9].

Developmental models are commonly explored using computational or simulation techniques. The simulation software may be general-purpose, intended to capture a variety of developmental processes depending on the input files, or special-purpose, intended to capture a specific phenomenon [10, 11]. Input data range from a few parameters in models capturing a fundamental mechanism to

thousands of measurements in calibrated descriptive models of specific plants. Standard numerical outputs (i.e. numbers or plots) may be complemented by computer-generated images and animations [12].

The content of bioactive compounds in plants varies with internal factors, as organs, age of the plant, phenological stage or external environmental factors [13]. The light intensity within the crop environment strongly increases its growth and yield. The light intensity can be identified as a key environment variable related to crop yields, phenological development, etc. The relationship between chemical composition and light intensity in *H. perforatum* was investigated in a previous study [14], but to author's knowledge there is no report on *H. triquetrifolium* in terms of the same relationship. In the present study, the effect of light intensity on phenolic compounds accumulation in *H. triquetrifolium* was quantitatively examined for the first time.

MATERIAL AND METHODS

Plant material and culture conditions

H. triquetrifolium plantlets were established from 5-month-old seeds collected on plants growing wild in the Erbaa district of Tokat, Turkey. Seeds were germinated in a float system, commonly used for seedling production of broad-leaves tobacco Burley and Flue-Cured-Virginia under a 16 h light/8 h dark cycle. Newly emerged seedlings were transferred to pots filled with the commercial peat tray substrate, 30 cm in diameter and watered daily until they reached maturity. Then, the pots were transferred to a greenhouse, separated into shaded and unshaded parts. Polyethylene cover of 50% transparency was used for shading. Plants were watered daily until they reached

* To whom all correspondence should be sent:
E-mail: mserhat@omu.edu.tr

maturity, then three times a week. Light intensities were measured at one-meter height over the plants with a Delta-T Sun Scan Canopy Analyzer. The measurements were performed daily in both shaded and unshaded parts separately. 100 pots were treated for each experimental part, thus a total of 200 pots were used. Ten pots (5 pots for shaded and unshaded parts) were harvested weekly and 20 samples were taken between May-September, 2007. The aerial parts of the plants were dried at room temperature ($20 \pm 2^\circ\text{C}$) and subsequently assayed for the phenolic concentrations by HPLC.

Preparation of plant extracts

Air-dried plant material was mechanically ground with a laboratory mill to obtain a homogenous drug powder. Samples of about 0.5 g (weighed with 0.0001 g precision) were extracted in 50 ml of 100 % methanol by ultrasonication at 40°C for 30 min. in a Sonorex Super model RK 225H ultrasonic bath. The prepared extracts were filtered through a membrane filter with pore size of $0.22\ \mu\text{m}$ (Carl Roth GmbH, Karlsruhe, Germany) and kept in a refrigerator until analysis, no longer than 3 h.

HPLC analysis

A Shimadzu Prominence LC-20A (Shimadzu Europa GmbH, Duisburg, Germany) chromatographic system equipped with two LC-20AD model pumps, a SIL-20AC auto-injector, a thermostat CTO-20AC and a SPD-M20A detector was used for HPLC analysis. Separation of all compounds was carried out using an YMC Pack Pro-C18 (YMC Europe GmbH, Dinslaken, Germany) column ($150\ \text{mm} \times 4\ \text{mm}$ i.d.; $3\ \mu\text{m}$ particle sizes) with 10 mm guard-precolumn. For mobile phase, 0.1 % aqueous trifluoroacetic acid (TFA) was used as eluent A and acetonitrile containing 0.1 % TFA as eluent B. The following binary gradient elution program was used: 0–1 min (B 5→5%), 1–14 min (B 5→20%), 14–20 min (B 20→80 %), 20–30 min (B 80→100 %), 30–39 min (B 100→100 %), 39–39.5 min (B 100→5 %), 39.5–45 min (B 5→5 %). The mobile phase was delivered with a flow rate of $1.0\ \text{mL min}^{-1}$; volume of extract injected was $10\ \mu\text{L}$. Detection was performed in the 210–790 nm wavelength range with a constant column temperature at 40°C . The eluted compounds were identified by comparison of their retention times and UV spectra with those of reference standards. The maximal absorption on the UV spectra of the compounds was obtained as follows: chlorogenic acid – 325 nm, rutin,

hyperoside and isoquercetin – 353 nm, quercitrin – 347 nm and quercetin – 368 nm wavelength.

The quantities of compounds were calculated from external standard calibration curves. The stock solutions of reference standards were prepared by dissolving in HPLC-grade methanol. Calibration curves were established on six concentrations in following ranges: 6.0–300 $\mu\text{g/mL}$ for chlorogenic acid and rutin, 3.0–300 $\mu\text{g/mL}$ for hyperoside and isoquercetin, 2.0–200 $\mu\text{g/mL}$ for quercitrin and quercetin. All calibration curves showed good linear regression ($r^2 \geq 0.999$) within the test range. Each sample was analyzed twice and the mean value was used for calculation. The concentration of compounds was expressed as mg/g dry mass (DM).

Chemicals

The reference substances chlorogenic acid (purity 98.03%), rutin trihydrate (purity 99.02%), isoquercetin (purity 99.0%), quercitrin (purity 99.0%), were purchased from Karl Roth (Germany). Hyperoside (purity 98.6%) and quercetin (purity 95.4%) reference materials were obtained from ChromaDex (USA). Acetonitrile and methanol of HPLC grade were supplied by Karl Roth (Germany).

Model construction

The general purpose of multiple regressions is to learn more about the relationship between several independent or predictor variables and a dependent or criterion variable. The linear regression model assumes that the relationship between the dependent variable y_i and the p -vector of the regressors x_i is linear. Some remarks on terminology and general use: y_i is called the dependent variable. The decision as to which variable in a data set is modelled as the dependent variable and which is modelled as the independent variable may be based on the presumption that the value of one of the variables is caused by, or directly influenced by the other variables. x_i is called independent variable. Usually a constant is included as one of the regressors. This variable captures all other factors that influence the dependent variable y_i other than the regressors x_i . The relationship between the error term and the regressors, for example, whether they are correlated, is a crucial step in formulating a linear regression model, as it will determine the method to be used for estimation [15].

The best estimating equations for the rooting percentage and root growth were determined with the R-program and formulized as $P_c = (a) + (b \times L) + (c \times L^2)$ where P_c is phenolic content, L is light intensity ($\mu\text{mol m}^{-2}\ \text{s}^{-1}$) and a , b and c are coefficients. Multiple regression analysis was carried out until the least sum of squares (R^2) was obtained.

RESULTS AND DISCUSSION

The light intensity is one of the major environmental factors affecting plant physiology, especially photosynthesis and plant development. Main function of plant secondary metabolites is thought to be the adaptation of plants to their environment. The physiological changes in plants in response to different stress factors may stimulate secondary metabolite production for the restoration of the defensive systems. The increase in secondary metabolite concentrations of plants observed in the present study under high light intensities may be attributed to those possible physiological changes. The development of prediction models for the content of phenolics, namely, chlorogenic acid, rutin, hyperoside, isoquercitrin, quercitrin and quercetin in *H. triquetrifolium* have potential using fields in pharmacological treatments. The developed mathematical models could be applied as very useful tools for prediction of phenolic compounds content for *H. triquetrifolium* instead of using expensive and time-consuming analytical devices. The obtained results are also important for plant physiology, agronomy and phytochemical studies on *H. triquetrifolium*.

In the present study, prediction equations were developed for estimation of the contents of chlorogenic acid, rutin, hyperoside, isoquercitrin, quercetin and quercitrin. Results of the statistical analysis revealed that most of variations in phenolic compounds levels in plant material could be explained by differences in light intensity.

The variation in the content of chlorogenic acid was explained by 97% of changing environmental parameters. The equation for chlorogenic acid was as follows: $P_{chol} = (27.659) - (0.124 \times L) - (1.43E^{-3} \times L)$, where P_{cho} : chlorogenic acid content in the

aerial parts (Table 1). Relationship between actual and predicted content of chlorogenic acid is shown in Figure 1.

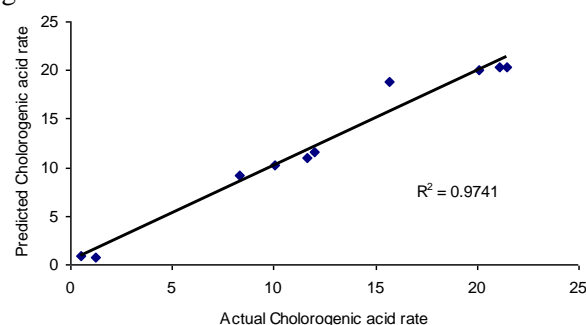


Fig. 1. Relationship between actual and predicted content of chlorogenic acid (mg/g DM) in greenhouse-grown *Hypericum triquetrifolium*.

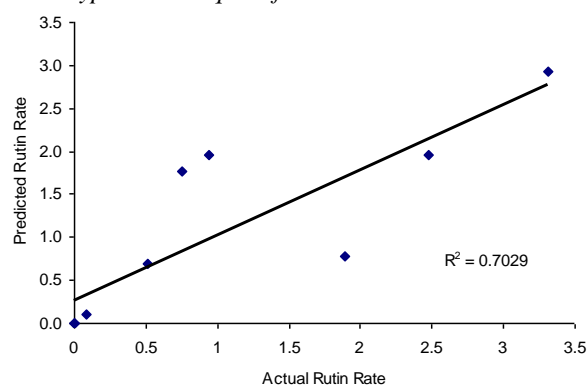


Fig. 2. Relationship between actual and predicted content of rutin (mg/g DM) in greenhouse-grown *Hypericum triquetrifolium*.

The variation between actual and predicted contents for hyperoside was explained by 86%. The equation for hyperoside was as follows: $P_{hyp} = (62.518) - (0.245 \times L) + (2.27 \times 10^{-4} \times L^2)$, where P_{hyp} : hyperoside acid content in the aerial part of the plant (Table 1). Relationship between actual and predicted content of hyperoside is shown in Figure 3.

Table 1. Coefficients, their standard errors and r^2 values of the new produced equations predicting phenolic compounds contents in greenhouse-grown *Hypericum triquetrifolium*.

Secondary metabolites (mg/g) with standard errors	Coefficient (a)	L (b)	L ² (c)	r ²
Chlorogenic acid	27.659 ± 10.269***	-0.124 ± 0.0361***	1.43E ⁻⁴ ± 2.99E ⁻⁵ ***	0.97***
Rutin	5.715 ± 8.483***	-0.023 ± 0.030***	2.32E ⁻⁵ ± 2.5E ⁻⁵ ***	0.70***
Hyperoside	62.518 ± 34.327***	-0.245 ± 0.121***	2.27 E ⁻⁴ ± 9.98E ⁻⁵ ***	0.86***
Isoquercetrin	70.328 ± 51.083***	-0.276 ± 0.179***	2.58 E ⁻⁴ ± 1.49E ⁻⁴ ***	0.86***
Quercitrin	15.588 ± 23.689***	-0.062 ± 0.0833***	6.11E ⁻⁵ ± 6.89E ⁻⁵ ***	0.87***
Quercetin	6.867 ± 5.683***	-0.025 ± 0.020***	2.21E ⁻⁵ ± 1.65E ⁻⁵ ***	0.85***

R²: regression coefficient, SE: standard error, L: light ($\mu\text{mol m}^{-2} \text{s}^{-1}$) of produced equations.

***: Significant at the level of $p < 0.001$.

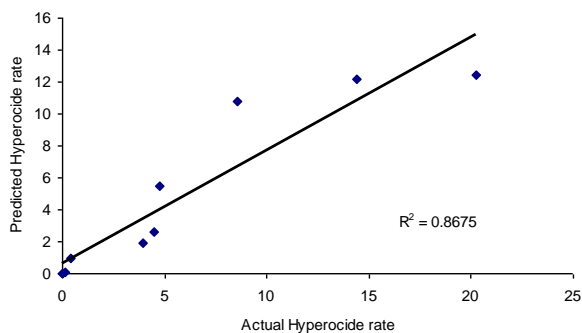


Fig. 3. Relationship between actual and predicted content of hyperoside (mg/g DM) in greenhouse-grown *Hypericum triquetrifolium*.

The variation explained by the parameters for isoquercetrin was 86%. The equation for isoquercetrin was $P_{\text{isoq}} = (70.328) - (0.276 \times L) + (2.58E^{-4} \times L^2)$, where P_{isoq} : isoquercetrin content in the aerial parts of the plant (Table 1). Relationship between actual and predicted content of isoquercetrin in *H. triquetrifolium* is shown in Figure 4.

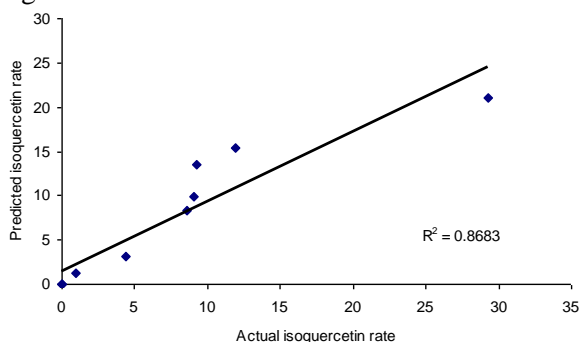


Fig. 4. Relationship between actual and predicted content of isoquercetrin (mg/g DM) in greenhouse-grown *Hypericum triquetrifolium*.

As for quercitrin, the variation explained by the parameters was 87%. The equation for quercitrin was: $P_{\text{qcitrin}} = (15.588) - (0.062 \times L) - (2.76E^{-3} \times L) + [6.11E^{-5} \times L]$, where P_{qcitrin} : quercitrin content in the aerial parts of the plant (Table 1). Relationship between actual and predicted content of quercitrin in *H. triquetrifolium* is shown in Figure 5.

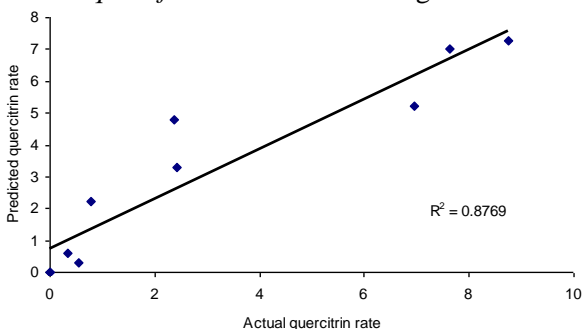


Fig. 5. Relationship between actual and predicted content of quercitrin (mg/g DM) in greenhouse-grown *Hypericum triquetrifolium*.

The variation explained by the parameters for quercetin was 85%. The equation for quercetin was: $P_{\text{qctin}} = (6.867) - (0.025 \times T) - (0.025 \times L) + (2.21E^{-5} \times L^2)$, where P_{qctin} : quercetin content in the aerial parts of the plant (Table 1). Relationship between actual and predicted content of quercetin in *H. triquetrifolium* is shown in Figure 6.

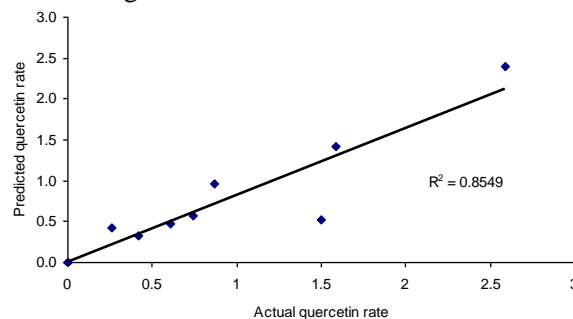


Fig. 6. Relationship between actual and predicted content of quercetin (mg/g DM) in greenhouse-grown *Hypericum triquetrifolium*.

H. triquetrifolium was treated during different phenological phases: vegetative, floral budding, full flowering, fresh fruiting, mature fruiting. In the present study, the contents of chlorogenic acid, rutin, hyperoside, isoquercetrin, quercetin and quercitrin increased in greenhouse-grown plants in response to elevating temperatures from 20 to 30 °C. We observed that increases in light intensities from 789.4 $\mu\text{mol m}^{-2} \text{s}^{-1}$ to 1716.6 $\mu\text{mol m}^{-2} \text{s}^{-1}$ resulted in a continuous increase in the contents of chlorogenic acid, rutin, hyperoside, isoquercetrin, quercetin and quercitrin. The obtained results are also important for plant physiology, agronomy and phytochemical studies on *H. triquetrifolium*.

CONCLUSION

Environmental factors have a prominent effect on secondary metabolism resulting in high variability of phytochemical contents of wild/cultivated plants. On the other hand, they determine the quality of the products derived from the corresponding plants. Hence, description of the effect of different environmental factors on secondary metabolism seems to be the first step in optimizing the production technologies of medicinal plant materials in terms of chemical profile. In the present study, we have developed prediction models for the secondary metabolite contents in *H. triquetrifolium*. The phenolic contents determined by the produced models (chlorogenic acid, rutin, hyperoside, isoquercetrin, quercitrin and quercetin) were found statistically acceptable ($R^2=0.70 - 0.97$). Thus, the models produced in the present study can be used safely by researchers for the standardization of *H. triquetrifolium* plant material quality.

Acknowledgements: The research was partially funded by a grant (No. MIP-57/2010) from the Research Council of Lithuania.

REFERENCES

1. J. C. Crocetta, N. K. B. *Med Aromat Plant Sci Biotechnol.*, **5**(1), 1 (2011).
2. B. Demirci, K. H. C. Baser, S. Croclett, I. A. Khan, *Journal of Essential Oil Research*, **17**, 659-663 (2005).
3. J. Patocka, *Journal of Applied Biomedicine*, **1**, 61 (2003).
4. R. C. Shelton, *J Clin Psychiat*, **70**, 23 (2009).
5. C. Cirak, J. Radusiene, V. Janulis, L. Ivanauskas, *Natural Product Communications*, **5**(6), 897 (2010).
6. C. Cirak, J. Radusiene, V. Janulis, L. Ivanauskas, N. Camas, A. K. Ayan, *Turkish Journal of Biology*, **35**, 449 (2011).
7. N. Camas, J. Radusiene, A. K. Ayan, C. Cirak, V. Janulis, L. Ivanauskas, *Natural Product Communications*, **3**, 1713 (2008).
8. L. Pistelli, A. Bertoli, I. Morelli, F. Menichini, R. A. Musmanno, T. Di Maggio, G. Coratza, *Phytotherapy Research*, **19**, 787 (2005).
9. D. Fraternalia, A. Bertoli, L. Giamperi, A. Bucchini, D. Ricci, F. Menichini, E. Trinciarelli, L. Pistelli, *Natural Product Communications*, **1**, 1117 (2006).
10. O. Caliskan, M. S. Odabas, C. Cirak, *Journal of Medicinal Plant Research*, **3**, 965 (2009).
11. M.S. Odabas, J. Radusiene, C. Cirak, N. Camas, *Pharmaceutical Biology*, **47**, 1117 (2009).
12. P. Prusinkiewicz, *Current Opinion in Plant Biology*, **7**, 79 (2004).
13. O. Caliskan, M. S. Odabas, C. Cirak, F. Odabas, *Journal of Medicinal Plant Research*, **4**, 542 (2010).
14. M. S. Odabas, N. Camas, C. Cirak, J. Radusiene, V. Janulis, L. Ivanauskas, *Natural Product Communications*, **4**, 535 (2010).
15. I. Erper, M. Turkkan, M. S. Odabas, *Žemdirbystė = Agriculture*, **98**, 195 (2011).

МОДЕЛ, ПРЕДСКАЗВАЩ ЕФЕКТА НА ИНТЕНЗИВНОСТТА НА СВЕТЛИНАТА ВЪРХУ ФЕНОЛНОТО СЪДЪРЖАНИЕ В *HYPERICUM TRIQUETRIFOLIUM* TURRA

М. С. Одабаш^{1*}, Дж. Радусиене², Б. Карпавичиене², Н. Камаш¹

¹Университет Ондукуз Майис, Професионална гимназия в Бафра, Самсун, Турция

²Природно-изследователски център, Институт по ботаника, Zaliuji ežeri 49, Вилнюс LT-08406, Литва

Получена на 17 февруари 2014 г.; ревидирана на 25 Август 2014 г.

Целта на настоящото изследване е да се разработи модел, предсказващ фенолното съдържанието в *Hypericum triquetrifolium* Turra с множествена регресия. Най-добрите изчислителни уравнения за съдържанието на фенолните съединения (хлорогенова киселина, рутин, хеперозид, изокверцетин, кверцитрин и кверцетин) са представени като $PC = (a) + (b \times L) + (c \times L^2)$, където PC е фенолното съдържание, L е интензитетът на светлината ($\text{mmol m}^{-2} \text{сек}^{-1}$) и , V и C са коефициенти. Множествин регресионен анализ се провежда, докато се получи сумата от най-малките квадрати (R^2). R^2 стойност е 0,70 за рутин и 0.97 за хлорогеновата киселина. Стандартните грешки се оказаха значителни при ниво $p < 0.001$.

EPR study of free radicals in pasta products

R. B. Mladenova*, N. D. Yordanov

Institute of Catalysis, Bulgarian Academy of Sciences, Acad. G. Bonchev St., Sofia, Bulgaria

Received June 12, 2013; Revised August 13, 2014

The features of the EPR spectra of different kinds of pasta products purchased from the local market and other home-made products are reported. All commercially available samples exhibited one singlet EPR line with $g=2.0049\pm 0.0003$ and line width $\Delta H=0.95\pm 0.05$ mT. The only difference between the EPR signal intensities at equal weights of different pasta products is that those prepared from wheat flour and water only exhibited a three to fifteen times lower signal in comparison with these containing additives as fats, milk, and egg powder.

The effect of drying parameters on the relative free radical concentration in freshly home-made spaghetti was also studied. The used wheat flour itself showed a very weak EPR singlet line with $g=2.0040\pm 0.0003$ and $\Delta H=0.83\pm 0.02$ mT. The spaghetti prepared from it and water were dried in open air at 28, 65, 75 and 93 ± 1 °C. After drying all samples exhibited an EPR signal with $g=2.0047\pm 0.0003$. At equal weights the relative number of paramagnetic species depends on the temperature and time of drying. At low drying temperature this effect may be attributed to the oxidation processes whereas at higher temperatures (65, 75, 93 °C) additionally Maillard reaction takes place. Upon storing the pasta products in inert atmosphere the number of free radicals remains constant in comparison with those exposed to open air where the significant increase in the number of free radicals is attributed to the development of an additional oxidation process.

Keywords: Pasta, spaghetti, drying, free radicals, EPR.

INTRODUCTION

The pasta is a widely consumed food. It is assumed that the best quality pasta is that produced in accordance with French (9 July 1999, law № 99-574), Italian (Presidential decree №187, 9 February 2001) or Greek (Ministries of Finance and Commerce. Approval of the Decision No 359/93 of the Supreme Chemical Council Food Code – Article 115 “Pasta”) laws from durum wheat semolina flour and water. The traditional pasta is dried at 40-50°C for a long time (up to 40 h). However, such drying cycles, called “low-temperature” (LT), can cause hygienic and qualitative problems because the combined effects of low temperature, high relative humidity and long drying time open the possibility of promoting microbiological growth. On the other hand, there is a big variety of pasta containing many ingredients added to their dough as fats, eggs, milk, spices, cheeses, etc. These ingredients, as well as the drying process in production of the pasta products influence their color [1-3], structural [4], textural [4,5] and technological [6] properties. Commercially available pasta products are typically dried at high (HT) (60-75°C) or very high

temperature (VHT) (75-100°C) for a short time (2-15 h depending on the temperature). The resulting product is characterized with less sticky, firmer consistence, lower cooking loss and improved color properties. On the other hand, in contrast to LT cycles, it is established that at HT and VHT drying cycles the Maillard reaction takes place [1-3] causing browning of the product. However, in previous studies from this laboratory it was shown that in the early stages of the Maillard reaction free radicals are recorded [7-9]. Other authors assigned them to radical cations of the type of 1,4-bis(5-amino-5-carboxy-1-pentyl)pyrazinium (CROSSPY) assuming that the latter are transient products in the process of protein oligomerization and melanoidins formation [10-13].

In the first part of the present study EPR spectra of different kinds of pasta products available on the local market were recorded, in order to find more thorough information on the semiquantitative concentration of free radicals present in them. The second part is devoted to the influence of the drying and storing conditions on the free radical generation in home-made pasta.

*To whom all correspondence should be sent:

E-mail: ralitsa@ic.bas.bg

Table 1. Pastas studied in the present paper

Type of pasta products	Origin	Content
Pasta "Pagani" (alfabeta)	Italy	Durum wheat flour
Macaroni "Stella" (helical)	Greece	100 % durum wheat semolina
Macaroni "Stella" (tubes)	Greece	100 % durum wheat semolina
Spaghetti "Melissa-Primo Gusto"	Greece	100 % durum wheat semolina
Vermicelli "Melissa-Primo Gusto"	Greece	100 % durum wheat semolina
Spaghetti "Gold ear"	Bulgaria	Wheat flour and water
Pasta "Cala" (helical)	Bulgaria	Common wheat semolina flour, water, natural color flours
Macaroni (over done) "Etar"	Bulgaria	Wheat semolina and water
Home made noodles "Etar"	Bulgaria	Flour type 500, semolina, salt, vegetable fat, egg powder
Noodles "Inko"	Bulgaria	Wheat flour type 500, wheat semolina, salt, milk, egg powder
Spaghetti "Choice" with vegetables (semi-cooked)	Korea	Wheat flour, palm fat, salt, soya sauce, onion, garlic, red and black pepper
Vermicelli "Zagaria"	Bulgaria	Durum wheat semolina, common wheat semolina and water

EXPERIMENTAL

Materials and method

Wheat flour and different types of pasta products (spaghetti, macaroni, noodles and vermicelli) produced by different producers were purchased from the local market. The type of pasta products, their origin and content are shown in Table 1.

Sample preparation, storage and kinetic measurements

The commercially available samples were crushed and accommodated in quartz EPR sample tubes ($\phi = 5\text{mm}$) up to 40 mm length.

In order to study the effect of drying conditions on the free radical generation, fresh home-made spaghetti were prepared and dried at different temperatures and atmospheres for different periods of time. The spaghetti dough obtained by kneading of wheat flour produced from common wheat semolina and distilled water were extruded in form of cylinders ($d = 1.5 \pm 0.2\text{ mm}$, length 60 mm). The samples were dried in a laboratory oven at 28, 65, 75, $93 \pm 1^\circ\text{C}$ for different times. The process of drying was monitored by weighing the samples. The samples were regularly taken out from the oven and weighed. The moment when the samples were dry was when the weight of two consecutive measurements was constant. After finishing the drying process, the home-made spaghetti were crushed and one part of the samples was accommodated into quartz EPR sample tubes in open air. Another part was accommodated in sample tubes closed with special rubber caps. Through this cap the sample was flushed with argon and heated in a drying oven at $65 \pm 1^\circ\text{C}$ for a given time. The EPR spectra were recorded regularly with time. A third part was lyophilized in

order to study the effect of oxygen on the relative number of free radicals during the drying process. In all cases the sample tubes were filled up to a 40 mm height and were with equal weight.

EPR measurements

EPR spectra were recorded at room temperature on a Bruker ER 200D SRC spectrometer operating in X-band. The g-values of all samples were estimated using "EPR marker" available in the "FF Lock" module (ER 033) of the ER 200D SRC spectrometer, calibrated in advance with DPPH for which $g = 2.0036$ [14]. The filled part of the sample tube was positioned exactly in the centre of the cavity. Every point in the kinetic studies was obtained as an average of at least three independent measurements.

The changes in the relative number of free radicals (N) in the studied samples per gram, was calculated using the formula $N \sim I_{pp}(\Delta H_{pp})^2$, where I_{pp} is the peak-to-peak intensity and ΔH_{pp} is the peak-to-peak line width of the first derivative of the EPR signal.

RESULTS AND DISCUSSION

EPR spectra of commercially available pasta samples

The pasta prepared only from wheat flour and water exhibited a weak singlet EPR line with $g = 2.0049 \pm 0.0003$ and $\Delta H = 0.95 \pm 0.05\text{ mT}$. The g-factors of the recorded spectra of the pasta suggest that the detection of O-centered radicals [15] is probably due to starch free radicals in the wheat flour. If this pasta is additionally backed, it exhibits about three times more intensive spectrum with the same EPR parameters. Most probably, the thermo-generated free radicals may be attributed to the development of a Maillard reaction [10-13].

The pasta containing additives such as fats, milk, egg powder, etc., showed about three to fifteen (in noodles) times more intensive EPR line with the same g -factor. The intensive spectrum may be due to oxidation processes of fats from the additives to pasta in addition to the Maillard reaction.

EPR spectra of home-made pasta

The wheat flour sample exhibited a weak singlet EPR signal with $g=2.0040\pm 0.0003$ and $\Delta H=0.83\pm 0.02$ mT, suggesting C-centered free radicals [15]. This EPR signal is probably due to mechanically induced free radicals in the process of milling the wheat grains. This assumption is in concert with the data available in the literature reporting that the intensity of the EPR signal increases with the extent of grinding [16].

After kneading a dough from flour and distilled water, the EPR parameters of the samples dried at 28, 65, 75 and $93 \pm 1^\circ\text{C}$ changed to $g=2.0047\pm 0.0002$ and $\Delta H=0.93\pm 0.03$ mT. This result may be connected with the fact that in starch and proteins, which are the major components of wheat semolina, structural transformation during pasta processing takes place [17-19] and forms free radicals [7].

The experimental results showed that the relative number of paramagnetic species depends on the drying temperature and time (Fig. 1).

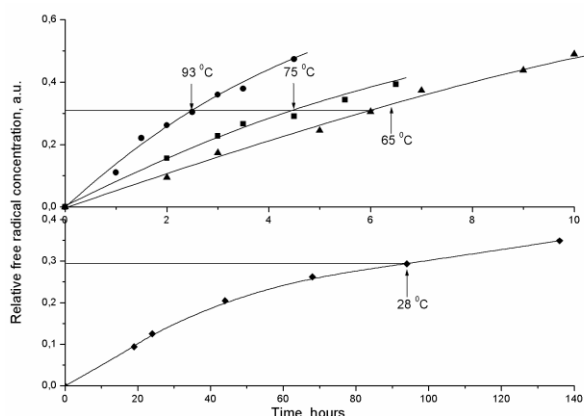


Fig. 1. Changes in the relative free radical concentration of home-made spaghetti during the process of drying in a laboratory oven at 28, 65, 75 and $93 \pm 1^\circ\text{C}$. The arrows show the points at which the weight of the samples becomes constant.

The home-made spaghetti were dried at different temperatures, as follows:

at 28°C for 94 h; at 65°C for 6.5 h; at 75°C for 4.5 h; at 93°C for 2.5 h.

The relative number of free radicals in these samples was approximately equal at these drying conditions. Samples dried at 28°C needed longer

time and probably oxidation processes took place at the high drying temperatures ($65, 75, 93^\circ\text{C}$). In addition, development of a Maillard reaction was expected. Realization of oxidation processes was confirmed by the fact that samples dried at room temperature for equal times in air and under vacuum, exhibited different free radicals number. The sample dried in absence of oxygen atmosphere was EPR silent.

In order to investigate the influence of storage conditions on the relative free radical concentration two home-made samples dried at room temperature in open air were taken – the one was kept in open air whereas the other - in argon atmosphere. The two samples were heated at $65\pm 1^\circ\text{C}$ for 50 h. The results presented in Figure 2 clearly show that the relative free radical concentration in the sample stored in argon atmosphere remains constant during the whole period of study whereas the number of free radicals in the sample kept in air was almost constant up to the 30th hour, then sharply increased.

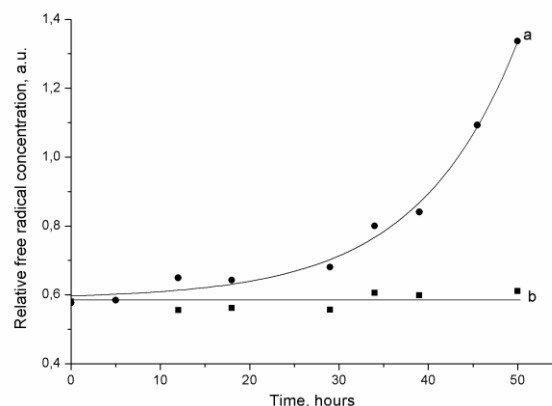


Fig. 2. Changes in the relative free radical concentration of dry home-made spaghetti samples heated at $65 \pm 1^\circ\text{C}$ in a laboratory oven for a time interval of 0-50 h and stored in: a) open air and b) in argon atmosphere.

It may be assumed that at the beginning (up to the 30th hour), some antioxidants naturally present in the pasta protected it from oxidation [20]. After their consumption, the sharp increase in the number of free radicals suggests that a typical chain oxidation reaction [21] takes place. From these results it could be concluded that during the storage period, oxidation processes take place in spaghetti samples if kept in air access.

CONCLUSIONS

The present EPR studies of pasta show that:

Under kneading of wheat flour and water a chemical reaction takes place and free radicals with $g=2.0047\pm 0.0003$ are generated;

The increase in relative free radical concentration in the drying samples on increasing the heating temperature may be most probably attributed to free radicals generation by oxidation processes at 28 °C whereas at higher temperatures (65, 75, 93 °C) the increase may be attributed to the development of an additional Maillard reaction. In conclusion, the processes of free radicals generation taking place in pasta products are lipid oxidation and Maillard reaction in presence of heat;

Drying under vacuum prevents the pasta samples from free radicals generation;

Storage of pasta in an inert atmosphere prevents it from developing of oxidation processes.

REFERENCES

1. M. Anese, M. C. Nicoli, R. Massini, C. R. Leric, *Food Res. Int.*, **32**, 193 (1999).
2. A. Sensidoni, D. Peressini, C. M. Pollini, *J. Sci. Food Agric.*, **79**, 317 (1999).
3. R. Acquistucci, *LWT - Food Sci. Technol.*, **33**, 48 (2000).
4. C. Zweifel, S. Handschin, F. Escher, B. Conde-Petit, *Cereal Chem.*, **80**, 159 (2003).
5. E. Marconi, M. Carcea, M. Schiavone, R. Cubadda, *Cereal Chem.*, **79**, 634 (2002).
6. G. Doxastakis, M. Papageorgiou, D. Mandalou, M. Irakli, E. Papalamprou, A. D'Agostina, D. Resta, A. Arnoldi, *Food Chem.*, **101**, 57 (2007).
7. N. D. Yordanov, N. G. Stoilova-Ivanova, *Bull. Chem. Technol. Macedonia*, **15**, 67 (1996).
8. N. D. Yordanov, R. Mladenova, *Spectrochim. Acta A*, **60**, 1395 (2004).
9. R. Mladenova, N. D. Yordanov, *Bulg. Chem. Commun.*, **39**, 128 (2007).
10. T. Hofmann, W. Bors, K. Stettmaier, *J. Agric. Food Chem.*, **47**, 391 (1999).
11. T. Hofmann, W. Bors, K. Stettmaier, *J. Agric. Food Chem.*, **47**, 379 (1999).
12. T. Hofmann, W. Bors, K. Stettmaier, in: "Free Radicals in Foods: Chemistry, Nutrition, and Health", M. J. Morello, F. Shahidi, Ch.-T. Ho (Eds.), ACS Symp. Ser. 807, American Chemical Society, Washington, DC, 2002, p. 49.
13. R. Stoesser, J. Klein, S. Peschke, A. Zehl, B. Cämmerer, L.W. Kroh, *Spectrochim. Acta A: Mol. Biomol. Spectrosc.*, **67**, 1161 (2007).
14. N. D. Yordanov, *Appl. Magn. Reson.*, **10**, 339 (1996).
15. K. M. Schaich, (2002) in: "Free Radicals in Foods: Chemistry, Nutrition, and Health", M. J. Morello, F. Shahidi, Ch.-T. Ho (Eds.), ACS Symp. Ser. 807, American Chemical Society, Washington, DC, 2002, p. 12.
16. M. Korkmaz, M. Polat, *Radiat. Phys. Chem.*, **58**, 169 (2000).
17. M. Petitot, J. Abecassis, V. Micard, *Trends Food Sci. Tech.*, **20**, 521 (2009).
18. J. M. Johnson, E. A. Davis, J. Gordon, *Cereal Chem.*, **67**, 286 (1990).
19. S. S. Paes, I. Yakimets, J. R. Mitchell, *Food Hydrocolloid*, **22**, 788 (2008).
20. R. Hirawan, W. Y. Ser, S. D. Arntfield, T. Beta, *Food Chem.*, **119**, 258 (2010).
21. N. M. Emanuel, G. E. Zaikov, Z. K. Maizus, Rol sredi in radikalno-zepnih reakzijah okislenija organicheskikh soedinenni, Nauka, Moscow, 1973 (in Russian).

EPR ИЗСЛЕДВАНЕ НА СВОБОДНИТЕ РАДИКАЛИ В МАКАРОНЕНИ ИЗДЕЛИЯ

Р. Б. Младенова*, Н. Д. Йорданов

Институт по катализ, Българска академия на науките, ул. „Акад. Г. Бончев“, София, България

Received June 12, 2013; Revised August 13, 2014

(Резюме)

Характеристиките на ЕПР спектрите на различни видове тестени изделия, закупени от местния пазар и на други домашно приготвени продукти са докладвани. Всички налични в търговската мрежа проби, показаха една синглетна ЕПР линия с $g=2.0049\pm 0.0003$ и ширина на линията $\Delta H=0.95\pm 0.05$ mT. Единствената разлика, в интензитета на ЕПР сигналите, при равни тегла на различните тестени изделия е, че тези, приготвени само от пшенично брашно и вода показват от три до петнадесет пъти по-нисък сигнал в сравнение с тези, съдържащи добавки, като мазнини, мляко и яйца на прах.

Ефектът от параметрите на сушене върху относителната концентрация на свободните радикали в прясно приготвени домашни спагети, също е изследван. Използваното пшенично брашно показва много слабо интензивна синглетна ЕПР линия с $g=2.0040\pm 0.0003$ и $\Delta H=0.83\pm 0.02$ mT. Спагетите, приготвени от него и вода бяха сушени на открито при 28, 65, 75 и 93 ± 1 °C. След изсушаване, всички проби показват ЕПР сигнал с $g= 2,0047 \pm 0,0003$. Относителния брой на парамагнитни частици зависи от температурата и времето на сушене, при еднакви тегла на пробите. При ниска температура на сушене, този ефект може да се дължи на окислителните процеси, докато при по-високи температури (65, 75, 93 °C), в допълнение протича и Майлардова реакция. При съхранение на паста продуктите в инертна атмосфера, броя на свободните радикали остава постоянен в сравнение с тези, които са изложени на открит въздух, където значителното нарастване на броя на свободните радикали се дължи на развитието на допълнителен процес на окисление.

Regeneration of surface plasmon resonance chips for multiple use

A. Sankiewicz*, A. Tokarzewicz, E. Gorodkiewicz

Department of Electrochemistry, Institute of Chemistry, University of Białystok, Al.J.Pilsudskiego 11/4, PL-15-443
Białystok, Poland

Received October 7, 2013, Revised November 18, 2014

The aim of this work was to investigate the possibility for regeneration of used biosensors SPRI using a special cleaning mixture. The presented procedure regenerates the thiol surface without affecting its surface properties and reproducibility of determination. Surface chip control before and after regeneration demonstrates the efficiency of the presented regeneration method. What is new is the use of a known mixture of regeneration yielding clean chips with the appropriate structure (layers of photopolymer and various monolayer immobilized substance).

Keywords: regeneration, surface plasmon resonance, biosensor

INTRODUCTION

The Surface Plasmon Resonance Imaging (SPRI) technique operating jointly with specific biosensors is a very promising tool for medical diagnosis [1-5]. In many cases, SPRI provided a diagnostic opportunity which was previously unavailable. A significant factor for popularization of SPRI is the reduced cost of a single measurement [6,7]. Therefore, the aim of this work was to investigate the possibility for regeneration of used biosensors and evaluation of their analytical applicability.

In terms of transduction, SPRI biosensors are optical biosensors. Several optical techniques are based on the phenomenon of surface plasmon resonance (SPR) and its modified versions: SPRI and Multi-Parametric Surface Plasmon Resonance (MP-SPR) [8-11]. These techniques are used for "label-free" detection. The effect of molecular interactions may be analyzed directly on a surface. The effect of SPR occurs when polarized light hits a prism covered by a thin metal layer. Under certain conditions (wavelength, polarization and incidence angle), a thin layer of metal on a high refractive index glass surface can absorb laser light, producing electron waves (surface plasmons) on the metal surface [8]. A thin layer of gold is the most suitable one for SPR measurements. The SPR signal is directly proportional to mass changes on the metal surface. SPR has also been used to monitor the adsorption of biological molecules onto a chemically modified gold surface [8-10]. The

SPR signal is converted into an image in the SPRI technique.

Biosensor design should be adapted to the use of a specific receptor-analyte response. Generally, a unmodified gold layer is not a suitable surface environment for biomolecular interaction. Therefore, gold on chips is modified with a thiol monolayer. The thiol monolayer is formed by the gold interaction with thiol sulphur. Interaction energy is of the order of chemical bond energy. A specific receptor for analyte molecules can be immobilized on the thiol surface. Various immobilization strategies can be used: adsorption, covalent bonds or hydrophobic interaction [12,13]. The most important parameters for biosensors are specificity, chemical stability, sensitivity, and reproducibility.

Two biosensors based on regenerated chips were investigated: (i) the biosensor for podoplanin determination, and (ii) the biosensor for proteasome 20S determination. The biosensor for podoplanin determination used immobilized podoplanin antibody as a receptor. The receptor was immobilized onto the chip surface by covalent bond through formation of an amide bond between a thiol with a terminal amino group (cysteamine (2-aminoethanethiol)) and an antibody, i.e. a molecule with an active carboxyl group. This system was used for AFM microscopic observation of surface changes on new and regenerated biosensors.

The determination of proteasome 20S with application of new and regenerated biosensors was an example of the effectiveness of such an approach in terms of quantitative determination. An immobilized PSI inhibitor (Z-Ile-Glu(OBut)-Ala-

* To whom all correspondence should be sent:
E-mail: ania@uwb.edu.pl

Leu-H) was used as a receptor. The latter was immobilized by covalent interaction between a thiol with a terminal amino group (cysteamine (2-aminoethanethiol) and PSI. The only opportunity considered in this work was the alkaline cleavage of the biosensor surface layer with regeneration of the gold surface covered with thiol. Such an approach is more universal. Different regenerated biosensors have the same state of surface (gold covered with thiol), provided that the same thiol was used as a linker. The opportunity to only remove an analyte layer during regeneration was not considered in this work. It was necessary to check that the procedure used for regeneration of different types of biosensors can be adapted to the regeneration of the above mentioned biosensors.

EXPERIMENTAL

Chemicals

The proteasome 20S (mammalian) of concentration 12 mg/ml was prepared in a solution of composition: 20 mM Tris-HCl, pH 7.5, 1 mM EDTA, 1 mM DTT, 1 mM sodium azide (AFFINITI Research Products Ltd, Mamhead, United Kingdom). Z-Ile-Glu(OBut)-Ala-Leu-H (PSI) ($C_{32}H_{50}O_8N_4$, 618.77 Da) (BIOMOL, Lörach, Germany), recombinant human podoplanin and sheep antibody (IgG) specific for podoplanin (R&D System, Inc.), 11-aminoundecanethiol hydrochloride (MUAM) (PROBIOR, München, Germany) cysteamine hydrochloride, N-ethyl-N'-(3-dimethylaminopropyl) carbodiimide (EDC), HEPES sodium salt (all SIGMA, Steinheim, Germany), 1-octadecanethiol (ODM), N-hydroxysuccinimide (NHS) (ALDRICH, Munich, Germany), dichloroethane (FLUKA, Munich, Germany), absolute ethanol (POCh, Gliwice, Poland), photopolymer ELPEMER SD 2054, hydrophobic protective paint SD 2368 UV SG-DG (PETERS, Kempen, Germany) were used as received. Aqueous solutions were prepared with filtered milliQ water (Simplicity®MILLIPORE).

Biosensor preparation

The biosensor was manufactured in several stages. Initially, a 1nm Cr layer was deposited on BK7 glass slides and then a 50 nm thick gold layer was also deposited [14]. Next, in order to protect the surface, the chip was covered with photopolymer ELPEMER SD 2054. The photopolymer was dried at 70°C for 30 min and irradiated with UV light for 2 min. The photopolymer layer was covered with a

hydrophobic photomask by application of the screen printing technique. The paint was irradiated with a UV lamp. Thus, the free gold surface of the obtained sensor was separated with a photopolymer and a hydrophobic photomask [3]. 9 places with 12 free gold surfaces were obtained. Chips were rinsed with ethanol and water and dried in an argon flow. A thiol monolayer was formed on the prepared chip. The kind of thiol used is dependent on the type of molecules used to capture the analyte from the sample. Generally, two thiol types were used: a thiol with a terminal amino group ('short' cysteamine (2-aminoethanethiol) and a 'long' MUAM (11-amino-undecane-1-thiol), as well as a thiol with a terminal alkyl group ODM (octadecyl thiol). The chips were then immersed in 20 mM cysteamine ethanolic solution or in 1 mM MUAM ethanolic solution for at least 2 h, or alternatively in 2.7 mM ODM ethanolic solution for at least 24 h. The chips were then rinsed with ethanol and water and dried in an argon flow. The inhibitor, or antibody or phospholipids were immobilized on the thiol monolayer under the suitable conditions [15,16]. Some inhibitors or phospholipids were immobilized on the ODM monolayer, while other inhibitors or antibodies were immobilized on the cysteamine or MUAM monolayer. Hydrophobic inhibitor or phospholipid solutions were placed on the thiol-modified surface, and incubated at room temperature for 24 h. For covalent attachment of antibodies or inhibitors, they were activated with NHS (250 mM) and EDC (250 mM), placed on the amine-modified surface and incubated at 37°C for 1 h. These molecules specifically react with the species-to-be-determined. The biosensor is then ready for analyte concentration measurement.

Chip regeneration procedure

Successful regeneration of SPRI chips and possibility of re-using the biosensor are important, especially when the latter is applied for diagnostic tests.

The cleaning procedure of the chip to a layer of gold has been previously studied [17]. We have used ethanol, Triton X-100 (1% solution), SDS (0.1 mol/l in water), chromic acid ($K_2Cr_2O_7$ saturated in concentrated H_2SO_4), dichloroethane/ethanol (pure/pure), Triton X-100/methanol (1% /pure).

The most commonly used conditions for antibody receptor regeneration included low pH (e.g. 10 mM glycine in HCl at pH 1.5-3) [18]. Although the pH range of inhibitor-protein interaction is very broad, usually the surfaces are regenerated satisfactorily by the use of base or acid hydrolysis.

A mixture of Triton X-100 (1%) containing NaOH (100 mM) was applied as the cleaning agent [19]. Used biosensors were rinsed extensively with this mixture. In this way, the deposited receptors (inhibitors or antibodies) and the analyte layer were removed from the sensor surface. The chips with the remaining thiol monolayer were washed by flushing with water for 5 min and put into water overnight. The last step was repeated 3-4 times. The rinsed chips were dried in an argon flow. In this manner, the prepared chips with the thiol layer were regenerated.

Atomic Force Microscopy (AFM) and Surface Plasmon Resonance Imaging (SPRI) measurements

AFM measurements were performed with a commercial Ntegra Prima scanning probe microscope (NT-MDT, Russia) using a tapping mode in air. In order to increase lateral resolution, high aspect ratio (5:1) ETALON probes (NT-MDT) were used. AFM measurements were performed to confirm the creation of subsequent layers (gold, thiol and protein layer) and to check the chip surface after regeneration. All measurements were done in ambient conditions.

SPRI measurements for protein array were performed as described in a previous paper [3]. On the basis of the registered images, the signal was measured twice - after immobilisation of the PSI inhibitor and after interaction with proteasome 20S. The SPRI signal, which is proportional to the mass of coupled biomolecules, was obtained by subtraction of the signal after and before interaction with a biomolecule, for each spot separately. Then the SPRI signal was integrated over the spot area. NIH Image J version 1.32 software was used to evaluate the SPRI images in 2D form.

Preparation of the standard curve

The response of the analytical SPRI signal for the proteasome 20S concentration was measured over the concentration range between 2 and 25 nM. The chip surface was covered by a monolayer of cysteamine and a layer of immobilized PSI inhibitor (Z-Ile-Glu(OBt)-Ala-Leu-H, C₃₂H₅₀O₈N₄) with concentration of 80 nM. The chip was then treated with the proteasome 20S solution. Time of interaction was 10 min. Experiments were performed at pH=7.4 [4].

Precision of the method for proteasome 20S determination

The precision of the method was tested under optimal conditions, i.e. pH=7.4 and inhibitor concentration at the chip preparation stage equal to

80 nM. The precision of proteasome 20S determination was tested for a concentration of 4 nM.

Determination of proteasome in biological samples

The procedure of biological samples (human plasma) preparation and the method for proteasome 20S determination were described in a former paper [4].

RESULTS AND DISCUSSION

The architecture of the applied chip is shown in Fig. 1. Nine different solutions can be simultaneously measured without mixing of the tested samples. Twelve single SPRI measurements can be performed from one solution.

Manufacturing and regeneration of the biosensor was controlled by observation of subsequent layers using Atomic Force Microscopy.

The presented AFM pictures confirm that the stages of the creation of each layer on the biosensor surface have really taken place. As indicated in Fig.1, thiol (Fig.1C) or protein (Fig.1D) immobilization significantly alters surface morphology. The receptor layer (podoplanin antibody 1,5 µg/ml) (Fig.1D) has globular domains. Fig. 1E shows a picture obtained after applying the regeneration procedure. The chip surface after regeneration has very similar morphology to that of the fresh thiol surface (see Fig. 1C).

Surface chip control before and after regeneration demonstrates the efficiency of the regeneration method. Only a thiol monolayer remains on the chip after the regeneration and the regenerated chip with the thiol layer can be reused. After immobilization of a new receptor (inhibitor, antibody, etc.), the biosensor is ready for analyte determination.

The measured SPRI signal before and after regeneration confirmed that the thiol layer remained on the chip surface.

Proteasome 20S determination with a PSI inhibitor (80 nM) as a receptor was used as an example for demonstrating the analytical applicability of the regenerated biosensors. In order to verify the analytical signal before and after regeneration, calibration curves of proteasome 20S with the application of the new and the re-used chip were prepared (Fig. 2A). The response of the analytical SPRI signal for proteasome 20S concentration was measured over the concentration range between 2 and 25 nM. Both calibration curves are of Langmuir's isotherm type. The roughly linear sections of these curves are within the range of 2 - 10 nM and this range is useful for

analytical purposes. The plateau of the curve corresponds to saturation of the active sites of the sensor. The analytical SPRI signal of proteasome 20S obtained with the regenerated biosensor is roughly the same as that obtained with the new biosensor, taking into account the precision error [4].

The number of successful regenerations of a single chip was also investigated. The determination of proteasome 20S (6 nM) with the

biosensor with PSI inhibitor (80 nM) as the receptor was used as an example. The results are given in Fig. 2B. Generally, the regenerated chips exhibit a slightly lower and gradually decreasing signal. After the first regeneration the analytical signal is reduced to about 98% and after the fifth regeneration even to 85% of the initial signal. This loss can be compensated by construction of a calibration curve with a regenerated biosensor.

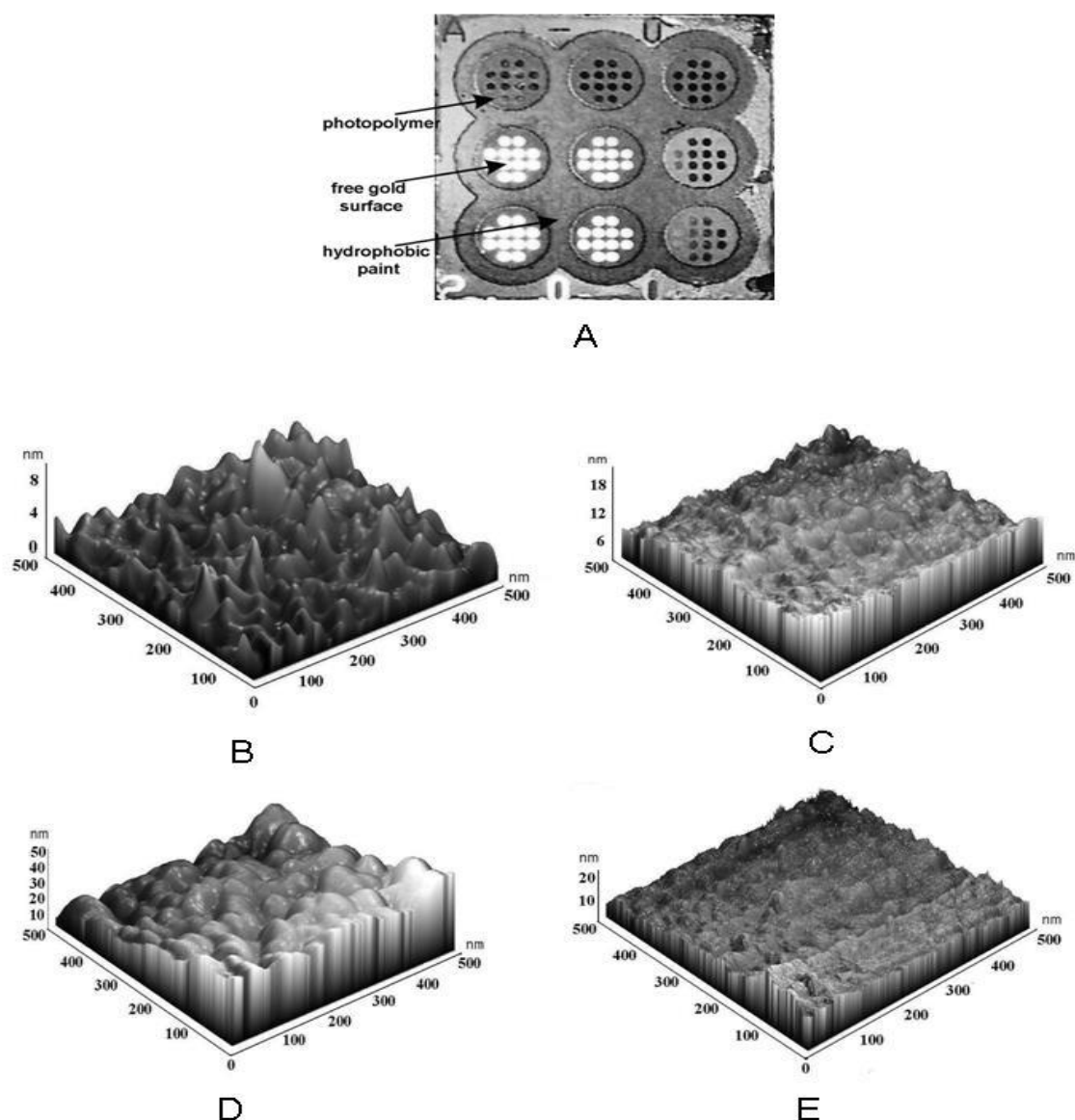


Fig. 1. Picture of chip (A) and AFM pictures of bare gold (B), thiol (cysteamine 20 mM) (C), podoplanin antibody (1.5 µg/ml) (D), thiol after regeneration (E). Initial antibody concentration: 1.5 µg/ml. Initial podoplanin concentration: 1 ng/ml.

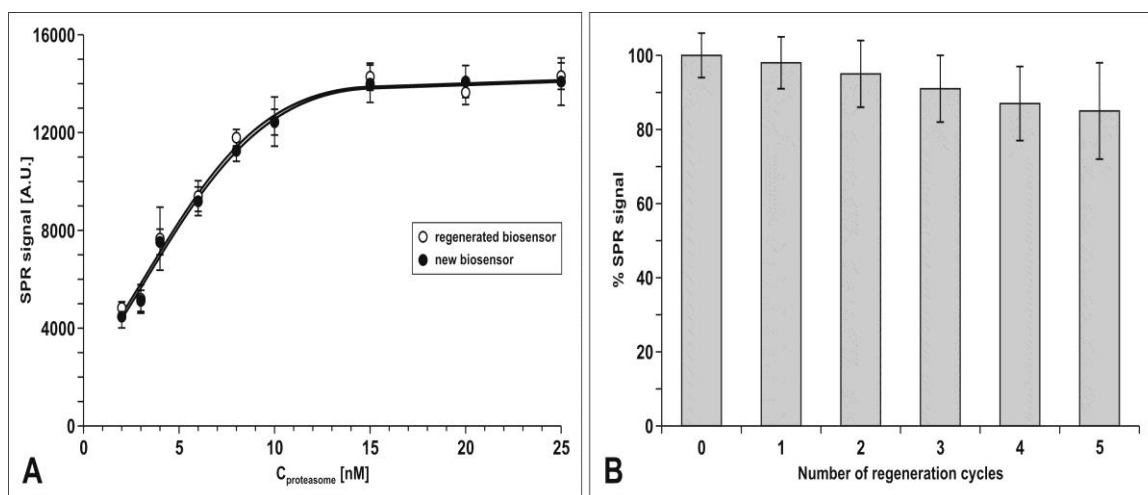


Fig. 2. (A) Dependence of SPR signal (Arbitrary Units) on proteasome 20S concentration for the PSI inhibitor (80 nM) (B) Effect of repeated chip regeneration on the proteasome 20S SPR signal on the PSI inhibitor. Concentration of proteasome 20S: 6 nM. pH value of proteasome solution: 7.4.

Table 1. Precision of the concentration measurement of proteasome 20S. The results were evaluated using calibration graphs constructed with biosensors having the same number of regenerations.

	Number of regeneration cycles	No of meas.	Added [nM]	Found [nM]	Recovery [%]	S.D. [nM]	Confidence limit (95%) [nM]
Proteasome 20S determination	0	24	4.00	4.10	102	0.41	0.27
	2	24	4.00	4,05	101	0.39	0.22
	5	24	4.00	3.97	99	0.40	0.23

Table 2. Proteasome 20S concentration in blood plasma of healthy volunteers. The results were evaluated using calibration graphs constructed with biosensors having the same number of regenerations.

Number of sample	Proteasome 20S concentration in blood plasma [nM]		
	New chip	Chip after two regeneration cycles	Chip after five regeneration cycles
1	5.73±0.43	5.80±0.54	5.69±0.81
2	17.12±2.93	16.99±1.76	17.01±2.42
3	11.93±4.12	11.76±2.45	11.99±3.05
4	8.27±2.50	7.97±3.13	8.03±2.76
5	19.40±6.25	18.70±4.15	19.04±3.97
6	14.91±1.78	14.66±2.87	14.97±3.51
7	15.50±5.86	15.42±4.34	15.60±3.39
8	12.62±2.49	11.99±2.24	12.33±3.07
9	14.07±2.02	14.39±3.11	13.97±4.48
Mean value	13.91 ± 2.78	13.08 ± 2.56	13.12 ± 2.61

The precision of proteasome 20S determination was tested for a new and a re-used chip. The results are shown in Table 1.

Standard deviation and confidence limit, at a confidence level of 95%, are very similar for all chips. Generally, the precision of a single measurement is poor, however, the precision of the

average value, as well as the confidence limits are much better and acceptable. The spike recoveries on the new and regenerated biosensors are very good, due to the application of suitable calibration graphs.

The proteasome 20S determination in blood plasma from 9 healthy volunteers was performed using new and reused chips. The results are given in Table 2.

The proteasome 20S concentration range in blood plasma of healthy volunteers is: on the new chip 13.91 ± 2.78 nM, after second regeneration of chip 13.08 ± 2.56 nM and after fifth regeneration 13.12 ± 2.61 nM. Similar values are obtained in the cases of all 9 analysed samples. Thus, the regeneration process does not significantly affect the determination of the concentration of the analyte.

Generally, it was shown that the chip cleaning procedure allows a removal of the immobilized protein layers. Only the thiol layer remains on the chip surface because thiol sulfur forms a strong bond with gold [20]. In the case of a biosensor with thiol containing a terminal amino group, the amine bond of the receptor with the analyte is hydrolyzed by NaOH contained in the cleaning mixture. This process restores the $-NH_2$ groups of the immobilized thiol. Triton X-100, also contained in

the cleaning mixture, is a non-denaturing surfactant, which can disrupt a hydrophobic interaction and lead to the removal of hydrophobically linked molecules [21].

It was shown that the sensor with a thiol monolayer can be reused and the regenerated chip can be used up to five times for the creation of a biosensor. The regeneration process, to a certain degree, affects the surface properties, including the level of surface binding capacity. However, this destructive process occurs gradually and several regenerations do not significantly affect the determination. On the other hand, chip regeneration allows skipping some steps in the biosensor preparation and saves time and cost of single determination.

The developed regeneration procedure can be used for biosensors having cysteamine (2-aminoethanethiol), MUAM (11-amino-undecane-1-thiol), or ODM (octadecyl thiol) (thiol with a terminal alkyl group) as a linker, as well as immobilized enzyme inhibitor, antibody or phospholipid as a receptor, which was experimentally checked in numerous examples.

REFERENCES

1. I. E. Tothill, *Semin. Cell. Dev. Biol.*, **20**, 55 (2009).
2. M. Mascini, S. Tombelli, *Biomarkers*, **13**, 637 (2008).
3. E. Gorodkiewicz, *Protein. Pept. Lett.*, **16**, 1379 (2009).
4. E. Gorodkiewicz, H. Ostrowska, A. Sankiewicz, *Microchim. Acta*, **175**, 177 (2011).
5. E. Gorodkiewicz, R. Charkiewicz, A. Rakowska, P. Bajko, L. Chyczewski, J. Nikliński, *Microchim. Acta*, **176**, 337 (2012).
6. S. Van Vlierberghe, K. De Wael, H. Buschop, A. Adriaens, E. Schacht, P. Dubruel, *Macromol. Biosci.*, **8**, 1090 (2008).
7. S. K. Vashist, *Anal. Biochem.*, **423**, 23 (2012).
8. J. Homola, *Anal. Bioanal. Chem.*, **377**, 528 (2003).
9. J. Homola, H. Vaisocherova, J. Dostalek, M. Piliarik, *Methods*, **37**, 26 (2005).
10. E. Helmerhorst, D. J. Chandler, M. Nussio, C. D. Mamotte, *Clin. Biochem. Rev.*, **33**, 161 (2012).
11. M. Robinson, J. Kuncova-Kallio, N. Grangvist, J.W. Sadowski, *Nanotech.*, **1**, 42 (2012).
12. A. Sassolas, L. J. Blum, B. D. Leca-Bouvier, *Biotechnol. Adv.*, **30**, 489 (2012).
13. S. Scarano, M. Mascini, A. P. Turner, M. Minunni, *Biosens. Bioelectron.*, **25**, 957 (2010).
14. E. Gorodkiewicz, J. Luszczyn, *Protein Pept. Lett.*, **14**, 443 (2007).
15. E. Gorodkiewicz, E. Regulska, K. Wojtulewski, *Microchim. Acta*, **173**, 407 (2011).
16. E. Gorodkiewicz, A. Sankiewicz, Z. A. Figaszewski, *Folia Histochem. Cytobiol.*, **48**, 687 (2010).
17. E. Gorodkiewicz, A. Fernandez-Gonzalez, A. Akkoyun, G. Steiner, R. Salzer, *Chem. Anal. (Warsaw)*, **50**, 103 (2005).
18. K. Anderson, D. Areskoug, E. Handerborg, *J. Mol. Recognit.*, **12**, 310 (1999).
19. R. J. Whelan, T. Wohland, L. Neumann, B. Huang, B. K. Kobilka, R. N. Zare, *Anal. Chem.*, **74**, 4570 (2002).
20. J. C. Love, L.A. Estroff, J. K. Kriebel, R. G. Nuzzo, and G. M. Whitesides, *Chem. Rev.*, **105**, 1103 (2005).
21. L. M. Hjelmeland, *Proc. Natl. Acad. Sci. USA*, **77**, 6368 (1980).

РЕГЕНЕРАЦИЯ НА ЧИПОВЕ С ПОВЪРХОСТЕН РЕЗОНАНС ЗА МНОГОКРАТНА УПОТРЕБА

А. Санкиевич*, А. Токажевич, Е. Городкевич

Департамент по електрохимия, Институт по химия, Университет в Бялисток, Полша

Получена на 7 октомври 2013 г.; коригирана на 18 ноември, 2014 г.

(Резюме)

Целта на тази работа е изследването на регенерацията на употребявани биосензори SPRI използвайки специална течност за почистване. С нейна помощ се регенерира тиоловата повърхност без да се влияе на повърхностните свойства и възпроизводимостта на определяне. Контролът на чиповете преди и след регенерацията показва приложимостта на настоящия метод на генерация. Нова е употребата на известна смес за почистване на чиповете с подходяща структура (слоеве от фотополимери и различни имбилизиращи вещества).

Phase formation and catalytic activity of Cu-Co-spinel catalyst deposited on Al/Si/Mg – support

D. D. Stoyanova*, D. R. Mehandjiev

Institute of General and Inorganic Chemistry, Bulgarian Academy of Sciences, Acad. G. Bontchev Str., 11, Sofia, Bulgaria

Received November 20, 2013; Revised May 19, 2014

The paper is devoted to Cu-Co oxide catalysts deposited on a commercially available high-temperature support containing aluminum, magnesium and silicon, calcined at different temperatures: 350, 450, 550, 650 and 750°C. The samples are prepared by impregnation with aqueous solutions of Cu and Co nitrates. The catalysts are characterized by X-ray photoelectron spectroscopy (XPS), X-ray diffraction (XRD), scanning electron microscopy (SEM), differential thermal analysis (DTA), and BET method. Chemical analysis of the samples is also carried out. The phase formation at different preparation temperatures and the catalytic activity of copper cobaltite in the reaction of CO oxidation with oxygen at two space velocities (20 000 and 100 000 h⁻¹) are investigated. The stability of the specimens to catalytic poisons at the same space velocities is studied. It is established that the most promising catalysts regarding the catalytic activity and stability to poisoning with SO₂ are the catalysts calcined in the range 350 – 550°C. At these temperatures a Cu-Co oxide spinel - like phase is formed. These results give us the reason to suppose a possible implementation of the high-temperature support in the preparation of catalysts for the purification of toxic emissions of gaseous fluids in the practice.

Key words: Cu-Co oxide catalysts, oxidation of CO + O₂, CO + O₂ + SO₂

INTRODUCTION

An important task in the investigations focused on the development of catalysts designed for environment protection, is to elaborate supports of various shape, porosity and thermal stability. The chemical nature of the support plays an important role for the catalytic activity, stability and resistance of the supported active phase to catalytic poisons. Therefore, the creation of such a support is decisive with a view to the industrial application of the catalyst. The spinels based on 3d-transition metals are known to possess high catalytic activity in reactions of complete oxidation of organic compounds, CO and also in the reduction of nitrogen oxides [1–4]. This enables their utilization in processes of neutralization of harmful components in industrial waste gases and in transport exhaust gases. For example, such a catalyst is the spinel copper cobaltite (CuCo₂O₄) applied as active phase in the MPB-11 and RILA catalysts [5, 6]. The activities of these catalysts depend on the formation of spinel structure and on the stoichiometry of the active phase. For this reason, the above cited patents are making use of γ -Al₂O₃ as support, which also possesses spinel

structure thus enabling epitaxial growth of the copper cobaltite active phase on the surface of the γ -Al₂O₃ support. It was ascertained that when the spinel stoichiometry is close to that of CuCo₂O₄, the activity is high and the sensitivity to catalytic poisons is low, including even SO₂ [7-9]. The question arises: is there another type of support, having different nature of the surface in comparison to that of γ -Al₂O₃, which would allow the formation of a spinel phase of copper cobaltite on the carrier surface manifesting high activity in oxidation reactions and at the same time non-sensitivity (resistance) to catalytic poisons including SO₂.

For this reason, the aim of the present work was to investigate the phase formation process at various synthesis temperatures and to observe the respective catalytic activity of copper cobaltite supported on an alumina-silica-magnesia carrier.

EXPERIMENTAL

Preparation of the catalyst samples

Ceramic filter containing alumina, silica and magnesia, manufactured by the company “Hofmann Consult Bulgarien GmbH” was used as a support in the synthesis of the catalyst samples. Its parameters were as follows: diameter 95 mm, thickness 22 mm, porosity 10 PPI, specific surface area $S = 0.7 \text{ m}^2\text{g}^{-1}$

* To whom all correspondence should be sent:
E-mail: dsto@svr.igic.bas.bg

and it was calcined at 1450°C. The deposition of the active phase containing Cu and Co was accomplished by the impregnation method using an aqueous solution – mixture of the nitrates of the two components. The technology involves the following steps: preliminary heating of the impregnating solution containing 7 g Cu/100 ml + 14 g Co/100 ml, up to 80°C, immersion of the filters in the solution, whereupon the temperature was maintained constant for 1 h. There follows drying at room temperature for 24 h and consecutive calcinations for 3 h at five different temperatures: 350, 450, 550, 650 and 750°C. The obtained catalyst samples are denoted as follows below:

AMC_350 – catalyst sample calcined at T=350°C

AMC_450 – catalyst sample calcined at T=450°C

AMC_550 – catalyst sample calcined at T=550°C

AMC_650 – catalyst sample calcined at T=650°C

AMC_750 – catalyst sample calcined at T=750°C

Characterization of the catalyst samples

The structure and the phase composition of the support and of the so prepared catalyst samples were identified on the X-ray diffractometer Bruker Advance, using CuK α radiation equipped with SolX detector, whose 2 θ value comprises 20 - 800 at a step of 0.04°.

The express BET method (single point) was applied for the evaluation of the specific surface area, based on low-temperature adsorption of nitrogen at the boiling point of liquid nitrogen 77K. The relative error of the method amounts to about 8%.

The chemical analysis of the samples was carried out on a FAAS M5-Thermo Fisher apparatus.

The X-ray photoelectron spectra (XPS) were recorded using monochromatic radiation AlK α (1486.6eV) on a VG ESCALAB MK II spectrometer at base pressure of 1×10^{-8} and 1 eV resolution of the apparatus. The charge effect was corrected (calibrated) based on the C1s peak, related to binding energy of 285 eV. The photoelectron signals of C 1s, O 1s, Al 2p, Mg 2p, Cu 2p $_{3/2}$, Co 2p $_{1/2}$ were recorded and corrected by subtraction of the background of the Shirley type and they were evaluated quantitatively on the basis of the peak area and the cross-sections of photo-ionization following Scofield's algorithm.

The morphology of the surface of the studied catalyst samples was observed by means of a scanning electron microscope JEOL JSM – 5300.

The differential thermal analysis was performed on a combined DTA/TG apparatus

LABSYSTM EVD manufactured by the SETARAM Company (France). Synthetic air was used as carrier gas, fed at a flow rate of 20 ml/min. The rate of heating was 10°C/min. A corundum crucible and a Pt/Pt-Rh thermocouple were used. The maximum achieved temperature upon heating reached 750°C.

The catalytic activity tests were carried out on a continuous-flow catalytic reactor described in [10]. The activities of the catalyst samples were measured in the reaction of CO oxidation by oxygen, whereupon the concentration of CO in the feed was 0.5 vol. %. The experimental runs were carried out at two different space velocities – $W = 20\,000\text{ h}^{-1}$ and $100\,000\text{ h}^{-1}$. The stability of the contact masses with respect to the catalyst poison SO $_2$ was ascertained in the reaction of CO oxidation by air, where the CO concentration was 0.5 vol%, while that of SO $_2$ was 0.03 vol%. This test was also carried out at the same two space velocities $W = 20\,000\text{ h}^{-1}$ and $100\,000\text{ h}^{-1}$.

RESULTS AND DISCUSSION

In order to determine the conditions of synthesis, DTA of dried catalyst (sample AMC_350) was carried out after depositing a phase of the precursors – nitrates of copper and cobalt (Figure 1).

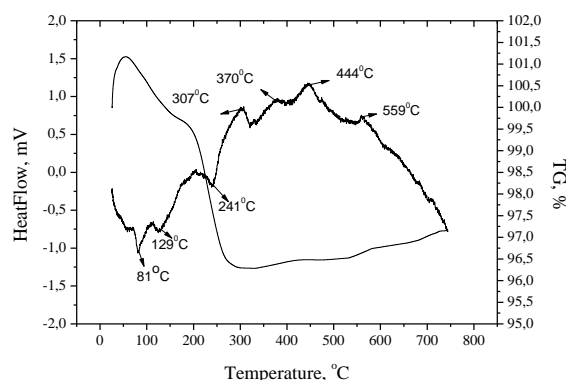


Fig. 1. DTA and TG curves of dry AMC_350 sample, after deposition of the precursors (Cu, Co nitrates)

The low-temperature region displays several endothermic effects at temperatures of 81 and 129°C, which could be attributed to processes of desorption of the water molecules, pre-adsorbed on the sample. Upon increasing the temperature, another endothermic peak is registered at 241°C, which could be attributed to the decomposition of the nitrates and is probably an initial step in the formation of the phases. The endothermic phase transition is accompanied by loss of mass $\Delta m = 4.83\%$ (TG curve), which starts at T~180°C and is completed at T~295°C. Going higher beyond this temperature there are no changes observable in the TG curve. The next increase in the temperature is leading to several exothermic effects, registered at the following temperatures: 307, 370,

444 and 559°C. According to the literature data, these can be explained by decomposition of the copper cobaltite into Co_3O_4 and CuO phases [11-13]. The latter exothermal peak at 559°C can be attributed to consecutive reduction of Co_3O_4 to CoO , as well as to crystallization processes of the oxides and growth of the crystallites. A slight increase in the mass is observed at the same temperature in the TG curve, which is attributed to the same processes. Table 1 lists the data from the chemical analysis of the catalyst samples, the specific surface area and the observed phases in the XRD patterns. As it is seen from the data in the table, the content of copper and cobalt increases with the increase of the synthesis temperature up to 550°C. The ratio between the contents of the two elements is preserved but the ratio does not reach the value 1:2 as in the case of normal spinel composition. This fact gives evidence that the stoichiometric spinel CuCo_2O_4 cannot be formed on the support but non-stoichiometric spinel may be formed. The dependence of the specific surface area of the samples also passes through a maximum, which is due to the formation of new phases on the surface of the support. The data from the XRD analysis of the support and the obtained catalyst samples reveal the presence mainly of the high-temperature modification of Al_2O_3 (i.e. $\alpha\text{-Al}_2\text{O}_3$) and a spinel phase of composition $\text{Cu}_{0.15}\text{Co}_{2.8}\text{O}_4$ judging from the XRD patterns (Figure 2 and Table 1).

It was established that at the different temperatures of calcination of the catalyst samples the degree of dispersion of the spinel phase is changing, whereupon in the case of

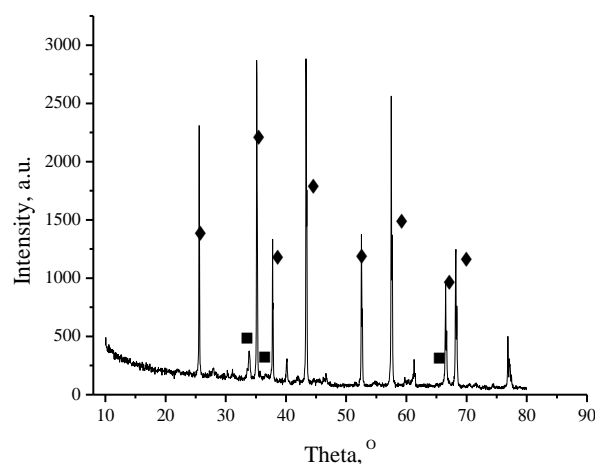


Fig. 2. XRD prevailing phases: \blacklozenge - $\alpha\text{-Al}_2\text{O}_3$, \blacksquare - $\text{Cu}_{0.15}\text{Co}_{2.84}\text{O}_4$ and SiO_2 -quartz

catalyst sample AMC_350 the size is 28.4 nm, while for the catalyst sample AMC_750 it reaches 89 nm (Figure 2). In the catalyst samples AMC_650 and AMC_750 calcined at the highest temperatures, there occurs decomposition of the copper cobaltite and the products of this decomposition Co_3O_4 and CuO are so finely dispersed, that it is impossible to register them by XRD measurements. Partial reduction of Co_3O_4 to CoO is also possible at the high temperatures. The analysis of the surface of the formed copper-cobalt mixed oxides on the alumina supports calcined at various temperatures was made by the XPS method. The obtained photoelectron spectra of copper and cobalt are shown in Figure 3, while the data from the analysis are systematized in Table 2.

Table 1. Cu, Co contents, phase composition, specific surface area of the synthesized samples and mechanical strength of the support

Sample Support	Cu, wt %	Co, wt %	Co/Cu	Phase composition, XRD	S_{BET} , m^2g^{-1}	Mechanical strength, kg cm^{-2}
AMC_350	0.84	1.33	1.58	Al_2O_3 , SiO_2 quartz - traces, $\text{Cu}_{0.15}\text{Co}_{2.84}\text{O}_4$	0.7 1.32	650 -
AMC_450	1.30	2.15	1.65	Al_2O_3 , SiO_2 quartz - traces, $\text{Cu}_{0.15}\text{Co}_{2.84}\text{O}_4$	1.14	-
AMC_550	1.45	2.48	1.71	Al_2O_3 , SiO_2 quartz - traces, $\text{Cu}_{0.15}\text{Co}_{2.84}\text{O}_4$	1.13	-
AMC_650	1.55	2.47	1.59	Al_2O_3 , SiO_2 quartz - traces, $\text{Cu}_{0.15}\text{Co}_{2.84}\text{O}_4$ - traces	1.01	-
AMC_750	1.40	2.35	1.68	Al_2O_3 , SiO_2 quartz - traces, $\text{Cu}_{0.15}\text{Co}_{2.84}\text{O}_4$ - traces	0.48	-

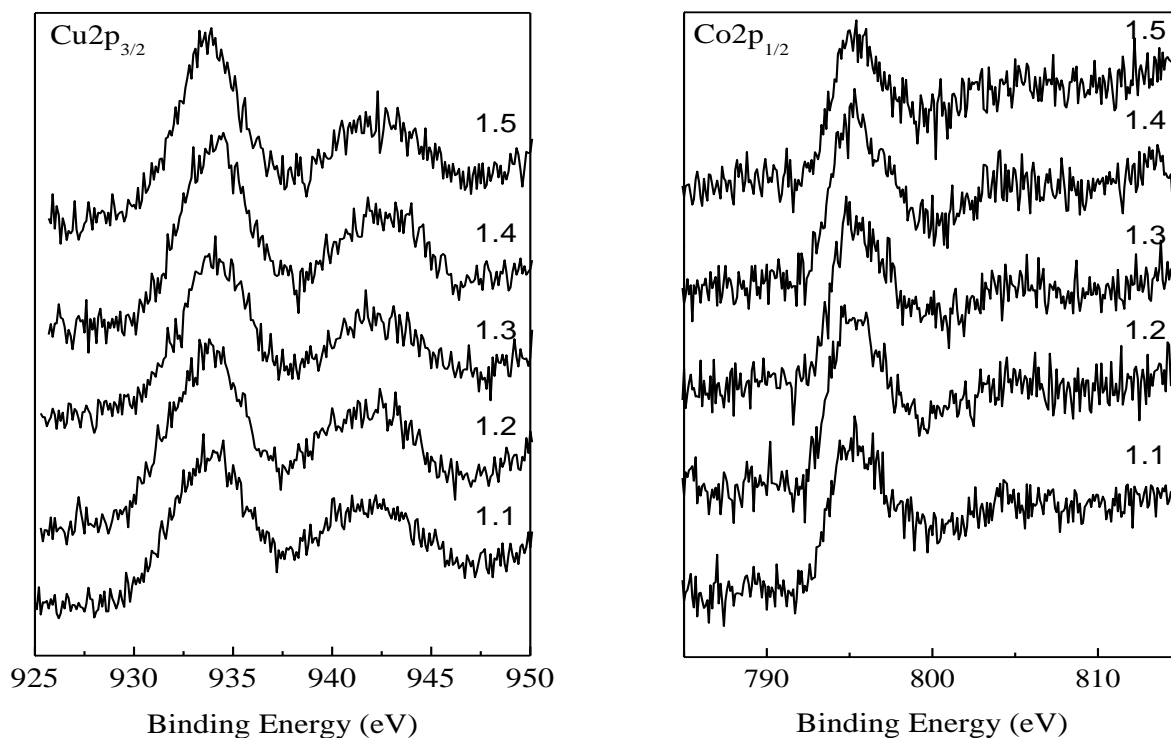


Fig. 3. The Cu2p_{3/2} and Co2p_{1/2} photoelectron spectra of AMC₃₅₀ (1.1), AMC₄₅₀ (1.2), AMC₅₅₀ (1.3), AMC₆₅₀ (1.4) and AMC₇₅₀ (1.5) catalysts.

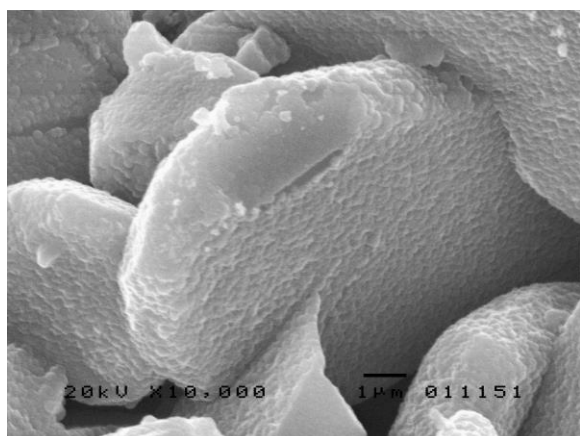
Table 2. XPS binding energies (eV) in the synthesized samples

Samples	Binding energies, eV			
	Co2p _{1/2}	Cu2p _{3/2}	Is/Im	Co-Cu
AMC ₃₅₀	795.1	933.9	0.70	1.41
AMC ₄₅₀	795.3	933.9	0.64	1.47
AMC ₅₅₀	795.0	934.2	0.59	1.44
AMC ₆₅₀	795.2	934.3	0.58	1.11
AMC ₇₅₀	795.1	933.8	0.57	1.33
CuO Merck	-	934.2	0.56	-

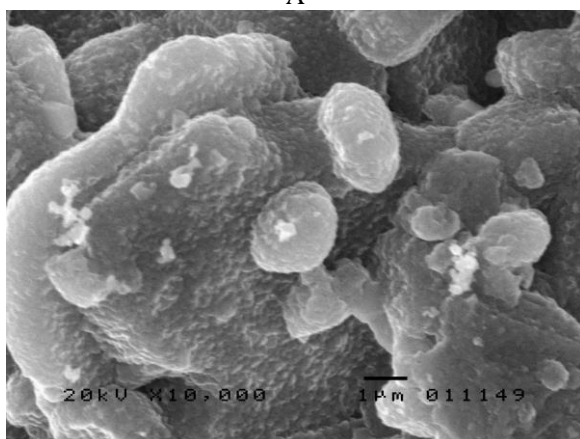
It is obvious from the results for the photoelectron signal of cobalt that it is in the Co³⁺ state, but one cannot exclude the presence of cobalt in the Co²⁺ oxidation state. It is clearly observable in the figure that the copper peak displays a satellite, characteristic of copper in the Cu²⁺ state. The catalyst samples AMC₃₅₀ to AMC₅₅₀ have a distinctly expressed asymmetry of the main photoelectron peak, which is missing in the other two samples AMC₆₅₀ and AMC₇₅₀ calcined at the highest temperatures. The single oxygen peak at about 541.4 eV was estimated to belong to the alumina phase. The calculated ratio between the intensity of the satellite and that of the main copper peak is decreasing and it becomes near to that of CuO - Merck (0.56). This fact gives us the reason to suppose that at low temperatures of calcination copper cobaltite is being formed on the surface, as it has already been observed in our previous studies

[14], while the increase in the temperature of calcination is probably leading to formation of separate phases of copper and cobalt oxides on the surface. These results coincide with the data from the XRD analysis of the same samples. Figure 4 presents SEM micrographs of the catalyst samples AMC₄₅₀, AMC₆₅₀ and AMC₇₅₀, respectively (Fig. 4A, 4B and 4C).

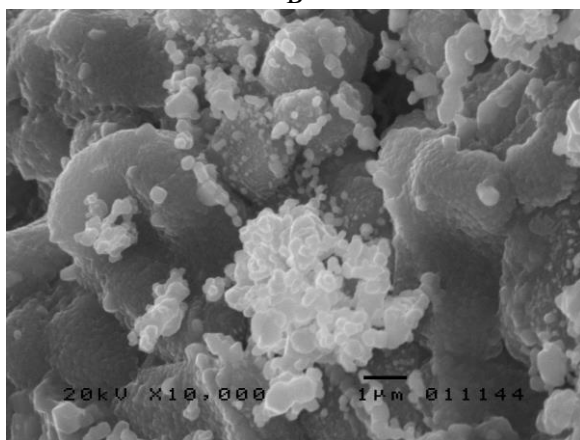
Separate particles of prevailing spherical form are observed in the catalyst sample AMC₄₅₀ (Fig. 4A), whereupon the size of the biggest ones is below 0.36 μm. In the case of catalyst sample AMC₆₅₀ (Fig. 4B) the shape of the particles is also spherical, whereupon the size of the smallest ones is below 0.7 μm. The largest particles have sizes less than 2 μm. Agglomeration of the particles is observed at this temperature. Further, in the case of the highest temperature sample AMC₇₅₀ (Fig. 4C) agglomerates are observed consisting of small particles of spherical shape, with sizes of the order of 0.15 – 0.30 μm and some larger ones of dimensions 0.50 – 0.80 μm, with prevailing spherical shape, which form chain clusters of size below 3 μm. The analysis of the results from the SEM micrographs shows that the particle size is dependent on the calcination temperature of the catalyst samples and it corresponds to the calculations made on the basis of Scherrer's rule in the course of the XRD investigations.



A



B



C

Fig. 4 SEM images for catalysts A – (AMC_450), B – (AMC_650) and C – (AMC_750)

The activities (conversion degrees η) of the catalyst samples in the CO oxidation reaction at different space velocities are shown in Figures 5 and 6.

One can observe the close values of the temperatures at which η is 50% with the catalyst samples AMC_350, AMC_450 and AMC_550 – $T_{50\%} = 175^\circ\text{C}$ at space velocity $W = 20\,000\text{ h}^{-1}$ (contact time $0.53 - 0.54\text{ h g-cat/mol}$). This is due to the formation of copper cobaltite spinel at these

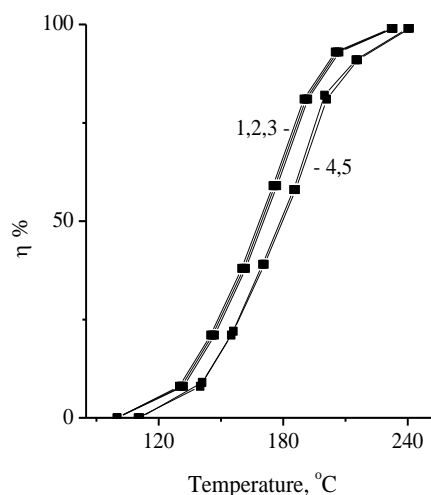


Fig. 5. CO conversion (η %) as a function of temperature of the catalysts: 1-AMC_350, 2-AMC_450, 3-AMC_550, 4-AMC_650, 5-AMC_750, space velocity, $W = 20\,000\text{ h}^{-1}$

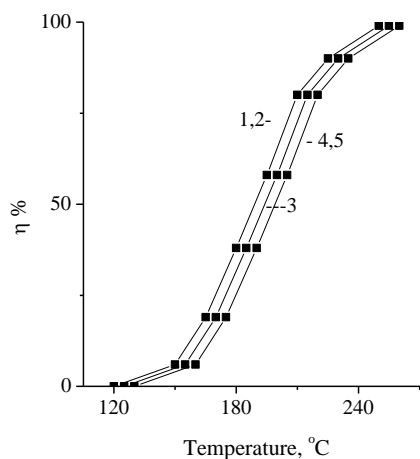


Fig. 6. CO conversion (η %) as a function of temperature of the catalysts: 1-AMC_350, 2-AMC_450, 3-AMC_550, 4-AMC_650, 5-AMC_750, space velocity, $W = 100\,000\text{ h}^{-1}$

temperatures. In the cases of the catalyst samples, calcined at 650 and 750°C, the temperature of the 50% conversion degree is shifted to higher values. Increasing the space velocity up to $100\,000\text{ h}^{-1}$ (contact time $0.11 - 0.12\text{ h g-cat/mol}$), the tendency is preserved, whereupon the catalyst samples AMC_350, AMC_450, AMC_550 are slightly more active than the samples calcined at the higher temperatures.

An analogous picture is obtained in regard to the activity, if the experimental results are presented by means of I_g , which denotes the amount of CO oxidized by 1g of catalyst per hour. These data are shown in Figures 7 and 8. This index also indicates AMC_350 as the most active catalyst sample. Similar activities were manifested by the catalyst samples AMC_450, AMC_550. The samples AMC_650 and

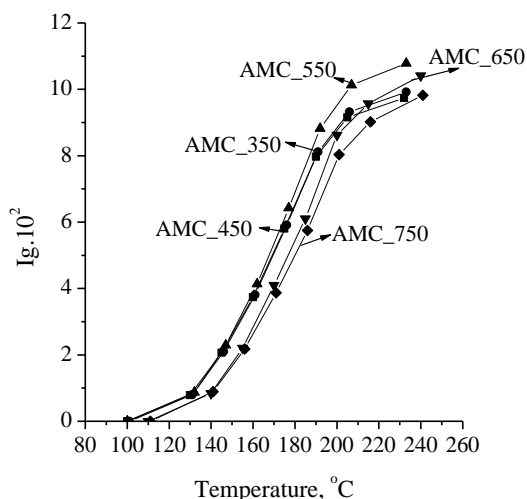


Fig. 7. CO oxidation (milligrams) by 1 g catalyst (I_g) versus temperature for the catalysts: AMC_350, AMC_450, AMC_550, AMC_650, AMC_750 space velocity, $W = 20\,000\text{ h}^{-1}$

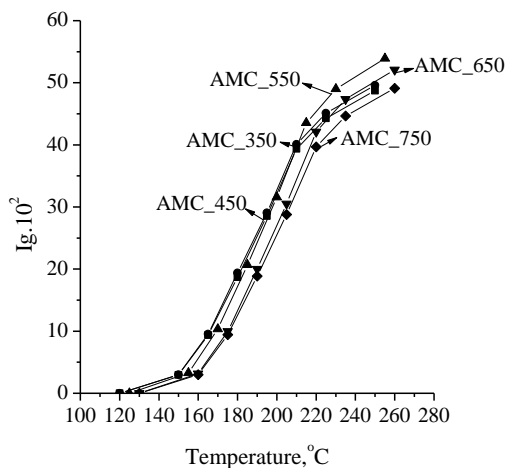


Fig. 8. CO oxidation (milligrams) by 1 g catalyst (I_g) versus temperature for the catalysts: AMC_350, AMC_450, AMC_550, AMC_650, AMC_750 space velocity, $W = 100\,000\text{ h}^{-1}$

AMC_750 display lower activities. It should be noted that the content of copper and cobalt on the surface of the AMC_350 sample (as a sum of the two) is the lowest one - 2.17 wt. %, while in the other catalyst samples it is higher than 3 wt. % and nevertheless, this catalyst sample is the most effective.

In order to check the sensitivity of the catalyst samples with respect to the catalyst poison sulfur dioxide, after reaching 98% conversion degree 30 ppm of SO_2 are fed into the inlet gas mixture flow. After a certain time interval the feeding of SO_2 is discontinued in order to observe whether the poisoning is reversible or irreversible. As it is seen in Figure 9 at space velocity $W = 20\,000\text{ h}^{-1}$, the

activities of the catalyst samples are gradually decreasing with the increase of the time interval of feeding the poison, but they are completely recovered after discontinuing the SO_2 flow. The difference in the performance of the high-temperature catalyst samples and that of the other samples is negligibly small. Quite different is the behavior of the samples at the higher space velocity $W = 100\,000\text{ h}^{-1}$ (Figure 10).

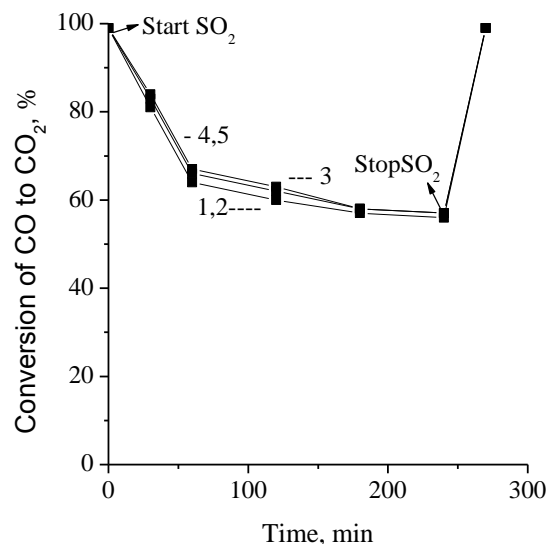


Fig. 9. Poisoning of the catalysts: 1-AMC_350, 2-AMC_450, 3-AMC_550, 4-AMC_650, 5-AMC_750 during the reaction oxidation of $\text{CO} + \text{O}_2$, space velocity, $W = 20\,000\text{ h}^{-1}$

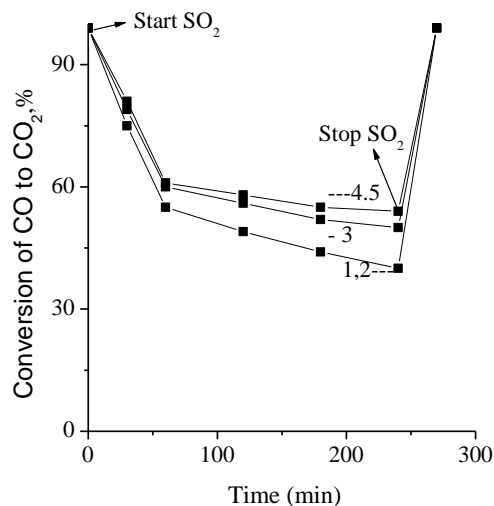


Fig. 10. Poisoning of the catalysts: 1-AMC_350, 2-AMC_450, 3-AMC_550, 4-AMC_650, 5-AMC_750 during the reaction oxidation of $\text{CO} + \text{O}_2$, space velocity, $W = 100\,000\text{ h}^{-1}$

During the feeding of the SO_2 poison the catalyst samples AMC_350, AMC_450 lower their activities down to 40%, while in the cases of the other samples the activities decrease to 50 – 55%. In this case it is also observable that the poisoning of the catalyst

samples is reversible. This is probably due to blocking of a fraction of the active sites participating in the CO+O₂ reaction, by the poison, which occurs as a result of formation of unstable superficial sulfate complexes under the effect of SO₂, which is followed by their desorption after stopping the SO₂ flow.

These results show that the formation of a spinel phase of copper cobaltite alters the sensitivity towards this strong catalyst poison – sulfur dioxide. It is known that the oxides of the transition metals, in particular the oxides of copper and cobalt, are active catalysts in oxidation reactions, but in the presence of this poison they lose 100 % of their activity. The poisoning is also reversible in the case of these two metal oxides and the initial activity is restored after discontinuing the poison flow. In the present investigation, the oxides present in the catalyst samples lose their activity and effectiveness completely, but the spinel phase is preserved and it continues its action, as it is non-sensitive to sulfur dioxide and therefore these catalyst samples preserve a comparatively high activity.

Additional information can be obtained if the data on the activity of the catalyst samples are presented by means of the quantity I_g, at one and the same reaction temperature, in dependence of the synthesis temperature of the catalyst samples.

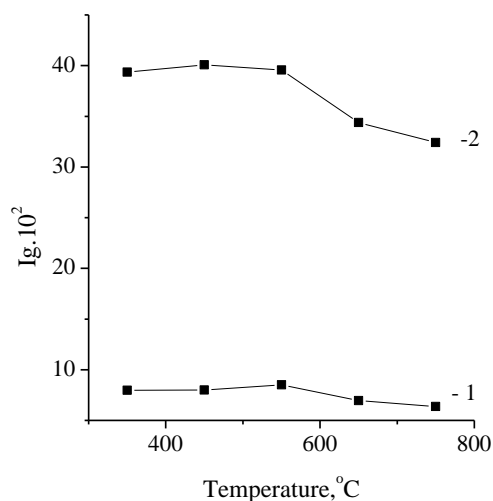


Fig. 11. CO oxidation by 1 g catalyst versus temperature and different space velocity:

- at T=190°C, space velocity W = 20 000 h⁻¹ (curve 1)
- at T=210°C, space velocity W = 100 000 h⁻¹ (curve 2)

Figure 11 illustrates this dependence for the studied catalyst samples at the two space velocities. As it can be seen from the figure, the catalyst samples obtained at lower temperatures, having a higher content of the spinel phase, preserve their high effectiveness. In the cases of higher synthesis

temperatures – above 650°C, at which the spinel is probably starting to decompose, the activities are lower and the sensitivity towards catalytic poisons increases.

CONCLUSION

On the basis of the results from the present investigation it was ascertained that:

The phase formation process in the synthesized catalyst samples deposited on high-temperature alumina-silica-magnesia support plays an essential role with respect to both the catalytic activity in the reaction of CO oxidation by oxygen from the air and the stability/resistance to catalyst poisons, in particular SO₂.

Of substantial importance for obtaining a spinel-like active phase are the structure and the texture of the support, as well as the solid-state processes occurring during the thermal treatment of the contact mass.

Most promising with a view to the activity in the studied reaction and stability to poisoning by SO₂ are the catalyst samples calcined within the temperature interval 350 – 550°C, enabling the synthesis of a spinel-like Cu/Co oxide phase.

This gives us the reason to propose practical application of the high-temperature support for depositing catalysts for purification of toxic emissions of gaseous fluids.

Acknowledgements: The authors thank the National Science Fund of Bulgaria (Grant N^o TO1/6) for the financial support.

REFERENCES

1. Suskil Kumar, K. K. Pant, *International journal of hydrogen energy*, **36**, 13352 (2011).
2. I. Spassova, M. Khristova, D. Panayotov, D. Mehandjiev, *Journal of Catalysis*, **185**, (1), 43 (1999).
3. I. Spassova, D. Mehandjiev, *Reac.Kinet. Catal. Lett.*, **69**, 2, 231 (2000).
4. V. Georgescu, D. Bombos, R. Scurtu, I. Spassova, D. Mehandjiev, L. D. Dumitrache, *Revista de Chimie* **59**, 2, 243 (2008).
5. D. Mehandjiev, B. Piperov, G. Bliznacov, *L'Acad. Bulg. Sci.*, **31**, 11, 1433 (1978).
6. D. Mehandjiev, *BG Patent* 10 6344 (2002).
7. D. Mehandjiev, E. Nikolova, *Thermochim. Acta* **23**, 117 (1978).
8. S. Angelov, D. Mehandjiev, B. Piperov, V. Zarcov, A. Terlecki - Baricevic, D. Jovanovic, Z. Jovanovic. *Appl. Catal.* **16**, 431 (1985).
9. D. Stoyanova, M. Christova, P. Dimitrova, J. Marinova, N. Kasabova, D. Panayotov, *Appl.Catal. B: Environmental*, **17**, 233 (1998).
10. D. Stoyanova, PhD Thesis, IONH, Sofia, 2002.

11. J.L.Cao, Y.Wang, T.Y. Zhang, S.H. Wu, Z.Y. Yuan, *Appl. Catal. B*: **78**, 120 (2008).
12. C.Q.Hu, *Journal. Chem. Eng.* **159**, 129 (2010).
13. Zhi-Gang Liu, S.H. Chai, A.Binder, Y.Li, L.T.Ji, C.Sh. Dai, *Appl. Catal.: General* **451**, 282 (2013).
14. P. Stefanov, I. Avramova, D. Stoichev, N. Radic, B.Grbic, Ts. Marinova, *Applied Surface Science* **245**, 65 (2005).

ФАЗООБРАЗУВАНЕ И КАТАЛИТИЧНА АКТИВНОСТ НА Cu – Co ШПИНЕЛЕН КАТАЛИЗАТОР НАНЕСЕН ВЪРХУ Al/Si/Mg – НОСИТЕЛ

Д. Д. Стоянова, Д. Р. Механджиев

Институт по обща и неорганична химия, Българска академия на науките,
ул. "акад. Г. Бончев" бл. 11, 1113 София, България

Получена на 20 ноември 2013 г.; коригирана на 19 май, 2014 г.

(Резюме)

В работата са представени Cu-Co оксидни катализатори, нанесени върху фирмен високотемпературен носител, съдържащ алуминий, магнезий и силиций и накалиени при различни температури: 350, 450, 550, 650 и 750⁰C. Образците са получени по метода на пропиването от водни разтвори на нитрати, съдържащи Cu и Co. Катализаторите са охарактеризирани посредством рентгенови фотоелектронни спектри, рентгенофазов анализ, диференциален термичен анализ, сканираща електронна микроскопия и по метода на БЕТ. Направен е химически анализ на образците. Изследвано е фазообразуването, при различни температури на получаване и каталитичната активност на меден кобалтит в реакцията на окисление на CO с кислород при две обемни скорости (20 000 и 100 000h⁻¹). Проследена е и устойчивостта на образците към каталитични отрови като SO₂ при същите обемни скорости (20 000 и 100 000h⁻¹). Установено е, че най-добра перспективност по отношение активността на разглежданата реакция и стабилност спрямо отравяне и активност съчетана с SO₂ показват катализаторите, накалиени в температурен интервал 350 – 550⁰C, при която температура се синтезира шпинелоподобната Cu-Co оксидна фаза. Това ни дава основание за възможната приложимост на високотемпературния носител за нанесени катализатори за очистиране от токсични емисии на газове флуиди.

Numerical analysis of mass and momentum transfer in co-axial cylinders with rotating inner cylinder

H. Ahmari¹, S. Zeinali Heris^{2*}

¹Ph.D. Student, Department of Chemical Engineering, Faculty of Engineering, Ferdowsi University of Mashhad, Mashhad, Iran

² Associated Professor, Department of Chemical Engineering, Faculty of Engineering, Ferdowsi University of Mashhad, Mashhad, Iran

Received December 18, 2013; Revised September 21, 2014

Bearing is one of the most commonly used tools in the industry that the distance between the two cylinders is filled with a fluid. Given the possibility of oil pollution, the emission behavior of mass and momentum transfer within the fluid appears to be necessary. In this paper, the coaxial cylinders with rotating inner cylinder and a non-Newtonian fluid is simulated. Differential equations of mass and momentum transfer with simple problem situation are introduced and the boundary conditions for solving these equations are obtained. The results showed that there was insignificant radial velocity. Even if there was an appendage of the outer cylinder, the change of radial velocity was very low, but, it did not affect diffusion. Also, variations of the Reynolds number, the radial velocity and diffusion as well as concentration are studied.

Keywords: Bearings, Co-axial cylinders, Momentum, Mass transfer, Non-Newtonian fluid

INTRODUCTION

Coaxial cylinders are used in many experimental analyses [1, 2] and industrial applications such as medicine filter industries. Some studies have focused on momentum transfer and behavior of system and some have addressed problems of heat flow in composite cylinders, as mentioned in the literatures [3-8]. However, mass transfer in coaxial cylinders has rarely been investigated. On the contrary, mass transfer in the laminar flow of non-Newtonian fluids between rotating coaxial cylinders is used in most industrial processes, such as the catalytic chemical reactors, filtration devices, plant cell bioreactors, liquid-liquid extractors [4], cylinder extraction columns, high efficiency batch distillation columns, cyclone chambers, Journal bearings and rotating electrical machinery [9].

Molki et al. [10] investigated convective heat/mass transfer characteristics of the laminar flow in a circular annulus with a rotating inner cylinder in the presence of a laminar axial flow. Sung et al. [11] measured the local mass transfer from a cylinder placed in a pulsating free stream. Flowers et al. [9] did an experimental study on the transport properties of a system in which a stream

of air flows axially in the long annulus between a rotating cylinder and a stationary coaxial outer tube. Also, they compared mass and momentum transfer in streams containing secondary flows [12]. Zeraibi et al. [13] presented a numerical investigation of the thermal convection for a thermo-dependent non-Newtonian fluid in an annular space between the two coaxial rotating cylinders. Jeng et al. [14] investigated the effects of jet flow and flow outlet configuration on the fluid flow in an annulus between co-axis cylinders. Laminar conjugate heat transfer by natural convection and conduction in a vertical annulus formed between co-axial cylinders was studied by Shahi et al. [15]. Ogawa et al. studied the relationship between the wave length of Taylor vortices and the lapse of time related to the spin-up time in the wide gap between coaxial cylinders in details [2]. Sedahmed and Nirdosh [16] measured the free convection mass transfer rates at the outer surface of the inner duct of a horizontal square annular duct by an electrochemical technique. Cheng presented a modeling of the heat transfer of upward annular flow in a smooth tube and a spirally internally ribbed tube [17]. Various method of predicting the transition to annular flow in an upward, two-phase, gas-liquid flow in a vertical

* To whom all correspondence should be sent:
E-mail: zeinali@um.ac.ir

tube were tested against a large set of experimental data by Rezkallah and Sims[18].

A bearing is a specific device that allows a relative motion, typically rotational or linear, between two or more pieces. Bearings can be widely classified. A layer of fluid bearings with a lubricant or compressed gas can prevent the collision of two surfaces and reduce the vertical forces between the two surfaces [19]. Also, the bearing rotational speed is generally low.

Dust and dirt usually find their way to a bearing and mix with the oil. However, sometimes these dust and dirt come from inside a bearing. Therefore, the bearing fluid should be able to take out this matter to protect itself against rubbing. The fluid must be able to pass through the material as quickly as possible.

In this study, the ways of transferring mass within the fluid bearing and the interaction between mass and momentum transfer are studied. Also, the effect of baffles on the fluid flow and diffusion is investigated. The variation of velocity, Reynolds number, concentration of diffuser and diffusion intensity between two walls vs. destination is plotted. The equations of mass transfer are solved in transient conditions, while momentum transfer is in stationary conditions.

Theory

The two dimensional geometry of the study is illustrated in Fig. 1. The inner cylinder moves with constant angular velocity. The outer cylinder is at rest, as the material on the wall is diffused into the fluid. The liquid is in the annular gap between the two vertical coaxial cylinders, by which the concentration difference across the thin liquid layer is supplied. Since the velocity of inner cylinder is low, the flow remains laminar. It is because the shear flow is replaced by an actually symmetric three-dimensional secondary flow when the rotational speed of the inner cylinder exceeds a certain value [9].

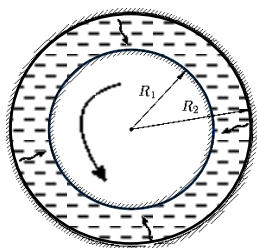


Fig. 1. Geometry of the system.

In the first geometry, Navies–Stock's (Momentum) equation is simplified and solved to provide more details about the velocity distribution

of the system. There is no radial velocity ($v_r = 0$) and from continuity equation:

$$\frac{\partial v_r}{\partial r} + \frac{\partial v_\theta}{\partial \theta} = 0 \quad (1)$$

Results:

$$\frac{\partial v_\theta}{\partial \theta} = 0 \quad (2)$$

Then:

$$v_\theta = v_\theta(r) \quad (3)$$

From momentum equations for r:

$$\rho \frac{v_\theta^2}{r} = \frac{dp}{dr} \quad (4)$$

And from momentum equation for θ :

$$\frac{1}{r} \frac{d}{dr} \left(r \frac{dv_\theta}{dr} \right) - \frac{v_\theta}{r^2} = 0 \Rightarrow \frac{d}{dr} \left(\frac{1}{r} \frac{d}{dr} (rv_\theta) \right) = 0 \quad (5)$$

$$v_\theta = \frac{A}{2} r + \frac{B}{r} \quad (6)$$

$$v_\theta|_{r=r_1} = r_1 \omega \quad (7)$$

$$v_\theta|_{r=r_2} = 0 \quad (8)$$

Then:

$$v_\theta = \frac{1}{r_1^2 - r_2^2} \left(r_1^2 \omega r - \frac{r_1^2 r_2^2 \omega}{r} \right) \quad (9)$$

As can be seen v_θ is a function of r_1 , r_2 and ω and it is time independent. Exact solutions of Navies–Stock's equation are of paramount importance in terms of both theoretical and practical values [20].

To investigate the concentration of fluid, the concentration equation is solved with $\frac{\partial C}{\partial \theta} = 0$:

$$\frac{\partial C}{\partial t} = D \left(\frac{1}{r} \frac{\partial}{\partial r} \left(r \frac{\partial C}{\partial r} \right) \right) \quad (10)$$

$$\frac{\partial C}{\partial r} \Big|_{r=r_1} = 0 \quad (11)$$

$$C|_{r=r_2} = C_0 \quad (12)$$

Equation (10) does not have an analytical solution. It shows that the concentration and momentum equations do not exhibit the expected analogous relationship [12]. The concentration of fluid between coaxial cylinders changes relative to time and radial velocity. Concentration and diffusion are not dependent on the angular velocity of fluid. Angular velocity homogenizes fluid in a certain angular line. This results in radial diffusion, which is not affected by the fluid flow. On the other hand, both phenomena, i.e., mass and momentum

transfer, are independent and need to be investigated separately.

In the geometry “with baffles”, the radial velocity affects the diffusion phenomena. Hence, the equation (10) is rewritten by v_r .

$$v_r \frac{\partial C}{\partial r} + \frac{\partial C}{\partial t} = D \left(\frac{1}{r} \frac{\partial}{\partial r} \left(r \frac{\partial C}{\partial r} \right) \right) \quad (13)$$

Radial velocity creates convective mass transfer in the system. To solve the equations of mass and momentum transfer, the finite element method is used.

To ensure the presence of the laminar flow, it should be tested with Taylor number. A definition of Taylor number is [21]:

$$Ta = \frac{\rho^2 v_\theta^2 R_i (R_o - R_i)^3}{\mu^2} \quad (14)$$

Here, the critical Taylor number is about 1700. In this study, given the assumed properties, the maximum permissible angular velocity is 0.77-0.98.

In the first geometry, $r_1 = 6$ cm and $r_2 = 8$ cm, the inner cylinder rotates with a speed of 0.005 m/sec, and for mass transfer analysis, the concentration of outer cylinder is 10 mol/m^3 . In the second geometry, 4 baffles with 0.1×0.1 dimensions are used. The fluid is non-Newtonian based on the power law model with a consistency index (k) and behavior index (n) of 0.5 and 0.7, respectively. The density of fluid is 1000 kg/m^3 . Finally, the value of diffusion coefficient of fluid (irrespective of its variation) is constant and equal to $1 \times 10^5 \text{ m}^2/\text{sec}$.

RESULTS AND DISCUSSION

The grid independency of the numerical solutions was investigated meticulously to ensure the accuracy of the numerical solution [22]. Order velocity was studied on a number of different quantities mesh elements. The results are shown in Fig. 2. In accordance with the increase of the number of mesh to 1200, velocity is independent of the number of mesh elements. As a result, the same mesh was used for the calculations.

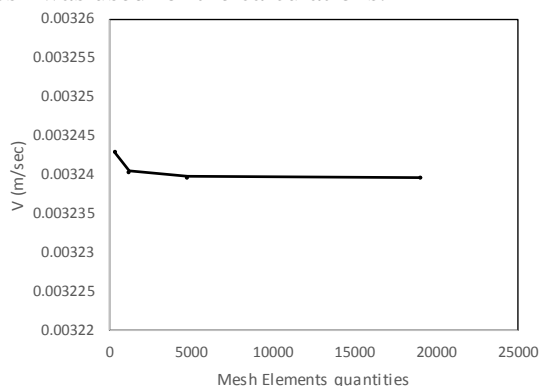


Fig. 2. Velocity vs. mesh quantity in certain point.

Momentum Transfer

Fig. 3 shows contour lines in both geometries. In the first geometry, the fluid layers turn in a constant circular line, meaning that the fluid is not mixed with the system. In the second geometry, contour lines turn uniformly but at a closer distance than the first geometry, except near the baffles where lines are closer together.

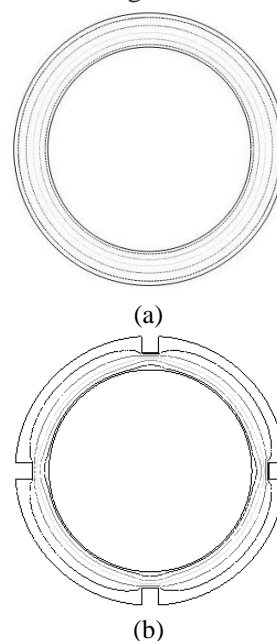


Fig. 3. Velocity contours in Both Geometry, without (a) and with Baffle (b).

As shown in Fig.4, in the absence of baffles, radial velocity is not created, while, in present of baffles it is created and changed by destination. The velocity reaches its maximum point near the inner cylinder. Maximum rate is about 5.5×10^{-6} with an average of 2.42×10^{-6} , which is very low. Unlike the first geometry, in the presence of baffle, the concentration is increased up to 3% in certain points. In other words, the fluid motion in the radial direction is negligible in the presence of baffles.

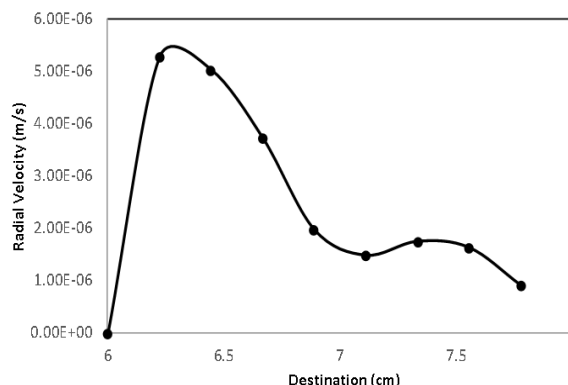


Fig. 4. Radial velocity vs. Destination in Geometry with the Baffle.

Fig. 5 illustrates the variation of Re number vs. destination. Re number is defined as [5]:

$$Re = \frac{\rho v R_o (R_o - R_i)}{\mu} \quad (15)$$

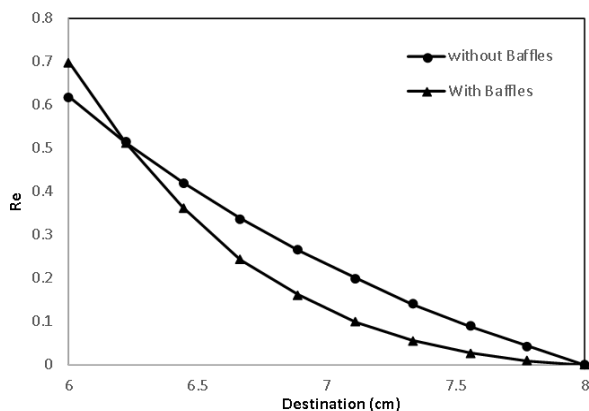


Fig. 5. Re number vs. Destination in both Geometries.

According to the above equation, Re number is the direct velocity magnitude-dependent and reversed apparent viscosity-dependent. In all points with baffle, velocity is lower than the points without baffle, which is due to the dramatic increase of surface after the baffle. The apparent viscosity in “with baffle” case is divided into two parts: areas near the inner cylinder and the areas outside it. In the former, the viscosity of points “with baffles” is less than the points “without baffles”, whereas in the latter, the viscosity is greater in the case “without baffle”. As a result, as shown in Fig. 5, Reynolds number in the case with baffles is less than the case without baffles, but in the vicinity of the inner cylinder, the slowdown is greater than the increased viscosity. Therefore, the Reynolds number is greater in the case without baffle.

Mass transfer

In this section, the system diffusion is investigated in both geometries. The radial velocity, which only appears in the first geometry, is generated in the system by baffles. However, the magnitude of velocity is negligible and ineffective in the radial mass transfer. As a result, the radial convection mass transfer is not produced in system. Mass transfer is carried out through diffusion mechanism.

Fig. 6 shows concentration in the system vs. destination at several points after the inception of diffusion. The numerical analysis of Equation (10) results variation of concentration vs. radius, which is nonlinear. As the time goes by, curves show a tendency toward nonlinearity.

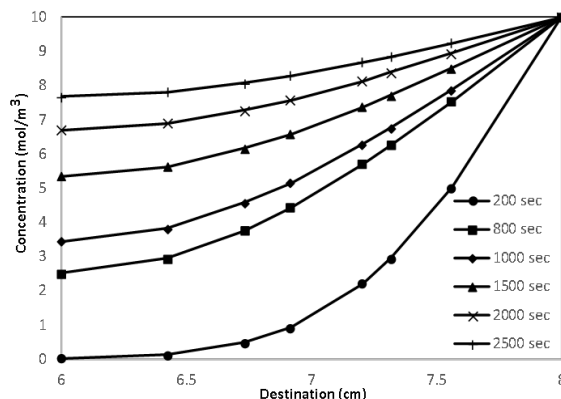


Fig. 6. Concentration vs. Destination at different times.

In certain points, concentration changes vs. time, as plotted in Fig. 7. In the first one, the range of curve is high because of the significant concentration difference and diffusion rate. However, the concentration difference reduces with time, the slope decreases and gives a linear curve.

Fig. 8 shows the variation of diffusion against the destination. At the initial time, the rate of diffusion is greater near the outer cylinder, but it decreases dramatically as the distance from the outer cylinder is furthered, because at that point its concentration is equal to zero. In other words, in the initial times, the substance is either non-existent or its value is very low for diffusion.

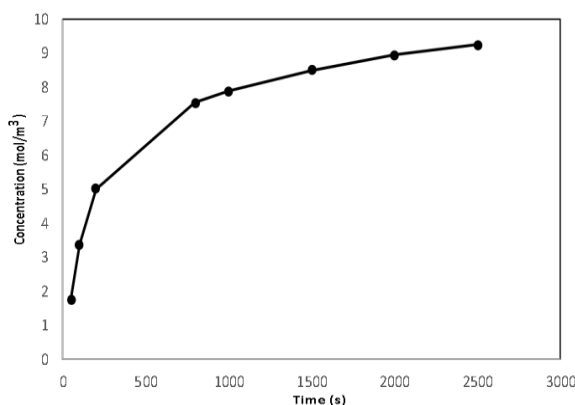


Fig. 7. Concentration vs. Time in r = 7.56 cm.

Over time, the radial diffusion appears in these areas and the concentration changes will be the same, though curves shrink gradually. This happens because concentration changes relative to the distance and time, as shown in Fig. 9. As mentioned earlier, the intensity of diffusion decreases over time. Also, radial diffusion decreases with time due to the concentration difference. This decline is sharp at the beginning of the process but it gradually becomes smoother.

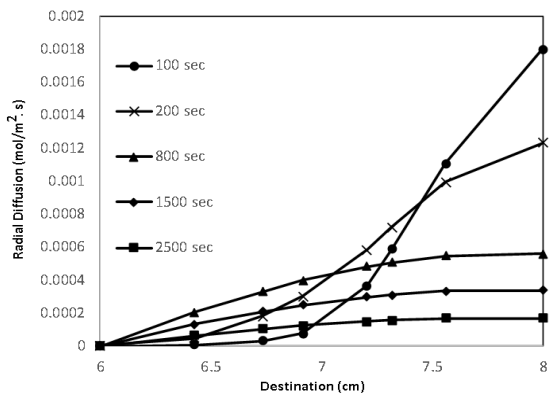


Fig. 8. Diffusion Flux vs. Destination in different times.

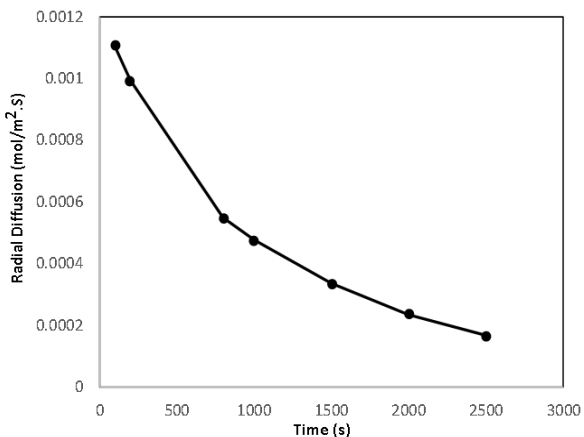


Fig. 9. Radial diffusion vs. time in $r=7.56$ cm.

CONCLUSION

In this research, mass and momentum transfer in co-axial cylinders was examined. The inner cylinder rotates at a constant velocity and the outer cylinder has a certain concentration. The simplification of the differential equation showed that both phenomena were distinct and could be solved separately. In this regard, the fluid turned uniformly and the radial velocity did not appear. The single mechanism of mass transfer is diffusion. The convection mass transfer is not achieved because the radial velocity is approximately zero. In the second case, baffles were used to change the flow model. At low velocities, the pattern of stream changed, but the creation of radial velocity was very low and it did not affect the radial mass transfer. Variations of concentration and diffusion mass transfer were also studied. The results showed

that at initial times, the starting point of diffusion had high rate of diffusion, but the rate reduced over the time.

REFERENCES

1. E. W. Billington, A. S. Huxley, *J. Colloid Interface Sci.*, **22**, 257 (1966).
2. A. Ogawa, Y. Fujita, N. Nagabayashi, *Chem. Eng. Comm.*, **37**, 209 (1985).
3. J. L. Chu, S. Lee, *Mechanics of Materials*. **20**, 105 (1995).
4. M. Amoura, N. Zeraibi, A. Smati, M. Gareche, *Int. Comm. Heat Mass Transfer*, **33**, 780 (2006).
5. H. R. Mozayyeni, A. B. Rahimi, *Scientia Iranica*, **19**, 91, (2012).
6. C. C. Liao, C. A. Lin, *Int. J. Heat Mass Transfer*, **55**, 6638 (2012).
7. O. Mahian, S. Mahmud, S. Zeinali Heris, *J. Heat Transfer*. **134**, 101704, (2012).
8. S.-C. Tzeng, *Int. Comm. Heat Mass Transfer*, **33**, 737 (2006).
9. J.R. Flower, N. Macleod, A.P. Shahbenderian, *Chem. Eng. Sci.*, **24**, 637 (1969).
10. M. Molki, K. N. Astill, E. Leal, *Int. J. Heat Fluid Flow*, **11**, 120 (1990).
11. H. J. Sung, K. S. Hwang, J. M. Hyun, *Int. J. Heat Mass Transfer*, **37**, 2203 (1994).
12. J. R. Flower, N. Macleod, *Chem. Eng. Sci.*, **24**, 651 (1969).
13. N. Zeraibi, M. Amoura, A. Benzaoui, M. Gareche, *Int. Comm. Heat Mass Transfer*, **34**, 740 (2007).
14. T. M. Jeng, S. C. Tzeng, H. L. Chang, *Int. Comm. Heat Mass Transfer*, **39**, 1119 (2012).
15. M. Shahi, A. H. Mahmoudi, F. Talebi, *Int. Comm. Heat Mass Transfer*, **38**, 533 (2011).
16. G.H. Sedahmed, I. Nirdosh, *Chem. Eng. Comm.*, **191**, 208 (2004).
17. L. Cheng, *Chem. Eng. Comm.*, **194**, 975 (2007).
18. K. S. Rezkallah, G. E. Sims, *Chem. Eng. Comm.*, **104**, 49 (1991).
19. A. Harnoy, *Bearing Design in Machinery Engineering Tribology and Lubrication*. Marcel Dekker, New York, 2002.
20. A.U. Sultangazin, K.N. Umbetov, *Math. Comput. Simulation*, **67**, 467 (2004).
21. F. M. White, *Fluid Mechanics*. Mc Graw-Hill, Boston, 2003.
22. Q. Lin, Z. Wei, Y. Tang, *Procedia CIRP*. **3**, 197 (2012).

ЧИСЛЕН АНАЛИЗ НА ПРЕНОСА НА МАСА И ЕНЕРГИЯ ПРИ КОАКСИАЛНИ ЦИЛИНДРИ ПРИ ВЪРТЯЩ СЕ ВЪТРЕШЕН ЦИЛИНДРИ

Х. Ахмари, С. Зейнали Херис*

Департамент по инженерна химия, Инженерен факултет, Университет "Фирдоуси" в Маишад, Иран

Постъпила на 18 декември, 2013 г., коригирана на 21 септември, 2014 г.

(Резюме)

Лагерите са едни от най-често срещаните средства в промишлеността, при които разстоянието между два цилиндъра е запълнено с флуид. Опасността от замърсяване на околната среда с масла налага оптимизирането на масопренасянето и преноса на енергия в тези флуиди. В настоящата работа се моделира не-Нютоновото течение между два коаксиални цилиндъра около въртящ се вътрешен цилиндър. Използвани са диференциалните уравнения за преноса на маса и енергия с необходимите гранични условия. Резултатите показват незначителна радиална компонента на скоростта с нищожно влияние върху дифузията. Изследвани са освен това измененията в числото на Рейнолдс и влиянието му върху радиалната компонента на скоростта, дифузията и концентрацията на пренасяното вещество.

Nano-TiO₂: An efficient and useful catalyst for the synthesis of 3-cyano-2(1H)-pyridone derivatives

B. Baghernejad*

Department of Chemistry, School of Sciences, Payame Noor University (PNU), 19395-3697, i.r. of Iran

Received December 29, 2013; Revised September 1, 2014

A highly efficient procedure for the synthesis of 3-cyano-2(1H)-pyridones and their 2-imino isosteres *via* a one-pot multicomponent reaction of 3,4-dimethoxyacetophenone, malonitrile or ethyl cyanoacetate, an aldehyde and ammonium acetate in the presence of nano-TiO₂ is achieved in good yields. Short reaction times, simple work-up, isolation of the products in high yields with high purity, mild reaction conditions are features of this new procedure.

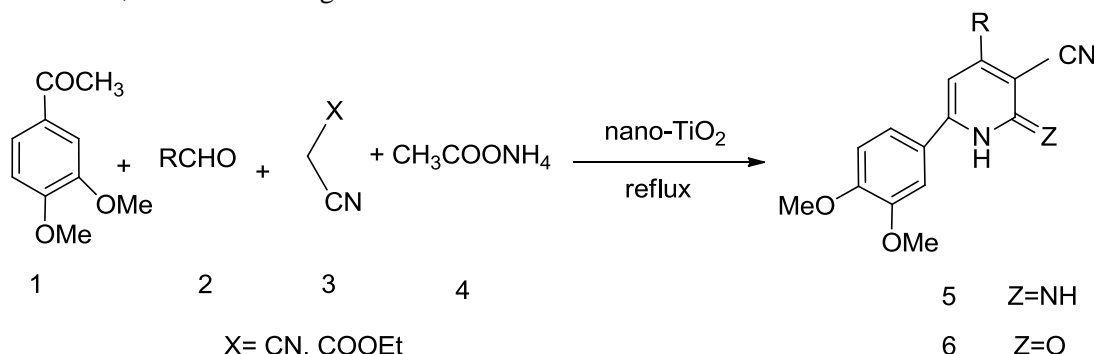
Keywords: 3-Cyano-2(1H)-pyridones, 2-Imino, Cardiotoxic, nano-TiO₂

INTRODUCTION

Among the various classes of nitrogen containing heterocyclic compounds, pyridine derivatives display a broad spectrum of biological activities. Substituted 3-cyano pyridines are important intermediates in pharmaceuticals, anti-inflammatory and dyes and therefore development of efficient procedures towards functionalized pyridines is an attractive target for organic synthesis.

Cardiac glycosides (digoxin and digitoxin), discovered in the 18th century, still represent the corner stone of therapy for congestive heart failure (CHF), despite their low therapeutic index and their propensity to cause life-threatening arrhythmia [1-3]. The newer sympathomimetic agents (dobutamine, dopamine) are orally inactive and may lead to tachyphylaxis due to β -receptor down regulation [4, 5]. Because of the need for safer and orally effective drugs, the synthesis of milrinone analogues as a series of nonglycosidic, non-sympathomimetic, cardiotoxic agents has been

developed [6]. 3-cyano-2(1H)-pyridinones and their 2-imino isosteres are milrinone analogues which also can be used as nonsteroidal cardiotoxic agents [7] and their syntheses are categorized by the following three types: (i) Knoevenagel and Hantzsch condensation chemistry from β -keto esters [8-10] (ii) pyridine synthesis from α , β -unsaturated ketones [11, 12] (iii) Krohnke type cyclization with 1,5-diketone and ammonium acetate [13], but many of reported methods have drawbacks such long reaction times, harsh reaction conditions, the use of stoichiometric reagents or of toxic and inflammable solvents, difficult work-ups or low yields of products. Consequently, there is a need to develop new methods for the synthesis of these compounds. In this communication we wish to report the application of nano-TiO₂ in the synthesis of 3-cyano-2(1H)-pyridones and their 2-imino isosteres. (Scheme 1)



Scheme 1.

* To whom all correspondence should be sent:
E-mail: address: bitabaghernejad@yahoo.com

RESULTS AND DISCUSSION

As part of our program aimed at developing new selective and environmental friendly methodologies for the preparation of fine chemicals, we performed the synthesis of 3-cyano-2(1H)-pyridones and their 2-imino isosteres through one-pot multi-component reaction of 3,4-dimethoxyacetophenone, malonitrile or ethyl cyanoacetate, an aldehyde and ammonium acetate in the presence of nano-TiO₂.

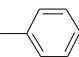
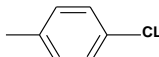
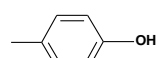
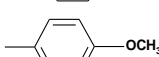
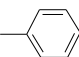
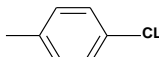
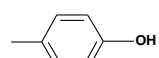
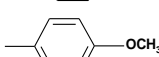
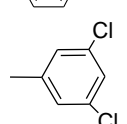
This reaction proceeded smoothly and rapidly to give the corresponding pyridones and 2-imino analogues in good yields (Table 1). Initially, we examined the effect of varying the solvent on the synthesis of 5b. This reaction was carried out in various solvents such as water, DMF, chloroform, ethanol, CH₂Cl₂ and toluene. As shown in Table 2, the best results in terms of yield and time are obtained in ethanol.

By carrying out reactions with different amounts of ammonium acetate, it was found that 8 mmol of ammonium acetate furnished the maximum yield for 1 mmol of the reactants. When ethyl cyanoacetate was used instead of malonitrile, the corresponding 2-pyridone was obtained in good yield (Table 1, entries 6-10).

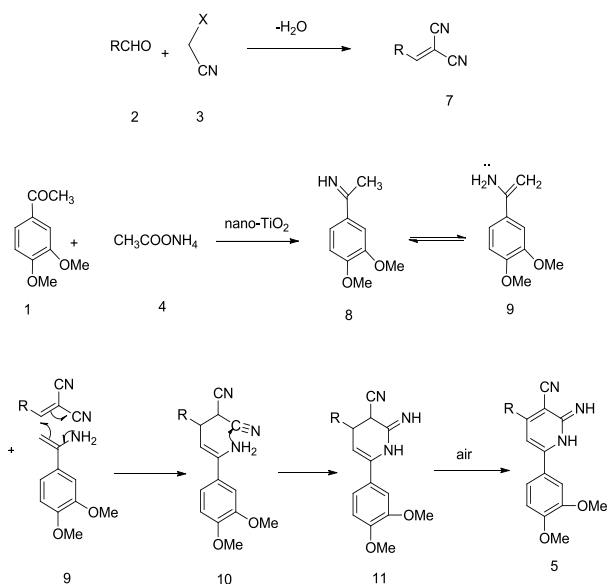
Under optimized reaction conditions, various aromatic aldehydes reacted very well with malonitrile and ethyl cyanoacetate as the active methylene compounds to give the corresponding 2(1H)-pyridones and their 2-imino isosteres in good yields (Table 1). The effect of temperature in ethanol as a solvent was studied by carrying out the reactions at different temperatures [room temperature (25 °C), 45 °C and under refluxing temperature (78 °C)]. As it is shown in Table 1, the yields of the reactions increased as the reaction temperature was raised. From these results it was decided that refluxing temperature would be the best temperature for all reactions. The reaction proceeds very cleanly under reflux and is free from side products.

A reasonable mechanism for this reaction is shown in Scheme 2. The enamine formed from dimethoxyacetophenone and ammonia adds to the aldol condensation product of the aldehyde and malonitrile. Subsequent addition to a cyano group followed by dehydrogenation affords the desired product 5.

Table 1. Synthesis of 3-cyano-2(1H)-pyridones with nano-TiO₂

Entry	R	X	Z	Product	Time (h)	Yield(%) ^a		
						25°C	45°C	78°C
1	-CH ₃	CN	NH	5a	3	45	65	83
2		CN	NH	5b	3	45	70	85
3		CN	NH	5c	3	40	68	87
4		CN	NH	5d	3	45	72	84
5		CN	NH	5e	3	50	71	84
6	-CH ₃	COOEt	O	6a	3	45	65	85
7		COOEt	O	6b	3	45	72	86
8		COOEt	O	6c	3	40	70	86
9		COOEt	O	6d	3	45	72	85
10		COOEt	O	6e	3	50	75	83
11		COOEt	O	6f	3	45	70	89

^aYield of isolated products.



Scheme 2.

Table 2. Synthesis of 5b with nano-TiO₂ in the presence of different solvents

Entry	Solvent	Temperature	Time(h)	Yield (%) ^a
1	Ethanol	Reflux	3	82
2	Acetonitrile	Reflux	3	80
3	Ethyl acetate	Reflux	4	78
4	THF	Reflux	4	75
5	Dichloromethane	Reflux	6	65

^aYield of isolated products.

It is known that the specific surface area and the surface-to-volume ratio increase dramatically as the size of a material decreases. The high surface area brought about by nanoparticle size is beneficial to many TiO₂-based devices, as it facilitates reaction/interaction between the devices and the interacting media [14]. TiO₂ nanoparticles have been widely investigated in the past decades due to their multiple potential catalytic activity for esterification [15], degradation of methyl parathion [16], photodecomposition of methylene blue [17], rhodamine B degradation [18], synthesis of β -acetamido ketones [19], 2-alkylbenzimidazoles and indazole [20], β -amino ketones [21], bis(indolyl)methanes [22], 2-indolyl-1-nitroalkane [23], selective oxidation of sulphides [24], Friedel-Crafts alkylation of indoles [25] and photocatalytic synthesis of quinaldines [26].

The investigation on nano-TiO₂ catalytic activity for the synthesis of many organic molecules is a current work in our laboratory. The dimensions of the applied TiO₂ nanoparticles were determined with SEM and are 38 nm (Fig. 1).

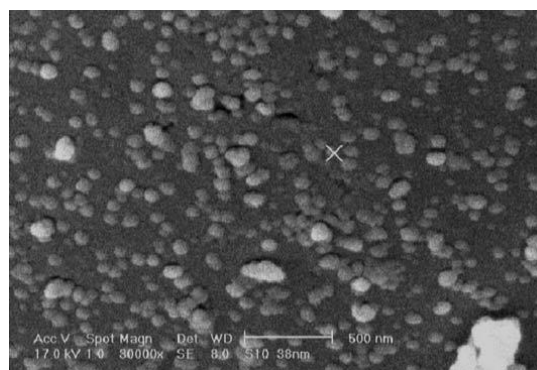


Fig.1. SEM photograph of nano-TiO₂

EXPERIMENTAL

All products are known compounds and were characterized by m.p., IR, ¹HNMR and GC/MS. Melting points were measured by the capillary tube method with an Electrothermal 9200 apparatus (Germany). ¹HNMR spectra were recorded on a Bruker AQS AVANCE-500 MHz spectrometer (Germany) using TMS as an internal standard (CDCl₃ solution). IR spectra were recorded from KBr disks on the FT-IR Bruker Tensor 27 (Germany). GC/MS spectra were recorded on an Agilent Technologies 6890 network GC system supplied with an Agilent 5973 network mass selective detector (United States). Thin layer chromatography (TLC) on commercial aluminum-backed plates of silica gel, 60 F254 was used to monitor the progress of reactions. All products were characterized by spectral and physical data.

Typical procedure for preparation of 4-aryl(alkyl)-3-cyano-6-(3,4-dimethoxyphenyl)-2(1H)-iminopyridines (5a-e):

A mixture of 3,4-dimethoxyacetophenone (1 mmol), malononitrile (1 mmol), the appropriate aldehyde (1 mmol), ammonium acetate (8 mmol) and nano-TiO₂ (5 mol%) in ethanol (5 mL) was refluxed for 3 h. The progress of the reaction was monitored by TLC (hexane-ethylacetate (2:1)). After completion of the reaction, the solvent was evaporated and the mixture was washed with chloroform and filtered to recover the catalyst. The filtrate was evaporated and the crude product was recrystallized from ethanol.

Typical procedure for preparation of 4-aryl(alkyl)-6-(3,4-dimethoxyphenyl)-3-cyano-2(1H)-pyridinones (6a-e):

The foregoing method was carried out except that malononitrile was replaced by ethyl cyanoacetate (Table 1, entries 6-10).

Synthesis of nano-TiO₂

A 500 mL three-necked flask containing 5 mL of titanium tetrachloride was equipped with a

condenser, a gas trap and a water steam producer. The titanium tetrachloride was heated to 130 °C. By adding water steam to hot titanium tetrachloride for 15 min, a milky solution was formed. After washing the condenser, the milky solution was filtered to obtain a white solid. By heating the white solid in an oven at 400 °C for 7 h, the TiO₂ nanoparticles formed a white crystalline powder.

Reusability of nano-TiO₂

Next, we investigated the reusability and recycling of nano-TiO₂. At the end of the reaction, the catalyst could be recovered by a simple filtration. The recycled catalyst was washed with methanol and subjected to a second run of the reaction process. To assure that catalysts were not dissolved in methanol, they were weighed after filtration and before using and reusing for the next reaction. The results show that these catalysts are not soluble in methanol. In Table 3, the comparison of the efficiency of nano-TiO₂ in the synthesis of 5a after five runs is reported. As it is shown in Table 3, the first reaction using recovered nano-TiO₂ afforded a similar yield to that obtained in the first run. In the following runs the yield gradually decreased.

Table 3. Reuse of nano-TiO₂ for the synthesis of 5a

Entry	Time/h	Yield/% ^a
1	3	83
2	3	81
3	3	80
4	3	75
5	3	70

(a) Isolated yields

Selected physical data

5c: Mp: 207 °C (lit.203-207[21]). IR (KBr) (ν_{\max} , cm⁻¹): 2225, 3340. ¹H NMR (DMSO-D₆, 500 MHz) δ H (ppm): 3.75 (s, 3H, 3-OCH₃), 3.89 (s, 3H, 4-OCH₃), 7.12–7.58 (m, 8H, aromatic), 10.51 (brs, 1H, NH), 10.62 (brs, 1H, NH). GC/MS: 365 (M⁺).

5d: Mp: 202 °C (lit.205-207 [21]). IR (KBr) (ν_{\max} , cm⁻¹): 2246, 3345. ¹H NMR (DMSO-D₆, 500 MHz) δ H (ppm): 3.85 (s, 3H, 3-OCH₃), 3.91 (s, 3H, 4-OCH₃), 7.12–7.58 (m, 8H, aromatic), 9.86 (brs, 1H, NH), 9.98 (brs, 1H, NH), 10.65 (1H, OH), GC/MS: 347 (M⁺).

6a: Mp: 255 °C (lit.255-257 [21]). IR (KBr) (ν_{\max} , cm⁻¹): 1670, 2220, 3320. ¹H NMR (DMSO-D₆, 500 MHz) δ H (ppm): 2.43 (s, 3H, CH₃), 3.75 (s, 3H, 3-OCH₃), 3.89 (s, 3H, 4-OCH₃), 7.01–7.49 (m, 4H, aromatic), 12.05 (brs, 1H, NH). GC/MS: 270 (M⁺).

6b: Mp: 285 °C (lit.287-289 [21]). IR (KBr) (ν_{\max} , cm⁻¹): 1641, 2228, 3330. ¹H NMR (DMSO-500

D₆, 500 MHz) δ H (ppm): 3.89 (s, 3H, 3-OCH₃), 4.01 (s, 3H, 4-OCH₃), 7.09–7.52 (m, 9H, aromatic), 12.51 (brs, 1H, NH). GC/MS: 332 (M⁺).

CONCLUSION

In summary, we have developed a simple and efficient protocol for the synthesis of 3-cyano-2(1H)-pyridones and their 2-imino isosteres with nano-TiO₂. Short reaction times, simple work-up, isolation of the products in high yields with high purity, mild reaction conditions are features of this new procedure.

REFERENCES

1. E. Braunwald, *Am. Heart. J.*, **102**, 486 (1981).
2. J.E. Muller, Z.G. Turi, P.H. Stone, R.E. Rude, D.S. Raabe, A.S. Jaffe, H.K. Gold, N. Gustafson, W.K. Poole, E. Passamani, T.W. Smith, E. Braunwald, *New Engl. J. Med.*, **314**, 265 (1986).
3. S. Yusuf, J. Wittes, K. Bailey, C. Furberg, *Circulation*, **73**, 14 (1986).
4. C.M. Lathers, J. Roberts. *Life Sci.*, **27**, 1713 (1980).
5. Y.S. Su, T.K. Harden, Perkins, J.P. *J. Biol. Chem.*, **255**, 7410 (1980).
6. P. Dorigo, D. Fraccarollo, G. Santostasi, R.M. Gaion, I. Maragno, M. Floreani, F. Carpenedo, *II Farmaco*, **49**, 19 (1994).
7. A. Abadi, O. Al-Deeb, A. Al-Afify, H. El-Kashef, *II Farmaco*, **54**, 195 (1999).
8. M.F. Gordeev, D.V. Patel, J. Wu, E.M. Gordon, *Tetrahedron Lett.*, **37**, 4643 (1996).
9. A. Bhandari, B. Li, M. A. Gallop, *Synthesis*, **11**, 1951 (1999).
10. J.G. Breitenbucher, G. Figliozzi, *Tetrahedron Lett.*, **41**, 4311 (2000).
11. A.L. Marzinzik, E.R. Felder, *J. Org. Chem.*, **63**, 723 (1998).
12. A.R. Katritzky, L. Serdyuk, C. Chassaing, D. Toader, X. Wang, B. Forood, B. Flatt, C. Sun, K. Vo, *J. Comb. Chem.*, **2**, 182 (2000).
13. C. Chiu, Z. Tang, J. Ellingboe, *J. Comb. Chem.*, **1**, 73 (1999).
14. X. Chen, S.S. Mao, *Chem. Rev.*, **107**, 2891 (2007).
15. H. Yu, Y. Zhu, C. Liu, *Chin. J. Catal.*, **30**, 265 (2009).
16. J. Wang, W. Sun, Z. Zhang, *J. Mol. Catal. A: Chem.*, **27**, 84 (2007).
17. C.H. Lin, Y.C. Lin, C.L. Chang, *React. Kinet. Catal. Lett.*, **90**, 267 (2007).
18. F. Sayilkan, M. Asilturk, S. Sener, *Turk. J. Chem.*, **31**, 220 (2007).
19. B.F. Mirjalili, A. Akbari, *Naturforsch.*, **64**, 347 (2009).
20. K. Selvam, B. Krishnakumar, R. Velmurugan, *Catal. Commun.*, **11**, 280 (2009).
21. M. Samet, B. Eftekhari, M.M. Hashemi, *Synth. Commun.*, **39**, 4441 (2009).

22. M. Rahimizadeh, Z. Bakhtiarpoor, H. Eshghi, *Monatsh. Chem.*, **140**, 1465 (2009).
23. M.L. Kantam, S. Laha, J. Yadav, P. Srinivas, *Synth. Commun.*, **39**, 4100 (2009).
24. M. Rahimizadeh, G. Rajabzadeh, S.M. Khatami, J. *Mol. Catal. A: Chem.*, **323**, 59 (2010).
25. K. Selvam, M. Swaminathan, *Tetrahedron Lett.*, **51**, 4911 (2010).
26. M.L. Kantam, S. Laha, J. Yadav, B. Sreedhar, *Tetrahedron Lett.* **47**, 6213 (2006).

НАНО-TiO₂: ЕФЕКТИВЕН И ПОЛЕЗЕН КАТАЛИЗАТОР ЗА СИНТЕЗА НА 3-ЦИАНО-2 (1H) -ПИРИДОНИ ПРОИЗВОДНИ

Б. Багернеджад *

Катедра по химия, училище за науки, Университет Паям Нур (PNU), 19395-3697, ИР Иран

Получена на 29 декември, 2013 г.; ревизирана на 1 септември 2014 г.

(Резюме)

Постигната е високо ефективна процедура за синтез на 3-циано-2 (1H) -пиридони и техните 2-имино изостери чрез едностодийна многокомпонентна реакция на 3,4-диметоксиацетофенон, малонитрил или етил цианоацетат, алдехид и амониев ацетат в присъствие на нано-TiO₂ с добри добиви. Характеристика на тази нова процедура са кратки реакционни времена, проста работа, изолиране на продуктите с високи добиви и висока степен на чистота, меки реакционни условия.

NaBH₄/I₂ mediated one-pot synthesis of 4-(substituted-anilinomethyl-3-(6-methoxy-2-naphthyl)-1-phenyl-1H-pyrazoles and their antimicrobial screening

N. Goel¹, S. Kumar², S. Bawa^{*2}

¹ Maharaja Surajmal Institute of Pharmacy, (Affiliated to GGSIP University, New Delhi) C-4, Janakpuri, New Delhi

² Dept. Of Pharmaceutical Chemistry, Faculty of Pharmacy, Jamia Hamdard, New Delhi

Received January 6, 2014; Revised March 4, 2014

A series of compounds (**Va-VI**) was synthesized *via* direct reductive amination of 3-(naphthalen-2-yl)-1-phenyl-1H-pyrazole-4-carbaldehyde with various substituted aromatic amines using NaBH₄ in the presence of I₂ as a reducing agent. The reaction was carried out in anhydrous methanol under neutral conditions at room temperature. The structures of the synthesized compounds (**Va-VI**) were established on the basis of IR, ¹H and ¹³C-NMR, and mass spectral data. All 4-(substituted-anilinomethyl-3-(2-naphthyl)-1-phenyl-1H-pyrazole derivatives (**Va-VI**) were tested *in vitro* for antifungal and antibacterial activities against different fungal and bacterial strains. Most of the compounds exhibited considerable antifungal activity but poor antibacterial activity against the test strains. The compounds **Vg**, **Vj** and **Vk** showed excellent antifungal activity against the fungal strain *Aspergillus niger* MTCC 281 and *Aspergillus flavus* MTCC 277 (% inhibition in the range of 47.7-52.8).

Keywords; Reductive amination, Pyrazole, Naphthalene, Antimicrobial activity

INTRODUCTION

Pyrazole scaffold represent one of the most active class of heterocyclic compounds possessing a wide spectrum of biological activities including anti-inflammatory–analgesic [1-3], antimicrobial [4,5], antihypertensive [6,7] etc. Some of the analogues have also shown potent antitumor [8,9], antidepressant - anticonvulsant [10,11] and hypoglycemic activities [12,13]. The significance of pyrazole scaffold may be realized by the fact that, there are numerous pyrazole containing drugs has been approved by USFDA for appropriate therapeutic indications some of which includes

Celecoxib, Lanazolac, Sulphinpyrazone and Cefoselis etc. Crizotinib (Xalkori) an anticancer drug recently approved by USFDA for the treatment of non-small cell lung carcinoma (NSCLC) is pyrazole derivative [14]. Fig. 1 shows some of the pyrazole derived therapeutic agents and represent the molecular diversity of pyrazole nucleus. Owing to the immense importance and varied bioactivities of pyrazole scaffold and in the continuation of our ongoing research on biologically active pyrazole derivatives [15, 16], it was thought of interest to synthesized some new 6-methoxy naphthalene incorporated pyrazole derivatives. In the present study

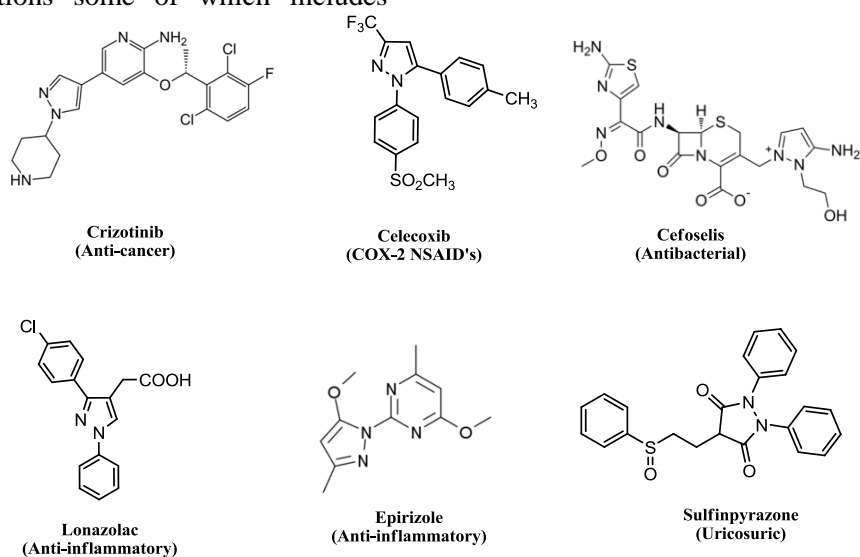


Fig. 1. Chemical structures of various pyrazole containing drugs.

* To whom all correspondence should be sent:
E-mail: drsbawa@reffimail.com

we performed the one-pot synthesis of 4-(substituted-anilinomethyl-3-(6-methoxy-2-naphthyl)-1-phenyl-1H-pyrazoles and their antimicrobial screening against a panel of bacterial and fungal strains.

EXPERIMENTAL

Melting points were determined by the open capillary method with electrical melting point apparatus and are uncorrected. IR spectra were recorded as KBr (pallet) on Nicolet, Protege 460 FTIR spectrophotometer and ^1H & ^{13}C -NMR spectra recorded on Bruker DPX 300 MHz spectrophotometer using DMSO-d_6 or CDCl_3 as a NMR solvent. TMS used as internal standard and chemical shift data reported in parts per million (in ppm) where s, bs, d, t, and m designated as singlet, broad singlet, doublet, triplet and multiplet respectively. Mass spectra (MS-ESI) were recorded on a JEOL-AccuTOF JMS-T100LS mass spectrometer with a DART (Direct Analysis in Real Time) and elemental analysis on C,H,N Analyzer Perkin Elmer 2400. Thin Layer Chromatography (TLC) was performed to monitor progress of the reaction and purity of the compounds, spot being located under iodine vapour or UV-light.

Synthesis of 1-[1-(6-methoxynaphthalen-2-yl)ethylidene]-2-phenylhydrazine (III).

A mixture of 2-acetyl-6-methoxynaphthalene **I** (2.0 g or 0.01 mol) and phenyl hydrazine **(II)** (0.012 mol) was refluxed in round bottom flask containing absolute ethanol (30 ml) for 2.0 hrs in presence of few drops of acetic acid. The content of the flask was cooled to give solid product which was filtered, washed with water, dried and recrystallized from ethanol as a yellow crystalline solid. The purity of compound was checked by TLC using (TEF) (5:4:1) as mobile phase.

1-[1-(6-Methoxynaphthalen-2-yl)ethylidene]-2-phenylhydrazine (III). Yellowish white solid, yield 90 %; m.p. 183 °C; IR (KBr) ν_{max} (cm^{-1}): 3357 (NH), 1605 (C=C), 1590 (C=N). ^1H -NMR (300 MHz, DMSO-d_6) δ : 2.36 (s, 3H, CH_3), 3.91 (s, 3H, OCH_3), 6.77-6.82 (m, 1H, Ar-H), 7.10-7.18 (m, 1H, Ar-H), 7.21-7.34 (m, 4H, Ar-H), 7.69-7.79 (m, 3H, Ar-H), 7.93 (s, 1H, Ar-H), 8.14-8.17 (d, 1H, Ar-H, $J = 8.7$ Hz), 10.4 (bs, 1H, NH) Anal. calcd. for : $\text{C}_{19}\text{H}_{18}\text{N}_2\text{O}$; C 78.59, H 6.25, N 9.65 % Found : C 78.33, H 6.29, N 9.72 %.

Synthesis of 3-(6-methoxynaphthalen-2-yl)-1-phenyl-1H-pyrazole-4-carbaldehyde (IV).

To a cold solution of 6-methoxy naphthyl hydrazones **III** (4.35 g or 0.015 mol) in DMF (25 ml) was added POCl_3 (5 ml) and resulting mixture was stirred at 55-60 °C for 6 hrs. The mixture was

cooled to room temperature and poured in to ice-cold water, latter a saturated solution of sodium bicarbonate was added to neutralize the solution. The precipitate so formed was filtered, washed with water, dried and recrystallized from ethanol as crystalline solid.

3-(6-Methoxynaphthalen-2-yl)-1-phenyl-1H-pyrazole-4-carbaldehyde (IV). Light yellow solid, yield 70%, m. P. 152 °C; IR (KBr) ν_{max} (cm^{-1}): 1671 (C=O), 1610 (C=C), 1595 (C=N). ^1H -NMR (300 MHz, DMSO-d_3) δ (ppm): 3.97 (s, 3H, OCH_3), 7.19-7.21 (m, 2H, Ar-H), 7.37-7.42 (m, 1H, Ar-H), 7.49-7.55 (m, 2H, Ar-H), 7.81-7.93 (m, 5H, Ar-H), 8.25 (s, 1H, Ar-H), 8.56 (s, 1H, Ar-H), 10.15 (s, 1H, CHO). ^{13}C -NMR (DMSO-d_6 , 75 MHz) δ (ppm) : 55.4 (OCH_3), 103.6, 114.5, 116.9, 119.7, 125.8, 126.6, 128.0, 128.9, 129.5, 130.2, 131.8, 132.0, 137.6, 141.2, 157.5, 162.4, 184.0 (CHO). MS (ESI) m/z: 328 (M^+), 300 (M-28), Anal. calcd. for : $\text{C}_{21}\text{H}_{16}\text{N}_2\text{O}_2$, C 76.81, H 4.91, N 8.53 %, Found C 76.48, H 4.95, N 8.61.

General procedure for the synthesis of compounds (Va-VI).

To a solution of 3-(6-methoxynaphthalen-2-yl)-1-phenyl-1H-pyrazole-4-carbaldehyde **IV** (1.0 mmol) in 10 ml of methanol, substituted aniline (1.2 mmol) was added and then 50 mg iodine (0.4 mmol) was added with stirring at room temperature. To the stirred solution 55 mg of sodium borohydride (1.4 mmol) was added slowly, stirring further for 3-6 hrs. The precipitate was formed which was filtered, washed with water, dried and recrystallized from ethanol/methanol to give crystalline product (**Va-VI**). The progress of reaction and purity of the compound was checked by (TLC), using benzene: acetone (9.5:0.5) as mobile phase.

4-Anilinomethyl-3-(6-methoxy-2-naphthyl)-1-phenyl-1H-pyrazole (Va). Light brown solid, yield 75%, m. P. 130-132 °C; IR (KBr) ν_{max} (cm^{-1}) 3406 (N-H), 1619 (C=C), 1596 (C=Vmax), 1021 (C-N). ^1H -NMR (300 MHz, CDCl_3) δ (ppm) : 3.90 (s, 3H, OCH_3), 4.47 (s, 2H, CH_2), 4.72 (s, 1H, NH, D_2O -exchangeable), 6.61-6.64 (d, 2H, Ar-H, $J = 8.4$ Hz), 7.04-7.07 (d, 2H, Ar-H, $J = 8.1$ Hz), 7.10-7.15 (m, 3H, Ar-H), 7.29-7.35 (m, 2H, Ar-H), 7.46-7.55 (m, 3H, Ar-H), 7.70-7.81 (m, 2H, Ar-H), 7.98-8.09 (m, 2H, Ar-H), 8.21 (s, 1H, Ar-H). ^{13}C -NMR (75 MHz, CDCl_3) δ (ppm) : 38.4 (CH_2), 55.4 (OCH_3), 103.2, 114.6, 116.4, 117.8, 119.2, 120.0, 125.3, 126.4, 127.6, 129.5, 128.2, 128.9, 129.5, 130.7, 132.1, 138.6, 140.9, 142.3, 149.4, 162.4. DEPT-135; (-ve) 38.6 (CH_2). MS (ESI) m/z: 405 (M^+). Anal. calcd. for $\text{C}_{27}\text{H}_{23}\text{N}_3\text{O}$: C 79.97, H 5.72, N 10.39 % ; Found: C 79.73, H 5.76, N 10.44%.

4-(4-Chloroanilinomethyl-3-(6-methoxy-2-naphthyl)-1-phenyl-1H-pyrazole (Vb). Cream colored solid, yield 70%, m. P. 119-121 °C; IR (KBr) ν_{\max} (cm⁻¹): 3411 (N-H), 1612 (C=C), 1596 (C=N), 1036 (C-N). ¹H-NMR (300 MHz, CDCl₃) δ (ppm): 3.93 (s, 3H, OCH₃), 4.46 (s, 2H, CH₂), 4.78 (bs, 1H, NH, D₂O-exchangeable), 6.67-6.69 (d, 2H, Ar-H, *J* = 8.0 Hz), 7.09-7.17 (d, 4H, Ar-H, *J* = 7.8 Hz), 7.22-7.29 (m, 2H, Ar-H), 7.40-7.48 (m, 3H, Ar-H), 7.69-7.74 (m, 2H, Ar-H), 7.95-8.03 (m, 2H, Ar-H), 8.16 (s, 1H, Ar-H). MS (ESI) *m/z*: 439 (M)⁺, 441 (M+2). Anal. calcd. for C₂₇H₂₂ClN₃O: C 73.71, H 5.04, N 9.55 %, Found: C 73.82, H 5.09, N 9.62 %.

3-(6-Methoxy-2-naphthyl)-1-phenyl-4-(4-toluidinomethyl)-1H-pyrazole. (Vc). Yellowish brown solid, yield 74%, m. P. 144 °C; IR (KBr) ν_{\max} (cm⁻¹): 3433 (N-H), 1620 (C=C), 1591 (C=N), 1030 (C-N). ¹H-NMR (300 MHz, CDCl₃) δ (ppm): 2.26 (s, 3H, CH₃), 3.93 (s, 3H, OCH₃), 4.46 (s, 2H, CH₂), 4.80 (s, 1H, NH, D₂O-exchangeable), 6.61-6.64 (d, 2H, Ar-H, *J* = 8.4 Hz), 7.01-7.03 (d, 2H, Ar-H, *J* = 8.1 Hz), 7.12-7.15 (m, 2H, Ar-H), 7.25-7.30 (m, 2H, Ar-H), 7.43-7.48 (m, 2H, Ar-H), 7.68-7.80 (m, 3H, Ar-H), 7.92-7.99 (m, 2H, Ar-H), 8.16 (s, 1H, Ar-H). ¹³C-NMR (75 MHz, CDCl₃) δ : 20.4 (CH₃), 37.9 (CH₂), 55.4 (OCH₃), 104.1, 114.4, 116.6, 117.4, 119.2, 120.6, 125.7, 126.3, 127.2, 127.8, 128.2, 128.8, 129.6, 130.2, 132.6, 135.8, 137.1, 138.2, 140.5, 142.8, 149.1, 162.8. DEPT-135; (-ve) 37.9 (CH₂). MS (ESI) *m/z*: 419 (M)⁺, Anal. calcd. for C₂₈H₂₅N₃O: C 80.16, H 6.01, N 10.02 %, Found: C 80.34, H 6.06, N 10.7 %.

4-(4-Bromoanilinomethyl-3-(6-methoxy-2-naphthyl)-1-phenyl-1H-pyrazole. (Vd). brownish solid, yield 68%, m. P. 189-192 °C; IR (KBr) ν_{\max} (cm⁻¹): 3424 (N-H), 1624 (C=C), 1596 (C=N), 1028 (C-N). ¹H-NMR (300 MHz, CDCl₃) δ (ppm): 3.90 (s, 3H, OCH₃), 4.49 (s, 2H, CH₂), 5.01 (bs, 1H, NH, D₂O-exchangeable), 6.70-6.73 (d, 2H, Ar-H, *J* = 8.0 Hz), 7.08-7.15 (m, 3H, Ar-H, *J* = 7.8 Hz), 7.20-7.25 (m, 2H, Ar-H), 7.30-7.34 (m, 1H, Ar-H), 7.42-7.51 (m, 3H, Ar-H), 7.72-7.78 (m, 2H, Ar-H), 7.90-7.98 (m, 2H, Ar-H), 8.18 (s, 1H, Ar-H). Anal. calcd. for C₂₇H₂₂BrN₃O: C 66.95, H 4.58, N 8.67 % Found: C 66.72, H 4.63, N 8.73 %.

4-(3-Chloroanilinomethyl-3-(6-methoxy-2-naphthyl)-1-phenyl-1H-pyrazole. (Ve). Beize colored solid, yield 65%, m. P. 110-112 °C; IR (KBr) ν_{\max} (cm⁻¹): 3418 (N-H), 1621 (C=C), 1593 (C=N), 1027 (C-N). ¹H-NMR (300 MHz, CDCl₃) δ (ppm): 3.94 (s, 3H, OCH₃), 4.47 (s, 2H, CH₂), 4.82 (bs, 1H, NH, D₂O-exchangeable), 6.69-6.72 (d, 2H, Ar-H, *J* = 8.0 Hz), 6.83-6.87 (m, 1H, Ar-H), 7.01-

7.08 (m, 3H, Ar-H), 7.18-7.25 (m, 2H, Ar-H), 7.37-7.45 (m, 3H, Ar-H), 7.68-7.78 (m, 2H, Ar-H), 6.97-7.03 (m, 2H, Ar-H), 8.20 (s, 1H, Ar-H). Anal. calcd. for C₂₇H₂₂ClN₃O: C 73.71, H 5.04, N 9.55 % Found: C 73.54, H 5.01, N 9.62 %.

4-(4-Methoxyanilinomethyl)-3-(6-methoxy-2-naphthyl)-1-phenyl-1H-pyrazole (Vf). Yellowish brown solid, yield 71%, m. P. 103-105 °C; IR (KBr) ν_{\max} (cm⁻¹): 3420 (N-H), 1628 (C=C), 1597 (C=N), 1029 (C-N). ¹H-NMR (300 MHz, CDCl₃) δ (ppm): 3.69 (s, 3H, OCH₃), 3.94 (s, 3H, OCH₃), 4.50 (s, 2H, CH₂), 4.78 (bs, 1H, NH, D₂O-exchangeable), 6.60-6.72 (d, 2H, Ar-H, *J* = 8.0 Hz), 6.96-6.98 (d, 2H, Ar-H, *J* = 8.0 Hz), 7.10-7.19 (m, 3H, Ar-H), 7.23-7.27 (m, 1H, Ar-H), 7.36-7.48 (m, 3H, Ar-H), 7.71-7.79 (m, 2H, Ar-H), 6.98-7.05 (m, 2H, Ar-H), 8.19 (s, 1H, Ar-H). Anal. calcd. for C₂₈H₂₅N₃O₂: C 77.22, H 5.79, N 9.65 % Found C 77.47, H 5.82, N 9.73 %.

4-(4-Fluoroanilinomethyl-3-(6-methoxy-2-naphthyl)-1-phenyl-1H-pyrazole (Vg). Light brown solid, yield 78%, m. P. 134-136 °C; IR (KBr) ν_{\max} (cm⁻¹): 3420 (N-H), 1628 (C=C), 1597 (C=N), 1029 (C-N). ¹H-NMR (300 MHz, CDCl₃) δ (ppm): 3.91 (s, 3H, OCH₃), 4.52 (s, 2H, CH₂), 4.79 (bs, 1H, NH, D₂O-exchangeable), 6.63-6.65 (d, 2H, Ar-H, *J* = 8.0 Hz), 7.01-7.04 (m, 1H, Ar-H), 7.09-7.15 (m, 2H, Ar-H), 7.24-7.30 (m, 3H, Ar-H), 7.41-7.45 (m, 2H, Ar-H), 7.73-7.80 (m, 3H, Ar-H), 7.01-7.06 (m, 2H, Ar-H), 8.15 (s, 1H, Ar-H). Anal. calcd. for C₂₇H₂₂FN₃O: C 76.58, H 5.24, N 9.92 % Found C 76.27, H 5.29, N 9.97 %.

3-(6-Methoxy-2-naphthyl)-4-(4-nitroanilinomethyl)-1-phenyl-1H-pyrazole (Vh). Yellowish brown solid, yield 75%, m. P. 168-170 °C; IR (KBr) ν_{\max} (cm⁻¹): 3428 (N-H), 1631 (C=C), 1590 (C=N), 1033 (C-N). ¹H-NMR (300 MHz, CDCl₃) δ (ppm): 3.92 (s, 3H, OCH₃), 4.48 (s, 2H, CH₂), 4.76 (bs, 1H, NH, D₂O-exchangeable), 6.60-6.63 (d, 2H, Ar-H, *J* = 8.0 Hz), 7.06-7.11 (m, 2H, Ar-H), 7.17-7.20 (m, 1H, Ar-H), 7.28-7.33 (m, 3H, Ar-H), 7.43-7.47 (m, 2H, Ar-H), 7.80-7.88 (m, 3H, Ar-H), 8.02-8.07 (m, 2H, Ar-H), 8.21 (s, 1H, Ar-H). Anal. calcd. for C₂₇H₂₂N₄O₃: C 71.99, H 4.92, N 12.44 % Found: C 72.21, H 4.96, N 12.51 %.

3-(6-Methoxy-2-naphthyl)-1-phenyl-4-(3-toluidinomethyl)-1H-pyrazole (Vi). Light brown solid, yield 75%, m. P. 106-107 °C; IR (KBr) ν_{\max} (cm⁻¹): 3417 (N-H), 1625 (C=C), 1594 (C=N), 1031 (C-N). ¹H-NMR (300 MHz, CDCl₃) δ (ppm): 2.24 (s, 3H, CH₃), 3.89 (s, 3H, OCH₃), 4.50 (s, 2H, CH₂), 4.81 (bs, 1H, NH, D₂O-exchangeable), 6.59-6.62 (d, 2H, Ar-H, *J* = 8.0 Hz), 6.93-6.97 (m, 2H, Ar-H), 7.07-7.13 (m, 2H, Ar-H), 7.21-7.24 (m, 1H, Ar-H), 7.40-7.49 (m, 3H, Ar-H), 7.68-7.77 (m, 3H, Ar-H), 8.01-8.07 (m, 2H, Ar-H), 8.17 (s, 1H, Ar-H). Anal. calcd. for

C₂₈H₂₅N₃O : C 80.16, H 6.01, N 10.02 %, Found : C 80.01, H 6.06, N 10.08 %.

4-(3-Chloro-4-fluoroanilinomethyl-3-(6-methoxy-2-naphthyl)-1-phenyl-1H-pyrazole (Vj). Brownish solid, yield 67%, m. P. 124-125 °C; IR (KBr) ν_{max} (cm⁻¹) : 3422 (N-H), 1630 (C=C), 1593 (C=N), 1034 (C-N). ¹H-NMR (300 MHz, CDCl₃) δ (ppm) : 3.92 (s, 3H, OCH₃), 4.48 (bs, 2H, CH₂), 4.71 (bs, 1H, NH, D₂O-exchangeable), 6.50-6.53 (m, 1H, Ar-H), 6.68-6.70 (m, 1H, Ar-H), 6.91-6.97 (m, 1H, Ar-H), 7.07-7.23 (m, 3H, Ar-H), 7.39-7.54 (m, 3H, Ar-H), 7.67-7.96 (m, 4H, Ar-H), 8.04 (s, 1H, Ar-H), 8.12 (s, 1H, Ar-H), Anal. calcd. for C₂₇H₂₁ClFN₃O : C 70.82, H 4.62, N 9.18% Found : C 70.63, H 4.67, N 9.24 %.

4-(3,4-Dichloroanilinomethyl-3-(6-methoxy-2-naphthyl)-1-phenyl-1H-pyrazole (Vk). Light brown solid, yield 69 %, m. P. 176-177 °C; IR (KBr) ν_{max} (cm⁻¹) : 3428 (N-H), 1631 (C=C), 1598 (C=N), 1033 (C-N). ¹H-NMR (300 MHz, CDCl₃) δ (ppm) : 3.93 (s, 3H, OCH₃), 4.46 (s, 2H, CH₂), 4.86 (bs, 1H, NH, D₂O-exchangeable), 6.52-6.55 (m, 1H, Ar-H), 6.70-6.72 (m, 1H, Ar-H), 6.91-6.97 (m, 1H,), 7.10-7.24 (m, 3H, Ar-H), 7.42-7.51 (m, 3H, Ar-H), 7.70-7.98 (m, 4H, Ar-H), 8.06 (s, 1H, Ar-H), 8.18 (s, 1H, Ar-H), Anal. calcd. for C₂₇H₂₁Cl₂N₃O : C 68.36, H 4.46, N 8.86 Found : C 68.15, H 4.49, N 8.92 %.

3-(6-Methoxy-2-naphthyl)-4-(4-hydroxyanilino methyl)-1-phenyl-1H-pyrazole (Vh). Dark yellowish solid, yield 65 %, m. P. 165-166 °C; IR (KBr) cm ν_{max} (cm⁻¹) : 3432 (N-H), 3389(OH) 1634 (C=C), 1594 (C=N), 1031 (C-N). ¹H-NMR (300 MHz, CDCl₃) δ (ppm) : 3.93 (s, 3H, OCH₃), 4.46 (s, 2H, CH₂), 4.82 (bs, 1H, NH, D₂O-exchangeable), 6.74-6.76 (d, 2H, Ar-H, J = 7.4 Hz), 7.09-7.12 (m, 2H, Ar-H), 7.18-7.20 (m, 1H, Ar-H),

7.30-7.36 (m, 3H, Ar-H), 7.42-7.48 (m, 2H, Ar-H), 7.86-7.93 (m, 3H, Ar-H), 8.03-8.07 (m, 2H, Ar-H), 8.24 (s, 1H, Ar-H), 9.79 (bs, 1H, OH). Anal. calcd. for C₂₇H₂₃N₃O₂ : C 76.94, H 5.50, N 9.97 % Found : C 76.73, H 5.52, N 10.02 %.

Antimicrobial activity

The newly synthesized compounds were screened for their antifungal and antibacterial activities against the test organism viz. *Candida albicans* MTCC-183, *Aspergillus niger* MTCC 281, *Aspergillus flavus* MTCC 277, *Escherichia coli* NCTC 10418, *Staphylococcus aureus* NCTC 6571, *Pseudomonas aeruginosa* NCTC 10662 in DMSO by cup plate method [17]. Potato dextrose agar and nutrient agar were used as culture medium for antibacterial and antifungal activity respectively. Using an agar punch, wells were made on these seeded agar plates and dilution of 500 µg/ml of test compounds in DMSO was added into each well, labeled previously. A control was also prepared using solvent DMSO. The petri plate were prepared and maintained at 30° for 72 hrs for fungi and at 37 °C for 24 hrs for bacteria. Each experiment was repeated twice and the average of the two independent determinations was recorded. Antimicrobial activity was determined by measuring zone of inhibition and results were reported as percentage inhibition and calculated as 100(C-T)/C, where C is the average diameter of fungal or bacterial growth on the control plate and T is the average diameter of fungal or bacterial growth on test plate. Activity of each compound was compared with standard Fluconazole for antifungal and Ciprofloxacin for antibacterial activity. Results of antimicrobial activity have been summarized in Table 1

Table 1. In-vitro antimicrobial activity data of compounds (Va-VI).

Compd. No.	Antimicrobial activity as % inhibition					
	Antifungal activity			Antibacterial activity		
	C. albicans	A. flavus	A. niger	E. coli	S. aureus	P. auroginosa
Va	28.1	33.8	31.7	19.6	13.7	—
Vb	38.2	42.0	43.6	16.9	17.4	—
Vc	26.0	30.8	32.3	22.5	13.8	—
Vd	31.8	39.6	38.0	21.7	18.7	—
Ve	38.4	45.7	46.1	18.6	14.3	—
Vf	26.1	32.5	30.3	24.9	18.2	—
Vg	38.9	48.9	48.7	20.9	15.6	—
Vh	14.8	18.6	15.7	32.3	21.5	—
Vi	24.7	26.8	28.8	15.7	10.8	—
Vj	42.2	49.6	51.0	22.9	18.2	—
Vk	44.8	52.8	50.3	23.7	20.4	—
VI	34.6	38.3	40.6	33.6	27.9	—
Ciprofloxacin	NT	NT	NT	84.8	78.7	80.6
Fluconazole	81.5	89.8	92.6	NT	NT	NT

NT: not tested, (—): no activity observed.

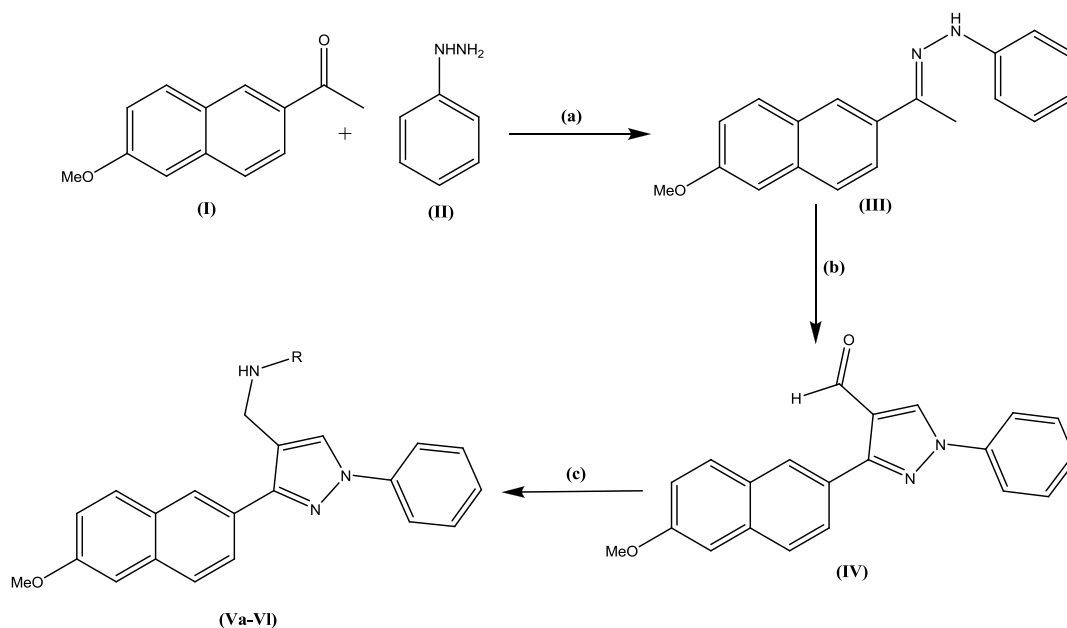


Fig. 2. Route of synthesis for compounds (**Va-VI**). Reagent and conditions: (a) Abs. EtOH, reflux (b) DMF/POCl₃, 55-60 °C, warm (c) aromatic amines, NaBH₄/I₂, MeOH, stirring

RESULTS AND DISCUSSION

Chemistry

The compounds (**Va-VI**) were synthesized by direct reductive amination of 3-(6-methoxynaphthalen-2-yl)-1-phenyl-1H-pyrazole-4-carbaldehyde with suitable aromatic amine using NaBH₄ in the presence of I₂ as reducing agent in absolute methanol as outlined in Fig. 2. The structure of synthesized amines (**Va-VI**) were elucidated by combined use of IR, ¹H & ¹³C-NMR and mass spectral data. Combustion analysis of compounds was found to be within the range of ±0.4 %. The synthesis of compounds was confirmed on the basis of functional group transformation of -CHO in compound **IV** into -CH₂NH- in compounds (**Va-VI**) and this was established on the basis of IR, ¹H, ¹³C-NMR including mass spectral data. In FTIR the characteristic carbonyl (C=O) stretching band which was observed at 1671 cm⁻¹ in compound **IV** disappeared in FTIR spectra of compounds (**Va-VI**). This was further supported by ¹H-NMR spectra. The ¹H-NMR spectrum of compound **IV**, the signal due to aldehydic proton which resonated as a singlet at δ value 10.15, disappeared in spectra of compounds (**Va-VI**) and a new signal observed at high upfield δ values ranging from 4.46 to 4.52 integrating for two protons. The signal due to the NH proton was observed at δ value 4.72–5.01. The methylene group of -CH₂NH- appeared as a singlet or broad singlet (bs) due to coupling effect of NH

proton whereas the NH signal was observed as a broad singlet. Furthermore in the ¹³C-NMR spectrum of the compound **IV** the signal due to the carbonyl carbon observed at δ value 184.0. No carbonyl carbon signal was found in the spectra of compounds (**Va-VI**) and a new signal due to methylene carbon of -CH₂NH- appeared at δ value 38.4 and 38.9 in compound **Va** and **Vc** respectively. The functional group transformation was again inveterate by ¹³C-NMR spectra using DEPT-135 technique, which records inverse (-ve) peak for CH₂ carbon. The DEPT-135 spectra of compound **Va** and **Vc** exhibit inverse (-ve) peak at 38.6 and 37.9 respectively. The above spectral analysis suggest the successful reductive amination of pyrazole carbaldehydes **IV**. This fact was further supported by MS(ESI) spectra of prototype compounds **Va**, **Vb** and **Vc**, in which M⁺ ion peak was observed at m/z 405, 439 and 419 respectively. In ¹H-NMR the protons of naphthalene and phenyl rings were observed in aromatic region as multiplets due to coupling and overlapping of signals. While a singlets integrating for one proton appeared at δ value 8.12-8.24 arising due to H-5 proton of the pyrazole nucleus. These data are in agreement with structures assigned to the compounds (**Va-VI**).

Antimicrobial activity of (**Va-VI**).

All the pyrazolyl amines (**Va-VI**) displayed variable growth inhibitory effects against the fungal strains at concentration of 500 mg/ml in DMSO as shown in Table No 1 Among the series of compounds (**Va-VI**) compounds **Vb**, **Ve**, **Vg**, **Vj** and **Vk** showed good antifungal activity against *Candida albicans*. The

growth inhibitory effect of compounds (**Va-VI**) was more pronounced against the fungal strain *Aspergillus niger* MTCC 281 and *Aspergillus flavus* MTCC 277. In this series compound **Vg**, **Vj** and **Vk** showed excellent antifungal activity against the fungal strain *Aspergillus niger* MTCC 281 and *Aspergillus flavus* MTCC 277 (% inhibition in the range of 47.7-52.8). While rest of the compounds such as **Va**, **Vc**, **Vd**, **Vf**, **Vi** and **VI** displayed moderate antifungal activity. Only one derivative expressed weak antifungal activity viz. **Vh**.

All the pyrazolyl amines (**Va-VI**) were also evaluated for antibacterial activity against the strains *Escherichia coli* NCTC 10418, *Staphylococcus aureus* NCTC 6571, *Pseudomonas aeruginosa* NCTC 10662 at concentration of 500 mg/ml in DMSO by cup plate method. A careful examination of Table revealed that most of molecules of series (**Va-VI**) exhibited moderate to weak antibacterial activity against the test organism *E. coli* NCTC 10418, *Staphylococcus aureus* NCTC 6571 at the conc. of 500 µg/ml. Compounds were completely inactive against the strain *Pseudomonas aeruginosa* NCTC 10662.

CONCLUSION

The study provides successful one-pot synthesis 4-(substituted-anilinomethyl-3-(6-methoxy-2-naphthyl)-1-phenyl-1H-pyrazols (**Va-VI**) using NaBH_4/I_2 as reducing agent. The process offers advantages such as good yield, simple procedure, use easily available reagents etc. The results of antimicrobial screening suggest that compounds were more active towards the fungal strains compared to the bacterial strains, In the series compound **Vg**, **Vj**, **Vk**, showed excellent antifungal activity against the fungal strain *Aspergillus niger* MTCC 281 and *Aspergillus flavus* MTCC 277 (% inhibition in the range of 47.7-52.8).

Acknowledgment: The author (NG) expresses sincere thanks to Maharaja Surajmal Institute of Pharmacy, Janakpuri, New Delhi for providing necessary facilities. Thanks are due to CDRI, Lucknow, India and IIT for recording spectral data.

REFERENCES

1. S. Sugiura, S. Ohno, O. Ohtani, K. Izumi, T. Kitamikado, H. Asai, K. Kato, M. Hori, M. Fujimura. *J. Med. Chem.*, **20**, 80 (1977).
2. T.D. Penning, J.J. Talley, S.R. Bertenshaw, J.S. Carter, P. W. Collins, S. Docter, M.J. Graneto, L.F. Lee, J.W. Malecha, J.M. Miyashiro, R.S. Rogers. *J. Med. Chem.*, **40**, 1347 (1997).
3. A.A. Bekhit, H.M. Ashour, A-D. Bekhit, S.A. Bekhit. *Med. Chem.*, **05**, 103 (2009).
4. A. Tanitame, O. Keiko, Y. Hiyama, S. Kenji, et. al.. *J. Med. Chem.*, **47**, 3693 (2004).
5. A.M. Gilbert, Y. Yang, A. Failli, J. Shumsky, A. Severin, G. Singh, et al., e. *J. Med. Chem.*, **49**, 6027 (2006).
6. L.M. Bonesi, G.A. Statti, S. Michel, F. Tillequin, F. Menichini. *Bioorg. Med. Chem. Lett.*, **20**, 1990 (2010).
7. A. Monge, I. Aldana, T. Alvarez, M.J. Losa, M. Font, E. Cenarruzabeiti, B. Lasheras, D. Frechill, E. Castiella, E. Fernandez-Alvarez. *Eur. J. Med. Chem.*, **26**, 655 (1991).
8. M. Anzaldi, A.C. Macciò, M. Mazzei, R. Gangemi, P. Castagnola, M. Miele, C. Rosano, M. Viale. *Eur. J. Med. Chem.*, **46**, 5293 (2011).
9. X. Li, X. Lu, M. Xing, X. Yang, T. Zhao, H. Gong, H. Zhu. *Bioorg. Med. Chem. Lett.*, **22**, 3589 (2012).
10. M. Abdel-Aziz, G-D. Abu-Rahma, A.A. Hassan. *Eur. J. Med. Chem.*, **44**, 3480 (2009).
11. O. Ruhoğlu, Z. Ozdemir, U. Caliş, B. Gümüşel, A.A Bilgin. *Arzneimittel forschung.*, **55**, 431 (2005).
12. B. Cottineau, P. Toto, C. Marot, A. Pipaud, J. Chenault. *Bioorg. Med. Chem. Lett.*, **19**, 2105 (2002).
13. D. Wu, F. Jin, W. Lu, J. Zhu, C. Li, W. Wang, Y. Tang, H. Jiang, J. Huang, G. Liu, J. Li. *Chem. Biol. Drug Des.*, **79**, 897 (2012).
14. <http://www.accessdata.fda.gov/scripts/cder/drugsatfda/index.cfm?fuseaction=SearchDrugDetails>
15. S. Bawa, H. Kumar. *Indian J. Heterocycl. Chem.*, **14**, 249 (2005).
16. S. Bawa, S. Kumar, S. Drabu, B.P. Panda, R. Kumar. *J. Pharm. Bioall. Sci.*, **01**, 32 (2009)
17. Kumar S, Bawa S, Kaushik D, Panda BP. *Arch Pharm Chem Life Sci.*, **344**, 474 (2011).

ЕДНОСТАДИЙНА СИНТЕЗА НА 4- (ЗАМЕСТЕН-АНИЛИНОМЕТИЛ-3- (6-МЕТОКСИ-2-НАФТИЛ) -1-ФЕНИЛ-1H-ПИРАЗОЛИ ПОСРЕДСТВОМ NaBH₄ / I₂ И ТЯХНАТА АНТИМИКРОБНА ОЦЕНКА

Н. Гоел¹, С. Кумар², С. Бава^{2*}

¹ *Институт по фармация „Махараджа Сураджмал“, (филиал на университет GGSIP, Ню Делхи) С-4, Джанакпури, Ню Делхи*

² *Катедра по фармацевтична химия, Фармацевтичен факултет, Джамия Хамдард, Ню Делхи*

Получена на 6 януари 2014 г.; Ревизирана на 4 март 2014г.

(Резюме)

Серия от съединения (Va-VI) бяха синтезирани чрез директно редуцивно аминирание на 3- (нафтален-2-ил) -1-фенил-1 H-пиразол-4-карбалдехид с различни заместени ароматни амини, използвайки NaBH₄ в присъствието на I₂ като редуциращ агент. Реакцията се извършва в безводен метанол при неутрални условия и стайна температура. Структурите на синтезираните съединения (Va-VI), са определени въз основа на IR, ¹H и ¹³C-ЯМР и мас спектрални данни. Всички 4- (заместен-анилинометил-3- (2-нафтил) -1-фенил-1H-пиразолови производни (Va-VI) бяха тествани ин витро за противогъбична и антибактериална активност срещу различни гъбични и бактериални щамове. Повечето от съединенията показват значителна противогъбична активност, но лоша антибактериална активност срещу тестваните щамове. Съединенията V_g, V_j и V_k, показват отлична противогъбична активност срещу гъбичните щам *Aspergillus Niger* MTCC 281 и *Aspergillus flavus* MTCC 277 (% инхибиране в обхвата от 47.7-52.8).

High photocatalytic activity in nitrate reduction by using Pt/ZnO nanoparticles in the presence of formic acid as hole scavenger

A. Fallah Shojaei*, F. Golriz

Department of Chemistry, Faculty of Science, University of Guilan, P.O. Box 1914, Rasht, Iran

Received January 26, 2014; revised July 23, 2014

In this work, the photocatalytic reduction of nitrate in water was examined using zinc oxide loaded with platinum nanoparticles and formic acid as a hole scavenger (electron donor). The data obtained in the structural characterization and in the nitrate photoreduction experiments showed that 1wt% Pt/ZnO photocatalyst had the highest photocatalytic activity and selectivity toward nitrogen. Selectivity and conversion were higher than 98 and 70%, respectively. This system effectively promoted the photocatalytic reduction of NO_3^- to N_2 . Nitrite ions were not observed during the reaction and a negligible amount of ammonia was formed.

Keywords: Pt/ZnO; Hole scavenger; Formic acid; Nitrate; Photocatalytic reduction; Zinc oxide.

INTRODUCTION

Increased groundwater contamination by nitrate has received attention all over the world [1–3] due to the intensive use of fertilizers from agricultural activities [4, 5], the disposal of massive amounts of livestock manure [5], and the discharge of poorly treated wastewater [6]. Nitrate has been known to be hazardous to human health, which can cause methaemoglobinaemia and blue baby syndrome, fatal disease to babies under 6 months of age [7], and leads to the formation of carcinogenic nitrosamine in the human body [8]. In the efforts to control nitrate contamination in groundwater, United States Environmental Protection Agency (USEPA) set regulations on maximum contaminant level of nitrate at 10 mg/L nitrate-nitrogen (NO_3^- -N) [9]. Remediation technologies such as advanced biological nutrient treatment, electro-kinetic denitrification, reverse osmosis, and chemical reduction [10–15] have been developed to solve compelling issues of nitrate contamination in groundwater. However, these technologies suffer from sludge generation [11], high operational cost [12–14], and undesirable by-product formation [15].

Catalytic reduction of nitrate to harmless nitrogen gas has drawn attention as a promising alternative for nitrate treatment since Vorlop and Tacke [16] demonstrated the effectiveness of bimetallic catalysts in 1989. Enormous efforts to find out the most effective metal combination in catalytic nitrate reduction have been made by

loading Cu, Sn, Ni, Pd, Pt, Au, and Rh on diverse supporting materials [17–21]. At present, supported catalysts have been investigated and widely applied in many industrial fields [22–24].

Photocatalytic denitrification (photoreduction of nitrate to innocuous nitrogen gas through the action of a photocatalyst) is an economically viable process having also environmental benefits compared to other treatments available for the removal of nitrogen from aqueous media, such as advanced filtration and biological denitrification [25–27].

There are several reports on the successful photoreduction of nitrate promoted by metal catalysts supported on TiO_2 [28–36], SnO_2 [37], and ZnS [38, 39]. However, there are limited reports on the photocatalytic reduction of nitrate over a metal-loaded ZnO catalyst system so far [40–41].

In our previous published research works [42–48], we synthesized several catalytic systems and described the catalytic activities of the prepared catalysts in different reactions. In the present work, we were interested in exploring the utility of Pt/ZnO (NPs) as a reusable, economical and commercially available catalyst for the photoreduction of nitrate to nitrogen gas. The effect of different operating parameters such as content of metal and hole scavenger, catalyst amount and initial nitrate concentration, was investigated.

EXPERIMENTAL

Instrumentation

X-ray diffraction (XRD) patterns were obtained on a Philips pw 1840 powder diffractometer using $\text{Cu K}\alpha$ ($\lambda = 1.54178\text{\AA}$) radiation (2θ from 0° to 70°)

* To whom all correspondence should be sent:
E-mail: a.f.shojaie@guilan.ac.ir

at a scanning rate of 2.4°/min. Transmission electron microscopy (TEM) was carried out on a Philips CM-10 model instrument operating at 100 keV. Before photographing, the samples were dropwise added onto the surface of a carbon membrane and dried at ambient temperature.

Preparation of the photocatalyst Pt/ZnO (NPs)

Pt-doped ZnO nanoparticles were prepared by a direct precipitation method using zinc acetate dihydrate ($\text{Zn}(\text{CH}_3\text{COO})_2 \cdot 2\text{H}_2\text{O}$) and platinum (IV) chloride (PtCl_4) as the precursors of zinc and platinum, respectively. First, $\text{Zn}(\text{CH}_3\text{COO})_2 \cdot 2\text{H}_2\text{O}$ and Na_2CO_3 were dissolved separately in distilled water to obtain 0.5 mol/L solutions. Zinc acetate solution (50 ml, 0.5 mol/L) was slowly added to 50 ml of 0.5 mol/L Na_2CO_3 solution under vigorous stirring. Afterwards, platinum (IV) chloride in the required stoichiometry was slowly added to the mix under stirring for 30 min yielding a yellow precipitate. The latter was filtered, rinsed repeatedly with distilled water and washed twice with ethanol. The resultant solid product was dried at 100°C for 12 h and calcined at 300°C for 2 h. ZnO nanoparticles were prepared by the same procedure without the addition of platinum (IV) chloride solution. The doping concentrations of Pt are expressed in wt%.

Photocatalytic reduction test

In order to investigate the effect of platinum doping on the photocatalytic activity of ZnO, the photocatalytic reduction of nitrate was carried out in a ZnO or Pt/ZnO suspension under UV irradiation. The photocatalytic experiments were performed in a reactor at ambient temperature and atmospheric pressure. A 400 W high-pressure mercury lamp was used as a light source. The reaction suspensions were prepared by adding 25 mg of catalyst and 3 ml of 0.008 M formic acid to 25 ml of aqueous nitrate solution with an initial NO_3^- concentration of 60 mg/l. Prior to illumination, the reaction suspension was stirred in the dark for 15 min to ensure adsorption/desorption equilibrium. The aqueous suspension containing nitrates and photocatalyst was then irradiated by UV. The reaction mixture was magnetically stirred to maintain the catalyst in suspension. The sample solution was periodically withdrawn and the powdered catalyst was immediately separated from the aqueous phase by centrifugation. The remaining solution was divided in three portions and the concentration of nitrate, nitrite and ammonium was determined by measuring the absorption in the

presence of brucine, Griess and Nessler reagents at 410, 520, and 392 nm, respectively, as shown in Figs. 1 - 3. At the end of the reaction, no nitrite ions and very small amounts of ammonium ions were detected, therefore, the selectivity towards nitrogen according to Eq. 1 was estimated to be about 100%. [49-51].

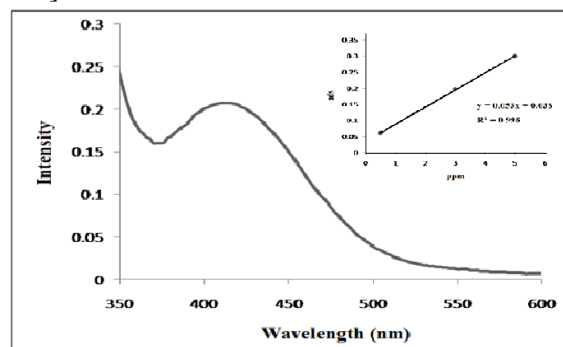


Fig. 1. Absorption spectrum and calibration curve of brucine - nitrate at 410 nm

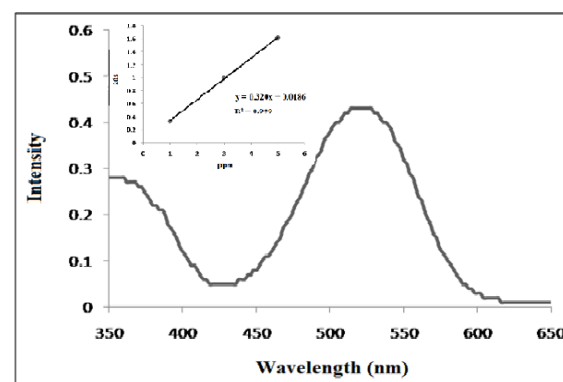


Fig. 2. Absorption spectrum and calibration curve of Griess-nitrite at 520 nm

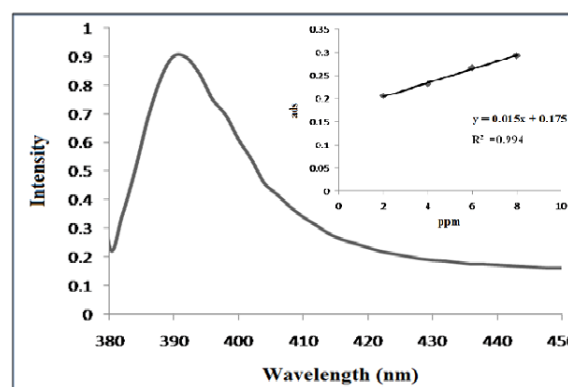


Fig. 3. Absorption spectrum and calibration curve of Nessler - ammonium at 392 nm

Determination of catalytic activity and selectivity

The catalytic activity for the reduction of nitrate is defined as the amount of reduced nitrate ions per time and catalyst weight ($\text{mmol g}_{\text{cat}}^{-1} \text{h}^{-1}$). The selectivity to nitrogen is defined as the ratio of the

amount of formed nitrogen to the amount of reduced nitrate, based on the assumption that no products other than nitrite and ammonia are formed. N_2 selectivity is calculated according to Eq. (1):

$$S_{N_2} = \frac{[\text{nitrate}]_0 - [\text{nitrate}]_t - [\text{nitrite}]_t - [\text{ammonia}]_t}{[\text{nitrate}]_0 - [\text{nitrate}]_t} \times 100 \quad (1)$$

where S_{N_2} is N_2 selectivity, $[\text{nitrate}]_0$ is the initial nitrate concentration, and $[\text{nitrate}]_t$, $[\text{nitrite}]_t$ and $[\text{ammonia}]_t$ are the residual concentrations of nitrate, nitrite and ammonia after reaction for 1 h, respectively [31].

RESULTS AND DISCUSSION

Photocatalytic nitrate reduction over metal-modified catalysts

Various metal-modified catalysts were tested for the reduction of nitrate to nitrogen. It can be seen that under the given conditions (initial concentration of nitrate = 60 ppm, photocatalyst = 25 mg and reaction time = 60 min), pure ZnO has low activity (18.5%). The experimental results shown in Fig. 4 demonstrate that after 60 min of reaction time, the concentration of nitrate in all suspensions was reduced. Among these catalysts, 1 wt% Pt/ZnO showed the maximum photocatalytic activity and thereby was selected as a model catalyst in this study.

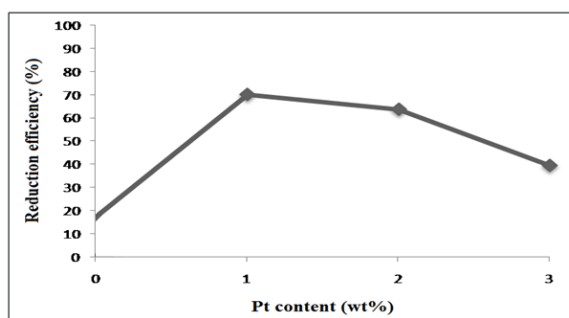


Fig. 4. Influence of metal content on the photocatalytic reduction activity of nitrate ions over Pt/ZnO catalysts (initial concentration of nitrate = 60 ppm, photocatalyst = 25 mg and reaction time = 60 min).

Effect of total metal content

As shown in Fig. 4, high metal content (2 wt% and 3 wt%) is not beneficial to the reduction of nitrate and the optimum reduction is obtained at a metal content of 1 wt%. This suggests that active atomic arrangement and active particle size on the surface of the catalyst may have a greater influence on the removal of nitrate than the amount of loaded

metal. Several research groups have suggested that, at a metal content higher than the optimal one, the overaccumulation of electrons on the metal deposits could attract photogenerated holes to the metal sites [52, 53]. This may promote the recombination of charge carriers, the metal deposits reversely behaving as recombinant centers. In addition, higher surface loadings of metal deposits may decrease the catalytic efficiency of the semiconductor due to the reductive availability of semiconductor surface for light absorption and pollutant adsorption [54].

XRD analysis of 1 wt% Pt/ZnO photocatalyst

Fig. 5 shows the XRD pattern of 1 wt% Pt/ZnO. There are two sets of diffraction peaks for each sample, indicating that the synthesized samples are composite materials. As shown, the diffraction peaks at $2\theta = 31.7^\circ$, 34.4° , and 36.2° are indexed to diffractions of hexagonal structured ZnO (wurtzite) (JCPDS Card No. 36-1451). The peaks located at $2\theta = 40.5^\circ$ and 47° are characteristic to diffractions of Pt [55]. XRD test shows the presence of ZnO and Pt phases in the samples. Its average crystal size is determined to be 41 nm according to the Debye-Scherrer formula ($L = 0.89\lambda/\beta\cos\theta$).

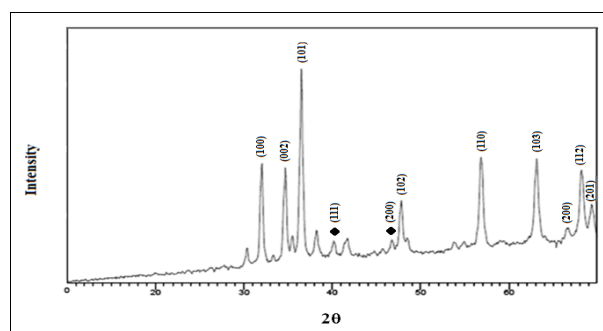


Fig. 5. XRD pattern of 1 wt% Pt/ZnO

TEM micrograph of 1 wt% Pt/ZnO photocatalyst

In order to further observe the morphology of ZnO and 1 wt% Pt/ZnO catalyst, TEM images of the catalysts were taken and representative photographs are shown in Fig. 6. TEM images show that the size of ZnO particles is larger than that of zinc oxide loaded with platinum nanoparticles and the size of most of the nanoparticles of 1 wt% Pt/ZnO is about 40-50 nm. The results are consistent with the results of XRD.

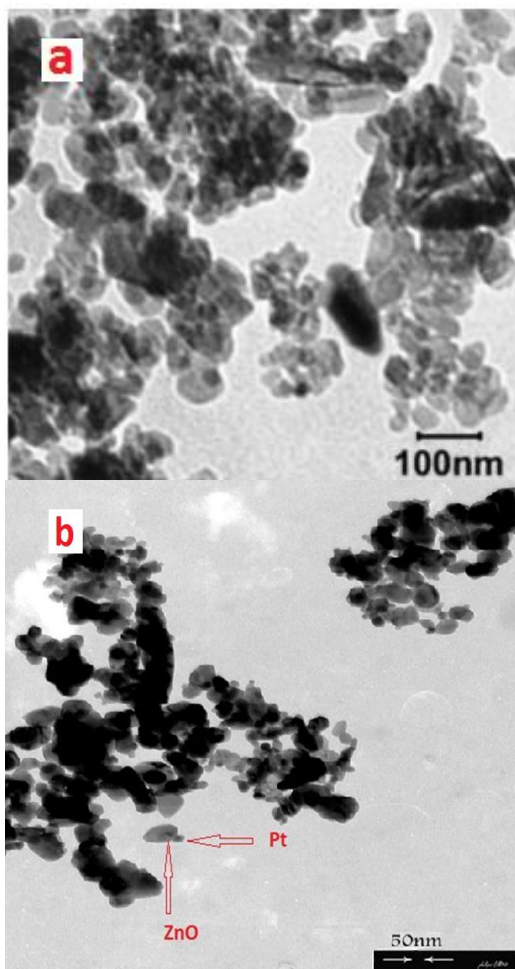


Fig. 6. TEM image of a) ZnO b) 1 wt% Pt/ZnO

Effect of catalyst amount

As shown in Fig. 7, pure ZnO (0 % Pt) has low catalytic activity (18.5%) and the optimum catalyst amount for NO_3^- removal is 25 mg. However, further increase in catalyst dosage decrease the photo-degradation efficiency of nitrate. The photo-decomposition rates of pollutants are influenced by the active site and the photo-absorption of the catalyst used. Adequate loading of the semiconductor increases the generation rate of electron-hole pairs for promoting the degradation of pollutants. However, the addition of a high dose of the semiconductor decreases the light penetration through the photocatalyst suspension [56].

On the other hand, additional experiments were carried out to evaluate the efficiency of nitrate degradation by 1 wt% Pt/ZnO at higher initial nitrate concentrations (e.g., 100 ppm). The reduction of nitrate ions at concentrations of 60 and 100 ppm with 1 wt% Pt/ZnO with time is shown in Figure 8. The maximum percentages of nitrate removal from water were observed at 69.5% and 50% respectively.

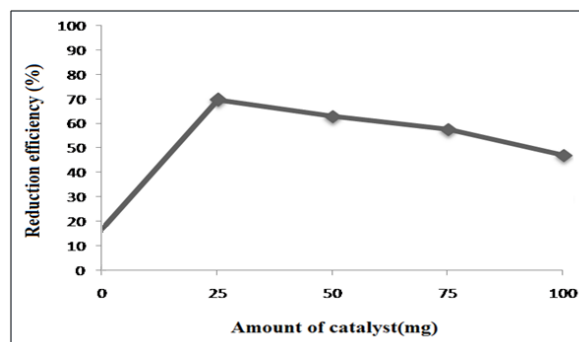


Fig. 7. Influence of catalyst amount on the photocatalytic reduction activity of nitrate ions over 1 wt% Pt/ZnO catalyst (initial concentration of nitrate = 60 ppm, reaction time = 60 min).

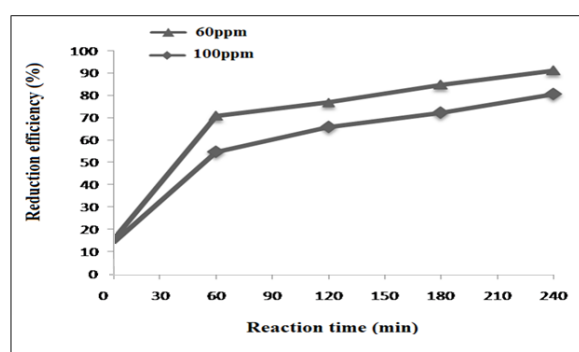


Fig. 8. Influence of initial nitrate concentration on the photocatalytic reduction activity over 1 wt% Pt/ZnO catalyst

Mechanism and role of Pt

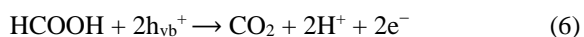
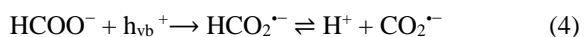
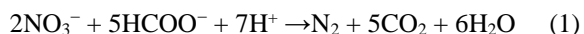
Loading a small amount of Pt (1 wt%) on ZnO leads to the enhancement of its photocatalytic activity. With 1 wt% Pt loading, the photocatalytic activity reaches a maximum. Increasing the amount of Pt loading to 3 wt% decreases the photocatalytic activity. Under UV irradiation, the electrons in the valence band of ZnO can be excited to their corresponding conduction band, thus, the efficient separation of photoinduced electrons and holes leads to the generation of photocurrent. Compared with the pure ZnO photocatalyst, loading a small amount of Pt on ZnO leads to an enhancement of its photocurrent. However, the further increase in the Pt loading to 3% results in a considerable decrease in its photocurrent. This observation reveals that the presence of excess Pt lowers the separation efficiency of photogenerated electrons and holes in the 3 % Pt/ZnO photocatalyst because the possibility of hole capture increases by the large number of negatively charged Pt particles on ZnO when Pt loading is above the optimum [57]. This process of hole capture probably takes place in a nonradiative pathway. Therefore, the lowest

photocatalytic activity of the 3 % Pt/ZnO photocatalyst is attributed to its lowest separation efficiency of photogenerated electrons and holes. This result indicates that the modification of ZnO with an appropriate amount of Pt can increase the separation efficiency of photogenerated electrons and holes in ZnO, which results in enhancement of its photocatalytic activity.

Effect of hole scavenger

When formic acid and nitrate are mixed in dark, no nitrate reduction occurs in the absence of a photocatalyst. Therefore, formic acid does not act as a direct reductant under these experimental conditions; it rather acts as a hole scavenger. It has been proved that a sacrificial reagent is necessary for the reduction of nitrate ions, and the different sacrificial reagents have distinct redox characteristics [58]. From Fig. 7 it can be seen that nitrate conversion is appreciably high when formic acid is used as the hole scavenger. Experimental parameters including pH, nitrate concentration, formate concentration, photocatalyst concentration, and metal loading were varied to demonstrate their effect on product selectivity. Under acidic conditions, nitrogen gas was the final product. However, under neutral pH conditions, only nitrite was formed [59].

In this work, the results have shown that the product was only nitrogen gas, so the reaction takes place according to Eq. (1). Consequently, two holes would have to be reduced by one formic acid molecule (Eq. 6). Formic acid first adsorbs on the surface of ZnO and disproportionates to a formate anion and a proton (Eq. 3). Formate reacts with one $h\nu^+$ to form the carbon dioxide anion radical, $CO_2^{\bullet-}$ (Eq. 4) After $CO_2^{\bullet-}$ forms, it reacts with an $h\nu^+$ (Eq. 5). So the total reaction for formic acid can be expressed as Eq. (6). [34, 60, 61]



CONCLUSIONS

In the present work, the enhancement of the photocatalytic activity of ZnO catalyst by doping with Pt was confirmed in the reaction of nitrate reduction in the presence of formic acid. It was found that a suitable amount (1 wt%) of the Pt

dopant effectively increases the photocatalytic activity of ZnO. The Pt particles doped on the ZnO surface behave as sites where electrons accumulate. Better separation of electrons and holes on the modified ZnO surface allows more efficient channeling of the charge carriers into useful reduction and oxidation reactions rather than recombination reactions. The experiments demonstrated that nitrate was degraded in aqueous Pt/ZnO suspension by more than 70% within 60 min. The reduction of nitrate eventually releases nitrogen gas.

Acknowledgement: The authors are grateful to the Research Council of the University of Guilan for the partial support of this study.

REFERENCES

1. B. T. Nolan, B. C. Ruddy, D. R. Helsel, *Environ. Tech.*, **31**, 2229 (1997).
2. A. Pintar, *Catal. Today*, **77**, 451 (2003).
3. D. C. Bouchard, M. K. Williams, R. Y. Surampalli, *J. Am. Water Works Ass.*, **84**, 85 (1992).
4. L.W. Canter, *Nitrates in Groundwater*, CRC Press, Boca Raton, 1996.
5. M. P. Maia, M. A. Rodrigues, F. B. Passos, *Catal. Today*, **123**, 171 (2007).
6. H. Constantin, M. Fick, *Water Res.*, **31**, 583 (1997).
7. L. Knobeloch, B. Salna, A. Hogan, J. Pstle, H. Anderson, *Environ. Health Persp.*, **108**, 675 (2000).
8. D. Majumdar, N. Gupta, *Indian J. Environ. Health*, **42**, 28 (2000).
9. H. H. Tsai, V. Ravindran, M.D. Williams, M. Pirbazari, *J. Environ. Eng. Sci.*, **3**, 507 (2004).
10. J. P. van der Hoek, P. J. M. van der Ven, A. Klapwijk, *Water Res.*, **22**, 679 (1988).
11. P. S. Barker, P. L. Dold, *Water Res.*, **30**, 769 (1996).
12. B. U. Bae, Y. H. Jung, W. W. Han, H. S. Shin, *Water Res.*, **36**, 3330 (2002).
13. A. C. A de Vooy, R. A. van Santen, J. A. R. van Veen, *J. Mol. Catal. A. Chem.*, **154**, 203 (2000).
14. J. J. Schoeman, A. Steyn, P. J. Scurr, *Water Res.*, **30**, 1979 (1996).
15. Y. H. Hwang, D. G. Kim, H.S. Shin, *J. Hazard. Mater.*, **185**, 1513 (2011).
16. K. D. Vorlop, T. Tacke, *Chem. Ing. Tech.*, **61**, 836 (1989).
17. Y. H. Liou, S. L. Lo, C. J. Lin, C. Y. Hu, W. H. Kuan, S. C. Weng, *Environ. Sci. Technol.*, **39**, 9643 (2005).
18. L. Calvo, M. A. Gilarranz, J. A. Casas, A. F. Mohedano, J. J. Rodriguez, *Indust. Eng. Chem. Res.*, **49**, 5603 (2010).
19. K. Daub, G. Emig, M. J. Chollier, M. Callant, R. Dittmeyer, *Chem. Eng. Sci.*, **54**, 1577 (1999).
20. U. Prüsse, K. D. Vorlop, *J. Mol. Catal. A. Chem.*, **173**, 313 (2001).
21. Y. H. Liou, C. J. Lin, S. C. Weng, H. H. Ou, S. L. Lo, *Environ. Sci. Technol.*, **43**, 2482 (2009).

22. R. Melendrez, G. Del Angel, V. Bertin, M. A. Valenzuela, J. Barbier, *J. Mol. Catal. A*, **157**, 143 (2000).
23. A. Pintar, J. Batista, *Catal. Today*, **53**, 35 (1999).
24. F. Epron, F. Gauthard, *J. Catal.*, **198**, 309 (2001).
25. W. Gao, R. Jin, J. Chen, X. Guan, H. Zeng, F. Zhang, N. Guan, *Catal. Today*, **90**, 331 (2004).
26. F. Zhang, R. Jin, J. Chen, C. Shao, W. Gao, L. Li, N. Guan, *J. Catal.*, **232**, 424 (2005).
27. N. Wehbe, M. Jaafar, C. Guillard, J. M. Herrmann, S. Miachon, E. Puzenat, N. Guilhaume, *Appl. Catal. A*, **368**, 1 (2009).
28. J. Anderson, A. Simultaneous, *Catal. Today*, **181**, 1 (2012).
29. R. Jin, W. Gao, J. Chen, H. Zeng, F. Zhang, Z. Liu, N. Guan, *J. Photochem. Photobiol. A: Chem.*, **162**, 585 (2004).
30. H. Kominami, H. Gekko, K. Hashimoto, *Phys. Chem. Chem. Phys.*, **12**, 15423 (2010).
31. L. Liyuan, X. Zhaoyi, L. Fengling, Sh. Yun, W. Jiahong, W. Haiqin, Zh. Shourong, *J. Photochem. Photobiol. A: Chem.*, **212**, 113 (2010).
32. K. T. Ranjit, T. K. Varadarajan, B. Viswanathan, *J. Photochem. Photobiol. A: Chem.*, **89**, 67 (1995).
33. F. X. Zhang, S. Miao, Y. L. Yang, X. Zhang, J. X. Chen, N. J. Guan, *J. Phys. Chem. C*, **112**, 7665 (2008).
34. K. Doudrick, T. Yang, K. Hristovski, P. Westerhoff, *Applied. Cat. B: Environ.*, **136**, 40 (2013).
35. K. T. Ranjit, B. Viswanathan, *J. Photochem. Photobiol. A: Chem.*, **108**, 79 (1997).
36. J. Sa, C. A. Aguera, S. Gross, J. A. Anderson, *Applied Catal. B: Environ.*, **85**, 192 (2009).
37. Y. N. Guo, J. H. Cheng, Y. Y. Hu, D. H. Li, *Applied Catal. B: Environ.*, **125**, 21 (2012).
38. O. Hamanoi, A. Kudo, *Chem. Lett.* **8**, 838 (2002).
39. K. T. Ranjit, R., Krishnamoorthy, B. Viswanathan, *J. Photochem. Photobiol. A: Chem.*, **81**, 55 (1994).
40. S. Park, H. J. Kim, J. S. Kim, K. Yoo, J. C. Lee, W. A. Anderson, J.H. Lee, *J. Nanosci. Nanotechnol.*, **7**, 4069 (2007).
41. K. T. Ranjit, T. K. Varadarajan, B. Viswanathan, *Indian J. Chem. A-Inorg. Bio-Inorg. Phys.Theore. Anal. Chem.*, **35**, 177 (1996).
42. H. F. Moafi, M. A. Zanjanchi, A. F. Shojaie *Mater. Chem. Phys.*, **139**, 856 (2013).
43. M. H. Loghmani, A. F. Shojaei, *J. Alloys Compd.*, **580**, 61 (2013).
44. M. A. Rezvani, A. F. Shojaie, M. H. Loghmani, *Catal. Commun.*, **25**, 36 (2012).
45. A. F. Shojaei, M. D. Rafie, M. H. Loghmani, *Bull. Korean Chem. Soc.*, **33**, 2748 (2012).
46. M. H. Loghmani, A. F. Shojaei, *Bull. Korean Chem. Soc.*, **33**, 3981 (2012).
47. H. F. Moafi, A. F. Shojaei, M. A. Zanjanchi, *Chem. Eng. J.*, **166**, 413 (2011).
48. A. F. Shojaei, M. H. Loghmani, *Chem. Eng. J.*, **157**, 263 (2010).
49. D. F. Boltz, J. A. Howell, "Colorimetric Determination of Non-metal", Wiley, New York, (1978).
50. Standard Methods for the Examination of Water and Wastewater, 14th Edition, Method 418A and 418B (1975), p 410.
51. Griess Reagent Kit for Nitrite Determination, *J. Biochem. Biophys. Res. Commun.* **161**, 420 (1989).
52. A. Sclafani, J. M. Herrmann, *J. Photochem. Photobiol. A: Chem.*, **113**, 181 (1998).
53. H. Tahiri, Y. A. Ichou, J. M. Herrmann, *J. Photochem. Photobiol. A: Chem.*, **114**, 219 (1998).
54. I. M. Arabatzis, T. Stergiopoulos, D. Andreeva, S. Kitova, S.G. Neophytides, P. Falaras, *J. Catal.*, **220**, 127 (2003).
55. P. Pawinrat, O. Mekasuwandumrong, J. Panpranot, *J. Catal. Commun.*, **10**, 1380 (2009).
56. A. Doongr, W. H. Chang, *J. Photochem. Photobiol. A: Chem.*, **116**, 221 (1998).
57. A. Sclafani, J. M. Hermann, *J. Photochem. Photobiol. A: Chem.*, **113**, 181 (1998).
58. M. Halmann, K. Zuckerman, *J. Chem. Soc., Chem. Commun.* 455 (1986).
59. J. R. Harbour, M. L. Hair, *J. Phys. Chem.*, **83**, 652 (1979).
60. D. M. Stanbury, *Adv. Inorg. Chem.*, **33**, 69 (1989).
61. L. L. Perissinotti, M. A. Brusa, M. A. Grela, *Langmuir*, **17**, 8422 (2001).

ВИСОКА ФОТОКАТАЛИТИЧНА АКТИВНОСТ НА НАНОЧАСТИЦИ ОТ Pt/ZnO ПРИ РЕДУКЦИЯТА НА НИТРАТИ В ПРИСЪСТВИЕ НА МРАВЧЕНА КИСЕЛИНА КАТО ДОНОР НА ЕЛЕКТРОНИ

А. Фалах Шоджаеи*, Ф. Голриц

Департамент по химия, Научен факултет, Университет „Гилан“, Рац, Иран

Постъпила на 26 януари, 2014 г., коригирана на 23 юли, 2004 г.

(Резюме)

В тази работа е изследвана фотокаталитичната редукция на нитрати във вода при използването на цинков оксид, зареден с наночастици от платина и мравчена киселина като донор на електрони. Получените данни за структурното охарактеризиране и фоторедукцията на нитрати показват, че фотокатализаторът с 1% (тегл.) Pt/ZnO има най-висока активност и селективност спрямо азота. Селективността и конверсията са по-високи от 98 и 70% съответно. Тази система повишава фотокаталитичната редукция на NO₃⁻ до N₂. Не са наблюдавани нитритни йони и пренебрежимо количество амоняк.

Crystal structure of *p*-[*N*-methyl(diethoxyphosphonyl)-(4-dimethylaminophenyl)]toluidine – a potential cytotoxic agent

I. Kraicheva^{*1}, B. L. Shivachev², R. P. Nikolova², A. Bogomilova¹, I. Tsacheva¹, E. Vodenicharova¹, K. Troev¹

¹*Institute of Polymers, Bulgarian Academy of Sciences, Sofia*

²*Institute of Mineralogy and Crystallography, Bulgarian Academy of Sciences, Sofia*

Received February 7, 2014; Revised August 21, 2014

The structure of an α -aminophosphonic acid diester, *p*-[*N*-methyl(diethoxyphosphonyl)-(4-dimethylaminophenyl)]toluidine, was determined by single-crystal X-ray diffraction. The compound is a racemic mixture and crystallizes as colourless prisms in a centrosymmetric manner in the monoclinic crystal system, space group $P2_1/c$, with two molecules in the asymmetric unit. One of the ethyl groups in one of the non-equivalent molecules exhibits a disorder. The bond lengths and angles, as well as the conformations of the two molecules, are comparable. Two intermolecular hydrogen bonds of the type N-H...O connect the non-equivalent molecules into dimers, and stabilize the crystal structure.

Keywords: single crystal X-ray diffraction analysis, aminophosphonic acid diesters, N-H...O hydrogen bonding.

INTRODUCTION

α -Aminophosphonic acid derivatives have attracted continuous interest owing to their pronounced biological activities. These compounds have been shown to serve as inhibitors of GABA receptors, inhibitors of various proteolytic enzymes like synthase, HIV protease, thrombin and serine proteases, and as inhibitors of bone resorption [1-4]. Aminophosphonates have been found to act as peptide mimics, antibiotics, antiviral and antitumor agents [5, 6]. They have been used as diagnostic imaging agents and contrast agents for magnetic resonance imaging [7].

The broad spectrum of pharmacological applications and utility of the aminophosphonic acid derivatives has stimulated extensive studies on various aspects of their chemistry and biochemistry and much attention has been paid to the investigation of their synthesis, structural and spectral characteristics, biological properties and relationship between structure and activity [8-10]. The biological activity of these compounds depends on their structural parameters and on the absolute configuration of the stereogenic α -carbon atom to phosphorus [11, 12]. Single-crystal X-ray analysis provides important information on the geometric parameters and the stereochemistry of the α -aminophosphonic acid derivatives; these studies establish the feasibility of hydrogen bonding that is essential for the interaction of the molecules with the biological systems [10, 13, 14]. Here we report

the crystal structure of the α -aminophosphonic acid diester *p*-[*N*-methyl(diethoxyphosphonyl)-(4-dimethylaminophenyl)]toluidine. The compound showed prominent cytotoxicity against the multi-drug-resistant cancer cell line HL-60/Dox [15].

EXPERIMENTAL

The title compound, $C_{20}H_{29}N_2O_3P$, was synthesized and tested *in vitro* for cytotoxicity against a panel of cell lines representative for some important types of human leukemia including the multi-drug-resistant model HL-60/Dox [15].

X-ray crystallography: A crystal of the title compound was mounted on a glass capillary and all data were collected at room temperature on an Oxford diffraction Supernova diffractometer using Mo-K α radiation ($\lambda = 0.71013 \text{ \AA}$) from a micro-focus source. The determination of cell parameters, data integration, scaling and absorption correction were carried out using the CrysAlisPro [16]. The structures were solved with ShelxS-2013 and refined using full-matrix least-squares on F^2 with the ShelxL-2013 package [17]. The N hydrogen atoms were positioned from difference Fourier map while all other hydrogen atoms were placed at idealized positions. The non-hydrogen atoms were refined anisotropically and hydrogen atoms were refined using the riding model.

ORTEP [18] drawing diagram of the molecular structures of the two molecules is shown in Fig.1.

* To whom all correspondence should be sent:
E-mail: igkraicheva@gmail.com

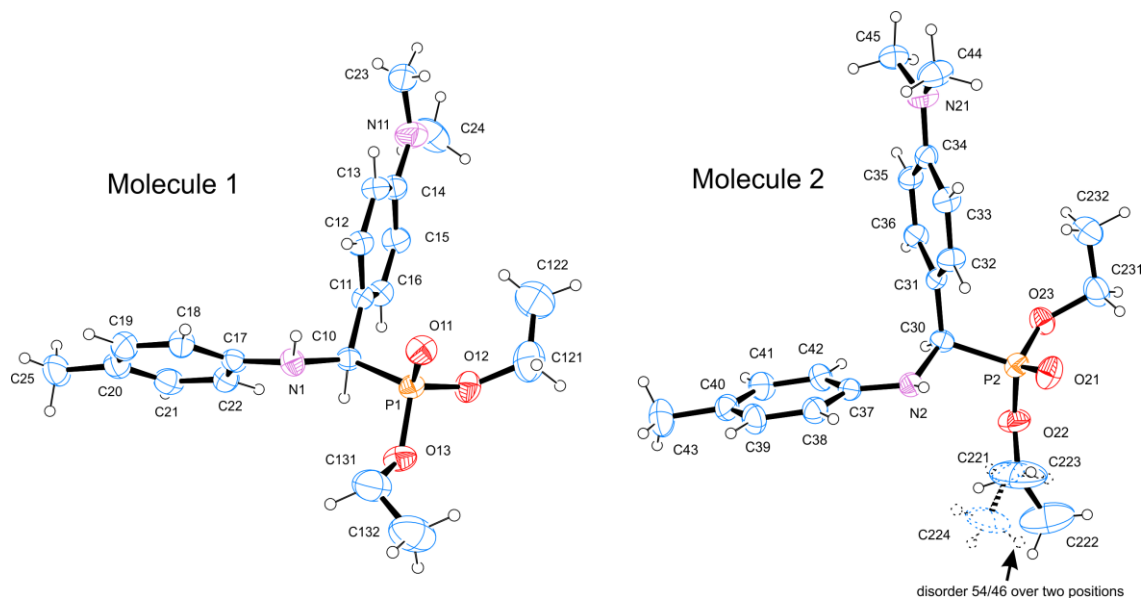


Fig. 1. ORTEP view and numbering scheme of the two molecules present in the asymmetric units of the title compound. H-atoms are presented with spheres of arbitrary size.

A summary of the fundamental crystal and refinement parameters is provided in Tables 1 and 2.

Table 1. Most relevant crystal data and refinement indicators

$C_{20}H_{29}N_2O_3P$	$F(000) = 1616$
$M_r = 376.42$	$D_x = 1.169 \text{ Mg m}^{-3}$
Monoclinic, $P2_1/c$	Melting point: 101–102 °C
Hall symbol: $-P 2ybc$	Mo $K\alpha$ radiation, $\lambda = 0.71073 \text{ \AA}$
$a = 18.1979 (12) \text{ \AA}$	Cell parameters from 1277 reflections
$b = 11.3948 (7) \text{ \AA}$	$\theta = 3.0\text{--}27.0^\circ$
$c = 22.3224 (13) \text{ \AA}$	$\mu = 0.15 \text{ mm}^{-1}$
$\beta = 112.506 (8)^\circ$	$T = 290 \text{ K}$
$V = 4276.3 (5) \text{ \AA}^3$	Prism, colourless
$Z = 8$	$0.23 \times 0.21 \times 0.15 \text{ mm}$
SuperNova, Dual, Cu at zero, Atlas diffractometer	7385 independent reflections
Radiation source: SuperNova (Mo) X-ray Source	3300 reflections with $I > 2\sigma(I)$
Mirror monochromator	$R_{\text{int}} = 0.103$
Detector resolution: 10.3974 pixels mm^{-1}	$\theta_{\text{max}} = 27.0^\circ$, $\theta_{\text{min}} = 3.0^\circ$
ω scans	$h = -18 \quad 21$
Absorption correction: multi-scan	$k = -14 \quad 12$
CrysAlisPro, Agilent Technologies,	$l = -28 \quad 25$
$T_{\text{min}} = 0.978$, $T_{\text{max}} = 1.000$	15622 measured reflections
Refinement on F^2	Primary atom site location: direct
Least-squares matrix: full	Secondary atom site location: from difference Fourier
$R[F^2 > 2\sigma(F^2)] = 0.079$	Hydrogen site location: mixed
$wR(F^2) = 0.188$	H-atom parameters constrained
S (GOF) = 0.99	$w = 1/[\sigma^2(F_o^2) + (0.0605P)^2]$, where $P = (F_o^2 + 2F_c^2)/3$
7385 reflections	$(\Delta/\sigma)_{\text{max}} < 0.001$
490 parameters	$\Delta\rho_{\text{max}} = 0.35 \text{ e \AA}^{-3}$
0 restraints	$\Delta\rho_{\text{min}} = -0.20 \text{ e \AA}^{-3}$
0 constraints	Extinction correction: none

Table 2. Hydrogen bond geometry (\AA and $^\circ$)

$D\text{---}H\cdots A$	$D\text{---}H$	$H\cdots A$	$D\cdots A$	$D\text{---}H\cdots A$
$N1\text{---}H1N1\cdots O21$	0.95	2.12	3.049 (5)	168
$N2\text{---}H1N2\cdots O11$	0.88	2.04	2.924 (4)	174

Crystallographic data (excluding structure factors) for the structural analysis were deposited at the Cambridge Crystallographic Data Centre, CCDC No 984798. A copy of this information may be obtained free of charge from: The Director, CCDC, 12 Union Road, Cambridge, CB2 1EZ, UK. Fax: +44 1223 336 033, e-mail: deposit@ccdc.cam.ac.uk, or www.ccdc.cam.ac.uk.

RESULTS AND DISCUSSION

The single-crystal X-ray study showed that the title compound crystallizes in a centrosymmetric manner (SG $P2_1/c$, No 14) with two molecules in the asymmetric unit. The bond lengths and angles of the two molecules are comparable. The aromatic ring systems present in the molecules are essentially planar. The values of the angle between the mean planes of the aromatic rings are comparable (86.19 and 81.32° for molecules 1 and 2, respectively). One of the ethyl groups in molecule 2 (O22, C221 and C222) exhibits a disorder over two positions, the major one being 54%. The values of the ADP of the second ethyl group (O23, C231 and C232) do not suggest a similar disorder over two positions.

The superposition of the two independent molecules of the title compound (Fig. 2) shows a slight rotation ($\sim 3\text{--}4^\circ$) of the 4-dimethylaminophenyl and toluidine moieties around the C-C and C-N bonds, respectively.

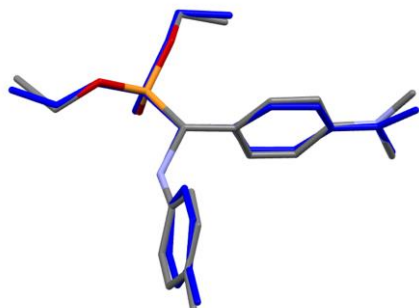


Fig. 2. Overlay of the two independent molecules present in the ASU.

The ethyl moieties are also slightly misaligned but this can be explained by their relative freedom of movement (expressed also as a disorder for O22, C221 and C222).

Having in mind the similarity (bond lengths and angles and also the superposition of the molecules) one should expect similar hydrogen bonding interactions. Indeed, two intermolecular N-H...O hydrogen bonds (Table 2 and Fig. 3) stabilize the molecular geometry of the two non-equivalent molecules.

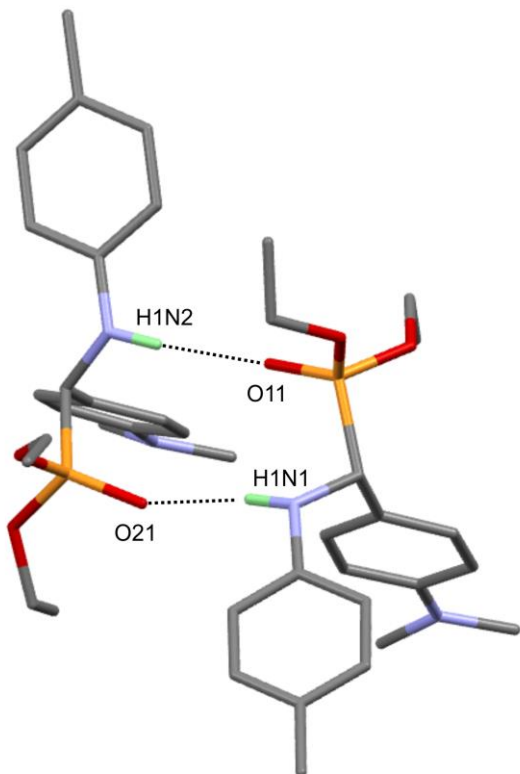


Fig. 3. Observed hydrogen bonding interactions in the title compound

Such type of hydrogen bonding interaction has also been observed in earlier reported crystal structures of two racemic anthracene-containing α -aminophosphonic acid diesters (dimethyl and diethyl) [19, 20], where both molecules form

“inversion” dimers linked by pairs of N-H...O hydrogen bonds.

Similarly to those compounds, the title compound crystallizes as a racemate. The three-dimensional packing (Fig. 4) also reveals that the crystal packing is governed by the hydrogen bonding interactions and thus the phosphonic and toluidine fragments are oriented toward each other producing hydrogen bonded dimers, while the 4-dimethylaminophenyl and ethyl moieties are oriented to minimize additional steric contacts.

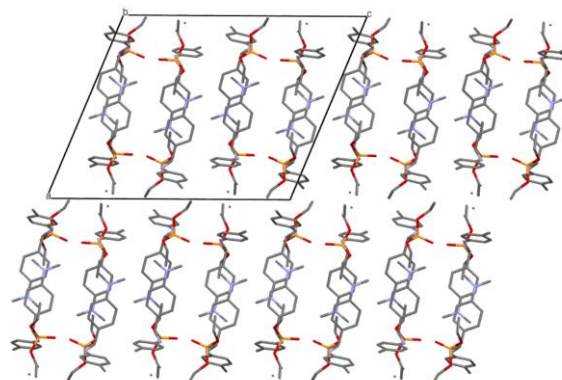


Fig. 4. Three-dimensional packing of the molecules of the title compound.

CONCLUSION

The compound *p*-[*N*-methyl (diethoxyphosphonyl)-(4-dimethylaminophenyl)] toluidine, exhibiting prominent cytotoxicity against a human leukemic multi-drug-resistant cell line, was characterized by single-crystal X-ray analysis. This revealed that the crystals are monoclinic, space group $P2_1/c$, with two molecules in the asymmetric unit. Important information on the structural parameters (bond lengths, bond angles and torsion angles, as well as intermolecular N-H...O hydrogen bonding) was obtained and a positional disorder of one of the ethyl groups was found. The obtained structural data of the compound could be useful in the further studies of its cytotoxicity mode of action.

Acknowledgement: Thanks are due to Bulgarian National Science Fund of the Ministry of Education and Science for the financial support: contract DTK-02/34(2009).

REFERENCES

- 1.L. Azema, R. Baron, S. Ladame, *Curr. Enzyme Inhibition*, **2**, 61 (2006).
- 2.M. Sienczyk, J. Oleksyszyn, *Curr. Med. Chem.*, **16**, 1673 (2009).
- 3.S.-L. Deng, I. Baglin, M. Nour, O. Flekhter, C. Vita, C. Cavé, *Phosphorus, Sulfur, and Silicon*, **182**, 951 (2007).

4. L. Rogers, I. Holen, J. *Translational Medicine*, **9**, 177 (2011).
5. P. Kafarski, B. Lejczak, *Curr. Med. Chem.-Anti-Cancer Agents*, **1**, 301 (2001).
6. L. Tušek-Božić, F. Frausin, V. Scarica, A. Furlani, *J. Inorg. Biochem.*, **95**, 259 (2003).
7. J. Galezowska, E. Gumienna-Kontecka, *Coordination Chem. Rev.*, **256**, 105 (2012).
8. J.-A. Ma, *Chem. Soc. Rev.*, **35**, 630 (2006).
9. M. Juribašić, L. Tušek-Božić, *J. Mol. Structure*, **924-926**, 66 (2009).
10. Y.-P. Hong, J.-A. Peng, D.-R. Cao, *Chinese J. Struct. Chem.*, **30**, 37 (2011).
11. Y. Belabassi, A. F. Gushwa, A. F. Richards, J.-L. Montchamp, *Phosphorus, Sulfur, and Silicon*, **183**, 2214 (2008).
12. R. A. Cherkasov, V. I. Galkin, *Usp. Khim.*, **67**, 940 (1998).
13. H. Gröger, Y. Saida, H. Sasai, K. Yamaguchi, J. Martens, M. Shibasaki, *J. Am. Chem. Soc.*, **120**, 3089 (1998).
14. Q. Wang, M. Zhu, R. Zhu, L. Lu, C. Yuan, S. Xing, X. Fu, Y. Mei, Q. Hang, *Eur. J. Med. Chem.*, **49**, 354 (2012).
15. I. Kraicheva, A. Bogomilova, I. Tsacheva, G. Momekov, K. Troev, *Eur. J. Med. Chem.*, **44**, 3363 (2009).
16. Agilent. Agilent Technologies, UK Ltd, Yarnton, England, 2011.
17. G. M. Sheldrick, *Acta Crystallographica Section A*, **64**, 112 (2008).
18. L. Farrugia, *Journal of Applied Crystallography*, **30**, 565 (1997).
19. I. Kraicheva, I. Tsacheva, E. Vodenicharova, E. Tashev, K. Troev, *Acta Cryst.*, **E 67**, o1980 (2011).
20. I. Kraicheva, I. Tsacheva, E. Vodenicharova, E. Tashev, K. Troev, *Acta Cryst.*, **E 67**, o2045 (2011).

КРИСТАЛНА СТРУКТУРА НА *p*-[*N*-МЕТИЛ(ДИЕТОКСИФОСФОНИЛ)-(4-ДИМЕТИЛАМИНОФЕНИЛ)]ТОЛУИДИН– ПОТЕНЦИАЛЕН ЦИТОТОКСИЧЕН АГЕНТ

И. Крайчева^{*1}, Б. Л. Шивачев², Р. П. Николова², А. Богомилова¹, И. Цачева¹,
Е. Воденичарова¹, К. Троев¹

¹Институт по полимери, Българска Академия на Науките, ул. „Акад. Г. Бончев“ бл. 103 А, 1113 София

²Институт по минералогия и кристалография, Българска Академия на Науките, ул. „Акад. Г. Бончев“ бл. 107, 1113 София

Постъпила на 7 февруари, 2014 г.; коригирана на 21 август, 2014 г.

(Резюме)

Структурата на диестер на α -аминофосфонова киселина, *p*-[*N*-метил(диетоксифосфонил)-4-(диметиламинофенил)]толуидин, беше определена чрез монокристален рентгено-дифракционен анализ. Съединението представлява рацемат и кристализира центросиметрично като безцветни призми от моноклинната система, в пространствена група $P2_1/c$, с две молекули в асиметричната клетка. Едната от етилните групи в една от нееквивалентните молекули показва безпорядък. Дължините на връзките и валентните ъгли, както и конформациите на двете молекули, са близки. Две междумолекулни водородни връзки от типа N-H \cdots O стабилизират структурата, свързвайки нееквивалентните молекули в димери.

Reversibility in monolithic dual membrane fuel cell

D. Vladikova^{1,*}, Z. Stoynov¹, A. Chesnaud², A. Thorel², M. Viviani³, A. Barbucci⁴, Ch. Nicoletta⁵, A. Bertei⁵, G. Raikova¹, P. Carpanese⁴, M. Krapchanska¹

¹ Institute of Electrochemistry and Energy Systems - Bulgarian Academy of Sciences, Sofia, Bulgaria

² Centre des Matériaux, Mines-ParisTech, Evry Cedex, France

³ Institute for Energetics and Interphases (IENI-CNR), National Research Council, Genova, Italy

⁴ Department of Chemical and Process Engineering (DICHeP), University of Genova, Genova, Italy

⁵ Department of Chemical Engineering, Università di Pisa, 2 Largo Lucio Lazzarino, 56126 Pisa, Italy

Received February 19, 2014; Accepted April 12, 2014

A promising direction in the development of solid oxide fuel cells (SOFC) is the reversible approach in which the device operates as a fuel cell and as an electrolyzer. A serious problem is the asymmetry of the system when operating in the two modes. A definitive breakthrough is the separation of the water production/consumption from the two electrodes. For fuel cell mode this idea has been realized in the innovative concept of the dual membrane fuel cell (dmFC). The cell consists of three independent chambers for hydrogen, oxygen and water. This work presents the reversibility studies of the dmFC. The first results are very promising. They show good reversibility without application of a special catalyst for enhancement of the water splitting.

Keywords: dual membrane fuel cell, fuel cell/electrolyzer, mechanistic model, reversible mode

INTRODUCTION

Fuel Cells and Hydrogen are part of the portfolio of technologies with expected contributions in the development of a sustainable and secure energy supply system in the medium and in the long-term strategic plans. The integration of a large share of renewable sources in the electricity production mix is one of the most crucial issues of the transformation into a low-carbon energy system. The development of efficient and cost competitive solutions for storing this renewable electricity in large quantities and for longer terms is one of the main priorities of the global energy policy. Hydrogen, as an energy carrier, is expected to play a key role in linking energy storage and power generation, in both transportation and stationary systems.

A promising direction in the development of high temperature fuel cells is the reversible approach in which the device operates as a solid oxide fuel cell (SOFC) and as an electrolyzer (SOEL), i.e. as an energy conversion/storage device. This mode of operation is very attractive for coupling with RES which usually require energy storage to meet specific power demands. However, still limited efforts are registered in reversibility studies [1,2].

SOEL and SOFC concepts are similar regarding materials and geometries. However, even if the systems are very close and can be operated in the same range of temperatures, optimum operation parameters may differ significantly, in particular in terms of current density, which is much higher in SOEL regime. In spite of the fact that the same global chemical reaction is used ($2H_2 + O_2 \leftrightarrow 2H_2O$), existing high temperature fuel cell systems and electrolyzers based on both SOFC and proton conducting pSOFC are strongly asymmetrical systems, with the production/consumption of water at the anode or cathode, respectively. This may cause implications concerning materials, microstructure, design, ageing, which introduces some constraints in the development of reversible systems.

A definitive breakthrough in the design would be the separation of the water production/consumption from the two electrodes where hydrogen and oxygen are generated and evacuated, without increase of the cell ohmic losses. This idea has been realized for the fuel cell mode in the innovative concept of the so called dual membrane fuel cell (dmFC), recently developed and proved [3-5]. The kernel of the new design is the introduction of a porous mixed ion conducting junction (central membrane CM) between the anode part of a pSOFC where protons are produced and the cathode part of a SOFC which produces oxide

* To whom all correspondence should be sent:

E-mail: d.vladikova@bas.bg

ions. The two types of ions meet in the CM, where water is produced and evacuated (Fig. 1). Thus the cell consists of three independent chambers for hydrogen, oxygen and water which could be separately optimized.

At electrolyzer operating conditions the steam should enter in the central membrane and split into protons and oxide ions. The two types of ions will propagate towards their respective electrode/electrolyte interfaces driven by potential/concentration gradients, where they will be transformed in the corresponding gases and evacuated through the porous electrodes structure.

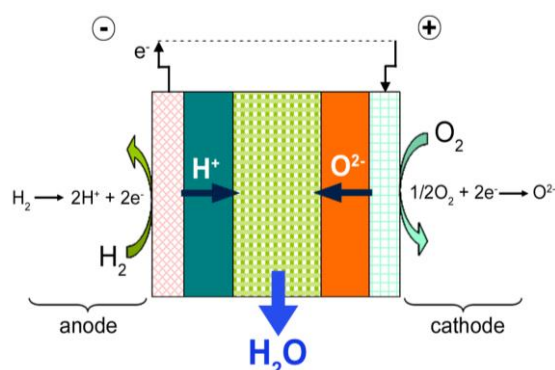


Fig. 1. Representation of the Dual membrane Fuel cell concept

The dmFC was proved [3,4] with cells in which the mixed conductivity of the CM was ensured by a composite of the two applied electrolytes: $\text{BaCe}_{0.85}\text{Y}_{0.15}\text{O}_{2.925}$ (BCY15) and $\text{Ce}_{0.8}\text{Y}_{0.15}\text{O}_{1.925}$ (YDC15). However, the application of composite structure decreases the effective triple phase boundary (BCY/YDC/pore) length and increases the ionic transport pathway tortuosity which causes enhancement of the CM internal resistance. Additional difficulties arise from the difference in the sinterability and thermal expansion of the two materials. The best solution towards optimization of the dmFC should be the replacement of the composite with a mixed ion conducting single ceramic phase.

BCY15 is well known in the literature as a good proton conductor [6,7]. Our conductivity measurements registered high proton and oxide ion conductivity at fuel cell operating temperatures. This result opens a pathway for the development of a new generation of dmFC in which YDC15 in the composite CM is replaced by BCY15. A total replacement of YDC with BCY, i.e. a “monolithic” design would strongly simplify the technology and the construction [8].

At electrolyzer mode the advantage of water splitting in the proton conducting material, which has natural properties to dissociate absorbed water,

is combined with absence of contact between the steam and the electrodes, and thus with no influence on their catalytic activity and thermo-mechanical stability, which is critical for the system durability. This work is focused on the development and first reversibility studies of the monolithic dual membrane fuel cell design. BCY15 pellets tested in water (temperature range 20-600°C) by differential thermal analysis and thermogravimetry combined with mass spectroscopy showed good chemical stability [9], which proved the applicability of this material for the performed investigations.

EXPERIMENTAL

The innovative part of the dmFC is the central membrane which has to combine high ionic (oxide ion and protonic) conductivity in the presence of sufficient porosity. The conductivity studies of the monolithic (porous BCY15) CM were successfully realized with the design of symmetrical CM supported half-cell Pt/BCY15porous/Pt. Fine powders ($d_{50} = 0.2 \mu\text{m}$) of $\text{BaCe}_{0.85}\text{Y}_{0.15}\text{O}_{2.925}$ (BCY15), prepared by the oxalate precipitation route, and delivered by Marion Technologies, were used. Previously estimated optimal porosity of about 30 v%, was ensured by applying graphite (TIMCAL, Switzerland) as pore former [10]. CM pellets with diameter ~ 2 cm and thickness ~ 2 mm were cold pressed and sintered at 1300°C for 5 hours. Platinum (Metalor) electrodes were painted and sintered in air following a procedure recommended by the producer. Since the studies concern the electrolytes part of the cell, including the CM, the application of Pt electrodes eliminates eventual influence of the electrodes composition and deposition technology on the electrolytes behaviour [11,12].

The electrolytes-central membrane assembly (ECMA) BCY15dense/BCY15porous/BCY15dense (ECMA) of monolithic button cells with diameter about 22 mm and thickness 1 to 2 mm was prepared by single stage cold pressing and sintering at 1300 °C for 5 hours (Fig. 2) and by platinum electrodes deposition.

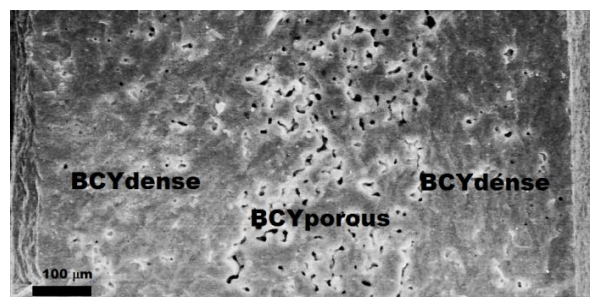


Fig. 2. SEM image of electrolytes-central membrane assembly (thickness 1,1mm)

The impedance measurements were performed on Solartron 1260 FRA in the temperature interval 100 – 800°C and frequency range from 10 MHz down to 0.01 Hz with a density of 5 points/decade and different modes and amplitudes of the AC signal. For registration and evaluation of the mixed ion conductivity, the half cell measurements were carried out at OCV in air (30 NmL/min) and in wet (3% H₂O) hydrogen (30 NmL/min). In order to acquire as much information as possible a wide frequency range was applied – from 10 MHz down to 10 mHz. During temperature scanning, the samples impedance changes from hundreds of megaohms down to milliohms. For data quality improvement different modes of operation were used [4]. At lower temperatures where the resistance of the sample is high the measurements were performed in potentiostatic regime with AC signal 20 – 200 mV, obeying the requirement for linearity. At high temperatures, where the sample's impedance is low, optimal galvanostatic mode was used. The impedance of the monolithic cells was measured in galvanostatic mode.

The low impedance at high operating temperatures increases the influence of the cell rig parasitic inductance and resistance and decreases the accuracy of the electrolyte resistance evaluation. For more precise analysis a procedure for parasitic inductance and resistance correction based on a previously developed algorithm [13,14] was applied.

RESULTS AND DISCUSSION

BaCe_{0.85}Y_{0.15}O_{2.925} is a good proton conductor [6,7]. Under humidified hydrogen atmosphere protonic defects are formed by dissociative absorption of water in the presence of oxygen

vacancies. Water vapor dissociates into a hydroxide ion which fills an oxide-ion vacancy, and a proton that forms a covalent bond with lattice oxygen, i.e. two proton defects are created stoichiometrically [14]. However, the presence of oxide-ion vacancies could be regarded as a precondition for oxide ion conductivity. Since mixed protonic and oxide ion conductivity is a phenomenon out of the scope of the classical SOFC and pSOFC applications the available information is an exception, rather than a rule [15,16]. For BaCe_{1-x}Y_xO₃, predominant protonic conductivity up to 700°C for x = 0.10 (BCY10) is reported, while for x = 0.25 (BCY25) mixed conductivity is found above 550°C [17]. For the development of the monolithic approach it was challenging to test the conductivity of BCY15 in hydrogen and in air. Impedance measurements on symmetrical half cells with dense and porous BCY15 (Fig. 3) confirmed high proton and oxide ion conductivity at operating temperatures. This result was a starting point for the development of the so called “monolithic concept”.

The replacement of the porous composite CM with a single phase of BCY15 should be *a priori* more efficient because it substitutes the triple phase boundary points with two-phase (ceramic/pore) boundary, decreases the pathway tortuosity and thus the cell ohmic resistance. Since solid-solid interfaces between different phases are expected to be the most resistive, their minimization by employing only one ionic conductor would be more effective. The 3-layered monolithic assembly - proton conducting electrolyte/mixed conducting porous CM/oxygen conducting electrolyte built from a single material with mixed conductivity should work as an oxide ion conductor in the

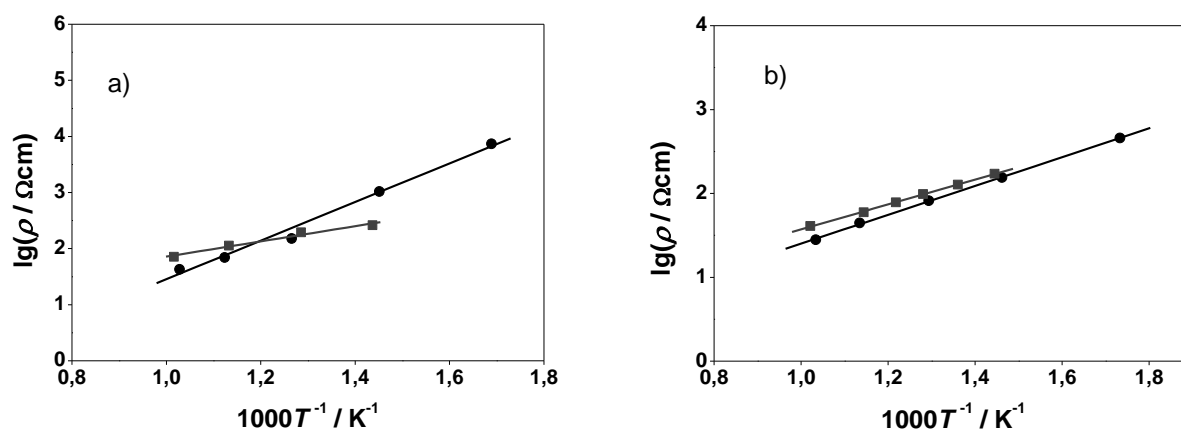


Fig. 3. Arrhenius plots of: a) dense BCY15; b) porous BCY15 measured in dry air (●) and wet hydrogen (■)

oxygen space, as a proton conductor in the hydrogen area and as a mixed conductor in the CM [8]. Experimental results obtained on the monolithic design are shown in Figure 4, which presents the current density/voltage and current density/power curves for cell with ECMA thickness of 1.1 mm (electrolyte I ~ 500 μm, CM ~ 200 μm; electrolyte II ~ 400 μm). The results are very promising - at 750°C power density of 86 mW/cm² is registered.

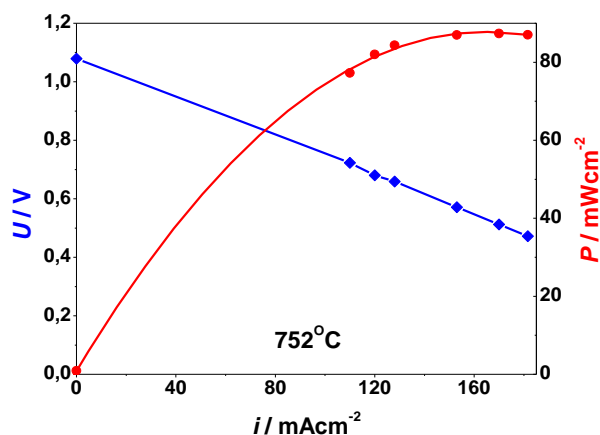


Fig. 4. Current density/voltage(■) and current density/power (●) curves of monolithic cell with thickness 1.1 mm (■) at gas flow 90% wet hydrogen and 90% oxygen

A separation of the ECMA resistance and the polarization resistance was performed based on the impedance measurements. If we accept that the polarization resistance is independent of ECMA thickness, a recalculation of the total cell resistance and the maximum power density can be done for thinner layers (Fig. 5). The results are very encouraging – the values exceed the best experimental results reported in the literature for pSOFC studies [18-20].

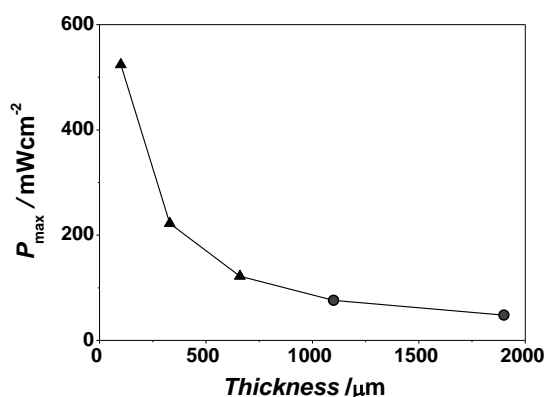


Fig. 5. Calculated values (▲) of the monolithic cell maximum power density (Pmax) for thinner configurations based on the measured data (●)

Since BCY15 has the natural property to split water (Eqn.1), it was supposed that the monolithic design would have a good performance as an electrolyzer. Water behavior studies in porous BCY15 membrane performed by complex permittivity measurements registered gigantic enhancement of the real component of the capacitance [21]. This phenomenon was connected with the formation of a semi-liquid dipole layer. The configuration of electrochemically active volumetric layer at the pores' surface in the CM would additionally improve the performance of the monolithic dmFC in electrolyzer mode [21]. For confirmation of this hypothesis, a specialized experiment was performed in which the cell was forced to behave periodically as a fuel cell and as an electrolyzer changing the operation mode. Under cathodic current the cell works as a fuel cell, filling the pores of the central membrane with the produced water. Under anodic current, the water from the pores splits to protons and oxide ions, propagating through the hydrogen and oxygen compartments, respectively.

The obtained results of operation in reversible mode are presented in Figure 6. They show good reversibility without application of a special catalyst or water vapour pressure for enhancement of the water splitting. The electrolyser mode of operation is characterized with lower overvoltage and thus with lower internal resistance. The performed experiment confirms the applicability of the monolithic dmFC design for operation in reverse mode.

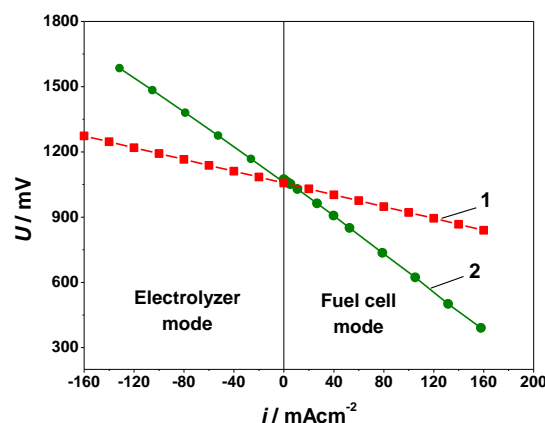
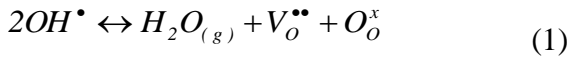


Fig. 6. Current density/voltage curves of monolithic dual membrane cell (● - measured) and central membrane (■ - calculated) in electrolyzer and in fuel cell operation mode at 700°C

The proof of the monolithic concept and its operation in reverse mode opens a new direction towards improvement of the performance. It is obvious that thinner cells should be produced.

However, in addition to the decrease of the electrolytes thickness, the CM should be optimized in respect to thickness and microstructure. For acceleration of the optimization towards operation in reverse mode, a mechanistic model of transport and reaction is under development. The first step concerns the CM. Since the CM is a porous layer of a mixed proton and oxide ion conductor, the model takes into account the following species, identified in Kröger-Vink notation: oxygen in the lattice (O_O^x), oxygen vacancies ($V_O^{\bullet\bullet}$), protonic defects (OH^\bullet) in the solid phase, gaseous water (H_2O) within the pores. The global reaction between these species is as follows [22]:



Eq. (1) represents a chemical reaction involving charged and uncharged species. Since no kinetic information about this reaction is available, an elementary kinetics is assumed:

$$r_w = \frac{k_d}{K} c_{OH}^2 - k_d p_w c_O c_{VO} \quad (2)$$

where r_w is the reaction rate, c_{oh} , c_o and c_{vo} are the concentrations per unit of perovskite cell of protonic defects, oxygen in the lattice and vacancies, p_w is the partial pressure of water in gas phase, k_d is the kinetic constant and K the equilibrium constant. It should be marked, that the simplified kinetic expression does not include the more complicated process of water adsorption/desorption and intermediate reaction steps, which were experimentally observed [21].

Assuming those simplifications, by imposing the electroneutrality of BCY and considering the total balance of oxygen sites, the concentration of vacancies and oxygen in the lattice can be expressed as a function of the concentration of protonic defects as $c_{VO} = (S - c_{OH})/2$ and $c_O = 3 - (S + c_{OH})/2$, where S is the dopant level [22] and c_{OH} is constrained between 0 and S .

Considering the reaction in Eq. (1), the balance equations on molar basis for protonic defects and vacancies along the thickness x of the CM result as follows:

$$\frac{dN_{OH}}{dx} = -2r_w a \quad \text{with} \quad N_{OH} = -D_{OH} f^{eff} \delta \frac{dc_{OH}}{dx} - \frac{F}{RT} D_{OH} f^{eff} \delta c_{OH} \frac{dV}{dx} \quad (3)$$

$$\frac{dN_{VO}}{dx} = r_w a \quad \text{with} \quad N_{VO} = -D_{VO} f^{eff} \delta \frac{dc_{VO}}{dx} - \frac{2F}{RT} D_{VO} f^{eff} \delta c_{VO} \frac{dV}{dx} \quad (4)$$

where the molar fluxes (i.e., N_{OH} and N_{VO}) account for diffusion and migration of the species [23]. The self-diffusivities, D_{OH} and D_{VO} , and the density of perovskite cells per unit volume δ are specific material properties and are taken from [24]. The morphological parameters, such as the effective conductivity factor f^{eff} and the specific surface area per unit volume a , are estimated from specific modeling studies on the basis of the particle size and porosity of the CM [25, 26].

The model is solved for the 2 dependent variables, the protonic defect concentration c_{OH} and the electric potential V , imposing, as boundary conditions, $N_{OH} = i/F$ and $N_{VO} = 0$ at the interface with the anodic electrolyte, $N_{OH} = 0$ and $V = 0$ at the interface with the cathodic electrolyte. The current density i is therefore imposed as a boundary condition: a positive current for fuel cell operation mode, a negative current for electrolysis operation mode. The solution of the model provides the value of the voltage at the anodic electrolyte interface, which is equal to the CM global overpotential.

Figure 6 shows the polarization curve of CM simulated for the operating conditions and CM geometry and microstructure of monolithic cell with thickness 1.1 mm. The polarization curve is less steep than the curve of the measured cell, since it includes in addition to the CM, the losses of electrodes and electrolytes. Although simplified in respect to water behavior in the CM, the first modeling results confirm the reversibility of the monolithic design and can be used for further development of the model, which should include the phenomena experimentally observed in this system.

CONCLUSIONS

The good performance of the monolithic design opens a new niche for the development of dual membrane-based configurations. The first reversibility results show that operation in both fuel cell and electrolyzer mode is a very promising direction for further work. Optimization of the CM geometry towards increase of water vapour evacuation/supply surface is necessary.

Acknowledgements: The research leading to these results has received funding from the European community's seventh framework programme (fp7/2007-2013) under grant agreement no 213389. powders were fabricated and supplied by Marion Technologies (MT).

The authors acknowledge also "Science and Business" BG051PO001/3.3-05-001 for the financial support that made possible the publication of this paper.

REFERENCES

1. Stuart PA, Unno T, Kilner JA, Skinner SJ. Solid oxide proton conducting steam electrolyzers. *Solid State Ionics* 2008;179:1120-1124.
2. Educhi U, Hatagishi T, Arai H. Power generation and steam electrolysis characteristics of an electrochemical cell with a zirconia- or ceria-based electrolyte. *Solid State Ionics* 1996;86-88:1245-1249.
3. Thorel AS, Abreu J, Ansar SA, Barbucci A, Brylewski T, Chesnaud A, et al. Proof of concept for the dual membrane cell: I. fabrication and electrochemical testing of first prototypes fuel cells, electrolyzers, and energy conversion. *J. Electrochem. Soc.* 2013;160(4):F360-F366.
4. Vladikova D, Stoyanov Z, Raikova G, Thorel A, Chesnaud A, Abreu J, et al. Impedance spectroscopy studies of dual membrane fuel cell. *Electrochim. Acta* 2011;56:7955-7962.
5. Thorel A. Cellule de Pile à Combustible Haute Température à Conduction Mixte Anionique et Protonique. In brevet français N° 0550696000, March 17th, 2005; international extension 06 726 255.0 in 2007 for Europe, USA and Japan.
6. Malavasi L, Fisher CAJ, Islam MS. Oxide-ion and proton conducting electrolyte materials for clean energy applications: structural and mechanistic features. *Chem. Soc. Rev.* 2010; 39: 4370-4387.
7. Ishihara T, Sammes NM, Yamamoto O. High Temperature Solid Oxide Fuel Cells: Fundamentals, Design and Applications. In S.C. Singhal and K. Kendall editors. Elsevier; 2003, p.83-117.
8. Thorel A, Vladikova D, Stoyanov Z, Chesnaud A, Viviani M, Presto S. In: Fuel cell with monolithic electrolytes membrane assembly, inventors. ARMINES patent #10 20120156573, June 17th, 2012.
9. Przybylski K, Prazuch J, Brylewski T, Amendola R, Presto S, Viviani M. Chemical stability study of Barium Cerate – based ionic conducting materials. In: Vladikova D, Stoyanov Z, editors. Proc. International Workshop Advances and Innovations in SOFCs, Sofia: Institute of Electrochemistry and Energy Systems; 2011, p. 62-71.
10. Krapchanska M, Vladikova D, Stoyanov Z, Chesnaud A, Thorel A, Raikova G, et al. Impedance Studies of Porous Electrolyte with Mixed Ion Conductivity. *Bulg Chem Commun.* 2013;45: in press.
11. Viviani M, Presto S, Barbucci A, Carpanese MP, Amendola R, Thorel AS, Chesnaud A, et al. MRS Proceedings1330;mrss11-1330-j05-04. doi:10.1557/opl.2011.1338.
12. Vladikova D, Stoyanov Z, Raikova G, Thorel A, Chesnaud A, Abreu J, et al. Electrochemical Impedance Spectroscopy – a Tool for Solid Oxide Fuel Cells Studies. Proc. 15th European Fuel Cell Forum 2011; Lucerne: Switzerland; Ch. 18/B1205, p. 29-41.
13. Stoyanov ZB, Vladikova DE. Electrochemical Impedance Spectroscopy. In: Garche J, Dyer C, Moseley P, Ogumi Z, Rand D, Scrosati B, editors. Encyclopedia of Electrochemical Power Sources, Vol 3. Amsterdam: Elsevier; 2009, p.632–642.
14. Iwahara H. Proton conducting ceramics and their applications. *Solid State Ionics* 1996; 86–88:9-15.
15. Iwahara H, Asakura Y, Katahira K, Tanaka M. Prospect of hydrogen technology using proton-conducting ceramics. *Solid State Ionics* 2004;168:299-310.
16. Bonanos N, Knight KS, Ellis B. Perovskite solid electrolytes: Structure, transport properties and fuel cell applications. *Solid State Ionics* 1995;79:161-170.
17. Suksamai W, Metcalfe IS. Measurement of proton and oxide ion fluxes in a working Y-doped BaCeO₃ SOFC. *Solid State Ionics* 2007;178:627-634.
18. Tsai CL, Schmidt VH. Fabrication, Performance, and Model for Proton Conductive Solid Oxide Fuel Cell. *J. Electrochem. Soc.* 2011;158(8):B885-B898
19. Meng G, Ma G, Ma Q, Peng R, Liu X. Ceramic membrane fuel cells based on solid proton electrolytes. *Solid State Ionics* 2007;178:697-703.
20. Guo Y, Ran R, Shao Z. A novel way to improve performance of proton-conducting solid-oxide fuel cells through enhanced chemical interaction of anode components. *Int J Hydrogen Energy* 2011;36:1683-1691.
21. Stoyanov ZB, Vladikova DE, Mladenova EA. Gigantic enhancement of the dielectric permittivity in wet yttrium-doped barium cerate. *J. Solid State Electrochem.* 2013;17:555-560.
22. Kreuer KD. Proton-conducting oxides. *Annu Rev Mater Res* 2003;33:333-359.
23. Bard AJ, Faulkner LR. *Electrochemical Methods: Fundamentals and Applications*. 2nd ed., New York:Wiley; 2001.
24. Coors GW. Protonic ceramic steam-permeable membranes. *Solid State Ionics* 2007;178:481-485.
25. Bertei A, Nucci B, Nicoletta C. Microstructural modeling for prediction of transport properties and electrochemical performance in SOFC composite electrodes. *Chem. Eng. Sci.* 2013;101:175-190.
26. Bertei A, Nucci B, Nicoletta C. Effective transport properties in random packings of spheres and agglomerates. *Chem. Eng. Trans.* 2013; 32:1531-1536.

ОБРАТИМОСТ В ДВОЙНО МЕМБРАННА ГОРИВНА КЛЕТКА

Д. Владикова^{1,*}, З. Стойнов¹, А. Чесно², А. Торел², М. Вивиани³, А. Барбучи⁴, К. Николела⁵, А. Бертей⁵,
Г. Райкова¹, П. Карпанезе⁴, М. Кръпчанска¹

¹ *Институт по електрохимия и енергийни системи "Акад. Е. Будевски" – БАН, ул. „Акад. Г. Бончев“, бл. 10, 1113, София, България*

² *Център по материалознание, Миньо – Тех Париж, ВР 87, 91003, Еври, Франция*

³ *Институт по енергетика и интерфейс, Национален съвет за научни изследвания, Генуа, Италия*

⁴ *Катедра по инженерна химия, Университет на Генуа, Генуа, Италия*

⁵ *Катедра по инженерна химия, Университет на Пиза, бул. „Лучо Лазарино“ №2, 56126 Пиза, Италия*

Получена на 19 февруари 2014 г.; приета на 12 април 2014 г.

(Резюме)

Една от перспективните посоки в по-нататъшното развитие на горивните клетки е тяхната работа в обратими режим, при който устройството работи като горивна клетка и като електролизьор. Един от сериозните проблеми е асиметрията на системата при работа в двата режима. Стъпка напред е възможността за получаване или разлагане на водата извън електродите. В режим на горивна клетка тази идея бе реализирана в иновативната концепция за двойно мембранна горивна клетка (ДМГК), която се състои от три независими камери за водород, кислород и вода. Настоящата работа представя изследвания на обратимостта в ДМГК. Първите резултати са много обещаващи. Те показват добра обратимост без прилагане на специален катализатор за разлагането на водата.

Relationships between particle size distribution and organic carbon of soil horizons in the Southeast area of Turkey

E. Sakin*, E. D. Sakin

Department of Soil Science and Plant Nutrition, Faculty of Agriculture University of Harran, 63040 Urfa, Turkey

Received February 17, 2014; revised March 20, 2014

The interdependent relationships between soil organic carbon and texture within the soil profile are little known. In order to determine this relationship, carbon and texture analyses were carried out on soil samples from Harran Plain. Soil samples were taken from 16 profiles (3 replications) in 1 m soil depth; all samples were taken from the same climate, vegetation and topography. Soil organic carbon (SOC) concentration was found to be directly related to soil texture at all depths. In statistical analysis ($p < 0.001$), the strongest relationship was found between clay ($R^2=96.0$) and silt ($R^2=95.0$). The relationship between sand and SOC was determined as ($R^2=65.46$). A very strong relationship was found between the organic carbon (OC) present in the soil and the texture in Harran Plain soils. The findings indicated that, in practice, areas containing low carbon should be preferred for use in carbon storage rather than areas containing high carbon stocks.

Keywords: carbon cycle, soil texture, soil organic carbon

INTRODUCTION

Soil texture (silt+clay+sand) protect soil organic matter (SOM) from being decomposed by physical, chemical and biological mechanisms (Six et al., 2002; Krull et al., 2003). It was suggested that chemical stabilization of organic molecules takes place *via* mineral-organic matter bonds from the start (Gonzalez and Laird, 2003). It was found that soil organic matter comprises approximately 60% of continental carbon pools and is generally very sensitive to agricultural land management (West and Post, 2002). It is suggested that agricultural practices resulted in the release of 55 Pg C from soil to the atmosphere in the 19th and 20th centuries (Paustian et al., 2000). When perennial vegetation constitutes agricultural areas, SOM accumulates, and thus a potential is created for atmospheric C sequestration (Post and Kwon, 2000; Follett, 2001). However, the factors affecting the importance, ratio and type of this accumulation are still not known (McLauchlan, 2006). The factors affecting soil formation for long periods, such as time – climate periods, organisms, relief and parent materials, can affect soil organic carbon accumulation (Jenny, 1941). Studies of the different pasture vegetation of North American Great Plains showed that organisms had minimum effect on SOC pools and accumulation rates (Vinton and Burke, 1997). Other studies indicated that parent material variations, different soil texture classes or clay concentrations are important variables in SOC

accumulation ratio and C sequestration (McLauchlan, 2006).

According to some evidence, clay concentration affects SOC accumulation in different ratios. It was found that maximum and medium SOC increased with increasing clay content in soil (Nichols, 1984; Burke et al., 1989). However, this relationship could not be generalized as SOC was sometimes much more strongly related to other factors in comparison to clay (Percival et al., 2000; Krull et al., 2003). The relationship between clay concentration and SOC content was expressed to be strong (at a sufficient level) according to SOM models such as Century (Parton et al., 1987) and RothC (Jenkinson, 1990). As clay concentration increases, SOM weathering decreases. It was found that, if other factors were fixed, as clay concentration increased, SOC accumulated faster (Jenkinson, 1990). Many studies showed that soil texture affected soil aggregation (Kemper and Koch, 1966; Chaney and Swift, 1984; Schlecht-Pietsch et al., 1994). As the clay constituents increase, they combine with SOC to form stable aggregates. For this reason, soil texture also plays direct and indirect role in chemical and physical protection mechanisms (Plante et al., 2006).

Clay content has a different effect on weathering of different SOC pools (Franzluebbers et al., 1996). For example, *in vitro* studies failed to find any relationship between clay and SOC (Wang et al., 2003; Muller and Hoper, 2004). It was determined that C mineralization rates in the natural environment generally decreased with increasing

* To whom all correspondence should be sent:

E-mail: esakin@harran.edu.tr
526

clay content (Hassink, 1997), but this trend could not always be demonstrated in the laboratory incubations (Scott et al., 1996). These observations suggest that clay particles protect some kinds of SOC from weathering (McLauchlan, 2006; Sakin, 2012).

The present study examined the effect of climate, temperature and rainfall, which are among the abiotic factors affecting SOC stocks and accumulation and texture. In order to determine the relationship between texture and SOC stocks, analyses were carried out on samples taken from 16 soil profiles in Harran Plain horizons.

EXPERIMENTAL

Material and Methods

Database

Soil Information

The study was carried out in the Harran Plain located in Southeastern Turkey; between 38° 48' to 39°12' E longitude and 37° 09' to 36° 42' N latitude. The total area of the plain is 225 000 ha. Rainfall is limited during most of the year, and the climate is arid. According to 33 years of data collection (1975–2008) by the Turkish State of Meteorology Service (TSMS, 2008), the average annual precipitation was 277.8 mm at Akcakale station and 448.1 mm at Sanliurfa station. The soil moisture regime of important parts of the plain is Xeric, and the temperature regime is Mesic. An Aridic soil humidity regime is established in parts of the areas near the south of the plain (Soil Survey Staff, 1996). Soil samples were taken from 16 series of genetic horizons on the Harran Plain and were taken as 3 replications from each horizon with profile depth of 1 m in the area of study. Analyses were carried out on 131 samples taken for the study.

Soil analysis was performed by the organic carbon-potassium dichromate acid method. Samples were titrated with dichromate iron sulphide. Before carrying out texture analysis, organic matter was burnt with hot hydrogen peroxide (H₂O₂). Sodium hexametaphosphate was used to determine the dispersion of particles. The hydrometer method was used to analyze particle-size distribution. Carbon stocks and bulk density

were determined according to methods for bulk density (Black, 1965).

RESULTS AND DISCUSSION

Soil texture analysis showed that the Harran Plain samples contained 65-28% clay, 41-22% silt and 3-31% sand. A summary of statistically analyses showing the distribution of carbon content and texture particle amounts of soil samples is presented in Table 1. Table 2 shows the statistical relationship between soil texture and organic carbon (p<0.001). As shown in Table 3, a strong relationship was found between SOC and soil texture (R²=92.01). Regression analysis of the relationship between soil texture particles and SOC is given in Eq. 1.

$$\text{SOC}(\text{kgCm}^{-2})=0.0305\text{Clay}\%+0.0015\text{Silt}\%+0.0162\text{Sand}\% \quad (1)$$

Table 1. Statistical distribution of texture class and organic carbon.

	N	Mean	Standard deviation
SOC (kg C m ⁻²)	131	1.870	1.019
Clay %	131	51.504	7.054
Silt %	131	33.298	4.989
Sand %	131	15.290	6.844

Statistical analyses of soil particles (clay-silt-sand) and SOC are given in Table 3. There is a very significant relationship between SOC and clay, silt and sand, with the strongest relationship in the order clay>silt>sand. Thus, it was observed that as the amount of clay in soil increased, the amount of SOC increased and a close relationship was detected between SOC and clay (R²=96.0). Although it is a physical disadvantage that soils of Harran Plain are very clayish, it is an advantage for accumulation and protection of SOC. Clay constitutes organo-mineral complexes by combining with SOC in soil and helps to retain carbon within the soil for long periods. Since the soils contain 2:1 type clay minerals, the carbon entering into the layers flips and is thus protected against oxidation and weathering of organisms. Some metals in soil clay minerals, Ca and Fe constitute complexes with carbon in soil and protect carbon.

Table 2. General relationship between soil texture and organic carbon

Source	DF	SS	MS	F	P	RMSE
Factor	3	183349.5	61116.5	1995.25	0.000	2.11
Error	520	15928.1	30.6			
Total	523	199277.6				

R² = 92.01

Table 3. Correlation relationship between texture particles (clay-silt-sand) and SOC

Source	DF	SS	MS	F	P<(0.001)
Factor	1	161359.3	161359.3	6352.97	0.000
Error	260	6603.7	25.4		
Total	261	167963.0			
Clay R ² = 96.07					
Factor	1	64693.8	64693.8	4990.64	0.000
Error	260	3370.4	13.0		
Total	261	68064.2			
Silt R ² = 95.05					
Factor	1	11796.2	11796.2	492.77	0.000
Error	260	6224.0			
Total	261	18020.2			
Sand R ² = 65.46					
Factor	2	165175.9	82588.0	3273.59	0.000
Error	390	9839.1	25.2		
Total	392	175015.0			
Clay+Silt	R ² = 94.38				

Plante et al. (2006) examined soils in Ohio and Saskatchewan, and found a statistically strong relationship ($r^2=0.48$; $P=0.012$) and ($r^2=0.46$; $P=0.0028$), between clay and SOC. According to their study, as the amount of clay increased, the amount of carbon retained in soil also increased. Nichols (1984) and Burke (1989) determined a strong relationship between clay and organic carbon concentration ($r=0.86$) in Southern Great Plains soils. Arrouays et al. (2006) detected a very strong correlation between SOC and clay content. Burke et al. (1989) and Schjonning (1999) found that SOC content and clay concentration were related. Many researchers reported a strong relationship between soil particles and SOC (Kern, 1994; Burke et al., 1995; Homann et al., 1998; Percival et al., 2000; Arrouays et al., 2006). In numerous studies it is suggested that SOC storage depends on soil texture (Scott and Cole, 1996; Bosatta and Agren, 1997; Hassink et al., 1997). In a study of New Zealand soils, Percival *et al.* (2000) found a weak relationship between clay and carbon concentration ($R=0.05$). Although there was no relationship between soil texture and soil carbon in many studies, Kölbl and Kögel-Knabner (2004) established that the amount of organic carbon in soil increased with the increase in the amount of clay. They also suggested that this relationship was not global, and sometimes depended on factors such as extractable aluminium, allophone content or physical surface area, that can extract more SOC than clay (Percival et al., 2000; Krull et al., 2003). The role of clay content is important within nitrogen cycle in the soil, and plays a key role in the mineralization of nitrogen (Cote et al., 2000). According to some studies, nitrogen mineralization

decreased with an increase in clay content (Giardina et al., 2001; McLauchlan et al., 2006).

A strong relationship was detected between soil silt particles and soil organic matter. A close relationship was found between soil organic carbon and silt ($R^2=95.0$). Therefore, it was concluded that the most important fraction in storing SOC was clay, followed by silt. A strong relationship was found between soil sand particles and SOC. However, this relationship was not as strong ($R^2=65.46$) as that found for clay and silt.

Hassink and Whitmore (1997) determined that, on the condition that soil organic carbon combined with clay and silt fractions of soil, SOC retention was maximized, which was suggested to cause excessive accumulation of organic carbon in soil. Hassink (1997), Kiem et al. (2002), Kiem et al. (2002), and Six et al. (2002) found that mineral soil particles (clay-silt) protected organic carbon against chemical weathering. Many studies indicated that soil texture affects aggregation (Kemper and Koch, 1996); Chaney and Swift, 1984; Schlecht-Pietsch et al., 1994), and thus increasing clay content combines with increasing aggregation or aggregate stability. It was found that, on the condition that soil aggregation increased, soil clay content indirectly affected carbon storage and thus protected soil carbon against oxidation and organisms. According to Plante et al. (2006), there was a statistically significant relationship between SOC and clay + silt ($P=0.99$, $r^2=0.76$) in Ohio and Saskatchewan soils. Many researchers found a strong relationship between SOC and clay + silt. This correlation was observed as: $R^2= 0.91$, $R^2= 0.97$, $R^2= 0.98$, $R^2= 0.86$ and $R^2= 0.93$, respectively

(Roscoe et al., 2001; Neufeldt et al., 2002; Ruggiero et al., 2002; Zinn et al., 2005).

Contrary to the findings of the present study and previous studies in the literature, some researchers have reported a very weak relationship between SOC and texture. McLauchlan (2006) reported a very weak relationship between SOC and texture, and thus texture had a lower effect on SOC storage in comparison to other parameters. According to Six et al. (2000), clay concentrations have a very weak effect on SOC accumulation rate and soil aggregate dynamics are relatively affected by low clay concentration. Plante et al. (2006) reported a direct proportional link between organic carbon concentration and silt + clay in the soil ($R^2=0.48$ and 0.46).

CONCLUSION

In worldwide studies, the effect of texture on SOC stocks was found to be very positive. In particular, the interaction of clay and silt fractions with SOC is extremely important. The present results from Harran Plain are similar to those of studies carried out in other parts of the world. A very strong relationship was found between these studies, since the quantity of clay and silt is high in Harran Plain soils. Another important finding of the present study is the statistically strong relationship between sand and SOC. The results suggest that retaining SOC in arid and semi-arid regions may depend on texture fractions.

REFERENCES

1. N. Arrouays, N. Sabic, C. Walter, B. Lemerrier, C. Schvartz, *Soil Use and Management*, **22**, 48 (2006).
2. C. A. Black, *Methods of Soil Analysis, Part II American Soc. of Agron Inc. Pub. No: 9* Madison WI, USA, 1965.
3. E. Bosatta, G. I. Agren, *Soil Biology and Biochemistry*, **29**, 1633 (1997).
4. I. C. Burke, Texture, *Soil Science Society of America Journal*, **53**, 800 (1989).
5. I. C. Burke, E. C. Elliot, C. V. Cole, *Ecological Applications*, **5**, 124 (1995).
6. K. Chaney, R. S. Swift, *J. Soil Sci.*, **35**, 223 (1984).
7. L. S. Cote, D. Brown, J. Pare, F. Fyles, J. Bauhaus, *Soil Biology & Biochemistry*, **32**, 1079 (2000).
8. R. F. Follett, *Soil and Tillage Research*, **61**, 77 (2001).
9. A. J. Franzluebbers, R. L. Haney, F. M. Hons, D. A. Zuberer, *Soil Biology and Biochemistry*, **28**, 1367 (1996).
10. C. P. Giardina, M. G. Ryan, R. M. Hubbard, D. Binkley, *Soil Science Society of America Journal*, **65**, 1272 (2001).
11. J. M. Gonzalez, D. A. Laird, *Soil Sci. Soc. Am. J.*, **67**, 1715 (2003).
12. J. Hassink, *Plant & Soil*, **191**, 77 (1997).
13. J. Hassink, A. P. Whitmore, J. Kubat, *European Journal of Agronomy*, **7**, 189 (1997).
14. J. Hassink, A. P. Whitmore, *Soil Science Society of America Journal*, **61**, 131 (1997).
15. P. S. Homann, P. Sollins, M. Fiorella, T. Thorson, J. S. Kern, *Soil Science Society of America Journal*, **62**, 789 (1998).
16. H. Jenny, *Factors of soil formation: a system of quantitative pedology*, McGraw Hill, New York, USA, 1941.
17. D. S. Jenkinson, *Biological Sciences*, **329**, 361 (1990).
18. R. Kiem, H. Knicker, I. Kogel-Knabner, *Org. Geochem.*, **33**, 1683 (2002).
19. W.D. Kemper, and E. J. Koch, *Aggregate stability of soils in Western United States and Canada*. U.S. Gov. Print. Office, Washington, DC, 1966.
20. J. S. Kern, *Soil Science Society of America Journal*, **58**, 439 (1994).
21. A. Kölbl & I. Kögel-Knabner, *J. Plant Nutr. Soil Sci.*, **167**, 45 (2004).
22. E. S. Krull, J. A. Baldock, J. O. Skjemstad, *Functional Plant Biology*, **30**, 207 (2003).
23. K. K. McLauchlan, *Geoderma*, **136**, 289 (2006).
24. K. K. McLauchlan, S. E. Hobbie, W. M. Post, *Ecological Applications*, **16**, 143 (2006).
25. T. Muller & H. Hoper, *Soil Biology and Biochemistry*, **36**, 877 (2004).
26. H. Neufeldt, D. V. S. Resck, M. A. Ayarza, *Geoderma*, **107**, 151 (2002).
27. J. D. Nichols, *Soil Science Society of America Journal*, **48**, 1382 (1984).
28. W. J. Parton, D. S. Schimel, C. V. Cole, D. S. Ojima. *Soil Science Society of America Journal*, **51**, 1173 (1987).
29. K. J. Paustian, E. T. Six, E. Elliott, H. W. Hunt *Biogeochemistry*, **48**, 147 (2000).
30. H. J. Percival, R. L. Parfitt, N. A. Scott, *Soil Science Society of America Journal*, **64**, 1623 (2000).
31. A. F. Plante, R. T. Conant, C. E. Stewart, K. Paustian, J. Six, *Soil Science Society of America Journal*, **70**, 287 (2006).
32. W. M. Post, K. C. Kwon, *Global Change Biology*, **6**, 317 (2000).
33. R. Roscoe, P. Buurman, E. J. Velthorst, C. A. Vasconcellos, *Geoderma*, **104**, 185 (2001).
34. P. G. C. Ruggiero, M. A. Batalha, V. R. Pivello, S.T. Meirelle, *Plant Ecol.*, **160**, 1 (2002).
35. E. Sakin, PhD Thesis, University of Harran, 2010, p. 234.
36. E. Sakin, A. Deliboran, E. D. Sakin, E. Tutar, *African Journal Agricultural Research*, **6**, 1750 (2010).
37. E. Sakin, A. Deliboran, E. D. Sakin, E. Tutar, *Notulae Botanicae Horti Agrobotanici Cluj-Napoca*, **38**, 151 (2010).
38. E. Sakin, A. Deliboran, E. D. Sakin, H. Aslan, *Romanian Agricultural Research*, **28**, 171 (2010).
39. E. Sakin, *Bulg. J. Agric. Sci.*, **18**, 626 (2012).

40. J. Six, E. T. Elliott, K. Paustian, *Soil Biology & Biochemistry*, **32**, 2099 (2000).
41. J. Six, R. T. Conant, E. A. Paul, K. Paustian, *Plant & Soil*, **241**, 155 (2002).
42. S. Schlecht-Pietsch, U. Wagner & T. H. Anderson, *Appl. Soil Ecol.*, **1**, 145 (1994).
43. P. Schjonning, *Geoderma*, **89**, 177 (1999).
44. N. A. Scott, C. V. Cole, E. T. Elliott, S. A. Huffman, *Soil Science Society of America Journal*, **60**, 1102 (1996).
45. Turkish State Meteorological Service (TSMS), Data of Climate Sanliurfa and Akcakale stations. Meteorological Bulten, Ankara, 2008.
46. M. A. Vinton, I. C. Burke, *Oecologia*. **110**, 393 (1997).
47. Y. L. Zinn, D. V. Resck, J. E. Silva, *For. Ecol. Manag.*, **166**, 285 (2005).
48. W. J. Wang, R. C. Dalal, P. W. Moody, C. J. Smith, Relationships of soil respiration to microbial biomass, substrate availability and clay content, *oil Biology and Biochemistry*, **35**, 273 (2003).
49. T. O. West, W. M. Post, *Soil Science Society of America Journal*, **66**, 1930 (2002).
50. Soil Survey Staff, Keys to soil taxonomy natural resources conservation service. Seventh Edition. 1996.

ВЗАИМОВРЪЗКИ МЕЖДУ РАЗПРЕДЕЛЕНИЕТО НА ЧАСТИЦИ ПО РАЗМЕРИ И ОРГАНИЧНИЯ ВЪГЛЕРОД В ПОЧВЕНИ ХОРИЗОНИ В ЮГОИЗТОЧНА ТУРЦИЯ

Е. Сакин *, Е. Д. Сакин

Департамент по почвознание и растениевъдство, Факултет по агронауки, Университет „Харан“, Урфа 63040, Турция

Постъпила на 17 февруари, 2014 г., коригирана на 20 март, 2014 г.

(Резюме)

Малко известни са взаимовръзките между текстурата на почвата и съдържанието на органичен въглерод в тях. За установяването на тези взаимовръзки са извършени анализи на въглерода и текстурата на проби от почвата в равнината Харан. Пробите (трикратно) за взимани от 16 профила на дълбочина до 1 м. Пробите за взимани от места с еднакъв климат, растителност и топография. Концентрацията на почвения органичен въглерод (SOC) се оказва пряко свързана с текстурата на почвата на всички дълбочини. Според статистическия анализ ($p < 0.001$) най-силна зависимост е намерена за глината ($R^2 = 96.0$) и тинята ($R^2 = 95.0$). При пясъка тази корелация спрямо SOC е $R^2 = 65.46$. Силна зависимост е намерена между органичния въглерод (OC) почвената текстура в равнината Харан. Получените резултати показват, че площите съдържащи органичен въглерод трябва да се предпочитат за съхранение на въглерод пред площите с високо въглеродно съдържание.

Design and synthesis of potential inhibitors of multienzyme systems included in Alzheimer's disease

I. Ivanov¹, L. Vezenkov¹, D. Danalev^{2,*}

¹University of Chemical Technology and Metallurgy, Organic Chemistry Department, 8 blvd. Kliment Ohridski, 1756,

²University of Chemical Technology and Metallurgy, Biotechnology Department, 8 blvd. Kliment Ohridski, 1756,

Received February 24, 2014, Revised May 15, 2014

Synthesis of a series of 6 peptides, potential inhibitors of β -secretase, analogues of the β -secretase inhibitor OM99-2 was designed and performed. Standard peptide synthesis in solution was applied by stepwise addition of amino acids from C- to N-terminus. All reactions gave very good yields (higher than 80%).

Key words: OM99-2 analogues, Alzheimer's disease, inhibitors of multienzyme systems

INTRODUCTION

Processes in the human body are usually related to the realization of a series of subsequent enzymatic reactions. For example, the blood coagulation cascade protects the organism from blood loss by thrombus formation [1,2]. Disorders of multienzyme cascade reactions in the most cases cause diseases.

Alzheimer's disease (AD) is a neurodegenerative illness, which affects millions of people worldwide. AD is characterized by progressive dementia, loss of memory, intellectual, speech and brain disturbances and inevitably leads to complete personality decay and lethal outcome. Designated neuropathological lesions associated with all forms of AD are senile plaques (SPs) and amyloid angiopathy, as well as neurofibril tangles. The amyloid hypothesis formulated in 1991 postulated that amyloid beta ($A\beta$) deposits, as the two dominant forms $A\beta_{40}$ and $A\beta_{42}$, are the fundamental reason of SPs formation and disease development [3,4]. The process of $A\beta_{40}$ and $A\beta_{42}$ formation includes multienzyme cascade reactions of proteolytic cleavage of wide sections from β -amyloid protein precursor (β APP) (the 695-770 amino acids) catalyzed by various proteases known as β - and γ -secretases [5]. Once released, β APP passes over to aggregation and SPs are obtained.

A possible approach for prevention of SPs formation is the inhibition of the multistage process of β APP cleavage. Tung *et al.* revealed in 2002 that the shortest analogue of β -secretase inhibitor OM99-2 with saved activity is Boc-Val-Asn-Leu-Ala-OH [6]. Several years later, in 2005, Ghosh *et al.* published a series of OM 99-2 analogues which

included benzylamine in their C-terminus with increased inhibition properties against β -secretase [7]. Additionally, they concluded that the presence of hydrophobic residues in P_3' and P_4' positions leads to increased activity. Herein we report on the design, synthesis and characterization of a series of new OM 99-2 mimetics including hydrophobic Ile, norvaline (Nva) and imidazol-4-acetic acid (Im-4-Ac) at P_3 position and Asn in P_2 position is replaced by Asp. Besides, both analogues with α - and β -Ala in P_1 position were synthesized in order to estimate their further influence on the inhibition activity.

EXPERIMENTAL

TBTU, TCTU or DCC/HOBt used as a coupling reagent according to the schemes presented in Results and Discussion part, were purchased from IRIS Biotech GmbH, Germany. All used amino acids were purchased from IRIS Biotech GmbH, Germany.

All reactions were monitored by TLC on pre-coated TLC-sheets ALUGRAM SIL G/UV₂₅₄ in the following chromatographic systems: (**S1**) $CHCl_3:CH_3COOH$ (9:1); (**S2**) $n-BuOH:CH_3COOH:H_2O$ (3:1:1); (**S3**) $pyridine:n-BuOH:CH_3COOH:H_2O$ (1:1,5:0,3:1,2).

The structure of all newly synthesized compounds was proven by ES-MS (Table 1). Melting points of all compounds were determined on a Kofler apparatus. The optical rotation was measured on a Quick polarimeter Russel-Jouan Type SL1D.

General procedure for coupling reaction using TBTU or TCTU

1 mmol of the starting compound with free amino function was dissolved in a minimal amount

* To whom all correspondence should be sent:
E-mail: dancho.danalev@gmail.com

of DMF. After cooling to $0^{\circ}\text{C} \div -5^{\circ}\text{C}$, 1 mmol of Et_3N (till pH 7) was added to deprotect the salt obtained in a previous deprotection procedure. Further 1.2 fold excess of carboxylic component and 1.4 mmol of TBTU (TCTU) was added. The reaction mixture was stirred for 6 h and quenched by addition of water. The product was extracted with EtOAc (3×10 ml) and the organic layer was washed with 5% NaHCO_3 (3×10 ml), H_2O (2×10 ml), 10% citric acid (3×10 ml) and H_2O to pH 7. The solvent was dried with Na_2SO_4 and removed *in vacuo* followed by recrystallization.

General procedure for coupling reaction using DCC/HOBt

1.00 mmol of the peptide (obtained from Boc-peptide ester by treatment with 10-fold excess of TFA) was dissolved in DMF (10 ml) and, after cooling to $0 \div 4^{\circ}\text{C}$, was neutralized to pH 7–7.5 with Et_3N . 1.20 mmol of Z- or Boc- amino acid, 1.20 mmol of DCC and 1.40 mmol of 1-HOBt were added. The reaction mixture was stirred at $0 \div 4^{\circ}\text{C}$ for 24 h and left at room temperature for 24 h. The obtained DC-urea was removed by filtration and then 30 ml of water was added. The product was extracted with EtOAc (3×10 ml) and the organic layer was washed with 5% NaHCO_3 (3×10 ml), H_2O (2×10 ml), 10% citric acid (3×10 ml) and H_2O to pH 7. The solvent was dried with Na_2SO_4 and removed *in vacuo* followed by recrystallization.

General procedure for Boc-group deprotection

1 mmol of the starting peptide was dissolved in 10-fold excess of TFA under stirring. The deblocking of the Boc-group was monitored by TLC in the system S1. At the end of the reaction TFA was evaporated *in vacuo* and the oil formed was further subjected to a condensation reaction without additional purification.

General procedure for deprotection of Z- groups by catalytic hydrogenolysis in the presence of Pd/C

1.00 mmol of the protected peptide was dissolved in MeOH and then Pd/C and 1.00 mmol of HCl or AcOH were added. Hydrogen was passed through the reaction mixture at 40°C . The deblocking was monitored by TLC in the system S1. After the end of the reaction, Pd/C was filtered off and MeOH was evaporated *in vacuo*. The oil formed was subjected to a condensation reaction without additional purification.

General procedure for –OBzl ester group deprotection in basic conditions

1 mmol of the starting peptide was dissolved in MeOH (10 ml) and 4-fold excess of 2N NaOH was added. The reaction was monitored by TLC in the S3 system. After completion of the reaction, the pH was reduced to 7 with 10% citric acid, and a part of the solvent was removed *in vacuo*. Afterwards the pH was reduced to 4–5 with 10% citric acid and the product was extracted with EtOAc (3×10 ml). The following extraction of the product from the organic phase was by 5% NaHCO_3 (3×10 ml), and after reducing the pH to 4–5 with 10% citric acid, it was extracted with EtOAc (3×10 ml). Finally, the organic layer was washed with H_2O (3×10 ml), dried with Na_2SO_4 and evaporated *in vacuo*.

RESULTS AND DISCUSSION

Initially, fragment condensation using DCC/1-HOBt and/or azide method was tried. A lot of side reactions took place. Because of that, the standard peptide synthesis in solution by stepwise addition of amino acids from C-to N-terminus of the aimed peptides was chosen. Aimed compounds were synthesized according to schemes 1 and 2 (Figs. 1 and 2). TBTU or DCC/1-HOBt was used as a coupling reagent for shorter fragments and TCTU was used as a coupling reagent for the peptides.

Removal of the protecting groups was realized as follows:

- Boc-group in all intermediate compounds was removed by treatment with 10-fold excess of TFA;
- Z-group was removed by catalytic hydrogenation in the presence of HCl (molar amount) and Pd/C;
- 2N NaOH was used for all ester hydrolyses.

All final compounds were characterized by TLC, m.p. and $[\alpha]_{546}^{22}$ and their structures were proven by ES-MS. All data are presented in Table 1.

The purity of all obtained intermediate peptides was monitored in the systems S2 and S3. The deblocking procedures of Boc and Z groups were controlled in the S1 system, and final deprotection of OBzl group of Asp was monitored in the S3 system. As it can be seen from Table 1, all reactions are run with very good yields (higher than 80%).

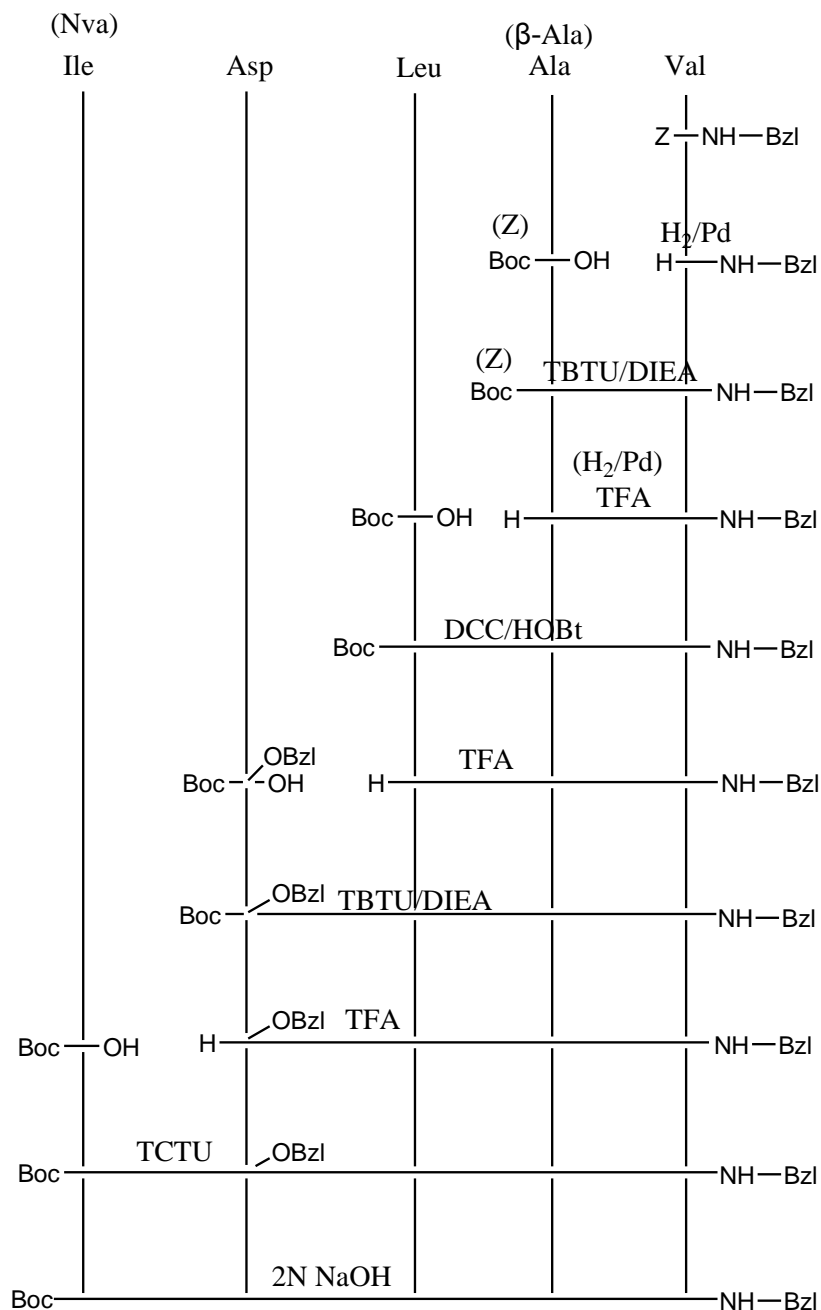


Fig. 1. Scheme of synthesis of pentapeptides Boc-Ile-Asp-Leu-Ala (β -Ala)-Val-NH-Bzl

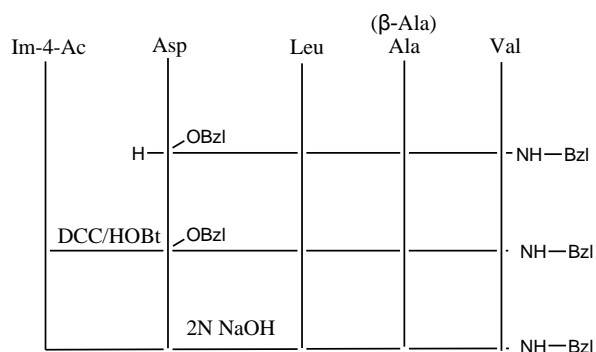


Fig. 2. Scheme of synthesis of pentapeptides Im-4-Ac-Asp-Leu-Ala (β -Ala)-Val-NH-Bzl

CONCLUSIONS

A series of 6 peptides, potential inhibitors of β -secretase, analogues of β -secretase inhibitor OM99-2 was designed. They were successfully synthesized using standard peptide synthesis in solution. All compounds were characterized by m.p., $[\alpha]_{546}^{22}$ and ESI-MS. Biological activity investigation is in a progress.

Table 1. MS data, melting points, yields and $[\alpha]_{546}^{22}$ of the newly synthesized compounds

N	Structure	MS data calc./found	M.p. [°C]	Yield [%]	* $[\alpha]_{546}^{22}$
1	Boc-Ile-Asp(OBzl)-Leu-β-Ala-Val-NH-Bzl	-	135-137	84	- 2.2
2	Boc-Ile-Asp-Leu-β-Ala-Val-NH-Bzl	718.4265/742.42 [M ⁺ +Na ⁺]	147-149	98	- 12.1
3	Boc-Nva-Asp(OBzl)-Leu-β-Ala-Val-NH-Bzl	-	186-189	87	- 4.4
4	Boc-Nva-Asp-Leu-β-Ala-Val-NH-Bzl	704.4109/727.42 [M ⁺ +Na ⁺]	210-214	97	- 14.0
5	Boc-Ile-Asp(OBzl)-Leu-Ala-Val-NH-Bzl	-	165-167	89	- 3.2
6	Boc-Ile-Asp-Leu-Ala-Val-NH-Bzl	718.4265/742.53 [M ⁺ +Na ⁺]	184-190	99	- 17.5
7	Boc-Nva-Asp(OBzl)-Leu-Ala-Val-NH-Bzl	-	146-148	89	- 2.0
8	Boc-Nva-Asp-Leu-Ala-Val-NH-Bzl	704.4109/727.27 [M ⁺ +Na ⁺]	187-189	99	- 9.2
9	Im-4-Ac-Asp(OBzl)-Leu-Ala-Val-NH-Bzl	-	161-163	79	- 1.1
10	Im-4-Ac-Asp(OBzl)-Leu-β-Ala-Val-NH-Bzl	-	192-194	77	- 2.3
11	Im-4-Ac-Asp-Leu-Ala-Val-NH-Bzl	728.4221/750.73 [M ⁺ +Na ⁺]	187-189	98	- 4.5
12	Im-4-Ac-Asp-Leu-β-Ala-Val-NH-Bzl	728.4221/750.73 [M ⁺ +Na ⁺]	198-200	99	- 28.0

* for all compounds $[\alpha]_{546}^{22}$ is determined for c = 1 in methanol

REFERENCES

1. D. Danalev, *Mini-review in Med. Chem.*, **12**, 721 (2012).
2. Z. Findrik, Đ. Vasiæ-Raëki, *Chem. Biochem. Eng. Q.* **23**, 545 (2009).
3. J. Hardy, D. Allsop, *Trends Pharmacol. Sci.*, **12**, 383 (1991).
4. A. Mudher, S. Lovestone, *Trends Neurosci.*, **25**, 22 (2002).
5. T. Nikolaev, D. McLaughlin, D. M. O'Leary, M. Tessier-Lavigne, *Nature*, **457**, 981 (2009).
6. J. S. Tung, D. L. Davis, J. P. Anderson, D. E. Walker, S. Mamo, N. Jewett, R. K. Hom, S. Sinha, E. D. Thorsett, V. John, *J. Med. Chem.*, **45**, 259 (2002).
7. A. K. Ghosh, T. Devasamudram, L. Hong, C. DeZutter, X. Xu, V. Weerasena, G. Koelsch, G. Bilcer, J. S. Tang, *Bioorg. Med. Chem. Lett.*, **15**, 15 (2005).

ДИЗАЙН И СИНТЕЗ НА ПОТЕНЦИАЛНИ ИНХИБИТОРИ НА МУЛТИЕНЗИМНИ СИСТЕМИ УЧАСТВАЩИ ПРИ БОЛЕСТТА НА АЛЦХАЙМЕР

Ив. Иванов¹, Л. Везенков¹, Д. Даналев^{2,*}

¹Химикотехнологичен и металургичен университет, Катедра по органична химия, бул. „Климент Охридски №8

²Химикотехнологичен и металургичен университет, Катедра по биотехнология, бул. „Климент Охридски №8

Получена на 24 февруари, 2014 г., ревизираната на 15 май, 2014 г.

(Резюме)

Проектирана и изпълнена беше синтеза на серия от 6 пептиди, потенциални инхибитори на β-секретаза, аналози на β-секретаза инхибитор ОМ99-2. Беше приложена стандартна пептидна синтеза в разтвор, чрез постепенно добавяне на аминокиселини от С-към N-края. Всички реакции дадоха много добри добиви (над 80%).

Changes of hardness and electrical conductivity of white gold alloy Au-Ag-Cu after aging treating

R. S. Perić^{*1}, Z. M. Karastojković², Z. M. Kovačević³, M. B. Mirić⁴, D. M. Gusković⁵

¹ „PERIĆ&PERIĆ“&Co. d.o.o., 12000 Požarevac, Dunavska 116, Serbia,

² Technical College, 11070 Novi Beograd, Blvd. Dr. Z. Đinđića 152a, Serbia

³ Institute of Testing of Materials, 11000 Beograd, Blvd. Vojvode Mišića, 43, Serbia;

⁴ Directorate of Measures and Precious Metals, M. Alasa 14, Belgrade, Department of the control subjects in precious metals, Gen. B. Jankovića 32, Nais, Serbia;

⁵ University of Belgrade, Technical Faculty Bor, 19210 Bor, V. Jugoslavije 12, Serbia.

Received February 26, 2014; revised May 22, 2014

Golden alloys which are able of strengthening after tempering, i.e. artificial aging, play an increased role in jewel production. According to customer's demands these alloys are produced as „yellow“ or „white“ gold. Commonly an alloy of 585 finesse, i.e., 58.5 wt.% of pure gold, is used.

In the appropriate literature most authors have investigated rather yellow gold than white gold. In fact, the white gold alloys are more complex in their nature than yellow alloys. In this paper the changes after precipitation (age) hardening of a white gold alloy with chemical composition corresponding to Au₅₈₅Ag₆₅Cu₂₇₇Zn₁₆Pd₅₇ are examined. The hardening of this alloy after aging at high temperature plays an important role in improving jewel quality. So, it is possible to produce a jewel either by hand- or machine making, beginning from an initial soft alloy (easily deformed and shaped) into a final product with increased hardness and strength. This aim could be realized by applying a rather simple heat-treatment, which includes annealing or non-hardening quenching. A jewel produced from white gold is hardened and strengthened after a period of time. Special attention was paid to the analysis of the changes in hardness and electrical conductivity in real time regimes, which are attainable during production in a gold shop. The used temperatures were from room temperature up to recrystallization temperatures.

Key words: white gold, alloy aging, recrystallization, hardness, electrical conductivity

INTRODUCTION

It is generally known that the principal role of jewels is the decoration, as a fashion detail. Through history, there are a lot of golden products representing both material value and art on high level. The skill in gold jewel production is basically a part of the culture of the nation at different epochs or artistic periods.

Jewels and artistic products made from golden alloys have been used since ancient times, and their colors (yellow, red or white) have also been of importance. In the production of jewels from gold of finesse 585, ternary alloys from the system Au-Ag-Cu represent the base material. Gold and copper are metals which possess color, so the golden alloys may have a broad range of different colors, depending of the kind and amount of alloying elements [1, 2].

The use of both „yellow“ and „white“ gold of 585 finesse for jewel making needs understanding and further investigation of these alloys. Approximately, up to the year 2000, white Au-Ag-Cu alloys were used with nickel additions but by laws in the European Union the nickel as alloying

element has been forbidden, mainly due to its allergic influence on customers [3, 4]. After that period, in the production of white gold palladium and zinc were used.

An increase in hardness and strength of the ternary alloys from the Au-Ag-Cu system could be achieved by artificial aging treatment at a high temperature, as a process of phase transformation and microstructural changes [5]. For these investigations the white alloy of composition Au₅₈₅Ag₆₅Cu₂₇₇Zn₁₆Pd₅₇ was used, which is acceptable according to market and law limitations. The sample preparation is done at a golden shop as a regular production schedule. The samples were casted in flat shape, cold rolled up to 0,5 mm in thickness, and then aged. The changes in the alloy after such a treatment were monitored by hardness and specific electrical conductivity measurements and metallography. It was established that electrical conductivity changes may serve for monitoring of the structural changes in metals [6]. Further, this alloy may be used not only in jewelry but also in electrotechnics and electronics, especially for telecommunication devices.

* To whom all correspondence should be sent:
E-mail: pericradisa@gmail.com

EXPERIMENT AND RESULTS

Preparation of alloy and strips

A binary Au-Ag alloy was first melted, then alloyed with copper, zinc and palladium. Melting was performed in an induction vacuum furnace for avoiding absorption of gases from the surrounding atmosphere. The molten alloy was casted as a rectangular bar, which was further cold rolled. The final thickness was 0.5 mm, with total height reduction of 66.66%. The obtained strips were aged at temperatures from 50 to 600°C, at steps of 50°C. The microhardness and electrical conductivity of these samples were measured and for typical changes (maxima and minima values) the microstructures were examined.

Hardness measurements

The hardness tests were performed using a 250 g load for 15 s. For every specimen 5 measurements were performed. After cold rolling with 66.67% of height reduction, the maximal hardness of 251.00 HV_{0.25} was achieved. The obtained results are shown in Fig. 1.

After aging treating, the maximal value of microhardness was reached at 300°C, for both 30 and 60 min of aging duration, while for 15 min of aging the maximal value of hardness was reached at 350°C. The exact value of maximal hardness was 307HV_{0.25}, Fig.1.

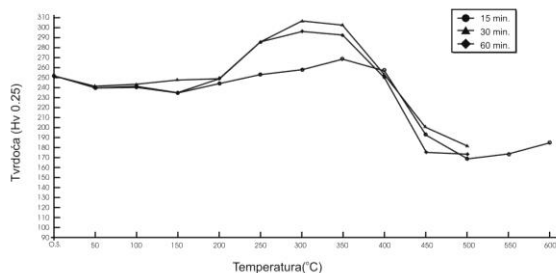


Fig. 1. Hardness changes after aging of white alloy Au585Ag65Cu277Zn16Pd57 for three durations over the temperature interval from 50°C to 600°C.

Electrical conductivity measurements

The electrical conductivity was measured by the *sigma test* on treated strips and the results were obtained as specific electrical conductivity, in Ms/m units, Fig.2.

The maximal value of the specific electrical conductivity was reached at 300°C, as can be seen from Fig.2. It is evident that specific electrical conductivity is more sensitive to the structural changes in the investigated alloy than microhardness.

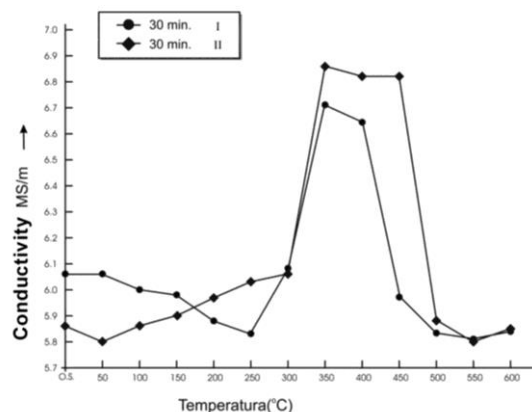


Fig.2. Changes of specific electrical conductivity for specimens of white alloy Au585Ag65Cu277Zn16Pd57 aged for 30 min.

Microstructure examinations

Metallographic examinations were done by optical microscopy. All specimens were examined in longitudinal and transverse directions, because they were rolled. The elongation of the crystal grains and their changes were more visible in longitudinal than in transverse direction of the rolled strip. For etching of all specimens an aqueous solution of 10% KCN and 10% (NH₄)₂S₂O₇ in a ratio of 1:1 was used. As a starting specimen the heavy cold rolled strip (66.67% height reduction) was chosen and its microstructure is shown in Figure 3.

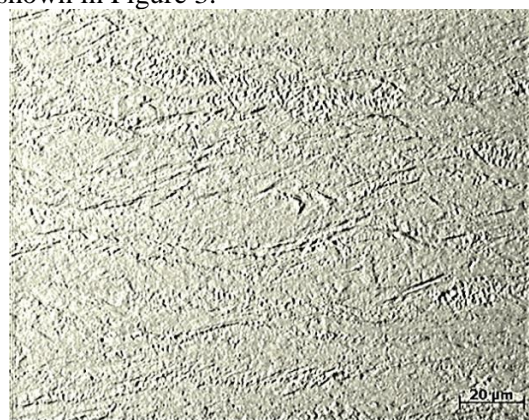


Fig. 3. Microstructure of a cold rolled strip of white alloy Au585Ag65Cu277Zn16Pd57 with 66.67% height reduction, longitudinal direction, ×500.

The aging treatment at 399°C for 30 min has produced the maximal hardness value of 307.80HV_{0.25}, according to Fig.1, and the microstructure of this specimen is shown in Fig.4.

The crystal grains are still elongated but very fine twins have appeared. The highest aging temperature of 600°C for 15 min produced a hardness of 186.50HV_{0.25} and the microstructure shows that recrystallization is finished, Figure 5.



Fig. 4. Microstructure of cold rolled and aged specimen of white alloy Au585Ag65Cu277Zn16Pd57 at 300°C, 30 min, twins, longitudinal direction, $\times 500$.

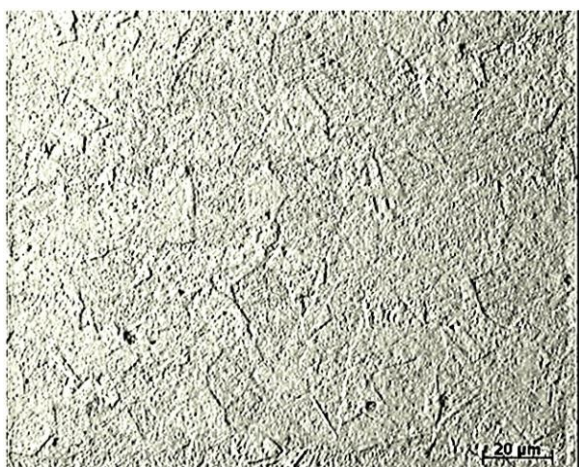


Fig. 5. Microstructure of fully recrystallized specimen of white alloy Au585Ag65Cu277Zn16Pd57 at 600°C, 15 min, longitudinal direction, $\times 500$

After the recrystallization was finished, further cold rolling could be performed if necessary.

DISCUSSION

In the process of aging, hardening of an alloy for jewel production from the system Au-Ag-Cu with additions of palladium and zinc could be performed in several ways: a) creation of annealing twins, almost for alloys with f.c.c. lattice [7,8], b) ordering of atoms in a kind of Au-Cu phases [8,9], c) precipitation at crystal grains of Ag-Cu phases [9,10], or d) spinodal decomposition of $\alpha_{(Au,Ag,Cu)} \leftrightarrow \alpha'_{(Au,Ag)} + \alpha''_{(Au,Cu)}$ [10,11].

In the applied regime of aging from 50°C to 600°C, the maximal hardness values for specimens of white alloy Au585Ag65Cu277Zn16Pd57 were achieved at 300°C with heating for 15 and 30 min; longer aging treating (60 min) produced lower maximal hardness at 350°C, see Figure 1.

The specific electrical conductivity for specimens of this white alloy reached the highest

values at temperatures about 300°C, Fig.2, and it seems that those changes are more sensitive to structural changes than the changes in hardness values.

The microstructural examination revealed twins at higher temperatures of aging, i.e. annealing, see Figure 4.

CONCLUSION

The aim of the present investigations was to produce a hard jewel starting from a relatively soft and easily deformable golden alloy by using annealing, ageing or quenching for achieving the hardening effects. Here, a common 585 gold alloy was additionally alloyed with 16/1000 g of zinc and 57/1000 g of palladium.

1. After applying cold rolling with 66.67% of height reduction, a hardness of 251HV_{0.25} was achieved.

2. Further increasing of the hardness values of the white alloy Au585Ag65Cu277Zn16Pd57 was achieved by aging treating at a high temperature. For a heavy cold rolled strip with 66.67% of height reduction, the aging at 300 – 350°C for 15 – 30 min was enough for achieving the maximal hardness values of about 300HV_{0.25}.

3. Such increase of hardness by additional alloying and aging is welcome for increasing the service life of jewels made from a soft golden alloy like the ternary 585 gold alloy.

REFERENCES

1. W. S. Rapson, , *Gold Bulletin*, **23**, 125 (1990)
2. C. Gretu, E.van der Lingen, *Coloured Gold Alloys*, Mintek, Private Bag X3015 Randburg 2125, South Africa, 1999, p. 31.
3. Direttiva 2004/96/CE della Commissione del 27 settembre 2004-Ni; Direttiva 2002/96/Ce del Parlamento Europeo del Consiglio del 27 gennaio 2003-Cd;
4. V. Ilić, V.Batanić, B. Jović, Epidemiološki i patogeni aspekti trovanja niklom, 2007, <http://www.publisher.medfak.ni.ac.rs>.
5. Y. O. Kim, H. I. Kim, M. H. Cho, S. Y. Cho, G. Y. Lee, Y. H. Kwon, H. J. Seol, Age-hardenability related to precipitation and lamellar-forming grain boundary reaction in dental low-carat gold alloy, Dept. of Dental Materials, Pusan National University, South Korea, Document N°MK110904, www.ijmr.de, p.1
6. W.D.Callister Jr., *Materials Science and Engineering An Introduction*, 7th Ed. John Willey & Sons, Inc., 2007.
7. L. Stuparević, D. Marković, D. Gusković, B. Stanojević, S. Ivanov, *Glasnik rudarstva i metalurgije*, **28**, 85 (1992).
8. K.Yasuda, , *Gold Bulletin*, **20**, 90 (1987).

9. H. Winn, Y. Tanaka, T. Shiraishi, K. Udoh, E. Miura, R. I. Hernandez, Y. Takuma, K. Hisatsune, *Journal of Alloys and Compounds*, **306**, 262 (2000).
10. Y. Le Bouar, A. Loiseau, A. G. Khachaturian, *Acta Mater.*, **46**, 2777 (1998).
11. R. Perić, Z. Karastojković, Z. Kovačević, Z. Janjušević, D. Gusković, *Journal Metalurgia*, **53**, 3 (2014).

ПРОМЕНИ В ТВЪРДОСТТА И ЕЛЕКТРОПРОВОДИМОСТТА НА СПЛАВТА „БЯЛО ЗЛАТО“ (Au-Ag-Cu) СЛЕД СТАРЕЕНЕ ЧРЕЗ ТЕРМИЧНО ТРЕТИРАНЕ

Р. С. Перич^{*1}, З. М. Карастойкович², З. М. Ковачевич³, М. Б. Мирич⁴, Д. М. Гускович⁵

¹ „Перич&Перич&Съдр. ООД, Пожаревац, Сърбия

² Технически колеж, 11070 Нови Белград, Сърбия

³ Институт по изпитание на материалите, 11000 Белград, Сърбия

⁴ Департамент по контрол на благородните метали, Директорат по измервания и благородни метали (Белград), Сърбия

⁵ Университет в Белград, Технически факултет в Бор, Сърбия

Постъпила на 26 февруари, 2014 г., коригирана на 22 май 2014 г.

(Резюме)

Златните сплави, които притежават способността на заякчаване след темпериране (изкуствено стареене) добиват все по-голямо значение в бижутерството. Според желанието на клиентите тези сплави се приготвят като „жълто“ или „бяло“ злато. Обикновено се използват сплави с проба 585, т.е. със съдържание на 58,5% (тегл.) чисто злато.

В литературата по-често се отбелязва „жълтото“ злато, докато бялото злато е слабо изследвано. Сплавите, наричани „бяло злато“ са по-сложни като състав. В настоящата работа се изследват промените след стареене и втвърдяване на такава сплав с химичен състав Au585Ag65Cu277Zn16Pd57.

Втвърдяването след стареене при висока температура на тази сплав има важна роля за подобряването качеството на бижутата. Например, възможно е да се изработи бижу ръчно или с машина, като се започне от мека сплав (лесна за формуване) и се стигне до краен продукт с повишена твърдост и якост. Тази цел може да бъде постигната чрез просто нагриване, заедно със накаливане или закаляване. Така изработените бижута от бяло злато се втвърдяват и заякчават за определено време. Специално внимание се дава на анализа на промяната на твърдостта и на електропроводимостта в реално време, допустимо в работата на златарско ателие. Изследваните температури са поддържани между стайните и тези на ре-кристализация.

Magnetic CuFe₂O₄ nanoparticles as an efficient catalyst for the oxidation of alcohols to carbonyl compounds in the presence of oxone as an oxidant

F. Sadri¹, A. Ramazani*², A. Massoudi¹, M. Khoobi³, S. W. Joo*⁴

¹Department of Chemistry, Payame Noor University, P.O. Box 19395-3697, Tehran, Iran

²Department of Chemistry, University of Zanjan, P O Box 45195-313, Zanjan, Iran

³Pharmaceutical Sciences Research Center, Tehran University of Medical Sciences, Tehran 14176, Iran

⁴School of Mechanical Engineering, Yeungnam University, Gyeongsan 712-749, Republic of Korea

Received February 27, 2014, Revised May 8, 2014

Nanomagnetic CuFe₂O₄ was used as an efficient, stable, and reusable catalyst for selective oxidation of alcohols to their corresponding carbonyl compounds using oxone (potassium hydrogen monopersulfate) as oxidant in the presence of water as solvent at room temperature. Primary and secondary alcohols gave the corresponding products in good yields. The oxidation of various primary and secondary alcohols was also examined and the corresponding products were obtained with good yields. The catalyst was investigated with XRD, SEM, ICP and IR techniques. Furthermore, the catalyst could be easily recovered and reused several times without loss of activity.

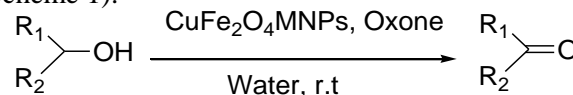
Keywords: Nanomagnetic catalyst, Copper ferrite, Oxidation, Alcohols, Carbonyl Compounds, Oxone.

INTRODUCTION

The oxidation of alcohols to their corresponding carbonyl compounds involves a basically important functional group transformation and takes a chief position in new synthetic organic chemistry [1]. They have normally been oxidized in noncatalytic ways with stoichiometric oxidants such as chromium and manganese compounds in the attendance of strong mineral acids, which produce enormous amounts of toxic metal salts as a waste [2]. Thus, the development of green oxidation systems using less poisonous catalysts, oxidants, and solvents became a crucial target for catalysis [3]. Although a variety of different catalytic systems for catalytic oxidation of alcohols has been developed, there is a growing interest in the search for new efficient metal catalysts for this concern [4-7]. Recently, sustainability and environmental friendliness are major elements in catalysis. While catalysis is an important process for the improvement of starting materials, fine chemicals and pharmaceuticals, green catalysis needs environmentally friendly catalysts which can be easily removed from the reaction media and used again many times with very high efficiency [8]. Nanoparticles display high catalytic activity and chemical selectivity under mild conditions [9]. In some reactions, the large surface area-to-volume ratio of metal oxide nanoparticles is mainly responsible for their catalytic performance [10]. In heterogeneous reactions, tedious methods like

centrifugation and filtration are utilized to recover catalysts and end in loss of solid catalyst in the process of separation. Magnetic separation supplies a convenient method to remove and recycle magnetized species by utilizing an appropriate magnetic field [11-13]. Magnetic spinel ferrite nanocrystals are considered as one of the most significant inorganic materials due to their electronic, electrical, optical, magnetic and catalytic features that are significantly different from those of their bulk counterparts [14-15]. Copper ferrite nanomaterial is one such reusable catalyst which shows high catalytic activity in organic synthesis [16].

Herein, copper ferrite nanoparticles were synthesized *via* the auto-combustion assisted sol-gel method [17-18]. We showed that nanomagnetic CuFe₂O₄ is an active and reusable catalyst through magnetic separation for oxidation of alcohols with oxone in the presence of water at room temperature (Scheme 1).



R₁, R₂ = Aryl, Alkyl, H

Scheme 1. Alcohols oxidation in the presence of nanomagnetic catalyst at room temperature

EXPERIMENTAL

General

Ferric nitrate nonahydrate Fe(NO₃)₃·9H₂O, copper nitrate trihydrate Cu(NO₃)₂·3H₂O, citric acid C₆H₈O₇, aliphatic and benzylic alcohols were

* To whom all correspondence should be sent:

purchased from Merck (Darmstadt, Germany) and Fluka (Switzerland) and used without further purification. The IR spectra were measured on a JASCO 6300 FT-IR spectrometer (KBr disks). The structural properties of the synthesized nanoparticles were studied by X-ray powder diffraction (XRD) on an X'pert-PRO advanced diffractometer using Cu (K α) radiation (wavelength: 1.5406 Å), operated at 40 kV and 40 mA at room temperature over the 2 θ range from 20 to 70°. The particulate morphology was characterized by scanning electron microscopy (Model: 1455VP, LEO Co., England). The disc was coated with gold in an ionization chamber. Elemental analyses were performed using inductively coupled plasma optical emission spectroscopy (ICP-OES, Model: VISTA-PRO). TLC and GC were used to monitor the reactions. The aliphatic products were detected by GC-FID (VARIAN C-P-3800 with FID detector, column CP-Sil 5 CB 30m \times 0.32mm).

Preparation of CuFe₂O₄ MNPs in aqueous solution

Copper ferrite nanoparticles were synthesized via the auto-combustion assisted sol-gel method from Cu²⁺ and Fe³⁺ ions (molar ratio 1:2) in ammonia solution [17,18]. Briefly, Fe(NO₃)₃·9H₂O, Cu(NO₃)₂·3H₂O and the chelating agent were dissolved in distilled water. The molar ratio of metal nitrate to citric acid was 1:1. The pH value was adjusted to 7 by dropwise adding ammonia solution (28%) to the reaction mixture under constant stirring. Then, the solution was evaporated on a water bath (60 °C) to form a sticky gel. The temperature was increased to 80 °C in order to obtain a thick gel. The gel was kept on a hot plate for auto-combustion and the temperature was increased to ca. 200 °C. A large amount of gases (CO₂, H₂O, and N₂) was released and auto-combustion occurred giving rise to a black ferrite powder. The powder was washed three times with distilled water and acetone and was isolated in a magnetic field.

General procedure for the oxidation of alcohol

Alcohol (1 mmol), water (2 mL) and 6 mol % of nanomagnetic CuFe₂O₄ (14 mg) were added to a round-bottomed flask. The mixture was stirred for two minutes. Then, oxone (0.7 mmol) was added in three portions for 15 min. The mixture was stirred at room temperature. The reaction was followed by TLC (EtOAc-cyclohexane, 2:10). After the completion of the reaction, the product was extracted in dichloromethane. The solvent was evaporated under reduced pressure to give the

corresponding pure aromatic products. Purification of the residue using flash column chromatography (silica gel) provided the pure carbonyl compounds. The products were identified by IR spectra. The aliphatic products in dichloromethane were dried using anhydrous MgSO₄ and were detected by GC-FID by comparison with standard samples of the corresponding alcohols and carbonyl compounds. The GC yields of the aliphatic products were calculated based on their gas chromatograms.

RESULTS AND DISCUSSION

Characterization of the catalyst

The FT-IR spectrum of the CuFe₂O₄ MNPs is presented in Fig. 1. A broad absorption band at about 3440 cm⁻¹ represents a stretching mode of H₂O molecules and indicates that a large number of OH groups are present on the surface of the MNPs [19]. In the range of 1000–400 cm⁻¹, two broad metal–oxygen bands are observed. A metal–oxygen absorption band typical for the spinel structure of the ferrite at ~580 cm⁻¹ was observed. This band strongly suggests intrinsic stretching vibrations of the metal (M \leftrightarrow O) at the tetrahedral site [20-21], whereas the lowest band, usually observed in the range 450–400 cm⁻¹, is assigned to octahedral metal stretching [22-24]. Fig. 2 shows the XRD pattern of the CuFe₂O₄ MNPs. Generally, XRD can be used to characterize the crystallinity of nanoparticles, and it gives the average diameters of all nanoparticles. The results indicate that the discernible peaks in Fig. 2 [18, 25] correspond to a cubic spinel structure of copper iron oxide (JCPDS card No. 01-077-0010). The diameter of the CuFe₂O₄ MNPs determined by the Debye-Scherrer equation using XRD data ($D = 0.94 \lambda / B \cos \theta$) was 57.9 nm. From the ICP- OES results, the atomic ratio of Cu-Fe was found to be 0.57, which is close to that of CuFe₂O₄ and 26.5% w/w is copper. The SEM analysis suggests that the CuFe₂O₄ MNPs are nanocrystalline and their shape is irregular spherical (Fig. 3). These results are in good agreement with the XRD analyses.

Optimization of alcohol oxidation conditions

We tried to convert 2-chlorobenzyl alcohol (1 mmol) to 2-chlorobenzaldehyde, as a model reaction in the presence of CuFe₂O₄ as a nanomagnetic catalyst (12 mg) and oxone (1 mmol added in three steps) in various solvents (2mL) at r.t. and the results are given in Table 1. The best result was achieved in the presence of water (Table 1, entry 4).

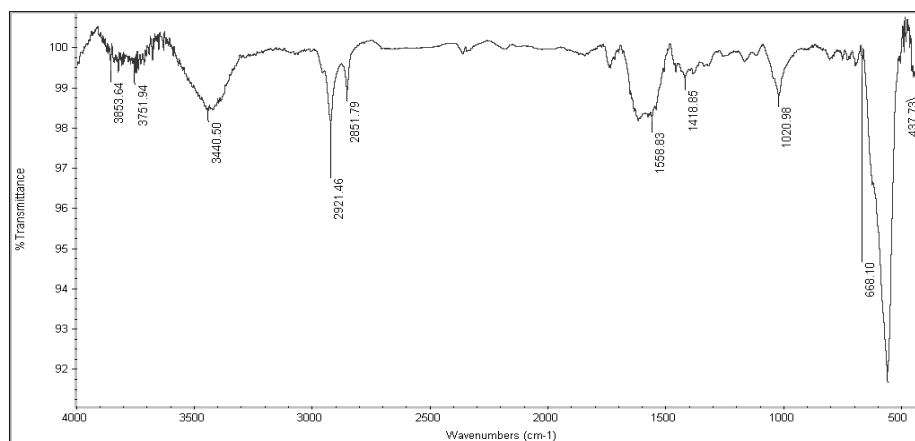


Fig. 1. FT-IR spectrum of the CuFe₂O₄ MNPs

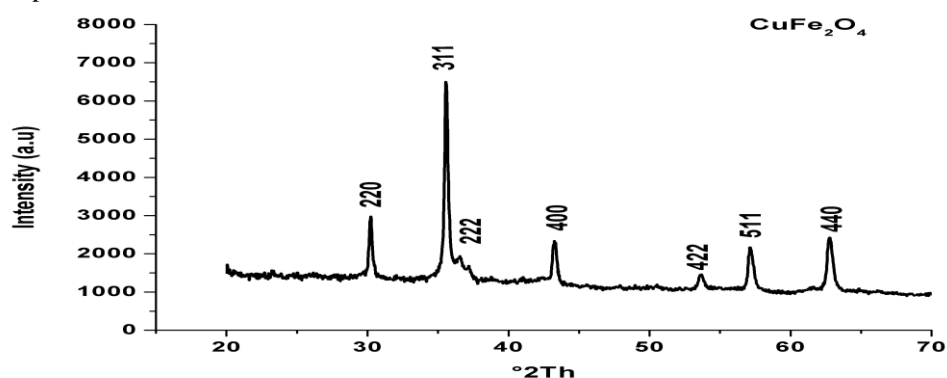


Fig. 2. XRD pattern of the CuFe₂O₄ MNPs

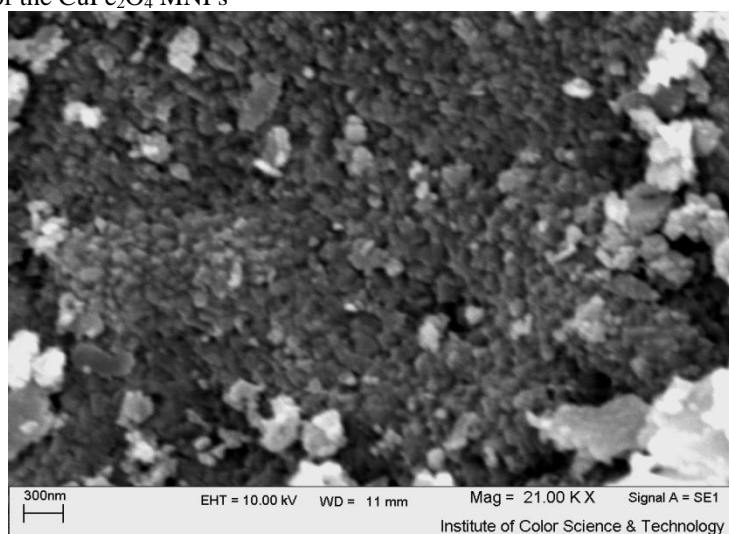


Fig. 3. SEM image of the CuFe₂O₄ MNPs

Table 1. Conversion of 2-chlorobenzyl alcohol to 2-chlorobenzaldehyde in different solvents with oxone in the presence of CuFe₂O₄ MNPs catalyst at r.t.

Entry	Solvent	Yield (%)	Time (min)
1	Dichloromethane	15	90
2	Cyclohexane	trace	90
3	Acetonitrile	22	90
4	Water	65	90
5	Ethanol	trace	90
6	Dry toluene	trace	90
7	Ethyl acetate	10	90

We also studied the oxidation of 2-chlorobenzyl alcohol to 2-chloro benzaldehyde with other oxidants in the presence of nanomagnetic CuFe₂O₄ catalyst in water at room temperature. These results showed that a higher yield was achieved with oxone as oxidant (Table 2, entry 3). We observed that in the absence of oxidant (in nitrogen atmosphere), 2-chlorobenzyl alcohol was not oxidized with this system, even for a long reaction time.

Catalyst and oxidant amounts were also optimized. The results showed that 14 mg of catalyst (6 mol%) and 0.7 mmol of oxidant were the best amounts for the oxidation of 1 mmol of alcohol (Table 3 and 4). In these reactions, the aldehyde selectivity was very high (>99%). No competing reaction such as overoxidation of aldehydes to the corresponding carboxylic acids was observed in any of the cases under the above conditions, but the reaction produced a byproduct (carboxylic acid) at high temperatures (>40 °C).

Application scope

The reaction conditions, which were optimized for 2-chlorobenzyl alcohol, can be easily applied to various primary and secondary alcohols. As indicated in Table 5, the CuFe₂O₄ MNPs catalyst showed high activity/selectivity and excellent reusability in oxidation processes. In most cases, the aldehyde selectivity was quite high (>99%). The oxidation of various benzylic alcohols gave carbonyl compounds in high yields and short reaction times. The electron withdrawing groups dramatically reduced the reaction rate (entry11) and the electron donor substituted group in the benzene ring of benzylic alcohols accelerated the reaction rate (entry14).

The oxidation times for aliphatic alcohols were fairly long (entries 17-19). No competing reaction such as overoxidation of aldehydes to the corresponding carboxylic acids was observed in any of the cases under the above conditions.

Table 2. Oxidation of 2-chlorobenzyl alcohol using various oxidants in water in the presence of CuFe₂O₄ MNPs catalyst at r.t.

Entry	Oxidizing agent (1mmol)	Yield (%)	Time (min)
1	H ₂ O ₂	20	90
2	O ₂ atmosphere	trace	90
3	Oxone	65	90
4	-	0	90

Table 3. Oxidation of 2-chlorobenzyl alcohol with oxone (1mmol) and different amounts of CuFe₂O₄ MNPs in water at r.t

Entry	Amount of nanomagnetic CuFe ₂ O ₄ catalyst (mol%)	Yield (%)	Time (min)
1	10	86	90
2	7	85	90
3	6	86	90
4	5	65	90
5	4	48	90
6	0	20	90

Table 4. Oxidation of 2-chlorobenzyl alcohol (1mmol) in water with different amounts of oxone in the presence of CuFe₂O₄ MNPs catalyst (6 mol%) at r.t

Entry	Amount of oxone (mmol)	Yield (%)	Time (min)
1	1	86	90
2	0.7	86	90
3	0.5	77	90
4	0.3	52	90
5	0.1	20	90

The catalyst was easily separated from the products by exposure of the reaction vessel to an external magnet and decantation of the reaction solution. The remaining catalyst was washed with acetone and water to remove residual products and dried. This catalyst could be reused in 6 further iterative cycles without obvious reduction in activity (Fig. 4). Measurements by ICP-OES showed that 26.3% of the catalyst weight in the 6th recycling was copper. Hence, there was no obvious decrease in the copper content of the catalyst in the 6th recycling. The XRD pattern of the CuFe₂O₄ MNPs in the 6th recycling showed no obvious difference in comparison with its first XRD pattern.

Proposed mechanism for the oxidation

Based on our experimental results and the related literature [26-28], we propose the following reaction mechanism for the oxidation of alcohols by oxone in water in the presence of CuFe₂O₄ MNPs catalyst (Scheme 2). Initially alcohol and catalyst were stirred and alcohol was grafted on the catalyst (Stage I). Then, oxone was added and was dissolved in water and HSO₅⁻ took electrons (Stage II). The procedure was followed by elimination of H⁺ (Stage III). It seems that a large number of OH groups are present on the surface of the catalyst (Fig. 1, absorption band at 3440 cm⁻¹). The OH groups cause some interactions in the water phase. Since the catalyst is present in the water phase, HSO₅⁻ takes electrons fairly rapidly. When the catalyst resides in the organic phase, HSO₅⁻ forms a separate aqueous phase, thus Fe(II) cannot donate an electron.

Table 5. Oxidation of various alcohols using CuFe₂O₄ MNPs as catalyst (6 mol%) in the presence of oxone (at r.t.) in water

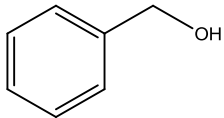
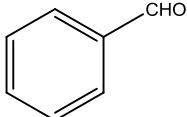
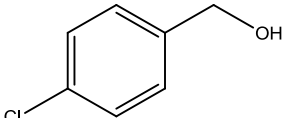
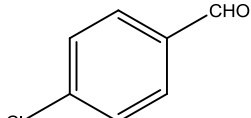
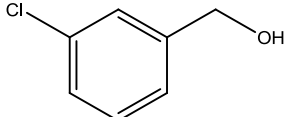
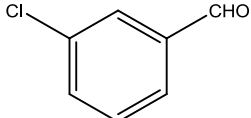
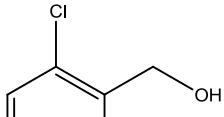
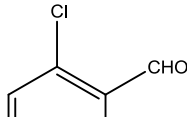
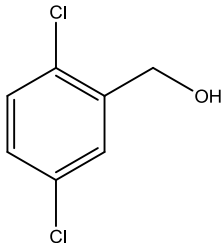
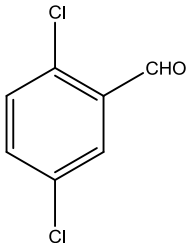
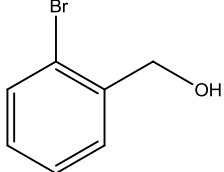
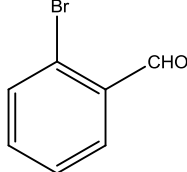
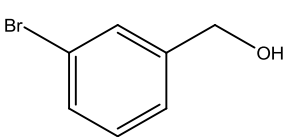
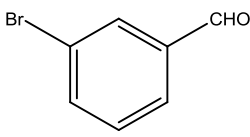
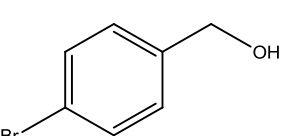
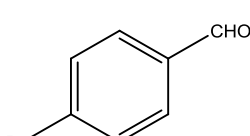
Entry	Substrate	Product	Yield ^a (%)	Time (min)
1	2	3	4	5
1			90	90
2			87	85
3			86	90
4			83	95
5			84	90
6			86	85
7			88	95
8			85	90

Table 5 continued

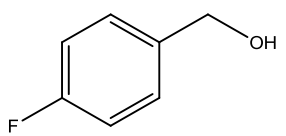
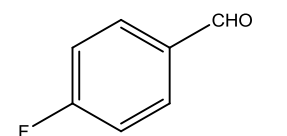
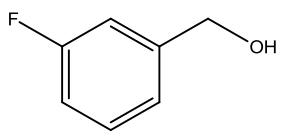
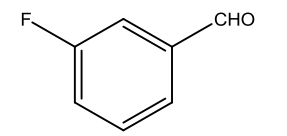
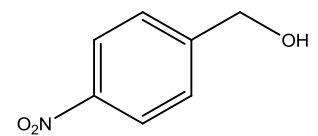
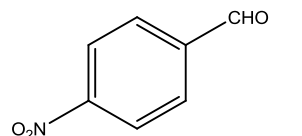
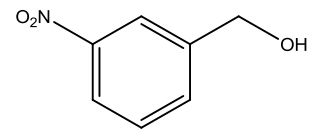
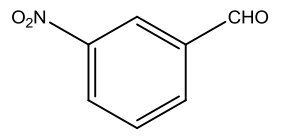
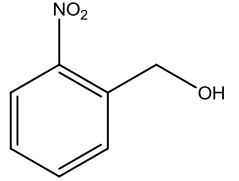
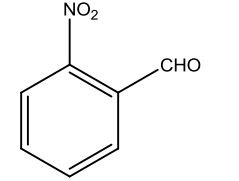
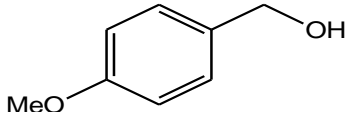
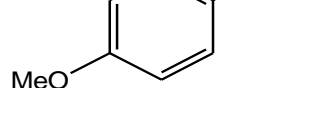
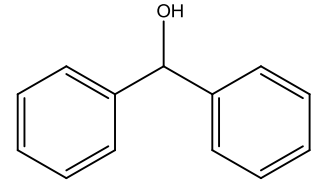
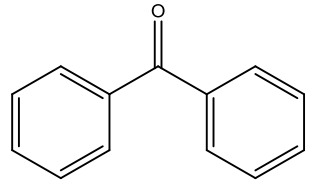
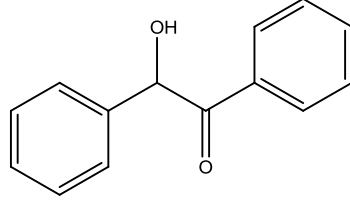
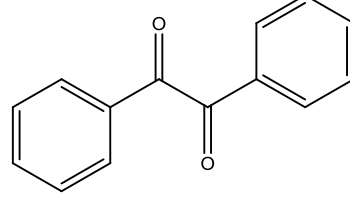
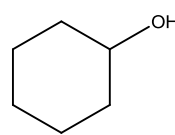
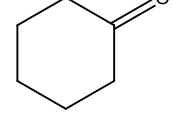
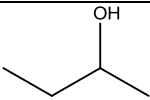
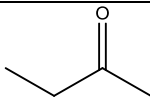
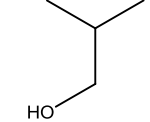
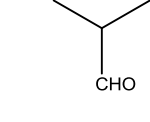
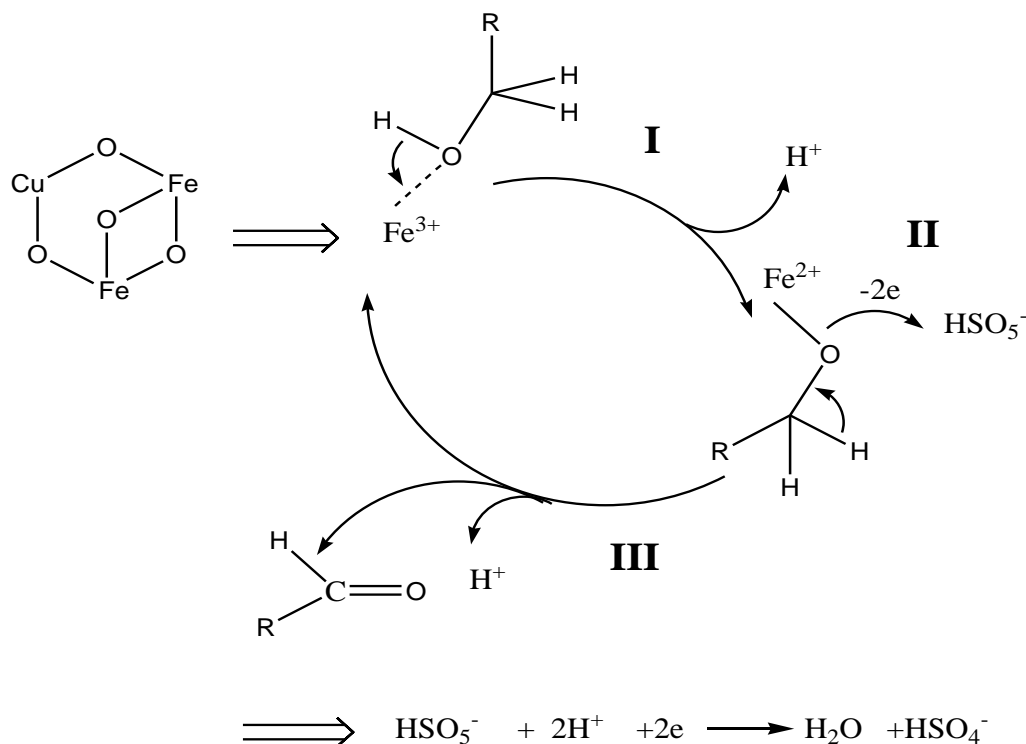
1	2	3	4	5
9			88	90
10			86	85
11			84	120
12			84	120
13			80	120
14			91	90
15			85	95
16			70	120
17 ^b			99.84	150

Table 5 continued

1	2	3	4	5
18 ^b			99.50	150
19 ^b			99.16	150

a- Yields refer to isolated products. The products were characterized by their spectral data (IR) and compared with authentic samples. b-The yields refer to GC analysis



Scheme 2. Proposed mechanism for the oxidation of alcohols by oxone oxidant in the presence of CuFe₂O₄ MNPs

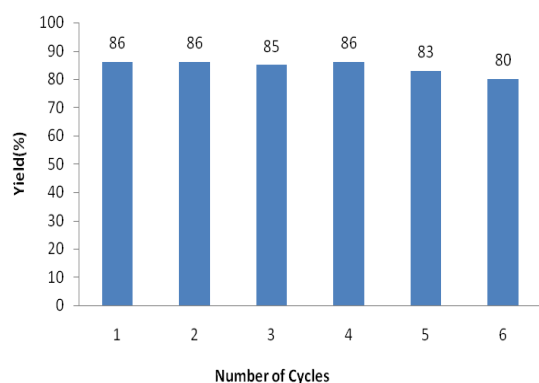


Fig. 4. Recycling of the catalyst for oxidation of 2-chlorobenzyl alcohol

CONCLUSIONS

To summarize, we have introduced a direct and effective method for the oxidation of alcohols to their corresponding carbonyl compounds using oxone in the presence of nanomagnetic CuFe₂O₄ catalyst as a reusable, non-toxic, non-corrosive, inexpensive and

commercially available heterogeneous catalyst in water. The method also offers some other advantages such as stability of the oxidation system, simplicity, short reaction times, good yields of the products and mild reaction conditions. The catalyst can be subsequently reused in 6 further iterative cycles with no decrease in activity. The extension of the application of this nanocatalyst to various oxidation reactions is currently under investigation in our laboratory.

Acknowledgment: This work was supported by the "Iran National Science Foundation: INSF".

REFERENCES

1. X. Wang, D. Z. Wang, *Tetrahedron*, **67**, 3406 (2011).
2. R. A. Sheldon, J. K. Kochi, *Metal-catalyzed Oxidation of Organic Compounds*, Academic, New York, 1981.
3. R. A. Sheldon, I. W. C. E. Arends, U. Isabel, *Green Chemistry and Catalysis*, Wiley-VCH, 2007.
4. J. March, *Advanced Organic Chemistry: Reactions, Mechanisms, and Structure*, 4th ed.; John Wiley and Sons: New York, 1992.
5. (a) M. Hudlicky, *Oxidations in Organic Chemistry*, American Chemical Society: Washington, DC, 1990. (b) R.C. Larock, *Comprehensive Organic Transformations: A Guide to Functional Group Preparations*, Wiley-VCH: New York, 1999.
6. G. Tojo, M. Fernandez, *Oxidation of Alcohols to Aldehydes and Ketones*, Springer: Berlin, 2006.
7. Y. Kuang, Y. Nabaie, T. Hayakawa, M. A. Kakimoto, M.a. *Appl. Catal. A: Gen.*, **423**, 52 (2012).
8. D. Astruc, *Transition-metal Nanoparticles in Catalysis: From Historical Background to the State of the Art*. In *Nanoparticles and Catalysis*, Wiley-VCH: Weinheim, Germany, 2008.
9. R. B. N. Baig, S. V. Rajender, *Chem. Commun.*, **49**, 7529 (2013).
10. A. T. Bell, *Science*, **299**, 1688 (2003).
11. J. A. Melero, R.V. Grieken, G. Morales, *Chem. Rev.*, **106**, 3790 (2006).
12. D. Astruc, F. Lu, J.R. Aranzaes, *Angew. Chem. Int. Ed.*, **44**, 7852 (2005).
13. S. Morent, S. Vasseur, F. Grasset, E. Duguet, *J. Mater. Chem.*, **14**, 2161 (2004).
14. B. Aslibeiki, P. Kameli, H. Salamati, M. Eshraghi, T. Tahmasebi, *J. Magn. Magn. Mater.*, **322**, 2929 (2010).
15. S. C. Tsang, V. Caps, I. Paraskevas, D. Chadwick, D. Thompsett, *Angew. Chem. Int. Edit.*, **43**, 5645 (2004).
16. M. L. Kantam, J. Yadav, L. Soumi, P. Srinivas, B. Sreedhar, F. Figueras, *J. Org. Chem.*, **74**, 4608 (2009).
17. A. A. Thant, S. Srimala, P. Kaung, M. Itoh, O. Radzali, M. N. Ahmad Fauzi, *J. Aust. Ceram. Soc.*, **46**, 11 (2010).
18. I. V. Kasi Viswanath, Y. L. N. Murthy, K. Rao Tata, R. Singh, *Int. J. Chem. Sci.*, **11**, 64 (2013).
19. V.K. Sankaranarayana, C. Sreekumar, *Curr. Appl. Phys.*, **3**, 205(2003).
20. P. Laokul, V. Amornkitbamrung, S. Seraphin, S. Maensiri, *Curr. Appl. Phys.*, **11**, 101 (2011).
21. S. Maensiri, M. Sangmanee, A. Wiengmoon, *Nanoscale Res Lett.*, **4**, 221(2009).
22. S. Hafner, *Z. Kristallogr.*, **115**, 331 (1961).
23. R.D. Waldron, *Phys. Rev.*, **99**, 1727 (1955).
24. N. Kasapoglu, A. Baykal, Y. Koseoglu, M. S. Toprak, *Scripta Mater.*, **57**, 441 (2007).
25. K. Ali, A. Iqbal, M. R. Ahmad, Y. Jamil, S. Aziz Khan, N. Amin, M.A. Iqbal, M. Z. Mat Jafri, *Sci. Int. (Lahore)*, **23**, 21 (2011).
26. K. S. Webb, S. J. Ruszkay, *Tetrahedron*, **54**, 401(1998).
27. Y. R. Wang, W. Chu, *Appl. Catal. B-Environ.*, **123**, 151 (2012).
28. S. P. Maradur, S.B. Halligudi, G. S. Gokavi, *Catal. Lett.*, **96**, 165 (2004).

МАГНИТНИ НАНОЧАСТИЦИ ОТ CuFe₂O₄ КАТО ЕФЕКТИВЕН КАТАЛИЗАТОР ЗА
ОКИСЛЯВАНЕТО НА АЛКОХОЛИ ДО КАРБОНИЛНИ СЪЕДИНЕНИЯ В ПРИСЪСТВИЕ
НА ОКСОН КАТО ОКИСЛИТЕЛ

Ф. Садри¹, А. Рамазани^{*2}, А. Масуди¹, М. Кхуби³, С. У. Джун^{*4}

¹Департамент по химия, Университет Паям Нур, Техеран, Иран

²Департамент по химия, Университет в Занджан, Иран

³Фармацевтичен научно-изследователски център, Университет по медицински науки в Техеран, Иран

⁴Училище по машиностроене, Университет Йоннам, Кьонсан 712-749, Република Корея

Постъпила на 27 февруари, 2014 г., коригирана на 8 май, 2014 г.

(Резюме)

Използвани са магнитни наночастици от CuFe₂O₄ като ефективен, устойчив катализатор за многократно употреба за селективното окисление на алкохоли до съответните им карбонилни съединения от оксон (натриев хидроген-персулфат) като окислител във водна среда при стайна температура. Първичните и вторичните алкохоли дават съответните продукти с добри добиви. Катализаторът е изследван с помощта на XRD, SEM, ICP и IR-методи. Катализаторът може лесно да се извлече и да се употребява многократно без загуба на активност.

Application of mechanochemical method as a new route for synthesis of β -phase AgI nanoparticles

M. Malekshahi Byranvand^{1*}, S. Shahbazi², A. Nemati Kharat¹, S. Afshar²

¹School of Chemistry, University College of Science, University of Tehran, Tehran, Iran

²Department of Chemistry, Iran University of Science and Technology, 16846-13114 Tehran, Iran

Received March 7, 2014, revised May 12, 2014

In this contribution, we introduce a one-pot, rapid solvent-free method for preparation of silver iodide nanoparticles (AgI NPs). The AgI NPs were characterized by X-ray powder diffraction patterns (XRD), energy dispersive X-ray spectroscopy (EDX), diffuse reflectance spectra (DRS), scanning electron microscopy (SEM) and dynamic light scattering (DLS). The XRD data indicated a wurtzite structure of the β -phase of AgI in the synthesized NPs. The EDX analysis confirmed the formation of a 100% pure AgI compound. The SEM images and the DLS data confirmed the nanosized spherical morphology of 25-70 nm. The DRS of the AgI nanoparticles showed a band gap about 2.7 eV.

Keywords: Nanoparticles; Semiconductors; Silver iodide; Solvent free synthesis.

INTRODUCTION

Silver iodide (AgI) is frequently used in photography and in cloud-seeding to promote rainfalls [1]. Also, the application of AgI-based superionic conducting glasses [2] has attracted much attention. The conductivity of the solid AgI is comparable to that of liquid sulfuric acid, and is even higher than that of liquid AgI [3]. At ambient temperature and pressure, AgI usually exists as a mixture of two phases, β -AgI and γ -AgI. The β -phase has a hexagonal wurtzite structure and the γ -phase has a cubic zinc blende structure [4]. Amongst the various types of nanomaterials, semiconductor nanoparticles attract special interest because they are expected to exhibit excellent properties compared to the corresponding bulk material [5]. Recently, there has been increasing interest in AgI in form of nanoparticles (NPs) which have different optical, electrical and superionic properties compared to the bulk compound [6].

We have recently reported the facile synthesis of CuI NPs by a mechanochemical method [7]. This method involves the mechanical activation of solid-state displacement reactions at low temperatures in a ball mill [8, 9]. When comparing the mechanochemical process with the hydrothermal [10], thermal decomposition [11], microemulsion and reverse micelles [6], laser-based synthesis [12], electrospinning [13] and sonochemical [14, 15] methods for the preparation of AgI NPs, it obvious that the mechanochemical reaction has many

advantages such as: one-pot synthesis, rapid reaction, solvent -free and safe reaction conditions. To the best of our knowledge, no reports for the preparation of AgI NPs under these conditions have been reported. Nevertheless, recently Hawari et al. synthesized AgI NPs using the mechanochemical method in the liquid-state over a long period of time (40–70 h) [16]. This study, for the first time, introduces a solid-state mechanochemical method for the synthesis of spherical β -AgI NPs. The proposed method is solvent-free and facile which would result in a lower cost and environmental safety.

MATERIALS AND METHODS

AgNO₃ (99%) and KI (99.5%) were purchased from Merck Company and were used without further purification. In a 10 ml stainless steel vial a mixture of AgNO₃ and KI solids with a molar ratio of 1:1 were milled using a Mixer Mill (Retsch MM-400) apparatus at 1800 rpm (30 Hz) for 40 min at room temperature. The resulting mixture was washed with deionized water to remove the potassium nitrate salt. The precipitate was then dried in a vacuum oven at 100 °C for 2 h to obtain the final yellow product.

X-ray powder diffraction patterns (XRD) were recorded on a SIEFERT XRD 3003 PTS diffractometer using Cu K α irradiation (λ 1.5418 Å). Diffuse reflectance spectra (DRS) were measured on a TU-1901 spectrophotometer. Scanning electron microscopy (SEM) and energy dispersive X-ray spectroscopy (EDX) were performed with a Hitachi S-4160 microscope with

* To whom all correspondence should be sent:
E-mail: mahdi.malekshahi@gmail.com

attached camera operating at 30 kV to determine the morphology, particle size and purity of the prepared synthesized salt. Dynamic light scattering (DLS) analysis was performed on a Zetasizer Nano-Z model apparatus to determine the size distribution of AgI NPs. All measurements were done at room temperature.

RESULTS AND DISCUSSION

The X-ray diffraction (XRD) pattern was used to investigate crystallinity and phase structure of the product before and after the washing process (Fig. 1a, b). As shown in Fig. 1a, peaks related to KNO_3 phases were indexed and before washing the peak intensity of the products was relatively high. Due to overlapping of AgI and KNO_3 peaks in a certain

region, after washing the sharpness of AgI peaks decreased (Fig. 1b). So it was concluded that AgI NPs were completely formed by the solid-state method. The β -AgI phase can be characterized by the peaks located at 2θ value of 22.32° , 23.71° , 25.35° , 32.76° , 39.20° , 42.63° and 45.57° , which are assigned to the (1 0 0), (0 0 2), (1 0 1), (1 0 2), (1 1 0), (1 0 3) and (1 1 2) planes of β -AgI crystal, respectively (Fig. 1 b)[17].

All diffraction peaks can be indexed to the hexagonal phase for the β -AgI with a wurtzite structure (space group P63mc, JCPDS card no. 3-0940). As we expected, all products generated from these simple mechanochemical reaction systems are pure AgI crystals, no diffraction signal from other byproducts such as Ag_2O was detected.

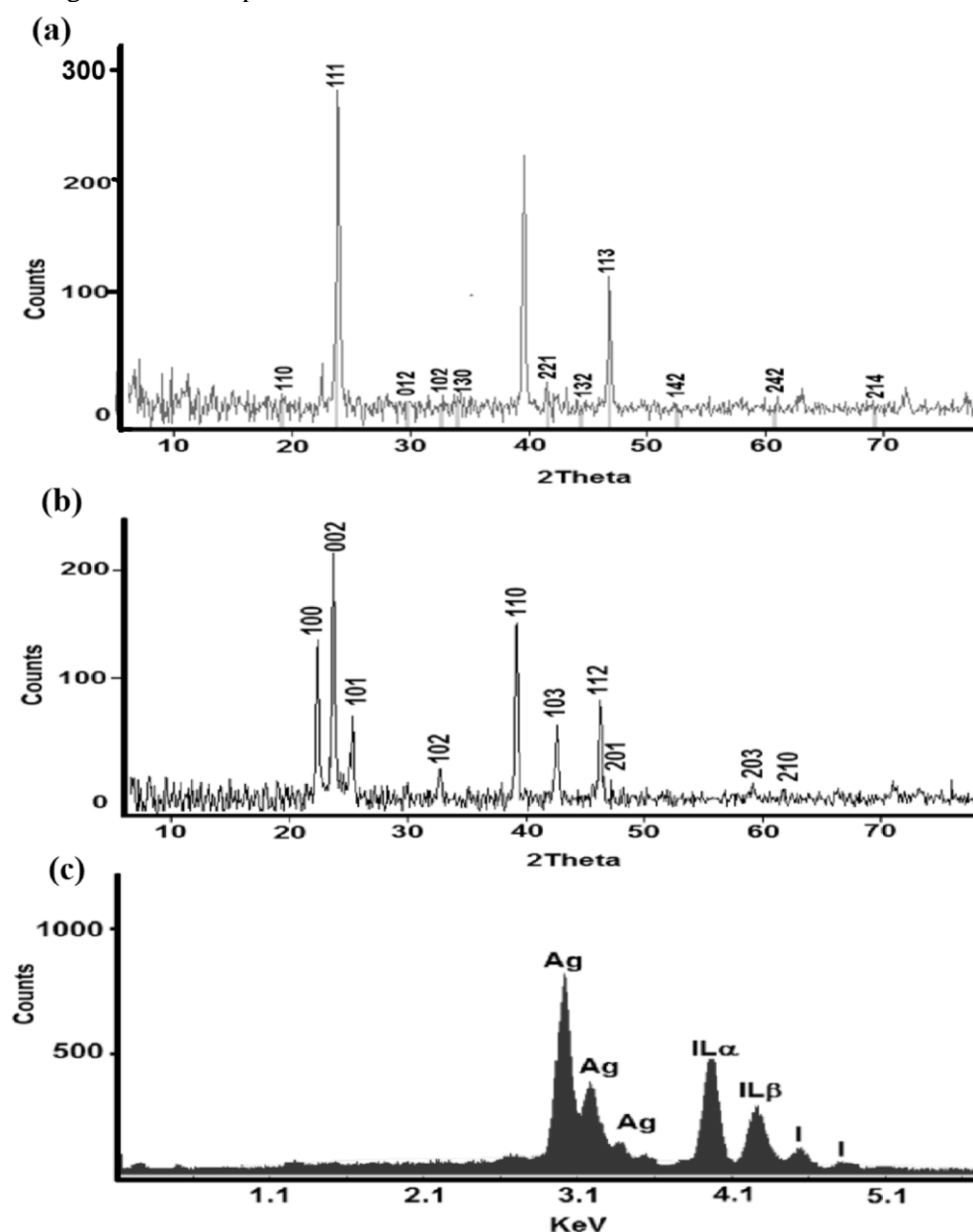


Fig. 1. (a) XRD pattern of the mixture of AgI NPs and KNO_3 salt (b) AgI NPs after the washing process; (c) EDX pattern of the synthesized product.

In the long history of investigation of AgI, one main difficulty was to obtain pure single phase crystals [18, 19]. According to our studies, AgI single phase crystals were obtained during mechanochemical reaction for 40 min at room temperature without any solvent. The estimated grain size of the AgI powder using Debye-Scherrer's formula [20] was found to be about 32 nm. The purity of the prepared AgI NPs was evidenced by the EDX pattern shown in Fig. 1c. The EDX analysis verified the existence of silver and iodide atoms in the final product. This analysis showed 100% purity of the synthesized compound which is in good agreement with the XRD data.

The morphology of the obtained product was investigated by SEM. As can be seen in Fig. 2a and b, the SEM images show that the AgI NPs powder consists of 25-50 nm spherical nanoparticles.

The DLS analysis was also used to estimate the particle size and size distribution. The particle size histogram in Fig. 2 c shows that size distribution is 25-70 nm and nanoparticles are uniformly aggregated, which is very close to the results obtained by SEM analysis. Optical absorption measurements were used extensively, because they are some of the most important methods to investigate the energy structures and optical properties of semiconductor nanocrystals [21, 22]. Based on the theory of optical absorption, the relation between the absorption coefficient and photon energy is as follows:

$$\alpha h\nu = A(h\nu - E_g)^{n/2} \quad (1)$$

where α is the absorption coefficient, ν is the frequency of photons, A is a constant, E_g is the band gap energy and n depends on the nature of the transition ($n=1$ for direct transitions) [23].

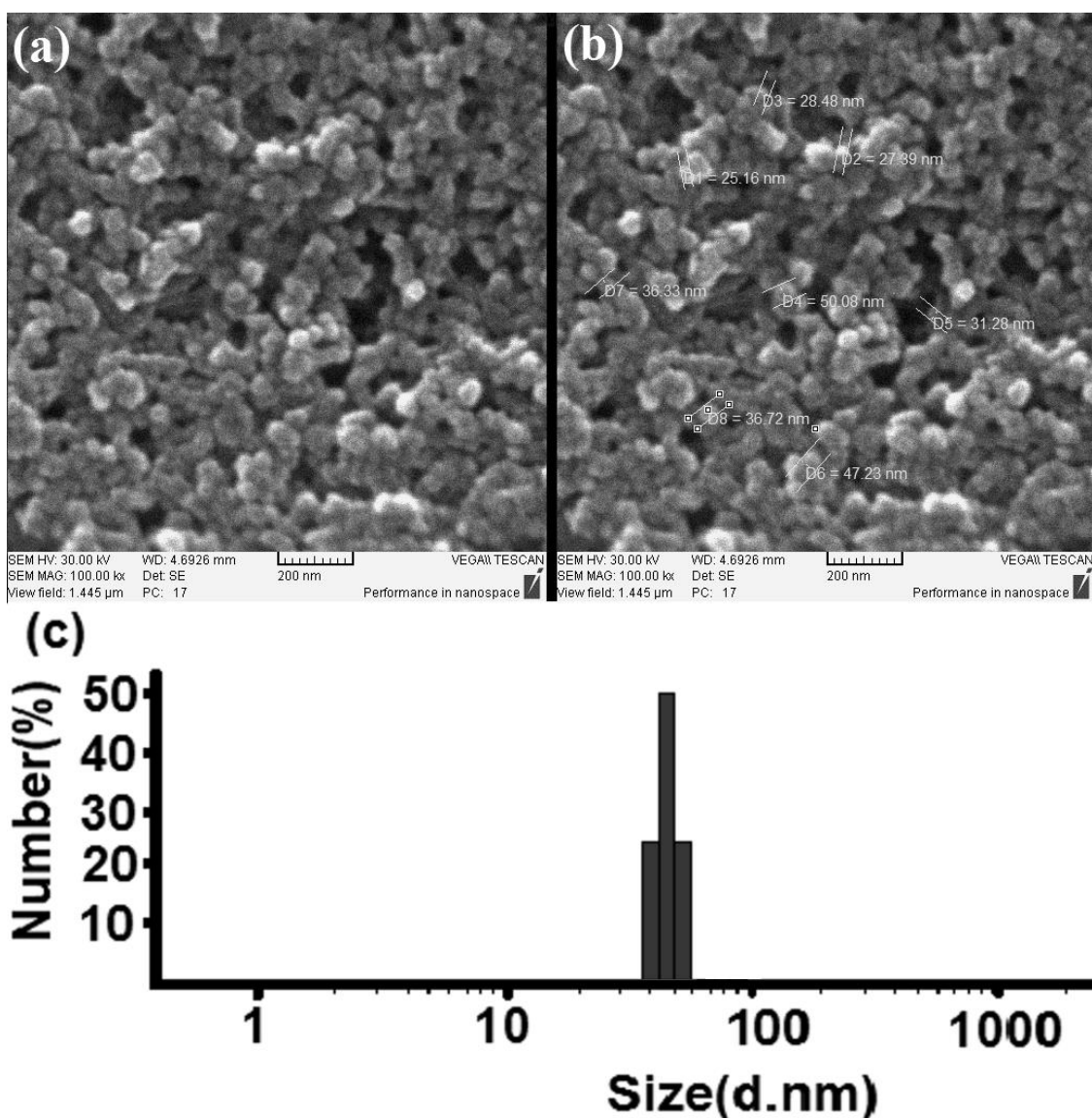


Fig. 2. (a, b) SEM images of AgI NPs; (c) Size distribution histogram extracted from DLS analysis data.

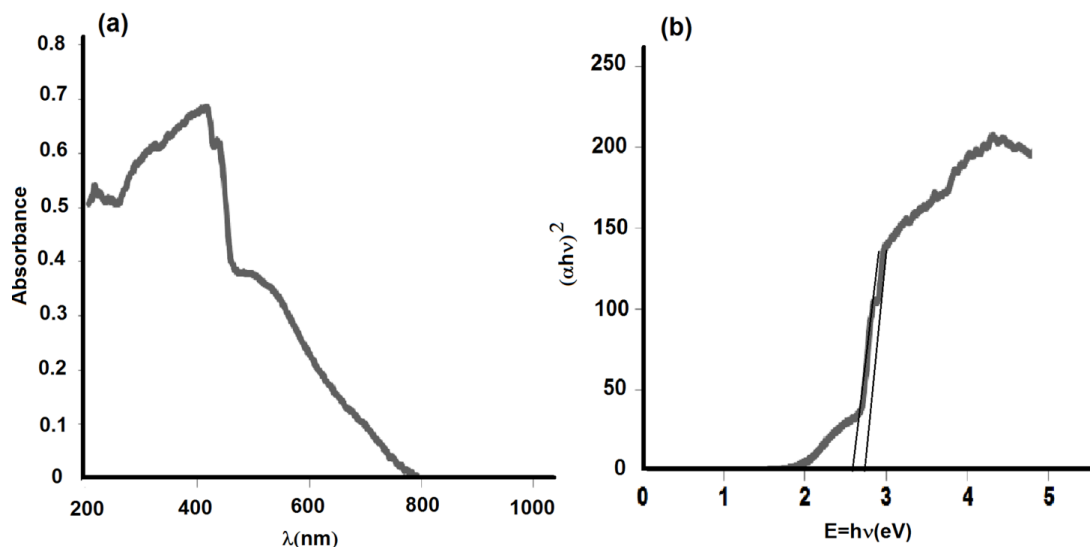


Fig. 3. (a) Optical absorption spectrum of obtained AgI NPs; (b) the plot of $(\alpha h\nu)^2$ vs. $h\nu$.

Figs. 3a and b show the optical absorption spectrum and the plot of $(\alpha h\nu)^2$ vs. $h\nu$ for the prepared AgI nanoparticles, respectively. There is a broad absorption peak with broader shoulders at about 495 nm and weak absorption peak at about 505 nm. According to the extrapolated values of the linear section, the band gap E_g is estimated to be 2.7 eV and 2.8 eV.

CONCLUSION

In this work, β -phase of AgI with spherical morphology of NPs was successfully synthesized using the mechanochemical method. The XRD and EDX analyses of these NPs revealed a pure β -phase. According to our studies, AgI NPs were obtained during mechanochemical reaction for 40 min without any solvent. This facile, solvent-free, short-time and one-pot method for the synthesis of AgI compound is reported for the very first time. The method proposed in this work has many advantages, such as solvent free characteristics which result in lower costs, environmental safety and a very easy procedure of synthesis. We believe that this simple method will be adopted in realizing other forms of nano-sized silver compounds on industrial scale.

REFERENCES

1. Z. Zheng, A. R. Liu, S. M. Wang, B. J. Huang, X. M. Ma, H. X. Zhao, D. P. Li, L. Z. Zhang, *Materials Research Bulletin*, **43**:2491(2008).
2. T. Usuki, S. Saito, K. Nakajima, O. Uemura, Y. Kameda, T. Kamiyama, M. Sakurai, *Journal of Non-Crystalline Solids*, **312–314**, 570 (2002) T. Usuki, S. Saito, K. Nakajima, O. Uemura, Y. Kameda, T. Kamiyama,
3. J. Non-Cryst. Solids, (2002), p.

4. S. Yamasaki, T. Yamada, H. Kobayashi, H. Kitagawa, *Chemistry – An Asian Journal*, **8**, 73 (2013).
5. C. Liang, K. Terabe, T. Tsuruoka, M. Osada, T. Hasegawa, M. Aono, *Advanced Functional Materials*, **17**, 1466 (2007).
6. M. Bangal, S. Ashtaputre, S. Marathe, A. Ethiraj, N. Hebalkar, S. W. Gosavi, J. Urban, and S. K. Kulkarni, *Hyperfine Interact.*, **160**, 81 (2005).
7. I. L. Validžić, I. A. Janković, M. Mitrić, N. Bibić, J. M. Nedeljković, *Materials Letters*, **61**, 3522 (2007).
8. S. Shahbazi, S. Afshar, *Materials Letters*, **115**, 190 (2014).
9. A. Tadjarodi, M. Izadi, M. Imani, *Materials Letters*, **92**, 108 (2013).
10. J. Huot, D. B. Ravnsbæk, J. Zhang, F. Cuevas, M. Latroche, T. R. Jensen, *Progress in Materials Science*, **58**, 30 (2013).
11. L. Chen, J. Ma, Q. Chen, R. Feng, F. Jiang, M. Hong, *Inorganic Chemistry Communications*, **15**, 208 (2012).
12. L. Yang, J. Lu, Z. Wang, L. Li, *Kuei Suan Jen Hsueh Pao/Journal of the Chinese Ceramic Society*, **39**, 929 (2011).
13. H. Tan, W. Y. Fan, *Chem Phys Lett.*, **406**, 289 (2005).
14. H. Liang, C. Li, J. Bai, L. Zhang, L. Guo, Y. Huang, *Applied Surface Science*, **270**, 617 (2013).
15. F. Mohandes, M. Salavati-Niasari, *Materials Research Bulletin*, **48**, 3773 (2013).
16. A. R. Abbasi, A. Morsali, *Ultrason Sonochem.*, **17**, 704 (2010).
17. N. L. Hawari, M. R. Johan, *Journal of Alloys and Compounds*, **509**, 2001 (2011).
18. S. Feng, H. Xu, L. Liu, Y. Song, H. Li, Y. Xu, J. Xia, S. Yin, J. Yan, *Colloids and surfaces A: Physicochemical and engineering aspects*, **410**, 23 (2012).
19. Y. Wang, J. Mo, W. Cai, L. Yao, L. Zhang, *Materials Letters*, **56**, 502 (2002).
20. H. He, Y. Wang, H. Chen, *Solid State Ionics*, **175**, 651 (2004).

21. M. Song, Z. Zhang, *Materials Research Bulletin*, **39**, 2273 (2004)
22. K.H. Schmidt, R. Patel, D. Meisel, *Journal of the American Chemical Society*, **110**, 4882 (1988).
23. J. Liu, X. Huang, Y. Li, K. M. Sulieman, X. He, F. Sun, *Crystal Growth & Design*, **6**, 1690 (2006).
24. B. Sharma, M. K. Rabinal, *Journal of Alloys and Compounds*, **556**, 198 (2013).

ПРИЛОЖЕНИЕ НА МЕХАНОХИМИЧНИ МЕТОДИ КАТО НОВ ПЪТ ЗА СИНТЕЗАТА НА β -ФАЗОВИ НАНОЧАСТИЦИ ОТ AgI

М. Малекшани Биранванд^{1*}, С. Шахбази², А. Н. Кхарат¹, С. Афшар²

¹ Училище по химия, Колеж за наука, Университет в Техеран, Иран

² Департамент по химия, Ирански университет по наука и технология 6846-13114 Техеран, Иран

Постъпила на 7 март, 2014 г., коригирана на 12 май, 2014 г.

(Резюме)

В настоящата работа се предлага едно-стадийна, бърза синтеза, без разтворител, за приготвянето на наночастици от сребърен йодид (AgI NPs). Наночастиците са охарактеризирани чрез прахова рентгенова дифракция (EDX), дифузионни отражателни спектри (DRS), сканираща електронна спектроскопия (SEM) и динамично светоразсейване (DLS). XRD-данните показват, че синтезираните наночастици имат структурата на вюрцит на β -фаза от сребърен йодид. В допълнение EDX-анализът потвърждава образуването на сребърен йодид със 100% чистота. Освен това SEM-образите и DLS-анализът потвърждават сферичната морфология на частиците с размери 25-70 nm. DRS-спектрите на продукта показват, че наночастиците от AgI имат забранена зона около 2.7 eV.

A green synthetic route to some supramolecules using molybdate sulfuric acid (MSA) as a highly efficient heterogeneous catalyst

A. Arami¹, B. Karami¹, S. Khodabakhshi*²

¹Department of Chemistry, Yasouj University, Yasouj, Zip Code: 75918-74831 P.O.Box 353, Iran

²Young Researchers and Elite Club, Robotkarim Branch, Islamic Azad University, Robotkarim, Iran

Received March 23, 2014, Revised August 5, 2014

A facile and simple procedure for the synthesis of some calix[4]resorcinarene derivatives was developed via reaction of aryl aldehydes with resorcinol in the presence of catalytic amounts of molybdate sulfuric acid under solvent-free conditions. This eco-friendly method has many appealing attributes, such as excellent yields, short reactions times, use of a green and recoverable catalyst, and simple work-up procedures.

Key words: Calix[4]resorcinarene; Aryl aldehyde; Molybdate sulfuric acid, Resorcinol.

INTRODUCTION

Supramolecular chemistry has attracted the attention of many chemists in recent years. Calix[4]resorcinarenes, a subclass of calixarenes, are large cyclic tetramers which have found many applications, as solid phases immobilising uranyl cations [1], macrocyclic receptors [2], dendrimers in biological systems [3], nanoparticles [4], nano-capsules [5], supramolecular tectons [6], optical chemosensors [7], host molecules or host-guest complexes [8,9], components in liquid crystals [10], photoresists [11], selective membranes [12], HPLC stationary phases [13], surface reforming agents [14] ion channel mimics [15], and metal ion extraction agents [16].

Although different synthetic methods have been used for the synthesis of calix[4]resorcinarene derivatives by employing some Lewis acid catalysts, however, some of them suffer from disadvantages such as low product yield, cumbersome isolation of the product and long reaction time. In the past few years, we have been involved in a program directed towards developing novel, simple and facile methods for the preparation of organic compounds using various catalysts and readily available starting materials [17-21]. For example, we used molybdate sulfuric acid (MSA) as an efficient catalyst for the synthesis of quinoxalines. In this case, the catalyst showed good recyclability [19]. The challenge in chemistry to develop practical methods, reaction media, conditions and/or materials based on the idea of green chemistry is one of the important issues in the

scientific community. However, preparing and employing a green catalyst in organic synthesis can be extremely valuable [22].

EXPERIMENTAL

Preparation of Catalyst

Firstly 25 mL of dry *n*-hexane was taken in a 100 mL round bottom flask, equipped with ice bath and overhead stirrer, and 4.118 g (20 mmol) of anhydrous sodium molybdate was added to the flask, then 0.266 mL (40 mmol) of chlorosulfonic acid was added dropwise to the flask for 30 min. The solution was stirred for 1.5 h. Afterwards the reaction mixture was gradually poured into 25 mL of chilled distilled water under agitation. The bluish solid which separated out was filtered. Then the catalyst was washed with distilled water five times till the filtrate showed negative test for chloride ions, and was dried at 120 °C for 5 h. The catalyst was obtained in a 90% yield as a bluish solid, which decomposed at 354 °C.

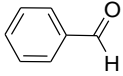
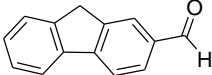
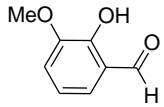
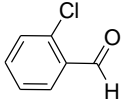
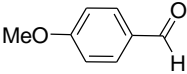
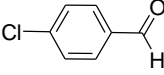
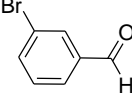
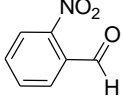
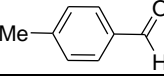
Preparation of calix[4]resorcinarene derivatives 4

A mixture of resorcinol 1 (1 mmol), aryl aldehyde 2 (1 mmol), and MSA (10 mol%) was stirred and heated at 120°C in a preheated oil bath for an appropriate time (Table 1). After completion of the reaction as indicated by TLC (AcOEt/hexane 7:3), the reaction mixture was dissolved in hot MeOH, then filtered to separate the catalyst and afford the pure product 4. At the end of the reaction, the catalyst was filtered, washed with ethanol, dried at 120 °C for 1 h, and reused in another reaction.

* To whom all correspondence should be sent:

E-mail: saeidkham@yahoo.com

Table 1. Synthesis of calix[4]resorcinarene derivatives catalyzed with MSA 1 at 120 °C under solvent-free conditions.

Entry	Product	Aldehyde	Time (min)	Yield ^a (%)	Melting point (°C) (decompose)
1	4a		150	84	297
2	4b		230	82	298
3	4c		180	82	264
4	4d		45	83	270
5	4e		155	94	262
6	4f		90	85	264
7	4g		70	95	269
8	4h		50	90	225
9	4i		150	88	240

^a Isolated yields.*Spectral Data*

Phenyl-calix[4]resorcinarene (4a): IR (KBr), cm^{-1} : 3400, 3022, 1611, 1510, 1230, 1090; ^1H NMR (400 MHz, DMSO), δ : 8.93-8.88; (m, 2H), 7.17-5.74 (m, 6H), 5.70 (s, 1H); ^{13}C NMR (100 MHz), δ : 156.68, 155.85, 153.42, 146.02, 130.53-125.29 (8c), 106.67, 105.83, 63.27; MS (m/z : 792).

2-Fluorenyl-phenyl-calix[4]resorcinarene (4b): IR (KBr), cm^{-1} : 3436, 2923, 1613, 1503, 1424, 1191, 1062, 767, 731; ^1H NMR (400 MHz, DMSO), δ : 8.68 (s, 1H), 8.50 (s, 1H), 7.05-7.17 (s, 4H), 6.50-6.64 (s, 3H), 6.10 (s, 1H), 5.97 (s, 1H), 5.60 (s, 1H), 3.50 (s, 2H).

2-Hydroxy-3-methoxy-phenyl-calix[4]resorcinarene (4c): IR (KBr), cm^{-1} : 3474, 2938, 2840, 1640, 1477, 1272, 1062, 778, 728; ^1H NMR(400 MHz, DMSO), δ : 8.17 (s, 1H), 8.14 (s, 1H), 8.13(s, 1H), 7.51(s, 1H), 7.49 (s, 1H), 6.43-6.25 (s, 3H), 6.01 (s, 1H), 5.96(s, 1H), 5.85 (s, 1H), 3.65 (s, 3H), 3.60 (s, 3H); ^{13}C NMR (100 MHz), δ : 153.16, 152.81, 152.72, 152.48, 146.91, 146.65, 143.42, 143.26, 132.81, 131.41, 123.51, 122.83, 122.25, 122.14, 120.26, 119.50, 117.67, 117.45,

108.84, 101.98, 56.28, 35.00, 34.43; MS (m/z : 974.8).

2-Chloro-phenyl-calix[4]resorcinarene (4d): IR (KBr), cm^{-1} : 3446, 2922, 2852, 1617, 1508, 1424, 1272, 1062, 731; ^1H NMR (400 MHz, DMSO), δ : 8.63 (s, 1H), 8.59 (s, 1H), 8.55 (s, 1H), 6.96-6.88 (s, 4H), 6.12 (s, 1H), 5.96 (s, 1H); ^{13}C NMR (100 MHz), δ : 153.59, 153.33, 143.96, 133.74, 130.02, 129.23, 128.85, 126.83, 125.94, 120.39, 118.34, 102.23; MS (m/z : 929.1).

4-Methoxy-phenyl-calix[4]resorcinarene (4e): IR (KBr) cm^{-1} : 3391, 3027, 3001, 1608, 1509, 824; ^1H NMR (400 Hz, DMSO) δ : 8.34 (s, 2H), 6.54 (s, 4H), 6.33 (s, 1H), 5.85 (s, 1H), 5.28 (s, 1H), 4.07 (s, 3H); MS (m/z : 912.4).

4-Chloro-phenyl-calix[4]resorcinarene (4f): IR (KBr) cm^{-1} : 3410, 3036, 2942, 1617, 1487, 1076; ^1H NMR(400 Hz, DMSO) δ : 8.48 (s, 2H), 6.79 (d, 2H, $J = 12$ Hz), 6.41 (d, 2H, $J = 12$ Hz), 5.98 (s, 2H), 5.39 (s, 1H); ^{13}C NMR (100 MHz) δ : 154.31, 146.15, 131.88, 131.25, 128.43, 121.46, 103.25, 42.56; MS (m/z : 929.1).

3-Bromo-phenyl-calix[4]resorcinarene (4g): IR (KBr) cm^{-1} : 3445, 2940, 1595, 1488, 1260, 1092,

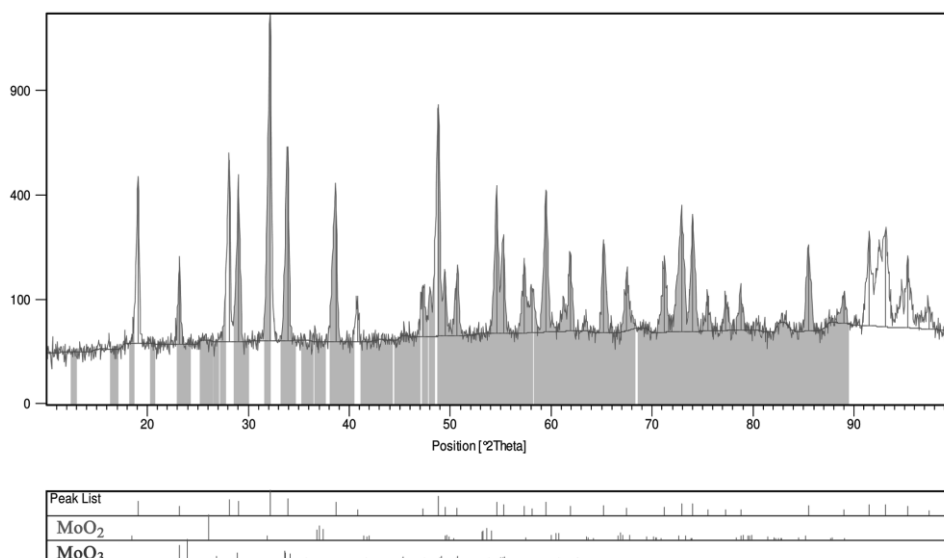


Fig. 1. XRD pattern for MSA 1.

880, 780, 690; ¹H NMR (400 MHz, DMSO) δ: 9.12-8.92 (m, 2H), 7.14-6.56 (m, 4H), 6.25-6.02 (m, 2H), 5.67 (s, 1H); ¹³C NMR (100 MHz) δ: 156.63, 155.80, 131.49, 129.93, 128.09, 121.50, 105.92, 102.64;

2-Nitro-phenyl-calix[4]resorcinarene (4h): IR (KBr) cm⁻¹: 3410, 3080, 2910, 1681, 1605, 1520, 1335, 1150, 730; ¹H NMR (400 MHz, DMSO) δ: 9.10-8.96 (m, 2H), 7.76-5.96 (m, 6H), 4.76 (s, 1H); ¹³C NMR (100 MHz) δ: 170.20, 157.13, 155.91, 154.07, 150.13, 149.30, 139.45, 132.40-124.23 (8C), 119.94, 106.66, 105.93, 102.69, 67.43; MS (*m/z*: 973.1).

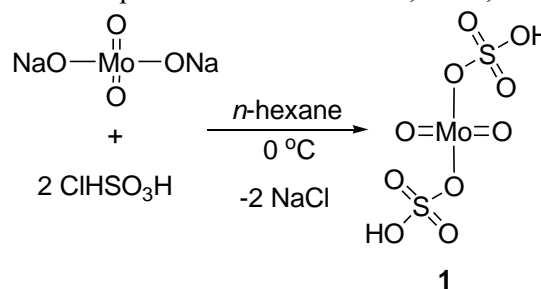
4-Methyl-phenyl-calix[4]resorcinarene (4i): IR (KBr) cm⁻¹: 3405, 3010, 2910, 1600, 1505, 1125.840; ¹H NMR (400 MHz, DMSO) δ: 9.10-8.88 (m, 2H), 7.10-6.20 (m, 6H), 5.67 (s, 1H), 2.19 (s, 3H); ¹³C NMR (100 MHz) δ: 158.91, 156.60, 130.16, 128.99, 128.37, 106.66, 105.81, 102.79, 21.04; MS (*m/z*: 854.7).

RESULTS AND DISCUSSION

The concept of “Green Chemistry” has emerged as one of the guiding principles of the environmentally safe organic synthesis. We found that anhydrous sodium molybdate reacts with chlorosulfonic acid (1:2 mole ratio) to give molybdate sulfuric acid (MSA **1**). The reaction is easy and clean and there is no gas production during the reaction (Scheme 1). The MSA **1** was characterized by X-ray diffraction, transmission electron microscopy, and Fourier transform infrared spectroscopy [23-25]. Figure 1 shows the XRD patterns for molybdate sulfuric acid (MSA **1**). It was reported that high degree mixing of Mo–S in chlorosulfonic acid often

led to the absence of XRD pattern for anhydrous sodium molybdate.

XRD patterns of sodium molybdate (Na₂MoO₄) show broad peaks at around 2θ 17.0°, 27.0°, 32.0°,



Scheme 1. Synthesis of molybdate sulfuric acid (MSA).

48.0°, 53.0°, 57.5°, 78.5°, 82.0° [26], some of which are absent in the XRD pattern of MSA due to high-degree mixing of Mo with sulfonic acid. The broad peaks around 2θ 23°, 29°, and 34° from the smaller inset can be attributed to the linking of Mo to sulfonic acid. The FT-IR spectra for anhydrous sodium molybdate and molybdosulfuric acid (MSA **1**) are shown in Figure 2.

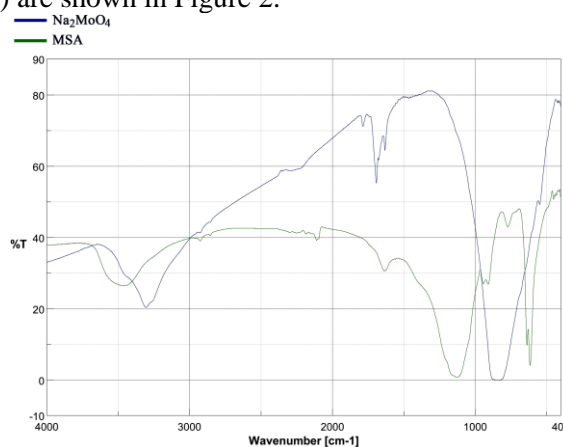


Fig. 2. FT-IR spectrum for MSA 1.

The spectrum of MSA **1** shows the characteristic bonds of anhydrous sodium molybdate and chlorosulfonic acid. The absorbance bands at 3459, 2110, 1635, 1129, 909, 771, 637, 616 and 451 cm^{-1} in the catalyst spectrum reveal both bonds in anhydrous sodium molybdate and $-\text{OSO}_3\text{H}$ group. Hence titration of the catalyst with NaOH (0.1 N) was done. Firstly, 1 mmol of the catalyst was dissolved in 100 mL of water. Then it was titrated with NaOH (0.1 N) in the presence of phenolphthalein as an indicator. In the equivalent point, 2 mmol of NaOH were utilized for 1 mmol of catalyst, which pointed to two acidic valences.

The XRF data of molybdate sulfuric acid (MSA **1**) indicate the presence of MoO_3 and SO_3 in the catalyst (Table 2). In this work, we describe a simple and green strategy based on the condensation of resorcinol **2** with aryl aldehyde **3** using MSA **1** as a powerful, recyclable and safe catalyst under solvent-free conditions for the preparation of calix[4]resorcinarene derivatives **4** (Scheme 2).

Table 2. XRF data of MSA **1**.

Entry	Compound	Concentration (% w/w)
1	SO_3	49.52
2	Na_2O	1.15
3	MoO_3	39.02
4	Cl	0.150
5	K_2O	0.064
6	Nb_2O_5	0.019
7	Fe_2O_3	0.012
8	CuO	0.010
9	LOI ^a	10.03
10	Total	99.98

^aLoss on Ignition.

The need to implement green chemistry principles (*e.g.* safer solvents, less hazardous chemical synthesis, atom economy and catalysis) is a driving force towards avoiding the use of toxic organic solvents. A solvent-free or solid-state reaction obviously reduces pollution, and brings down handling costs due to simplification of experimental procedure, work up technique and saving in labour. Interest in the environmental control of chemical processes has remarkably increased during the last three decades as a response to the public concern about the use of hazardous chemicals. Therefore, to improve the effectiveness of this method in

preventing chemical waste, it is important to optimize the reaction conditions. To determine the suitable reaction conditions, the reaction of benzaldehyde with resorcinol was taken as a model reaction. At first, we found that in the absence of MSA **1**, the reaction did not complete in a long reaction time (650 min). After examining the reaction using various amounts of MSA **1** at 120 °C, it was found that the reaction can be efficiently carried out by adding 10 mol% of the catalyst under solvent-free conditions for 150 min. The use of higher amounts of the catalyst does not increase the yield and reaction rate. According to Table 1, under the optimized reaction conditions, a number of aromatic aldehydes reacted with resorcinol in a molar ratio of 1:1 with the catalyst affording calix[4]resorcinarenes **4a-4i** in good to excellent yields.

Not only the ecological profile (through decreasing hazardous industrial waste), but also the economic profile (through eliminating expensive organic solvents) are further improved using a recyclable catalyst and solvent-free reaction conditions. In this process, as indicated in Figure 3, the recycled catalyst was used for four cycles of 150 min each. Actually, the catalyst showed an appreciable loss in catalytic activity after reusing. During catalyst recovery, as mentioned in previous studies, sometimes catalyst decomposition and/or leaching occurs [27,28].

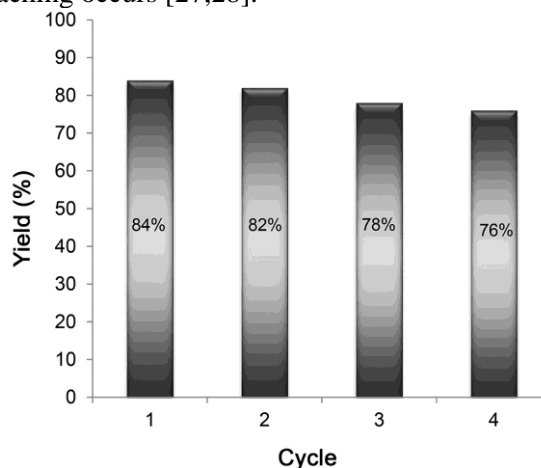
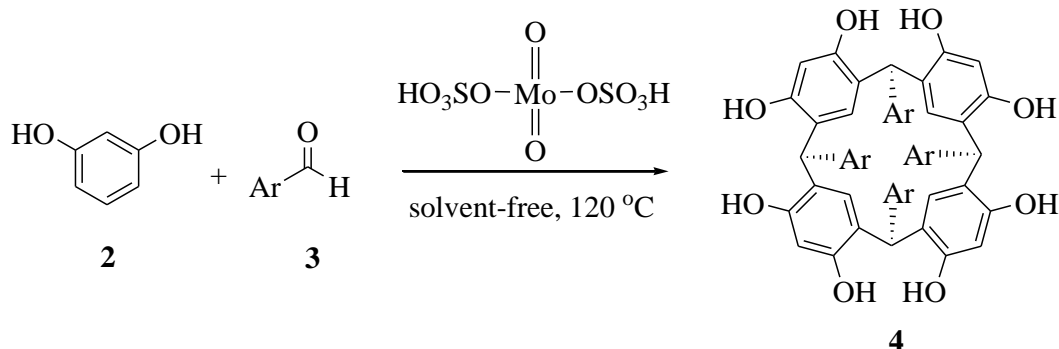


Fig. 3. Recyclability of MSA **1** catalyst in the synthesis of **4a** at 120 °C under solvent-free conditions (reaction time = 150 min).



Scheme 2. Synthesis of calix[4]resorcinarene derivatives using MSA 1.

CONCLUSION

In summary, a green synthetic route to some calix[4]resorcinarene derivatives using MSA 1 under solvent-free conditions is presented. This method not only gives high yield and purity but also is cheap, speedy, facile, and eco-friendly throughout the course of the reaction.

Acknowledgement: The authors gratefully acknowledge partial support of this work by the Yasouj University, Iran.

REFERENCES

1. E. B. Maroun, A. Hagege, C. Basset, E. Quemeneur, C. Vidaud, Z. Asfari, *Supramol. Chem.*, **21**, 585 (2009).
2. B. Botta, M.D.I. Cassani, D. Misiti, D. Subissati, G.D. Monache, *Curr. Org. Chem.*, **9**, 337 (2005).
3. Y. Ge, C. Yan, *J. Chem. Res.*, **33**, 279 (2004).
4. J. E. Gualbert, P. Shahgaldian, A. Lazar, A.W. Coleman, *J. Inclusion Phenom. Macrocycl. Chem.*, **48**, 37 (2004).
5. M. W. Heaven, C. L. Rastonb, J. L. Atwood, *Chem. Commun.*, **7**, 892 (2005).
6. L. R.; MacGillivray, J. L. Atwood, *J. Solid State Chem.*, **152**, 199 (2000).
7. T. W. Bell, N. M. Hext, *Chem. Soc. Rev.*, **33**, 589 (2004).
8. G. M. Martinez, C. R. Teran, O. A. Tlapanco, A. Toscano, R. Cruz-Almanza, *Fullerene Sci. Technol.*, **8**, 475 (2000).
9. P. Leyton, S. Sanchez-Cortes, M. Campos-Vallette, C. Domingo, J.V. Garcia-Ramos, C. Saitz, *Appl. Spectrosc.*, **59**, 1009 (2005).
10. K. Yonetake, T. Nakayama, M. Ueda, *J. Mater. Chem.*, **11**, 761 (2001).
11. T. Nakayama, D. Takhashi, K. Takeshi, M. Ueda, *J. Photopolym. Sci. Technol.*, **12**, 347 (1999).
12. N. Tbeur, T. Rhlalou, M. Hlaibi, D. Langevin, M. Metayer, J. F. Verchere, *Carbohydr. Res.*, **329**, 409 (2000).
13. O. Pietraszkiwicz, M. Pietraszkiwicz, *Phenom. Macrocyclic. Chem. J. Inclusion*, **35**, 261 (1999).
14. K. Ichimura, E. Kurita, M. Ueda, *Eur. Pat.*, EP 671220 (1995).
15. N. Yoshino, A. Satake, Y. Kobuke, *Angew. Chem. Int. Ed.*, **40**, 457 (2001).
16. E. Gaubert, H. Barnier, L. Nicod, A. Favre-Reguillon, J. Foos, A. Guy, C. Bardot, M. Lemaire, *Sep. Sci. Technol.*, **32**, 2309 (1997).
17. B. Karami, S. Khodabakhshi, F. Hashemi, *Tetrahedron Lett.*, **54**, 3583 (2013).
18. V. Kamaei, B. Karami, S. Khodabakhshi, *Polycyclic Aromat. Compds.*, **34**, 1 (2014).
19. B. Karami, S. Khodabakhshi, M. Nikrooz, *Polycyclic Aromat. Compds.* **31**, 97 (2011).
20. S. Khodabakhshi, B. Karami, *Catal. Sci. Technol.*, **2**, 1940 (2012).
21. B. Karami, V. Ghashghaee, S. Khodabakhshi, *Catal. Commun.*, **20**, 71 (2012).
22. J. L. C. Sousa, I. C. M. S. Santos, M. M. Q. Simoes, J. A. S. Cavaleiro, H. I. S. Nogueira, A. M. V. Cavaleiro, *Catal. Commun.*, **12**, 459 (2011).
23. B. Karami, S. Khodabakhshi, M. Jamshidi, *J. Chin. Chem. Soc.*, **60**, 1103 (2013).
24. F. Tamaddon, H. Kargar-Shooroki, A.A. Jafari, *J. Mol. Catal. A*, **66**, 368 (2013).
25. F. Tamaddon, M. Farahi, B. Karami, *J. Mol. Catal., A* **356**, 85 (2012).
26. Y. Ding, N. Hou, N. Chen, Y. Xia, *Rare Met.*, **25**, 316 (2006).
27. A. Molnar, *Chem. Rev.*, **111**, 2251 (2011).
28. J. A. Gladysz, *Pure Appl. Chem.*, **73**, 1319 (2001).

**“ЗЕЛЕН” СИНТЕТИЧЕН ПЪТ КЪМ НЯКОИ СУПРА-МОЛЕКУЛИ С ИЗПОЛЗВАНЕТО
НА МОЛИБДАТ-СЯРНА КИСЕЛИНА (MSA) КАТО ВИСОКО-ЕФЕКТИВЕН
КАТАЛИЗАТОР**

А. Арами¹, Б. Карами¹, С. Ходабахши *²

¹*Департамент по химия, Университет в Ясудж, Ясудж, Иран*

²*Младежки изследователски и елитен клуб, Клон Робаткарим, Ислямски университет «Азад»,
Робаткарим, Иран*

Постъпила на 23 март, 2014 г., коригирана на 5 август, 2014 г.

(Резюме)

Разработена е лесна и проста процедура за синтезата на някои каликс [4] резорцин-аренови производни чрез реакцията на арилови алдехиди с резорцинол в присъствие на катализатор от молибдат-сярна киселина в отсъствие на разтворител. Този екологично чист метод показва много примамливи качества, като отлични добиви, кратко време за реакция, “зелен” и възстановим катализатор и проста работна процедура.

Sunflower seed oil polymerization by ion exchange resins: acidic heterogeneous catalysis

B. Vafakish^{1*}, M. Barari¹, E. Jafari²

¹ Chemical, Polymeric and Petrochemical Technology Development Research Division, Research Institute of Petroleum Industry, P.O. Box 14115-143, Tehran, Iran

² Department of Agriculture, Shahr-e-Ghods Branch, Islamic Azad University, Tehran, Iran

Received April 8, 2014, Revised November 10, 2014

Sunflower seed oil, like other unsaturated triglycerides, is susceptible to thermal degradation and oxidation. Polymerization is an easy and economical way to decrease the number of double bonds and heterogeneous catalysis and is one of the best choices to produce high quality polymerized oil. In this paper the effect of time, temperature and catalyst concentration on the polymerization reaction is evaluated. As expected, the reaction rate increased in parallel with temperature and catalyst concentration. Time could affect the product properties. Finding the optimum conditions is crucial to control the properties of the polymerized oil. GPC and viscometry techniques were used to control the reaction extent. The product's behavior after polymerization was studied using TGA and FT-IR and its analysis was performed according to ASTM and USP.

Keywords: Sunflower seed oil, Heterogeneous Catalysis, Cationic Polymerization, Viscosity, Gel Permeation Chromatography

INTRODUCTION

The sunflower is a distinctive flowering plant (*Helianthus annuus L.*). The seeds of this plant contain a valuable edible oil that contains more vitamin E than any other vegetable oil.[1-2] Sunflower seed oil finds many industrial applications, e.g. in food, cosmetics, paints, surface coatings, lubricants and surfactants.[3-7]

This oil is a combination of monounsaturated and polyunsaturated fatty acids with low saturated ones.[8] The percentage of saturated fatty acids in the sunflower seed oil is about 5% while it reaches 45% for monounsaturated and 46% for polyunsaturated fatty acids. The total percentage of essential fatty acids (linoleic and linolenic) in sunflower seed oil is more than 50%. These unsaturated long chain fatty acids are useful in improving the low temperature properties of the finally polymerized oil.[9] The number of double bonds per molecule is about 5 and the remarkable point is that all of these double bonds are in "cis" configuration.[10] The chemical and physical properties of the vegetable oils strongly depend on the degree of unsaturation, which can be determined by measuring the iodine value (IV).[11-12]

The fatty acid percent composition of the deodorized sunflower seed oil is as follows:

palmitic acid 5-7.6%, stearic acid 2.7-6.5%, oleic acid 14-39%, linoleic acid 48-74%, linolenic acid <0.3%. The specification is shown in Table 1.[13-14]

Table 1. Typical properties of sunflower seed oil

No.	Items	Standard
1	Appearance	Yellowish transparent liquid
2	Specific Gravity at 25° C	0.915-0.919
3	Viscosity at 25° C	49 mPa.s
4	Saponification Value	188-194 mg KOH/g
5	Iodine Value	120-140 gI ₂ /100g
6	Titre	15-18° C
7	Insoluble impurities	~0.05%

High levels of oleic acid make the oil more susceptible to oxidation and hence more unsuitable for processes requiring high oxidative stability at high temperatures as in biodiesel and biolubricant applications.[15-17] To reduce the risk, the double bonds of the oil could be polymerized which is a less expensive approach compared to other methods, e.g. hydrogenation.[18] By controlling the polymerization conditions, the preferred viscosity, color and molecular weight could be achieved for a variety of vegetable oils with a broad range of iodine values and fatty acid compositions.[19]

From macromolecular viewpoint unsaturated oils are monomers with more than one functional group capable of polymerization.[20-21] There are

* To whom all correspondence should be sent:
E-mail: vafakishb@ripi.ir

two major industrial techniques for oil polymerization: thermal [22] and air blown methods.[23]

In the first process, the oil is simply heated to a temperature of 290-330 °C for 20-30 h with or without an inhibitor like antraquinone to control the molecular weight of the polymer. The reaction is time consuming and the product is a yellowish viscous liquid. The long time of the reaction is due to the low reactivity of non-conjugated double bonds in the oil structure.[24-25]

In the second one, the oil is heated to 100-110 °C for 30-50 h while air is purged in it. Many functional groups in the oil structure are oxidized under these conditions to ketones, aldehydes, hydroperoxides and carboxyl which are hazardous for human health.[26-27]

Cationic polymerization could be easily completed on the internal double bonds bearing alkyl electron donating substituents of unsaturated oils such as sunflower seed oil.[28-32] There are many reports in the literature for cationic polymerization of the double bonds in acidic conditions using homogenous catalysts, e.g. superacids [33] ($H_2S_2O_7$) or Lewis acids [34] (BF_3 and $TiCl_4$), and also heterogeneous ones like clay and zeolite.[35-36]

The aim of this paper was to use ion exchange resins as heterogeneous polymer-based catalysts to polymerize sunflower seed oil. Compared with others, they are high-capacity macroporous catalysts which could regenerate and tolerate severe conditions without degradation.[37] They showed more efficient and economical than acid catalysts and the reaction was performed in milder conditions than the previously reported unsaturated oil polymerization. The reduction of the double bonds is demonstrated by the decrease in iodine value from 120-140 to 70-90 $g\ I_2\ 100\ g^{-1}$.

The main economical advantage of using these catalysts is the simplicity of their isolation from the reaction mixture which makes the reaction a short time experience in comparison to similar processes. The optimum conditions were found by varying the reaction parameters such as time, temperature and concentration of catalyst. The polymerized oil was finally analyzed.[38]

EXPERIMENTAL

Materials

The used sunflower seed oil was commercially deodorized oil obtained from TEXTRON (Spain) with the specification of Table 1. A commercial strongly acidic polystyrene ion exchange resin was

used as heterogeneous catalyst under the brand name of AMBERLITE™ FPC23 H from Dow Company. The total exchange capacity of the resin was 2.2 eq L^{-1} . Sulfonate functional groups were activated before the reaction while the final H^+ content of 0.056 eq. was used in the reaction. All other materials were prepared from technical grade products of Merck Company.

Apparatus

The polymerization was carried out in a 2 liter 3-neck round bottom flask with mechanical overhead stirrer, thermometer, electrothermal heating mantle and nitrogen line to remove oxygen from the reaction mixture. The stirrer was equipped with a stainless steel shaft and four anchor-shaped stirrer blades in two different heights, one at the end of the shaft and the other in the lower one-third of it. There were also four small metallic mesh bags attached to the end of each blade filled with activated heterogeneous catalyst.

Reaction procedure

The sunflower seed oil (1000 g) was weighed in the flask (same amount in every reaction) equipped with stirrer, heating mantle, thermometer, nitrogen line to sparge nitrogen and filled bags of activated heterogeneous catalyst.[38] The reaction was performed at three different temperatures by controlling the temperature of the heating mantle at 60-90-150 °C. To find the best time, samples were withdrawn at different times from $t=0$ to $t=11$ h every 30 min. The catalyst concentrations were varied as 1.7, 1.9, 2.2, 2.5, 2.7 eq (per liter of oil). Pure nitrogen gas was purged in the reaction by a sparger with a rate of 5 $mL\ min^{-1}$ to prevent oxidation of the oil. At the end of the reaction time the product was evacuated from the flask and analyzed without any further purification.

Analytical procedure

Gel permeation chromatography:

Gel permeation chromatography was performed on a Shimadzu Class-LC10 GPC Prominence Model instrument. The stainless steel column with length of 300 mm and internal diameter of 7.7 mm was packed with high performance spherical gel made of styrene-divinylbenzene co-polymer with diameter of the particles: 5 μ , pore size: 100 Å of the equivalent in term of exclusion power and resolution. The column temperature was increased from room temperature to 60 °C with a rate of 5 °C $10\ min^{-1}$. The column was stored in toluene. A refractive index detector with a sensitivity at full scale at least 2 of refractive index was used. Flow

rate was 1 mL min⁻¹ and the eluent was tetrahydrofuran.

Viscometry

The extent of the reaction was monitored by viscometry on an Anton-Paar SVM 3000 viscometer at room temperature. This viscometer measures the dynamic viscosity according to ASTM D-7042.[39]

Thermogravimetric Analysis

Thermogravimetric analyzer TGA-DTA, model Diamond TG/DTA, Perkin Elmer Instruments was used. Measurements were performed under N₂ purge. Typically, 5-10 mg of sample were placed in a platinum pan and heated from 30 °C to 600 °C, at 10 °C min⁻¹.

RESULTS AND DISCUSSION

As expected, the sunflower seed oil polymerized in acidic conditions. After 20-30 min the color of the reaction mixture turned a little darker due to the formation of conjugated carbocations with double bonds. The various parameters such as time, temperature and concentration of catalyst were changed to find out the optimum conditions. Some physical characteristics of the finally obtained polymerized oil were determined. Gel permeation chromatography (GPC) and viscometry were used to follow up the reaction extent.

Effect of time on the reaction

Sampling of the reaction mixture and analysis by GPC showed the effect of time on the molecular weight (MW) which was low in the starting point. With time oligomers were formed (Fig. 1). About 10 wt % of the starting oil consisting of saturated fatty acids, e.g. stearic and palmitic acids will be unchanged.

The time effect was also followed by changing the viscosity of the reaction mixture. As demonstrated in Fig. 2, at $t = 90$ °C, the viscosity gradually increased in the first 4 h of the reaction but after that the viscosity growth was considerable. After 10 h the viscosity of the reaction mixture increased to around 20 Pa.s at 25 °C which is the desired viscosity. It is noticeable that the viscosity of the sunflower seed oil is 0.05 Pa.s at this temperature. As the desired viscosity was achieved for 10 h, this was considered as the optimum reaction time.

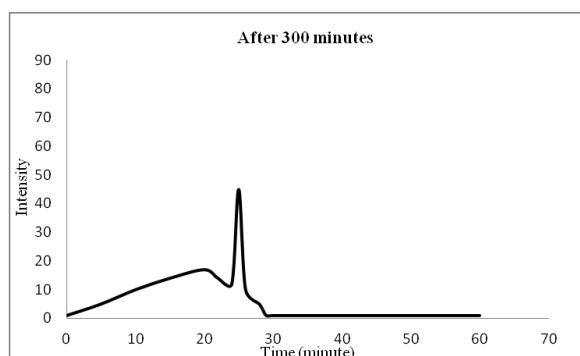
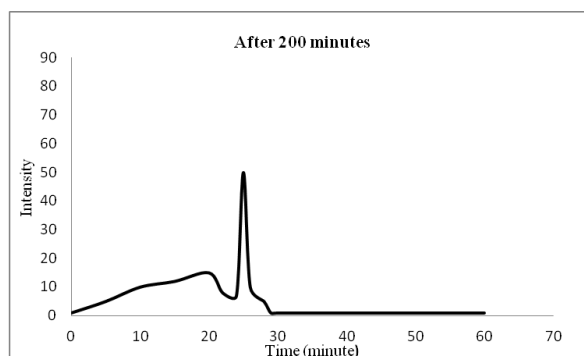
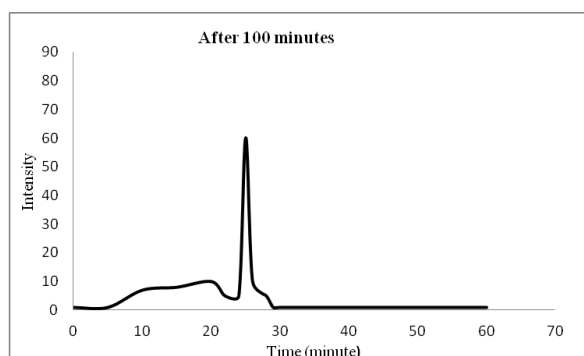
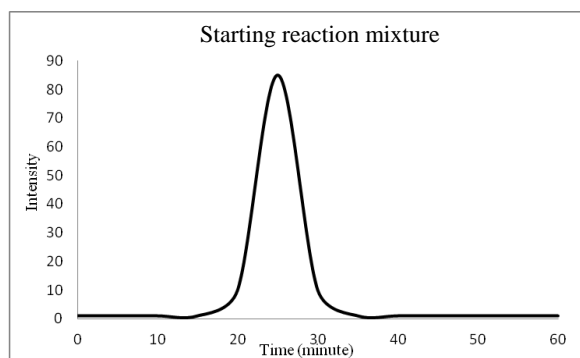


Fig. 1. GPC chromatograms of the reaction mixture at different times after the starting point. (reaction conditions as described in the experimental section).

Effect of temperature on the reaction

To study the effect of temperature on the reaction duration, the catalyst concentration was fixed at 2.2 eq H⁺ per liter of oil. The viscosity of the samples measured at different temperatures is shown in Fig. 2; the viscosity around 20 Pa.s was

considered to determine the optimum temperature. Compared to 60 °C, the reaction at 90 °C is rapid. By heating the reaction rate will go up; the reaction mixture will be solid at temperatures above 150 °C (Fig. 2). Considering high utility cost in the industry and the easier rate control of the reaction to prevent runaway, the $t=90$ °C was determined as the optimum temperature.

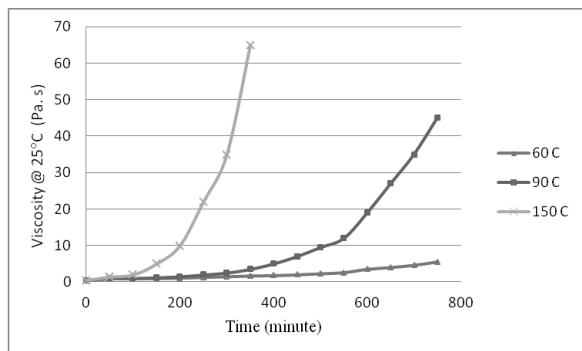


Fig. 2: Effect of reaction temperature on the viscosity of the product with time. (reaction conditions as described in the experimental section).

For preparing a more viscous product, higher temperature and longer time should be used [40-41].

Effect of catalyst concentration on the reaction

The reaction rate dependency on catalyst concentration was studied at 90 °C and catalyst concentrations of 1.7, 1.9, 2.2, 2.5, 2.7 eq (per liter of oil) were used to reach viscosity around 20 Pa.s. Actually the viscosity was used as an indication of the reaction extent. The results are demonstrated in Fig. 3. It is obvious that the reaction time was shortened proportional to the increase in catalyst concentration. If the chosen concentration was more than 2.2 eq. per liter of oil there was no noticeable increase in the reaction rate. Considering the high price of these catalysts, the concentration of 2.2 eq H^+ per liter oil was selected. In other words, the used catalyst was 25.5 mL per liter of oil which equals to 2.2 eq L^{-1} . [37]

Physical properties of the polymerized oil

At the end of the reaction ($t=10$ h, $T=90$ °C and catalyst concentration= 2.2 eq H^+ per liter oil), the polymerized oil was evacuated and some characteristics of cationic polymerized soybean oil were analyzed according to ASTM and USP.[42] (Table 2). The results were in the mentioned range of the polymerized oils.[43]

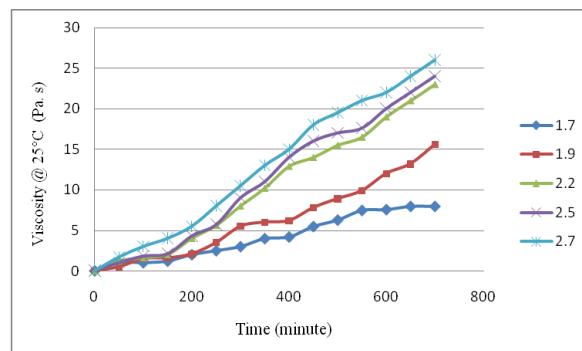


Fig. 3. Effect of catalyst concentration on the viscosity of the product with time. (reaction conditions as described in the experimental section).

Table 2. Characteristics of polymerized oil obtained from cationic polymerization after 10 h at $T=90$ °C and catalyst concentration of 2.2 eq H^+ per liter oil.

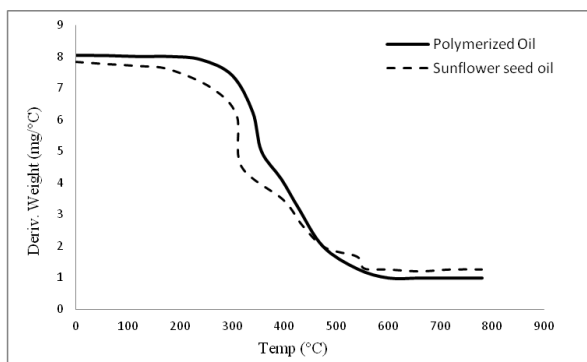
Items	Results	Analytical Method
Appearance	Yellowish Viscous Liquid	-
Color (Gardner)	Max. 7	ASTM D1544
Acid Value, mg KOH/g	Max. 5	ASTM D2076
Peroxide Value, meq/Kg	Max. 5	USP33-NF28
Saponification Value, mg KOH/g	82-90	ASTM D5558
Iodine Value, mg $I_2/100g$	70-90	ASTM D1959
Moisture	Max. 0.5%	ASTM E203
Insoluble impurities	Max. 0.1%	
Viscosity, 25 °C, Pa.s	17.52	ASTM D445
Average Molecular Weight	1900-2100	-

Thermal characterization of the sunflower seed oil compared to polymerized oil

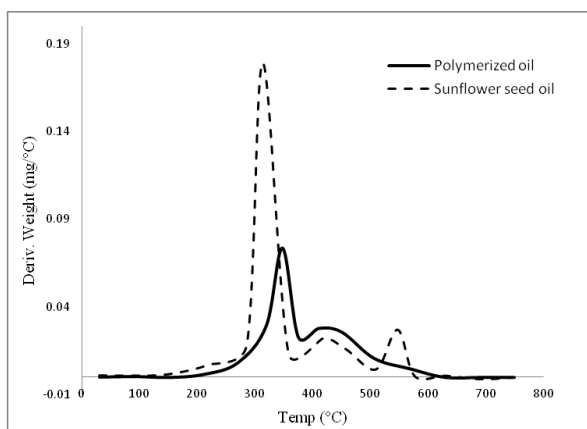
Thermal degradation was studied by means of thermogravimetric analysis (TGA). TGA tests were conducted for sunflower oil from ambient temperature to 800°C at a heating rate of 10°C/min in nitrogen environment with a flow rate of 100ml/min. By heating the oil was decomposed to aldehyde, ketones and alcohols which are volatile so the weight decreased [44, 45]. Figures 4a and 4b show the TGA curves and their derivatives. As can be seen in the figures, the thermal decomposition of sunflower seed oil occurs in three stages (peak

maxima at 314°C, 417°C and 547°C), related to the decomposition of polyunsaturated, monounsaturated and saturated fatty acids. The first step is the most vital one for the thermal stability of the oil, because this is the step where decomposition of the unsaturated fatty acids starts.

Polymerized oil shows two main peaks (peak maxima at 347 °C, 450 °C), attributed to different stages of the decomposition process and polymerization degrees. As expected, the thermal stability of the polymerized oil is higher than that of the raw oil.



(a)

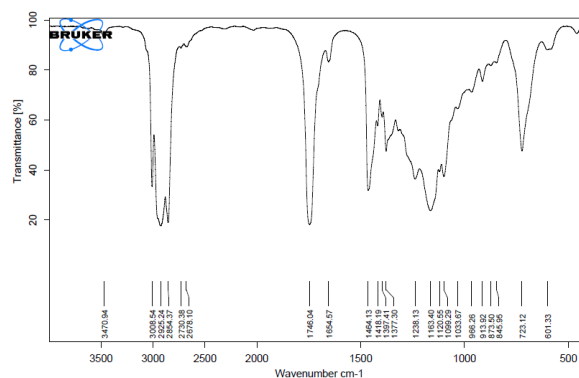


(b)

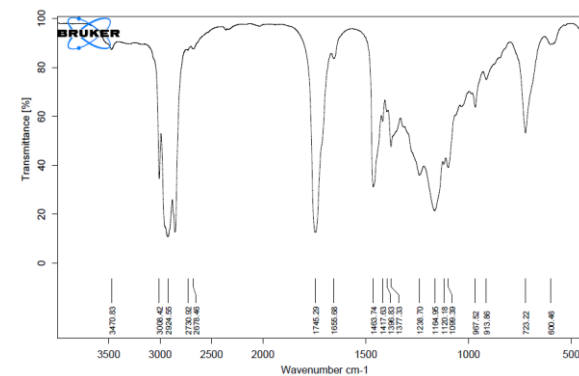
Fig. 4. TGA thermograms for sunflower seed oil and polymerized oil.

FT-IR spectra of polymerized oil compared to sunflower seed oil

The FT-IR spectra of sunflower seed oil and polymerized oil are shown in Figures 5a and 5b. The band around 3000 cm⁻¹ was assigned to the CH vibrations of CH, CH₂ and CH₃ groups in the two samples. The carbonyl groups displayed a sharp band at 1745 cm⁻¹[46]. It is worth noting that the 967 cm⁻¹ band in the polymerized oil spectrum was attributed to the trans double band while this band did not appear in the sunflower seed oil spectrum. This indicates a transformation of the cis to trans double bands during acid catalytic polymerization.



(a)



(b)

Fig. 5. FT-IR spectra of sunflower seed oil (a) and polymerized oil (b).

CONCLUSION

The polymerization reaction of sunflower seed oil by AMBERLITE™ FPC23 as a heterogeneous catalyst was investigated in a stirred batch reactor. The reaction mixture behavior was controlled by gel permeation chromatography and viscometry. The increase of viscosity with time is a direct measure of the efficiency of the process used for cationic polymerization of sunflower seed oil. The suitable conditions were: 90 °C, 10 h and catalyst concentration of 2.2 eq per liter of oil to reach a viscosity of the polymerized oil of around 20 Pa.s. The advantages of using these mild reaction conditions to other available methods are: low temperature, shorter time and no need for purification of the product after the reaction.

Acknowledgment: The authors thank the Kimyagarn Emrooz Chemical Industries Company (Tehran, Iran) for the financial support of this work.

REFERENCES

1. K. Chowdhury, L. Banu A. S. Khan, A. Latif Bangladesh, *J. Sci. Ind. Res.*, **42**, 311 (2007).
2. F. D. Gunstone, *Vegetable oils in food technology: composition, properties and uses*, 2nd ed. Wiley-Blackwell, 2011, p.11.

3. H. M. Deckers, G. Rooijen, J. Boothe, J. Goll, S. Mahmoud, M. M. Moloney, US Patent 6210742 (2001).
4. M. N. Belgacem, A. Gandini, Monomers, polymers and composites from renewable resources; Elsevier, Amsterdam, 2008, p.39.
5. K. Hill, *Pure Appl. Chem.*, **72**, 1255 (2000).
6. G F. S.üner, Y. Yağci, A. T. Erciyes, *Prog. Polym. Sci.*, **31**, 633 (2001).
7. M. A. R. Meier, J. O. Metzger, Schubert, *U. S. Chem. Soc. Rev.*, **36**, 1788 (2007).
8. D. C. Zimmerman, G. N. Fick, *J. Am. Oil Chem. Soc.*, **50**, 273 (1973).
9. Y. Xia, R. C. Larock, *Green Chem.*, **12**, 1893 (2010).
10. M. Plourde, K. Belkacemi, J. Arul, *Ind. Eng. Chem. Res.*, **43**, 2382 (2004).
11. G. J. Knothe, *Am. Oil Chem. Soc.*, **79**, 847 (2002).
12. C. E. Stauffer, Fats & Oils: Practical guides for the food industry; Eagan Press Handbook Series, Minnesota, USA, 1996.
13. G. S. Jamieson, W. F. Baughman, *J. Am. Chem. Soc.*, **44**, 2952 (1922).
14. J. Janick, A. Whipkey, Trends in new crops and new uses, ASHS Press, Alexandria, VA, 2002.
15. N. J. Fox, G. W. Stachowiak, *Tech. Int.*, **40**, 1035 (2007).
16. J. M. Fernández-Martínez, B. Pérez-Vich, L. Velasco, J. Domínguez, *HELIA*, **30**, 75 (2007).
17. H. Toppalar; Y. Bayrak; M. Iscan, *Tr. J. of Chem.*, **21**, 118 (1997).
18. Coenen J. W. E. J. *Am. Oil Chem. Soc.* **53**, 382 (1976).
19. V. Sharma, P. P. Kundu *Prog., Polym. Sci.*, **33**, 1199 (2008).
20. C. K. Williams, M. A. Hillmyer, *Polym. Rev.*, **48**, 1 (2008).
21. J. O. Metzger, U. Bornscheuer, *Appl. Microbiol. Biot.*, **71**, 13 (2006).
22. C. Wang, S. Erhan, *J. Am. Oil Chem. Soc.*, **76**, 1211 (1999).
23. E. Geiger, N. Becker, WO 2006094227 (2006).
24. P. O. Powers, *Journal of Polymer Science*, **5**, 741 (1950).
25. F. K Li, R. C. Larock, *Biomacromolecules*, **4**, 1018 (2003).
26. Christianson R.; US Patent 7262311 (2007).
27. R. Gorkum, E. Bouwman, *Coordin. Chem. Rev.*, **249**, 1709 (2005).
28. D. D. Andjelkovic, M. Valverde, P. Henna, F. Li, R. C. Larock, *Polymer*, **46**, 9674 (2005).
29. V. Sharma P. Kundu, *Prog. Polym. Sci.*, **31**, 983 (2006).
30. F. Li, R. C. Larock, Natural Fibers, Biopolymers and Biocomposites, eds. Mohanty A. K.; Misra M.; Drzal L. T.; CRC Press, Boca Raton, FL, 2005, p. 727.
31. Y. Lu, R. C. Larock, *ChemSusChem*, **2**, 136 (2009).
32. (a) F. Li, R. C. Larock, J. U. Otaigbe, *Polymer.*, **41**, 4849 (2000); (b) F. Li, D. W. Marks, R. C. Larock J. U. Otaigbe, *Polymer*, **41**, 7925 (2000).
33. G. A. Olah, G. K. S. Prakash, *Sommer J. Science*, **206**, 13 (1979).
34. A. Corma, H. Garcia, *Chem. Rev.*, **103**, 4307 (2003).
35. J. M. Adams, *Appl. Clay Sci.*, **2**, 309 (1987).
36. D. Marks, F. Li, C. M. Pacha, R. C. Larock, *J. Appl. Polym. Sci.*, **81**, 2001 (2001).
37. Chakrabarti A.; M. M. Sharma, *React. Polym.*, **20**, 1 (1993).
38. M. M. Sharma, *React. Func. Polym.*, **26**, 3 (1995).
39. Book of ASTM Standards. Philadelphia. American society for testing and material, 1965.
40. F. Li, R. C. Larock, *J. Polym. Sci. Poly. Phys.*, **38**, 2721 (2000).
41. F. Li, R. C. Larock, *J. Polym. Sci. Poly. Phys.*, **1**, 60 (2001).
42. US Pharmacopeia. USA, 2010.
43. S. N. Khot, J. J. Lascala, E. Can, S. S. Morye, G. I. Williams, G. R. Palmese, S. H. Kusefoglu, R. P. Wool, *J. Appl. Polym. Sci.*, **82**, 703 (2001).
44. V. M. Mello, G. V. Oliviera, J. M. G. Mandarino; M. C. C. Carrao-Panizzi, P. A. Z. Suarez, *Ind. Crop. Prod.*, **43**, 56 (2013).
45. N. Alemdar, A. T. Erciyes, N. Bicak, *Prog Org. Coat.*, **69**, 552 (2010).
46. L. A. Garcia-Zapateiro, J. M. Franco, C. Valencia, M. A. Delgado, C. Gallegos, M. V. Ruiz-Mendez, *Grasas Aceites*, **64**, 497 (2013).

ПОЛИМЕРИЗАЦИЯ НА СЛЪНЧОГЛЕДОВО МАСЛО С ЙОНООБМЕННА СМОЛА: КИСЕЛИНЕН ХЕТЕРОГЕНЕН КАТАЛИЗ

Б. Вакафиш^{1*}, М. Барари¹, Е. Джафари²

¹ *Изследователски отдел по химична, полимерна и нефтохимична технология, Изследователски институт по нефтена индустрия, Техеран, Иран*

² *Департамент по земеделие, Ислямски университет "Азад", Клон Шахр-е-Годс, Техеран, Иран*

Постъпила на 8 април, 2014 г., коригирана на 10 ноември, 2014 г.

(Резюме)

Слънчогледовото масло, както другите ненаситени триглицериди е чувствително към термично разлагане и окисление. Полимеризацията е лесен и икономичен начин да се намали броя на двойните връзки, а хетерогенният катализ е един от най-добрите способности за получаването високо-качествено полиемризирано олио. В тази работа са оценени ефектите на времето, температурата и концентрацията на катализатора върху полимеризацията. Както се очаква, скоростта на реакцията се повишава успоредно с температурата и концентрацията на катализатора. Времето влияе върху качествата на продукта. Оптималните условия на процеса са от ключово значение за контрола върху свойствата на полимеризиралото олио. За тази цел са използвани гел-проникваща хроматография и вискозиметрия. Отнасянията на продукта след полимеризация са изследвани с помощта на термо-гравиметричен анализ и инфрачервена спектrophотометрия (FT-IR), както данните са интерпретиране според стандартите ASTM и USP.

Cyanogenic glucoside determination in *Sorghum Halepense* (L.) Pers. leaves at the different growth stages

P. Ebrahimi^{1*}, M. Mohammad Esmaeili², S. Ganji², A. Sattarian², H. Sabouri²

¹Department of Chemistry, Faculty of Basic Sciences, Golestan University, P. O. Box 155, Post code 4913815759, Gorgan, Iran

²Gonbad-Kavous University, P. O. Box 163, Gonbad, Iran

Received April 13, 2014, Revised September 18, 2014

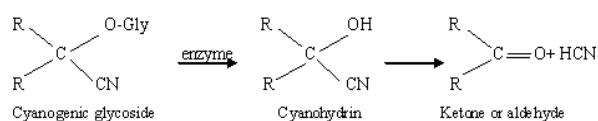
A simple, fast and accurate method of assessing dhurrin as cyanogenic glucoside in the leaves of *sorghum halepense* (L.) pers. plant was developed by polarography using a dropping mercury electrode (DME). Cyanide concentrations in the range 0.01-10 mg/L caused no toxicity problems. The good recovery and precision of CN⁻ determination in the plant shows that this method gives reasonably accurate results. The determination is also practicable in solutions containing sulfides and proteins. The results showed that other interferents are absent or present only in negligible amounts in the plant tissue. It was also found that the content of the cyanogenic glucoside dhurrin in sorghum varies depending on plant age and growth conditions. The highest cyanide potential was registered shortly after onset of germination. The sample preparation was performed by extraction of 30.0 g fresh plant tissue in 10% methanol at ambient temperature for 48 h. Then alkaline hydrolysis of the cyanogenic glycoside was carefully carried out under agitation for 8 h. The voltammetric method was shown to be useful, adequate and reliable as a quality control method in screening low cyanide contents in herbal medicines.

Keywords: *Sorghum halepense* (L.) pers.; Cyanogenic glucoside; Dhurrin; Polarography; Dropping mercury electrode.

INTRODUCTION

Cyanide occurs in the leaves of *sorghum halepense* (L.) pers. plant as the cyanogenic glucoside dhurrin [p-hydroxy-(S)-mandelonitrile β-D-glucopyranoside] derived from the parent amino acid L-tyrosine [1-4]. The biological roles of cyanogenic glycosides in plants include physiological processes and defense mechanisms against predators [5]. Degradation of dhurrin yields equimolar amounts of HCN, glucose, and p-hydroxybenzaldehyde (p-HB). The plants usually show variation in the amount of produced HCN. The production of HCN depends on both the biosynthesis of the cyanogenic glycosides and the existence (or absence) of its degrading enzymes. The biosynthetic precursors of the cyanogenic glycosides are different L-amino acids, these are hydroxylated, then the N-hydroxylamino acids are converted to aldoximes, these are turned into nitriles. The latter are hydroxylated to alpha-hydroxynitriles and are glycosilated to cyanogenic glycosides. The generation of HCN from cyanogenic glycosides is a two-step process involving deglycosilation and cleavage of the molecule (regulated by beta-glucosidase and alpha-hydroxynitrilase). The actual level of cyanogenic glycosides is determined by various factors, both

developmental and ecological ones [6-7]. One of the objectives of sorghum breeding programs is the reduction in the level of dhurrin since cyanide released from the plant tissues will be harmful to consuming livestock. Plant-breeding and genetic programs typically require the examination of large numbers of individual plants [8].



Various methods for the determination of cyanogenic glycosides in plants have been reported [9, 10]. Among these are colorimetric [8, 11-19], fluorometric [20], potentiometric [21], and titrimetric [22] procedures, all of which are based on the assay of hydrocyanic acid (HCN) released when the cyanogenic glucoside is chemically or enzymatically hydrolyzed to yield HCN, glucose, and aglycone. In most of the published procedures, hydrolysis of the cyanogen is accomplished enzymatically, using either endogenous or exogenous glucosidases. For colorimetric and fluorometric assays, the hydrolyzed sample is subjected to diffusion, distillation or aeration, and the volatilized HCN is trapped in an alkaline solution for subsequent assay. These time-consuming procedures help reducing the effects of interfering compounds, but they may result in erroneous values due to incomplete recovery of the

* To whom all correspondence should be sent:
E-mail: epouneh@yahoo.com; p.ebrahimi@gu.ac.ir

released HCN. The picrate method [12, 19, 23] and the Feigl-Anger spot test [24-26] have been also used to survey a wide range of plants for cyanogenesis. The latter method depends on the presence of an endogenous enzyme to catalyze hydrolysis of cyanoglucoside to cyanohydrin which then breaks down to hydrogen cyanide. If the enzyme is not present or the enzyme is inhibited by tannin, then such methods would give a negative or low result [27]. Since the sodium picrate procedure usually depends upon endogenous glycosidase for hydrolysis of the cyanogen, it may cause incomplete release of HCN from the tissues and consequently erroneously low results. In some reports [28] a cyanide selective electrode has been directly utilized to assess the HCN in the hydrolysate of various cultivars. However, the electrode is adversely affected by constituents of the crude extracts; equilibration is slow, and misleading results are sometimes obtained. Other determination methods of the cyanogenic glucoside dhurrin include the indirect classical photometric [22] and the direct chromatographic ones [29-35] in which its aglycone, p-hydroxybenzaldehyde (p-HB), exhibits strong absorption at 330 nm in alkaline solution.

The present study describes a rapid polarographic method for assay of the cyanogenic glucoside content in the leaves of *sorghum halepense* (L.) pers. at four growth stages: vegetative growth, before flowering, flowering and seed ripening, with relatively inexpensive equipment and supplies. The method does not involve enzymatic hydrolysis of dhurrin. At first, alkaline hydrolysis of the cyanogenic glycoside [36] was performed with 2.5% NaOH and then the free cyanide concentration was determined by a polarographic method. Cyanide concentration is proportional to the concentration of the cyanogenic glucoside.

EXPERIMENTAL

Reagents

Sodium hydroxide, potassium hydroxide, boric acid and potassium cyanide used in the study were obtained from Merck (Darmstadt, Germany). All reagents were of analytical grade and were used without further purification. Ultrapure water was obtained from a Millipore, Direct-Q® Water purification system (Millipore Co., Bedford, MA, France). Cyanide standard solution (1 g/L) was prepared by dissolving 0.2503 g of KCN in KOH 0.01 M and making up to 100 mL.

Plant Material

The leaves of *sorghum halepense* (L.) pers. were randomly collected at four growth stages in triplicate, that is, vegetative growing (in the early spring), before flowering, flowering (in June) and seed ripening (in September 2012) from the campus of the Gonbad-e-Kavous university (Gonbad-e-Kavous, Golestan province, Iran). The site is located in the Golestan province at 37° 26'N and 55° 21'E, at an altitude of 45 m above the mean sea level. The climate is Mediterranean, semi arid. The sorghum plant grew on celtic loam soil with pH 7.8.

Sample Preparation

The fresh plant material (30 g) was cut into small pieces and extracted with 10% methanol at ambient temperature for 6 h. The extracts were stored in dark and kept at -4 °C till further analysis. The lack of colour change after 48 h indicated that the extraction of cyanogenic glycoside was approximately completed. Then the filtered extract along with 20 mL of 2.5% NaOH was placed in a 250 mL flask and allowed to stay at room temperature for 2 h. The flask was connected to a vertical water-cooled condenser and heated under agitation for 8 h to permit alkaline hydrolysis of the cyanogenic glycoside to take place. Finally, the content of the flask was transferred to a 100 ml volumetric flask and made up to the volume. Following hydrolysis, the cyanide content of the extracts was determined by a polarographic method.

Polarographic measurement

The electrochemical experiments were carried out using a 746 VA trace analyzer and 757 VA Computrace (Metrohm). A dropping mercury electrode (DME) and a platinum wire were used as working and counter electrodes, respectively. All potentials were recorded against an Ag/AgCl, KCl sat. reference electrode. Pure N₂ was bubbled through the sample solutions for 300 s before the measurements. In order to remove contaminations, the voltammetric cell was washed with concentrated HNO₃. A volume of 10 mL sample solution and 10 mL supporting electrolyte was transferred to the voltammetric cell. Supporting electrolyte contained NH₃BO₃ 0.2 M (12.4 g/L) and KOH 0.17 M (11.2 g/L) with pH 10.2. After degassing, free cyanide was determined by differential pulse polarography (DP) using the standard addition method. The voltammetric parameters included: equilibration time 5 s, pulse amplitude 50 mV, stirring speed 2000 rpm, start potential 0 V, end potential -500 mV, voltage step 8

mV, voltage step time 0.8 s, sweep rate 10 mV/s and peak potential CN⁻ -240 mV.

RESULTS AND DISCUSSION

The results are shown in Figure 1 (A-D). Fig. 1 A shows that the cyanide value of sorghum rapidly increases during germination and vegetative growing, after which it declines with plant age. The results of this study are also summarized in Table 1. The measurements showed that the cyanogenic glycoside value in the vegetative growing stage of *sorghum halepense* was approximately 0.1% of the fresh weight and reached $2 \times 10^{-5}\%$ before flowering stage. No cyanide content was detected in the flowering and seed ripening stages. The method accuracy was investigated in recovery experiments in which a known amount of free cyanide at three concentration levels (0.05, 10, 35 ppm) was added to the plants collected in the flowering and seed ripening stages. Replicate analyses (n=3) were carried out for each solution by the polarographic method. Recovery of cyanide was calculated as follows:

$$\frac{(\text{amount measured} - \text{amount of pure extract}) \times 100}{\text{amount added}}$$

where the amount of pure extract was zero (Fig. 1C-D). As shown in Table 1, the recovery values (standard deviations in parentheses) in the flowering and seed ripening stages were 98.71 (0.48) and 98.84 (0.43), respectively. The good recovery of CN⁻ from the plant shows that this method gives reasonably accurate results and interfering constituents are absent or present only in negligible amounts in the plant tissue.

The linearity of the method was studied in the 0.01-10 mg/L range. Six concentration levels of CN⁻ were chosen and five determinations were carried out for each solution. The correlation graphs were constructed by plotting the peak height obtained *versus* the added amounts. An excellent linear response was observed over the range specified in this method, as confirmed by the correlation coefficient (0.9999).

The precision of the polarographic determination of free cyanide obtained from *sorghum halepense* (L.) Pers. was calculated in terms of intra-day repeatability and inter-day precision. To this purpose, two spiked samples at three concentration levels, 0.05, 1.5, 2.5 ppm, were prepared and analyzed in triplicate. The procedure was repeated on 3 different days to determine inter-day reproducibility. The results showed an RSD between 0.3-3.5 % indicating a good precision (Table 1).

Therefore, the plant of *sorghum halepense* (L.) Pers. in its new growing stage (such as newly emerged seedlings and young leaves), constitutes a health risk for humans and domestic animals [37] due to the cyanogenic potential. To increase food and feed safety, it is of great interest to know the effect of growth conditions and stages on cyanogenic glycoside accumulation to avoid incidences of cyanide intoxication due to occasionally unexpected high concentrations that cannot be handled using normal precautionary measures.

Table 1. Values of cyanogenic glycoside in *sorghum halepense* at the different growing stages, intra-day and inter-day precision and accuracy obtained in the polarographic determination of CN⁻.

Growth stages	CN ⁻ (%) ^a	0.050 ppm ^b (CV, %)	1.500 ppm ^b (CV, %)	2.500 ppm ^b (CV, %)	Amount added (mg/L)	Recovery (%±SD)	Mean recovery (%±SD)
vegetative growing before	0.1	-	-	-	-	-	-
flowering	2×10^{-5}	-	-	-	-	-	-
flowering	0	0.053 ^c (1.35)	1.538 ^c (1.01)	2.444 ^c (2.74)	0.05	98.13±0.35	98.71±0.48
		0.056 ^d (2.12)	1.359 ^d (2.80)	2.354 ^d (1.79)	10	95.53±0.68	
					35	102.47±0.34	
seed ripening	0	0.056 ^c (1.09)	1.540 ^c (0.92)	2.514 ^c (0.30)	0.05	98.27±0.50	98.84±0.43
		0.060 ^d (1.65)	1.154 ^d (3.59)	2.244 ^d (1.17)	10	94.06±0.31	
					35	104.18±0.46	

^a measured free cyanide in the plant at the different growth stages.

^b concentrations which were added to the plant at the flowering and seed ripening stages.

^c measured average value during a single day (n=3).

^d measured average value on three consecutive days

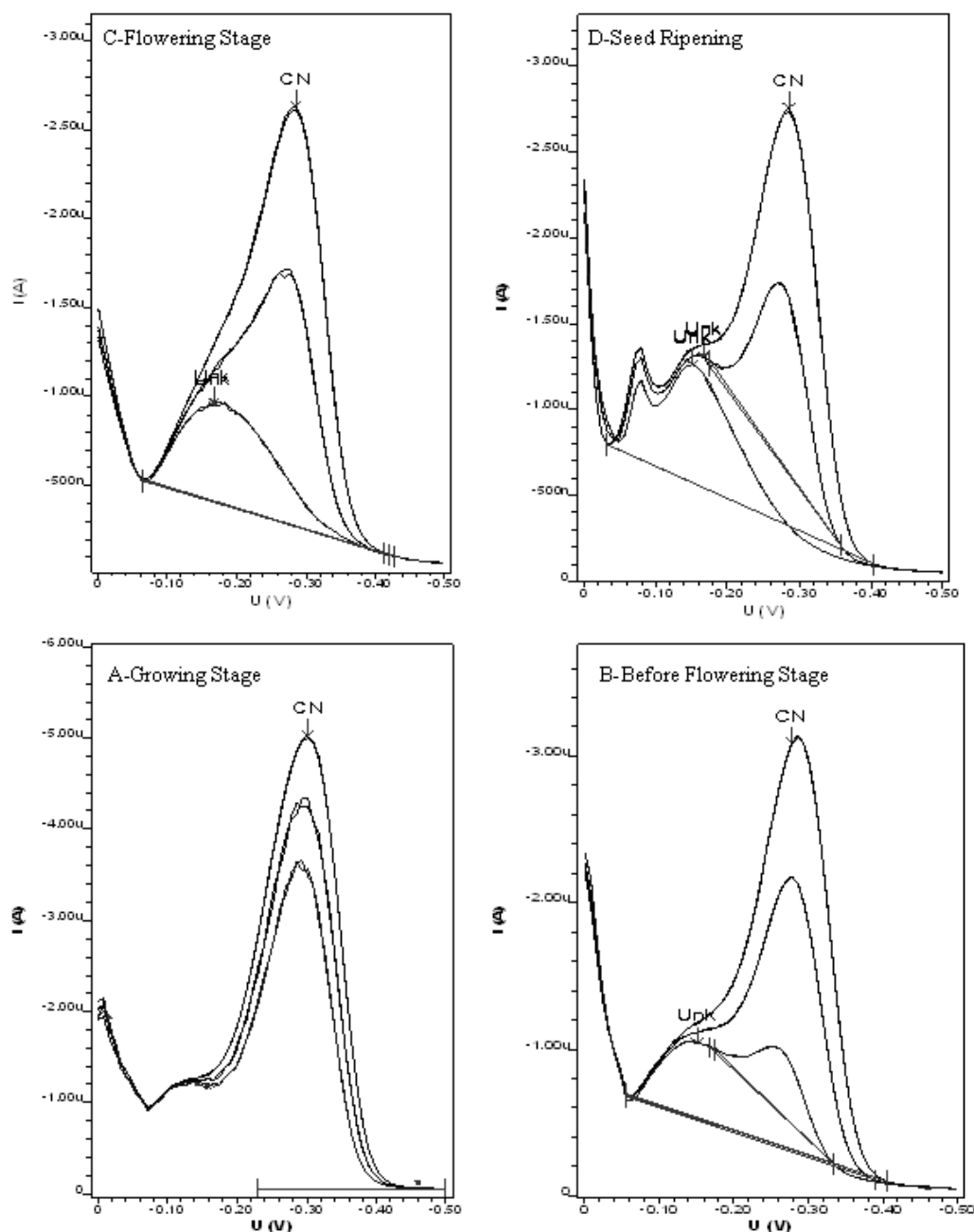


Fig. 1- Polarograms of *sorghum halepense* hydrolyzed extracts at the different growing stages: A) Growing stage; B) Before flowering stage; C) Flowering stage; D) Seed ripening. Voltammetric parameters: equilibration time 5 sec, pulse amplitude 50 mV, stirring speed 2000 rpm, start potential 0 V, end potential -500 mV, voltage step 8 mV, voltage step time 0.8 s, sweep rate 10 mV/s and peak potential CN^- -240 mV.

CONCLUSION

A simple method for the polarographic determination of cyanogenic glycoside in plants was developed. The method does not involve enzymatic hydrolysis of dhurrin. The study can serve as a reference to new studies on cyanoglucosides in all plants and can be used for the rapid and routine estimation of the dhurrin of sorghum. The free cyanide was determined in the alkaline hydrolysed extracts by differential pulse voltammetry technique with a dropping mercury electrode (DME). The polarographic signal was

proportional to the cyanide concentration and the linear range of calibration was from 0.01 to 10 mg/L cyanide with $r=0.9999$. The good recovery and precision of CN^- from the plant shows that this method gives reasonably accurate results and interfering constituents are absent or present only in negligible amounts in plant tissue. Therefore, it was suggested that the polarographic procedure can be used as an efficient tool in screening low cyanide contents of sorghum.

REFERENCES

1. P. K. Busk, B. L. Møller, *Plant Physiol.*, **129**, 1222 (2002).
2. D. Ganjewala, S. Kumar, S. A. Devi, K. Ambika, *Acta Biolog. Szegediensis*, **54**, 1 (2010).
3. [3] B. Goff, K. J. Moore, S. L. Fales, G. F. Pedersen, *J. Sci. Food Agr.*, **91**, 1523-1526 (2011).
4. D. G. Barceloux, Cyanogenic Foods (Cassava, Fruit Kernels, and Cycad Seeds). In *Medical Toxicology of Natural Substances: Foods, Fungi, Medicinal Herbs, Toxic Plants, and Venomous Animals*. Hoboken, NJ: John Wiley & Sons, 2008, p. 44.
5. D. A. Jones, *Phytochem.*, **47(2)**, 155 (1998).
6. S. Prasad, M. S. Dhanya, *J. Metabolomics Syst. Biol.*, **2(1)**, 10 (2011).
7. B. L. Møller, D. S. Seigler, Biosynthesis of cyanogenic glycosides, cyanolipids and related compounds. In *Plant amino acids biochemistry and biotechnology*, B. K. Singh (ed.), Marcel Dekker, 1999 p. 563.
8. F. A. Haskins, H. J. Gorz, R. M. Hill, *J. Agric. Food Chem.*, **36(4)**, 775 (1988).
9. A. Surleva, R. Gradinaru, G. Drochioiu, *Int. J. Criminal Invest.*, **2(2)**, 79 (2012).
10. J. Ma, P. Dasgupta, *Anal. Chim. Acta*, **673**, 117 (2010).
11. J. H. Bradbury, I. C. Denton, *Food Chem.*, **127**, 1755 (2011).
12. J. H. Bradbury, *Food Chem.*, **113**, 1329 (2009).
13. A. Surleva, G. Drochioiu, *Food Chem.*, **141**, 2788 (2013).
14. A. E. Burns, J. H. Bradbury, T. R. Cavagnaro, R. M. Gleadow, *J. Food Comp. Anal.*, **25**, 79 (2012).
15. S. Abban, L. Thorsen, L. Brimer, *Nat. Sci.*, **9**, 64 (2011).
16. M. R. Haque, J. H. Bradbury, *Food Chem.*, **85**, 27 (2004).
17. G. Drochioiu, *Anal. Bioanal. Chem.*, **372**, 744 (2002).
18. G. Drochioiu, K. Popa, D. Humelnicu, M. Murariu, I. Sandu, A. Cecal, *Toxicol. Envir. Chem.*, **90**, 221 (2007).
19. G. Drochioiu, C. Arsene, M. Murariu, C. Oniscu, *Food Chem. Toxicol.*, **46**, 3540–3545 (2008).
20. S. Takanashi, Z. Tamura, *Chem. Pharm. Bull.*, **18(8)**, 1633 (1970).
21. D. B. Easty, W. J. Blaedel, L. Anderson, *Anal. Chem.*, **43(4)**, 509 (1971).
22. T. Akazawa, P. Miljanich, E. E. Conn, *Plant Physiol.*, **35(4)**, 535 (1960).
23. A. Adersen, H. Adersen, L. Brimer, *Biochem. Sys. Ecol.*, **16(1)**, 65 (1988).
24. B. E. Van Wyk, *Biochem. Sys. Ecol.*, **17(4)**, 297 (1989).
25. K. M. Olsen, B. L. Sutherland, L. L. Small, *Mol. Ecol.*, **16**, 4180 (2007).
26. A. Takos, D. Lai, L. Mikkelsen, M. A. Hachem, D. Shelton, M. S. Motawia, C. E. Olsen, T. L. Wang, C. Martin, F. Rook, *The Plant Cell*, **22**, 1605 (2010).
27. M. Rezaul Haque, J. Howard Bradbury, *Food Chem.*, **77(1)**, 107 (2002).
28. W. J. Blaedal, D. B. Easty, L. Anderson, T. R. Farrell, *Anal. Chem.*, **43(7)**, 890 (1971).
29. R. Bacala, V. Barthet, *J. AOAC Int.*, **90**, 153 (2007).
30. [30] N. Bjarnholt, M. Laegdsmand, H. C. B. Hansen, O. H. Jacobsen, B. L. Møller, *Chemosphere*, **72**, 897 (2008).
31. G. R. De Nicola, O. Leoni, L. Malaguti, R. Bernardi, L. Lazzeri, *J. Agri. Food Chem.*, **59**, 8065 (2011).
32. D. Ganjewala, S. Kumar, S. A. Devi, K. Ambika, *Acta Biolog. Szegediensis*, **54**, 1 (2010).
33. B. Goff, K. J. Moore, S. L. Fales, G. F. Pedersen, *J. Sci. Food Agr.*, **91**, 1523 (2011).
34. W. Herchi, D. Arráez-Román, S. Boukhchina, H. Kallel, A. Segura-Carretero, A. Fernández-Gutierrez, *Afr. J. Biotech.*, **11**, 724 (2012).
35. S. Sornyotha, K. L. Kyu, K. Ratanakhanokchai, *Food Chem.*, **104**, 1750 (2007).
36. C.-H. Mao, L. Anderson, *J. Org. Chem.*, **30(2)**, 603 (1965).
37. J.B. Harborne, Plant toxins and their effects on animals. In: *Introduction to Ecological Biochemistry*. Academic Press, London, 1993, p. 71.

ОПРЕДЕЛЯНЕ НА ЦИАНОГЕННИ ГЛЮКОЗИДИ В ЛИСТАТА НА *Sorghum halepense* (L.) Pers. В
РАЗЛИЧНИ ЕТАПИ НА РАЗВИТИЕ

П. Ебрахими^{1*}, М. Мохамад Есмаели², С. Ганджи², А. Сатарян², Х. Сабури²

¹ Департамент по химия, Факултет по основни науки, Университет в Голестан, Горган, Иран

² Университет Гонбад-Кавус, Гонбад, Иран

Received January 8, 2014, Revised June 25, 2014

(Резюме)

Развит е прост, бърз и точен полярографски метод за определянето на dhurrin като цианогенен глюкозид в листата на *Sorghum halepense* (L.) pers. Концентрацията на цианиди в интервала 0.01-10 mg/L не предизвикват токсичност. Добрият добив и точността на определянето на CN⁻ в растенията показва, че методът дава твърде добри резултати. Определянето е също подходящо за разтвори, съдържащи сулфиди и протеини. Резултатите показват, че липсват пречещи вещества или те са в много ниски концентрации в растителните тъкани. Освен това е намерено, че съдържанието на цианогенния глюкозид dhurrin в растението варира в зависимост от възрастта на растението и условията на растеж. Най-висок цианиден потенциал е установен кратко време след началото на покълването. Пробите са подготвени чрез екстракция на 30 г. пресни растителни тъкани в 10% метанол при стайна температура за 48 ч. След това се провежда алкална хидролиза на цианогенния глюкозид при разбъркване за 8 часа. Волт-амперометричният метод се оказва полезен за скрийнинга на малки количества цианиди в лекарствени растения.

Preferential solvation of naproxen and piroxicam in ethanol + water mixtures

R. G. Sotomayor¹, D. R. Delgado², F. Martínez^{2*}

¹ Programa de Farmacia, Facultad de Química y Farmacia, Universidad del Atlántico, Barranquilla, Colombia.

² Grupo de Investigaciones Farmacéutico Fisicoquímicas, Departamento de Farmacia, Facultad de Ciencias, Universidad Nacional de Colombia, Cra 30 No. 45-03, Bogotá D.C., Colombia.

Received April, 30, 2014, Revised August 21, 2014

The preferential solvation parameters of naproxen (NAP) and piroxicam (PIR) in ethanol (EtOH) + water binary mixtures were obtained from their thermodynamic properties by means of the inverse Kirkwood-Buff integrals method. NAP and PIR are very sensitive to specific solvation effects, so the preferential solvation parameter by EtOH, $\delta x_{1,3}$, is negative in the water-rich mixtures but positive in all the other compositions for both drugs at temperatures of 293.15, 303.15 and 313.15 K. It is conjecturable that in water-rich mixtures the hydrophobic hydration around the aromatic and methyl groups of the drugs plays a relevant role in the solvation. The higher drugs solvation by EtOH in mixtures of similar solvent proportions and in EtOH-rich mixtures could be due mainly to polarity effects. In these mixtures both drugs would be acting as Lewis acids with the EtOH molecules because this co-solvent is more basic than water.

Key words: naproxen, piroxicam, ethanol, preferential solvation, IKBI.

INTRODUCTION

Naproxen (NAP, Fig. 1, 230.26 g mol⁻¹, (+)-(S)-2-(6-methoxynaphthalen-2-yl)propanoic acid, CAS number: 22204-53-1) and piroxicam (PIR, Fig. 2, 331.35 g mol⁻¹, 4-Hydroxy-2-methyl-N-2-pyridinyl-2H-1,2-benzothiazine-3-carboxamide 1,1-dioxide, CAS number: 36322-90-4) are non-steroidal anti-inflammatory drugs used as analgesics and antipyretics [1, 2]. Although NAP and PIR are widely used in current therapeutics, the physicochemical information about their solubilities in aqueous-rich and organic-rich media is not abundant [3]. Nevertheless, some physicochemical studies about their solution thermodynamics in pharmaceutical co-solvent mixtures conformed by water and ethanol (EtOH) have been reported [4, 5]. Moreover, some semiempirical methods have also been challenged to correlate their solubilities as a function of temperature. In particular the extended Hildebrand solubility approach [6] has been analyzed at 298.15 K for both drugs [7, 8]; the log-linear model of Yalkowsky and Roseman [9] and the Jouyban-Acree model [10] have also been studied for NAP at temperatures from 293.15 to 313.15 K [11, 12]. Nevertheless, none of these studies has been specifically carried out to study the preferential solvation of these drugs by the solvent components according to the mixtures composition.

In this way, the inverse Kirkwood-Buff integrals (IKBI) method is a powerful tool for evaluating the preferential solvation of non-electrolyte compounds in binary co-solvent mixtures, describing the local composition of both solvents around the solute molecules [13-18]. Specifically, in the case of aqueous ethanolic solutions this treatment depends on the values of the standard molar Gibbs energies of transfer of the drug from neat water to EtOH + water mixtures, as well as on the excess molar Gibbs energy of mixing of the co-solvent mixtures.

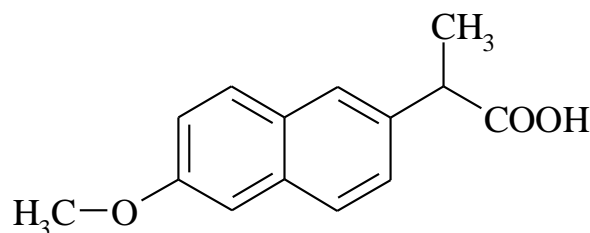


Fig. 1. Molecular structure of naproxen.

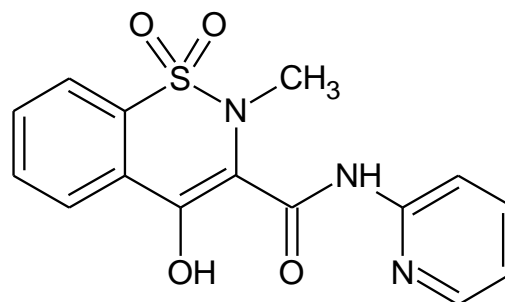


Fig. 2. Molecular structure of piroxicam.

* To whom all correspondence should be sent:
E-mail: fmartinezr@unal.edu.co

Thus, the main goal of this paper was to evaluate the preferential solvation of NAP and PIR in EtOH + water co-solvent mixtures, based on thermodynamic definitions, as has been made for several drugs in the same aqueous co-solvent mixtures [19-21]. These drugs were chosen for the present research because they have very different molecular structures, NAP being composed of C, H and O atoms; whereas PIR additionally contains N and S atoms. It is important to keep in mind that ethanol is the co-solvent more widely used in the development of homogeneous liquid pharmaceutical dosage forms [22, 23]. Thus, the results are expressed in terms of the preferential solvation parameter ($\delta x_{1,3}$) of the drugs by EtOH in the mixtures.

COMPUTATIONAL BACKGROUND

In binary EtOH + water mixtures the preferential solvation parameter by EtOH (component 1) is defined as:

$$\delta x_{1,3} = x_{1,3}^L - x_1 = -\delta x_{2,3} \quad (1)$$

where x_1 is the mole fraction of co-solvent in the bulk solvent mixture and $x_{1,3}^L$ is the local mole fraction of EtOH in the environment near to NAP or PIR (component 3). If $\delta x_{1,3} > 0$ then the drug is preferentially solvated by EtOH; on the contrary, if this parameter is < 0 the drug is preferentially solvated by water. Values of $\delta x_{1,3}$ are obtainable from the inverse Kirkwood-Buff integrals for the individual solvent components analyzed in terms of some thermodynamic quantities as shown in equations (2) and (3) [17-21]:

$$G_{1,3} = RT\kappa_T - V_3 + x_2 V_2 D/Q \quad (2)$$

$$G_{2,3} = RT\kappa_T - V_3 + x_1 V_1 D/Q \quad (3)$$

where κ_T is the isothermal compressibility of the co-solvent + water solvent mixtures (expressed in GPa^{-1}), V_1 and V_2 are the partial molar volumes of the solvents 1 and 2 in the mixtures (expressed in $\text{cm}^3 \text{mol}^{-1}$), similarly, V_3 is the partial molar volume of the drug in these mixtures (also expressed in $\text{cm}^3 \text{mol}^{-1}$). The function D is the derivative of the standard molar Gibbs energies of transfer of the drug, from neat water to the EtOH + water mixtures, with respect to the solvent composition (expressed in kJ mol^{-1} , as also is RT). Otherwise, the function Q involves the second derivative of the excess molar Gibbs energy of mixing of the two solvents (G_{1+2}^{Exc}) with respect to the water proportion in the mixtures (also expressed in kJ mol^{-1}), as defined in equations (4) and (5) [17-21]:

$$D = \left(\frac{\partial \Delta_{tr} G_{(3,2 \rightarrow 1+2)}^o}{\partial x_1} \right)_{T,p} \quad (4)$$

$$Q = RT + x_1 x_2 \left(\frac{\partial^2 G_{1,2}^{Exc}}{\partial x_2^2} \right)_{T,p} \quad (5)$$

Because the dependence of κ_T on composition is unknown for a lot of the systems investigated and because of the small contribution of $RT \kappa_T$ to the IKBI, the dependence of κ_T on composition could be approximated. This is made by considering

additive behavior, according to: $\kappa_{T,\text{mix}} = \sum_{i=1}^n x_i \kappa_{T,i}^o$,

where x_i is the mole fraction of component i in the mixture and $\kappa_{T,i}^o$ is the isothermal compressibility of the pure component i [24, 25]. Thus, the preferential solvation parameter by the co-solvent is calculated from the inverse Kirkwood-Buff integrals as follows:

$$\delta x_{1,3} = \frac{x_1 x_2 (G_{1,3} - G_{2,3})}{x_1 G_{1,3} + x_2 G_{2,3} + V_{\text{cor}}} \quad (6)$$

Here, the correlation volume (V_{cor}) is estimated by means of the following expression [17-21]:

$$V_{\text{cor}} = 2522.5 \left(r_3 + 0.1363 (x_{1,3}^L V_1 + x_{2,3}^L V_2) \right)^{1/3} - 0.085 \quad (7)$$

where r_3 is the drug molecular radius (expressed in nm). However, the definitive correlation volume requires iteration, because it depends on the local mole fractions. This iteration is done by replacing $\delta x_{1,3}$ in the Eq. (1) to calculate $x_{1,3}^L$ until a non-variant value of V_{cor} is obtained.

RESULTS AND DISCUSSION

The experimental solubility of NAP and PIR in EtOH + water systems was taken from the literature [4, 5]. As was mentioned earlier, the solubility of these drugs continuously increases from neat water to EtOH indicating higher affinity of NAP and PIR for semipolar organic media. Standard molar Gibbs energy of transfer of NAP and PIR from neat water to EtOH + water mixtures is calculated and correlated to regular third order polynomials from the drugs solubility data by using Eq. (8). Figure 3 shows the Gibbs energy of transfer behaviors at 293.15 K, whereas Table 1 also shows the behaviors at all the temperatures studied. The coefficients of the polynomials obtained are shown in Table 2.

Table 1. Gibbs energy of transfer (kJ mol^{-1}) of naproxen and piroxicam in ethanol + water co-solvent mixtures at several temperatures.

x_1^a	Naproxen ^b			Piroxicam ^c		
	293.15 K	303.15 K	313.15 K	293.15 K	303.15 K	313.15 K
0.0000	0.00	0.00	0.00	0.00	0.00	0.00
0.0417	-0.47	-1.12	-1.64	-1.41	-1.82	-2.21
0.0891	-2.70	-3.57	-4.51	-2.16	-4.02	-4.58
0.1436	-6.27	-7.66	-8.61	-4.43	-6.81	-7.38
0.2068	-9.91	-10.87	-11.61	-7.02	-8.70	-9.24
0.2812	-12.53	-13.42	-14.29	-9.36	-10.11	-10.79
0.3698	-14.65	-15.56	-16.60	-10.84	-11.54	-12.07
0.4772	-16.28	-17.12	-18.00	-12.20	-12.89	-13.37
0.6101	-17.54	-18.48	-19.41	-13.40	-14.03	-14.49
0.7788	-18.62	-19.51	-20.46	-14.50	-15.09	-15.40
1.0000	-19.42	-20.45	-21.39	-15.79	-15.63	-15.83

^a x_1 is the mole fraction of ethanol in the ethanol + water mixtures free of drug.^b Calculated from solubility values reported in Ref. [4].^c Calculated from solubility values reported in Ref. [5].**Table 2.** Coefficients of the equation (8) applied to the Gibbs energy of transfer of naproxen and piroxicam from neat water to ethanol + water mixtures at several temperatures.

Coefficient kJ mol^{-1}	Naproxen			Piroxicam		
	293.15 K	303.15 K	313.15 K	293.15 K	303.15 K	313.15 K
<i>a</i>	1.34	1.00	0.73	0.55	-0.03	-0.20
<i>b</i>	-65.67	-71.21	-75.94	-44.79	-52.30	-55.76
<i>c</i>	73.51	85.89	95.04	46.33	65.71	73.23
<i>d</i>	-28.51	-36.12	-41.26	-17.80	-29.15	-33.27

Table 3. *D* values (kJ mol^{-1}) for naproxen and piroxicam in ethanol + water mixtures at several temperatures.

x_1^a	Naproxen			Piroxicam		
	293.15 K	303.15 K	313.15 K	293.15 K	303.15 K	313.15 K
0.00	-65.67	-71.21	-75.94	-44.79	-52.30	-55.76
0.10	-51.83	-55.11	-58.17	-36.06	-40.04	-42.11
0.20	-39.69	-41.19	-42.87	-28.39	-29.52	-30.46
0.30	-29.27	-29.43	-30.05	-21.80	-20.75	-20.80
0.40	-20.56	-19.84	-19.71	-16.27	-13.72	-13.14
0.50	-13.55	-12.41	-11.84	-11.81	-8.45	-7.48
0.60	-8.26	-7.16	-6.45	-8.41	-4.93	-3.81
0.70	-4.68	-4.07	-3.53	-6.09	-3.15	-2.14
0.80	-2.81	-3.14	-3.09	-4.83	-3.12	-2.47
0.90	-2.65	-4.39	-5.12	-4.64	-4.84	-4.79
1.00	-4.20	-7.80	-9.63	-5.52	-8.31	-9.11

^a x_1 is the mole fraction of ethanol in the ethanol + water mixtures free of drug.**Table 4.** $G_{1,3}$ values ($\text{cm}^3 \text{mol}^{-1}$) for naproxen and piroxicam in ethanol + water mixtures at several temperatures.

x_1^a	Naproxen			Piroxicam		
	293.15 K	303.15 K	313.15 K	293.15 K	303.15 K	313.15 K
0.00	-663.6	-688.2	-706.3	-518.0	-561.6	-574.8
0.10	-580.6	-623.6	-668.6	-466.9	-510.5	-542.0
0.20	-480.7	-508.1	-540.2	-403.3	-423.3	-444.1
0.30	-390.7	-395.3	-403.8	-345.2	-339.9	-343.0
0.40	-320.4	-310.9	-306.0	-299.4	-278.5	-271.9
0.50	-268.5	-254.5	-245.8	-265.7	-238.6	-229.3
0.60	-230.3	-218.6	-211.1	-240.4	-214.5	-205.9
0.70	-202.4	-197.1	-193.0	-219.4	-201.5	-195.3
0.80	-185.4	-186.2	-185.7	-201.3	-195.3	-192.8
0.90	-178.6	-180.5	-181.2	-189.9	-190.1	-189.9
1.00	-175.5	-175.4	-175.3	-184.6	-184.5	-184.4

^a x_1 is the mole fraction of ethanol in the ethanol + water mixtures free of drug.

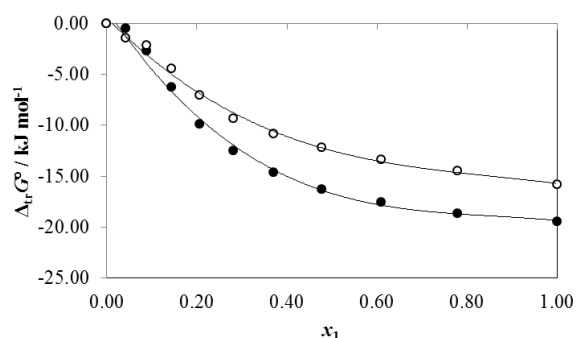


Fig. 3. Gibbs energy of transfer of naproxen (●) and piroxicam (○) from neat water to ethanol + water mixtures at 293.15 K.

$$\Delta_{tr}G_{3,2 \rightarrow 1+2}^{\circ} = RT \ln \left(\frac{x_{3,2}}{x_{3,1+2}} \right) = a + bx_1 + cx_1^2 + dx_1^3 \quad (8)$$

Thus D values are calculated from the first derivative of polynomial models, Eq. (9), solved according to the solvent mixtures composition. This procedure was done varying by 0.05 in mole fraction of EtOH but in the following tables, the respective values varying only by 0.10 are reported. D values are shown in Table 3.

$$D = b + 2cx_1 + 3dx_1^2 \quad (9)$$

Q and $RT \kappa_T$ values for EtOH + water binary mixtures, as well as the partial molar volumes of EtOH and water, at the three temperatures considered here, were taken from the literature [20, 21].

Otherwise, partial molar volumes of non-electrolyte drugs are not frequently reported in the literature. This is because of the large uncertainty obtained in its determination due to their low solubilities, in particular in aqueous media. For this reason, in the first approach, the molar volumes of NAP and PIR were considered as independent of co-solvent composition and temperature, as they are calculated according to the groups contribution method proposed by Fedors [26]. Thus, these values were taken from the literature as $V_3 = 178.3 \text{ cm}^3 \text{ mol}^{-1}$ for NAP [27] and $187.4 \text{ cm}^3 \text{ mol}^{-1}$ for PIR [8]. On the other hand, from these values the radii of the drug molecules were calculated by using: $r_3 = (3 \cdot 10^{21} \cdot V_3 / 4 \cdot \pi \cdot N_{Av})^{1/3}$, where N_{Av} is the Avogadro number, as $r_3 = 0.413 \text{ nm}$ and 0.420 nm for NAP and PIR, respectively.

Tables 4 and 5 show that the $G_{1,3}$ and $G_{2,3}$ values are negative for both co-solvent systems at all temperatures under study. Nevertheless, depending on co-solvent compositions in some cases $G_{1,3}$ values are larger in magnitude in comparison with $G_{2,3}$ values, but in other cases the behavior is opposite. As has been described in the literature, these differences are associated with the affinity of

both drugs to each of the components of the mixtures, EtOH or water [15, 16].

In order to apply the IKBI method, the correlation volume was iterated three times by using the equations (1), (6) and (7) to obtain the final values reported in Table 6. This property is almost independent on temperature in water-rich mixtures but increases to some extent in EtOH-rich mixtures. This would be expectable according to the variation of the respective molar expansibilities with the mixtures composition [28].

According to Fig. 4 the values of $\delta x_{1,3}$ vary non-linearly with the EtOH proportion in the aqueous mixtures at 293.15 K. In this way, the addition of EtOH to water tends to make negative the $\delta x_{1,3}$ values of NAP and PIR from pure water up to the mixtures of 0.23 in mole fraction of EtOH.

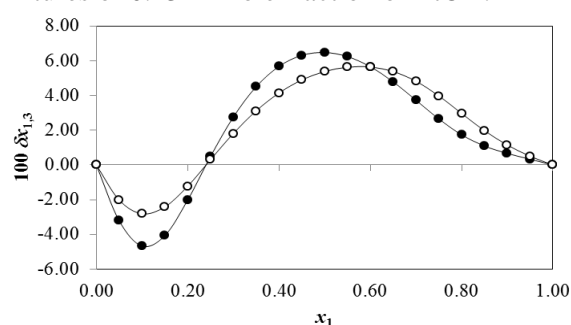


Fig. 4. $\delta x_{1,3}$ values for naproxen (●) and piroxicam (○) in ethanol + water mixtures at 293.15 K.

In these water-rich mixtures the maximum negative values are found in $x_1 = 0.10$ ($\delta x_{1,3} = -4.665 \times 10^{-2}$ for NAP and -2.806×10^{-2} for PIR, at 293.15 K). These magnitudes are similar to those found for some other drugs in the same mixtures [20, 21]. As was previously indicated, possibly the structuring of water molecules around the non-polar groups of this drug leading to hydrophobic hydration of the aromatic and methyl groups (Figs. 1 and 2), contributes to lowering of the net $\delta x_{1,3}$ to negative values in these water-rich mixtures. Similar behaviors are observed at the other temperatures as can be seen in Table 7. On the other hand, the maximum negative values increase with the temperature increase. The possibility of hydrophobic hydration of NAP and PIR in water-rich mixtures has been exposed previously from enthalpy-entropy compensation plots and some thermodynamic quantities of transfer [4, 5]. Additionally, the negative deviations to the log-linear model proposed by Yalkowsky and Roseman [9], exhibited by NAP in water-rich mixtures, have also been attributed to an increase of water-structuring in these compositions [11, 12].

Table 5. $G_{2,3}$ values ($\text{cm}^3 \text{mol}^{-1}$) for naproxen and piroxicam in ethanol + water mixtures at several temperatures.

x_1^a	Naproxen			Piroxicam		
	293.15 K	303.15 K	313.15 K	293.15 K	303.15 K	313.15 K
0.00	-177.2	-177.1	-177.1	-186.3	-186.2	-186.2
0.10	-311.9	-328.1	-345.2	-280.0	-295.9	-307.9
0.20	-413.6	-437.6	-465.4	-355.3	-372.8	-390.9
0.30	-473.0	-482.0	-496.1	-406.5	-401.0	-406.9
0.40	-497.7	-478.6	-469.4	-439.8	-394.6	-380.9
0.50	-496.0	-449.1	-420.1	-463.9	-371.1	-339.4
0.60	-467.6	-405.8	-366.3	-482.1	-343.3	-297.7
0.70	-403.4	-359.5	-324.8	-481.1	-327.2	-275.4
0.80	-320.3	-335.1	-330.0	-433.6	-343.1	-308.1
0.90	-277.4	-345.6	-375.6	-363.3	-372.3	-371.7
1.00	-275.9	-357.9	-396.0	-316.8	-379.0	-393.1

^a x_1 is the mole fraction of ethanol in the ethanol + water mixtures free of drug.**Table 6.** Correlation volume ($\text{cm}^3 \text{mol}^{-1}$) of naproxen and piroxicam in ethanol + water mixtures at several temperatures.

x_1^a	Naproxen			Piroxicam		
	293.15 K	303.15 K	313.15 K	293.15 K	303.15 K	313.15 K
0.00	814	815	817	839	840	841
0.10	857	853	849	898	896	895
0.20	959	961	963	993	996	1000
0.30	1076	1082	1090	1098	1103	1110
0.40	1177	1180	1185	1197	1196	1201
0.50	1260	1260	1262	1285	1277	1280
0.60	1331	1329	1331	1366	1352	1354
0.70	1393	1396	1400	1437	1426	1428
0.80	1453	1464	1473	1499	1500	1507
0.90	1520	1533	1545	1561	1572	1582
1.00	1588	1599	1610	1627	1638	1649

^a x_1 is the mole fraction of ethanol in the ethanol + water mixtures free of drug.**Table 7.** $\delta x_{1,3}$ values ($\times 100$) of naproxen and piroxicam in ethanol + water mixtures at several temperatures.

x_1^a	Naproxen			Piroxicam		
	293.15 K	303.15 K	313.15 K	293.15 K	303.15 K	313.15 K
0.00	0.000	0.000	0.000	0.000	0.000	0.000
0.10	-4.665	-5.364	-6.176	-2.806	-3.337	-3.736
0.20	-2.021	-2.214	-2.479	-1.224	-1.318	-1.421
0.30	2.755	2.906	3.119	1.812	1.781	1.858
0.40	5.677	5.239	5.019	4.145	3.284	3.027
0.50	6.479	5.359	4.690	5.385	3.405	2.765
0.60	5.660	4.337	3.520	5.640	2.847	1.983
0.70	3.736	2.964	2.371	4.825	2.225	1.390
0.80	1.740	1.909	1.834	2.970	1.855	1.429
0.90	0.668	1.112	1.301	1.153	1.203	1.190
1.00	0.000	0.000	0.000	0.000	0.000	0.000

^a x_1 is the mole fraction of ethanol in the ethanol + water mixtures free of drug.

The bigger preferential solvation parameters by water obtained for NAP compared with those obtained for PIR could be attributed to the differences in the drug polarities in comparison with the polarity of EtOH and water. Thereby, if the Hildebrand solubility parameters (δ) are considered, i.e. 23.4, 30.4, 26.5, and 47.8 $\text{MPa}^{1/2}$ for NAP, PIR, EtOH, and water, respectively [8, 27, 29], it follows that EtOH exhibits an intermediate polarity between both drugs, and NAP is the drug more

distant in polarity with respect to water. Accordingly, the hydrophobic hydration of NAP would be higher than the one for PIR.

In the EtOH + water mixtures with composition $0.23 < x_1 < 1.00$ the local mole fractions of EtOH are greater than the ones for water for both drugs.

In this way, the co-solvent action could be related to the breaking of the ordered structure of water (by hydrogen bonding) around the non-polar moieties of the drugs. This fact would increase the

drug solvation reaching maximum values in compositions near to $x_1 = 0.50$ and 0.60 for NAP and PIR, with $\delta x_{1,3} = 6.479 \times 10^{-2}$ and 5.640×10^{-2} at 293.15 K, respectively. These magnitudes are also similar to those found for other drugs in the same mixtures [19-21]. In opposite way to the water-rich mixtures behavior, the maximum positive values decrease with the temperature increase.

As has been indicated earlier, NAP and PIR could act in solution as Lewis acids due to the hydrogen atom in their $-OH$ groups (and also by the $-CO-NH-$ group for PIR, Figs. 1 and 2), in order to establish hydrogen bonds with proton-acceptor functional groups in EtOH and water (oxygen atom in $-OH$). In addition, these drugs could act as Lewis bases due to free electron pairs in oxygen atoms of hydroxyl and carbonyl groups (and also by the $-SO_2-$ group for PIR, Figs. 1 and 2) to interact with hydrogen atoms present in both solvents. In this context, NAP has one hydrogen-bonding donor and three hydrogen-bonding acceptor groups, whereas PIR has two hydrogen-bonding donor and four hydrogen-bonding acceptor groups, excluding the aromatic nitrogen [4, 5].

According to the preferential solvation results, it is conjecturable that in intermediate composition mixtures and EtOH-rich mixtures, NAP and PIR are acting as Lewis acids with the EtOH molecules because this co-solvent is more basic than water as indicated by the Kamlet-Taft hydrogen bond acceptor parameters (β), i.e. 0.75 for EtOH and 0.47 for water [24, 30]. In this way, these drugs would prefer EtOH instead of water.

CONCLUSIONS

According to the performed analyses, NAP and PIR are preferentially solvated by water in water-rich mixtures but preferentially solvated by EtOH in mixtures with intermediate composition and those rich in EtOH at all temperatures considered. It is important to note that these results are in good agreement with those described previously, based on classical thermodynamic and extra-thermodynamic treatments [4-8]. Nevertheless, the specific solvent-drug interactions remain unclear.

REFERENCES

1. S. Budavari, M. J. O'Neil, A. Smith, P. E. Heckelman, J. R. Obenchain, J. A. R. Gallipeau, M. A. D'Arecea, The Merck Index, An Encyclopedia of Chemicals, Drugs, and Biologicals, 13th ed., Merck & Co., Inc. Whitehouse Station, NJ, 2001.
2. G. R. Hanson, Analgesic, antipyretic, and anti-inflammatory drugs, in: Remington, The Science and

- Practice of Pharmacy, 20th ed., A. R. Gennaro (ed.), Lippincott, Williams & Wilkins, Philadelphia, 2000.
3. A. Jouyban, Handbook of Solubility Data for Pharmaceuticals, CRC Press, Taylor & Francis Group, Boca Raton, FL, 2010.
4. D. P. Pacheco, F. Martínez, *Phys. Chem. Liq.*, **45**, 581 (2007).
5. R. G. Sotomayor, A. R. Holguín, A. Romdhani, F. Martínez, A. Jouyban, *J. Solution Chem.*, **42**, 358 (2013).
6. A. Martin, P. Bustamante, A. H. C. Chun, Physical Chemical Principles in the Pharmaceutical Sciences, 4th edition, Lea & Febiger, Philadelphia, 1993.
7. D. M. Aragón, D. P. Pacheco, M. A. Ruidiaz, A. D. Sosnik, F. Martínez, *Vitae, Rev. Fac. Quím. Farm.*, **15**, 113 (2008).
8. R. G. Sotomayor, A. R. Holguín, D. M. Cristancho, D. Delgado, F. Martínez, *J. Mol. Liq.*, **180**, 34 (2013).
9. S. H. Yalkowsky, T. J. Roseman, Solubilization of drugs by cosolvents, in: Techniques of Solubilization of Drugs, S. H. Yalkowsky (ed.), Marcel Dekker, New York, 1981.
10. A. Jouyban, W. E. Acree, Jr., *J. Pharm. Pharmaceut. Sci.*, **9**, 262 (2006).
11. D. P. Pacheco, F. Martínez, *Rev. Acad. Colomb. Cienc.*, **32**, 403 (2008).
12. E. Vargas, A. Sosnik, F. Martínez, *Lat. Am. J. Pharm.*, **27**, 654 (2008).
13. A. Ben-Naim, *Pure Appl. Chem.*, **62**, 25 (1990).
14. Y. Marcus, *Pure Appl. Chem.*, **62**, 2069 (1990).
15. Y. Marcus, Solvent Mixtures: Properties and Selective Solvation, Marcel Dekker, Inc., New York, 2002.
16. Y. Marcus, Preferential solvation in mixed solvents, In: Fluctuation Theory of Solutions: Applications in Chemistry, Chemical Engineering, and Biophysics, P. E. Smith, E. Matteoli, J. P. O'Connell (eds.), CRC Press, Taylor & Francis Group, Boca Raton, FL, 2013.
17. Y. Marcus, *J. Mol. Liq.*, **140**, 61 (2008).
18. Y. Marcus, *Acta Chim. Slov.*, **56**, 40 (2009).
19. D. R. Delgado, A. R., Holguín, O. A. Almanza, F. Martínez, Y. Marcus, *Fluid Phase Equilib.*, **305**, 88 (2011).
20. D. R. Delgado, M. Á. Peña, F. Martínez, *Rev. Colomb. Cienc. Quím. Farm.*, **42**, 298 (2013).
21. D. R. Delgado, F. Martínez, *J. Mol. Liq.*, **193**, 152 (2014).
22. J. T. Rubino, Cosolvents and cosolvency, in: Encyclopedia of Pharmaceutical Technology, J. Swarbrick, J. C. Boylan (eds.), vol. 3, Marcel Dekker, Inc., New York, 1988.
23. S. H. Yalkowsky, Solubility and Solubilization in Aqueous Media, American Chemical Society and Oxford University Press, New York, 1999.
24. Y. Marcus, The Properties of Solvents, John Wiley & Sons, Chichester, 1998.
25. K. A. Connors, Thermodynamics of Pharmaceutical Systems: An Introduction for Students of Pharmacy, Wiley-Interscience, Hoboken, NJ, 2002.
26. R. F. Fedors, *Polym. Eng. Sci.*, **14**, 147 (1974).

27. G. A. Rodríguez, D. R. Delgado, F. Martínez, *Phys. Chem. Liq.*, **52**, 533 (2014).
28. J. Jiménez, J. Manrique, F. Martínez, *Rev. Colomb. Cienc. Quím. Farm.*, **33**, 145 (2004).
29. A. F. M. Barton, *Handbook of Solubility Parameters and Other Cohesion Parameters*, 2nd ed., CRC Press, New York, 1991.
30. M. J. Kamlet, R. W. Taft, *J. Am. Chem. Soc.*, **98**, 377 (1976).

ПРЕФЕРЕНЦИАЛНА СОЛВАТАЦИЯ НА НАПРОКСЕН И ПИРОКСИКАМ В СМЕСИ ОТ ЕТАНОЛ/ ВОДА

Р.Г. Сотомайор¹, Д.Р. Делгадо², Ф. Мартинес^{2*}

¹ Програма за фармация, Факултет по химич и фармация, Атлантически университет, Баранкия, Колумбия

² Група по физико-фармацевтични изследвания, Департамент по фармация, Научен факултет, Национален университет на Колумбия, Cra 30 No. 45-03, Богота, Колумбия

Постъпила на 30 април, 2014 г., коригирана на 21 август, 2014 г.

(Резюме)

Предпочитаните параметри на солватация за напроксен (NAP) и пироксин (PIR) в бинарни смеси на етанол (EtOH) и вода са получени от техните термодинамични свойства с помощта на метода на обратните интегрални на Kirkwood-Buff. NAP и PIR са много чувствителни спрямо специфичните ефекти на солватация, като преференциалният параметър на солватация с EtOH, $\delta\chi_{1,3}$, е отрицателен в смеси, богати на вода, но са положителни за всички други смеси за двете лекарства при температури 293.15, 303.15 и 313.15 K. Оказва се, че в богатите на вода смеси хидрофобната хидратация около ароматните и метиловите групи играе основна роля при солватацията. По-високата солватация с етанол в подобни смеси и в смеси, богати на етанол може би се дължи на полярни ефекти. В тези смеси двете лекарства се отнася като киселини на Lewis спрямо молекулите на етанола, тъй като този разтворител е по-базичен от водата.

A theoretical DFT study on the stability of imidazopyridine and its derivatives considering the solvent effects and NBO analysis

Z. Heidarnzhad^{1,2*}, M. Vahedpour¹, S. Ahmad Razavizadeh³

¹ Department of Chemistry, University of Zanjan, P.O. Box 45371-38791, Zanjan, Iran

² Young Researchers Club, Andimeshk Branch, Islamic Azad University, Andimeshk, Iran

³ Department of Chemistry, Payame Noor University, P.O. Box 19395-3697, Tehran, Iran

Received May 11 2014, Revised August 26, 2014

Computational calculations at B3LYP/cc-pvdz level were employed in the study of the predominant tautomeric forms of imidazopyridine derivatives (H, NO₂, Cl, OH, CH₃, CF₃) in gas phase and in selected solvents like benzene, tetrahydrofuran (THF), methanol and water. The tautomers were optimized in solvents according to the polarizable continuum method (PCM) and all structures were optimized at this level. The results show that the tautomer IP1 is more stable than the other tautomers. In addition, the stability of the tautomers in different solvents shows an interesting behavior. Variations of dipole moments and NBO charges on atoms in the solvents were studied.

Keywords: DFT study, NBO charges, Imidazopyridine, Dipole moments

INTRODUCTION

Tautomeric interconversions have been investigated by chemists during the last decades. Recently, the study of tautomerism received renewed attention due to its importance for the determination of compounds' properties and their area of applications. The imidazopyridines (IPs) are a class of short-acting hypnotic, antibacterial and anticonvulsant drugs related to benzodiazepines. The IP derivatives are structurally different from benzodiazepines.[1,2] Several other papers have been devoted to their hypnotic, [3-6] analgesic and antipyretic, as well as antiviral effects. [7-9] Two highly efficient one-pot annulation reactions are described for the synthesis of imidazopyridine derivatives (IPs). The first one allows the production of simpler IPs, the second leads to IPs with functionalized imidazole moiety [10]. Synthesis and SAR studies of very potent imidazopyridine antiprotozoal agents was also reviewed.[11] Molecular structure, vibrational energy levels and potential energy distribution of 1H-imidazo[4,5-b]pyridine, 3H-imidazo[4,5-b]pyridine, 5-methyl-1H-imidazo[4,5-b]pyridine, 6-methyl-1H-imidazo[4,5b]pyridine and 7-methyl-3H-imidazo[4,5-b]pyridine were determined using density functional theory(DFT) at the B3LYP/6-31G(d,p) level[12]. Thereupon compounds containing different tautomers can be the subject of

interest by theoretical chemists [13-15]. Many of the compounds possess clinically useful activity, especially as anticonvulsants (e.g., norantoin, mephenytoin, nirvanol, and methetoin). Many biological activities of hydantoin derivatives are known, as in their uses as herbicides and fungicides some N-substituted derivatives of hydantoin are employed as chlorinating or brominating agents in disinfectant/sanitizer or biocide products. Both the electron distribution and the stereochemistry of the hydantoins are important for their biological activity. For this reason and along with a research program to study the structure–activity relationships for this class of compounds, the solvent effects on the tautomerism of imidazopyridine and its derivatives were studied.

COMPUTATIONAL METHOD

All calculations were carried out on a corei7 personal computer by means of GAUSSIAN09 program package. First all compounds' structures were drawn using Gauss View 03 [16] and optimized by semi-empirical methods. To characterize the optimized geometries the vibrational frequencies for all conformers were done at B3LYP levels. The stationary structures are confirmed by ascertaining that all ground states have only real frequencies. The tautomers were also optimized in solvents according to the polarisable continuum method of Tomasi and co-workers, which exploits the generating polyhedra procedure [17-21] to build the cavity in the polarisable continuum medium, where the solute is

* To whom all correspondence should be sent:
E-mail: Z.heidarnzhad@gmail.com

accommodated. Atomic charges in all structures were obtained using the Natural Population Analysis (NPA) method within the Natural Bond Orbital (NBO) approach [22-27].

RESULTS AND DISCUSSION

Gas phase

Structures and numbering of imidazopyridine are depicted in Fig. 1 and the results of energy comparisons of five tautomers in gas phase and in different solvents are given in Table 1. In the gas phase IP1 forms are more stable than the other forms. The order of stability of all tautomers in the gas phase is IP1>IP2>IP3. But OH substitution is an exception. If the substituted hydroxyl interacts with double bond nitrogen, as shown in Figure 2, IP2(A) is predominant to IP3, otherwise IP3(A) is $[E2(\text{Hartree})-E1(\text{Hartree})] \times 627.5096 = 4.522 \text{ kcal.mol}^{-1}$ more predominant than IP2. The order of stability is IP1>IP3(A)>IP2.

The calculated dipole moments are presented in Table 2. For all conformer tautomers IP1 with Cl substituted has a lower dipole moment in gas phase as much as 1.3225D. Among all forms and in all

phases the highest dipole moment belongs to IP3 with NO₂ substitution in water solution with a value of 13.1005 Debye. The largest difference of dipole moments belongs to gas and water phases for IP3 form with NO₂ substitution (3.2652 Debye).

The calculated values of NBO charges using the Natural population Analysis (NPA) of optimized structures of imidazopyridine derivatives in gas and solvent phases are listed in Tables 3, 4, 5 and 6. Among all positions for all structures the N9 atom has the most negative charge. For all structures, N9, N10 and N11 atoms have the most negative charge compared to the other ones. The most negative charge on the carbons belongs to C1 and C2 atoms, and these positions will most effectively interact with electrophiles.

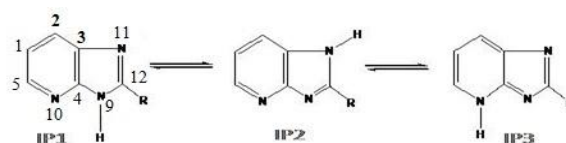


Fig.1. Tautomeric forms of imidazopyridines.

Table 1 . Total energies(Hartree) at B3LYP/CC-PVDZ in gas phase and in solvents.

R	Tautomer	Gas(1.0)	Benzene(2.2)	THF(7.6)	Methanol	Water(78.4)
	IP1	-600.447	-600.452	-600.456	-600.457	-600.457
NO2	IP2	-600.440	-600.448	-600.454	-600.455	-600.456
	IP3	-600.432	-600.444	-600.451	-600.454	-600.455
CF3	IP1	-732.990	-732.995	-732.997	-732.998	-732.998
	IP2	-732.984	-732.936	-732.995	-732.997	-732.997
	IP3	-732.977	-732.986	-732.991	-732.993	-732.994
CL	IP1	-855.550	-855.552	-855.557	-855.558	-855.558
	IP2	-855.544	-855.551	-855.555	-855.557	-855.557
	IP3	-855.539	-855.547	-855.552	-855.554	-855.555
H	IP1	-395.935	-395.940	-395.944	-395.945	-395.945
	IP2	-395.929	-395.936	-395.942	-395.943	-395.9442
	IP3	-395.920	-395.927	-395.932	-395.934	-395.934
CH3	IP1	-435.260	-435.265	-435.268	-435.269	-435.269
	IP2	-435.253	-435.261	-435.266	-435.268	-435.268
	IP3	-435.244	-435.251	-435.256	-435.257	-435.255
	IP1	-471.173	-471.179	-471.182	-471.183	-471.183
	IP1(A)	-471.173	-471.171	-471.176	-471.178	-471.767
	IP2	-471.155	-471.166	-471.174	-471.177	-471.177
OH	IP2(A)	-471.168	-471.175	-471.180	-471.182	-471.182
	IP3	-471.161	-471.169	-471.175	-471.176	-471.177
	IP3(A)	-471.162	-471.170	-471.175	-471.177	-471.177

Table 2. Calculated dipole moments of imidazopyridine (Debye).

R	Tautomer	Gas(1.0)	Benzene(2.2)	THF(7.6)	Methanol	Water(78.4)
NO ₂	IP1	4.017	4.495	4.830	4.961	4.984
	IP2	6.234	7.210	7.910	8.186	8.236
	IP3	9.835	11.415	12.562	13.018	13.101
CF ₃	IP1	2.085	2.294	2.438	2.493	2.503
	IP2	5.419	6.353	6.924	7.168	7.212
	IP3	7.846	9.057	9.911	10.243	10.302
CL	IP1	1.323	1.505	1.632	1.681	1.690
	IP2	5.291	6.172	6.796	7.039	7.083
	IP3	6.544	7.759	8.634	8.977	9.039
H	IP1	1.611	1.854	2.023	2.088	2.100
	IP2	5.458	6.353	6.984	7.230	7.274
	IP3	5.093	6.051	6.747	7.022	7.071
CH ₃	IP1	2.045	2.385	2.623	2.715	2.731
	IP2	5.482	6.448	7.186	7.406	7.454
	IP3	4.420	5.296	5.931	6.182	6.227
	IP1(A)	1.486	1.701	1.849	1.906	1.916
OH	IP2(A)	1.1 86	1.391	1.536	1.592	1.536
	IP2	6.898	7.995	8.762	9.060	9.113
	IP2(A)	4.267	5.020	5.555	5.736	5.801
	IP3	5.292	6.223	6.893	7.156	7.203
	IP3(A)	3.934	4.746	5.340	5.575	5.618

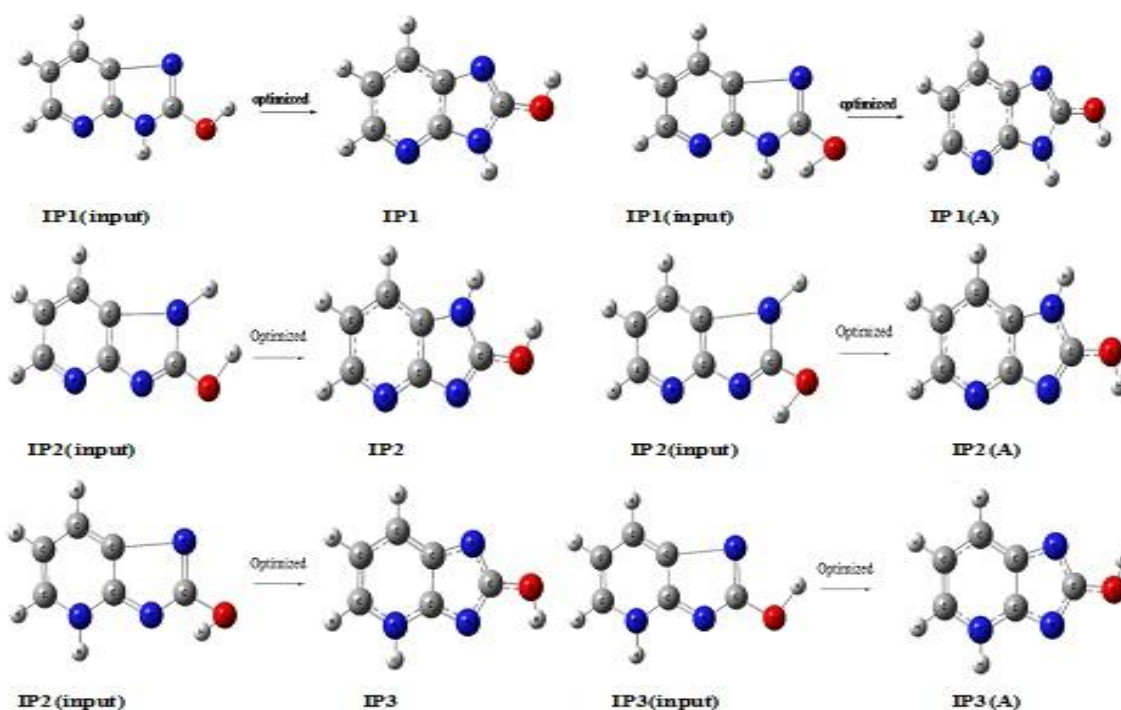


Fig.2. Optimized structures of IP1, IP2 and IP3 for 8-OH position.

Table 3. Calculated NBO charge on ring atoms of IP1.

R	e=	1.0	2.2	7.6	32.6	78.4
	Atom	IP1	IP1	IP1	IP1	IP1
CF3	C1	-0.2604	-0.2812	-0.2800	-0.2794	-0.2793
	C2	-0.2401	-0.1765	-0.1764	-0.1764	-0.1764
	C3	0.0228	0.0969	0.0969	0.0969	0.0969
	C4	0.3677	0.4126	0.4146	0.4153	0.4155
	C5	0.0581	0.0711	0.0722	0.0727	0.0728
	N9	-0.6388	-0.5974	-0.5937	-0.5924	-0.5921
	N10	-0.4831	-0.5154	-0.5208	-0.5226	-0.5229
	N11	-0.2477	-0.4949	-0.5039	-0.5073	-0.5079
	C12	0.5117	0.5579	0.5600	0.5607	0.5608
	C1	-0.2640	-0.2854	-0.2854	-0.2853	-0.2853
	C2	-0.2409	-0.1826	-0.1835	-0.1839	-0.1839
	C3	-0.0011	0.0944	0.0933	0.0928	0.0928
NO2	C4	0.3650	0.4037	0.4045	0.4048	0.4049
	C5	0.0521	0.0583	0.0576	0.0574	0.0574
	N9	-0.6204	-0.5925	-0.5891	-0.5878	-0.5876
	N10	-0.4935	-0.5183	-0.5238	-0.5256	-0.5259
	N11	-0.2747	-0.5146	-0.5246	-0.5284	-0.5290
	C12	0.2707	0.3337	0.3357	0.3364	0.3365
	C1	-0.2759	-0.2870	-0.2874	-0.2875	-0.2875
	C2	-0.2456	-0.1903	-0.1914	-0.1919	-0.1920
	C3	-0.0521	0.0956	0.0941	0.0935	0.0934
	C4	0.3665	0.4030	0.4037	0.4040	0.4040
	C5	0.0404	0.0484	0.0473	0.0469	0.0469
	N9	-0.6325	-0.6197	-0.6167	-0.6155	-0.6153
N10	-0.5176	-0.5214	-0.5269	-0.5288	-0.5291	
N11	-0.4225	-0.5479	-0.5586	-0.5625	-0.5632	
C12	-0.0663	0.4283	0.4302	0.4309	0.4310	
C1	-0.2678	-0.2919	-0.2929	-0.2933	-0.2933	
C2	-0.2421	-0.1913	-0.1935	-0.1943	-0.1945	
C3	-0.0259	0.0881	0.0862	0.0855	0.0854	
C4	0.3590	0.3954	0.3953	0.3953	0.3953	
C5	0.0464	0.0464	0.0443	0.0435	0.0434	
N9	-0.6257	-0.6112	-0.6083	-0.6073	-0.6071	
N10	-0.5024	-0.5251	-0.5310	-0.5330	-0.5334	
N11	-0.3121	-0.5513	-0.5643	-0.5691	-0.5699	
C12	0.2026	0.2831	0.2880	0.2898	0.2902	
C1	-0.2701	-0.2936	-0.2948	-0.2953	-0.2954	
C2	-0.2425	-0.1956	-0.1982	-0.1992	-0.1993	
C3	-0.0279	0.0953	0.0935	0.0928	0.0927	
C4	0.3657	0.4017	0.4016	0.4016	0.4016	
C5	0.0451	0.0409	0.0384	0.0375	0.0373	
N9	-0.6365	-0.6165	-0.6139	-0.6129	-0.6127	
N10	-0.5048	-0.5280	-0.5341	-0.5362	-0.5366	
N11	-0.3119	-0.5633	-0.5756	-0.5801	-0.5809	
C12	0.4087	0.4823	0.4876	0.4895	0.4898	

Table 4. Calculated NBO charge on ring atoms for IP2.

R	e= Atom	1.0 IP2	2.2 IP2	7.6 IP2	32.6 IP2	78.4 IP2
CF3	C1	-0.2604	-0.2812	-0.2800	-0.2794	-0.2793
	C2	-0.2401	-0.1765	-0.1764	-0.1764	-0.1764
	C3	0.0228	0.0969	0.0969	0.0969	0.0969
	C4	0.3677	0.4126	0.4146	0.4153	0.4155
	C5	0.0581	0.0711	0.0722	0.0727	0.0728
	N9	-0.6388	-0.5974	-0.5937	-0.5924	-0.5921
	N10	-0.4831	-0.5154	-0.5208	-0.5226	-0.5229
NO2	N11	-0.2477	-0.4949	-0.5039	-0.5073	-0.5079
	C12	0.5117	0.5579	0.5600	0.5607	0.5608
	C1	-0.2640	-0.2854	-0.2854	-0.2853	-0.2853
	C2	-0.2409	-0.1826	-0.1835	-0.1839	-0.1839
	C3	-0.0011	0.0944	0.0933	0.0928	0.0928
	C4	0.3650	0.4037	0.4045	0.4048	0.4049
	C5	0.0521	0.0583	0.0576	0.0574	0.0574
Cl	N9	-0.6204	-0.5925	-0.5891	-0.5878	-0.5876
	N10	-0.4935	-0.5183	-0.5238	-0.5256	-0.5259
	N11	-0.2747	-0.5146	-0.5246	-0.5284	-0.5290
	C12	0.2707	0.3337	0.3357	0.3364	0.3365
	C1	-0.2759	-0.2870	-0.2874	-0.2875	-0.2875
	C2	-0.2456	-0.1903	-0.1914	-0.1919	-0.1920
	C3	-0.0521	0.0956	0.0941	0.0935	0.0934
H	C4	0.3665	0.4030	0.4037	0.4040	0.4040
	C5	0.0404	0.0484	0.0473	0.0469	0.0469
	N9	-0.6325	-0.6197	-0.6167	-0.6155	-0.6153
	N10	-0.5176	-0.5214	-0.5269	-0.5288	-0.5291
	N11	-0.4225	-0.5479	-0.5586	-0.5625	-0.5632
	C12	-0.0663	0.4283	0.4302	0.4309	0.4310
	C1	-0.2678	-0.2919	-0.2929	-0.2933	-0.2933
CH3	C2	-0.2421	-0.1913	-0.1935	-0.1943	-0.1945
	C3	-0.0259	0.0881	0.0862	0.0855	0.0854
	C4	0.3590	0.3954	0.3953	0.3953	0.3953
	C5	0.0464	0.0464	0.0443	0.0435	0.0434
	N9	-0.6257	-0.6112	-0.6083	-0.6073	-0.6071
	N10	-0.5024	-0.5251	-0.5310	-0.5330	-0.5334
	N11	-0.3121	-0.5513	-0.5643	-0.5691	-0.5699
CH3	C12	0.2026	0.2831	0.2880	0.2898	0.2902
	C1	-0.2701	-0.2936	-0.2948	-0.2953	-0.2954
	C2	-0.2425	-0.1956	-0.1982	-0.1992	-0.1993
	C3	-0.0279	0.0953	0.0935	0.0928	0.0927
	C4	0.3657	0.4017	0.4016	0.4016	0.4016
	C5	0.0451	0.0409	0.0384	0.0375	0.0373
	N9	-0.6365	-0.6165	-0.6139	-0.6129	-0.6127
CH3	N10	-0.5048	-0.5280	-0.5341	-0.5362	-0.5366
	N11	-0.3119	-0.5633	-0.5756	-0.5801	-0.5809
	C12	0.4931	0.4829	0.4888	0.4910	0.4914

Table 5. Calculated NBO charge on ring atoms of IP3.

R	e=	1.0	2.2	7.6	32.6	78.4
	Atom	IP3	IP3	IP3	IP3	IP3
CF3	-0.2801	-0.2942	-0.2908	-0.2891	-0.2888	-0.2801
	-0.1998	-0.1478	-0.1452	-0.1443	-0.1441	-0.1998
	-0.0763	0.1071	0.1041	0.1029	0.1027	-0.0763
	0.4167	0.4195	0.4209	0.4214	0.4215	0.4167
	0.0644	0.0720	0.0848	0.0900	0.0910	0.0644
	-0.6156	-0.5846	-0.5917	-0.5942	-0.5947	-0.6156
	-0.5616	-0.5213	-0.5175	-0.5160	-0.5157	-0.5616
	-0.2197	-0.5396	-0.5504	-0.5545	-0.5552	-0.2197
	0.5130	0.5398	0.5329	0.5300	0.5295	0.5130
	-0.2840	-0.2979	-0.2958	-0.2948	-0.2946	-0.2840
NO2	-0.2043	-0.1571	-0.1558	-0.1554	-0.1553	-0.2043
	-0.0869	0.1058	0.1013	0.0995	0.0992	-0.0869
	0.4136	0.4213	0.4219	0.4220	0.4220	0.4136
	0.0605	0.0613	0.0717	0.0759	0.0767	0.0605
	-0.6170	-0.5998	-0.6077	-0.6106	-0.6111	-0.6170
	-0.5631	-0.5248	-0.5213	-0.5200	-0.5197	-0.5631
	-0.2440	-0.5525	-0.5635	-0.5677	-0.5684	-0.2440
	0.2705	0.3212	0.3133	0.3100	0.3095	0.2705
	-0.2847	-0.2957	-0.2942	-0.2934	-0.2932	-0.2847
	-0.2071	-0.1739	-0.1719	-0.1712	-0.1711	-0.2071
Cl	-0.0922	0.1120	0.1072	0.1054	0.1050	-0.0922
	0.4162	0.4251	0.4256	0.4257	0.4257	0.4162
	0.0572	0.0475	0.0580	0.0623	0.0630	0.0572
	-0.6396	-0.6172	-0.6248	-0.6276	-0.6281	-0.6396
	-0.5655	-0.5289	-0.5251	-0.5236	-0.5233	-0.5655
	-0.2575	-0.5844	-0.5960	-0.6004	-0.6011	-0.2575
	0.3301	0.4117	0.4057	0.4032	0.4027	0.3301
	-0.2876	-0.3016	-0.3005	-0.2999	-0.2997	-0.2876
	-0.2101	-0.1741	-0.1738	-0.1737	-0.1737	-0.2101
	-0.1011	0.1026	0.0975	0.0955	0.0951	-0.1011
H	0.4079	0.4145	0.4146	0.4145	0.4145	0.4079
	0.0544	0.0461	0.0553	0.0590	0.0597	0.0544
	-0.6391	-0.6248	-0.6330	-0.6359	-0.6364	-0.6391
	-0.5664	-0.5292	-0.5261	-0.5249	-0.5246	-0.5664
	-0.2705	-0.5884	-0.6011	-0.6058	-0.6067	-0.2705
	0.2019	0.2748	0.2674	0.2643	0.2637	0.2019
	-0.2882	-0.3019	-0.3016	-0.3013	-0.3013	-0.2882
	-0.2113	-0.1843	-0.1843	-0.1844	-0.1844	-0.2113
	-0.1079	0.1124	0.1071	0.1050	0.1046	-0.1079
	0.4155	0.4254	0.4254	0.4253	0.4253	0.4155
CH3	0.0514	0.0383	0.0468	0.0503	0.0509	0.0514
	-0.6483	-0.6326	-0.6406	-0.6434	-0.6439	-0.6483
	-0.5670	-0.5342	-0.5312	-0.5301	-0.5299	-0.5670
	-0.2781	-0.5978	-0.6102	-0.6149	-0.6158	-0.2781
	-0.2801	-0.2942	-0.2908	-0.2891	-0.2888	-0.2801

Table 6. Calculated NBO charge for (OH) substituted.

R	e= Atom	1.0	2.2	7.6	32.6	78.4	1.0	2.2	7.6	32.6	78.4
		IP1					IP2				
	C1	-0.2667	-0.2893	-0.2907	-0.2912	-0.2913	-0.2765	-0.2844	-0.2856	-0.2860	-0.2860
	C2	-0.2423	-0.2087	-0.2108	-0.2116	-0.2118	-0.2567	-0.2340	-0.2293	-0.2273	-0.2269
	C3	-0.0110	0.1023	0.1007	0.1001	0.1000	0.1536	0.1052	0.1074	0.1083	0.1085
	C4	0.3664	0.4008	0.4010	0.4011	0.4011	0.3607	0.3942	0.3910	0.3896	0.3894
OH	C5	0.0501	0.0307	0.0278	0.0268	0.0266	0.0576	0.0321	0.0279	0.0262	0.0259
	N9	-0.6589	-0.6434	-0.6419	-0.6413	-0.6412	-0.5883	-0.6039	-0.6241	-0.6318	-0.6332
	N10	-0.4965	-0.5269	-0.5335	-0.5358	-0.5362	-0.4299	-0.5056	-0.5224	-0.5289	-0.5300
	N11	-0.3162	-0.6305	-0.6382	-0.6409	-0.6414	-0.6794	-0.6516	-0.6458	-0.6434	-0.6430
	C12	0.6454	0.8097	0.8133	0.8146	0.8148	0.7731	0.8072	0.8123	0.8141	0.8145
		IP1(A)					IP2(A)				
	C1	-0.2637	-0.2889	-0.2902	-0.2907	-0.2902	-0.2818	-0.2847	-0.2862	-0.2866	-0.2867
	C2	-0.2394	-0.2069	-0.2107	-0.2122	-0.2107	-0.2371	-0.2326	-0.2286	-0.2269	-0.2265
	C3	-0.0130	0.1017	0.1001	0.0995	0.1001	0.1035	0.1054	0.1071	0.1077	0.1079
	C4	0.3644	0.3994	0.4000	0.4002	0.4000	0.3995	0.3957	0.3927	0.3914	0.3912
OH	C5	0.0495	0.0299	0.0267	0.0255	0.0267	0.0360	0.0313	0.0275	0.0259	0.0257
	N9	-0.6717	-0.6602	-0.6553	-0.6534	-0.6553	-0.6134	-0.6329	-0.6458	-0.6507	-0.6516
	N10	-0.4991	-0.5289	-0.5346	-0.5365	-0.5346	-0.4856	-0.5083	-0.5238	-0.5297	-0.5308
	N11	-0.3056	-0.6034	-0.6195	-0.6256	-0.6195	-0.6382	-0.6336	-0.6300	-0.6285	-0.6282
	C12	0.5994	0.8072	0.8119	0.8138	0.8119	0.8027	0.8094	0.8137	0.8153	0.8156
		IP3					IP3(A)				
	C1	-0.2868	-0.2948	-0.2956	-0.2957	-0.2957	-0.2933	-0.2952	-0.2955	-0.2954	-0.2954
	C2	-0.2125	-0.2062	-0.2063	-0.2064	-0.2064	-0.2083	-0.2079	-0.2073	-0.2070	-0.2070
	C3	-0.0868	0.1221	0.1171	0.1151	0.1147	0.1285	0.1217	0.1167	0.1147	0.1143
	C4	0.4124	0.4340	0.4339	0.4339	0.4339	0.4328	0.4338	0.4339	0.4338	0.4338
OH	C5	0.0559	0.0222	0.0310	0.0345	0.0352	0.0129	0.0230	0.0310	0.0342	0.0348
	N9	-0.6430	-0.6786	-0.6820	-0.6832	-0.6834	-0.6312	-0.6482	-0.6589	-0.6629	-0.6636
	N10	-0.5690	-0.5394	-0.5362	-0.5349	-0.5347	-0.5432	-0.5389	-0.5357	-0.5345	-0.5343
	N11	-0.2368	-0.6313	-0.6470	-0.6529	-0.6540	-0.6484	-0.6614	-0.6698	-0.6729	-0.6735
	C12	0.6770	0.7877	0.7842	0.7827	0.7824	0.7929	0.7887	0.7849	0.7833	0.7830

Solvent effects

Solvent effects are relevant in tautomer stability phenomena, since polarity differences among tautomers can induce significant changes in their relative energies in solution. We used PCM/B3LYP calculations to analyze the solvent effects on the tautomerism of imidazopyridine derivatives. It is important to stress that the PCM model does not consider the presence of explicit solvent molecules; hence specific solute–solvent interactions are not described and the calculated solvation effects arise only from mutual solute–solvent electrostatic polarization. The data presented in Table 1 show that polar solvents increase the stability of all forms compared to gas phase. The difference between the total energies of imidazopyridine and the other forms does not show a regular trend when changing from gas phase to most polar solvents (water). If in IP2 form with substituted hydroxyl, hydrogen interacts with double bond nitrogen N9 (Fig. 2) then the order of stability is IP1>IP2 (A)>IP3 in all phases. But if hydrogen of the substituted hydroxyl does not interact with double bond nitrogen (N4) in IP2 and intra-molecular hydrogen bond is not

formed, then the order of stability has two different sequences. In the first one hydrogen of the substituted hydroxyl interacts with double bond nitrogen (N7) in IP3, then the order of stability in all phases is IP1>IP3>IP2. The other sequence is when hydrogen of the substituted hydroxyl interacts with double bond nitrogen (N9) then the order of stability in gas phase, benzene, THF is IP1>IP3(A)>IP2 but in polar solvents like water and methanol is IP1>IP2>IP3. Also the dipole moment increases from gas phase to a more polar solvent, then the highest value belongs to IP3 with substituted NO₂ in water phase with 13.1005D. We have examined the charge distribution of tautomers in the solvent, as well as in gas phase by using calculated NBO charges. The charge distribution in solvents with increase in polarity differently varies for any atoms. Calculated Gibbs free energies of all structures at 298.15 K and one atmosphere at B3LYP/cc-pvdz level are illustrated in Table 7. The Gibbs free energy difference (ΔG) between IP3(A) and IP2 for (OH) substituted in gas phase is 2.58 kcal.mol⁻¹.

Table 7. Calculated Gibbs free energy of imidazopyridine (kcal.mol⁻¹).

R	Tautomer	Gas(1.0)	Benzene(2.2)	THF(7.6)	Methanol	Water(78.4)
	IP1	46.950	46.920	46.889	46.876	46.873
NO2	IP2	46.772	46.809	46.825	46.829	46.829
	IP3	46.222	46.829	46.958	46.986	46.991
	IP1	46.169	45.893	45.570	45.301	45.218
CF3	IP2	46.083	45.993	45.886	45.815	45.798
	IP3	46.586	48.392	48.431	48.414	48.414
	IP1	40.580	40.576	40.567	40.564	40.562
CL	IP2	40.363	40.434	40.476	40.491	40.494
	IP3	40.935	41.009	41.050	41.064	41.066
	IP1	48.037	48.084	48.109	48.116	48.118
H	IP2	47.820	47.940	48.011	48.036	48.040
	IP3	48.319	48.416	48.473	48.492	48.496
	IP1	63.583	63.620	63.632	63.635	63.635
CH3	IP2	63.279	63.431	63.517	63.546	63.551
	IP3	63.628	63.749	63.821	63.846	63.850
	IP1	50.062	50.011	49.971	49.954	49.951
	IP1(A)	49.056	50.011	49.253	49.260	49.261
OH	IP2	48.010	48.757	48.888	48.912	48.915
	IP2(A)	49.828	49.858	49.880	49.878	49.880
	IP3	50.542	50.555	50.555	50.554	50.554
	IP3(A)	50.598	50.606	50.604	50.601	50.601

REFERENCES

1. J.D. Hoehns, P.J. Perry, *Clin. Pharm.*, **12**, 814(1993).
2. M. Yoshimoto, H. Kamata, K. Yoshida, T. Shimizu, Y. Hishikawa, *Eur. Neuropsychopharmacol.*, **9**, 29 (1999).
3. H. D. Langtry, P. Benfield, *Drugs.*, **40**, 291(1990).
4. S.M. Evans, F.R. Funderburk, R.R. Griffiths, *Pharmacol. J. Exp. Ther.*, **255**, 1246 (1990).
5. A. Dureand, J.P. Thenot, G. Bianchetti, P.L. Morselli, *Drugs . Metab. Rev.*, **24**, 239 (1992).
6. I. Berlin, D. Warot, T. Hergueta, P. Molinier, C. Bagot, A.J. Puech, *J. Clin. Psychopharm.*, **13**, 100 (1993).
7. Y. Maruyama, K. Anarmi, Y. Katoh, *Arzneim. Forsch.*, **28**, 2102 (1978).
8. S. Mavel, J. L. Renou, C. Galtier, H. Allaouchi, R. Snoeck, G. Andrei, E. de Clerq, J. Balzarini, A. Gueiffier, *Bioorg. Med. Chem.*, **10**, 941 (2002).
9. K. S. Gudmundsson, B.A. Johns, *Org. Lett.*, **5**, 1369 (2003).
10. A.D. Parenty, L. Cronin, *Synthesis.*, **9**, 1479 (2008)
11. T. Biftu, D. Feng, G. Liang, X. Qian, A. Scribner, R. Dennis, S. Lee, P. A. Liberator, C. Brown, A. Gurnett, P. S. Leavitt, D. Thompson, J. Mathew, A. Misura, S. Samaras, T. Tamas, J. F. Sina, K. A. McNulty, C. G. McKnight, D. M. Schmatz, M. Wyvratt, *Bioorg. Med. Chem. Lett.*, **16**, 2479 (2006).
12. J. Lorenc, L. Dymisnska, Z. Talik, J. Hanuza, M. M. aczka, *J. Raman Spectrosc.*, **39**, 1 (2008).
13. Z. Heidarneshad, F. Heidarneshad, I. Ganiev, Z. Obidov, M. S. Sharifi, *Orient J. Chem.*, **29**(1), 53 (2013).
14. Z. Heidarneshad, F. Heidarneshad, I. Ganiev, Z. Obidov, *Chem. Sci. Trans.*, **2**(4), 1370 (2013).
15. Z. Heidarneshad, I. Ganiev, Z. Obidov, F. Heidarneshad, M. S. Sharifi, *Orient J. Chem.*, **28**(4), 1597 (2012).
16. M.J. Frisch, G.W. Trucks, H.B. Schlegel, et al., Gaussian 03, Revision B.03, Gaussian, Inc. Pittsburgh PA, 2003.
17. R. Dengton, T. Keith, J. Millam, K. Eppinnett, W. L. Hovell, R. Gilliland. GaussView, Version 309, Semichem, Inc, Shawnee Mission, KS, 2003.
18. S. Miertus, E. Scrocco, J. Tomasi, *J. Chem. Phys.*, **55**, 117 (1981).
19. M.T. Cancas, V. Mennucci, J. Tomasi, *J. Chem. Phys.*, **107**,3032 (1997).
20. M. Cossi, V. Barone, B. Mennucci, J. Tomasi, *Chem. Phys. Lett.*, **286**, 253 (1998).
21. V. Barone, M. Cossi, *J. Phys. Chem. A.*, **102**, 1995 (1998).
22. V. Barone, M. Cossi, J. Tomasi, *J. Comp. Chem.*, **19**, 404 (1998).
23. A.E. Reed, L.A. Curtiss, F. Wienhold, *Chem. Rev.*, **88**, 899 (1988).
24. A. Najafi-Chermahini, M. Nasr-Esfahani, Z. Dalirnasab, H.A. Dabbagh, A. Teimouri, *J. Mol. Struct. THEOCHEM.*, **820**, 7 (2007).
25. Z. Heidarneshad, F. Heidarneshad, F. Heydari, I. Ganiev, Z. Obidov, *Orient J. Chem.*, **29**(4), 1565 (2012)
26. H. Moghanian, A. Mohamadi, *Bulgarian Chem. Communications.*, **46**(1),43 (2014).
27. Z. Heidarneshad, F. Heidarneshad, F. Heydari, E. Bahramian, *Orient J. Chem.*, **29**(1), 69 (2013)

ТЕОРЕТИЧНО DFT-ИЗСЛЕДВАНЕ НА СТАБИЛНОСТТА НА ИМИДАЗОПИРИДИН И НЕГОВИ ПРОИЗВОДНИ ПРИ ОТЧИТАНЕ НА ЕФЕКТА НА РАЗТВОРИТЕЛЯ И НВО-АНАЛИЗ

З. Хейдарнежад^{1,*}, Ф. Хейдарнежад²

¹Младежки изследователски клуб, Клон Андимешк, Ислямски университет „Азад“, Андимешк, Иран
²Департамент по химия, Клон Андимешк, Ислямски университет „Азад“, Андимешк, Иран

Постъпила на 11 май, 2014 г., коригирана на 25 август, 2014 г.

(Резюме)

Извършени са изчисления на ниво В3LYP/сс за изследването на преобладаващите тавтомерни форми на производните на имидазопиридина (H, NO₂, Cl, OH, CH₃, CF₃) в газова фаза и избрани разтворители като бензен, тетраhydroфуран (THF), метанол и вода. Всички тавтомерни форми са оптимизирани според разтворителите съгласно метода на поляризирания континуум (PCM). Резултатите показват, че тавтомерите IP1 в различни разтворители са по-стабилни от останалите. Изследвани са диполните моменти и НВО-товарите на атомите в разтворителите.

Synthesis and characterization of Si and Mg substituted lithium vanadium(III) phosphate

S. M. Stankov^{1*}, A. Momchilov¹, I. Abrahams², I. Popov¹, T. Stankulov¹, A. Trifonova³

¹*Institute of Electrochemistry and Energy Systems “Acad. Evgeni Budevski”, Bulgarian Academy of Sciences, Acad. Georgi Bonchev Str., Block 10, 1113 Sofia, Bulgaria.*

²*Materials Research Institute, School of Biological and Chemical Sciences, Queen Mary University of London, Mile End Road, London E1 4NS, United Kingdom.*

³*AIT Austrian Institute of Technology GmbH, Giefinggasse 2, 1210 Vienna, Austria.*

Received May 12, 2014, Revised July 15, 2014

Active materials for lithium ion batteries based on Si and Mg substitution in lithium vanadium(III) phosphate, $\text{Li}_3\text{V}_2(\text{PO}_4)_3$ (LVP), were investigated using X-ray powder diffraction, thermal analysis, transmission electron microscopy, galvanostatic tests and cyclic voltammetry. $\text{Li}_3\text{V}_2(\text{PO}_4)_3$, $\text{Li}_{3.1}\text{V}_2(\text{SiO}_4)_{0.1}(\text{PO}_4)_{2.9}$, $\text{Li}_{3.5}\text{V}_2(\text{SiO}_4)_{0.5}(\text{PO}_4)_{2.5}$ and $\text{Li}_{3.04}\text{Mg}_{0.03}\text{V}_2(\text{SiO}_4)_{0.1}(\text{PO}_4)_{2.9}$ were prepared as carbon coated powders, through wet chemistry (sol-gel) followed by solid state routes under Ar. X-ray powder diffraction confirmed that the basic monoclinic structure of LVP was preserved in the substituted systems. Electrochemical testing on two electrode cells based on these materials at a charge-discharge rate of 0.2C in the range 2.8-4.4 V showed that the Mg substituted system delivers the highest discharge capacity of $124.8 \text{ mA h g}^{-1}$, achieving 94% of its theoretical capacity (133 mA h g^{-1}) in this voltage range. However, this material shows poor long-term cycling behavior, with approximately 20% capacity fade over 100 cycles. Generally it is found that Si substitution has a negative effect on initial capacity, but following a capacity fade of up to 15% in the first 15 cycles, the Si substituted systems show nearly constant capacity on further cycling.

Keywords: Lithium Vanadium Phosphate, Positive Active Material, Li-ion Battery

INTRODUCTION

Lithium-ion battery (LIB) technology has developed over the past two decades, due to the high energy density and output voltage of systems based on this technology. Cathode specific capacity is a limiting factor in LIBs, particularly for transport applications, so high energy density materials are being searched for. Lithium cobalt oxide, LiCoO_2 [1], is the most commonly used positive active material in the industry, but there are issues related to the environment and health care, as well as cost, which limit its widespread use for transport applications. Other layered oxides like $\text{Li}(\text{Ni}_{1/3}\text{Co}_{1/3}\text{Mn}_{1/3})\text{O}_2$ [2] and LiMn_2O_4 [3] have also found places in the market. Materials based on phosphate polyanions are very attractive because of their relatively high energy density, non-toxicity and inexpensiveness. LiFePO_4 [4] has already successfully been implemented in the industry and other phosphate and fluorophosphate materials such as $\text{Li}_3\text{V}_2(\text{PO}_4)_3$ [5], LiMnPO_4 [6], LiCoPO_4 [7], LiNiPO_4 [8], LiVPO_4F [9], *etc.* are being considered for the next generation of commercial materials. The main drawbacks of these materials are low electronic and ionic conductivity and

instability during operation [10-11]. Although the problem of low electronic conductivity has been addressed for some of these materials by applying so-called carbon coating [12-14], other issues like short cycle-life remain.

Among the above mentioned phosphates, $\text{Li}_3\text{V}_2(\text{PO}_4)_3$ (LVP) has the highest theoretical specific capacity of 197 mA h g^{-1} for removal of three moles of lithium per mole of LVP. Studies have confirmed de-intercalation at high potentials, with four characteristic plateaus *versus* Li/Li^+ at 3.6 and 3.68 V, corresponding to the first Li extraction, 4.2 V and over 4.5 V, corresponding to the second and third lithium extractions, respectively [15]. Due to structural instability at high potentials, with consequent rapid decline in discharge capacity, studies have focused on a more limited operational voltage range of 3.0 to 4.4 V [16-17]. In this voltage range, the theoretical specific capacity is $\sim 131.5 \text{ mA h g}^{-1}$ for two moles of lithium per mole LVP. To overcome the structural instability obstacle at high potentials, many groups have researched the effect of doping on LVP. Different elements like Cr, Mo, Y, Al, *etc.* [18-21] can partially replace vanadium, while oxygen in the phosphate group can be partially substituted by chlorine [21].

* To whom all correspondence should be sent:
E-mail: s.stankov@mail.bg

The aim of the present study was to investigate the effects of substitution of silicon for phosphorus in lithium vanadium phosphate on structure and electrochemical performance. Silicon and phosphorus show similar structural chemistry, adopting tetrahedral geometry in oxide systems, forming $(\text{SiO}_4)^{4-}$ and $(\text{PO}_4)^{3-}$, respectively. Two methods of charge balance are investigated in the system: (i) through additional Li^+ and (ii) through addition of Mg^{2+} .

EXPERIMENTAL

Preparations

Carbon coated samples of $\text{Li}_3\text{V}_2(\text{PO}_4)_3$ (LVPC), $\text{Li}_{3.1}\text{V}_2(\text{SiO}_4)_{0.1}(\text{PO}_4)_{2.9}$ (LVS10PC), $\text{Li}_{3.5}\text{V}_2(\text{SiO}_4)_{0.5}(\text{PO}_4)_{2.5}$ (LVS50PC) and $\text{Li}_{3.04}\text{Mg}_{0.03}\text{V}_2(\text{SiO}_4)_{0.1}(\text{PO}_4)_{2.9}$ (LMgVSPC) were synthesized *via* a three-step sol-gel method. Stoichiometric amounts of V_2O_5 (synthesized by decomposition of NH_4VO_3 , Fluka, >99% at 320°C), and $\text{H}_2\text{C}_2\text{O}_4 \cdot 2\text{H}_2\text{O}$ (Sigma-Aldrich, ≥98.5%) were dissolved in distilled water to give a blue-green solution. To this were added separate solutions of stoichiometric amounts of $\text{LiOH} \cdot \text{H}_2\text{O}$ (Sigma-Aldrich, ≥98%) and $(\text{NH}_4)_2\text{HPO}_4$ (Sigma-Aldrich, ≥98%) dissolved in distilled water. Colloidal silica (Silica sol, $m\text{SiO}_2 \cdot n\text{H}_2\text{O}$, Qingdao YuKai Import and Export Co.,Ltd) with SiO_2 30-31 wt% in solution, an average particle size of 10-20 nm and pH=8.5-10, was added to the mixture for LVS10PC, LVS50PC and LMgVSPC samples. $\text{MgCl}_2 \cdot 6\text{H}_2\text{O}$ (Merck, >98%) was employed as the magnesium precursor for the LMgVSPC material. Glycine ($\text{NH}_2\text{CH}_2\text{COOH}$, Sigma-Aldrich, ≥ 98.5 %) was used as a carbon source for all samples. For the LVPC sample acetylene black P1042 (AB) [22] was added to the mixture as an additional carbon source, as well as 1 to 2 drops of Triton X-100, which served as a surfactant for decreasing the surface tension around suspended AB particles. The final solution was evaporated with constant stirring at 80 °C for *ca.* 4 h until it became a gel. The gel was dried in an oven at 120 °C for 16 h and the resulting powder was heated at 370 °C for 4 h in Ar flow in order to remove ammonia and water. The intermediate precursor was ground for 30 min and then annealed at 800 °C for 10 h under Ar.

Sample characterization

X-ray powder diffraction (XRD) data were collected on a PANalytical X'Pert Pro diffractometer fitted with an X'Celerator detector, using Ni-filtered $\text{Cu-K}\alpha$ radiation ($\lambda = 1.5418 \text{ \AA}$), over the 2θ range 5-120°, with a step width of

0.033° and an effective scan time of 200 s per step at room temperature. Data were modeled by Rietveld analysis using the GSAS suite of programmers [23]. The structures of $\text{Li}_3\text{V}_2(\text{PO}_4)_3$ (with appropriate substitution of Si for P) [24], Li_3PO_4 [25] and VO [26], were used as starting models in the refinements. Thermogravimetric and differential thermal analyses were carried out for the LVPC precursor in Ar, on a Stanton Redcroft thermogravimetric analyzer in the range 20-760 °C, with a heating rate of 5 °C per min. Transmission electron microscopy (TEM) was carried out on a JEOL JEM 2010 microscope, with an accelerating voltage of 200 kV and a beam current of 106 μA .

Electrochemical testing

The obtained materials were electrochemically tested in two-electrode laboratory cells. The working electrodes were prepared by mixing active material (AM), PVDF (MTI corp., USA) and acetylene black (AB) P1042 in N-methyl-2-pyrrolidone (NMP, MTI corp., USA). The ratio of the slurry was AM:PVDF 70:10 wt.%, with acetylene black and the carbon coating of the active material constituting the remaining 20 wt.%. The slurries were stirred for 24 h and then coated onto aluminum foil. The coated foils were dried under vacuum at 120°C for 24 h. Cells were assembled using lithium foil (Alfa Aesar) as the counter electrode, with Freudenberg FS 2190 as a separator. The electrolyte used was 1M LiClO_4 (Alfa Aesar) in a 1:1 (v/v) mixture of ethylene carbonate (EC) and dimethyl carbonate (DMC) (both purchased from Alfa Aesar). Electrochemical galvanostatic tests were performed on a Neware Battery Testing System (V-BTS8-3), in the voltage range 2.8 - 4.4 V for all four materials and 2.8 - 4.8 V only for LVPC, at a C/5 (0.2C) rate, where C is the theoretical specific capacity for 3 moles of extracted Li, *i.e.* 197 mA h g^{-1} and 5 is the charge or discharge time in hours. Cyclic voltammetry (CV) was performed on a VersaSTAT MC (Princeton Applied Research) multi-channel potentiostat/galvanostat, with a step rate of 20 $\mu\text{V s}^{-1}$, where the counter Li electrode was also used as a reference, as its polarization is negligible.

RESULTS AND DISCUSSION

Thermogravimetric and differential thermal analyses (Fig. 1) were carried out for the LVPC gel precursor obtained after the first synthesis step. The differential thermogram shows significant endotherms at 131 and 142, 241 and 308 °C. These peaks are associated mostly with loss of water and ammonia which is in agreement with the

thermogravimetric measurement. The major weight loss is 55.5 wt.% in the range 20-388 °C. The exotherms in the range 350-600 °C correspond to the product formation. The weight loss is 12.34% in the range 388-760 °C.

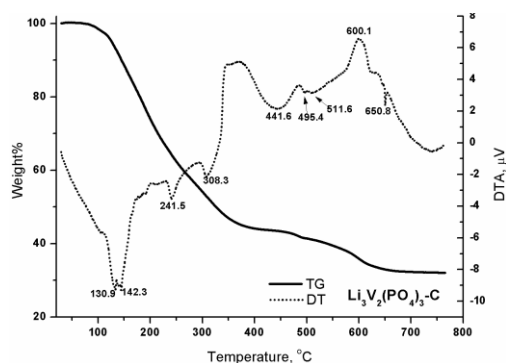


Fig. 1. Thermogravimetric (TG) and differential thermal (DT) analyses of LVPC precursor.

The X-ray powder diffraction data (Fig. 2) are similar and show a monoclinic $\text{Li}_3\text{V}_2(\text{PO}_4)_3$ type phase, in space group $P2_1/n$. Besides the desired phase, the patterns for LVPC and LVS50PC display peaks corresponding to Li_3PO_4 , while LVPC, LVS10PC and LVS50PC additionally show broad peaks from a cubic phase that appears to correspond to VO, suggesting some reduction of the vanadium to V^{2+} . Only LMgVSPC was isolated as a single phase. Table 1 summarizes the refined unit cell parameters and weight fractions obtained through Rietveld analysis of the data. None of the silicate containing samples showed the presence of a separate silicate phase and appeared to confirm successful substitution of Si for P in the main phase. Indeed, the increase in unit cell volume with increasing Si substitution, is consistent with the substitution of P(V) with Si(IV), with respective ionic radii of 0.17 Å and 0.26 Å [27].

Fig. 3 depicts TEM images of the obtained

Table 1. Refined cell dimensions of primary LVP type phase and weight fractions from Rietveld analysis of the studied materials.

Parameter	LVPC	LMgVSPC	LVS10PC	LVS50PC
Wtfrac. 1° phase	0.860(1)	1.00	0.9518(4)	0.731(2)
Wtfrac. Li_3PO_4	0.099(2)			0.19(3)
Wtfrac. VO	0.041(2)		0.048(1)	0.071(3)
1° phase <i>a</i> (Å)	8.5548(3)	8.6083(3)	8.6060(5)	8.6100(5)
1° phase <i>b</i> (Å)	8.6719(3)	8.5958(3)	8.5915(5)	8.5969(5)
1° phase <i>c</i> (Å)	11.9915(4)	12.0416(4)	12.0394(7)	12.0484(7)
1° phase β (°)	89.890(5)	90.564(2)	90.588(4)	90.569(4)
1° phase Vol. (Å ³)	884.06(6)	890.98(7)	890.1(1)	891.8(1)

materials. LVPC particles (Fig. 3a) are surrounded by large masses of carbon, most likely acetylene black P1040. LMgVSPC and LVS10PC (Figs. 3b and 3c) samples show the presence of large clusters composed of small particles of active material, which are held together by carbon. LVS50PC (Fig. 3d) displays an uneven distribution of active material and carbon. The particle (agglomerate) size varies from 30 nm to 5 μm for LVPC (with an average in the range 50-300 nm), 0.2-10 μm for LMgVSPC, 0.15-7.5 μm for LVS10PC and 0.2-8 μm for LVS50PC.

Second cycle charge-discharge curves for the test cells at a 0.2C rate, in the range 2.8–4.4 V are shown in Fig. 4. All curves show the characteristic three charge-discharge plateaus, corresponding to the three types of reversible phase transformation in $\text{Li}_{3-x}\text{V}_2(\text{PO}_4)_3$ ($x = 0, 0.5, 1.0, \text{ and } 2.0$) [15]. LMgVSPC delivers the highest discharge capacity of 124.8 mA h g⁻¹, achieving 94% of its theoretical capacity (133 mA h g⁻¹) in this voltage range. LVPC, LVS10PC and LVS50PC present discharge capacities of 116.5, 112.6 and 97.8 mA h g⁻¹, respectively. It is notable that increasing amount of Si appears to have a negative effect on the initial capacity, apart from LMgVSPC. For LVS10PC and LVS50PC the discharge profile below 3.5 V is not as steep compared to those of LVPC and LMgVSPC and is indicative of slower kinetics of ion diffusion in these samples.

The cycling performance of the test cells is shown in Fig. 5. LVPC shows a first specific discharge capacity of 118 mA h g⁻¹ and relatively good stability, with a capacity decline of 6.7% over 100 cycles and a coulombic efficiency of around 98%.

Of the four samples, LMgVPC displays the greatest initial capacity of $\sim 125 \text{ mA h g}^{-1}$, but it has poor cyclability.

Although the capacity is higher in the first 60 cycles compared to LVPC, the fading is 20.7% over 100 cycles and the coulombic efficiency varies from 90 to 98%. This result is somewhat surprising, since achieving charge balance through addition of Mg^{2+} ions rather than additional Li^+ ions yields compounds with lower theoretical discharge capacities. The other two silicate containing samples show similar cycling behavior to each other. In the first cycle, the discharge specific capacity of LVS10PC is 116 mA h g^{-1} and declines to $\sim 100 \text{ mA h g}^{-1}$, up to the 15th cycle, corresponding to a 14% loss. The material becomes stable after the 15th cycle and there is no further capacity loss up to the 60th cycle. The coulombic efficiency is 91-97% for this cell over the first 15 cycles and 97-98% thereafter. LVS50PC displays the lowest initial capacity of 102 mA h g^{-1} of all the test samples. For this cell, the capacity fades 16.8% over the first 15 cycles and then remains stable up to the 100th cycle. The coulombic efficiency is 88-96% up to the 15th cycle then rises to 97-99% up to the 100th cycle.

Cyclic voltammetry was performed on the four studied materials (Fig. 6). It is notable that there are

significant differences in the delivered currents, which do not correspond to the delivered capacities in galvanostatic mode in Fig. 4.

This is caused by the differences in the weight of the active material used in the electrodes. All four voltammograms show oxidation potentials at around 3.62, 3.70, 4.12 and 4.53 V, with those of LMgVSP by 15-20 mV higher.

These peaks are associated with the four stages of Li de-intercalation and the corresponding oxidation of vanadium. The third and fourth peaks in the oxidation curve are replaced by a single broad peak at around 3.8-3.9 V on reduction, reflecting a change in structure following de-intercalation of the third lithium. The last two reduction peaks are at around 3.63 and 3.56 V. The results show that LMgVSPC exhibits a higher polarization (100-250 mV) compared to the other three materials (70-150 mV).

This structural change is confirmed by the galvanostatic charge-discharge curves (Fig. 7) for LVPC, investigated at a rate of 0.2C, in the voltage range 2.8–4.8 V. These clearly show an absence of flat plateaus in the discharge profile following the first charge. The capacities of charge and discharge are 189.6 and 147 mAh g^{-1} , respectively, corresponding to a coulombic efficiency of 77.57%

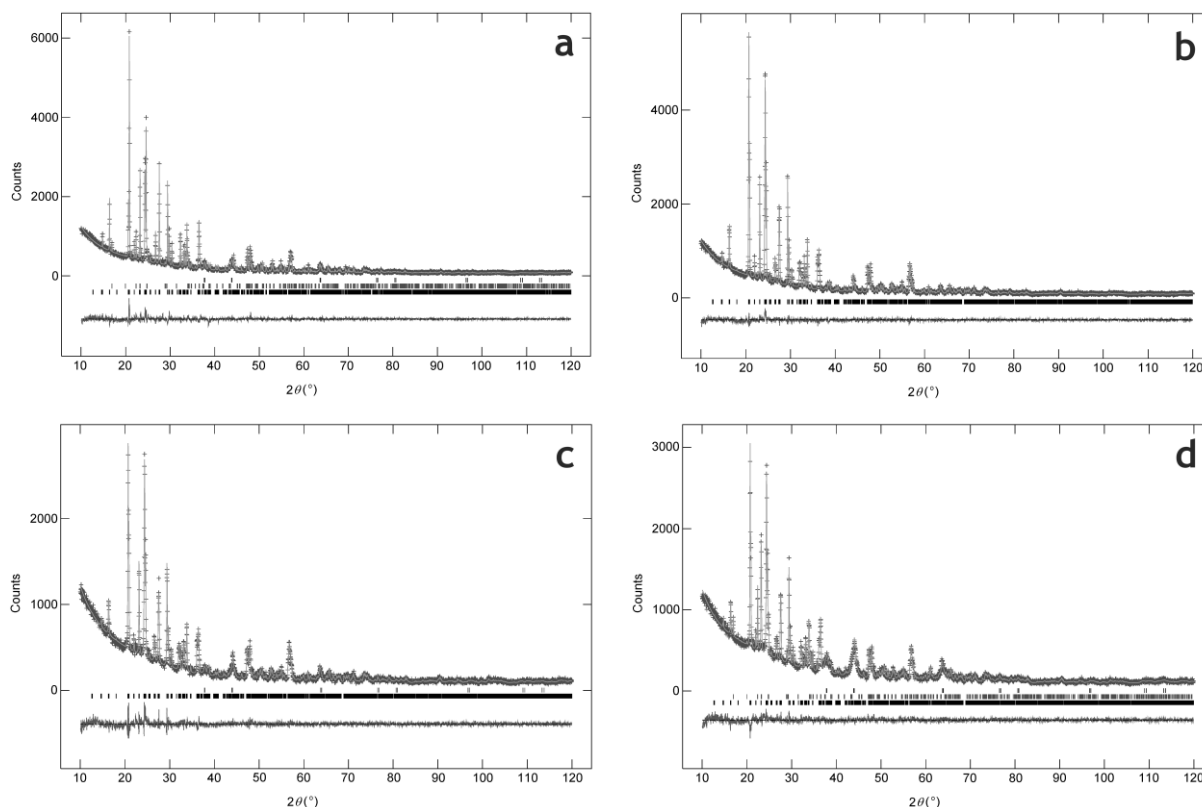


Fig.2. Fitted X-ray diffraction profiles for (a) LVPC, (b) LMgVSPC, (c) LVS10PC and (d) LVS50PC, showing observed (+ symbols), calculated (line), and difference (lower) profiles. Reflection positions are indicated by markers.

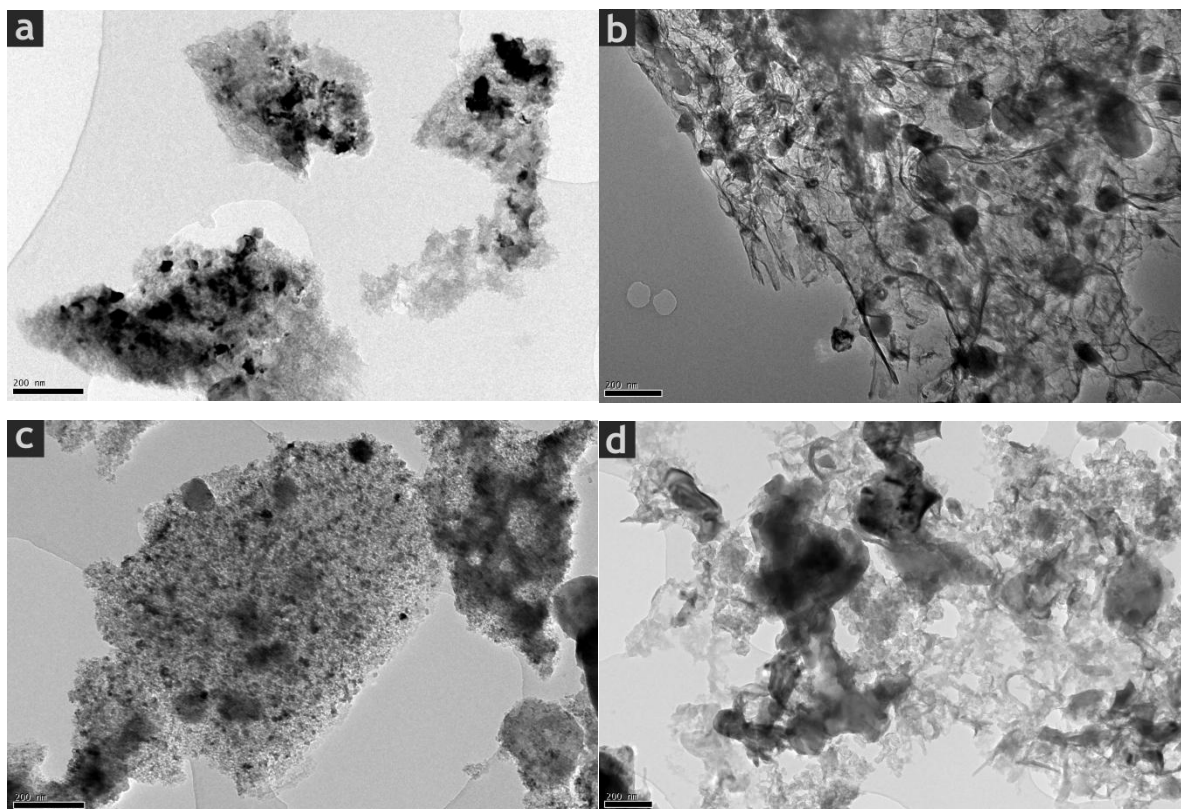


Fig. 3. TEM images of (a) LVPC, (b) LMgVSPC, (c) LVS10PC and (d) LVS50PC.

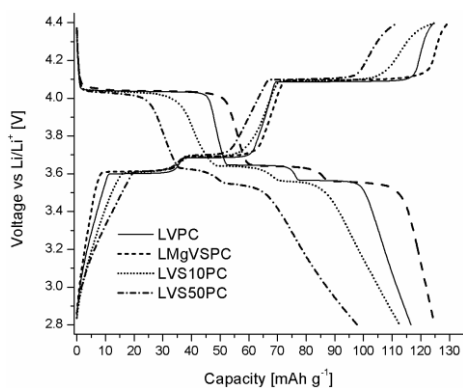


Fig. 4. Second cycle charge-discharge profiles of LVPC, LMgVSPC, LVS10PC and LVS50PC at 0.2C rate in the voltage range 2.8–4.4 V vs. Li/Li⁺.

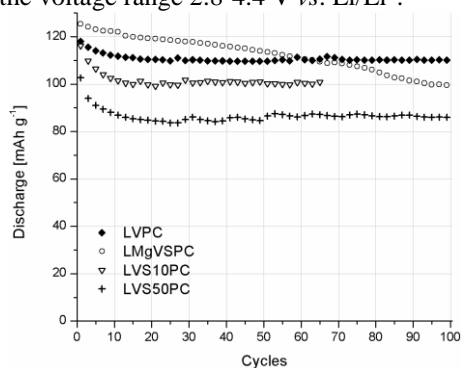


Fig. 5. Discharge capacities of LVPC, LMgVSPC, LVS10PC and LVS50PC recorded during cycling at 0.2C rate in the voltage range 2.8–4.4 V vs. Li/Li⁺.

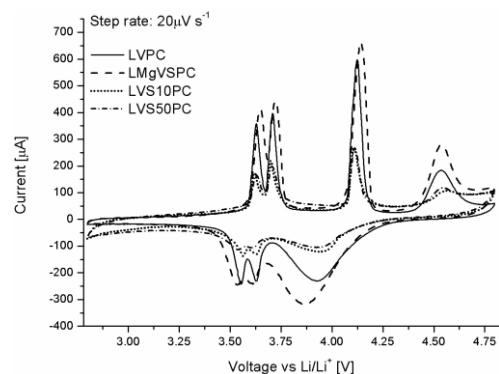


Fig. 6. Cyclic voltammograms of LVPC, LMgVSPC, LVS10PC and LVS50PC.

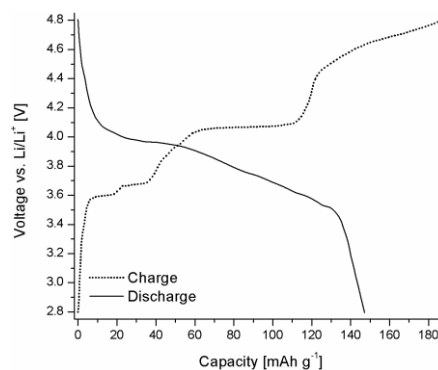


Fig. 7. Initial charge-discharge profiles for LVPC at 0.2C rate in the voltage range 2.8–4.8 V vs. Li/Li⁺.

CONCLUSIONS

Si can successfully be substituted for P in $\text{Li}_3\text{V}_2(\text{PO}_3)_3$. However, Si substitution is found to have a negative effect on initial discharge capacity in cells constructed using these compounds as active material. On cycling, cells using the Si substituted LVP show an initial capacity fade, but after the 15th cycle the capacity remains fairly constant. Inclusion of Mg in this system is found to increase the initial capacity of the Si substituted system, and although cycling behavior is degraded to some extent, the results are encouraging. Studies on the effects of Mg inclusion in isolation warrant further investigation.

Acknowledgements: This study was supported by Project BG051PO001/3.3-05-0001 "Science and Business", "Human Resources Development" Operational Programme co-financed by the European Social Fund of the EU and Bulgarian national budget. We wish to thank Dr R.M. Wilson at Queen Mary University of London for his help in X-ray data collection.

REFERENCES

1. K. Mitzushima, P.C. Jones, P.J. Wiseman, J.B. Goodenough, *Mater. Res. Bull.*, **15**, 783 (1980).
2. S.-K. Kim, W.-T. Jeong, H.-K. Lee, J. Shim, *Int. J. Electrochem. Sci.*, **3**, 1504 (2008).
3. M.M. Thackeray, W.I.F. David, P.G. Bruce, J.B. Goodenough, *Mater. Res. Bull.*, **18**, 461 (1983).
4. A.K. Padhi, K.S. Nanjundaswamy, J.B. Goodenough, *J. Electrochem. Soc.*, **144**, 1188 (1997).
5. J. Barker, M. Y. Saidi, Valence Technology Inc., US Patent 5,871,866 (1999).
6. Z. Bakenov, I. Taniguchi, *Electrochem. Commun.*, **12**, 75 (2010).
7. K. Amine, H. Yasuda, M. Yamachi, *Electrochem. Solid-State Lett.*, **3**, 178 (2000).
8. J. Wolfenstine, J. Allen, *J. Power Sources*, **142**, 389 (2005).
9. J. Barker, R.K.B. Gover, P. Burns, A. Bryan, M.Y. Saidi, J.L. Swoyer, *J. Power Sources*, **146**, 516 (2005).
10. K. Rissouli, K. Benkhouja, J.R. Ramos-Barrado, C. Julien, *Mater. Sci. Eng. B*, **98**, 185 (2003).
11. D. Morgan, A. Van der Ven, G. Ceder, *Electrochem. Solid State Lett.*, **7**, A30 (2004).
12. L. Wang, Z. Tang, L. Ma, X. Zhang, *Electrochem. Commun.*, **13**, 1233 (2011).
13. Y. Li, L. Hong, J. Sun, F. Wu, S. Chen, *Electrochim. Acta.*, **85**, 110 (2012).
14. Y. Lan, X. Wang, J. Zhang, J. Zhang, Z. Wu, Z. Zhang, *Powder Technol.*, **212**, 327 (2011).
15. M.Y. Saidi, J. Barker, H. Huang, J.L. Swoyer, G. Adamson, *J. Power Sources*, **119–121**, 266 (2003).
16. A. Tang, X. Wang, Z. Liu, *Mater. Lett.*, **62**, 1646 (2008).
17. Y.-Z. Li, Z. Zhou, M.-M. Ren, X.-P. Gao, J. Yan, *Mater. Lett.*, **61**, 4562 (2007).
18. Y. Chen, Y. Zhao, X. An, J. Liu, Y. Dong, L. Chen, *Electrochim. Acta*, **54**, 5844 (2009).
19. W. Yuan, J. Yan, Z. Tang, O. Sha, J. Wang, W. Mao, L. Ma, *Electrochimica Acta*, **72**, 138 (2012).
20. S. Zhong, L. Liu, J. Jiang, Y. Li, J. Wang, J. Liu, Y. Li, *J. Rare Earths*, **27**, 134 (2009).
21. J.N. Son, S.H. Kim, M.C. Kim, G.J. Kim, V. Aravindan, Y.G. Lee, Y.S. Lee, *Electrochim. Acta.*, **97**, 210 (2013).
22. R. Boukoureshlieva, S. Hristov, J. Milusheva, A. Kaisheva, *Bulg. Chem. Commun.*, **38**, 213 (2006).
23. A. C. Larson, R. B. Von Dreele, *Los Alamos National Laboratory Report*, No. LAUR-86-748, (1987).
24. S.-C. Yin, H. Grondey, P. Strobel, M. Anne, L.F. Nazar, *J. Am. Chem. Soc.*, **125**, 10402 (2003).
25. O.V. Yakubovich, V.S. Urusov, *Kristallografiya*, **42**, 301 (1997). (*In Russian*)
26. R.E. Loehman, C.N.R. Rao, J.M. Honig, *J. Phys. Chem.*, **73**, 1781 (1969).
27. R.D. Shannon, *Acta Crystallogr. A*, **32**, 751 (1976).

СИНТЕЗ И ОХАРАКТЕРИЗИРАНЕ НА ЛИТИЕВО ВАНАДИЕВ ФОСФАТ, ДОТИРАН СЪС СИЛИЦИЙ И МАГНЕЗИЙ

С. М. Станков^{1*}, А. Момчилов¹, И. Абрахамс², И. Попов¹, Т. Станкулов¹, А. Трифонова³

¹ *Институт по електрохимия и енергийни системи „Акад. Евгени Будевски“ – Българска академия на науките, ул. „Акад. Г. Бончев“ бл. 10, София 1113, България*

² *Изследователски институт по материали Училище по биологически и химически науки, Университет „Кралица Мери“, Майл енд роуд, Лондон E1 4NS, Великобритания.*

³ *AIT Австрийски институт за технологии, GmbH, Giefinggasse 2, 1210 Виена, Австрия.*

Постъпила на 12 май, 2014 г., коригирана на 15 юли, 2014 г.

(Резюме)

Активни материали за литиево-йонни батерии, базирани на дотиран с Si и Mg литиево ванадиев фосфат, $\text{Li}_3\text{V}_2(\text{PO}_4)_3$ (LVP), бяха синтезирани и изследвани чрез рентгеноструктурен, термогравиметричен и диференциално термичен анализи, трансмисионна електронна спектроскопия, галваностатични тестове и циклична волтаперометрия. $\text{Li}_3\text{V}_2(\text{PO}_4)_3$, $\text{Li}_{3.1}\text{V}_2(\text{SiO}_4)_{0.1}(\text{PO}_4)_{2.9}$, $\text{Li}_{3.5}\text{V}_2(\text{SiO}_4)_{0.5}(\text{PO}_4)_{2.5}$ и $\text{Li}_{3.04}\text{Mg}_{0.03}\text{V}_2(\text{SiO}_4)_{0.1}(\text{PO}_4)_{2.9}$ бяха получени чрез зол-гел метод, последван от твърдофазен синтез в аргонова атмосфера. Рентгеноструктурните анализи потвърдиха, че основната моноклинна кристалографска структура на LVP е запазена при дотираните съединения. Електрохимичните тестове, проведени в двуелектродни клетки, при токов режим 0.2С и диапазон от потенциали 2.8-4.4 V срещу Li/Li^+ , показаха, че съединението, дотирано с Mg и Si отдава най-голям капацитет от $124.8 \text{ mA h g}^{-1}$, достигайки 94% от теоретичния си капацитет (133 mA h g^{-1}) в този интервал от потенциали. Въпреки това, този материал показва лошо поведение при циклиране, като загубата на капацитет е около 20% за направени 100 цикъла. Като цяло бе установено, че дотирането със силиций има неблагоприятно влияние върху електрохимичното поведение, но след първоначалния спад на капацитета от около 15% в първите 15 цикъла, двата материала, дотирани само със силиций, показаха относителна стабилност в последващите цикли.

Geometric and energetic consequences of prototropy for neutral and ionized 4-aminopyrimidine in water solution

E. D. Raczynska*

Department of Chemistry, Warsaw University of Life Sciences (SGGW), 02-776 Warszawa, Poland

Received May 15, 2014, revised July 10, 2014

Quantum-chemical calculations were performed for the major, minor, and rare tautomers of neutral and ionized 4-aminopyrimidine (**4APM**, **4APM+•**, and **4APM-•**) in water solution at the PCM(water)//DFT(B3LYP)/6-311+G(d,p) level. Four tautomers were considered, one amine and three imine forms. Geometric isomerism of the exo =NH group was also taken into account. Ionization strongly influences the relative stabilities (ΔE) of the amino and imino forms in water solution. The amine tautomer is favored for **4APM**, whereas the imine ones have the lowest energies for the charged radicals, that is, the imine form with the labile proton at the endo N1 atom for **4APM+•** and the imine form with the labile proton at the endo C5 atom for **4APM-•**. The geometric parameters (HOMED - harmonic oscillator model of electron delocalization) estimated in water solution correlate well with those found in the gas phase {B3LYP/6-311+G(d,p)} for all tautomers of **4APM**, **4APM+•**, and **4APM-•**. A good relation also exists between the HOMED and ΔE values for the neutral and positively ionized forms in water solution. For the radical anions, the HOMED/ ΔE relation is more complex. The electron affinity seems to be a more important factor than aromaticity, and dictates the tautomeric preference.

Key words: 4-Aminopyrimidine, Tautomers, Ionization Effects, Relative stabilities, HOMED indices, DFT, PCM

INTRODUCTION

Prototropy and electron delocalization (particularly aromaticity) are well known phenomena that influence the structure and properties of many chemical compounds, natural products, and drugs [1-6]. Electron delocalization is a concept introduced for molecules (e.g., butadiene, benzene, guanidinium cation, pyridine, pyrimidine, etc.) displaying an exceptional stability, for which a single arrangement of atoms cannot be represented by one Lewis electronic structure, and the resonance hybrid has been proposed [7-9]. Prototropy is a concept introduced for chemical compounds (e.g. phenols, hydroxyazines, imidazoles, purines, nucleobases, etc.) displaying a particular case of isomerism of functional groups [1-6, 10]. It refers to a compound existing in an equilibrium between two or more isomers (tautomers) which differ by their constitution, i.e., by the positions of the labile proton(s). Consequently, tautomers differ by the positions of the double bond(s), and their structures can be explained by the resonance hybrids. A relation between prototropy and electron delocalization has been signaled more than fifty years ago by Pauling [10]. For example, phenol

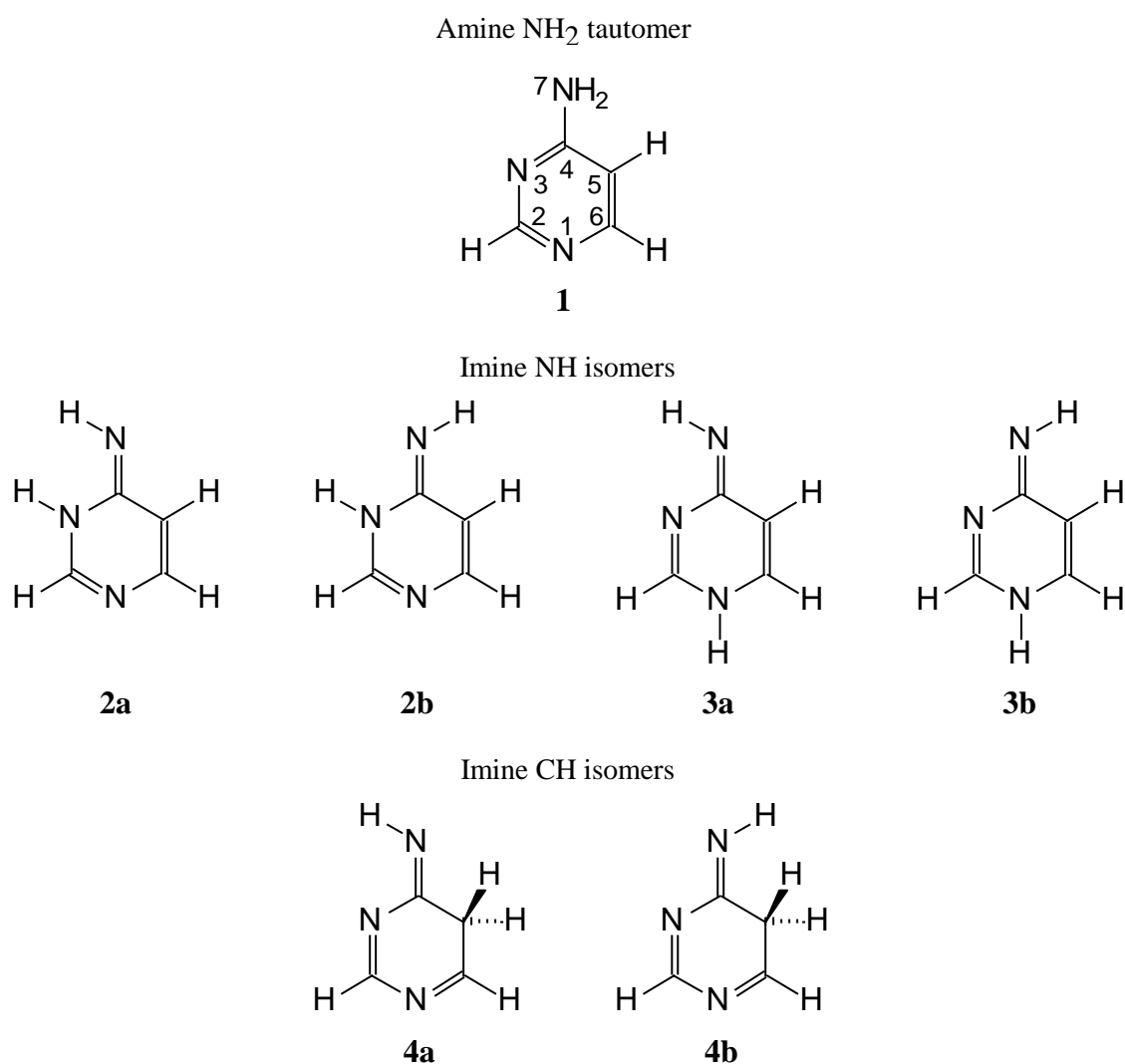
favors its enol form because of a complete electron delocalization (aromaticity) in the ring, whereas cyclohexanone takes preferentially the keto form [11, 12]. 2-aminopyrimidines prefer more aromatic amino than imino forms [13].

In the case of 4-aminopyrimidine (**4APM**), prototropy and electron delocalization have been recently discussed for isolated systems [14]. Since **4APM** is a convenient model for the nucleobases cytosine [15], vitamin B₁ thiamine molecules [16], and novel HIV inhibitors [17], investigations in water solution were undertaken in this paper. Four tautomers (Scheme 1): one amine form (**1**) and three imine forms (**2-4**) are possible for **4APM**. One proton can move between the exo NH₂ group and the endo N and C atoms. Due to geometric isomerism of the exo =NH group, two isomers can be considered for **2-4**, one with the imine H atom synperiplanar to the ring N3 atom (**a**) and the other one with this atom antiperiplanar (**b**). In the solid state, neutral **4APM** exists in the amine form **1** [18]. This form has been also found for isolated and associated neutral **4APM** [14, 19-25]. The ionized forms of **4APM** have been solely investigated by us in the gas phase [14]. Since ionization changes tautomeric equilibria [14], the complete tautomeric mixture of **4APM** was studied here in water solution.

* To whom all correspondence should be sent:
E-mail: ewa_raczynska@sggw.pl

It is well known that tautomeric conversions are very fast and reversible processes, and it is difficult to separate and to study the individual tautomers [1-6]. For this reason, quantum-chemical calculations were performed for all seven isomers of neutral, positively, and negatively ionized forms of 4-aminopyrimidine (**4APM**, **4APM⁺•**, and **4APM⁻•**) in water solution at the PCM(water)//DFT(B3LYP)/6-311+G(d,p) level. This level of theory has been chosen previously for investigations of the favored and rare tautomers of adenine in water solution [26]. The computations give the possibilities to study the variations of geometric and energetic consequences of

prototropy for all possible tautomers when proceeding from the gas phase {B3LYP/6-311+G(d,p)} to water solution {PCM(water)//B3LYP/6-311+G(d,p)}. Spectroscopic techniques (e.g., UV, IR, NMR, MW, MS, etc.) were not applied here to the tautomeric mixture, because their application gives solely an information on the major tautomers, signals of which have significant intensities. The minor and rare tautomers cannot be detected when their amounts are too small (< 0.1%) and their signals are in the background.



Scheme 1. Prototropic tautomers of 4-aminopyrimidine.

METHODS

Geometries of all seven neutral and charged isomers of 4-aminopyrimidine in their ground states were fully optimized without symmetry constraints employing the DFT(B3LYP) method [27-29] and the 6-311+G** basis set [30]. The restricted and unrestricted B3LYP functionals were used for the neutral and ionized forms, respectively. The solvent effect was studied with the PCM method [31, 32] applied to water as solvent. Geometries of all isomers were re-optimized at the PCM(water)//B3LYP/6-311+G(d,p) level, and the relative energies calculated. All calculations were performed using the Gaussian 03 program [33]. The adiabatic ionization potential (IP) and the adiabatic electron affinity (EA) were estimated using equations (1) and (2), respectively, where E_s are the total electronic energies of the optimized charged (**4APM**⁺• and **4APM**⁻•) and neutral isomers (**4APM**) of 4-aminopyrimidine. The geometry-based HOMED (harmonic oscillator model of electron delocalization) indices [34, 35] were estimated for the neutral and charged isomers optimized at the PCM//DFT level using equation (3) as described previously for purine [36]. In this equation, α is a normalization constant, R_0 is the optimum bond length (assumed to be realized for fully delocalized system), R_i are the running bond lengths in the system, and n is the number of bonds

taken into account. Equation (3) is the same as that for the original [37] and reformulated [38] HOMA (harmonic oscillator model of aromaticity) indices. Similarities and differences between HOMED and HOMA were described in details in refs [35, 36].

$$IP = E(\mathbf{4APM}^{+\bullet}) - E(\mathbf{4APM}) \quad (1)$$

$$EA = E(\mathbf{4APM}) - E(\mathbf{4APM}^{-\bullet}) \quad (2)$$

$$HOMED = 1 - \{\alpha \Sigma (R_0 - R_i)^2\} / n \quad (3)$$

RESULTS AND DISCUSSION

Geometric Parameters

For the seven isomers of neutral and charged 4-aminopyrimidine (Scheme 1), the minima with all real frequencies were found in the gas phase at the DFT(B3LYP)/6-311+G** level [14]. The PCM model with water as solvent does not change very much the geometries optimized in the gas phase. In water solution, the exo NH₂ group is planar solely for the radical cation (**1**⁺•). For the radical anion (**1**⁻•), this group takes the pyramidal conformation similar to the neutral form (**1**).

The transfer of the labile proton to the endo N atom in the structures **2a**, **2b**, **3a**, and **3b** (imine NH isomers) does not destroy the planarity of the ring for the neutral and ionized forms in water solution. Due to presence of the C-sp³ atom (C5), the structures **4a** and **4b** (imine CH isomers) lose the planarity of the ring at each oxidation state.

Table 1. Comparison of the HOMED indices estimated for the seven isomers of neutral and ionized 4-aminopyrimidine in water solution with those in the gas phase

(a) gas phase {B3LYP/6-311+G(d,p)} [14]

Isomer	Neutral form		Radical cation		Radical anion	
	HOMED6	HOMED7	HOMED6	HOMED7	HOMED6	HOMED7
1	0.991	0.981	0.950	0.960	0.904	0.843
2a	0.737	0.756	0.924	0.936	0.712	0.767
2b	0.707	0.736	0.938	0.949	0.775	0.818
3a	0.664	0.701	0.917	0.934	0.777	0.805
3b	0.663	0.702	0.921	0.936	0.773	0.804
4a	0.346	0.435	0.122	0.226	0.557	0.640
4b	0.170	0.297	0.106	0.210	0.470	0.574

(b) water solution {PCM(water)//B3LYP/6-311+G(d,p)}

Isomer	Neutral form		Radical cation		Radical anion	
	HOMED6	HOMED7	HOMED6	HOMED7	HOMED6	HOMED7
1	0.979	0.981	0.937	0.949	0.867	0.841
2a	0.797	0.816	0.957	0.958	0.786	0.828
2b	0.813	0.828	0.954	0.961	0.806	0.844
3a	0.765	0.795	0.935	0.949	0.749	0.801
3b	0.766	0.797	0.934	0.948	0.749	0.802
4a	0.384	0.470	0.199	0.287	0.556	0.641
4b	0.406	0.486	0.211	0.308	0.580	0.658

In water solution, the CC (1.375-1.416 Å) and CN (1.333-1.354 Å) bond lengths for the neutral amine NH₂ tautomer **1** are not very different from those calculated for fully delocalized benzene (1.396 Å) and *s*-triazine (1.335 Å), respectively. The HOMED indices (Table 1) estimated for the six-membered ring (HOMED₆ = 0.979) and for the whole tautomeric system including the exo NH₂ group (HOMED₇ = 0.981) are close to unity, confirming the aromatic character of **1**. The transfer of the labile proton from the exo NH₂ group to the endo N atom induces larger variations of the CC (1.349-1.461 Å) and CN (1.295-1.412 Å) bond lengths for the neutral imine NH isomers (**2a**, **2b**, **3a**, and **3b**) than for **1**. Consequently, the HOMED indices (< 0.9) for **2a**, **2b**, **3a**, and **3b** are lower than those for **1**. The neutral imine CH isomers (**4a** and **4b**) completely lose their aromatic character. The CC bond lengths (1.498-1.512 Å) for **4a** and **4b** are close to that for ethane (1.531 Å), and their CN bond lengths (1.413-1.415 Å and 1.273-1.285 Å) are close to those for methylamine (1.469 Å) and methylimine (1.270 Å). Hence, the HOMED indices estimated for **4a** and **4b** are lower than 0.5. All bond lengths for simple compounds (ethane, methylamine, benzene, and *s*-triazine) were calculated at the PCM(water)//B3LYP/6-311+G(d,p) level [36].

When going from the neutral isomers of 4-aminopyrimidine to the radical cations, variations of the CC and CN bond lengths are greater for the charged amine (**1**^{•+}) and imine CH isomers (**4a**^{•+} and **4b**^{•+}) than for the neutral ones. However, they are smaller for the charged imine NH isomers (**2a**^{•+}, **2b**^{•+}, **3a**^{•+}, and **3b**^{•+}) than for the neutral ones. Consequently, positive ionization decreases the HOMED indices for the amine NH₂ and imine CH isomers (by 0.03-0.04 and 0.18-0.20 HOMED units, respectively), and increases them for the imine NH ones (by 0.13-0.17 HOMED units). Quite a different situation takes place when proceeding from the neutral isomers to the radical anions of 4-aminopyrimidine for which resonance conjugations and variations of the CC and CN bond lengths are completely different. Negative ionization induces an exceptional increase of π -electron delocalization. Small variations of the CC and CN bonds are observed for the negatively ionized imine CH isomers (**4a**^{•-} and **4b**^{•-}). For the charged imine NH isomers (**2a**^{•-}, **2b**^{•-}, **3a**^{•-}, and **3b**^{•-}), delocalization of π -electrons also changes. However, it decreases for the charged amine isomer

(**1**^{•-}). Consequently, the HOMED indices increase for the imine CH tautomers (by ca. 0.17 HOMED units) and decrease for the amine NH₂ one (by 0.11-0.14 HOMED units). For the imine NH tautomers, the HOMED variations are not larger than ± 0.02 units.

Generally, trends observed in water solution are similar to those in the gas phase [14], that is, the aromatic amine NH₂ and imine NH isomers are more delocalized than the non-aromatic imine CH ones. Solvent decreases slightly the HOMED values for **1** and it increases them for **2-4**, for both the neutral and ionized forms. Although these solvent effects are different for the individual isomers, there is a good linear relationship between the HOMED values estimated in water solution and those in the gas phase for the pyrimidine ring - six bonds, and also for the whole tautomeric system - seven bonds (Fig. 1). This indicates that the solvent does not affect very much the resonance conjugations possible for the neutral and ionized isomers of 4-aminopyrimidine. Electron delocalization in water solution is parallel to that in the gas phase.

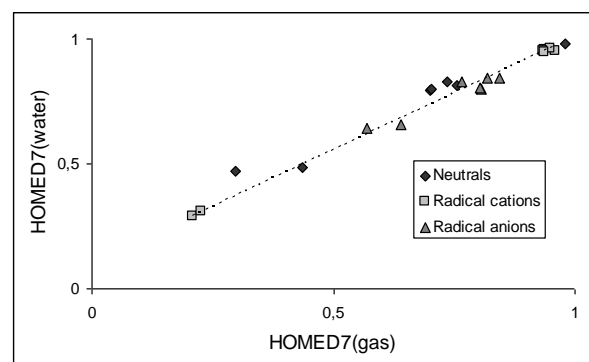


Fig. 1. Correlation between the HOMED7 values estimated in the gas phase and in water solution for the whole tautomeric system (seven bonds) of the neutral and ionized isomers of 4-aminopyrimidine

Relative Stabilities

The relative energies (ΔE) calculated in water solution for all neutral and charged isomers can be compared with those in the gas phase (Table 2). As it could be expected [14, 19-25], the amine tautomer **1** has the lowest energy for neutral **4APM**. Aromaticity of the six membered ring seems to be one of the most important factor that dictates the high stability of **1** and its tautomeric preference (100%) in both environments. The imine NH tautomers (**2** and **3**) possess considerably larger energies than **1** ($\Delta E > 10$ kcal mol⁻¹). They are lower in water solution (ΔE 10-12 kcal mol⁻¹) than in the gas phase (ΔE 13-22 kcal mol⁻¹). The

transfer of the labile proton to the endo C atom decreases exceptionally the stability of **4a** and **4b**. Their energies are larger than that of **1** by more than 30 kcal mol⁻¹ in both environments. The intramolecular favorable and unfavorable interactions possible for the structures **a** and **b** of the imine NH and CH tautomers differentiate their energies in higher degree in the gas phase (3-5 kcal mol⁻¹) than in water solution (ca. 1 kcal mol⁻¹). However, these effects do not influence the tautomeric preference. The percentage contents of the imine NH and CH tautomers are very low (< 0.001 %). Indeed, they cannot be experimentally detected for neutral **4APM**, and thus they may be neglected in the tautomeric mixture.

Positive ionization changes the tautomeric preferences in water solution for **4APM⁺**. Although the amine tautomer (**1⁺**) has the lowest energy in the gas phase [14], the imine NH isomer (**3a⁺**) dominates in water solution. Ionization and solvent also change the relative energies of the amine NH₂ (**1⁺**) and imine NH tautomers (**2a⁺**, **2b⁺**, **3a⁺**, and **3b⁺**), and the compositions of the tautomeric mixture are different in both environments. They are as follows: 88.3% of **1⁺**, 7.3% of **2⁺**, and 4.4% of **3⁺** in the gas phase, and 1.5% of **1⁺**, 27.0% of **2⁺**, and 71.5% of **3⁺** in water solution. This difference should be considered in electron-transfer reactions in which 4-aminopyrimidine loses one electron. It should be also taken into account for positively ionized cytosine, vitamin B₁ thiamine molecules, and some HIV inhibitors. The ΔE values for the imine CH isomers (**4a⁺** and **4b⁺**) are larger than 40 kcal mol⁻¹ in both environments. Thus, their percentage contents are very low (< 1·10⁻³⁰ %). As exceptionally rare isomers, they may be neglected in the tautomeric mixture of **4APM⁺**.

Negative ionization dramatically changes the tautomeric preference. For **4APM⁻**, the imine CH isomer (**4a⁻**) with the labile proton at the endo C5 atom has the lowest energy in water solution, as well as in the gas phase. Change of environment decreases solely the relative energies. In water solution, two tautomers should be considered in the tautomeric mixture of **4APM⁻**: **1⁻** (1.3%) and **4⁻** (98.7%), whereas only one (**4⁻**, 100%) in the gas phase. The amount of **1⁻** (0.03%) is very low in the gas phase. It may be considered as the rare

tautomer. The imine NH tautomers (**2⁻** and **3⁻**) possess considerably larger energies than **4⁻** (> 4 kcal mol⁻¹). They may be neglected in the tautomeric mixture of **4APM⁻** in both environments.

HOMED/ ΔE Relation

A parallelism of the ΔE and HOMED values for the neutral and positively ionized isomers indicates that some relation exists between prototropy and electron delocalization for 4-aminopyrimidine (Fig. 2). In water solution, the HOMED7 indices estimated for the neutral isomers of **4APM** correlate well with their ΔE values: HOMED7(water) = -0.014 ΔE + 0.972, R = -0.999. Similar relationship is found in the gas phase: HOMED7(gas) = -0.017 ΔE + 1.007, R = -0.977. The HOMED7/ ΔE correlation is slightly better in water solution than in the gas phase. Solvent diminishes intramolecular interactions between the exo and endo functional groups, and influences the relative energies and the HOMED indices. The energetic effects are larger than the geometric ones. Electron delocalization (aromaticity) seems to be one of the main factors that influences the stability of the neutral forms. It is also an important factor for the radical cations. A good linear relationship between the HOMED7 and ΔE values is observed in water solution {HOMED7(water) = -0.013 ΔE + 0.967, R = -0.999}. The parameters of this relationship do not differ very much from those found for the neutral isomers. Negative ionization differentiates the imine CH isomers from the family of other ones (NH₂ and NH). In this case, the HOMED/ ΔE relation is more complex. The electron affinity seems to be more important factor than aromaticity and dictates the tautomeric preference.

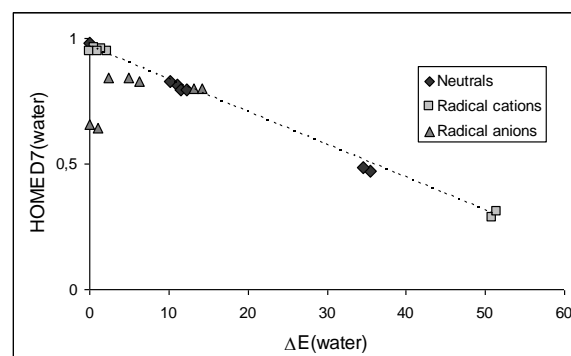


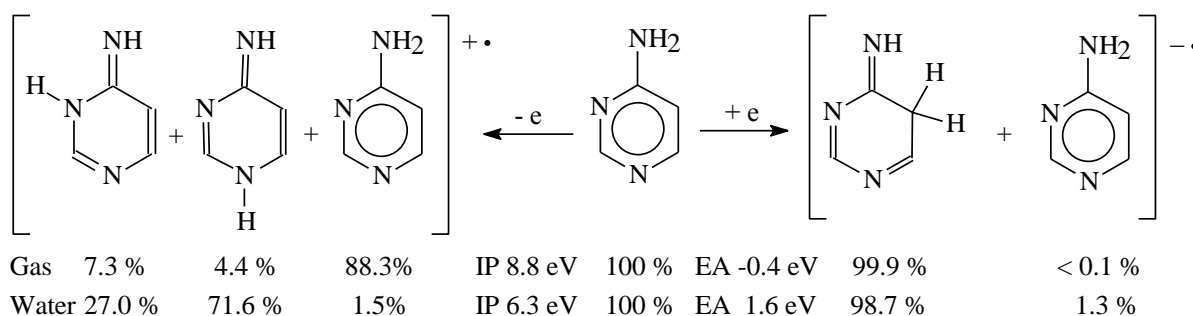
Fig. 2. HOMED7/ ΔE plot for the neutral and ionized isomers of 4-aminopyrimidine in water solution.

Table 2. Comparison of the relative energies (in kcal mol⁻¹ at 0 K) calculated for the seven isomers of neutral and ionized 4-aminopyrimidine in water solution with those in the gas phase

Isomer	Neutral form		Radical cation		Radical anion	
	Gas	Water	Gas	Water	Gas	Water
1	0.0	0.0	0.0	2.2	6.4	2.4
2a	16.1	11.0	4.5	1.5	10.2	6.3
2b	12.9	10.1	0.9	0.6	6.8	4.9
3a	18.3	11.5	1.4	0.0	17.7	13.2
3b	22.5	12.3	6.2	1.1	21.6	14.2
4a	37.8	35.5	45.4	50.9	4.8	1.0
4b	33.2	34.5	44.8	51.5	0.0	0.0

Table 3. The adiabatic ionization potentials (IP) and the adiabatic electron affinities (EA) estimated for all isomers of 4-aminopyrimidine in the gas phase and in water solution (in eV at 0 K, 1 eV = 23.06037 kcal mol⁻¹)

Positive ionization	IP		Negative ionization	EA	
	Gas	Water		Gas	Water
1 - e → 1 ^{+•}	8.8	6.4	1 + e → 1 ^{-•}	-0.6	1.6
2a - e → 2a ^{+•}	8.3	5.9	2a + e → 2a ^{-•}	-0.1	1.9
2b - e → 2b ^{+•}	8.3	5.9	2b + e → 2b ^{-•}	-0.1	1.9
3a - e → 3a ^{+•}	8.1	5.8	3a + e → 3a ^{-•}	-0.3	1.6
3b - e → 3b ^{+•}	8.1	5.8	3b + e → 3b ^{-•}	-0.3	1.6
4a - e → 4a ^{+•}	9.3	7.0	4a + e → 4a ^{-•}	1.1	3.2
4b - e → 4b ^{+•}	9.1	7.0	4b + e → 4b ^{-•}	1.1	3.2

**Scheme 2.** The favored ionization reactions for 4-aminopyrimidine

Ionization Processes

A simple one-electron loss or one-electron gain may be observed during positive or negative ionization in the mass spectrometer. Consequently, 4-aminopyrimidine may be transformed to its positively ($4\text{APM} - e \rightarrow 4\text{APM}^{+\bullet}$) or negatively ionized ($4\text{APM} + e \rightarrow 4\text{APM}^{-\bullet}$) very reactive states. In the presence of oxidizing or reducing agents, neutral 4-aminopyrimidine may also lose or gain one electron. The mechanisms of chemical redox reactions, anodic oxidations or cathodic reductions of 4-aminopyrimidine, may be very complex and may depend on reaction conditions such as solvent, reagent, catalyst, etc.. The redox

processes may pass through different intermediates among which the charged forms, $4\text{APM}^{+\bullet}$ and $4\text{APM}^{-\bullet}$, are possible.

A direct comparison of the energetic parameters for the ionized and neutral isomers of 4-aminopyrimidine suggests that one-electron loss is less endothermic process in water solution than in the gas phase, and one-electron gain is more profitable process than one-electron loss in both environments (Table 3). This means that 4-aminopyrimidine may take spontaneously one electron from a reducing agent. Interestingly, change of the position of the imine H atom vis-à-vis the ring N3 atom from synperiplanar to antiperiplanar has no important effect on the values

of the adiabatic ionization potential (IP) and of the adiabatic ionization affinity (EA). This suggests that favorable and unfavorable interactions possible for the neutral and ionized isomers are similar. However, the IP and EA values are different for the amine (NH₂) and imine (NH and CH) tautomers. The ionization mechanisms are not the same. An analysis of the distribution of the spin density and charge computed in the gas phase and in water solution shows evidently the differences. For the NH₂ and NH tautomers, the exo N atom may lose preferentially one of the non-bonding electrons, whereas the endo N atoms may participate in one-electron loss for the CH isomers. On the other hand, the pyrimidine ring may gain one excess electron for the NH₂ and NH tautomers, whereas the exo N atom may participate in one-electron gain. This tendency is similar in both environments. When going from the gas phase to water solution, the IP and EA values vary by ca. 2 eV.

If we consider solely the major and minor tautomers for neutral, positively, and negatively ionized 4-aminopyrimidine, the following ionization processes can be proposed (Scheme 2), and the following IP and EA values can be estimated for 4-aminopyrimidine in the gas phase and in water solution (ground states): IP 8.8 and 6.3 eV, EA -0.4 and 1.6 eV at 0K, respectively. The IP (8.5 and 6.3 eV) and EA values (-0.4 and 1.8 eV) found for 2-aminopyrimidine at the same levels of theory are of the same order of magnitude [39]. Unfortunately, there are no experimental data in the literature for the ionization potential (IP) and for the electron affinity (EA) of **4AMP** and no comparison can be made. However, it should be mentioned here that the IP values in the gas phase for pyrimidine (9.3 eV [40]), 2- and 4-aminopyridine (8.5 and 8.8 eV, respectively [41]) are of the same order of magnitude as the DFT-estimated IP for **4APM**. The literature EA value for unsubstituted pyrimidine is not very large in the gas phase (> -0.24999 eV [42]). The negative value suggests that the anion is not higher in energy than the corresponding neutral form, and hence unstable in the gas phase. However, the anion can be studied in water solution. The calculated EA value is positive for **4APM** in water solution. Similar tendencies on the IP and EA values in the gas phase and in water solution have been reported for nucleobases [26, 43, 44]. 4-Aminopyrimidine models well the redox properties of cytosine and adenine, containing the exo NH₂ group at the same

position vis-à-vis the endo N atoms in the pyrimidine ring.

CONCLUSIONS

Quantum-chemical calculations performed for all possible amine and imine tautomers-isomers of neutral 4-aminopyrimidine (**4APM**) and of its charged forms (**4APM**⁺• and **4APM**⁻•) show evidently important changes of the tautomeric preference when proceeding from the gas phase to water solution (Scheme 2). The neutral tautomeric mixture of **4APM** consists mainly of the amine NH₂ tautomer (100%). This is independent on environment. Positive and negative ionizations dramatically change the composition of the tautomeric mixture. The tautomeric preference for **4APM**⁺• depends on the medium. In the gas phase, the amine NH₂ tautomer is favored for **4APM**⁺•, whereas the imine NH isomer with the labile proton at the N1 atom dominates in water solution. For **4APM**⁻•, the C5 atom takes preferentially the labile proton and the imine CH isomer is favored in the gas phase and also in water solution. Solvent has slight effect on the composition of the tautomeric mixture of **4APM**⁻•.

The geometric HOMED indices, which measure electron delocalization for the individual isomers, change little when proceeding from the gas phase to water solution. Larger variations take place for the relative energies (ΔE), which measure prototropic conversions. However, the HOMED and ΔE values correlate well for the neutral and positively ionized isomers of 4-aminopyrimidine (Fig. 2). Some discrepancies occur for the radical anions, for which the HOMED/ ΔE relation seems to be more complex. In this case, two factors (electron affinity and aromaticity) influence the tautomeric conversions. For the favored ionization processes, the adiabatic ionization potentials and the adiabatic ionization affinities change by ca. 2 eV when proceeding from the gas phase to water solution. This solvent effect is similar to that reported for nucleobases [43, 44].

REFERENCES

1. J. Elguero, C. Marzin, A.R. Katritzky, P. Linda, *The Tautomerism of Heterocycles*, Academic Press, New York, 1976.
2. A.F. Pozharskii, A.T. Soldatenkov, A.R. Katritzky, *Heterocycles in Life and Society*, Wiley, New York, 1997.

3. A.R. Katritzky, K. Jug, D.C. Oniciu, *Chem. Rev.*, **101**, 1421 (2001).
4. J.S. Kwiatkowski, B. Pullman., *Adv. Heterocyclic Chem.* **18**, 199 (1975).
5. J.S. Kwiatkowski, W.B. Person, In *Theoretical Biochemistry and Molecular Biology*, D.L. Beveridge, and R. Lavery (Eds.), Academic Press, New York, 1990.
6. E.D. Raczyńska, W. Kosińska, B. Ośmiałowski, R. Gawinecki, *Chem. Rev.* **105**, 3561 (2005), and references therein.
7. G.W. Wheland, *Resonance in Organic Chemistry*, John Wiley & Sons, New York, 1955.
8. Y.K. Syrkin, M.E. Dyatkina, *Structure of Molecules and the Chemical Bond*, Interscience Publishers, New York, 1950.
9. C.A. Coulson, *Valence*, Calendron Press, Oxford, 1952.
10. L. Pauling, *The Nature of Chemical Bond*, Cornell University Press, Third Edition, New York, 1960.
11. *The Chemistry of Phenols*, Z. Rappoport, Ed., John Wiley & Sons, Chichester, 2003.
12. *The Chemistry of Enols*, Z. Rappoport Ed., Wiley, Chichester, 1990.
13. I. Alkorta, J. Elguero, *J. Org. Chem.* **67**, 1515 (2002).
14. E.D. Raczyńska, K. Kolczyńska, T.M. Stępniewski, *J. Mol. Model.*, **18**, 3523 (2012).
15. W. Saenger, *Principles of Nucleic Acid Structure*, Springer, New York, 1994.
16. A. Schellenberger, *Biochim. Biophys. Acta* **1385**, 177 (1998).
17. V.R. Gadhachanda, B. Wu, Z. Wang, K.L. Kuhen, J. Caldwell, H. Zondler, H. Walter, M. Havenhand, Y. He, *Bioorg. Med. Chem. Lett.* **17**, 260 (2007).
18. L. Van Meervelt, K. Uytterhoeven, *Z. Kristallogr. - New Cryst. Struct.* **218**, 481 (2003).
19. J. Smets, L. Adamowicz, G. Maes, *J. Phys. Chem.* **99**, 6387 (1995).
20. K. Balci, S. Akyuz, *J. Mol. Struct.* **744-747**, 909 (2005).
21. S. Akyuz, T. Akyuz, Y. Akkaya, E. Akalin, *J. Mol. Struct.*, **834-836**, 403 (2007).
22. S. Akyuz, T. Akyuz, *J. Mol. Struct.* **924-926**, 37 (2009).
23. J.J. Szymczak, T. Muller, H. Lischka, *Chem. Phys.*, **375**, 110 (2010).
24. D. Nachtigallová, M. Barbatti, J.J. Szymczak, P. Hobza, H. Lischka, *Chem. Phys. Lett.*, **497**, 129 (2010).
25. T. Zeleny, P. Hobza, D. Nachtigallová, M. Ruckebauer, H. Lischka, *Collect. Czech. Chem. Commun.*, **76**, 631 (2011).
26. E.D. Raczyńska, M. Makowski, K. Zientara-Rytter, K. Kolczyńska, T.M. Stępniewski, M. Hallmann, *J. Phys. Chem. A.*, **117**, 1548 (2013).
27. R.G. Parr, W. Yang, *Density Functional Theory of Atoms and Molecular Orbital Theory*, Oxford University Press, New York, 1989.
28. A.D. Becke, *J. Chem. Phys.*, **98**, 5648 (1993).
29. C. Lee, W. Yang, R.G. Parr, *Phys. Rev. B*, **37**, 785 (1988).
30. W. J. Hehre, L. Radom, P.v.R. Schleyer, J.A. Pople, *Ab initio Molecular Theory*, Wiley, New York, 1986
31. S. Miertus, J. Tomasi, *Chem. Phys.*, **65**, 239 (1982).
32. S. Miertus, E. Scrocco, J. Tomasi, *Chem. Phys.*, **55**, 117 (1981).
33. M.J. Frisch, G.W. Trucks, H.B. Schlegel, G.E. Scuseria, M.A. Robb, J.R. Cheeseman, J.A. Jr. Montgomery, T. Vreven, K.N. Kudin, J.C. Burant, J.M. Millam, S.S. Iyengar, J. Tomasi, V. Barone, B. Mennucci, M. Cossi, G. Scalmani, N. Rega, R. Petersson, H. Nakatsuji, M. Hada, M. Ehara, K. Toyota, R. Fukuda, J. Hasegawa, M. Ishida, T. Nakajima, Y. Honda, O. Kitao, H. Nakai, M. Klene, X. Li., J.E. Knox, H.P. Hratchian, J.B. Cross, V. Bakken, C. Adamo, R. Jaramillo, R. Gomperts, R.E. Stratmann, O. Yazyev, A.J. Austin, R. Cammi, C. Pomelli, J.W. Ochterski., P.Y. Ayala, K. Morokuma, G.A. Voth, P. Salvador, J.J. Dannenberg, V.G. Zakrzewski., S. Dapprich, A.D. Daniels, M.C. Strain, O. Farkas, D.K. Malick., A.D. Rabuck, K. Raghavachari, J.B. Foresman, J.V. Ortiz., Q. Cui, A.G. Baboul, S. Clifford, J. Cioslowski, B.B. Stefanov, G. Liu, A. Liashenko, P. Piskorz, I. Komaromi, R.L. Martin, D.J. Fox, T. Keith, M.A. Al-Laham, C.Y. Peng, A. Nanayakkara, M. Challacombe, P.M.W. Gill, B. Johnson, W. Chen, M.W. Wong, C. Gonzalez, J.A. Pople, Gaussian-03, Revision E.01, Gaussian, Inc., Wallingford CT, 2004.
34. E.D. Raczyńska, T.M. Krygowski, K. Duczmal, M. Hallmann, *XVIII International Conference on Physical Organic Chemistry*, Warsaw, 2006, p. 31 (Book of abstracts).
35. E.D. Raczyńska, M. Hallmann, K. Kolczyńska, T.M. Stępniewski, *Symmetry*, **2**, 1485 (2010).
36. E.D. Raczyńska, B. Kamińska, *J. Mol. Model.* **19**, 3947-3960 (2013).
37. J. Kruszewski, T. M. Krygowski, *Tetrahedron Lett.*, **13**, 3839 (1972).
38. T.M. Krygowski, *J. Chem. Int. Comput. Sci.* **33**, 375 (1993).
39. E.D. Raczyńska, *Comput. Theor. Chem.*, **1031**, 56 (2014).
40. S.G. Lias, *Ionization energy evaluation*, in NIST Chemistry WebBook, NIST Standard Reference Database Number 69. Eds. P.J. Linstrom and W.G. Mallard, National Institute of Standards and Technology, Gaithersburg MD, 20899, <http://webbook.nist.gov>.
41. D. Stefanovic, H.F. Grützmacher, *Org. Mass Spectrom.*, **9**, 1052 (1974).
42. I.Nenner, G.J. Schultz, *J. Chem. Phys.*, **62**, 1747 (1975).
43. D.M. Close, *J. Phys. Chem. A*, **108**, 10376 (2004).
44. X. F. Li, Z.L. Cai, M.D. Sevilla, *J. Phys. Chem.. A*, **106**, 1596 (2002).

ГЕОМЕТРИЧНИ И ЕНЕРГИЙНИ СЛЕДСТВИЯ ОТ ПРОТОТРОПИЯТА НА НЕУТРАЛЕН И ЙОНИЗИРАН 4-АМИНОПИРИМИДИН ВЪВ ВОДНИ РАЗТВОРИ

Е.Д. Рачинска*

Департамент по химия, Варшавски университет по науките за живота, Варшава, Полша

Постъпила на 15 май, 2014 г., коригирана на 10 юли, 2014 г.

(Резюме)

Извършени са квантово-химични пресмятания за тавтомерните форми (главни, малки, редки) на неутрален и йонизиран 4-аминопиримидин (**4АРМ**, **4АРМ⁺** и **4АРМ⁻**) във водни разтвори на РСМ(вода)//DFT(B3LYP)/6-311+G(d,p) ниво. Разгледани са четири тавтомери – една аминна и три иминни форми. Отчетен е и изометризмът на екзо =NH групите. Йонизацията силно влияе върху относителната стабилност (ΔE) на amino- и имино-формите във водни разтвори. Амино-тавомерите са предпочитани при **4АРМ**, докато иминните имат най-ниска енергия на натоварените радикали, т.е. имино-формите имат лабилен протон при ендо N 1 атома за **4АРМ⁺**, а имино-формата е с лабилен протон при ендо C5-атом за **4АРМ**. Геометричните параметри (НОМЕД – модел на хармоничен осцилатор на електронна делокализация), оценени за воден разтвор се корелират добре с намерените за газова фаза {B3LYP/6-311+G(d,p)} за всички тавтомери - **4АРМ**, **4АРМ⁺** и **4АРМ⁻**. Добра релация съществува между стойностите на НОМЕД и ΔE за неутрални и положително йонизираните форми във воден разтвор. Релацията НОМЕД/ ΔE за анион-радикалите е по-сложна. Изглежда, че електронният афинитет е по-важен фактор и ароматната природа и определя предпочитането на тавтомерните форми.

One-pot synthesis of tetrahydrobenzo[*b*]pyran and dihydropyrano[*c*]chromene derivatives using ammonium Alum in green media

M. A. Bodaghifard*, N. Ahadi

Department of Chemistry, Faculty of Science, Arak University, 38156-88138, Arak, Iran.

Received May 31, 2014, Revised August 25, 2014

A variety of 4*H*-benzo[*b*]pyran and pyrano[*c*]chromene derivatives have been efficiently synthesized under green conditions. This inexpensive, non-toxic, eco-friendly protocol afforded the products in good to high yields.

Keywords: green chemistry, multi-component, benzopyran, pyranochromene, ammonium alum.

INTRODUCTION

The increasing attention during the past decade for environment protection has led to a new area called green chemistry. Elimination of dangerous toxic solvents and replacing it with water and environmentally friendly solvents is very important in green chemistry [1]. Development of chemical processes with the highest efficiency, lowest cost and use of non-toxic reagents and catalysts and also use of solvent-free mediums have been found of special interest [1]. In recent years, the use of water as a green solvent has been developed. Replacing of organic solvents with water has advantages such as availability, low cost and safety for the environment [2].

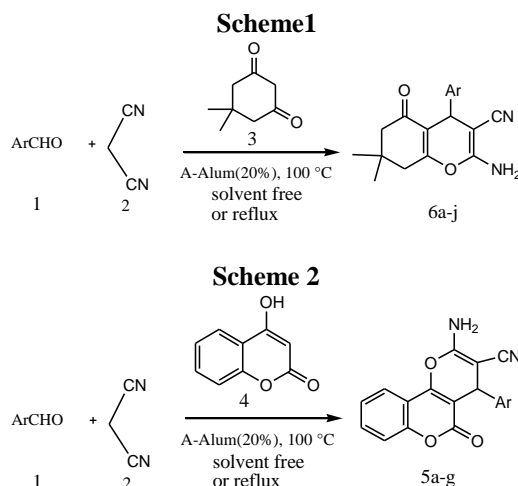
Multi-component reactions are powerful synthetic tools for the synthesis of compounds with biological activity [3]. Tetrahydrobenzo[*b*]pyran and dihydropyrano[*c*]chromene derivatives have been exhibited biological and pharmaceutical properties including anticancer and anticoagulation [4], diuretics [5], anti-Alzheimer's [6], anti leukemic [7], anti anaphylactic [8], anti-malarial [9], emetic [10]. Also these compounds have been used in pigments and cosmetics [5, 11].

Several methods have been reported for the synthesis of tetrahydrobenzo[*b*]pyrans and dihydropyrano[*c*]chromenes. These compounds have been synthesized in the presence of various catalysts, such as di-ammonium hydrogen phosphate (DHAP) [12], TBAB [13], K₂CO₃ under microwave irradiation [14], S-proline [15], MgO [16], and sulfonic acid functionalized silica (SiO₂-PrSO₃H) [17]. Each of these reported methods has its own merits, with at least one of the limitation of drastic condition, long reaction times, low yields, and effluent pollution.

Ammonium alum (A-Alum) with mild acidity, involatility, inexpensivity and incorrosivity is insoluble in common organic solvents and partially soluble in water [18]. Hence it is good candidate for catalysis in green organic synthesis.

To the best of our knowledge, there are no reports on the use of A-Alum in organic reactions as a catalyst.

In continuation of our research devoted to the development of green organic chemistry and one-pot multi-component reactions for the synthesis of various heterocyclic compounds [19], herein we wish to report an efficient and green procedure for the preparation of tetrahydrobenzo[*b*]pyrans and dihydropyrano[*c*]chromenes via a domino Knoevenagel-cyclocondensation reaction using (NH₄)Al(SO₄)₂·12H₂O (A-Alum) as a catalyst in aqueous medium.



EXPERIMENTAL

All of the products are known compounds and were identified by their physical and spectroscopic data with those reported in literature. Melting

* To whom all correspondence should be sent:
E-mail: mbodadgi2007@yahoo.com

points were measured by using capillary tubes on an electro thermal digital apparatus and are uncorrected. The progress of reactions was monitored by TLC using *n*-hexane/ EtOAc (1:1 v/v) as eluent. IR spectra were recorded as KBr disc on a galaxy series FT-IR 5000 spectrometer. NMR spectra were recorded on 300 MHz brucker spectrometer in DMSO-*d*₆ with TMS as an internal standard. Microanalyses were performed by the Elemental Analyzer (Elemental, Vario EL III) at the Arak University.

General procedure for the synthesis of tetrahydrobenzo[b]pyran and dihydroprano[c]chromene derivatives:

Method A: A mixture of an aldehyde (1 mmol), malononitrile (1 mmol), dimedone or 4-hydroxy coumarin (1 mmol) and A-Alum (20% mol) in 3 ml H₂O/EtOH (2:1) was refluxed with stirring for Adequate time. After the reaction completion (monitored by TLC), the reaction mixture was cooled to room temperature, filtered and washed with cool water. The crud product recrystallized with hot ethanol.

Method B: A mixture of an aldehyde (1 mmol), malononitrile (1 mmol), dimedone or 4-hydroxy coumarin (1 mmol) and A-Alum (20% mol) was heated at 100 °C under solvent free conditions. Completion of the reaction was followed by TLC, after the reaction was completed, the reaction mixture was cooled to room temperature and washed with cool water and then recrystallized with hot ethanol.

Selected data of products:

(6a): IR (KBr) (ν_{\max}): 3393, 3317, 3185, 2958, 2196, 1687, 1652, 1367 cm⁻¹. ¹H NMR (DMSO-*d*₆): δ_{H} : 0.94 (3H, s, Me), 1.04 (3H, s, Me), 2.08 (1H, d, *J* = 16.0 Hz, H-6), 2.23 (1H, d, *J* = 16.0 Hz, H-6'), 2.50 (2H, m, CH₂), 4.11 (1H, s, H-4), 7.06 (2H, br s, NH₂), 7.19 (3H, m, H-Ar), 7.33 (2H, m, H-Ar) ppm. Anal. calcd for C₁₈H₁₈N₂O₂: C, 73.45; H, 6.16; N, 9.52. Found: C, 73.97; H, 6.79; N, 9.42.

(6d): IR (KBr) (ν_{\max}): 3533, 3364, 3153, 2966, 2193, 1685, 1658, 1367 cm⁻¹. ¹H NMR (DMSO-*d*₆): δ_{H} : 1.00 (3H, s, Me), 1.06 (3H, s, Me), 2.11 (1H, d, *J* = 16.0 Hz, H-6), 2.27 (1H, d, *J* = 16.0 Hz, H-6), 2.47–2.61 (2H, m, CH₂), 4.70 (1H, s, H-4), 7.15 (2H, br s, NH₂), 7.25 (1H, d, *J* = 8.4 Hz, H-Ar), 7.39 (1H, d, *J* = 8.4 Hz, H-Ar), 7.56 (1H, s, H-Ar) ppm. Anal. calcd for C₁₈H₁₆Cl₂N₂O₂: C, 59.52; H, 4.44; N, 7.71. Found: C, 59.91; H, 4.63; N, 7.63.

(6g): IR (KBr) (ν_{\max}): 3381, 3321, 3209, 2962, 2191, 1682, 1656, 1367 cm⁻¹. ¹H NMR (DMSO-

*d*₆): δ_{H} : 0.97 (3H, s, Me), 1.06 (3H, s, Me), 2.10 (1H, d, *J* = 16.0 Hz, H-6), 2.27 (1H, d, *J* = 16.0 Hz, H-6'), 2.47–2.55 (2H, m, CH₂), 2.87 (6H, s, -N(Me)₂), 4.06 (1H, s, H-4), 6.66 (2H, d, *J* = 8.7 Hz, H-Ar), 6.95 (2H, br s, NH₂), 6.97 (2H, d, *J* = 8.7 Hz, H-Ar) ppm. Anal. Calcd for C₂₀H₂₃N₃O₂: C, 71.19; H, 6.87; N, 12.45. Found: C, 71.49; H, 6.71; N, 12.33.

(6i): IR (KBr) (ν_{\max}): 3387, 3323, 3213, 2968, 2191, 1683, 1656, 1520, 1346 cm⁻¹. ¹H NMR (DMSO-*d*₆): δ_{H} : 0.99 (3H, s, Me), 1.06 (3H, s, Me), 2.14 (1H, d, *J* = 16.0 Hz, H-6), 2.30 (1H, d, *J* = 16.0 Hz, H-6), 2.53–2.57 (2H, m, CH₂), 4.39 (1H, s, H-4), 7.24 (2H, br s, NH₂), 7.48 (2H, d, *J* = 8.4 Hz, H-Ar), 8.21 (2H, d, *J* = 8.4 Hz, H-Ar) ppm.

(5a): IR (KBr) (ν_{\max}): 3378, 3285, 3180, 2199, 1710, 1675, 1638, 1607, 1491, 1382, 1059 cm⁻¹. ¹H NMR (DMSO-*d*₆): δ_{H} : 4.45 (1H, s, H-4), 7.21–7.35 (5H, m, H-Ar), 7.42 (2H, s, NH₂), 7.44–7.68 (2H, m, H-Ar), 7.89 (1H, d, *J* = 1.5 Hz, H-Ar), 7.92 (1H, d, *J* = 1.5 Hz, H-Ar) ppm.

(5b): ¹H NMR (300 MHz, DMSO-*d*₆): δ_{H} : 3.72 (3H, s, -OCH₃), 4.40 (1H, s, H-4), 6.87 (2H, d, *J* = 8.1 Hz, H-Ar), 7.18 (2H, d, *J* = 8.1 Hz, H-Ar), 7.37 (2H, br s, NH₂), 7.45 (1H, d, *J* = 8.3 Hz, H-Ar), 7.49 (1H, t, *J* = 7.8 Hz, H-Ar), 7.70 (1H, t, *J* = 7.7 Hz, H-Ar), 7.89 (1H, d, *J* = 7.7 Hz, H-Ar) ppm.

RESULTS AND DISCUSSIONS

For the primary study, the condensation reaction of benzaldehyde with malononitrile and dimedone in the presence of A-Alum was carried out in order to optimization of reaction conditions, such as the amount of catalyst, temperature and solvent of the reaction. As shown in Table 1 and 2, the best conditions for this reaction were 20% mol of A-Alum, reflux in Water/ethanol (2:1) as a green solvent or solvent-free at 100 °C.

Table 1. Optimization of catalyst amount and temperature.

Ent.	Ar	Prod.	Solvent	Time (min)	Yield (%)
1	C ₆ H ₅	6a	EtOH/H ₂ O	110	85 ^a
2	C ₆ H ₅	6a	H ₂ O	180	65 ^a
3	C ₆ H ₅	6a	CHCl ₃	120	10 ^a
4	C ₆ H ₅	6a	CH ₃ CN	120	35 ^a
5	C ₆ H ₅	6a	EtOH	120	70 ^a

^a Aqueous medium,

^b Solvent-free medium.

To explore the generality of the reaction, we extended our study using different aromatic aldehydes containing both electron withdrawing and donating substituents to prepare a series of 2-amino-7,7-dimethyl-5-oxo-4-(aryl)-5,6,7,8-tetrahydro-4*H*-chromene-3-carbonitrile derivatives

(Table 3). Also a series of 2-amino-4-(aryl)-5-oxo-4, 5-dihydropyrano [3,2-*c*]chromene-3-carbonitrile derivatives synthesized in good yields. Condensation of aldehydes, malononitrile and 4-hydroxycoumarin under same conditions, afforded the above mentioned products (Table 4).

Table 2. Solvent selection for the reaction

Ent.	Ar	Prod.	Solvent	Time (min)	Yield (%)
1	C ₆ H ₅	6a	EtOH/H ₂ O	110	85 ^a
2	C ₆ H ₅	6a	H ₂ O	180	65 ^a
3	C ₆ H ₅	6a	CHCl ₃	120	10 ^a
4	C ₆ H ₅	6a	CH ₃ CN	120	35 ^a
5	C ₆ H ₅	6a	EtOH	120	70 ^a
6	C ₆ H ₅	6a	Neat	75	90 ^b

^a Reflux, 20% A-Alum.^b 100 °C, 20% A-Alum.**Table 3.** Synthesis of tetrahydrobenzo[b]pyran.

Ent	Ar	Prod.	Metod A		Metod B	
			Time (min)	Yield (%)	Time (min)	Yield (%)
1	C ₆ H ₅	6a	110	85	75	90
2	4-Cl-C ₆ H ₄	6b	90	92	17	93
3	4-CH ₃ O-C ₆ H ₄	6c	100	95	30	94
4	2,4-Cl ₂ -C ₆ H ₃	6d	90	85	45	90
5	3-OH-C ₆ H ₄	6e	90	80	30	91
6	2,4-(CH ₃ O) ₂ -C ₆ H ₃	6f	90	91	25	96
7	4-N(Me) ₂ -C ₆ H ₄	6g	110	89	20	87
8	2-Cl-C ₆ H ₄	6h	120	83	45	85
9	4-NO ₂ -C ₆ H ₄	6i	120	90	35	95
10	2,4-Cl ₂ -C ₆ H ₃	6j	120	91	30	92

Method A: Reaction carried out in water/ethanol, reflux, 20% A-Alum.

Method B: Reaction carried out under solvent-free condition, 100 °C, 20% A-Alum.

Table 4. Synthesis of dihydropyrano[*c*]chromenes

Ent.	Ar	Prod.	Metod A		Metod B	
			Time (min)	Yield (%)	Time (min)	Yield (%)
1	C ₆ H ₅	5a	140	83	80	90
2	4-CH ₃ O-C ₆ H ₄	5b	123	64	115	93
3	2,6-Cl ₂ -C ₆ H ₃	5c	60	52	45	90
4	3-OH-C ₆ H ₄	5d	105	43	105	89
5	2,4-(CH ₃ O) ₂ -C ₆ H ₃	5e	65	75	50	90
6	4-N(Me) ₂ -C ₆ H ₄	5f	60	79	25	94
7	2-Cl-C ₆ H ₄	5g	90	69	50	89

Method A: Reaction carried out in water/ethanol, reflux, 20% A-Alum.

Method B: Reaction carried out under solvent-free condition, 100 °C, 20% A-Alum.

CONCLUSION

We have been reported an efficient and simple method for synthesis of Tetrahydrobenzo[*b*]Pyrans and dihydropyrano[*c*]Chromenes. The use of

inexpensive and environmentally friendly catalyst, elimination of toxic solvents, using water/ethanol as a green solvent, simple workup procedure, good yields and short reaction times are some advancement of this method.

Acknowledgments: We gratefully acknowledge for financial support from the Research Council of Arak University.

REFERENCES

1. R. Ballini (ed), Eco-Friendly Synthesis of Fine Chemicals, RSC Publishing, Cambridge (UK), 2009.
2. R. N. Butler, A.G. Coyne, *Chem. Rev.*, **110**, 6302 (2010).
3. J. Zhu; H. Bienayme, (Eds.); Multicomponent Reactions; Weinheim, Germany, 2005.
4. A. Fallah-Tafti, R. Tiwari, A. N. Shirazi, T. Akbarzadeh, D. Mandal, A. Shafiee, K. Parang, A. Foroumadi, *Med. Chem.*, **7**, 466 (2011).
5. E. A. A. Hafez, M. H. Elnagdi, A. G. A. Elagamey, F. M. A. EL-Taweel, *Heterocycles*, **26**, 903 (1987).
6. T. A. Bayer, S. Schafer, H. Breyh, O. Breyhan, C. Wirths, G. A. Treiber, *Clin. Neuropathol.*, **25**, 163 (2006).
7. N. Fokialakis, P. Magiatis, L. Chinou, S. Mitaka, F. Tilleguin, *Chem. Pharm. Bull.*, **50**, 413 (2002).
8. C. Biot, G. Glorian, L. A. Maciejewski, J. S. Brocard, O. Domarle, G. Blampain, P. Blampain, A. J. Georges, H. Abessolo, D. Dive, J. Lebib, *J. Med. Chem.*, **40**, 3715 (1997).
9. L. Bonsignore, G. Loy, D. Secci, A. Calignano, *Eur. J. Med. Chem.*, **28**, 517 (1993).
10. J.G. Cannon, R.R. Khonji, *J. Med. Chem.*, **18**, 110 (1975).
11. Y. Morinaka, K. Takahashi, Jpn Patent JP520174998, (1997).
12. S. Abdolmohammadi, S. Balalaie, *Tetrahedron Lett.*, **48**, 3299 (2007).
13. J. M. Khurana, S. Kumar, *Tetrahedron Lett.*, **50**, 4125 (2009).
14. M. Kidwai, S. Saxena, *Synth. Commun.*, **36**, 2737 (2006).
15. S. Balalaie, M. Bararjanian, A. M. Amani, B. Movassagh, *Synlett*, **263** (2006).
16. M. Seifi, H. Sheibani, *Catal. Lett.*, **126**, 275 (2008).
17. G. Mohammadi Ziarani, A. Badiie, M. Azizi, P. Zarabadi, *Iran. J. Chem. Chem. Eng.*, **30**, 59 (2011).
18. J. T. Baker, Aluminum Ammonium Sulfate Material Safety Data Sheet, 2009.
19. (a) A. Mobinikhaledi, M.A. Bodaghi Fard, F. Sasani, M.A. Amrollahi, *Bulg. Chem. Commun.* **45**, 353, 2013. (b) M.A. Bodaghi Fard, A. Mobinikhaledi, M. Hamidinasab, *Synth. React. Inorg. Met.-Org. Nano-Met. Chem.*, **44**, 567 (2014)

ЕДНОСТАДИЙНА СИНТЕЗА НА ТЕТРАХИДРОБЕНЗО[*b*]ПИРАНОВИ И
ДИХИДРОПИРАНО [*c*]ХРОМЕНОВИ ПРОИЗВОДНИ С АМОНИЕВ АЛУМ В „ЗЕЛЕНА“
СРЕДА

М. А. Бодагифард*, Н. Ахади

Департамент по химия, Научен факултет, Университете в Арак, Иран.

Постъпила на 31 май, 2014 г., коригирана на 25 август 2014 г.

(Резюме)

Синтезирани са различни 4*H*-бензо[*b*]пиранови и пирано [*c*]хроменови производни при „зелени“ условия. Тези евтени, не-токсични, екологично съвместими се получават при добри до вискои добиви.

ZSM-5-SO₃H as an efficient catalyst for the one-pot synthesis of 2,4,5-trisubstituted and 1,2,4,5- tetrasubstituted imidazoles under solvent-free conditions

M. Vosoughi, F. Mohebbali, A. Pesaran Seiied Bonakdar, H. Ardeshiri Lordegani, A. R. Massah*

Department of Chemistry; Shahreza Branch, Islamic Azad University, Shahreza, Isfahan, 86145-311, Iran

Received June 5, 2014, Revised October 21, 2014

A simple one-pot three-component synthetic method is reported for the synthesis of 2,4,5-trisubstituted imidazole by three-component cyclocondensation of benzil, aromatic aldehydes and ammonium acetate under solvent-free conditions in the presence of ZSM-5-SO₃H as a catalyst. Moreover, the utility of this protocol was further explored for the one-pot, four-component synthesis of 1,2,4,5-tetrasubstituted imidazoles from benzil, aromatic aldehydes, primary amines and ammonium acetate in good to high yield and purity.

Keywords: ZSM-5-SO₃H; 2,4,5-trisubstituted imidazoles; 1,2,4,5-tetrasubstituted imidazoles; Solvent-free.

Multi-component reactions (MCRs) have proved to be remarkably successful in generating products in a single synthetic operation. These reactions are classified in various ways based on the number of components involved in the reaction or their intrinsic variability. Nowadays organic chemical syntheses involving multi-component condensation strategy attained greater value, as the target molecules are often obtained in a single step rather than multiple steps, which minimizes the tedious work-up procedures and environmentally hazardous wastes [1].

The imidazole ring system is a vital heterocyclic nucleus found in a large number of natural products and pharmacologically active compounds. These compounds are known to have several therapeutic applications such as antimicrobial [2], antitubercular [3], cytotoxic [4], anti-inflammatory [5], and anticancer [6] activities. Several methods have been reported for the construction of this important structure. The most common method for preparation of these compounds involves three- and four-component condensations of a 1,2-diketone derivative with an aldehyde, ammonium acetate and primary amine using acidic conditions, such as zeolite [7], NaHSO₄-SiO₂ [8], HClO₄-SiO₂ [9], FeCl₃-6H₂O [10], BF₃-SiO₂ [11], trifluoroacetic acid [12], zeolite supported reagents [13], dicationic magnetic ionic liquid [14], MCM-41 or *p*-TsOH [15], 1-butyl-3-methylimidazolium bromide [16], silica-bonded propylpiperazine-*N*-sulfamic [17], *N*-methyl-2-pyrrolidonium hydrogen sulfate [18], and DABCO [19]. These methods are suitable for

certain synthetic conditions; however, many of these procedures suffer from one or more disadvantages such as the use of expensive reagents, long reaction times, tedious separation procedures, and large amounts of catalyst loadings which in turn result in the generation of a large amount of wastes into the environment. Therefore, the development of mild, generalized and environmentally friendly approaches to overcome these shortcomings still remains an ongoing challenge for the synthesis of highly substituted imidazoles.

Solid acids are beginning to play a significant role in the greening of chemicals manufacturing processes. Recently, in continuation of our studies on solid acid catalysts [20], ZSM-5-SO₃H was synthesized for the first time in our group and was used in acylation of aldehydes [21] and Mannich reaction [22]. Based on these findings, we report here a simple approach for the synthesis of 2,4,5-trisubstituted imidazole (scheme 1) and 1,2,4,5-tetrasubstituted imidazoles (scheme 2) by the condensation of benzil, aldehydes, ammonium acetate and primary amines using ZSM-5-SO₃H as a mild heterogeneous catalyst.

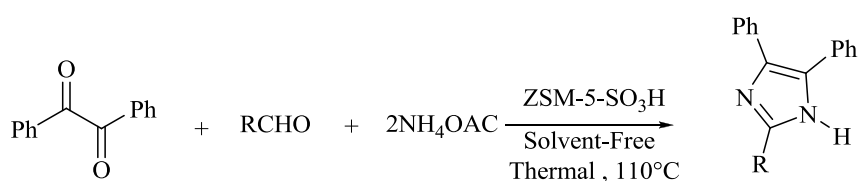
To optimize the reaction conditions including solvents, molar ratios and temperature for the synthesis of 2,4,5-trisubstituted imidazoles, the reaction of benzil, 4-chlorobenzaldehyde and ammonium acetate was chosen as a model reaction. In order to determine the most appropriate choice of solvent system, we have screened solvents such as methanol, ethanol, acetonitrile and also used solvent-free conditions. Even though the reactions in ethanol led to a high yield of the product in shorter reaction times, the maximum yield was

* To whom all correspondence should be sent:
E-mail: Massah@iaush.ac.ir

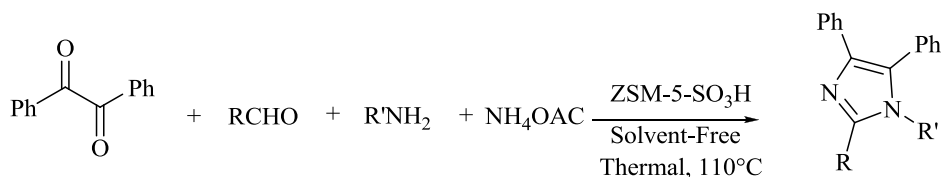
obtained under solvent-free conditions (Table 1, entry 4). Also, the reaction was examined at 50, 80 and 110 °C under solvent-free conditions (Table 1, entries 4-6). The results demonstrated that the yield at 110°C was better than those at the other temperatures. The effect of catalyst amount on the yield of reaction was also studied (Table 1, entries 4 and 7-10). When the amount of the catalyst was increased from 0.01 g to 0.03 g, the yield increased from 50 % to 90 %. Higher amounts of the catalyst did not further improve the yields. In the absence of the catalyst, the reaction proceeded sluggishly (Table 1, entry 11). So, the optimum conditions were chosen as follows: benzil (1 mmol), aldehyde (1 mmol), ammonium acetate (7 mmol) and ZSM-

5-SO₃H (0.03 g), heating at 110°C under solvent-free conditions.

We next examined a wide variety of aldehydes to establish the scope of this catalytic transformation (Table 2). Several aromatic aldehydes bearing electron donating and electron withdrawing substituents were subjected to this one-pot, three-component cyclocondensation to furnish 2,4,5-trisubstituted imidazoles in good to high yields. Various functional groups were found to be compatible under the reaction conditions. In general, the reactions were clean and no side products were detected. The aliphatic aldehydes lead to the corresponding imidazoles in lower yields in comparison to aromatic ones.



Scheme 1. ZSM-5-SO₃H catalyzed synthesis of 2,4,5-trisubstituted imidazoles



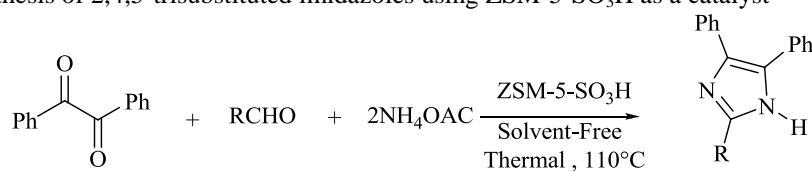
Scheme 2. ZSM-5-SO₃H catalyzed synthesis of 1,2,4,5-tetrasubstituted imidazoles

Table 1. Synthesis of imidazole under different conditions ^a

Entry	Solvent	ZSM-5-SO ₃ H (g)	Temperature (°C)	Time (min)	Yield (%) ^b
1	MeOH	0.03	65	170	33
2	EtOH	0.03	78	140	71
3	CH ₃ CN	0.03	81	200	51
4	Solvent-free	0.03	110	90	90
5	Solvent-free	0.03	50	90	56
6	Solvent-free	0.03	80	90	68
7	Solvent-free	0.01	110	90	50
8	Solvent-free	0.02	110	90	76
9	Solvent-free	0.06	110	90	90
10	Solvent-free	0.1	110	90	90
11	Solvent-free	-	110	240	20

^a 4-Chlorobenzaldehyde (1.0 mmol), benzil (1.0 mmol) and ammonium acetate (7.0 mmol)

^b Isolated yield

Table 2. Synthesis of 2,4,5-trisubstituted imidazoles using ZSM-5-SO₃H as a catalyst

Entry	Compd.	R	Time (min)	Yield ^a (%)	M.p. (°C)	
					Found	Reported [Ref.]
1	1a	4-HOC ₆ H ₄	120	71	235-239	233-234 [23]
2	1b	4-MeOC ₆ H ₄	90	85	219-222	222-223 [23]
3	1c	4-ClC ₆ H ₄	90	90	265-268	262-264 [18]
4	1d	C ₆ H ₅	130	62	269-272	267-269 [18]
5	1e	4-CH ₃ C ₆ H ₄	85	86	224-228	229-232 [27]
6	1f	4-O ₂ NC ₆ H ₄	100	73	240-243	242-243 [23]
7	1g	3-O ₂ NC ₆ H ₄	110	65	261-264	265-267 [18]
8	1h	2,4-Cl ₂ C ₆ H ₃	100	76	174-176	176-178 [18]
9	1i	3-ClC ₆ H ₄	95	81	284-287	287-289 [18]
10	1j	CH ₃ CH ₂ CH ₂	150	59	277-279	277-278 [23]

^a Isolated yield

The same reaction conditions were applied for the synthesis of 1,2,4,5-tetrasubstituted imidazoles *via* one-pot, four-component condensation of benzil (1 mmol), an aldehyde (1 mmol), a primary amine (1 mmol) and ammonium acetate (6 mmol) in the presence of 0.02 g of catalyst (Table 3). The substrate scope of the reaction was then evaluated by varying differently substituted aldehydes and primary amines including both electron-donating and electron-withdrawing groups. The use of a heterocyclic amine such as aminothiazole leads to the corresponding imidazole in high yield and purity.

To our delight, the 1,2,4,5-tetrasubstituted imidazoles were obtained in good to high yields and no side products, for example, 2,4,5-trisubstituted imidazoles, were formed.

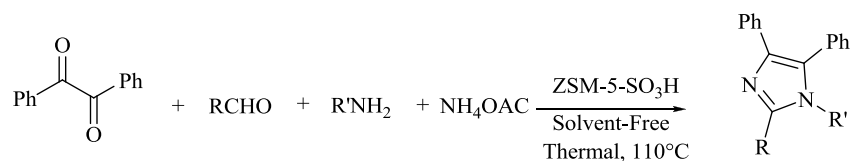
To show the merits of the present work in comparison with reported results in the literature, we compared ZSM-5-SO₃H with some reported heterogeneous catalysts in the synthesis of 2,4,5-trisubstituted and 1,2,4,5-tetrasubstituted imidazoles. As shown in Tables 4 and 5, ZSM5-

SO₃H acts as a suitable catalyst with respect to reaction times, yields of the products, temperature under solvent-free conditions.

Finally, the reusability of the catalysts was studied. For this purpose the recovered catalyst from the experiment was washed with ethyl acetate (3×5 mL), then was dried in oven at 60°C and used in the reaction. The results show that the catalyst can be reused 3 times without any modification and no significant loss of activity/selectivity performance was observed.

In summary, an efficient and environmentally friendly approach was introduced for the synthesis of imidazole derivatives *via* condensation of benzil with various aromatic aldehydes, a primary amine and ammonium acetate using ZSM-5-SO₃H as a catalyst. The solvent-free conditions, simplicity of operation, easy work-up, lower catalyst amount and cost efficiency render this approach as an interesting alternative to the existing methods.

Table 3. Synthesis of 1,2,4,5-tetrasubstituted imidazoles using ZSM-5-SO₃H



Entry	Compd.	R	R'	Time (min)	Yield (%)	M.p. (°C)	
						Found	Reported [Ref.]
1	2a	4-ClC ₆ H ₄	4-MeOC ₆ H ₄	50	94	182-185	180-183 [25]
2	2b	C ₆ H ₅	4-ClC ₆ H ₄	40	86	239-242	237-240 [25]
3	2c	4-HOC ₆ H ₄	4-ClC ₆ H ₄	30	85	203-207	207-210 [24]
4	2d	4-ClC ₆ H ₄	4-ClC ₆ H ₄	50	90	186-189	187-189 [28]
5	2e	4-ClC ₆ H ₄	C ₆ H ₅	30	78	158-160	163-165 [9]
6	2f	4-ClC ₆ H ₄	4-CH ₃ C ₆ H ₄	30	93	193-195	197-199 [18]
7	2g	4-O ₂ NC ₆ H ₄	4-MeOC ₆ H ₄	55	64	168-170	167-170 [18]
8	2h	4-MeOC ₆ H ₄	CH ₂ C ₆ H ₅	50	73	162-167	164-165 [25]
9	2i	4-CH ₃ C ₆ H ₄	C ₆ H ₅	35	91	179-183	177-180 [26]
10	2j	4-HOC ₆ H ₄	CH ₂ C ₆ H ₅	55	79	235-238	232-235 [26]
11	2k	4-ClC ₆ H ₄	aminothiazole	60	81	227-229	226-228 [24]
12	2l	C ₆ H ₅	4-CH ₃ C ₆ H ₄	30	90	165-167	168-170 [11]
13	2m	4-ClC ₆ H ₄	CH ₂ C ₆ H ₅	60	70	166-169	162-164 [23]
14	2n	C ₆ H ₅	C ₆ H ₅	40	85	218-220	220-221 [18]
15	2o	4-O ₂ NC ₆ H ₄	C ₆ H ₅	60	63	209-212	212-214 [24]
16	2p	4-HOC ₆ H ₄	C ₆ H ₅	55	77	284-289	281-283 [24]
17	2q	CH(Me) ₂	C ₆ H ₅	100	51	231-233	232-234 [25]

^a Isolated yield

Table 4. Comparison of various catalysts with ZSM-5-SO₃H in the synthesis of 2,4,5-trisubstituted imidazoles from 4-chloro benzaldehyde, benzyl and ammonium acetate

Entry	Catalyst (g)	Solvent	Temperature (°C)	Time (min)	Yield (%)	Ref.
1	InCl ₃ ·3H ₂ O	MeOH	140	540	71	[23]
2	NiCl ₂ ·6H ₂ O/Al ₂ O ₃	EtOH	80	360	80	[25]
3	ZSM-5	EtOH	80	60	80	[24]
4	Silica gel	Solvent-free	140	120	68	[18]
5	L-proline	MeOH	60	540	88	[25]
6	Pb(NO ₃) ₂	EtOH	80	300	52	[23]
7	ZSM-5-SO ₃ H	Solvent-free	110	90	90	This work

Table 5. Comparison of various catalysts with ZSM-5-SO₃H in the synthesis of 1,2,4,5-tetrasubstituted imidazole from benzaldehyde, benzil, 4-chloro aniline and ammonium acetate

Entry	Catalyst (g)	Solvent	Temperature (°C)	Time (min)	Yield (%)	Ref.
1	InCl ₃ ·3H ₂ O	MeOH	140	440	79	[23]
2	Co(NO ₃) ₂ /MCM-41	Solvent-free	120	90	11	[13]
3	Cu(NO ₃) ₂ /zeolite-HY	EtOH	70	180	53	[13]
4	SnCl ₄	Solvent-free	140	120	60	[26]
5	MgCl ₂	Solvent-free	140	120	50	[18]
6	AlCl ₃	MeOH	60	120	53	[23]
7	Cu(NO ₃) ₂ /zeolite-HY	MeOH	65	180	56	[13]
8	ZSM-5-SO ₃ H	Solvent-free	110	40	86	This work

EXPERIMENTAL

The chemicals were purchased from Merck and Aldrich and were used without additional purification. The products were characterized by comparison with authentic samples and by spectroscopy data (IR, ¹H NMR and ¹³C NMR spectra). The NMR spectra were recorded on a Bruker BioSpin GmbH 400 MHz instrument. FT-IR spectra were recorded on a Perkin Elmer spectrometer. The yields refer to isolated products after purification.

Synthesis of Catalyst

Zeolite ZSM-5 was prepared under hydrothermal conditions with SiO₂/Al₂O₃ = 80. Sodium chloride (2.50 g) and aluminum sulfate (0.59 g) were dissolved at room temperature in distilled water (10.12 g) then 1.89 g tetrapropyl ammonium bromide (TPA), distilled water (7.12 g) and sulfuric acid (1.09 g) were added to this solution and stirred to dissolve completely. At the end 15.00 g of sodium silicate was added and the synthesis was carried out under stirring at room temperature for 1 h or more to obtain a milky homogeneous mixture. Then the mixture was moved to the reactor and kept at 110 °C for 2 h and at 230 °C for 5.5 h. The solution was filtered and washed with distilled water. Template removal was performed by calcination at 550 °C for 6 h. ZSM-5-SO₃H was synthesized following the procedure previously reported by Zolfigol for the synthesis of silicasulfuric acid.

General procedure for the synthesis of 2,4,5-trisubstituted imidazoles:

Aldehyde (1mmol) and ZSM-5-SO₃H (0.03 g) were ground in a mortar for a few seconds. Then, benzil (1 mmol) and ammonium acetate (7 mmol) were added to the mixture and heated at 110 °C under solvent-free conditions. After completion of

the reaction, monitored by TLC, the mixture was cooled to room temperature and ethyl acetate (30 mL) was added and the catalyst was separated by filtration. The organic layer was washed with water (15 mL) and dried over sodium sulfate. After evaporation of the solvent the product was purified by recrystallization from ethanol.

General procedure for the synthesis of 1,2,4,5-tetrasubstituted imidazoles:

Aldehyde (1 mmol) and ZSM-5-SO₃H (0.02 g) were ground in a mortar for a few seconds. Then, benzil (1 mmol), aryl amine (1 mmol) and ammonium acetate (6 mmol) were added to the mixture and heated at 110 °C under solvent-free conditions. After completion of the reaction, monitored by TLC, the product was separated and purified as the above procedure.

Selected spectral data:

2-(4-chlorophenyl)-1-(4-methoxyphenyl)-4,5-diphenyl-1H-imidazole (2a): Yield 94%, m.p. 182-185 °C, IR (KBr, cm⁻¹): 3056, 1600, 1510, 1248; ¹H NMR (400 MHz, CDCl₃) δ (ppm) = 3.81 (s, 3H), 6.80 (d, 2H, *J* = 8.8 Hz), 6.97 (d, 2H, *J* = 8.8 Hz), 7.16 (d, 2H, *J* = 9.6 Hz), 7.21–7.32 (m, 8H), 7.41 (d, 2H, *J* = 9.3 Hz), 7.56 (d, 2H, *J* = 9.6 Hz); ¹³C NMR (100 MHz, CDCl₃) δ (ppm) = 55.4, 114.4, 126.7, 127.4, 128.1, 128.2, 128.4, 128.5, 129.1, 129.4, 129.6, 130.1, 130.5, 131.1, 131.4, 134.2, 134.3, 138.2, 145.9, 159.3;

2-(4-chlorophenyl)-1,4,5-triphenyl-1H-imidazole (2e): Yield 78%, m.p. 158-160 °C, IR (KBr, cm⁻¹): 3058, 1595, 1490, 1245; ¹H NMR (400 MHz, DMSO) δ (ppm) = 7.19 (d, 2H, *J* = 8.0 Hz), 7.23–7.34 (m, 11H), 7.36 (d, 2H, *J* = 8.0 Hz), 7.38 (d, 2H, *J* = 8.0 Hz), 7.52 (d, 2H, *J* = 8.0 Hz); ¹³C NMR (100 MHz, CDCl₃) δ (ppm) = 126.3, 126.6, 128.1, 128.3, 128.4, 128.6, 128.7, 128.8, 129.1, 129.2, 129.8, 130.2, 131.1, 131.5, 133.1, 134.2, 136.4, 136.9, 144.8;

2-(4-chlorophenyl)-4,5-diphenyl-1-p-tolyl-1H-imidazole (2f): Yield 93%, m.p. 191-193 °C, IR (KBr, cm⁻¹): 3045, 1606, 1499, 1248; ¹H NMR (400 MHz, CDCl₃) δ (ppm) = 3.36 (s, 3H), 6.94 (d, 2H, J = 8.0 Hz), 7.09 (d, 2H, J = 8.0 Hz), 7.15 (d, 2H, J = 8.0 Hz), 7.08–7.30 (m, 8H), 7.41 (d, 2H, J = 8.0 Hz), 7.61 (d, 2H, J = 8.4 Hz).

Acknowledgements: Support from Islamic Azad University, Shahreza Branch (IAUSH) Research Council is gratefully acknowledged.

REFERENCES

1. J. Zhu, H. Bienayme (Eds), Multicomponent reactions, Wiley-VCH, Weinheim, 2005.
2. L. Nagarapu, A. Satyender, B. Rajashaker, K. Srinivas, P. R. Rani, K. Radhika, G. Subhashini, *Bioorg. Med. Chem. Lett.*, **18**, 1167 (2008).
3. P. Gupta, S. Hameed, R. Jain, *Eur. J. Med. Chem.*, **39**, 805 (2004).
4. J. Arrowsmith, S. A. Jennings, A. S. Clark, M. F. G. Stevens, *J. Med. Chem.*, **45**, 5458 (2002).
5. L. Navidpour, H. Shadnia, H. Shafaroodi, M. Amini, A. R. Dehpour, A. Shafiee, *Bioorg. Med. Chem.*, **15**, 1976 (2007).
6. C. Kus, G. Ayhan-Kilcigil, S. Ozbey, F. B. Kaynak, M. Kaya, T. Coban, B. Can-Eke, *Bioorg. Med. Chem.*, **16**, 4294 (2008).
7. A. Bamoniri, B.F. Mirjalili, S. Nazemian, N.Y. Mahabadi, *Bulg. Chem. Commun.*, **46**, 79 (2014).
8. A. R. Karimi, Z. Alimohammadi, J. Azizian, A. A. Mohammadi, M. R. Mohammadzadeh, *Catal. Commun.*, **7**, 728 (2006).
9. S. Kantevari, S. V. N. Vuppapapati, D. O. Biradar, L. Nagarapu, *J. Mol. Catal. A: Chem.*, **266**, 109 (2007).
10. M. M. Heravi, F. Derikvand, M. Haghghi, *Monatsh. Chem.*, **139**, 31 (2008).
11. B. Sadeghi, B. B. F. Mirjalili, M. M. Hashemi, *Tetrahedron Lett.*, **49**, 2575 (2008).
12. M. R. Mohammadzadeh, A. Hasaninejad, M. Bahramzadeh, *Synth. Commun.*, **39**, 3232 (2009).
13. K. Sivakumar, A. Kathirvel, A. Lalitha, *Tetrahedron Lett.*, **51**, 3018 (2010).
14. B. Mombani Godajdar., A. R. Kiasat, *Iran. J. Catal.*, **3**, 229 (2013).
15. R. Hekmat Shoar, G. Rahimzadeh, F. Derikvand, M. Farzaneh, *Synth. Commun.*, **40**, 1270 (2010).
16. A. Hassaninejad, A. Zare, M. Shekouhy, J. A. Rad, *J. Comb. Chem.*, **12**, 844 (2010).
17. K. Niknam, A. Deris, F. Naeimi, F. Majleci, *Tetrahedron Lett.*, **52**, 4642 (2011).
18. H. R. Shaterian, M. Ranjbar, *J. Mol. Liq.*, **160**, 40 (2011).
19. S. Narayana Murthy, B. Madhav, Y. V. D. Nageswar, *Tetrahedron Lett.*, **51**, 5252 (2010).
20. (a) A. R. Massah, B. Asadi, M. Hoseinpour, A. Molseghi, R. J. Kalbasi, H. J. Naghash, *Tetrahedron*, **65**, 7696 (2009). (b) H. Adibi, A. R. Massah, M. B. Majnooni, S. Shahidi, M. Afshar, R. Abiri, H. J. Naghash, *Synth. Commun.*, **40**, 2753 (2010). (c) A. R. Massah, H. Adibi, R. Khodarahmi, R. Abiri, M. B. Majnooni, S. Shahidi, B. Asadi, M. Mehrabi, M. A. Zolfigol, *Bioorg. Med. Chem.*, **16**, 5465 (2008); (d) A. R. Massah, M. Dabagh, S. Shahidi, H. J. Naghash, A. R. Momeni, H. Aliyan, *J. Iran Chem. Soc.*, **6**, 405 (2009); (e) F. Kazemi, A. R. Massah, H. J. Naghash, *Tetrahedron*, **63**, 5083 (2007).
21. A. R. Massah, R. J. Kalbasi, A. Shafiei, *Monatsh. Chem.*, **143**, 643 (2012).
22. A. R. Massah, R. J. Kalbasi, N. Samah, *Bull. Korean Chem. Soc.*, **32**, 1703 (2011).
23. S. D. Sharma, P. Hazarika, D. Konwar, *Tetrahedron Lett.*, **49**, 2216 (2008).
24. A. Teimouri, A. N. Chermahini, *J. Mol. Catal. A: Chem.*, **346**, 39 (2011).
25. S. Samai, G. C. Nandi, P. Singh, M. S. Singh, *Tetrahedron*, **65**, 10155 (2009).
26. F. K. Behbahani, T. Yektanezhad, *Monatsh. Chem.*, **143**, 1529 (2012).
27. J. Safari, Z. Zarnegar, *Iran J. Catal.*, **3**, 121 (2012).
28. L. Nagarapu, S. Apuri, S. Kantevari, *J. Mol. Catal. A: Chem.*, **266**, 104 (2007).

ZSM-5-SO₃H КАТО ЕФИКАСЕН КАТАЛИЗАТОР ЗА ЕДНО-СТАДИЙНАТА СИНТЕЗА НА 2,4,5-ТРИ-ЗАМЕСТЕНИ И 1,2,4,5-ТЕТРА-ЗАМЕСТЕНИ ИМИДАЗОЛИ В ОТСЪСТВИЕ НА РАЗТВОРИТЕЛ

М. Восуги, Ф. Мохебали, А.П.С. Бонакдар, Х.А. Лордегани, А.Р. Масах *

Департамент по химия, Ислямски университет „Азад“, Клон Шахреза, Шахреза, Исфahan, Иран

Постъпила на 5 юни, 2014 г., коригирана на 21 октомври, 2014 г.

(Резюме)

В работата се съобщава за едно-стадийна три-компонентна метод за синтезата на 2,4,5-тризаместен имидазол чрез три-компонентна цикло-кондензация на бензил-ароматни алдехиди и амониев ацетат в отсъствие на разтворител в присъствие на ZSM-5-SO₃H като катализатор. Освен това прилагането на този протокол е изпитан за едно-стадийна четири-компонентна синтеза на 1,2,4,5-тетразаместени имидазолови производни от бензил, ароматни алдехиди, първични амини и амониев ацетат с високи добиви и чистота.

Exploring the interactions of enkephalin and dalargin analogues with the μ -opioid receptor

F. I. Sapundzhi¹, T. A. Dzimbova*², N. S. Pencheva¹, P.B. Milanov^{1,3}

¹South-West University "Neofit Rilski", Bulgaria, 2700 Blagoevgrad

²Institute of Molecular Biology, Bulgarian Academy of Sciences, Bulgaria, 1113 Sofia

³Institute of Mathematics and Informatics, Bulgarian Academy of Sciences, Bulgaria, 1113 Sofia

Received June 30, 2014, Accepted August 14, 2014

The μ -opioid receptor (MOR) is an important target in the search for novel analgesics. The recently published crystal structure of MOR gives the possibility of *in silico* investigations. The aim of the present work is to evaluate the method for finding the relationship between structure and activity of the selective ligands of MOR in order to develop a reliable approach for designing new potent analogues. We performed docking with enkephalin and dalargin selective analogues to MOR with GOLD 5.2 and we found a correlation between data obtained *in vitro* and the scoring function from the computational method. The docking procedure can help to explain *in vitro* results and could be successfully used in design of new agonists of the MOR receptor.

Keywords: Docking, scoring functions, μ -opioid receptor, correlation, GOLD.

INTRODUCTION

Opioid receptors are a family of G-protein-coupled receptors. This family consists of three principal receptor subtypes, termed μ -opioid receptor (MOR), δ -opioid receptor and κ -opioid receptor [1]. Opioid agonist drugs are potent analgesics that are used clinically for pain management [2]. Knockout mouse studies have shown that MOR is the opioid receptor subtype primarily responsible for mediating the analgesic and rewarding effects of opioid agonist drugs [3]. However, chronic use of opioid agonist drugs may cause tolerance and dependence, thus limiting their therapeutic efficacy [3]. Development of new opioid drugs that provide analgesia without producing dependence is important for pain treatment.

In the last decades computer-aided drug design has taken a more significant place in the field of natural sciences. Predicting the binding modes and affinities of compounds when they interact with a protein-binding site lies at the heart of structure-based drug design. Consequently, the number of algorithms available for protein–ligand docking is large. DOCK [4], FlexX [5], PRO_LEADS [6], and GOLD [7, 8] are examples of docking programs, but many more are reported in the literature (for an overview of docking strategies see Taylor *et al.* [9]). Most approaches consider the protein to be (mostly) rigid and allow the ligand to be flexible. A characteristic of a good docking program is the ability of its scoring function to score and rank

ligands according to their experimental binding affinities.

In this article, we describe the implementation of the ChemScore function as a scoring function for GOLD 5.2 and its usefulness to perform docking precisely, to predict the binding energies, and to realise the biological effects of investigated compounds.

MATERIALS AND METHODS

Objects

- *Receptor-MOR*

The crystal structure of MOR published in RCSB Protein Data Base (PDB id: 4dkl, www.rcsb.org) was used. It was obtained by X-ray diffraction with 2.8 Å resolution.

- *Ligands*

[Cys(O₂NH₂)²-Leu⁵]-enk, [Cys(O₂NH₂)²-Met⁵]-enk, dalargin, dalarginamide, dalarginethylamide, DAMGO ([D-Ala²,N-Me-L-Phe⁴,Gly-ol⁵]-enkephalin), [D-Phe⁴]-dalarginamide, [L-Ala²]-dalargin, [Leu⁵]-enkephalin, [Met⁵]-dalargin, [Met⁵]-enkephalin, N-Me-[D-Phe⁴]-dalarginamide, and N-Me-[L-Phe⁴]-dalarginamide.

Software:

- *Avogadro Version 1.1.0.*

Ligand preparation was done with Avogadro: an open-source molecular builder and visualization tool (Version 1.1.0, <http://avogadro.openmolecules.net>).

Avogadro is an advanced molecule editor and visualiser designed for use in computational

* To whom all correspondence should be sent:
E-mail: tania_dzimbova@abv.bg

chemistry, molecular modeling, bioinformatics, materials science, and related areas. It offers flexible high-quality rendering and powerful plugin architecture. The Molecular builder/editor is developed as a cross-platform for Windows, Linux, and Mac OS X. All source codes are available under the GNU GPL. Plugin architecture for developers includes: rendering, interactive tools, commands, and Python scripts. The Avogadro python API (Application-Programming Interface) resembles the [C++ API] as much as possible. This means that the C++ documentation also applies to Python. In addition to serving as a set of user-level tools, Open Babel offers a C++ library and interface in other languages (e.g., Perl and Python) for general chemical software development, both in-house and to encourage open source chemistry packages.

- **GOLD 5.2**

GOLD 5.2 has proven successful in virtual screening, lead optimisation, and identifying the correct binding mode of active molecules. GOLD 5.2 is highly configurable allowing full advantage to be taken of the knowledge of a protein-ligand system in order to maximise docking performance. GOLD 5.2 enables complete user control over speed *versus* accuracy settings, from efficient virtual screening of large compound libraries, to highly accurate exhaustive sampling for lead optimisation. With a wide range of available scoring functions and customisable docking protocols, GOLD 5.2 provides consistently high performance across a diverse range of receptor types. Most parts of the GOLD 5.2 program have been described by Jones et al. [7,8]. Like all other docking programs, GOLD 5.2 consists of three main parts.

The first part is a *scoring function* to rank different binding modes. The ChemScore scoring function [10] estimates the total free energy change that occurs on ligand binding:

$$(1) \Delta G_{binding} = \Delta G_0 + \Delta G_{hbond} S_{hbond} + \Delta G_{metal} S_{metal} + \Delta G_{lipo} S_{lipo} + \Delta G_{rot} H_{rot}$$

where S_{hbond} is score for hydrogen bonding, S_{metal} is score for acceptor-metal bonding, S_{lipo} is lipophilic interactions, H_{rot} –loss of conformational entropy of the ligand upon binding to the protein, and ΔG are coefficients derived from a multiple linear regression analysis. The expression for the ChemScore function [10] was adapted for docking by Baxter *et al.* [11], where they added the following three elements to the so called free energy of binding of a ligand to a protein ($\Delta G_{binding}$): a protein–ligand clash–energy term, (E_{clash}), a ligand–

internal–energy term, (E_{int}) and a covalent energy term, (E_{cov}):

$$(2) \Delta G'_{binding} = \Delta G_{binding} + E_{clash} + E_{int} + E_{cov}$$

The second part is a *mechanism for placing the ligand* in the binding site. GOLD 5.2 uses a unique method to do this, which is based on fitting points. It adds fitting points to hydrogen-bonding groups on the protein and ligand, and maps acceptor points on the ligand on donor points in the protein and *vice versa*. Additionally, GOLD 5.2 generates hydrophobic fitting points in the protein cavity onto which the ligand CH groups are mapped.

The last part is a *search algorithm* to explore possible binding modes. GOLD 5.2 uses a genetic algorithm in which the following parameters are modified/optimised: - dihedrals of ligand rotatable bonds; - ligand ring geometries (by flipping ring corners); - dihedrals of protein OH groups and NH_3^+ groups; - the mappings of the fitting points (i.e., the position of the ligand in the binding site). Of course, at the start of a docking run, all these variables are randomised.

Molegro Molecular Viewer (MMV)

MMV is an application for studying and analysing how ligands interact with macromolecules. MMV can be used to: (1) inspect docking results consisting of high-scoring poses found by Molegro Virtual Docker (MVD) – the molecular docking software product offered by Molegro; (2) inspect and visualize molecular structures obtained from other sources, such as the Protein Data Bank.

The main focus of MVD and MMV is on studying protein-ligand interactions. MMV does not currently support DNA and RNA molecules. The MolDock scoring function (MolDock Score) used by MVD [12] is derived from the PLP scoring functions originally proposed by Gehlhaar *et al.* [13, 14] and later extended by Yang *et al.* [15]. The MolDock scoring function further improves these scoring functions with a new hydrogen bonding term and new charge schemes. The docking scoring function, E_{score} is defined by the following energy terms:

$$(3) E_{score} = E_{inter} + E_{intra}$$

where E_{inter} is the ligand-protein interaction energy and E_{intra} is internal energy of the ligand.

- **GraphPad Prism®**

GraphPad Prism combines non-linear regression (curve fitting), basic biostatistics, and scientific graphing (www.graphpad.com). Prism uses the term

“analyze” more generally than many programs. The term includes data manipulation (i.e. mathematical transforms) as well as statistical analyses and regression. Prism quantifies correlations by calculating the Pearson correlation coefficient, r . In statistics, the Pearson product-moment correlation coefficient (sometimes referred to as the PPMCC or PCC, or Pearson's r) is a measure of the correlation (linear dependence) between two variables X and Y , giving a value between +1 and -1 inclusive. It is widely used in science as a measure of the strength of linear dependence between two variables. Pearson's correlation coefficient between two variables is defined as the covariance of the two variables divided by the product of their standard deviations. The form of the definition involves a "product moment" i.e. the mean (the first moment about the origin) of the product of the mean-adjusted random variables; hence the modifier *product-moment* in the name. Pearson's correlation coefficient when applied to a sample is commonly represented by the letter r and may be referred to as the *sample correlation coefficient* or the *sample Pearson correlation coefficient*. We can obtain a formula for r by substituting estimates of the covariance and variances based on a sample into the formula above. That formula for r is:

$$(4) r = \frac{\sum_{i=1}^n (X_i - \bar{X})(Y_i - \bar{Y})}{\sqrt{\sum_{i=1}^n (X_i - \bar{X})^2} \sqrt{\sum_{i=1}^n (Y_i - \bar{Y})^2}}$$

Concerning the choice of the criterion it has to be kept in mind that the Spearman correlations are based on ranks, not actual values, and so it could be assumed that in our investigation, the proper criterion would be that of Pearson.

- *Docking of ligands*

Thirteen peptides ([Cys(O₂NH₂)²-Leu⁵]-enk, [Cys(O₂NH₂)²-Met⁵]-enk, dalargin, dalarginamide, dalarginethylamide, DAMGO, [D-Phe⁴]-dalarginamide, [L-Ala²]-dalargin, [Leu⁵]-enkephalin, [Met⁵]-dalargin, [Met⁵]-enkephalin, N-Me-[D-Phe⁴]-dalarginamide, and N-Me-[L-Phe⁴]-dalarginamide) were chosen for docking with the receptor. All of them were synthesised, *in vitro* biologically tested, and have already been published [16, 17]. Docking was carried out with GOLD 5.2 software, which uses a generic algorithm and considers full ligand conformational flexibility and partial protein flexibility. From the literature [18], the binding site for MOR was defined as residues within 10 Å radius of aspartic acid of the third TM domain, which is involved in the most crucial interaction. In the case of MOR this is Asp147. The ChemScore algorithm was used and scoring function was calculated for each ligand. The conformations of

the ligands with best scoring functions were selected and parameters of the scoring functions were used in order to find correlations between them and the *in vitro* results (Table 1).

RESULTS AND DISCUSSION

Docking results

Docking was performed with MOR and all 13 ligands. The results of docking studies of ligands are described below and the best and the worst of them are presented in Fig. 1.

All of the ligands bind to the receptor by forming many H-bonds. A very important residue in the receptor sequence is Asp147, which forms a salt bridge with NH₃⁺ of the ligand's molecule. Less potent MOR ligand N-Me-[L-Phe⁴]-dalarginamide does not bind to Asp147. However the effect of the compounds is not connected to this interaction, because in the case of dalarginamide there is no such interaction, but it is still very potent. A key part of the ligand structure is the phenolic hydrogen group (Tyr residue). In all cases, except for dalargin and [D-Phe⁴]-dalarginamide, it binds to different residues in the receptor structure.

The best poses obtained from docking for each ligand with MOR are described in Table 2 and the ligands with the best and the worst scoring functions are presented in Fig. 1.

According to this observation at least one of these interactions must be present in order to have some biological effect.

Number of interactions does not correlate with biological activity, only their strength is important. All the potent ligands bind to MOR electrostatically.

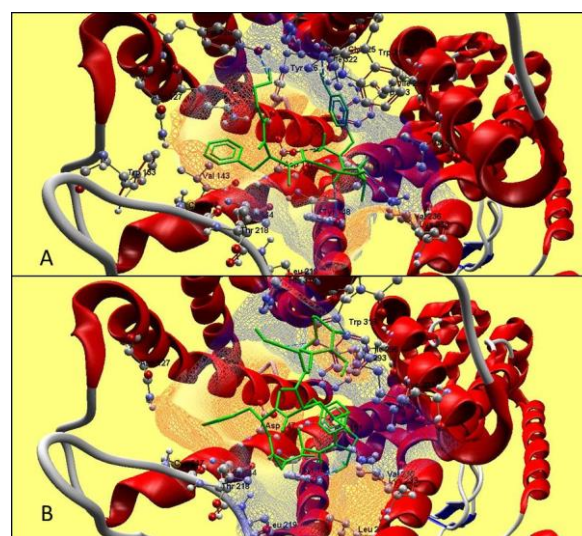


Fig. 1. Ligands with the best (A – DAMGO) and the worst (B–[D-Phe⁴]-dalarginamide) scoring functions.

Table 1. The inhibitory effect (IC₅₀, nM) [17, 18] of: - dalargin, its analogues, endogenous ligands – [Leu⁵]-enkephalin and [Met⁵]-enkephalin and μ -selective ligand – DAMGO, on electrically evoked contractions of the myenteric plexus-longitudinal muscle of the guinea-pig (μ -selective tissue).

Ligands	IC ₅₀ , (nM)	Score	Total Energy
[Cys(O ₂ NH ₂) ² -Leu ⁵]-enk	3960±740	20.44	-111.281
[Cys(O ₂ NH ₂) ² -Met ⁵]-enk	1378±245	19.6	-107.904
Dalargin	12.3±1.7	22.05	-135.245
Dalarginamide	5.8±0.7	20.67	-148.221
Dalarginethylamide	6.0±0.7	28.75	-163.106
DAMGO	5.8±0.4	29.02	-93.278
[D-Phe ⁴]-Dalarginamide	5300±408	14.31	-115.856
[L-Ala ²]-Dalargin	234±46	21.28	-130.171
[Leu ⁵]-enkephalin	65.3±8.2	25.95	-148.483
[Met ⁵]-dalargin	11.9±1.7	23.27	-173.298
[Met ⁵]-enkephalin	28.6±8.4	25.11	-120.651
N-Me-[D-Phe ⁴]-Dalarginamide	3350±850	19.17	-115.122
N-Me-[L-Phe ⁴]-Dalarginamide	0.57±0.08	20.08	-107.216

Table 2. Interactions of ligands with MOR.

Designations: the symbols in *italic* are the Asp residue in the binding site of the MOR, while the Tyr residue of the ligand molecule is shown in **bold**.

Ligand	Number of H-bonds	Residues and groups involved in interactions
[Cys(O ₂ NH ₂) ² -Leu ⁵]-enk	5	Tyr128 – SO, Asp147 – COOH, Asp147 – OH (Tyr) , Trp318 – SO, Tyr326 – COOH
[Cys(O ₂ NH ₂) ² -Met ⁵]-enk	7	Gln124 – COOH, Tyr128 – COOH, Tyr128 – CO, Asp147 – NH ₃ ⁺ , Leu219 – SO, Lys233 – CO, His297 – OH (Tyr)
Dalargin	4	Tyr128 – NH, Asp147 – NH ₃ ⁺ , Lys233 – COOH, Tyr326 – CO
Dalarginamide	8	Tyr128 – CO, Tyr148 – NH, Tyr148 – NH ₃ ⁺ , Leu219 – CO, 2 H-bonds His297 – OH (Tyr) , Trp318 – CO, Tyr326 – CO
Dalarginethylamide	7	Tyr128 – CO, Tyr148 – NH ₃ ⁺ , Lys233 – CO, 2 H-bonds His297 – OH (Tyr) , Gln314 – Gu, Trp318 – CO
DAMGO	5	Tyr128 – OH, Asp147 – NH ₃ ⁺ , Tyr148 – CO, Ile322 – OH (Tyr) , Lys233 – CO
[D-Phe ⁴]-Dalarginamide	4	Tyr148 – NH ₃ ⁺ , Tyr148 – NH, Trp318 – CO, His319 – NH ₂ (amide)
[L-Ala ²]-Dalargin	7	Tyr128 – COOH, Asp147 – NH ₃ ⁺ , Tyr148 – CO, Lys233 – CO, Trp318 – COOH, Cys321 – OH (Tyr) , Ile322 – OH (Tyr)
[Leu ⁵]-enkephalin	5	Gln124 – COOH, Tyr128 – COOH, Asp147 – NH ₃ ⁺ , His297 – OH (Tyr)
[Met ⁵]-dalargin	8	Asn127 – COOH, Asp147 – NH ₃ ⁺ , 2 H-bonds Asp147 – Gu-group, Tyr148 – CO, Cys217 – COOH, Ile322 – OH (Tyr) , Tyr326 – OH (Tyr)
[Met ⁵]-enkephalin	5	Asp147 – NH, Asp147 – NH ₃ ⁺ , Cys217 – COOH, Leu219 – COOH, Ile322 – OH (Tyr)
N-Me-[D-Phe ⁴]-Dalarginamide	5	Asp147 – NH ₃ ⁺ , Tyr148 – CO, Lys233 – CO, Trp318 – CO, Ile322 – OH (Tyr)
N-Me-[L-Phe ⁴]-Dalarginamide	6	Asp147 – NH ₂ (amide), Tyr148 – NH, Lys233 – CO, Ile306 – OH (Tyr), 2 H-bonds Ile322 – Gu –group

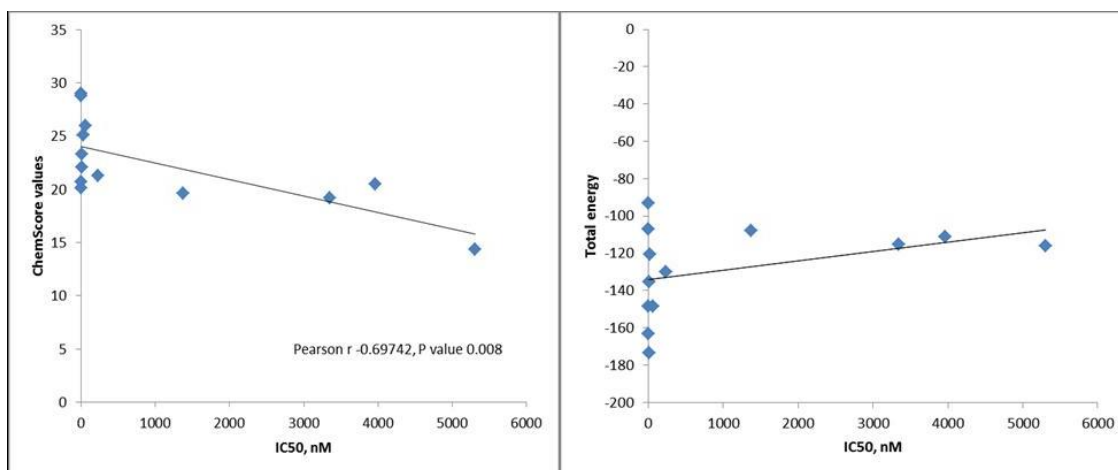


Fig. 2. Pearson's correlation between: A- IC₅₀ and ChemScore function; and B - IC₅₀ and Total energy.

Correlations

Correlations of docking data and *in vitro* experiments results were performed with GraphPad Prism 3.0. Scoring function was taken for all compounds and compared with the results of *in vitro* experiments. Good Pearson's correlation was obtained between scoring function from the GOLD5.2 docking procedure and IC₅₀ value in the guinea-pig myenteric plexus.

Total energies of all compounds were calculated in MMV after docking (MolDoc algorithm). They were also compared with the results from *in vitro* experiments, but the correlation was not significant (Pearson $r = 0.69742$, P value = 0.008). (Fig. 2).

According to the correlations obtained, we can conclude that the ChemScore algorithm is more suitable for docking studies of MOR with this series of enkephalin analogues, as compared with MolDoc algorithm.

CONCLUSIONS

Previously published results from *in vitro* experiments significantly correlate with docking data obtained with GOLD5.2, using the ChemScore algorithm. The docking procedure can help to explain *in vitro* results and could be successfully used for *in silico* design of new potent agonists of μ -opioid receptor, saving time, experimental animals and expense.

Acknowledgments: This work is partially supported by the project of the Bulgarian National Science Fund, entitled: "Bioinformatics research: protein folding, docking and prediction of biological activity", code NSF I02/16, 12.12.14.

REFERENCES

1. P.Y. Law, Y.H. Wong, H.H. Loh, *Ann.Rev.Pharmacol.Toxicol.*, **40**, 389 (2000).
2. J.K. Zubietta, Y.R. Smith, J.A. Bueller, Y. Xu, M.R. Kilbourn, D.M. Jewett, C.R. Meyer, R.A. Koeppe, C.S. Stohler, *Science*, **293**, 311 (2001).
3. H.W.D. Matthes, R. Maldonado, F. Simonin, O. Valverde, S. Slowe, I. Kitchen, K. Befort, A. Dierich, M. Le Meur, P. Dollé, E. Tzavara, J. Hanoune, B.P. Roques, B.L. Kieffer. *Nature*, **383**, 819 (1996).
4. S. Makino, I. D. Kuntz, *J. Comput. Chem.*, **18**, 1812 (1997).
5. M. Rarey, B. Kramer, T. Lengauer, G. Klebe, *J. Mol. Biol.*, **261**, 470 (1996).
6. C.A. Baxter, C.W. Murray, D.E. Clark, D.R. Westhead, M.D. Eldridge, *Proteins*, **33**, 367 (1998).
7. G. Jones, P. Willett, R.C. Glen, A.R. Leach, R. Taylor, *J. Mol. Biol.*, **267**, 727 (1997).
8. G. Jones, P. Willett, R.C. Glen, *J. Mol. Biol.*, **245**, 43 (1995).
9. R.D. Taylor, P.J. Jewsbury, J.W. Essex, *J. Comput.-Aided Mol. Des.*, **16**, 151 (2002).
10. M.L. Verdonk, J. C. Cole, M.J. Hartshorn, C.W. Murray, R.D. Taylor, *Proteins*, **52**, 609 (2003).
11. C. A. Baxter, C. W. Murray, D. E. Clark, D. R. Westhead, M. D. Eldridge, *Proteins*, **33**, 367 (1998).
12. R. Thomsen, M. H. Christensen, *J. Med. Chem.*, **49**, 3315 (2006).
13. D. K. Gehlhaar, G. Verkhivker, P. A. Rejto, D. B. Fogel, L. J. Fogel, S. T. Freer, Proceedings of the Fourth International Conference on Evolutionary Programming, 1995, p. 615.
14. D. K. Gehlhaar, D. Bouzida, P. A. Rejto, Proceedings of the Seventh International Conference on Evolutionary Programming, 1998, p. 449.
15. J-M. Yang, C-C. Chen, *Proteins*, **55**, 288 (2004).
16. N. Pencheva, J. Pospínek, L. Hauzerova, T. Barth, P. Milanov, *Br. J. Pharmacol.*, **128**, 569 (1999).
17. N. Pencheva, L. Vezenkov, E. Naydenova, P. Milanov, T. Pajpanova, S. Malamov, L. Bojkova, *Bul. Chem. Comm.*, **33**, 47 (2001).
18. K. Befort, L. Tabbara, S. Bausch, C. Chavkin, C. Evans, B. Kieffer, *Mol. Pharmacol.*, **49**, 216 (1996).

ИЗСЛЕДВАНЕ НА ВЗАИМОДЕЙСТВИЯТА НА ЕНКЕФАЛИНОВИ И ДАЛАРГИНОВИ АНАЛОЗИ С μ -ОПИОИДЕН РЕЦЕПТОР

Ф. И. Сапунджи¹, Т. А. Дзимбова², Н. С. Пенчева¹, П. Б. Миланов^{1,3}

¹Югозападен Университет „Неофит Рилски“, България, 2700, Благоевград

²Институт по молекулярна биология „Румен Цанев“, БАН, България, 1113, София

³Институт по математика и информатика, БАН, България, 1113, София

Постъпила на 30 юни, 2014 г., приета на 14 август 2014 г.

(Резюме)

Мюопиоидният рецептор (МОР) е особено важен в процеса на търсене на нови аналгетици. Наскоро публикуваната кристална структура на МОР дава възможност за *in silico* изследвания. Целта на представената работа е да се оцени метода за намиране на връзката структура-активност на селективните лиганди на МОР и да се разработи надежден подход за създаване на нови мощни аналози. Проведени са докинг изследвания на енкефалинови и даларгинови селективни МОР аналози с GOLD 5.2. и е установена корелация между данните получени от *in vitro* тестовете и оценъчната функция. Докинг процедурата може да помогне за обясняването на резултатите от *in vitro* тестовете и за успешно използване при дизайна на нови агонисти на МОР.

Synthesis, characterization and melt functionalization of high density poly (ethylene) with zinc salt

V. Parthasarathy¹, V. Dhanalakshmi², R. Anbarasan^{2*}

¹Department of Physics, Hindustan University, Padur – 603 103, Chennai, Tamilnadu, India.

²Department of Polymer Technology, Kamaraj College of Engineering and Technology, Virudhunagar – 626 001, Tamilnadu, India.

Received December 9, 2013 Revised October 9, 2014

Zinc dimethacrylate (Zn DMA) was synthesized by a chemical method and characterized by different analytical tools like Fourier transform infrared spectroscopy (FTIR), X-ray diffraction (XRD) analysis, differential scanning calorimetry (DSC) and high resolution transmission electron microscopy (HRTEM). Synthesized Zn DMA was melt-functionalized with high density polyethylene (HDPE) at 160 °C in nitrogen atmosphere. For melt functionalization reaction, dicumyl peroxide initiator (DCP) and Zn DMA were used in 1:1 ratio. FTIR spectroscopy was used to confirm the quantitative chemical grafting of Zn DMA onto HDPE backbone. FTIR-Relative Intensity (FTIR-RI) method was used to find out the order of melt functionalization reaction. The results were analyzed and critically compared with literature reports. HRTEM report confirmed the chemical grafting of Zn DMA onto HDPE backbone. A plausible reaction mechanism was proposed.

Key Words: Zinc dimethacrylate, FTIR, DSC, HRTEM, Melt functionalization

INTRODUCTION

Recently, many astonishing industrial developments have been registered particularly in the engineering plastic field because of the rapidly increasing use of plastics in varied applications in the automobile and packaging sectors. However, plastics are inactive towards bio-degradability due to the absence of functional groups in their backbone thus causing environmental pollution. Melt grafting is a way to minimize the undesired properties by introducing additional functions in a polymer. By using the melt functionalization method, functional compounds are chemically grafted onto the backbone of polyolefins to make them environment friendly, i.e., to make them active towards the bio-degradation process. Different techniques are available for the functionalization process. For example, Garmabi and co-workers [1] reported the free radical grafting of glycidyl methacrylate onto HDPE by the response surface method. PE backbone was modified with heparin for the improvement of antithrombogenicity [2]. HDPE was grafted with acrylic acid [3], chloromethyl styrene [4], epoxide [5] ethylmercapto propionate [6], butyl-3-mercapto propionate and ethyl-2-mercapto propionate [7]. Currently, melt grafting of metal salts onto the polyolefin backbone is a fascinating field of

research because of their ester functionalization and active double bond present as a side chain for further structural modification. The recent literature indicates that different metal salts were synthesized, characterized and grafted onto polyolefin backbone [8, 9]. In 2005, Sadeghi [10] reported on the synthesis and characterization of Zn salts containing polymerizable double bond. Poly(siloxane)-Zn DMA composites were prepared and characterized by various analytical tools [11]. Other authors also reported on the synthesis, characterization and application of Zn DMA [12-15]. The thorough literature survey did not reveal, however, reveal any report on the synthesis, characterization and melt grafting of zinc dimethacrylate (Zn DMA) onto HDPE backbone in the presence of dicumyl peroxide as a free radical initiator. In the present investigation, we successfully synthesized, characterized and grafted Zn DMA onto HDPE in the presence of dicumyl peroxide (DCP) as a free radical initiator at 160 °C in nitrogen atmosphere.

After the melt functionalization process, the amount of Zn DMA grafted onto HDPE backbone can be determined by chemical or instrumental analytical methods. Generally, the chemical methods cause environmental pollution because of the utilization of toxic and hazardous solvents. The instrumental analytical methods are eco-friendly and inexpensive and provide more accurate results. For these reasons, we preferred the FTIR

* To whom all correspondence should be sent:
E-mail: anbu_may3@yahoo.co.in

spectroscopy method to find out the amount of ester grafted onto HDPE backbone. FTIR spectroscopy is used for both qualitative [16,17] and quantitative [18-25] analysis. Recently, Kaith *et al.* [26] and Chauhan *et al.* [27-29] explained the thermal properties of structurally modified polymers.

No report was found in the literature on the FTIR-RI based determination of kinetics of melt functionalization of Zn DMA onto HDPE backbone. The novelty of the present investigation is the conversion of non-biodegradable HDPE into biodegradable, processable and eco-friendly HDPE by a simple melt functionalization reaction. Moreover, metal salts are also eco-friendly. The FTIR-RI method was used to determine the amount of melt grafted Zn DMA onto HDPE backbone. In such a way, environmental issues related to the plastic pollution can be solved.

MATERIALS AND METHODS

Zinc carbonate (SD Fine Chemicals, AR grade, India) and methacrylic acid (MA, SD Fine Chemicals) were used as received. High density poly(ethylene) (HDPE, Rayson, India, of average molecular weight 1,25,000 Da) was purified by the procedure followed in our earlier publication [5]. Toluene (Chemspure, AR, India) and acetone (Merck) were used without further purification. Dicumyl peroxide (DCP, Across Chemicals, UK) and cyclohexane (Paxy chemicals, AR, India) were used as received.

Purification of HDPE

5g of HDPE powder sample was dissolved in 100 mL of toluene at 130 °C for 3h in order to remove antioxidants added during its long period of storage. During the dissolution process, the toluene solvent was boiled and evaporated. In order to avoid the loss of solvent molecules, the condenser unit was circulated with cold water. After dissolving the HDPE powder samples in toluene, 800 mL of acetone was added to precipitate the HDPE [5]. The contents were filtered and dried at 60 °C for 24 h under vacuum. The dissolution and precipitation processes were repeated thrice to further purify the HDPE. Finally, the dried samples were weighed and stored in a zipper bag.

Synthesis of zinc dimethacrylate (Zn DMA)

10g ZnCO₃ was dissolved in 100 mL of 0.01M HCl solution in a three-necked round bottom (RB) flask. 10 mL of methacrylic acid was dropwise added to the acidified ZnCO₃ solution followed by 0.03 g of antimony trioxide, the esterification catalyst, to catalyze the metal salt formation

process. The contents were sparged with nitrogen gas to create an inert atmosphere inside the RB flask. The latter was connected to a water condenser and the solution was boiled with vigorous stirring at 90 °C for 3h. There is a chance for the polymerization of MA under these conditions, but due to the dominant reaction of zinc chloride with methacrylic acid, the double bond remains unaltered. During this reaction, HCl is obtained as a by-product. Zn DMA thus formed is insoluble in water and was hence purified from HCl by repeated washing with doubly distilled water. Finally, the Zn DMA was washed with acetone and the sample was dried, weighed and stored in a zipper bag. Synthesis of Zn DMA and melt functionalization with HDPE are the novel contributions of the present investigation.

Synthesis of HDPE-g-Zn DMA

1g of pure HDPE powder sample was mixed with 1% w/w of Zn DMA in 25 mL of cyclohexane-dichloromethane (1:9 v/v) solvent mixture in a 100 mL beaker under mild stirring. Then 1% w/w of DCP was added to the contents of the beaker and the stirring was continued for further 1h. The solvent mixture was used to distribute the DCP and Zn DMA onto HDPE backbone uniformly, otherwise agglomeration would occur. In the present investigation, both DCP and ester were used in equal concentrations at a 1:1 ratio, after many trial experiments. DCP was selected as a free radical initiator due to its normal dissociation rate at 160 °C with minimum side products. After 1h of mixing, the solvents dichloromethane and cyclohexane were removed by rotary evaporation. The complete removal of the solvent mixture from the reaction mixture was confirmed by the constant weight. Then the reaction mixture was transferred to a test tube reactor and de-aerated for 30 min with sulphur-free nitrogen gas. After degassing, the temperature of the reactor was raised to 160 °C (at a heating rate of 10 °C/min) for 2.5 h without stirring. During the melt functionalization process, the same was dissolved in the molten HDPE and produced a homogeneous medium. After the melt functionalization process, the reactor was removed from the oil bath, cooled to room temperature and the samples were collected and cut into small pieces. These were put in toluene at 130 °C for 30 min for the purpose of isolation. The functionalized, non-cross-linked samples were dissolved in toluene, while the functionalized cross-linked samples did not dissolve in toluene. The dissolved samples were re-precipitated by adding 600 mL of acetone and the cross-linked samples were isolated. It is very difficult to isolate the non-cross linked HDPE from

the functionalized HDPE because of its solubility. Even after the functionalization process, the grafting occurred in a random way. The non-cross linked sample was collected and dried under vacuum at 60 °C. After drying, the sample was weighed and stored in a zipper bag. FTIR spectrum was recorded and quantitative calculations were done with the non-cross linked, functionalized polymers.

Characterization

FTIR spectra were recorded on a 8400 S Shimadzu FTIR spectrometer in KBr pellets in the range from 400 to 4000 cm⁻¹. 7 mg of metal salt functionalized HDPE sample was grinded with 200 mg of KBr and made as a pellet under 750 tons of pressure. In order to avoid errors while recording the FTIR spectrum, corrected peak areas were considered. To cross check the corrected peak area values, the FTIR spectra were recorded for the same sample disc in different parts. After proper base line correction (to avoid error) with the aid of FTIR software, the same corrected peak area values were obtained. FTIR spectrum was recorded thrice for the same sample disc and the same corrected peak area values have been obtained. In such a way, the errors were nullified. Further the efficiency of FTIR software was cross checked manually by predicting the lower and upper limits and the corrected peak area was determined. In this case also we got the same corrected peak area value as reported previously. Three-point (4000, 2000 and 450 cm⁻¹) baseline correction was made to nullify the error in peak area measurement for accurate calculation. For the quantitative determination of % ester grafting, the following corrected areas of the peaks, which were assigned at 1730 (C=O) and 720 (C-H out of plane bending vibration) cm⁻¹ were determined and the relative intensity (RI) was calculated as mentioned below. For the RI measurement, the C-H bending mode appeared at 1450 cm⁻¹ can also be considered because of its sharpness and more dense nature. The present investigation followed the literature report [5, 6] strictly because of the availability of proportionality constant for the A₁₇₃₀/A₇₂₀.

$$RI \text{ of carbonyl ester } (RI_{[C=O/C-H]}) = A_{1730}/A_{720} \dots (1)$$

$$\% \text{ Ester grafting} = \frac{RI_{[C=O/C-H]} \times W}{C \times 1.5} \times 100 \dots (2)$$

where, W is the weight of non-cross linked ester grafted polymer taken for FTIR study, C is the % weight of peroxide used, 1.5 is the proportionality constant as mentioned in our earlier publication

[20]. During the melt functionalization reaction, gel formation due to the cross-linking (C.L.) reaction is also possible. At higher degree of functionalization, the % C.L. was low. The cross-linked gel was insoluble in any of the solvents available at the laboratory. For the ease of dissolution purpose, we chose the soluble part of the functionalized HDPE sample alone. At the same time, melt functionalization occurred in the cross-linked gel too. In the present investigation, we considered the non-cross linked HDPE with ester functionalized samples only. The % C.L. was determined by the following formula:

$$\% \text{ cross-linking} = \frac{[\text{Weight of polymer taken for functionalization}] - [\text{Weight of non-cross linked polymer obtained after functionalization}]}{\text{Weight of polymer taken for functionalization}} \times 100 \dots (3)$$

DSC of the sample was recorded using the Universal V4.3A TA instrument under nitrogen atmosphere at a heating rate of 10 °C/min from room temperature to 300 °C. XRD was recorded using the Rigaku Rint 2000 (Japan) diffractometer at room temperature with CuKα1 radiation in the 2 theta value range of 20 to 60°. The voltage and current of X-ray tubes were 40 kV and 100 mA, respectively. Elemental analysis was carried out using Elementor GmbH Vario El instrument. Synthesized nano material topography and size were observed by HRTEM on a JEM-200 CX transmission electron microscope.

RESULTS AND DISCUSSION

For the sake of convenience, the results and discussion part is sub-divided in: 1) synthesis and characterization of Zn DMA and 2) melt surface grafting of Zn DMA onto HDPE backbone.

Synthesis and characterization of Zn DMA

FTIR study

Figure 1 shows the FTIR spectrum of Zn DMA. The important functional groups present in Zn DMA are characterized below. The Zn DMA spectrum contains free hydroxyl stretching (3617 cm⁻¹), C-H symmetric stretching (2842 cm⁻¹), C-H anti-symmetric stretching (2926 cm⁻¹), C=O stretching (1738 cm⁻¹), C=C stretching (1646 cm⁻¹), C-H bending vibration (1562 cm⁻¹), C-O-C linkage (1141 cm⁻¹), C-H out of plane bending vibration (814 cm⁻¹) and Zn-O stretching (460 cm⁻¹). Appearance of these peaks confirmed the chemical functionalities of Zn DMA. The hydroxyl stretching is associated with the intercalated water molecules in Zn DMA [30] and the presence of the same can be further confirmed by DSC analysis.

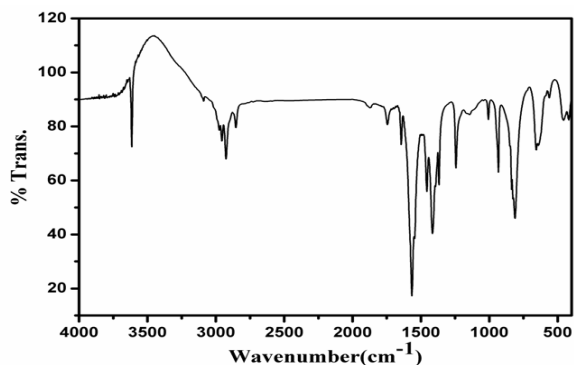


Fig. 1. FTIR spectrum of Zn DMA

DSC study

Figure 2 shows the DSC of Zn DMA. The DSC thermogram exhibits two endothermic peaks at 179.5 °C and 235.5 °C for the removal of intercalated water molecules and the melting temperature (T_m) of Zn DMA respectively. Recently, Anbarasan and co-workers [25] reported the DSC of Ca DMA with very high melting temperature. The present system also yielded a similar result.

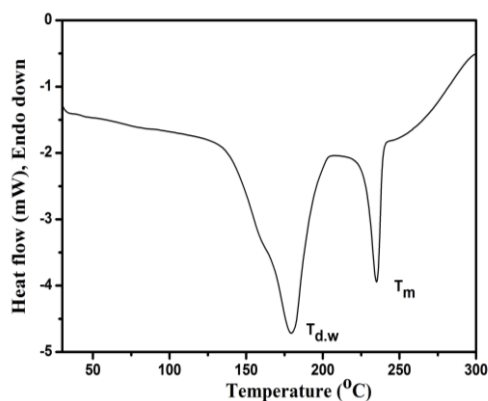


Fig. 2. DSC of Zn DMA

XRD analysis

Figure 3 represents the XRD of Zn DMA. The diffractogram shows many sharp crystalline peaks of Zn DMA. This confirmed that Zn DMA is a crystalline powder. Appearance of a peak at the 2 theta value of 22.80° confirmed the presence of d_{111} crystal plane. Other important crystal planes such as d_{100} (31.6°) and d_{101} (36.1°) were also available. Thus, the XRD confirmed the highly crystalline nature of Zn DMA.

Elemental analysis

Further, the structural composition of Zn DMA was confirmed by elemental analysis. Zn DMA produced the following data on elemental analysis: C-38.08%, H-3.51%, O-58.41% and supported the following structural formula: $C_8H_{10}O_4Zn \cdot 2H_2O$.

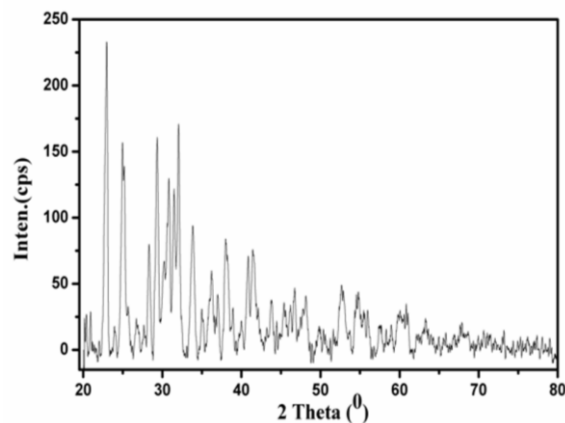


Fig. 3. XRD of Zn DMA

HRTEM report

Figure 4 shows the HRTEM images of Zn DMA. Figure 4a exhibits the distorted layered structural arrangement of different crystal planes of zinc ions. The layered structure of Zn^{2+} ion was broken by the salt formation with methacrylic acid. The length and breadth of the zinc ion in Zn DMA was found to be 10-12 nm and <0.10 nm, respectively. Figure 4b represents the nanosphere-like structure of Zn DMA with a diameter of <5 nm.

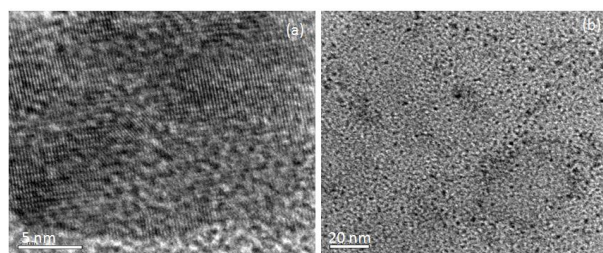


Fig. 4. HRTEM of Zn DMA

Melt functionalization of HDPE with Zn DMA

Effect of (% w/w of Zn DMA) on the RI values of carbonyl group and % C.L

The synthesized Zn DMA was melt functionalized with HDPE in the presence of equal concentration of DCP, a free radical initiator, under nitrogen atmosphere at 160 °C. The % w/w of Zn DMA was varied from 1 to 5%. Figure 5a shows the FTIR spectrum of pristine HDPE. The important peaks are characterized below: A broad peak around 2900 cm^{-1} is due to the C-H anti-symmetric stretching vibration. A small hump at 2646 cm^{-1} corresponds to the C-H symmetric stretching vibration. The C-H bending vibration appears at 1469 cm^{-1} . A sharp peak at 721 cm^{-1} is ascribed to the C-H out of plane bending vibration. Figure 5 b-f shows the FTIR spectra of HDPE after melt functionalization with 1 to 5 w/w % of Zn DMA. The system exhibits some new peaks. They are explained below: The OH stretching due to the intercalated water molecules is observed around 3500 cm^{-1} . The metal salt carbonyl group is

observed at 1721 cm^{-1} . The -OH bending vibration (due to the intercalated water molecules in the basal spacing of Zn DMA) is observed at 1646 cm^{-1} . A broad peak at 1586 cm^{-1} accounts for the presence of C=C double bond. This indicates that among the two double bonds, one C=C is freely available and the remaining one is involved in the melt functionalization reaction. The ester C-O-C linkage is observed at 1048 cm^{-1} . A peak at 609 cm^{-1} indicates the presence of Zn-O stretching. Appearance of these new peaks confirmed the chemical grafting of Zn DMA onto HDPE backbone.

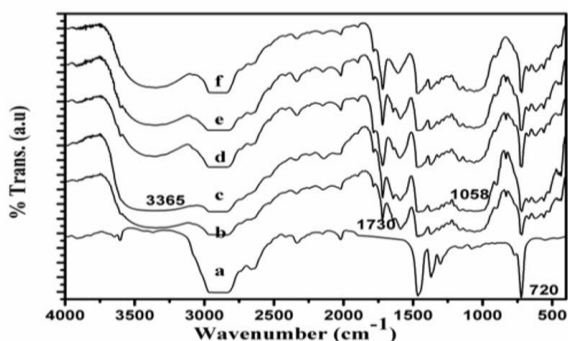


Fig. 5. FTIR spectra of HDPE functionalized with Zn DMA at a) 0% w/w, b) 1% w/w, c) 2% w/w, d) 3% w/w, e) 4% w/w, f) 5% w/w

While increasing the % w/w of Zn DMA and keeping the other experimental conditions constant, the FTIR-RI of carbonyl group linearly increased. The increase in carbonyl peak intensity is due to the Zn DMA grafting through active C=C double bond. In order to find the order of the functionalization reaction, the log-log plot was drawn between % w/w of DCP and $RI_{[C=O/CH]}$ (Figure 6a). The plot shows a linear increase in RI with the increasing % w/w of DCP. The reaction order was determined as 1.17 from the slope of the plot. This inferred that the melt functionalization reaction followed the 1.25 order of reaction with respect to % w/w of DCP, i.e., 1.25 mol of Zn DMA is required to functionalize one mol of HDPE. The rate of functionalization reaction (R_f) can be written as follows: $R_f \propto (\% \text{weight of Zn DMA})^{1.17}$. In this system, one can expect melt graft copolymerization reaction due to the presence of two double bonds in Zn DMA. Due to the absence of abnormal increase in $RI_{[C=O/CH]}$, no graft copolymerization reaction took place here. Moreover, the spectra indicated the availability of a free double bond. This means that one double bond of Zn DMA was involved in the melt functionalization reaction whereas the other one remained free. This is in accordance with the literature report [21]. The % grafting values are given in Table 1.

Table 1. Effect of % w/w of Zn DMA on % functionalization and % C.L.

% w/w Loading	HDPE-ZnDMA	
	% Functionalization	% Crosslinking
1	61.6	8.4
2	67.3	13.2
3	71.2	19.6
4	75.7	25.9
5	77.8	31.3

The % C.L. values on varying the % w/w of Zn DMA are indicated in Table 1. The % C.L. values varied from 8 to 31%. When compared with the mercapto ester grafting [7], the present system yielded higher % C.L. values due to the poor radical forming nature of Zn DMA. Moreover, it contains two double bonds and leads to cross-linking reaction. In order to find the order of % C.L. reaction, the plot of $\log(\% \text{weight of Zn DMA})$ vs $\log(\% \text{C.L.})$ (Figure 6b) was drawn and the slope was determined as 1.60. This confirmed the 1.50 order of C.L. reaction. The rate of C.L. ($R_{C.L.}$) can be written as follows: $R_{C.L.} \propto (\% \text{weight of Zn DMA})^{1.60}$. This infers that 1.60 mol of Zn DMA is required to cross-link one mol of HDPE backbone.

The % grafting values of the present system are low when compared with the mercapto ester grafting onto HDPE backbone [7]. This is due to the slow free radical formation nature of Zn DMA. The low % grafting of Zn DMA is due to the higher melting temperature and crystalline behaviour. Even though Zn DMA has a higher T_m , it was dissolved in the molten HDPE medium and was involved in the melt functionalization reaction with higher % C.L. values.

HRTEM report of HDPE-g-Zn DMA

Figure 7 shows the HRTEM image of Zn DMA grafted HDPE backbone. The Zn salt is uniformly distributed on the HDPE backbone with a size of less than 20 nm. This confirmed the chemical grafting of Zn salt onto HDPE backbone in the presence of a free radical initiator. Some agglomerated portion is also noticed.

Melt grafting mechanism

Anbarasan *et al.* [5, 7] explained the mechanism of free radical grafting of thioester onto HDPE backbone. A similar type of mechanism was applied to the present system too. However, the presence of two double bonds at the ends leads to different possible reactions. Melt functionalization reaction proceeds *via* free radical reaction. Free

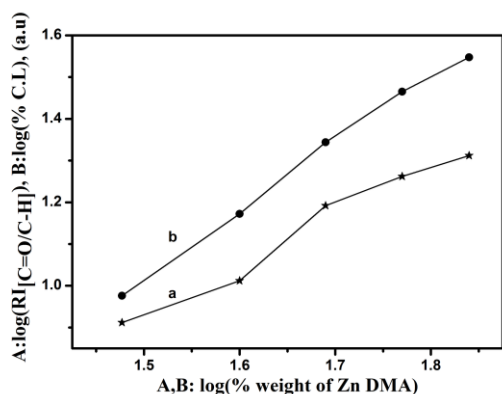


Fig. 6. Effect of (% w/w of Zn DMA) on a) RI_[C=O/C-H] and b) % C.L of HDPE

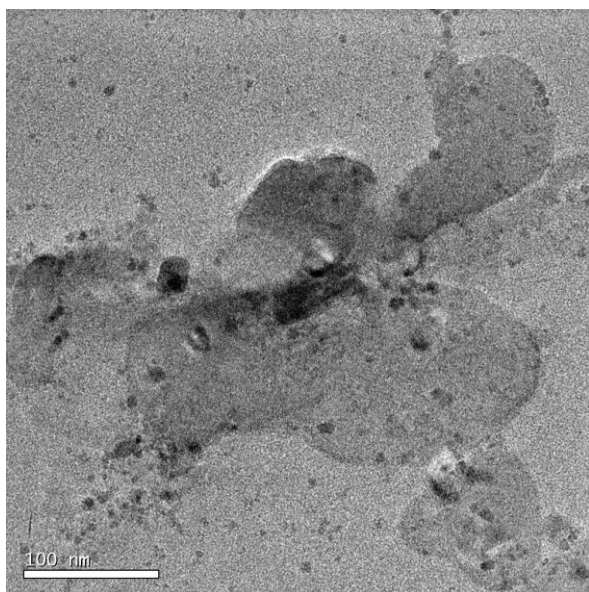
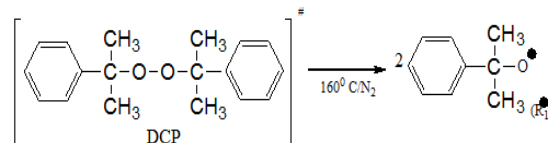
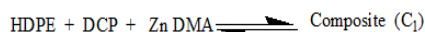


Fig. 7. HRTEM image of HDPE-g-Zn DMA

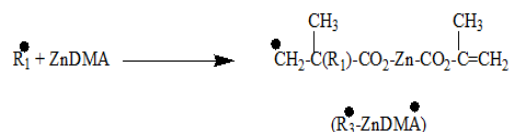
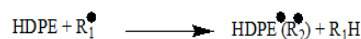
radical reactions proceed in three steps, namely, initiation, propagation and termination (Scheme 1).

DCP, a free radical initiator, produced two cumyloxy radicals on heating to 160 °C at a normal dissociation rate. Formation of free radicals is the initiation step of the melt functionalization reaction. In the first step, DCP undergoes dissociation to form two cumyloxy radicals. These radicals can interact either with HDPE or with Zn DMA. Following interaction with HDPE, HDPE macro radicals will be formed. Following interaction with Zn DMA, a Zn DMA radical will be formed. The coupling of a HDPE macro radical and a Zn DMA radical leads to the formation of metal salt functionalized HDPE. This means that the formed free radicals interacted with HDPE and produced HDPE macro radicals for functionalization and C.L. reactions. In the present investigation we used a 1:1:1 ratio of HDPE, Zn DMA and DCP. Coupling of HDPE macro radicals led to C.L. reactions.

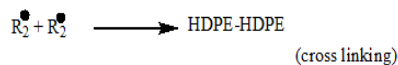
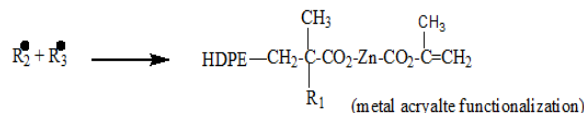
Initiation



Propagation



Termination



Scheme-1 Melt functionalization of HDPE with Zn DMA

CONCLUSIONS

The FTIR spectrum and DSC report confirmed the presence of intercalated water molecules in Zn DMA. A peak at 609 cm⁻¹ in the FTIR spectrum confirmed the chemical grafting of Zn DMA onto HDPE backbone. Further, a melting temperature (T_m) of 235.5 °C was observed on the DSC thermogram of Zn DMA. HRTEM revealed the nanosize of Zn ions in Zn DMA with broken layered structure and showed the sphere-like structure of Zn DMA. XRD revealed the crystalline structure of Zn DMA with d₁₁₁ plane. The melt functionalization of Zn DMA onto HDPE followed the 1.25 order of reaction for functionalization and 1.5 order of reaction for crosslinking. The lowest % functionalization of Zn DMA was due to higher melting temperature and more crystalline structure. According to the adopted reaction mechanism, the melt functionalization reaction proceeded through a free radical process.

Acknowledgement: DST, New Delhi is gratefully acknowledged for their financial support (Ref. No. SR/FTP/CS-39/2005).

REFERENCES

1. M. R. Saeb, and H. Garmabi, *J. Appl. Polym. Sci.*, **111**, 1600 (2009).
2. Z. Guowei, C. Yashao, D. Tao, W. Xiaoli, *Plast. Sci. Tech.*, **9**, 202 (2007).
3. A. H. Ashour, H. M. Saad, M.M. Ibrahim, *Egypt. J. Solids.*, **29**, 351 (2006).
4. Y. Hamabe, R. Matsuura, A. Jyo, A. Kotakai, *React. Funct. Polym.*, **69**, 1 (2009).
5. R. Anbarasan, O. Babot, B. Maillard, *J. Appl. Polym. Sci.*, **97**, 761 (2005).
6. R. Anbarasan, O. Babot, B. Maillard, *J. Appl. Polym. Sci.*, **97**, 766 (2005).
7. V. Parthasarathy, V. Dhanalakshmi, R. Anbarasan, *Polym. Eng. Sci.*, **50**, 474 (2010).
8. R. Anbarasan, V. Dhanalakshmi, *Spectrochim. Acta Part A.*, **76**, 37 (2010).
9. R. Anbarasan, V. Dhanalakshmi, M. Sudha, *J. Mater. Sci.*, **45**, 3289 (2010).
10. S.M.T. Sadeghi, Iran. *Polym. J.*, **14**, 657 (2005).
11. Y. Meng, Z. Wei, Y. L. Liu, L. Q. Zhang, *Xpress Polym. Lett.*, **6**, 882 (2012).
12. J. Tsuchida, Y. Saito, S. Sato, Y. Takewaki, *Polym. J.*, **45**, 1007 (2013).
13. Y. Cao, N. Gu, S. Hu, R. Jin, J. Zhang, *Appl. Mech. Mater.*, **182**, 47 (2012).
14. Y.N.Hsio, W.T.Wang, S.H.Lin, K.Y. Hsu, *Jpn. J. Appl. Phys.*, **45**, 8699 (2006).
15. C.Xu, L.Fang, Y.Chen, *Polym. Eng. Sci.*, **54**, 2321 (2014).
16. J.S. Wang, J.S. Shi, J.G. Wu, *World J. Gastro.*, **9**, 1897 (2003).
17. I. Xueref, F. Domine, *Atmos. Chem. Phys.*, **3**, 1779 (2003).
18. S. Rathika, I. Baskaran, R. Anbarasan, *J. Mater. Sci.*, **44**, 3542 (2009).
19. K. Duraimurugan, S. Rathika, R. Anbarasan, *Chin. J. Polym. Sci.*, **26**, 393 (2008).
20. M. Saule, S. Navarre, O. Babot, B. Maillard, *Macromolecules.*, **36**, 7469 (2003).
21. M. Saule, S. Navarre, O. Babot, B. Maillard, *Macromolecules.*, **38**, 77 (2003).
22. S. Navarre, B. Maillard, *J. Polym. Sci. Part A Polym. Chem.*, **38**, 2957 (2000).
23. M.F. Parveen, V. Dhanalakshmi, R. Anbarasan, *J. Mater. Sci.*, **44**, 5852 (2009).
24. M.F. Parveen, V. Dhanalakshmi, R. Anbarasan, *NANO.*, **4**, 147 (2009).
25. A. Yelilarasi, J.L. Jayakumari, R. Anbarasan, *Spectrochim. Acta Part A.*, **74**, 1229 (2009).
26. B. Kaith, R. Jindal, J.K. Bhatia, *J. Macromol. Sci.*, **48**, 299 (2011).
27. A. Chauhan, B. Kaith, *J. Anal. Bioanal. Tech.*, **3**, 7 (2012).
28. A. Chauhan, B. Kaith, *J. Chil. Chem. Soc.*, **57** (2012).
29. A. Chauhan, B. Kaith, *J. Nat. Fiber*, **8**, 308 (2011).

СИНТЕЗА, ОХАРАКТЕРИЗИРАНЕ И ФУНКЦИОНАЛИЗИРАНЕ В СТОПИЛКА НА ПОЛИЕТИЛЕН ВИСОКА ПЛЪТНОСТ С ЦИНКОВА СОЛ

В. Паргасаратхи¹, Ж. Дханалакшми², Р. Анбаразан^{2*}

¹Департамент по физика, Индустански университет, Падур-603103, Ченаи, Тамилнаду, Индия

²Департамент по полимерни технологии, Колеж по технологии и инженерство "Камарадж", Вирудхунагар, Тамилнаду, Индия

Постъпила на 9 декември, 2013 г.; коригирана на 9 октомври 2014 г.

(Резюме)

Синтезиран е цинков диметакрилат (Zn DMA) и е охарактеризиран чрез аналитични методи, например инфрачервена спектроскопия с Фурие-трансформация (FTIR), рентгенова дифракция (XRD), диференциална сканираща калориметрия (DSC) и трансмисионна електронна микроскопия с висока разделителна способност (HRTEM). Синтезираният Zn DMA е подложен на функционализиране в стопилка с полиетилен висока плътност (HDPE) при 160°C в среда на азот. За реакцията на функционализиране е използван Като инициатор ди-кумил пероксид (DCP) в отношение 1:1 спрямо цинковата сол. FTIR-спектроскопията и HRTEM-методът потвърждават количествено химическото присаждане на Zn DMA върху макромолекуления скелет на полиетилена. Методът на относителния интензитет (FTIR-RI) е използван за откриването на реакцията на функционализиране в стопилка. Предложен е правдоподобен механизъм на реакцията.

Synthesis and anti-inflammatory evaluation of novel piperazine derivatives of mefenamic acid

A. Ahmadi

Young Researchers & Elite Club, Pharmaceutical Sciences Branch, Islamic Azad University, Tehran, Iran

Received February 24, 2014; revised May 24, 2014

In order to explore novel anti-inflammatory agents, some novel mefenamic acid derivatives as potential non-steroidal anti-inflammatory agents (NSAIDs) were synthesized and characterized by IR, $^1\text{H-NMR}$, $^{13}\text{C-NMR}$, mass and elemental analysis. The anti-inflammatory activities of the target compounds were evaluated *via* the croton oil-induced ear oedema test in mice. According to screened results, compounds **I** and **II** show potential anti-inflammatory activity comparable to aspirin.

Keywords: Non-steroidal anti-inflammatory drugs (NSAIDs), Mefenamic acid derivatives, Cyclooxygenase (COX).

INTRODUCTION

Inflammation is defined as a complex series of tissue changes that result in pain and fever [1]. During the last three decades the development of non-steroidal anti-inflammatory drugs (NSAIDs) has shown to be one of the major advancements in chemotherapeutical research [2,3]. These agents are among the most widely used drugs worldwide and represent a mainstay in the therapy of acute and chronic pain, fever and inflammation by blocking the formation of prostaglandins (PGs). PGs are well-known as the mediators of inflammation, pain and swelling. They are produced by the action of cyclooxygenase (COX) enzyme on arachidonic acid. COX is the principal target of NSAIDs. Pharmacological inhibition of COX can provide relief from symptoms of inflammation and pain. NSAIDs, such as aspirin and ibuprofen, exert their effects through inhibition of COX. The three main groups of prostanoids: prostaglandins, prostacyclins and thromboxanes are each involved in the inflammatory response. In the 1990s, researchers discovered that two different COX enzymes existed, now known as COX-1 and COX-2. Cyclooxygenase-1 (COX-1) is known to be present in most tissues. In the gastrointestinal tract, COX-1 maintains the normal lining of the stomach. The enzyme is also involved in kidney and platelet function. Cyclooxygenase-2 (COX-2) is primarily present at sites of inflammation. While both COX-1 and COX-2 convert arachidonic acid to prostaglandin, resulting in pain and inflammation,

their other functions make inhibition of COX-1 undesirable while inhibition of COX-2 is considered desirable [4, 5]. Selective COX-2 inhibitors are still under development [6,7]; they were proposed as drugs with higher selectivity for COX-2 tending to induce cardiovascular disease [8-10]. The present study aimed at design, synthesis and preliminary evaluation of new mefenamic acid derivatives as potential NSAIDs.

EXPERIMENTAL

Material and equipments

All chemicals and solvents were purchased from Merck (Darmstadt, Germany) and Sigma-Aldrich Chemical Co. (U.S.A.). Melting points (uncorrected) were determined with a digital Electrothermal melting point apparatus (model 9100, Electrothermal Engineering Ltd., Essex, UK). ^1H and $^{13}\text{C-NMR}$ spectra were recorded with a Bruker 300 MHz (model AMX, Karlsruhe, Germany) spectrometer (internal reference: TMS). IR spectra were recorded with a Thermo Nicolet FT-IR (model Nexus-870, Nicolet Instrument Corp., Madison, Wisconsin, U.S.A.) spectrometer. Mass spectra were recorded with an Agilent Technologies 5973, mass selective detector (MSD) spectrometer (Wilmington, USA). Elemental analyses were carried out using a Perkin-Elmer, CHN elemental analyzer model 2400.

Synthesis of 2-(2, 3-dimethylphenylamino) benzoic anhydride (I)

Mefenamic acid (5.0 g, 0.02 mol) was dissolved in THF (30 ml), and dicyclohexyl carbodiimide (DCCI) (2.06 g, 0.01 mol) was added. The reaction

* To whom all correspondence should be sent:

E-mail: ahmadikiau@yahoo.com

mixture was continuously stirred at room temperature for 4 h. The reaction was completed (monitored by TLC) and a white precipitate of dicyclohexylurea (DCU) was formed and separated by filtration. The filtrate was evaporated under vacuum to obtain compound (I) [11, 12].

White-gray powder; 73% yield; m.p. 142-144 °C; IR (KBr, cm⁻¹): 3330, 2921, 2845, 1800, 1752, 1625, 1530, 1522, 1275, 1169.

General procedure for the synthesis of (II-IV)

To a solution of the appropriate 1-(2-substituted phenyl) piperazine (0.01 mol) in dioxane (20 ml) were added: compound I (2.5 g, 0.005 mol), zinc powder (catalyst, 0.01 g), glacial acetic acid (0.5 ml) and 10 mg benzyltriethylammonium chloride as phase transfer catalysts. The reaction mixture was gently refluxed for 90 min. After reaction completion (monitored by TLC), the reaction mixture was neutralized, extracted with ethyl acetate or brine, dried over MgSO₄ and evaporated under vacuum. Re-crystallization from ethyl acetate-petroleum ether (60-80 °C) mixture was carried out to obtain the desired compounds (II-IV).

[2-(2,3-Dimethyl-phenylamino)-phenyl]-(4-phenyl-piperazin-1-yl)-methanone (II)

White-light brown powder, m.p. 202-204 °C; 68% yield; IR (KBr, cm⁻¹): 3340, 3080, 2850, 2851, 1690, 1600, 1524, 1468, 1389, 1316, 1250, 973, 790. ¹H-NMR (CDCl₃) (ppm): 2.15 (6H, m, CH₃), 3.39 (4H, m, CH₂), 3.85 (4H, m, CH₂), 6.3-7.7 (12H, m, phenyl), 10.57 (br, s, NH). ¹³C-NMR (CDCl₃) (ppm): 6.6, 12.4, 48.4, 54.6, 57.5, 113.0, 117.9, 118.5, 118.6, 121.2, 122.3, 126.4, 127.9, 130.1, 131.9, 145.2, 145.7, 168.7. Anal. Calcd. for C₂₅H₂₇N₃O: C, 77.89; H, 7.06; N, 10.90. Found: C, 77.75; H, 7.10; N, 10.83. MS: m/z (regulatory intensity): 385 (100), 386 (30).

[2-(2,3-Dimethyl-phenylamino)-phenyl]-(4-pyridin-2-yl-piperazin-1-yl)-methanone (III)

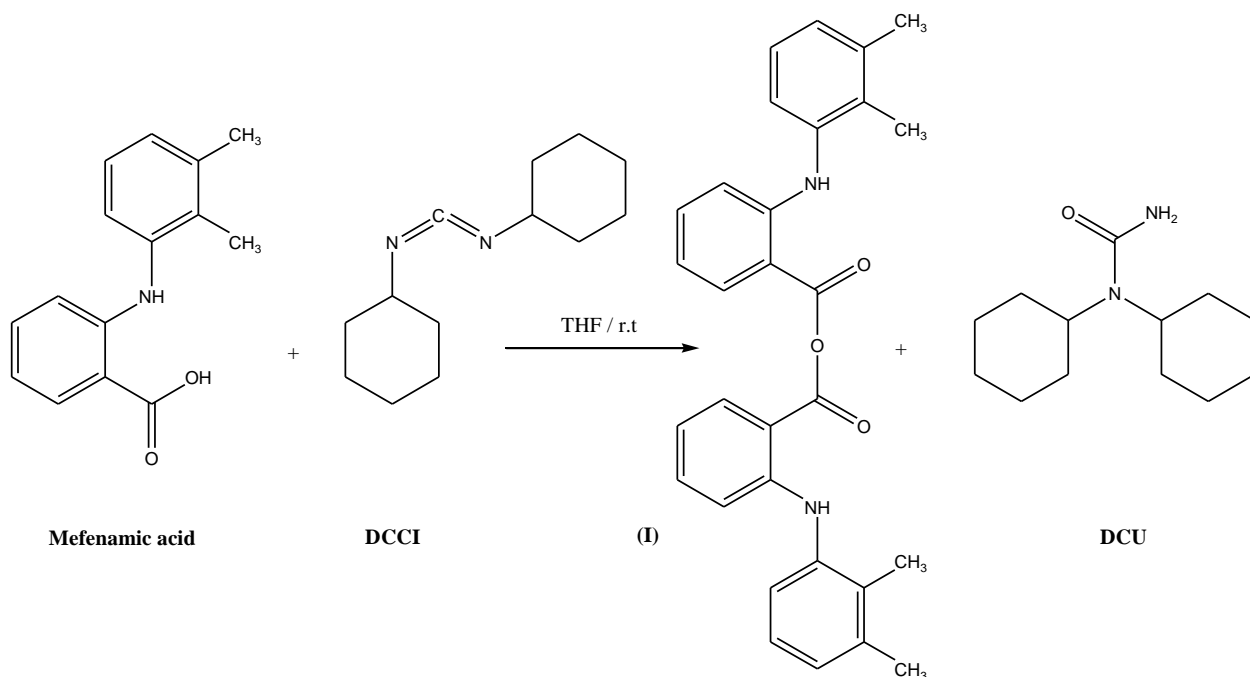
White-light yellow powder, m.p. 192-194 °C; 63% yield; IR (KBr, cm⁻¹): 3330, 3095, 2978, 2851, 1698, 1625, 1554, 1458, 1389, 1316, 1266, 1118, 780. ¹H-NMR (CDCl₃) (ppm): 2.10 (6H, m, CH₃), 3.41 (4H, m, CH₂), 3.77 (4H, m, CH₂), 6.45-8.4 (11H, m, phenyl), 10.62 (br, s, NH). ¹³C-NMR (CDCl₃) (ppm): 5.9, 13.3, 49.4, 55.6, 60.5, 115.0, 119.9, 121.5, 123.6, 124.2, 125.3, 126.4, 127.9, 133.1, 135.9, 146.2, 149.7, 170.1. Anal. Calcd. for C₂₄H₂₆N₄O: C, 74.58; H, 6.78; N, 14.50. Found: C, 74.65; H, 6.80; N, 14.43. MS: m/z (regulatory intensity): 386 (100).

[2-(2,3-Dimethyl-phenylamino)-phenyl]-(2,3,5,6-tetrahydro-[1,2']bipyrazinyl-4-yl) methanone (IV)

White-light orange powder, m.p. 188-190 °C; 59 % yield; IR (KBr, cm⁻¹): 3430, 3065, 2958, 2833, 1675, 1625, 1502, 1458, 1378, 1330, 1226, 1118, 750. ¹H-NMR (CDCl₃) (ppm): 2.18 (6H, m, CH₃), 3.44 (4H, m, CH₂), 3.69 (4H, m, CH₂), 6.35-7.95 (10H, m, phenyl), 10.70 (br, s, NH). ¹³C-NMR (CDCl₃) (ppm): 6.1, 12.3, 50.1, 54.9, 61.7, 116.3, 119.3, 122.3, 123.8, 124.1, 125.8, 126.7, 127.1, 134.2, 137.1, 147.1, 148.3, 169.5. Anal. Calcd. for C₂₃H₂₅N₅O: C, 71.29; H, 6.50; N, 18.07. Found: C, 71.35; H, 6.55; N, 17.95. MS: m/z (regulatory intensity): 387 (100).

Pharmacological Methods

The topical anti-inflammatory activity was evaluated as inhibition of the croton oil-induced ear oedema in Swiss mice [13]. Male mice (18-22 g), at the beginning of the experiment, were randomly housed in a temperature-controlled colony room under 12 h light/dark cycle. Rats were given free access to water and standard laboratory rat chow. All experiments were conducted between 7 a.m. and 7 p.m., under normal room light at 25°C. Groups (each group containing 10 mice) were used in all tests. The tested compounds and the reference drug were suspended in 0.5% sodium carboxymethyl cellulose (CMC). Inflammation was always induced in the late morning (10 a.m.-12 p.m.). Mice were anaesthetized with ketamine hydrochloride (145 mg/kg, intra-peritoneally) and inflammatory response was induced on the inner surface of the right ear (surface: about 1 cm²) by application of 20 µL of 2% croton oil suspended in 42% aqueous ethanol. Control animals received only the irritant, whereas the other animals received the irritant together with the tested substances. At the maximum of the oedematous response, 6 h later, mice were sacrificed and a plug (φ=8 mm) was removed from both the treated (right) and the untreated (left) ears. Oedema was measured as the mass difference between the two plugs. The anti-inflammatory activity was expressed as the percentage of oedema reduction in treated mice compared to that in the control mice. As reference, the non-steroidal anti-inflammatory drug ibuprofen was used. The results were expressed as mean±SD and statistical analysis was performed by means of Student's t-test or by one-way analysis of variance followed by the Dunnett's test for multiple comparisons of unpaired data. Statistically, a P value of less than 0.05 was considered to be significant and a P value of less than 0.01 was considered to be very significant.



Scheme 1. Scheme of the synthesis of intermediate (I)

RESULTS AND DISCUSSION

Chemistry

New piperazine derivatives of mefenamic acid (**II-IV**) were successfully synthesized as shown in Schemes 1 and 2. The conversion of the carboxylic acid group of mefenamic acid to benzamide group by conjugating the selected moiety of the heterocyclic compounds may produce new non-steroidal anti-inflammatory agents. Spectroscopic (IR, ^1H and ^{13}C -NMR, mass) and elemental (CHN) data confirmed the structure of the synthesized compounds. The purity of every compound was checked by TLC with ethyl acetate-hexane as the eluent. Preliminary pharmacological evaluation was done for the designed compounds.

Biological Evaluation

The anti-inflammatory effects of the target compounds were investigated by the croton oil-induced ear oedema test, and the results show that

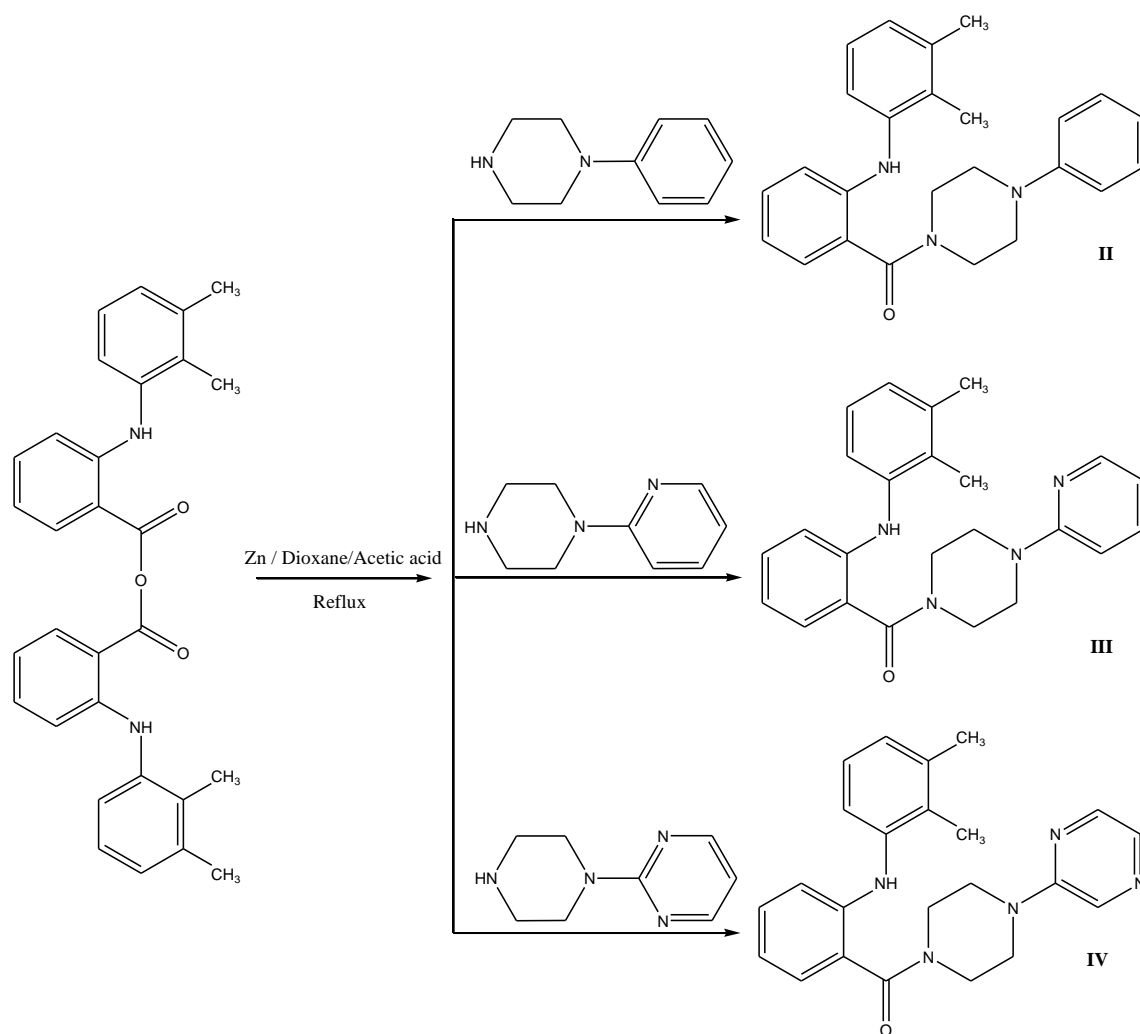
some target compounds induced oedema reduction. It was found that these compounds exhibit anti-inflammatory effects comparable to that of aspirin (Table 1).

Table 1. Anti-inflammatory activity of target compounds on ear oedema induced by croton oil after topical administration at a dose of 200 mg/kg in mice.

Compound	Swelling (mg, $\bar{X} \pm \text{SD}$)	Inhibition (%)	<i>P</i>
Control *	13.44 \pm 8.25		
Aspirin	7.87 \pm 3.05	47.58	<0.01
II	9.81 \pm 5.18	28.21	<0.05
III	9.76 \pm 6.08	26.87	<0.05
IV	11.89 \pm 4.50	11.56	

*0.5% sodium carboxymethyl cellulose aqueous solution.

Acknowledgements: The author gratefully acknowledges financial support of Islamic Azad University for this research project.



Scheme 2. Scheme of the synthesis of the final compounds (**II-IV**)

REFERENCES

1. A. C. Guyton, J. E. Hall, Resistance of body to infection: Leucocytes, granulocytes, the monocyte macrophage system and inflammation. In: Textbook of medical physiology (10th ed.). Harcourt Asia PTE LTD, Philadelphia, 2000, p. 397
2. R. A. Harvey, P. C. Champe, Lippincott illustrated reviews: pharmacology (3rd ed.). Lippincott Williams and Wilkins, Philadelphia, 2006, p. 495.
3. B. G. Katzung, Basic and clinical pharmacology (9th ed.). Mc-Graw-Hill, New York, 2004, p.298.
4. R. N. Dubois, S. B. Abramson, L. Grofferd, *FASEB J.*, **12**, 1063 (1998).
5. C. J. Hawkey, *Lancet*, **353**, 307 (1999).
6. C. Velazquez, P. N. Rao, R. McDonald, E. E. Knausdi, *Bioorg. Med. Chem.*, **13**, 2749 (2005).
7. Q. H. Chen, P. N. Rao, E. E. Knaus, *Bioorg. Med. Chem.*, **13**, 2459 (2005).
8. J. M. Dogne, C. T. Supuran, D. Pratico, *J. Med. Chem.*, **7**, 2251 (2005).
9. L. A. Garcia Rodriques, H. Jick, *Lancet*, **343**, 769 (1994).
10. L. A. Garcia Rodriques, C. Gattaruzzi, M. G. Troncon, L. Agostins, *Arch. Intern. Med.*, **158**, 33 (1998).
11. K. Pradip, J. Baner, L. Gordon, *J. Pharm. Sci.*, **70**, 1299 (1981).
12. M. F. Mahdi, *Iraqi. J. Pharmaceut. Sci.*, **17**, 7 (2008).
13. N. Erdemoglu, E. K. Akkol, E. Yesilada, I. Caliş, *J. Ethnopharmacol.*, **119**, 172 (2008).

СИНТЕЗА И ПРОТИВО-ВЪЗПАЛИТЕЛНО ДЕЙСТВИЕ НА НОВИ ПРОИЗВОДНИ НА
ПИПЕРАЗИНА НА МЕФЕНАМИНОВАТА КИСЕЛИНА

А. Ахмади

*Младежки изследователски и елитен клуб, Отделение по фармацевтични науки, Ислямски университет
„Азад“, Иран*

Постъпила на 24 февруари, 2014 г., коригирана на 24 май, 2014 г.

(Резюме)

Синтезирани са нови производни на мекенаиновата киселина и е изследвана тяхната противовъзпалителна активност като не-стероидни агенти (NSAIDs). Те са охарактеризирани чрез IR, ¹H-NMR, ¹³C-NMR, масов и елементарен анализ. Противовъзпалителната активност на целевите съединения е оценена върху ушен едем при мишки, индуциран от кротеново масло. Според резултатите от скрийнинга съединения **I** и **II** показват потенциален противовъзпалителен ефект сравним с аспирин.

NMR and NBO study of vinblastine as a biological inhibitor

S. Joohari*, M.Monajjemi

Department of Chemistry, Science and Research Branch, Islamic Azad University, Tehran, Iran

Received July 14, 2014, Revised September 11, 2014

Vinblastine is a potent biological inhibitor that has been clinically applied against a variety of neoplasms. In this work, the molecular structure of vinblastine was optimized using HF and B₃LYP level of theory with 6-31 G(d) as a basis set. Theoretical computations were performed to study thermodynamic parameters, NMR chemical shift data and NBO analysis. Accordingly, some electronic properties such as E_{HOMO}, E_{LUMO}, E_{bg} (energy gap between LUMO and HOMO), atomic charges, were calculated. Moreover, thermodynamic parameters such as relative energy (ΔE), standard enthalpy (ΔH), entropy (ΔS), Gibbs free energy (ΔG) and constant volume molar heat capacity (C_v) values of vinblastine were evaluated. In NMR investigation, magnetic shielding tensor (σ , ppm), shielding asymmetry (η), magnetic shielding anisotropy (σ_{aniso}) and skew of a tensor (K) at various rotation angles around a characteristic rotation were estimated. Also, the calculated chemical shifts were compared with experimental data in CDCl₃ and DMSO. The calculated data showed in some cases acceptable agreement with experimental ones.

Keywords: vinblastine, NBO, *ab initio*, biological, inhibitor.

INTRODUCTION

Alkaloids are known as biologically active molecules that originate from natural sources [1-3] as found in the late 1950s [4-7]. Since that time, more than eighty alkaloids extracted from *C. roses* have been identified. Alkaloids have shown various biological properties such as anticancer, antimicrobial, anti-hypertensive and some other biomedical activities [8]. Two alkaloids of vinblastine (VLB) and vincristine (VCR) have been obtained from the famous Madagascar periwinkle plant, formally known as *Vinca-rosea* [2, 3]. These two compounds are very similar in structure. Molecular structure of vinblastine is presented in scheme 1.

Vinblastine is a biological inhibitor that has been clinically applied against a variety of neoplasms. Vinblastine acts an anti-metabolic agent. It affects the metaphase stage of meiosis. Vincristine is also an anti-metabolic agent, but it can affect the metaphase stage of mitosis. Some differences are found between these two stages of meiosis and mitosis. But both in meiosis and mitosis, in metaphase stage, chromosomes are placed in the middle of the cell nucleus so that microtubules are attached to them very hardly and are ready to divide the chromosomes. When we use

vinblastine or its analogue (vincristine), the cancer cells will not grow because these two matters bind to the microtubule and make them loose so the cell division is stopped at the metaphase stage [9-12].

Microtubules are highly dynamic polymers of heterodimers of α and β tubulin, arranged parallel to a cylindrical axis to form tubes of 25 nm diameter that may be many μm long. Polymerization of microtubules is initiated by a nucleation-elongation mechanism in which the formation of a short microtubule 'nucleus' is followed by elongation of the microtubule *via* a reversible non-covalent addition of tubulin dimers [12]. Microtubules are not simple polymers. They exhibit complex polymerization dynamics that apply energy released *via* hydrolysis of GTP. These complicated dynamics are suggested to be important for their cellular functions. Various chemical materials are bound to tubulin or microtubules that inhibit cell proliferation by acting on microtubules. Many of these bound compounds have been known as drugs that are highly applicable against various forms of cancer or are currently in clinical trials. An important class of these drugs inhibiting the microtubule polymerization at high drug concentrations is found to be the *Vinca* alkaloids [12-16]. The *Vinca* alkaloids can bind to both tubulin and microtubules, and therefore their biological activities are highly

* To whom all correspondence should be sent:
E-mail: shjoohari@yahoo.com

dependent on the drug concentration [16]. At relatively high concentrations of these alkaloids, the microtubule depolymerization is stopped, spindle microtubules are dissolved and therefore cells arrest at mitosis [18-20]. In contrast, at low concentrations, the *vinca* alkaloids decrease microtubule dynamics without depolymerizing spindle microtubules, but remain able to arrest mitosis and induce apoptosis [12]. All of these compounds can affect mitotic progression and cause apoptosis in cancer cells [21-23].

In continuation of previously experimental studies, in this work, the molecular structure of vinblastine was optimized using HF and B₃LYP level of theory with 6-31 G(d) as a basis set. Theoretical computations were performed to study thermodynamic parameters, NMR chemical shift data and NBO analysis.

THEORETICAL BACKGROUND

The chemical shift refers to the phenomenon associated with the secondary magnetic field created by the induced motions of the electrons surrounding the nucleus when it is subjected to an applied external magnetic field. The energy of a magnetic momentum, μ , in a magnetic field, B, is as follow:

$$E = -\mu \cdot (1 - \sigma) B$$

where σ refers to the differential resonance shift due to the induced motion of the electrons. The chemical shielding is defined by a real three-by-three Cartesian matrix, which can be divided into a single scalar term, three anti symmetric pseudo vector components, and five components corresponding to a symmetric tensor [23]. Only the single scalar and the five symmetric tensor elements can be seen in the normal NMR spectra of the solids. For brevity, these six resonance shifts are usually referred to as the shielding tensor:

$$\begin{bmatrix} \sigma_{xx} & \sigma_{xy} & \sigma_{xz} \\ \sigma_{yx} & \sigma_{yy} & \sigma_{yz} \\ \sigma_{zx} & \sigma_{zy} & \sigma_{zz} \end{bmatrix}$$

that can be obtained by averaging the off-diagonal values of the complete tensor [24]. The chemical shielding tensor is generally referred to as the chemical shift anisotropy tensor (CSA) according to the possession of second rank properties. The measurement or calculation of the diagonal components ($\sigma_{xx}, \sigma_{yy}, \sigma_{zz}$) or ($\sigma_{11}, \sigma_{22}, \sigma_{33}$) in the principal

axis system (PAS) allows the complete description of the CSA tensor. The CSA tensor can also be illustrated by three additional parameters, as reported previously [25]. In various areas of chemical physics, a careful prediction of molecular response properties to external fields is necessary. Since the NMR data have gained substantial importance in chemistry and biochemistry, they are studied with two parameters isotropic (σ_{iso}) and anisotropic (σ_{aniso}) shielding as shown in the following relationships. If $|\sigma_{11} - \sigma_{iso}| \geq |\sigma_{33} - \sigma_{iso}|$, σ , chemical shift anisotropy, η , asymmetry parameter and δ are obtained as shown below [26]:

$$\Delta\sigma = \sigma_{11} - \frac{\sigma_{22} + \sigma_{33}}{2}$$

$$\eta = \frac{\sigma_{22} - \sigma_{33}}{\delta}$$

$$\delta = \sigma_{11} - \sigma_{iso}$$

If $|\sigma_{11} - \sigma_{iso}| \leq |\sigma_{33} - \sigma_{iso}|$:

$$\Delta\sigma = \sigma_{33} - \frac{\sigma_{22} + \sigma_{11}}{2}$$

$$\eta = \frac{\sigma_{22} - \sigma_{11}}{\delta}$$

$$\delta = \sigma_{33} - \sigma_{iso}$$

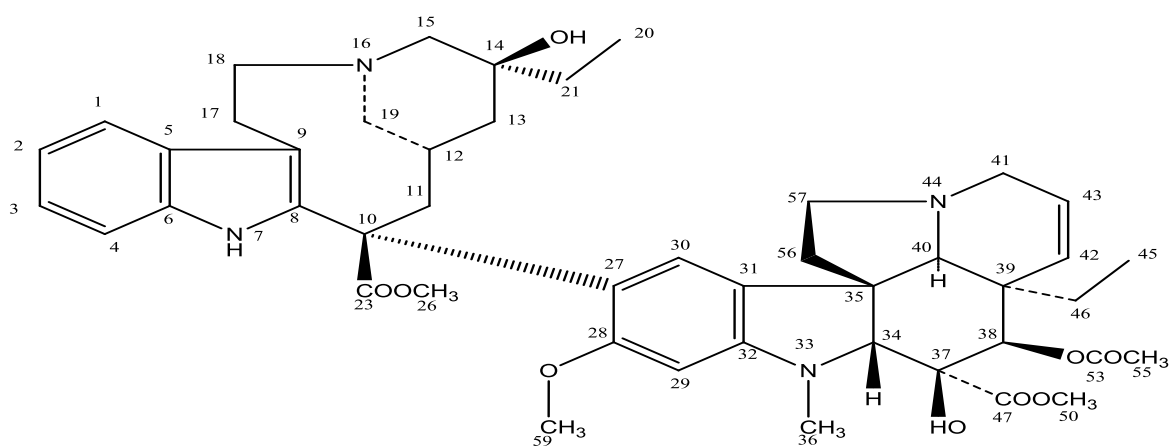
For both cases, skew (K) is shown as:

$$K = \frac{3 * (\sigma_{iso} - \sigma_{22})}{\sigma_{33} - \sigma_{11}}$$

It is to be noted that the skew is a measure of the asymmetry of the probability distribution of a real-valued random variable about its mean.

Computational Methods

Molecular structure of vinblastine was optimized using HF and B₃LYP levels of theory with 6-31G(d) as a basis set. Computations were carried out to study thermodynamic parameters, NMR chemical shift data and NBO analysis [27]. All calculations were carried out using the Gaussian 09 program package. Gaussian 09 is a computational chemistry software package applicable to present interaction of electrons in atoms and molecules. It uses numerical methods to find solutions to wave functions. Molecular orbital energies, bond energies, molecular geometries and energies, and vibrational frequencies, along with many other properties are evaluable by this package. The term *ab initio* is given to calculations that are



Scheme 1. Molecular structure of vinblastine

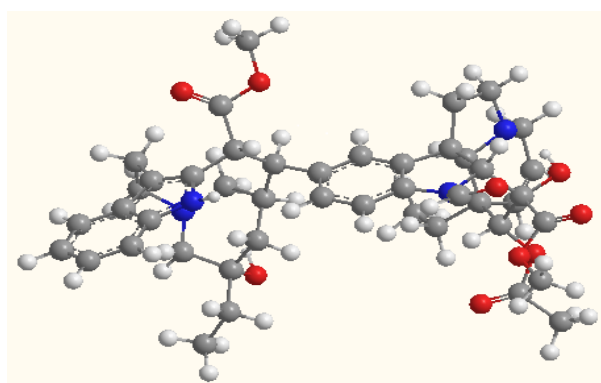


Fig. 1. Optimized geometric structure of vinblastine.

obtained exactly from theoretical principles without adding any experimental data [28]. The optimized geometric structure of vinblastine is shown in Fig. 1.

RESULTS AND DISCUSSION

In this work we have theoretically studied the magnetic properties of atomic nuclei to determine physical and chemical properties of atoms in the title compound. *Ab initio* calculation of nuclear magnetic shielding has become an aid for the analysis of molecular structure. So, NMR is based on the quantum mechanical properties of the nuclei. Based on NMR study, calculated magnetic shielding tensor (σ , ppm), shielding asymmetry (η), magnetic shielding anisotropy (σ_{aniso} , ppm), the skew of a tensor (K), chemical shift anisotropy ($\Delta\sigma$) and chemical shift (δ) were calculated. These results are listed in Tables 1 and 2. The graphs of these

calculated parameters *versus* the number of atoms of vinblastine were sketched as shown in Figs. 2a-2e, respectively.

As seen in Figures 2a-2e, at HF level, O₅₈ has a maximum value of σ_{iso} (280.8046); O₂₄ has a maximum value of σ_{aniso} (763.7363); O₂₄ has a maximum value of $\Delta\sigma$ (763.7363), C₅₅ has a maximum value of K (0.825985) and C₄₅ has a maximum value of η (0.994694) and at B3LYP level O₂₂ has a maximum value of σ_{iso} (246.9817); O₂₄ has a maximum value of σ_{aniso} (664.3599); O₂₄ has a maximum value of $\Delta\sigma$ (664.3599), C₁₅ has a maximum value of K (0.820206), finally C₈ has a maximum value of η (0.987734).

The calculated chemical shifts by HF and B3LYP methods as compared with experimental data in CDCl₃ and DMSO [29] are collected in Table 3. As shown in Table 3, in some cases the chemical shifts calculated by HF are close to the experimental data while in some other cases, the results computed by B3LYP are comparable with experimental data.

Moreover, some electronic properties such as energy of the highest occupied molecular orbital (E_{HOMO}), energy of the lowest unoccupied molecular orbital (E_{LUMO}), energy gap (E_{bg} ; the gap between LUMO and HOMO energies) and atomic charges, were evaluated. The results are tabulated in Tables 4 and 5. The values of E_{HOMO} , E_{LUMO} and E_{bg} were evaluated as -0.25936, 0.12368 and 0.38304 eV, respectively. The maximum Mulliken negative charge was calculated for 58H and the maximum positive charge was computed for 47c.

Table 1. Magnetic shielding tensor (σ , ppm), magnetic shielding anisotropy (σ_{aniso} , ppm) and chemical shift anisotropy ($\Delta\sigma$) calculated by HF and B3LYP models with 6-31G(d) basis set for C, N, O in vinblastine.

Atomic label	HF/ 6-31G(d)			B3LYP/ 6-31G(d)		
	σ_{Iso}	σ_{Aniso}	$\Delta\sigma$	σ_{Iso}	σ_{Aniso}	$\Delta\sigma$
1c	82.2239	177.1057	177.10575	81.4572	155.5608	155.56085
2c	86.3922	170.8911	170.89115	81.9852	152.4802	152.48025
3c	80.8488	178.6912	178.69115	79.8344	155.5389	155.5389
4c	93.7094	154.9596	154.95955	90.7186	136.607	136.607
5c	73.1957	163.5265	163.52645	68.1407	145.5024	145.50245
6c	63.9003	166.0338	166.0338	63.4268	140.3232	140.3232
7N	138.4154	51.8364	-75.6211	116.3844	48.4883	-71.75595
8c	68.5629	122.45	-137.2326	65.238	102.7925	-103.4267
9c	85.6121	132.781	132.781	79.1179	116.9933	116.9933
10c	154.2052	22.6749	22.6749	139.5491	20.9796	-21.8936
11c	154.7359	24.7421	24.74215	133.3454	22.3519	22.35185
12c	168.6329	24.6203	24.6203	150.2322	25.4396	25.43955
13c	171.3767	32.7447	32.74465	155.2889	34.6152	34.61515
14c	137.8163	42.1837	42.18375	116.7567	42.1362	42.13625
15c	149.6165	31.286	31.28605	132.3138	34.7518	34.75185
16N	244.2934	47.564	47.56405	209.9096	51.2007	51.20065
17c	181.5312	22.2527	-35.2348	167.0131	25.5394	-37.2209
18c	160.483	43.4438	43.44375	143.2538	45.0838	45.08385
19c	163.4631	33.0308	33.0308	146.3866	36.0842	36.08405
20c	199.4931	15.4888	15.48885	187.3711	15.9159	15.91585
21c	171.8519	37.7055	37.70545	155.214	39.0024	39.0023
22O	273.5037	159.3895	159.3895	246.9817	161.2745	161.27455
23c	12.5103	127.1395	-186.23915	16.5554	89.0413	-142.3802
24O	-167.7572	763.7363	763.7363	-133.997	664.3599	664.3599
25O	175.3948	211.9189	-330.0435	127.8043	193.0803	-316.96325
26c	157.9504	62.3724	62.37245	144.5365	65.5015	65.5016
27c	68.0566	170.9488	170.9488	63.2549	151.6022	151.60225
28c	44.9724	134.9123	134.91235	39.9634	106.072	106.07205
29c	98.8318	146.4449	146.44485	96.431	131.7501	131.75015
30c	74.2976	157.3851	157.3851	73.3478	132.0677	132.0677
31c	73.3031	144.0565	144.05655	67.7907	125.3065	125.30645
32c	49.4952	144.72	144.72	46.1149	116.6732	116.6733
33N	205.2028	82.9149	82.9148	169.211	80.0504	80.0504
34c	132.4978	31.215	31.215	111.4526	30.3105	30.3105
35c	154.2238	30.2564	30.25645	133.5051	29.9711	29.199
36c	165.3309	59.1434	59.14335	151.3953	63.4749	63.47485
37c	121.0346	21.8353	21.8353	102.1689	23.6388	23.63885
38c	137.0632	37.5001	-46.3665	117.5051	35.957	-316.96325
39c	165.9838	13.5246	13.52465	144.9849	14.1888	14.1888
40c	147.0094	32.4146	32.41455	127.0656	35.9774	35.97745
41c	160.8988	37.662	37.66205	143.0828	40.9629	40.9629
42c	76.1156	159.1929	-181.62215	70.2006	143.8221	-149.7878
43c	76.9451	153.362	-176.30675	73.8942	137.5253	-145.59015
44N	218.0582	38.0472	-67.1081	185.1565	36.8617	-63.62375
45c	198.666	13.8161	-13.8528	186.5266	14.7872	14.78715
46c	180.0201	22.1054	-22.3894	162.9237	23.1603	-24.57635
47c	11.6178	134.2036	-176.01545	16.6645	95.1436	-134.0453
48O	-129.3067	711.0296	711.0296	-109.4652	628.0083	628.0083
49O	173.3682	207.8216	-339.364787	126.1173	186.0971	-322.11535
50c	158.3326	61.399	61.399	144.8955	64.434	64.434
51O	272.5608	57.1822	-63.4529	238.7188	47.4807	-51.59265
52O	161.4416	183.5647	-305.59205	115.4793	163.0053	-295.2175
53c	17.3794	125.56	-192.1905	22.4825	87.237	-150.53115
54O	-148.8274	711.1191	711.11915	-119.6978	616.7324	616.73245
55c	180.815	49.865	49.86505	171.534	47.9299	47.92985
56c	163.9835	50.9283	50.9284	147.9227	52.59	52.59
57c	161.0108	54.8761	54.8761	143.6472	58.7531	58.75315
58O	280.8046	86.7669	-128.33215	236.4346	87.2229	-132.0352
59c	154.7926	67.179	67.1789	140.8168	72.0584	72.05835

Table 2. Skew of a tensor (K) and shielding asymmetry (η) calculated by HF and B3LYP levels of theory with 6-31G(d) as a basis set for C, N, O in vinblastine.

Atomic label	NMR chemical shielding tensors data								
	HF/ 6-31G(d)		B3LYP/ 6-31G(d)		Atomic label	HF/ 6-31G(d)		B3LYP/ 6-31G(d)	
	K	η	K	η		K	η	K	η
1c	0.177746	0.776260	0.219067	0.727788					
2c	0.112513	0.855405	0.145127	0.815425	31c	0.276995	0.661891	0.371120	0.559648
3c	0.147455	0.812604	0.170245	0.785195	32c	0.125273	0.839664	0.251150	0.691001
4c	0.175871	0.778491	0.221297	0.725207	33N	0.528391	0.400984	0.492250	0.436180
5c	0.622574	0.312561	0.689458	0.252510	34c	0.148045	0.811888	0.317799	0.616855
6c	0.371780	0.558950	0.433252	0.495228	35c	0.370729	0.560056	0.387924	0.541991
7N	-0.559824	0.370951	-0.58051	0.351476	36c	0.718357	0.227231	0.799340	0.158441
8c	-0.170777	0.784560	-0.00922	0.987734	37c	0.030498	0.959757	0.159907	0.797584
9c	0.155445	0.802948	0.427788	0.500800	38c	-0.317158	0.617553	-0.54897	0.218313
10c	0.149083	0.810632	-0.06395	0.916516	39c	0.009060	0.987966	0.06443	0.915891
11c	0.551140	0.379192	0.484246	0.444078	40c	0.419833	0.508942	0.58679	0.345603
12c	0.634505	0.301690	0.744221	0.204938	41c	0.156974	0.801111	0.12501	0.839977
13c	0.592674	0.340126	0.571183	0.360227	42c	-0.197431	0.753013	-0.06095	0.920344
14c	0.455015	0.473211	0.414851	0.514065	43c	-0.249748	0.759093	-0.08545	0.889212
15c	0.722875	0.223311	0.820206	0.141191	44N	-0.829084	0.133906	-0.79898	0.158740
16N	0.030366	0.959914	0.082559	0.892865	45c	-0.003984	0.994694	0.046761	0.938608
17c	-0.677471	0.263108	-0.55838	0.372315	46c	-0.019144	0.974628	-0.08899	0.884760
18c	0.661427	0.277410	0.620945	0.314051	47c	-0.404345	0.524907	-0.50920	0.419573
19c	0.219159	0.727685	0.055836	0.926892	48O	0.706988	0.237128	0.597656	0.335504
20c	0.202640	0.746908	0.212412	0.735526	49O	-0.720728	0.225174	-0.80292	0.155468
21c	0.661431	0.277403	0.645588	0.291652	50c	0.601598	0.331852	0.556313	0.374280
22O	0.807507	0.151672	0.699200	0.243943	51O	-0.155939	0.802349	-0.12451	0.840599
23c	-0.565766	0.365336	-0.69145	0.250754	52O	-0.748394	0.201370	-0.86559	0.104306
24O	0.597302	0.335833	0.520315	0.408785	53c	-0.629082	0.306620	-0.79860	0.159055
25O	-0.653871	0.284187	-0.72866	0.218313	54O	0.493689	0.434764	0.485922	0.442417
26c	0.660716	0.278048	0.612208	0.322068	55c	0.825985	0.136445	0.681357	0.259663
27c	0.702762	0.240822	0.807988	0.151269	56c	0.572955	0.358561	0.695674	0.247039
28c	0.054552	0.928561	0.226644	0.719034	57c	0.386805	0.543159	0.462369	0.465832
29c	0.384853	0.545204	0.470383	0.457831	58O	-0.579711	0.352224	-0.61314	0.321207
30c	0.120913	0.845027	0.135531	0.827103	59c	0.667287	0.272174	0.704061	0.239687

Thermodynamic calculations

Thermodynamic parameters levels such as relative energy (ΔE), standard enthalpies (ΔH), entropies (ΔS), Gibbs free energy (ΔG) and constant volume molar heat capacity (C_v) values of vinblastine were computed by Freq method using HF/6-31G(d) obtained. The values are tabulated in Table 6. The resultant data show that relative energy, Gibbs free energy and standard enthalpies of vinblastine are negative indicating the stable character of its structure.

Natural bond orbital (NBO) analysis:

In computational chemistry, NBO is a calculated bonding orbital that contains maximum electron density. The NBO is one of a sequence of natural localized orbital sets that include "natural atomic orbitals (NAO), natural hybrid orbitals (NHO) and natural (semi-)localized molecular orbitals (NLMO). These natural localized sets are intermediate between basis atomic orbitals (AO) and molecular orbitals (MO)[30, 31]. In quantum chemistry, the distribution of electron densities on

atoms and the bonds between them are investigated by NBO analyses. NBOs contain the highest possible percentage of the electron density, ideally close to 2.000 [31-32]. This is performed by considering all possible interactions between filled donor and empty acceptor NBOs and evaluating their energetic importance by the second-order perturbation theory. For each donor NBO (i) and acceptor NBO (j), the stabilization energy $E^{(2)}$ associated with electron delocalization between donor and acceptor is evaluated by the equation:

$$E^{(2)} = -q_i \frac{(F)_{i,j}^2}{\epsilon_j - \epsilon_i}$$

where q_i is the orbital occupancy, ϵ_i , ϵ_j are diagonal characters and $F_{i,j}$ is the off-diagonal NBO Fock matrix element [32].

In this study we investigated the nature of bonding in vinblastine molecular structure (scheme 1), by the aid of NBO analyses. It is suggested that the results from NBO calculations can provide a new vision into the electronic structure of the molecule. The obtained results of NBOs analyses such as occupancy, bond orbital, coefficients and

hybrids at the HF level of theory are compiled in Table 7.

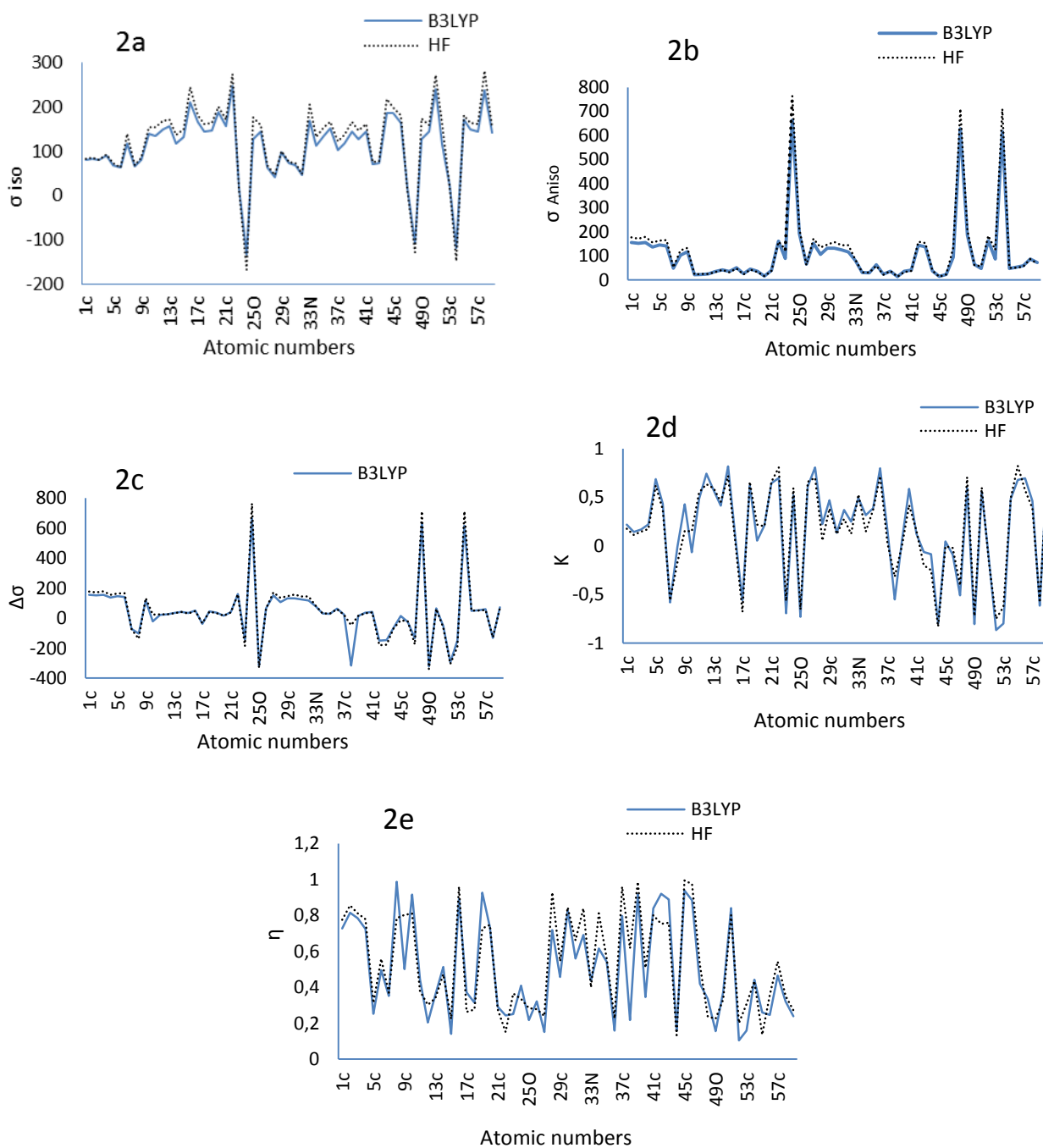


Fig. 2. Graphs of a) σ_{iso} , b) σ_{aniso} , c) $\Delta\sigma$ d) K, e) η versus atoms of vinblastine in gas phase at the B3LYP / 6-31G (d) and HF/ 6-31G (d) basis set.

Table 3. Experimental (in CDCl₃ and DMSO) and calculated chemical shifts by B3LYP and HF levels of theory with 6-31 G(d) as basis set.

NMR chemical shift data (δ)									
Atomic label	Calculation		Experimental		Atomic label	Calculation		Experimental	
	HF method	B3LYP method	CDCl ₃ solvent	DMSO solvent		HF method	B3LYP method	CDCl ₃ solvent	DMSO solvent
1c	118.0705	103.7072	118.5	117.7	29c	97.6299	87.8334	94.2	94.2
2c	113.9274	101.6535	118.8	118	30c	104.9234	88.0451	123.6	123.8
3c	119.1274	103.6926	122.2	121.1	31c	96.0377	83.5376	122.7	122.3
4c	103.3063	91.0713	110.5	111.4	32c	96.48	77.7822	152.7	152.2
5c	109.0176	97.0016	129.6	128.7	34c	20.81	20.207	83.4	82.2
6c	110.6892	93.5488	135.0	135.4	35c	20.171	19.466	53.3	52.9
8c	-91.4884	-68.9511	131.5	131.3	36c	39.4289	42.3166	38.4	38.1
9c	88.5207	77.9955	117.1	115.8	37c	14.5568	15.7592	79.7	79.4
10c	15.1166	-14.5957	55.8	55.2	38c	-30.911	-34.7096	76.5	75.9
11c	16.4948	14.9012	34.4	34.2	39c	9.0164	9.4592	42.7	42.1
12c	16.4135	16.9597	30.2	29.6	40c	21.6097	23.985	65.6	63.9
13c	21.8298	23.0768	41.6	40.7	41c	25.108	27.3086	50.3	49.5
14c	28.1225	28.0908	69.7	67.3	42c	-121.0814	-99.8585	130.1	130.3
15c	20.8574	23.1679	64.4	63.9	43c	-114.5378	-97.0601	124.5	124.0
17c	-23.4899	-24.8139	28.8	27.9	45c	-9.2352	9.8581	8.4	7.8
18c	28.9625	30.0559	55.8	56.2	46c	-14.9263	-16.3842	30.9	30.7
19c	22.0205	24.0562	48.2	46.9	47c	-117.3436	-89.3635	171.7	171.1
20c	10.3259	10.6105	6.9	7.0	50c	40.9327	42.956	52.2	51.5
21c	25.137	26.0015	34.4	34.2	53c	-128.127	-100.3541	170.9	170.0
23c	-124.1594	-94.9201	174.9	174.5	55c	33.2434	31.9533	21.2	20.9
26c	41.5816	43.6677	52.4	51.9	56c	33.9523	35.06	44.6	44.6
27c	113.9659	101.0682	121.2	121.1	57c	36.5841	39.1688	50.4	48.9
28c	89.9416	70.7147	158.1	157.6	59c	44.7859	48.0389	55.8	56.0

Table 4. Some electronic properties of vinblastine

E _{HOMO} (ev)	E _{LUMO} (ev)	E _{bg} (ev)
-0.25936	0.12368	0.38304

Table 8 collects the second-order perturbative estimations of donor-acceptor interactions. This analysis is done by considering all probable interactions between filled donor Lewis-type NBOs and empty acceptor non-Lewis NBOs, and evaluating their energetic necessity by the 2nd-order perturbation theory. Since these interactions cause a loss of occupancy from the localized NBOs of the idealized Lewis structure into the empty non-Lewis orbitals, this is known as delocalization corrections to the zero-order natural Lewis structure. The stabilization energy E^2 along with delocalization between donor NBO (i) and acceptor NBO (j) can be calculated based on the equation mentioned previously using the values shown in Table 8.

The strongest interaction in vinblastine is found for BD(1) C₅-H₉ → BD* (1) C₈-C₁₀ with $E^2= 9.40$ Kcal/mol and BD(2) C₃₁-C₃₂ → BD* (2) C₂₇-C₃₀ with $E^2= 48.42$ Kcal/mol.

Vinblastine molecule can be rotated around its bonds and NMR analyses are performed at each status. In this way, we changed the

torsion angle around the C₁₁- C₁₀- C₂₇- C₂₈ and then NMR analyses were performed for each torsion angle. Based on these analyses, magnetic shielding tensor (σ , ppm), shielding asymmetry (η), magnetic shielding anisotropy (σ_{aniso}) and skew of a tensor (K) were evaluated and the graphs of this calculated parameters *versus* the torsion angle for some atoms were sketched, as shown in Fig. 3. As can be seen, skew parameter changes *versus* torsion angles for O₂₅ and N₄₄ obey a polynomial order 4 and Dirac delta function, respectively. The changes of σ_{iso} and σ_{Aniso} *versus* torsion angles for O₄₉ and O₂₄ are obtained as Dirac delta function (positive and negative, respectively) with maximum value in torsion angle of 80°. It is to be noted that this angle is the one found at the optimum structure of vinblastine. The plot of shielding asymmetry changes (η) *versus* torsion angles for O₂₄ is found to be of polynomial order 6.

Table 5. Calculated Mullikan atomic charges for all atoms in vinblastine molecular structure.

Atomic label	Mullikan Charge	Atomic label	Mullikan Charge	Atomic label	Mullikan Charge	Atomic label	Mullikan Charge
1c	-0.13619	31c	-0.02926	61H	0.184648	91H	0.164775
2c	-0.22792	32c	0.265	62H	0.186518	92H	0.146818
3c	-0.21732	33N	-0.77152	63H	0.196788	93H	0.272845
4c	-0.14082	34c	0.073628	64H	0.43771	94H	0.159914
5c	-0.21191	35c	-0.08953	65H	0.254383	95H	0.141219
6c	0.308355	36c	-0.26553	66H	0.230143	96H	0.180493
7N	-1.00778	37c	0.222878	67H	0.163308	97H	0.188434
8c	0.282342	38c	0.127902	68H	0.21347	98H	0.179906
9c	0.154342	39c	-0.11579	69H	0.137191	99H	0.142957
10c	-0.2793	40c	0.067632	70H	0.168751	100H	0.162479
11c	-0.16864	41c	-0.11388	71H	0.165403	101H	0.163872
12c	-0.11404	42c	-0.09274	72H	0.197505	102H	0.176901
13c	-0.26947	43c	-0.17035	73H	0.164002	103H	0.177369
14c	0.211056	44N	-0.63763	74H	0.158911	104H	0.18265
15c	-0.02414	45c	-0.45698	75H	0.133441	105H	0.180525
16N	-0.7204	46c	-0.30954	76H	0.172843	106H	0.181985
17c	-0.32805	47c	0.875485	77H	0.151748	107H	0.421133
18c	-0.05787	48O	-0.58357	78H	0.148429	108H	0.202064
19c	-0.09774	49O	-0.71443	79H	0.173915	109H	0.213386
20c	-0.45233	50c	-0.1453	80H	0.154205	110H	0.195012
21c	-0.31385	51O	-0.70344	81H	0.16537	111H	0.174738
22O	-0.74841	52O	-0.75784	82H	0.141191	112H	0.178543
23c	0.785359	53c	0.800234	83H	0.395133	113H	0.138989
24O	-0.55927	54O	-0.56415	84H	0.188259	114H	0.180177
25c	-0.72328	55c	-0.50742	85H	0.180898	115H	0.186719
26c	-0.14027	56c	-0.31379	86H	0.177623	116H	0.195058
27c	-0.03382	57c	-0.07669	87H	0.234449	117H	0.167143
28c	0.392776	58H	-0.82446	88H	0.227144		
29c	-0.18419	59H	-0.16245	89H	0.231773		
30c	-0.20595	60H	0.202366	90H	0.208582		

Table 6. Calculated thermodynamic parameters of vinblastine using HF/6-31G(d) level

Zero point energy (Hartree)	ΔE (Hartree) ^a	ΔG (Hartree)	ΔH (Hartree)	S (cal/molK)	CV (cal/molK)
-2664.946395	-2664.898065	-2665.022405	-2664.89712	263.683	197.316

^a consider that 1 Hartree= 627.5095 Kcal/mol

Table 7. Results of NBOs analyses at the HF level of theory with 6-31 G(d).

Bond_{No.ele}^{BD}	Coefficients hybrids	Bond_{No.ele}^{BD}	Coefficients hybrids
1	2	3	4
C1 – C2_{1.97855}^σ	0.7096 SP ^{1.76} + 0.7046 SP ^{1.78}	C17 – H73_{1.98192}^σ	0.7876 SP ^{3.22} + 0.6162 S
C1 – C2_{1.74662}^π	0.6918 SP + 0.7220 SP	C18 – H74_{1.98482}^σ	0.7836 SP ^{3.09} + 0.6213 S
C1 – C5_{1.97347}^σ	0.6983 SP ^{1.92} + 0.7158 SP ^{1.77}	C18 – H75_{1.98994}^σ	0.7793 SP ^{2.94} + 0.6266 S
C1 – H60_{1.98225}^σ	0.7868 SP ^{2.38} + 0.6172 S	C19 – H76_{1.98964}^σ	0.7866 SP ^{2.96} + 0.6174 S
C2 – C3_{1.97878}^σ	0.7059 SP ^{1.90} + 0.7083 SP ^{1.87}	C19 – H77_{1.98617}^σ	0.7802 SP ^{3.01} + 0.6255 S
C2 – H61_{1.98304}^σ	0.7866 SP ^{2.38} + 0.6175 S	C20 – C21_{1.99085}^σ	0.7018 SP ^{2.71} + 0.7124 SP ^{2.77}
C3 – C4_{1.97704}^σ	0.7033 SP ^{1.80} + 0.7109 SP ^{1.75}	C20 – H78_{1.99069}^σ	0.7841 SP ^{3.13} + 0.6207 S
C3 – C4_{1.75437}^π	0.6965 SP + 0.7176 SP	C20 – H79_{1.99158}^σ	0.7885 SP ^{3.08} + 0.6150 S
C3 – H62_{1.98290}^σ	0.7866 SP ^{2.40} + 0.6174 S	C20 – H80_{1.99167}^σ	0.7834 SP ^{3.12} + 0.6215 S
C4 – C6_{1.97541}^σ	0.6987 SP ^{1.97} + 0.7154 SP ^{1.61}	C21 – H81_{1.98160}^σ	0.7879 SP ^{3.21} + 0.6159 S
C4 – H63_{1.98257}^σ	0.7865 SP ^{2.34} + 0.6176 S	C21 – H82_{1.98422}^σ	0.7826 SP ^{3.34} + 0.6225 S
C5 – C6_{1.96490}^σ	0.7073 SP ^{2.25} + 0.7069 SP ^{1.94}	O22 – H83_{1.98960}^σ	0.8608 SP ^{4.36} + 0.5089 S
C5 – C6_{1.61719}^π	0.7249 SP + 0.6889 SP ^{99.99}	C23 – O24_{1.99675}^σ	0.5800 SP ^{2.00} + 0.8146 SP ^{1.43}
C5 – C9_{1.96426}^σ	0.7137 SP ^{2.02} + 0.7005 SP ^{2.30}	C23 – O24_{1.99208}^π	0.5348 SP ^{99.99} + 0.8450 SP ^{99.99}
C6 – N7_{1.98442}^σ	0.6249 SP ^{2.64} + 0.7807 SP ^{1.95}	C23 – O25_{1.98208}^σ	0.5524 SP ^{2.74} + 0.8336 SP ^{2.37}
N7 – C8_{1.98134}^σ	0.7866 SP ^{2.08} + 0.6174 SP ^{2.91}	O25 – C26_{1.99313}^σ	0.8349 SP ^{2.43} + 0.5504 SP ^{3.91}
N7 – H64_{1.98080}^σ	0.8625 SP ^{2.51} + 0.5061 S	C26 – H84_{1.99632}^σ	0.7853 SP ^{2.71} + 0.6191 S
C8 – C9_{1.97203}^σ	0.7086 SP ^{1.47} + 0.7057 SP ^{1.79}	C26 – H85_{1.99624}^σ	0.7838 SP ^{2.72} + 0.6210 S
C8 – C9_{1.87436}^π	0.7023 SP ^{99.99} + 0.7119 SP ^{99.99}	C26 – H86_{1.99223}^σ	0.7832 SP ^{2.86} + 0.6217 S
C8 – C10_{1.97420}^σ	0.6982 SP ^{1.96} + 0.7159 SP ^{2.59}	C27 – C28_{1.97149}^σ	0.7082 SP ^{1.97} + 0.7060 SP ^{1.64}
C9 – C17_{1.97701}^σ	0.7151 SP ^{1.96} + 0.6990 SP ^{2.78}	C27 – C30_{1.96919}^σ	0.7097 SP ^{1.90} + 0.7045 SP ^{1.81}
C10 – C11_{1.96775}^σ	0.7196 SP ^{2.65} + 0.6944 SP ^{3.01}	C27 – C30_{1.67501}^π	0.7233 SP + 0.6905 SP
C10 – C23_{1.97450}^σ	0.7102 SP ^{3.40} + 0.7040 SP ^{1.52}	C28 – C29_{1.97476}^σ	0.7059 SP ^{1.61} + 0.7083 SP ^{1.91}
C10 – H65_{1.95995}^σ	0.8031 SP ^{3.53} + 0.5959 S	C28 – C29_{1.69659}^π	0.6795 SP + 0.7337 SP
C11 – C12_{1.97338}^σ	0.7180 SP ^{2.63} + 0.6960 SP ^{2.83}	C28 – O58_{1.99158}^σ	0.5644 SP ^{3.23} + 0.8255 SP ^{2.17}
C11 – C27_{1.97129}^σ	0.6972 SP ^{2.89} + 0.7168 SP ^{2.13}	C29 – C32_{1.97041}^σ	0.7038 SP ^{1.80} + 0.7104 SP ^{1.68}
C11 – H66_{1.97329}^σ	0.7954 SP ^{3.57} + 0.6061 S	C29 – H87_{1.97762}^σ	0.7917 SP ^{2.33} + 0.6109 S
C12 – C13_{1.98056}^σ	0.7096 SP ^{2.81} + 0.7046 SP ^{2.81}	C30 – C31_{1.97003}^σ	0.6992 SP ^{1.83} + 0.7150 SP ^{1.73}
C12 – C19_{1.97916}^σ	0.7116 SP ^{2.94} + 0.7026 SP ^{2.71}	C30 – H88_{1.97988}^σ	0.7900 SP ^{2.43} + 0.6131 S
C12 – H67_{1.97554}^σ	0.7890 SP ^{3.48} + 0.6144 S	C31 – C32_{1.96735}^σ	0.7087 SP ^{2.10} + 0.7055 SP ^{1.83}
C13 – C14_{1.97846}^σ	0.7046 SP ^{2.88} + 0.7096 SP ^{2.65}	C31 – C32_{1.65024}^π	0.7314 SP + 0.6819 SP ^{99.99}
C13 – H68_{1.97955}^σ	0.7966 SP ^{3.08} + 0.6045 S	C31 – C35_{1.96553}^σ	0.7078 SP ^{2.21} + 0.7064 SP ^{2.87}
C13 – H69_{1.98370}^σ	0.7824 SP ^{3.28} + 0.6228 S	C32 – N33_{1.98226}^σ	0.6335 SP ^{2.68} + 0.7737 SP ^{2.53}

Table 7 continued

1	2	3	4
C14 – C15 $\sigma_{1.97286}$	0.7123 SP ^{2.85} + 0.7019 SP ^{2.76}	N33 – C34 $\sigma_{1.98004}$	0.7837 SP ^{2.54} + 0.6211 SP ^{3.75}
C14 – C21 $\sigma_{1.98101}$	0.7091 SP ^{2.59} + 0.7051 SP ^{2.75}	N33 – C36 $\sigma_{1.98375}$	0.7899 SP ^{2.53} + 0.6132 SP ^{3.33}
C14 – O22 $\sigma_{1.99275}$	0.5602 SP ^{4.33} + 0.8284 SP ^{2.10}	C34 – C35 $\sigma_{1.97273}$	0.7044 SP ^{2.64} + 0.7098 SP ^{3.16}
C15 – N16 $\sigma_{1.98549}$	0.6245 SP ^{3.26} + 0.7810 SP ^{2.38}	C34 – C37 $\sigma_{1.96735}$	0.6963 SP ^{2.88} + 0.7178 SP ^{2.58}
C15 – H70 $\sigma_{1.98379}$	0.7843 SP ^{3.04} + 0.6204 S	C34 – H89 $\sigma_{1.98008}$	0.7999 SP ^{2.89} + 0.6001 S
C15 – H71 $\sigma_{1.98834}$	0.7856 SP ^{2.97} + 0.6187 S	C35 – C40 $\sigma_{1.96804}$	0.7141 SP ^{2.92} + 0.7001 SP ^{2.86}
N16 – C18 $\sigma_{1.98633}$	0.7847 SP ^{2.26} + 0.6199 SP ^{3.31}	C35 – C56 $\sigma_{1.96740}$	0.7227 SP ^{3.03} + 0.6912 SP ^{2.80}
N16 – C19 $\sigma_{1.98429}$	0.7787 SP ^{2.50} + 0.6274 SP ^{3.37}	C36 – H90 $\sigma_{1.99078}$	0.7912 SP ^{2.86} + 0.6115 S
C17 – C18 $\sigma_{1.97913}$	0.7068 SP ^{2.96} + 0.7074 SP ^{2.70}	C36 – H91 $\sigma_{1.99112}$	0.7834 SP ^{2.96} + 0.6215 S
C17 – H72 $\sigma_{1.98346}$	0.7918 SP ^{3.08} + 0.6107 S	C36 – H92 $\sigma_{1.99668}$	0.7796 SP ^{2.89} + 0.6263 S
C37 – C38 $\sigma_{1.97382}$	0.7110 SP ^{2.62} + 0.7032 SP ^{2.76}	C46 – H103 $\sigma_{1.98319}$	0.7894 SP ^{3.25} + 0.6139 S
C37 – C47 $\sigma_{1.97407}$	0.7076 SP ^{3.23} + 0.7066 SP ^{1.57}	C47 – O48 $\sigma_{1.99697}$	0.5780 SP ^{1.94} + 0.8160 SP ^{1.38}
C37 – O51 $\sigma_{1.98942}$	0.5845 SP ^{3.84} + 0.8114 SP ^{2.39}	C47 – O48 $\pi_{1.99263}$	0.5254 SP ^{99.99} + 0.8508 SP ^{99.99}
C38 – C39 $\sigma_{1.96986}$	0.7077 SP ^{2.50} + 0.7066 SP ^{3.14}	C47 – O49 $\sigma_{1.99218}$	0.5550 SP ^{2.67} + 0.8319 SP ^{2.36}
C38 – O52 $\sigma_{1.98883}$	0.5475 SP ^{4.49} + 0.8368 SP ^{2.17}	O49 – C50 $\sigma_{1.98285}$	0.8338 SP ^{2.48} + 0.5520 SP ^{3.91}
C38 – H93 $\sigma_{1.97761}$	0.8042 SP ^{2.74} + 0.5943 S	C50 – H104 $\sigma_{1.99123}$	0.7841 SP ^{2.85} + 0.6207 S
C39 – C40 $\sigma_{1.97025}$	0.7084 SP ^{2.94} + 0.7058 SP ^{2.57}	C50 – H105 $\sigma_{1.99603}$	0.7838 SP ^{2.72} + 0.6210 S
C39 – C42 $\sigma_{1.96975}$	0.7193 SP ^{2.96} + 0.6947 SP ^{2.20}	C50 – H106 $\sigma_{1.99696}$	0.7840 SP ^{2.72} + 0.6208 S
C39 – C46 $\sigma_{1.96999}$	0.7219 SP ^{2.97} + 0.6920 SP ^{2.82}	O51 – H107 $\sigma_{1.98762}$	0.8671 SP ^{4.13} + 0.4981 S
C40 – N44 $\sigma_{1.97970}$	0.6349 SP ^{3.57} + 0.7726 SP ^{2.58}	O52 – C53 $\sigma_{1.99158}$	0.8370 SP ^{2.39} + 0.5472 SP ^{2.69}
C40 – H94 $\sigma_{1.98178}$	0.7844 SP ^{3.12} + 0.6203 S	C53 – O54 $\sigma_{1.99691}$	0.5800 SP ^{1.93} + 0.8146 SP ^{1.41}
C41 – C43 $\sigma_{1.98003}$	0.7106 SP ^{2.66} + 0.7036 SP ^{2.24}	C53 – O54 $\pi_{1.99310}$	0.5294 SP ^{99.99} + 0.8484 SP ^{99.99}
C41 – N44 $\sigma_{1.98515}$	0.6265 SP ^{3.32} + 0.7795 SP ^{2.46}	C53 – C55 $\sigma_{1.98516}$	0.7077 SP ^{1.57} + 0.7065 SP ^{3.01}
C41 – H95 $\sigma_{1.98365}$	0.7805 SP ^{3.04} + 0.6252 S	C55 – H108 $\sigma_{1.98898}$	0.7936 SP ^{2.97} + 0.6085 S
C41 – H96 $\sigma_{1.98160}$	0.7891 SP ^{3.02} + 0.6142 S	C55 – H109 $\sigma_{1.98033}$	0.7956 SP ^{3.00} + 0.6059 S
C42 – C43 $\sigma_{1.98194}$	0.7092 SP ^{1.52} + 0.7050 SP ^{1.53}	C55 – H110 $\sigma_{1.98239}$	0.7922 SP ^{3.02} + 0.6103 S
C42 – C43 $\pi_{1.97100}$	0.7088 SP + 0.7054 SP	C56 – C57 $\sigma_{1.98633}$	0.7095 SP ^{2.94} + 0.7047 SP ^{2.78}
C42 – H97 $\sigma_{1.97840}$	0.7894 SP ^{2.45} + 0.6139 S	C56 – H111 $\sigma_{1.98740}$	0.7882 SP ^{3.04} + 0.6154 S
C43 – H98 $\sigma_{1.97970}$	0.7861 SP ^{2.37} + 0.6182 S	C56 – H112 $\sigma_{1.98626}$	0.7887 SP ^{3.15} + 0.6148 S
N44 – C57 $\sigma_{1.98476}$	0.7793 SP ^{2.61} + 0.6266 SP ^{3.41}	C57 – H113 $\sigma_{1.99091}$	0.7793 SP ^{2.97} + 0.6266 S
C45 – C46 $\sigma_{1.99067}$	0.7033 SP ^{2.69} + 0.7109 SP ^{2.77}	C57 – H114 $\sigma_{1.98671}$	0.7886 SP ^{2.90} + 0.6149 S
C45 – H99 $\sigma_{1.99164}$	0.7812 SP ^{3.13} + 0.6243 S	O58 – C59 $\sigma_{1.99256}$	0.8320 SP ^{2.58} + 0.5548 SP ^{3.85}
C45 – H100 $\sigma_{1.98955}$	0.7868 SP ^{3.13} + 0.6173 S	C59 – H115 $\sigma_{1.99579}$	0.7844 SP ^{2.71} + 0.6202 S
C45 – H101 $\sigma_{1.99176}$	0.7864 SP ^{3.09} + 0.6177 S	C59 – H116 $\sigma_{1.98033}$	0.7864 SP ^{2.85} + 0.6059 S
C46 – H102 $\sigma_{1.98324}$	0.7886 SP ^{3.23} + 0.6150 S	C59 – H117 $\sigma_{1.98033}$	0.7797 SP ^{2.77} + 0.6261 S

Table 8. Second- order interaction energy (E^2 , Kcal/mol) between donor and acceptor orbitals in vinblastine^a.

Donor NBO (i)	Acceptor NBO (j)	$E_{\text{acceptor}(i)}-E_{\text{Donor}(j)}$ •Fack Matrix (F_{ij} , a.u.)	E^2 (Kcal/mol)	Donor NBO (i)	Acceptor NBO (j)	$E_{\text{acceptor}(i)}-E_{\text{Donor}(j)}$ •Fack Matrix (F_{ij} , a.u.)	E^2 (Kcal/mol)
1	2	2	4	5	6	7	8
C1 – C2σ	C1 – C5 σ^*	$ \psi\rangle=\text{BD (1)-BD}^* (1)=1.79$ *0.085	5.10	C12 – C13 σ	C14 – C21 σ^*	$ \psi\rangle=\text{BD (1)-BD}^* (1)=1.35$ *0.031	2.18
C1 – C2π	C3 – C4 π^*	$ \psi\rangle=\text{BD (2)-BD}^* (2)=0.50$ *0.126	38.91	C12 – C19 σ	N16 – C18 σ^*	$ \psi\rangle=\text{BD (1)-BD}^* (1)=1.35$ *0.032	3.03
C1 – C5σ	C5 – C9 σ^*	$ \psi\rangle=\text{BD (1)-BD}^* (1)=1.80$ *0.080	6.64	C12 – H67 σ	C10 – C11σ^*	$ \psi\rangle=\text{BD (1)-BD}^* (1)=1.20$ *0.080	6.63
C1 – H60σ	C2 – C3 σ^*	$ \psi\rangle=\text{BD (1)-BD}^* (1)=1.59$ *0.052	4.99	C13 – C14 σ	C11 – C12 σ^*	$ \psi\rangle=\text{BD (1)-BD}^* (1)=1.36$ *0.059	3.21
C2 – C3σ	C3 – C4 σ^*	$ \psi\rangle=\text{BD (1)-BD}^* (1)=1.79$ *0.050	4.26	C13 – H68 σ	C12 – H67σ^*	$ \psi\rangle=\text{BD (1)-BD}^* (1)=1.27$ *0.030	2.79
C2 – H61σ	C1 – C5 σ^*	$ \psi\rangle=\text{BD (1)-BD}^* (1)=1.59$ *0.052	5.11	C13 – H69 σ	C12 – C19σ^*	$ \psi\rangle=\text{BD (1)-BD}^* (1)=1.28$ *0.028	3.64
C3 – C4σ	C6 – N7 σ^*	$ \psi\rangle=\text{BD (1)-BD}^* (1)=1.77$ *0.076	7.17	C14 – C15 σ	N16 – C18 σ^*	$ \psi\rangle=\text{BD (1)-BD}^* (1)=1.36$ *0.032	3.51
C3 – C4π	C5 – C6 π^*	$ \psi\rangle=\text{BD (2)-BD}^* (2)=0.52$ *0.116	34.18	C14 – C21 σ	C12 – C13σ^*	$ \psi\rangle=\text{BD (1)-BD}^* (1)=1.39$ *0.051	2.34
C3 – H62σ	C4 – C6 σ^*	$ \psi\rangle=\text{BD (1)-BD}^* (1)=1.59$ *0.074	5.10	C14 – O22 σ	C21 – H81σ^*	$ \psi\rangle=\text{BD (1)-BD}^* (1)=1.81$ *0.040	1.19
C4 – C6σ	C5 – C6 σ^*	$ \psi\rangle=\text{BD (1)-BD}^* (1)=1.81$ *0.078	6.68	C15 – N16 σ	C19 – H77σ^*	$ \psi\rangle=\text{BD (1)-BD}^* (1)=1.48$ *0.037	1.95
C4 – H63σ	C5 – C6 σ^*	$ \psi\rangle=\text{BD (1)-BD}^* (1)=1.54$ *0.078	4.94	C15 – H70 σ	N16 – C19σ^*	$ \psi\rangle=\text{BD (1)-BD}^* (1)=1.25$ *0.025	4.60
C5 – C6σ	C4 – C6 σ^*	$ \psi\rangle=\text{BD (1)-BD}^* (1)=1.75$ *0.087	6.20	C15 – H71 σ	C14 – O22 σ^*	$ \psi\rangle=\text{BD (1)-BD}^* (1)=1.26$ *0.046	2.29
C5 – C6π	C1 – C5 π^*	$ \psi\rangle=\text{BD (2)-BD}^* (2)=0.48$ *0.129	41.82	N16 – C18 σ	C14 – C15 σ^*	$ \psi\rangle=\text{BD (1)-BD}^* (1)=1.49$ *0.044	1.87
	N7 – H64σ^*	$ \psi\rangle=\text{BD (2)-BD}^* (1)=1.04$ *0.031	0.98				
C5 – C9σ	C8 – C10 σ^*	$ \psi\rangle=\text{BD (1)-BD}^* (1)=1.72$ *0.047	9.40	N16 – C19 σ	C15 – H70σ^*	$ \psi\rangle=\text{BD (1)-BD}^* (1)=1.60$ *0.036	1.83
C6 – N7σ	C8 – C10 σ^*	$ \psi\rangle=\text{BD (1)-BD}^* (1)=1.86$ *0.070	3.45	C17 – C18 σ	C15 – N16σ^*	$ \psi\rangle=\text{BD (1)-BD}^* (1)=1.36$ *0.061	3.47
					C8 – C9π^*	$ \psi\rangle=\text{BD (1)-BD}^* (2)=0.98$ *0.059	3.69
N7 – C8σ	C4 – C6 σ^*	$ \psi\rangle=\text{BD (1)-BD}^* (1)=1.82$ *0.048	5.65	C17 – H72 σ	C5 – C9 σ^*	$ \psi\rangle=\text{BD (1)-BD}^* (1)=1.45$ *0.075	4.80
					C8 – C9π^*	$ \psi\rangle=\text{BD (1)-BD}^* (2)=0.89$ *0.021	0.56
N7 – H64σ	C8 – C9 σ^*	$ \psi\rangle=\text{BD (1)-BD}^* (1)=1.79$ *0.056	2.16	C17 – H73 σ	C8 – C9 σ^*	$ \psi\rangle=\text{BD (1)-BD}^* (1)=1.61$ *0.076	4.45
	C8 – C9 π^*	$ \psi\rangle=\text{BD (1)-BD}^* (2)=1.07$ *0.032	1.09		C8 – C9π^*	$ \psi\rangle=\text{BD (1)-BD}^* (2)=0.89$ *0.035	1.54
C8 – C9σ	C8 – C10 σ^*	$ \psi\rangle=\text{BD (1)-BD}^* (1)=1.81$ *0.084	5.95	C18 – H74 σ	N16 – C19σ^*	$ \psi\rangle=\text{BD (1)-BD}^* (1)=1.27$ *0.071	4.99
C8 – C9π	C5 – C6 π^*	$ \psi\rangle=\text{BD (2)-BD}^* (2)=0.52$ *0.109	24.23	C18 – H75 σ	C9 – C17σ^*	$ \psi\rangle=\text{BD (1)-BD}^* (1)=1.35$ *0.060	3.32
	N7 – H64σ^*	$ \psi\rangle=\text{BD (2)-BD}^* (1)=1.09$ *0.030	0.96				
C8 – C10σ	C8 – C9 σ^*	$ \psi\rangle=\text{BD (1)-BD}^* (1)=1.62$ *0.051	6.43	C19 – H76 σ	C11 – C12 σ^*	$ \psi\rangle=\text{BD (1)-BD}^* (1)=1.26$ *0.049	2.36
C9 – C17σ	C8 – C9 σ^*	$ \psi\rangle=\text{BD (1)-BD}^* (1)=1.64$ *0.048	6.50	C19 – H77 σ	C12 – C13 σ^*	$ \psi\rangle=\text{BD (1)-BD}^* (1)=1.28$ *0.023	1.94
C10 – C11σ	C23 – O24 σ^*	$ \psi\rangle=\text{BD (1)-BD}^* (1)=1.72$ *0.032	3.06	C20 – C21 σ	C13 – C14σ^*	$ \psi\rangle=\text{BD (1)-BD}^* (1)=1.37$ *0.050	2.32
	C8 – C9 π^*	$ \psi\rangle=\text{BD (1)-BD}^* (2)=1.00$ *0.044	2.02				
C10 – C23σ	O25 – C26 σ^*	$ \psi\rangle=\text{BD (1)-BD}^* (1)=1.53$ *0.052	3.91	C20 – H78 σ	C14 – C21 σ^*	$ \psi\rangle=\text{BD (1)-BD}^* (1)=1.26$ *0.066	4.27
	C8 – C9 π^*	$ \psi\rangle=\text{BD (1)-BD}^* (2)=1.08$ *0.036	1.37				

Table 8 continued

1	2	2	4	5	6	7	8
C10 – H65^σ	C8 – C9^{σ*}	$ \psi\rangle=BD(1)-BD^*(1)=1.64$ *0.084	5.30	C20 – H79^σ	C21 – H81^{σ*}	$ \psi\rangle=BD(1)-BD^*(1)=1.28$ *0.024	3.46
	C23 – O24^{π*}	$ \psi\rangle=BD(1)-BD^*(2)=0.84$ *0.073	7.66				
C11 – C12^σ	C10 – C11^{σ*}	$ \psi\rangle=BD(1)-BD^*(1)=1.31$ *0.034	1.01	C20 – H80^σ	C21 – H82^{σ*}	$ \psi\rangle=BD(1)-BD^*(1)=1.29$ *0.023	3.28
	C27 – C30^{π*}	$ \psi\rangle=BD(1)-BD^*(2)=0.93$ *0.046	2.43				
C11 – C27^σ	C27 – C28^{σ*}	$ \psi\rangle=BD(1)-BD^*(1)=1.34$ *0.030	3.67	C21 – H81^σ	C14 – O22^{σ*}	$ \psi\rangle=BD(1)-BD^*(1)=1.17$ *0.075	6.03
C11 – H66^σ	C27 – C28^{σ*}	$ \psi\rangle=BD(1)-BD^*(1)=1.31$ *0.056	6.04	C21 – H82^σ	C14 – C15^{σ*}	$ \psi\rangle=BD(1)-BD^*(1)=1.25$ *0.064	4.10
O22 – H83^σ	C14 – C15^{σ*}	$ \psi\rangle=BD(1)-BD^*(1)=1.47$ *0.073	4.51	C36 – H90^σ	C32 – N33^{σ*}	$ \psi\rangle=BD(1)-BD^*(1)=1.32$ *0.067	4.16
C23 – O24^σ	C10 – C23^{σ*}	$ \psi\rangle=BD(1)-BD^*(1)=1.99$ *0.045	1.22	C36 – H91^σ	N33 – C34^{σ*}	$ \psi\rangle=BD(1)-BD^*(1)=1.23$ *0.064	4.17
C23 – O24^π	C10 – C11^{σ*}	$ \psi\rangle=BD(2)-BD^*(1)=1.10$ *0.035	1.35	C36 – H92^σ	N33	$ \psi\rangle=BD(1)-RY^*(1)=1.98$ *0.040	1.04
C23 – O25^σ	C8 – C10^{σ*}	$ \psi\rangle=BD(1)-BD^*(1)=1.79$ *0.045	1.39	C37 – C38^σ	C47 – O49^{σ*}	$ \psi\rangle=BD(1)-BD^*(1)=1.37$ *0.040	2.48
O25 – C26^σ	C10 – C23^{σ*}	$ \psi\rangle=BD(1)-BD^*(1)=1.63$ *0.064	3.09	C37 – C47^σ	O49 – C50^{σ*}	$ \psi\rangle=BD(1)-BD^*(1)=1.40$ *0.049	3.94
C26 – H84^σ	O25	$ \psi\rangle=BD(1)-RY^*(1)=2.22$ *0.045	0.51	C37 – O51^σ	N33 – C34^{σ*}	$ \psi\rangle=BD(1)-BD^*(1)=1.60$ *0.045	1.56
					C47 – O48^{π*}	$ \psi\rangle=BD(1)-BD^*(2)=1.23$ *0.040	1.54
C26 – H86^σ	C23 – C25^{σ*}	$ \psi\rangle=BD(1)-BD^*(1)=1.23$ *0.062	3.81	C38 – C39^σ	C45 – C46^{σ*}	$ \psi\rangle=BD(1)-BD^*(1)=1.34$ *0.038	2.69
					C42 – C43^{π*}	$ \psi\rangle=BD(1)-BD^*(2)=1.03$ *0.040	1.93
C27 – C28^σ	C28 – C29^{σ*}	$ \psi\rangle=BD(1)-BD^*(1)=1.56$ *0.066	5.89	C38 – O52^σ	C53 – C55^{σ*}	$ \psi\rangle=BD(1)-BD^*(1)=1.64$ *0.041	2.41
C27 – C30^σ	C30 – C31^{σ*}	$ \psi\rangle=BD(1)-BD^*(1)=1.80$ *0.093	5.97	C38 – H93^σ	C37 – O51^{σ*}	$ \psi\rangle=BD(1)-BD^*(1)=1.20$ *0.076	5.98
C27 – C30^π	C11 – C12^{σ*}	$ \psi\rangle=BD(2)-BD^*(1)=0.92$ *0.058	3.88	C39 – C40^σ	N44 – C57^{σ*}	$ \psi\rangle=BD(1)-BD^*(1)=1.36$ *0.047	2.37
	C28 – C29^{π*}	$ \psi\rangle=BD(2)-BD^*(2)=0.46$ *00134	47.35				
C28 – C29^σ	C27 – C28^{σ*}	$ \psi\rangle=BD(1)-BD^*(1)=1.57$ *0.069	6.60	C39 – C42^σ	C42 – C43^{σ*}	$ \psi\rangle=BD(1)-BD^*(1)=1.37$ *0.049	4.53
C28 – C29^π	C31 – C32^{σ*}	$ \psi\rangle=BD(1)-BD^*(1)=0.51$ *0.138	45.08	C39 – C46^σ	C37 – C38^{σ*}	$ \psi\rangle=BD(1)-BD^*(1)=1.32$ *0.051	2.52
					C42 – C43^{π*}	$ \psi\rangle=BD(1)-BD^*(2)=1.01$ *0.050	3.15
C28 – O58^σ	C29 – C32^{σ*}	$ \psi\rangle=BD(1)-BD^*(1)=1.99$ *0.050	1.56	C40 – N44^σ	C31 – C35^{σ*}	$ \psi\rangle=BD(1)-BD^*(1)=1.54$ *0.064	3.35
C29 – C32^σ	C31 – C32^{σ*}	$ \psi\rangle=BD(1)-BD^*(1)=1.81$ *0.103	7.33	C40 – H94^σ	C34 – C35^{σ*}	$ \psi\rangle=BD(1)-BD^*(1)=1.24$ *0.069	4.76
C29 – H87^σ	C31 – C32^{σ*}	$ \psi\rangle=BD(1)-BD^*(1)=1.55$ *0.051	5.27	C41 – C43^σ	N44 – C57^{σ*}	$ \psi\rangle=BD(1)-BD^*(1)=1.48$ *0.027	3.48
C30 – C31^σ	C31 – C32^{σ*}	$ \psi\rangle=BD(1)-BD^*(1)=1.56$ *0.064	7.37	C41 – N44^σ	C43 – H98^{σ*}	$ \psi\rangle=BD(1)-BD^*(1)=1.47$ *0.047	2.01
C30 – H88^σ	C31 – C32^{σ*}	$ \psi\rangle=BD(1)-BD^*(1)=1.42$ *0.025	5.64	C41 – H95^σ	C42 – C43^{π*}	$ \psi\rangle=BD(1)-BD^*(2)=0.93$ *0.060	4.85
					C42 – C43^{σ*}	$ \psi\rangle=BD(1)-BD^*(1)=1.69$ *0.028	0.59
C31 – C32^σ	C29 – C32^{σ*}	$ \psi\rangle=BD(1)-BD^*(1)=1.80$ *0.100	6.91	C41 – H96^σ	C40 – N44^{σ*}	$ \psi\rangle=BD(1)-BD^*(1)=1.25$ *0.067	4.51
					C42 – C43^{π*}	$ \psi\rangle=BD(1)-BD^*(2)=0.93$ *0.043	2.52
C31 – C32^π	C27 – C30^{π*}	$ \psi\rangle=BD(2)-BD^*(2)=0.49$ *0.138	48.42	C42 – C43^σ	C39 – C42^{σ*}	$ \psi\rangle=BD(1)-BD^*(1)=1.64$ *0.076	4.40
	C35 – C56^{σ*}	$ \psi\rangle=BD(2)-BD^*(1)=0.89$ *0.065	5.00				

Table 8 continued

1	2	2	4	5	6	7	8
C31 – C35^σ	C30 – C31^{σ*}	$ \psi\rangle=BD(1)-BD^*(1)=1.66$ *0.056	5.49	C42 – C43^π	C41 – H95^{σ*}	$ \psi\rangle=BD(2)-BD^*(1)=0.95$ *0.050	4.04
C32 – N33^σ	C30 – C31^{σ*}	$ \psi\rangle=BD(1)-BD^*(1)=1.78$ *0.051	3.20	C42 – H97^σ	C41 – C43^{σ*}	$ \psi\rangle=BD(1)-BD^*(1)=1.27$ *0.059	7.79
N33 – C34^σ	C29 – C32^{σ*}	$ \psi\rangle=BD(1)-BD^*(1)=1.76$ *0.085	5.19	C43 – H98^σ	C39 – C42^{σ*}	$ \psi\rangle=BD(1)-BD^*(1)=1.33$ *0.095	8.49
N33 – C36^σ	C31 – C35^{σ*}	$ \psi\rangle=BD(1)-BD^*(2)=1.07$ *0.047	2.13	N44 – C57^σ	C39 – C40^{σ*}	$ \psi\rangle=BD(1)-BD^*(1)=1.47$ *0.061	3.15
C34 – C35^σ	C30 – C31^{σ*}	$ \psi\rangle=BD(1)-BD^*(1)=1.66$ *0.083	5.15	C45 – C46^σ	C38 – C39^{σ*}	$ \psi\rangle=BD(1)-BD^*(1)=1.33$ *0.048	2.18
C34 – C37^σ	C38 – O52^{σ*}	$ \psi\rangle=BD(1)-BD^*(1)=1.28$ *0.058	3.25	C45 – H99^σ	C46 – H103^{σ*}	$ \psi\rangle=BD(1)-BD^*(1)=1.38$ *0.026	2.93
	C47 – O48^{π*}	$ \psi\rangle=BD(1)-BD^*(2)=0.96$ *0.043	2.31				
C34 – H89^σ	C37 – C38^{σ*}	$ \psi\rangle=BD(1)-BD^*(1)=1.25$ *0.058	3.34	C45 – H100^σ	C39 – C46^{σ*}	$ \psi\rangle=BD(1)-BD^*(1)=1.24$ *0.071	5.05
C35 – C40^σ	C31 – C32^{π*}	$ \psi\rangle=BD(1)-BD^*(2)=0.96$ *0.035	1.31	C45 – H101^σ	C46 – H102^{σ*}	$ \psi\rangle=BD(1)-BD^*(1)=1.28$ *0.024	3.16
	C39 – C40^{σ*}	$ \psi\rangle=BD(1)-BD^*(1)=1.37$ *0.064	1.97				
C35 – C56^σ	C31 – C32^{π*}	$ \psi\rangle=BD(1)-BD^*(2)=0.94$ *0.050	2.83	C46 – H102^σ	C39 – C42^{σ*}	$ \psi\rangle=BD(1)-BD^*(1)=1.30$ *0.062	3.71
	C39 – C40^{σ*}	$ \psi\rangle=BD(1)-BD^*(1)=1.35$ *0.066	4.03				
C46 – H103^σ	C39 – C40^{σ*}	$ \psi\rangle=BD(1)-BD^*(1)=1.25$ *0.065	4.21	C55 – H108^σ	O52 – C53^{σ*}	$ \psi\rangle=BD(1)-BD^*(1)=1.22$ *0.074	5.45
C47 – O48^σ	C37 – C47^{σ*}	$ \psi\rangle=BD(1)-BD^*(1)=1.98$ *0.044	1.17	C55 – H109^σ	C53 – O54^{σ*}	$ \psi\rangle=BD(1)-BD^*(1)=1.54$ *0.058	2.70
					C53 – O54^{π*}	$ \psi\rangle=BD(1)-BD^*(2)=0.87$ *0.068	6.33
C47 – O48^π	C37 – O51^{σ*}	$ \psi\rangle=BD(2)-BD^*(1)=1.09$ *0.034	1.99	C55 – H110^σ	C53 – O54^{σ*}	$ \psi\rangle=BD(1)-BD^*(1)=1.54$ *0.060	2.89
					C53 – O54^{π*}	$ \psi\rangle=BD(1)-BD^*(2)=0.87$ *0.065	5.78
C47 – O49^σ	C37 – C39^{σ*}	$ \psi\rangle=BD(1)-BD^*(1)=1.70$ *0.042	1.30	C56 – C57^σ	C41 – N44^{σ*}	$ \psi\rangle=BD(1)-BD^*(1)=1.43$ *0.052	3.09
O49 – C50^σ	C37 – C47^{σ*}	$ \psi\rangle=BD(1)-BD^*(1)=1.60$ *0.065	3.26	C56 – H111^σ	C35 – C40^{σ*}	$ \psi\rangle=BD(1)-BD^*(1)=1.27$ *0.047	2.20
C50 – H104^σ	C47 – C49^{σ*}	$ \psi\rangle=BD(1)-BD^*(1)=1.23$ *0.062	3.79	C56 – H112^σ	C34 – C35^{σ*}	$ \psi\rangle=BD(1)-BD^*(1)=1.24$ *0.058	3.37
C50 – H105^σ	O49	$ \psi\rangle=BD(1)-RY^*(2)=2.17$ *0.036	0.76	C57 – H113^σ	C59 – H111^{σ*}	$ \psi\rangle=BD(1)-BD^*(1)=1.25$ *0.029	1.20
C50 – H106^σ	O49	$ \psi\rangle=BD(1)-RY^*(2)=2.17$ *0.034	0.66	C57 – H114^σ	C40 – N44^{σ*}	$ \psi\rangle=BD(1)-BD^*(1)=1.25$ *0.057	3.26
O51 – H107^σ	C34 – C37^{σ*}	$ \psi\rangle=BD(1)-BD^*(1)=1.46$ *0.076	4.87	O58 – C59^σ	C27 – C28^{σ*}	$ \psi\rangle=BD(1)-BD^*(1)=1.88$ *0.069	3.13
					C28 – C29^{π*}	$ \psi\rangle=BD(1)-BD^*(2)=1.20$ *0.028	0.66
O52 – C53^σ	C55 – H108^{σ*}	$ \psi\rangle=BD(1)-BD^*(1)=1.84$ *0.040	1.07	C59 – H115^σ	C59 – H116^{σ*}	$ \psi\rangle=BD(1)-BD^*(1)=1.42$ *0.025	0.56
C53 – O54^σ	C53 – C55^{σ*}	$ \psi\rangle=BD(1)-BD^*(1)=2.01$ *0.041	1.05	C59 – H116^σ	C28 – O58^{σ*}	$ \psi\rangle=BD(1)-BD^*(1)=1.26$ *0.064	4.09
C53 – O54^π	C55 – H109^{σ*}	$ \psi\rangle=BD(2)-BD^*(1)=1.27$ *0.024	1.50	C59 – H117^σ	C28 – C58^{σ*}	$ \psi\rangle=BD(1)-BD(1)=1.27$ *0.025	0.62
C53 – C55^σ	C38 – O52^{σ*}	$ \psi\rangle=BD(1)-BD^*(1)=1.34$ *0.068	4.28				

^aBD and BD*refer to bonding and anti-bonding, respectively.

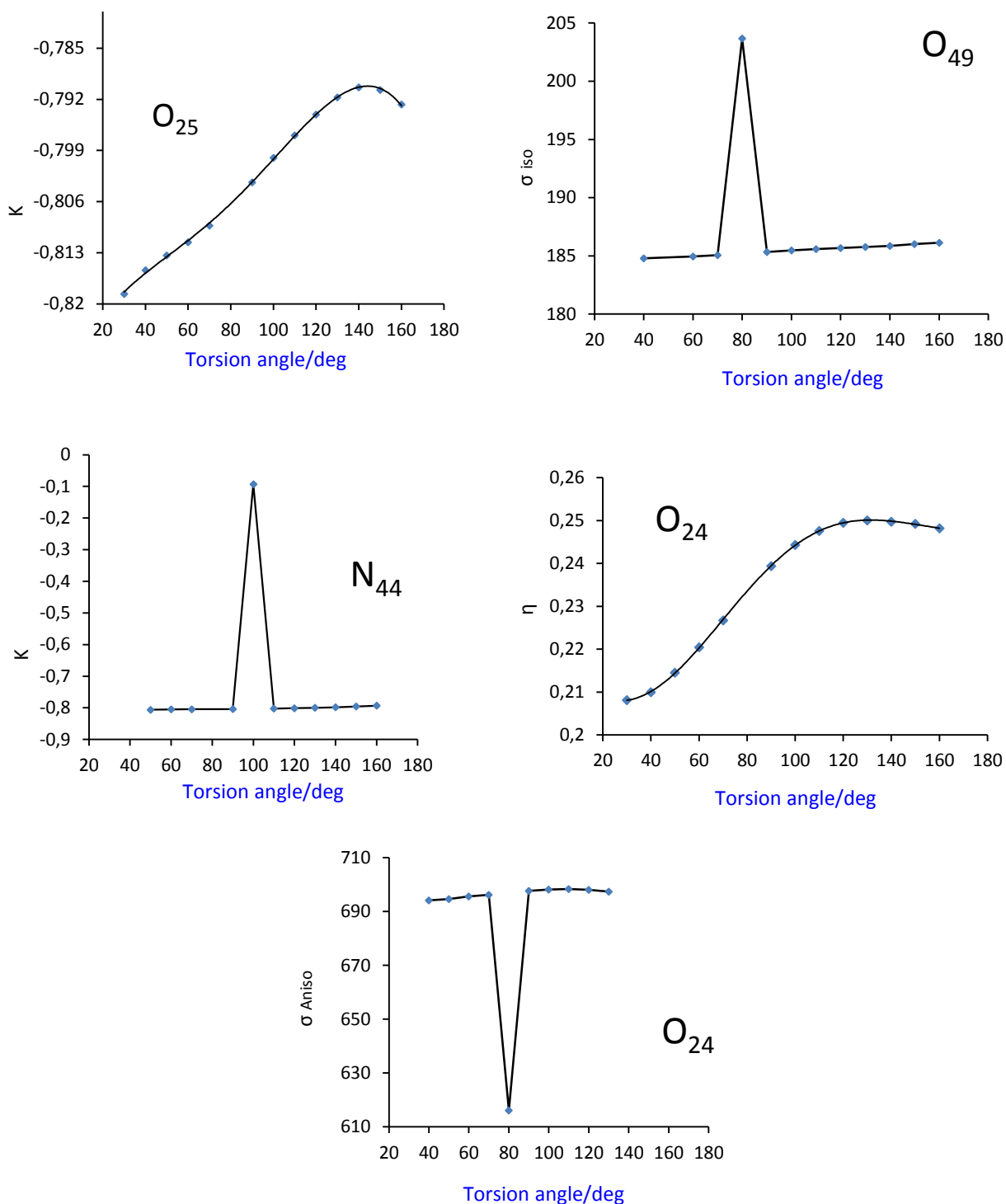


Fig. 3 Calculated parameters of NMR (K , η , σ_{iso} , σ_{Aniso}) versus the torsion angle around the C₁₁- C₁₀- C₂₇- C₂₈ of the structure for some atoms of vinblastine.

CONCLUSION

In this work, we theoretically investigated the structure features of vinblastine as a biological active compound. Chemical shift anisotropy asymmetry (η), isotropy (σ_{iso}), anisotropy (σ_{aniso}), $\Delta\sigma$, K and chemical shift tensor (δ) were calculated based on theoretical data obtained from BL3Y/6-31G(d) and HF/6-31G(d) levels of theory. Moreover, NBO analyses were performed and then stabilization energies, electron occupation at each bond and hybridization character around each atom were evaluated. Furthermore, Freq computation was done for investigation of thermodynamic parameters such as enthalpy, entropy, Gibbs free energy and heat capacity. Mullikan atomic charges for all atoms of the title compounds were also calculated. The values of E_{HOMO} , E_{LUMO} and E_{bg} were evaluated too. Based on the calculated results on NMR chemical shifts, it seems that the HF level has more consistency with experimental data.

Acknowledgement: Partial support of this work (PhD thesis) by Science and Research Branch, Islamic Azad University, Tehran, Iran is appreciated.

REFERENCES

1. W. H. Chen, Y. Qin, Z. Cai, C. L. Chan, G. A. Luo, Z. H. Jiang, *Bioorg. Med. Chem.*, **13**, 1859 (2005).
2. Y. Qin, J. Y. Pang, Chan, W. H. Cai, Z. H. Jiang, *Bioorg. Med. Chem.*, **14**, 25 (2006).
3. W. N. Hait, E. Rubin, E. Alli, S. Goodin, *Update on cancer therapeutics*, **2**, 1 (2007).
4. G. H., Svoboda, *J. Phnrm. Sci.*, **47**, 834 (1958).
5. R. L. Noble, C. T. Beer, J. H. Cutts, N. Y. Ann, *Acad. Sci.*, **76**, 882. (1958).
6. R. L. Noble, *Biochem. Cell. Biol.*, **68**, 1344 (1990).
7. G. A. Cordell, G. Blasko, in *The Alkaloids* (Brossi, A. and Suffness, M., eds), Vol. 37, Academic Press, New York, 1990, p. 1.
8. H. Blcskei, in: V.G. Kartsev (Ed.), *The Chemistry and Biological Activity of Natural Indole Systems*, ICFSP, Moscow, 2005, p.166.
9. M. A. Jordan, W. Leslie, *Nature Reviews cancer*, **4**, 253 (2004).
10. S. Lobert, J. W. Ingram, J. J. Correia, *Biophysical chemistry*, **126**, 50 (2007).
11. K. H. Dowling, E. Nogals, *Current Opinion in Cell Biology*, **10**, 16 (1998).
12. M. A. Jordan, *Curr. Med. Chem. Anti-Cancer Agents*, **2**, 1 (2002).
13. S. Modoka, P. Hydeb, H. R. Mellor, T. Rooseb, R. Callaghana, *European Journal of Cancer*, **42**, 2404 (2004).
14. M. A. Jordan, L. Wilson, *Curr. Opinion in Cell Biol.*, **10**, 123 (1998).
15. T. Kosjek, T. Dolinšek, D. Gramec, E. Heath, P. Strojjan, G. Serša, M. Čemažar, *Talanta*, **116**, 887 (2013).
16. M. Monajjemi, L. Saedi, F. Najafi, F. Mollaamin, *International Journal of the Physical Sciences*, **5**, 1609 (2010).
17. M. A. Jordan, D. Thrower, L. Wilson, *Cancer Res.*, **51**, 2212 (1991).
18. M. A. Jordan, R. L. Margolis, R. H. Himes, L. Wilson, *J. Mol. Biol.*, **187**, 61 (1986).
19. H. P. Erickson, N. Y. Ann, *Acad. Sci.*, **253**, 51 (1975).
20. R. H. Himes, *Pharmacol. Ther.*, **51**, 257 (1991).
21. A. Duflos, A. Kruczynski, J. M. Barret, *Curr. Med. Chem. Anti- Canc Agents*, **2**, 55 (2002).
22. E. Hamel, *Pharmacol. Ther.*, **55**, 31 (1992).
23. J. C. Facelli, *Encyclopedia of Nuclear Magnetic Resonance*; D. M. Grant, R. K. Harris, Eds., London: John Wiley & Sons., **9**, 323 (2002).
24. T. H. Sefzic, D. Turco, R. J. Iuliucci, J.C. Facelli, *J. Phys. Chem. A*, **109**, 1180 (2005).
25. M. Mousavi, A. R. Ilkhani, Sh. Sharifi, J. Mehrzad, A. Eghdami, M. Monajjemi *International Journal of Microbiology Research and Reviews*, **1**, 32 (2013).
26. M. Monajjemi, L. Kharghanian, M. Khaleghian, H. Chegini, *Fullerenes, Nanotubes, and Carbon Nanostructures*, **22**, 709 (2014).
27. A. E. Reed, L. A. Curtiss, F. Weinhold, *Chem. Rev.*, **88**, 899 (1988).
28. D. C. Young, *Computational Chemistry: A Practical Guide for Applying Techniques to Real-World Problems*, John Wiley: New York. 2001.
29. Zs. Dubrovay, V. Hada, Z. Beni, Cs. Szantay Jr., *J. Pharm. Biomed. Anal.*, **84**, 293 (2012).
30. <http://www.wikipedia.org>
31. <http://www.cup.uni-muenchen>
32. R. Ghiasi, E. EbrahimiMokaram, *Journal of Applied Chemical Research*, **20**, 7 (2012).

NMR И НВО-ИЗСЛЕДВАНЕ НА ВИНБЛАСТИН КАТО БИОЛОГИЧЕН ИНХИБИТОР

С. Джохари *, М. Монайеми

Департамент по химия, Научно-изследователски клон, Ислямски университет „Азад“, Техеран, Иран

Постъпила на 14 юли, 2014 г., коригирана на 11 септември, 2014 г.

(Резюме)

Винбластинът е мощен биологичен инхибитор, който се прилага клинично срещу различни неоплазми. В тази работа е оптимизирана молекулната структура на винбластин с помощта на флуороводород и B_3LYP -ниво на теорията с 6-31 G(d) като основна мрежа. Представени са теоретични изчисления, които да изследват термодинамични параметри, Theoretical computations were performed to study thermodynamic parameters, ЯМР-химичното отместване и НВО-анализ (естествени орбитали на връзките). Заедно с това са изчислени някои електронни свойства, като E_{HOMO} , E_{LUMO} , E_{bg} (забранената зона между LUMO и HOMO) и атомните заряди. Освен това са оценени термодинамични параметри, като относителната енергия (ΔE), стандартната енталпия (ΔH), ентропията (ΔS), термодинамичният потенциал по Гибс (ΔG) и постоянният обемен моларен топлинен капацитет (C_v) за винбластин. В ЯМР-изследването са оценени магнитният екраниращ тензор (σ , ppm), екраниращата асиметрия (η), магнитнато-екраниращата анизотропия (σ_{aniso}) и отместването на тензор (K) на различни ъгли на ротация около характеристичната ос на ротация. Изчислени са химическите отмествания спрямо експериментални данни с $CDCl_3$ и DMSO. Пресметнатите данни показват в приемливо съгласие с експерименталните в някои случаи.

Physico-chemical and antibacterial studies on the coordination compounds of N-(2-carbamoylfuranyl)-C-(3'-carboxy-2'-hydroxyphenyl) thiazolidin-4-one

D. Kumar¹, D. Dass², A. Kumar^{3*}

¹Department of Chemistry, National Institute of Technology, Kurukshetra 136119, Haryana,

²Department of Chemistry, Shri Krishan Institute of Engineering & Technology, Kurukshetra 136118, Haryana,

³Department of Chemistry, Haryana College of Technology & Management, Kaithal, 136027, Haryana, India

Received March 26, 2014, Revised July 31, 2014

An equimolar mixture of 3-formylsalicylic acid and furoic acid hydrazide, refluxed in MeOH, forms the Schiff base (**I**). The latter upon reacting with mercaptoacetic acid in dry benzene, undergoes cyclization and forms N-(2-carbamoylfuranyl)-C-(3'-carboxy-2'-hydroxyphenyl)thiazolidin-4-one, LH₃ (**II**). A MeOH solution of **II** reacts with Co(II), Ni(II), Zn(II), Fe(III) and MoO₂(VI) ions and forms the coordination compounds [M(LH)(MeOH)₂] [where M = Co(II), Ni(II)], [Zn(LH)], [FeCl₃(LH₃)] and [MoO₂(acac)(LH₂)] (here acacH = pentane-2,4-dione). The coordination compounds were characterized on the basis of elemental analyses, molar conductance, molecular weight, spectral (IR, reflectance, NMR) studies and magnetic susceptibility measurements. All coordination compounds are non-electrolytes ($\Lambda_M = 2.8-11.7 \text{ mho cm}^2 \text{ mol}^{-1}$) in DMF. **II** behaves as a monobasic bidentate OS donor ligand in [MoO₂(acac)(LH₂)], neutral tridentate ONO donor ligand in [FeCl₃(LH₃)], and dibasic tetradentate OONO donor ligand in [M(LH)(MeOH)₂] [where M = Co(II), Ni(II)] and [Zn(LH)]. All compounds are monomers in diphenyl. The absolute coordination number of Zn(II) ion is 4 and those of Co(II), Ni(II), Fe(III) and MoO₂(VI) are 6. Tetrahedral structure for [Zn(LH)] and octahedral structure for the rest of the compounds are proposed. The ligand (**II**) and its compounds show antibacterial activities towards *E. Coli* (Gram Negative) and *S. Aureus* (Gram positive).

Keywords: thiazolidin-4-one, coordination compounds, monomeric, magnetic susceptibility, complexometric titration, strong field, covalent character.

INTRODUCTION

Thiazolidinones are derivatives of thiazolidine belonging to an important group of heterocyclic compounds. 4-Thiazolidinone, with a carbonyl group at 4th position is a topic of numerous reports concerning its chemistry and applications. The presence of a thiazolidine ring in penicillin and related derivatives was the first recognition of its occurrence in nature [1]. These heterocyclic compounds containing S and N as heteroatoms may bear imine or carboxyl groups. Thiazolidine possesses two donor sites situated at the =NH group and the sulphur atom of the ring, whereas for its derivatives additional coordination sites appear. All above mentioned donor atoms are responsible for the formation of various complexes with transition metal ions [2]. Due to their pharmaceutical importance, thiazolidin-4-ones have played an important role in medicinal chemistry. They have been extensively studied because of their biological activities such as antioxidant [3], antitubercular [4], antimicrobial [5], antibacterial [6], anticonvulsant

[7], antifungal [8] etc.

Metal complexes play an important role in plant and animal life due to their physico-chemical and biological properties. Organosulphur compounds, in the form of their metal complexes, exhibit a wide range of biological properties. Most of the drugs have improved pharmacological properties in the form of metal complexes. Transition metal based drugs are more effective than the uncomplexed drugs [9]. These facts motivated us to study the coordination behaviour of newly synthesized thiazolidinone complexes with some transition metals.

A perusal of the literature indicates that relatively little work has been carried out on the coordination compounds of thiazolidinones [10,11] and there is no report on the coordination compounds of N-(2-carbamoylfuranyl)-C-(3'-carboxy-2'-hydroxyphenyl)thiazolidin-4-one, LH₃ (**II**) as shown in Figure-1 and its coordination compounds with Co(II), Ni(II), Zn(II), Fe(III) and MoO₂(VI) ions. These compounds are very well coordinated and biologically active.

* To whom all correspondence should be sent:
E-mail: amit_vashista2004@yahoo.co.in

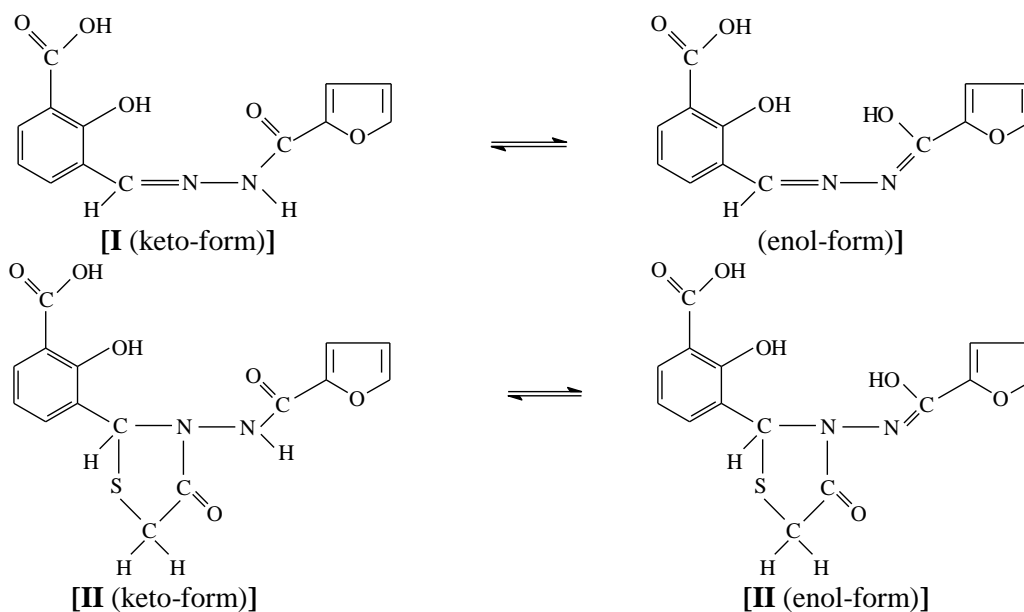


Fig.1

EXPERIMENTAL

Materials

Furoic acid hydrazide [Aldrich]; nickel (II) acetate tetrahydrate, iron (III) chloride (anhydrous) [Sarabhai]; zinc(II) acetate dihydrate [SD's Fine]; cobalt (II) acetate tetrahydrate, ammonium molybdate(VI) tetrahydrate, methanol, ethanol, mercaptoacetic acid, dry benzene, sodium bicarbonate [Ranbaxy] were used as supplied for the syntheses. 3-Formylsalicylic acid and bis(acetylacetonato)dioxomolybdenum(VI) were synthesized following the reported procedures [12].

Analyses and Physical Measurements

The organic skeleton of the respective coordination compounds was decomposed by slow heating of ~ 0.1 g of the latter with conc. HNO_3 . The residue was dissolved in a minimum amount of conc. HCl and the corresponding metal ions were determined as follows: the Ni(II) content of the coordination compound was determined by complexometric titration with standardized EDTA solution using murexide as the indicator. The Co(II) and Zn(II) contents in the respective coordination compounds were determined by complexometric titration with standardized EDTA solution using xylenol orange as an indicator. The Fe(III) ions were reduced to Fe(II) ions with aqueous SnCl_2 and then determined with a standard $\text{K}_2\text{Cr}_2\text{O}_7$ solution using N-phenylanthranilic acid as an indicator. The molybdenum content was estimated gravimetrically after decomposing the given $\text{MoO}_2(\text{VI})$ compound with a few drops of conc. HNO_3 and conc. H_2SO_4 and then igniting the residue in an electric Bunsen burner at 500°C . MoO_3 obtained was dissolved in

6N NaOH and then molybdenum was determined as bis (8-hydroxyquinolinato)dioxomolybdenum (VI). The C, H and N contents of LH_3 and its coordination compounds were determined on a CHN Eager analyzer model-300. The S and Cl contents were determined gravimetrically as BaSO_4 and AgCl , respectively. The molecular weight measurements were carried out by the Rast method using diphenyl as the solvent [13]. The molar conductances (Λ_M) of the coordination compounds were measured in DMF with the help of a Toshniwal conductivity bridge (CL01-02A) and a dip type cell calibrated with KCl solutions. The IR spectra were recorded in KBr pellets ($4000\text{--}400\text{ cm}^{-1}$) on a Beckman-20 spectrophotometer. The reflectance spectra were recorded on a Beckmann DU spectrophotometer with a reflectance arrangement. The magnetic susceptibility measurements were carried out at room temperature using $\text{Hg}[\text{Co}(\text{NCS})_4]$ as the standard [14]. The diamagnetic corrections were computed using Pascal's constants. The magnetic susceptibilities were corrected for the temperature independent paramagnetism term (TIP) [14] using a value of 200×10^{-6} cgs units for Ni(II) and Co(II), and zero for Fe(III) ions.

Synthesis of the Schiff base (I)

The title compound was synthesized following the published procedure [15].

Synthesis of N-(2-carbamoylfuranyl)-C-(3'-carboxy-2'-hydroxyphenyl)thiazolidin-4-one (II)

A dry benzene solution of I (2.74 g, 10 mmol) and mercaptoacetic acid (0.92 g, 10 mmol) was refluxed for 12 h on a water bath. The mixture was

cooled to room temperature and then washed with 10% sodium bicarbonate solution. The benzene layer was separated using a separating funnel. The evaporation of the excess of solvent gave a solid product which was filtered, washed with benzene and recrystallized from petroleum ether. The compound was dried *in vacuo* at room temperature over silica gel. Yield = 17%. *Anal*: (**II**, C₁₅H₁₂N₂O₆S) (obsd: C, 51.42%; H, 3.34%; N, 8.17%; S, 9.35%. calcd.: C, 51.72%; H, 3.45%; N, 8.04%; S, 9.20%); IR bands (KBr): 2850 cm⁻¹ [$\nu(\text{O}-\text{H})$] (intramolecular H-bonding), 1695 cm⁻¹ [$\nu(\text{C}=\text{O})$] (thiazolidinone ring), 1670 cm⁻¹ [$\nu(\text{C}=\text{O})$] (carboxylic), 1645 cm⁻¹ [$\nu(\text{C}=\text{O})$] (amide), 1565 cm⁻¹ [$\nu(\text{C}-\text{N})$] (thiazolidinone ring), 1532 cm⁻¹ [$\nu(\text{C}-\text{O})$] (phenolic), 1090 cm⁻¹ [$\nu(\text{C}-\text{O}-\text{C})$] (furan ring) and 825 cm⁻¹ [$\nu(\text{C}-\text{S})$] (thiazolidinone ring).

Syntheses of the coordination compounds of **II**

A MeOH solution (30-50 mL) of the appropriate metal salt (10 mmol) was added to a MeOH solution (50 mL) of **II** (3.48 g, 10 mmol) and the mixture was then refluxed for 3-4 h. The solid products formed were suction filtered, washed with MeOH and were then dried as mentioned above. Yield = 30–60%.

RESULTS AND DISCUSSION

The Schiff base **I** in a dry benzene solution reacts with mercaptoacetic acid and forms N-(2-carbamoylfuranyl)-C-(3'-carboxy-2'-

hydroxyphenyl) thiazolidin-4-one, LH₃ (**II**). The reaction of the latter with appropriate metal salts in 1:1 molar ratio in MeOH produces the coordination compounds [M(LH)(MeOH)₂] [where M = Co(II), Ni(II)], [Zn(LH)], [FeCl₃(LH₃)] and [MoO₂(acac)(LH₂)] (here acacH = pentane-2,4-dione). The compounds are stable in air at room temperature. They are insoluble in H₂O, partially soluble in MeOH, EtOH and completely soluble in DMSO and DMF. The molar conductance measurements ($\Lambda_M = 2.8-11.7$ mho cm² mol⁻¹) indicate their non-electrolytic nature. The analytical data of **II** and its coordination compounds are given in Table 1.

Infrared Spectral Studies

The infrared spectra of **II** and its coordination compounds were recorded in KBr and the prominent peaks (in cm⁻¹) are shown in Table 2. **I** exhibits a $\nu(\text{C}=\text{N})$ (azomethine) stretch at 1630 cm⁻¹. This band disappears in **II** and a new band appears at 1565 cm⁻¹ due to the $\nu(\text{C}-\text{N})$ (thiazolidinone ring) stretch [16] indicating the conversion of **I** into **II**. The formation of **II** is further supported by the appearance of a new band at 825 cm⁻¹ due to the $\nu(\text{C}-\text{S})$ (thiazolidinone ring) stretch [17]. The $\nu(\text{C}-\text{N})$ (thiazolidinone ring) stretch of **II** shifts to lower energy by 50-72 cm⁻¹ in the coordination compounds of Co(II), Ni(II) and Zn(II) ions suggesting the involvement of the ring N atom towards coordination [17].

Table 1. Analytical, molar conductance (Λ_M) and molecular weight data of **II** and its coordination compounds.

Compound	Mol. formula	Λ_M (mho cm ² mol ⁻¹)	Mol. wt obsd (calcd)	obsd(calcd)%					
				M	C	H	N	S	Cl
LH ₃ (II)	C ₁₅ H ₁₂ N ₂ O ₆ S	–	348.0 ^a (348.0)	–	51.42 (51.72)	3.34 (3.45)	8.17 (8.04)	9.35 (9.20)	–
[Co(LH)(MeOH) ₂]	CoC ₁₇ H ₁₈ N ₂ O ₈ S	5.3	464.9 ^b (468.9)	12.51 (12.56)	43.23 (43.51)	3.77 (3.84)	5.89 (5.97)	6.60 (6.82)	–
[Ni(LH)(MeOH) ₂]	NiC ₁₇ H ₁₈ N ₂ O ₈ S	2.8	465.4 ^b (468.7)	12.40 (12.52)	43.22 (43.52)	3.74 (3.84)	5.88 (5.97)	6.91 (6.83)	–
[Zn(LH)]	ZnC ₁₅ H ₁₀ N ₂ O ₆ S	8.2	427.2 ^b (411.4)	15.69 (15.92)	43.82 (43.74)	2.51 (2.43)	6.68 (6.81)	7.96 (7.78)	–
[FeCl ₃ (LH ₃)]	FeC ₁₅ H ₁₂ N ₂ O ₆ SCl ₃	11.7	528.1 ^b (510.5)	10.72 (10.97)	34.98 (35.26)	2.19 (2.35)	5.66 (5.48)	6.05 (6.27)	20.50 (20.86)
[MoO ₂ (acac)(LH ₂)]	MoC ₂₀ H ₁₈ N ₂ O ₁₀ S	7.3	558.1 ^b (573.9)	16.54 (16.71)	41.61 (41.82)	3.16 (3.14)	4.73 (4.88)	5.51 (5.58)	–

Abbreviation; ^aMass spectral data, ^bRast method data

Table 2. IR, reflectance spectral data (cm^{-1}) and magnetic moments of the coordination compounds of **II**

Compound	$\nu(\text{C-N})$ (thiazolidinone)	ν (C-O) ϕ	ν_{as} (COO)	ν_{s} (COO)	$\nu(\text{C=O})$ (amide)	$\nu(\text{C-O})$ (MeOH)	ν_{max}	Mag. moment (B. M.)
LH ₃ (II)	1565	1532	–	–	1645	–	–	Diamagnetic
[Co(LH)(MeOH) ₂]	1515	1542	1566	1348	1628	976	8900,13290, 19400	4.78
[Ni(LH)(MeOH) ₂]	1500	1541	1568	1358	1620	970	9460,17215, 26000	3.26
[Zn(LH)]	1493	1542	1560	1350	1611	–	–	Diamagnetic
[FeCl ₃ (LH ₃)]	1565	1532	–	–	1645	–	13150, 16900, 24750	5.97
[MoO ₂ (acac)(LH ₂)]	1565	1541	–	–	1645	–	–	Diamagnetic

However, the existence of this band at the same energy in the coordination compounds of Fe(III) and MoO₂(VI) ions indicates the non-involvement of the ring N atom towards coordination. **II** exhibits a strong band at 2850 cm^{-1} due to the intramolecular H-bonded OH groups of phenolic and/or carboxylic acid moieties [18]. The appearance of this band at almost the same energy in [FeCl₃(LH₃)] is indicative of the non-involvement of the OH groups of the above moieties towards coordination. On the other hand, the coordination compounds of the other metal ions do not show this band indicating the breakdown of H-bonding and subsequent deprotonation of the OH groups followed by the involvement of phenolic and carboxylic O atoms in coordination. The $\nu(\text{C=O})$ (thiazolidinone ring) stretch [19] of **II** occurs at 1695 cm^{-1} . This band shifts to 1660 cm^{-1} in [FeCl₃(LH₃)] indicating coordination through the O atom of the carbonyl group of the thiazolidinone moiety. However, the above band remains unchanged in the rest of the coordination compounds suggesting the non-involvement of the above O atom in coordination. The $\nu(\text{C=O})$ (carboxylic) stretch [20] of **II** occurs at 1670 cm^{-1} . This band remains unchanged in the coordination compounds of Fe(III) and MoO₂(VI) ions indicating the non-involvement of the O atom of the carboxylic group in coordination. However, the remaining coordination compounds display two new bands between 1560-1568 cm^{-1} and 1348-1358 cm^{-1} . These bands are assigned to the $\nu_{\text{as}}(\text{COO})$ and $\nu_{\text{s}}(\text{COO})$ stretches of the carboxylato ligand, respectively. The energy separation ($\Delta\nu = 210\text{-}218$ cm^{-1}) between the $\nu_{\text{as}}(\text{COO})$ and $\nu_{\text{s}}(\text{COO})$ stretches is indicative of the monodentate nature of the carboxylato ligand [21]. The presence of a strong band at 1645 cm^{-1} due to the $\nu(\text{C=O})$ (amide) stretch in **II** indicates that it occurs in the keto-form [12]. This band shifts to lower energy by 17-34 cm^{-1} in the coordination compounds of Co(II), Ni(II) and Zn(II) ions, suggesting the involvement of the keto O atom in coordination. However, the

existence of this band at the same energy in the coordination compounds of Fe(III) and MoO₂(VI) ions indicates the non-involvement of the keto O atom in coordination. The $\nu(\text{C-O})\phi$ stretch [22] (1532 cm^{-1}) of **II** undergoes a positive shift by ≤ 10 cm^{-1} in the coordination compounds of Co(II), Ni(II), Zn(II) and MoO₂(VI) ions. This band remains unchanged in the Fe(III) compound indicating the non-involvement of phenolic O in coordination. The $\nu(\text{C-S})$ (thiazolidinone ring) stretch [16] of **II** shifts from 825 cm^{-1} to lower energy by 42 cm^{-1} in [MoO₂(acac)(LH₂)] suggesting the formation of a bond between the metal ions and the S atom. However, it remains unchanged in the rest of the coordination compounds indicating non-involvement of S atom in coordination. The [$\nu(\text{C-O-C})$ (furan moiety)] stretch of **II** occurs at 1090 cm^{-1} . The appearance of a band at the same energy in the coordination compounds of Co(II), Ni(II), Zn(II), and MoO₂(VI) ions indicates the non-involvement of the O atom of the furan moiety in coordination. On the other hand, the negative shift by 60 cm^{-1} of this band in [FeCl₃(LH₃)] indicates the coordination through the O atom of the furan moiety. The presence of a broad band between 3300-3400 cm^{-1} due to $\nu(\text{O-H})$ (MeOH) stretch and the decrease in $\nu(\text{C-O})$ (MeOH) stretch [23] from 1034 cm^{-1} to lower energy by 58-64 cm^{-1} in the coordination compounds of Co(II) and Ni(II) ions indicate the involvement of the O atom of MeOH in coordination [23]. The absence of a band between 820-860 cm^{-1} in [FeCl₃(LH₃)] precludes the presence of a $\nu(\text{Fe-O-Fe})$ bridged structure [24]. The molecular weight data (Table 1) also suggest the same. The appearance of two new bands due to the $\nu_{\text{s}}(\text{O=Mo=O})$ stretch (940 cm^{-1}) and the $\nu_{\text{as}}(\text{O=Mo=O})$ stretch (910 cm^{-1}) in [MoO₂(acac)(LH₂)] are indicative of a *cis*-MoO₂ configuration [20]. The new non-ligand bands in the present coordination compounds in the low frequency region are assigned to $\nu(\text{M-O})$ (538-563 cm^{-1}), $\nu(\text{M-N})$ (418-456 cm^{-1}) and $\nu(\text{M-S})$ (342-369 cm^{-1}) vibrations [25].

NMR Spectral Studies

The NMR spectra of **II** and [Zn(LH)] were recorded in DMSO-*d*₆. The chemical shifts (δ) are expressed in ppm downfield from TMS. The prominent resonance signals of these compounds were compared with the reported peaks [26]. **II** exhibits a singlet at δ 17.5 ppm due to the carboxylic proton, a sharp singlet at δ 13.61 ppm due to phenolic proton, a singlet at δ 10.8 ppm (due to CONH proton) and at δ 11.3 ppm (due to HO-C=N, tautomeric protons), and multiplets between δ 7.36-7.71 ppm due to aromatic protons. The absence of the signal at δ 17.5 ppm due to the COOH proton in [Zn(LH)] indicates the deprotonation of the COOH group, followed by the involvement of its O atom in coordination. The absence of the resonance signal at δ 13.61 ppm due to the phenolic proton in [Zn(LH)] indicates the deprotonation of the phenolic OH group followed by its involvement in coordination [27]. The singlet at δ 10.4 ppm due to CONH proton remains unchanged in the complex which shows involvement of keto oxygen in the coordination.

Reflectance Spectral Studies

The presence of three bands at 8900, 13290 and 19400 cm^{-1} due to ${}^4T_{1g}(F) \rightarrow {}^4T_{2g}(v_1)$, ${}^4T_{1g}(F) \rightarrow {}^4A_{2g}(v_2)$ and ${}^4T_{1g}(F) \rightarrow {}^4T_{1g}(v_3)$ transitions, respectively, in [Co(LH)(MeOH)₂] suggests an octahedral arrangement of **II** around the Co(II) ions [28]. The v_3/v_1 value is 2.18 which lies in the usual range (2.00-2.80) reported for the majority of octahedral Co(II) coordination compounds [28]. The parameters are: $Dq = 1004 \text{ cm}^{-1}$, $B' = 776 \text{ cm}^{-1}$, $\beta = B'/B = 0.80$, $\beta^0 = 20\%$ and $\text{CFSE} = -96.13 \text{ kJ mol}^{-1}$. The reduction of Racah parameter from the free ion value of 971 cm^{-1} to 776 cm^{-1} and the β^0 value (20%) indicate the covalent nature of the compound and the strong field nature of the ligand [14]. [Ni(LH)(MeOH)₂] exhibits three bands at 9460, 17215 and 26000 cm^{-1} due to ${}^3A_{2g}(F) \rightarrow {}^3T_{2g}(F)(v_1)$, ${}^3A_{2g}(F) \rightarrow {}^3T_{1g}(F)(v_2)$ and ${}^3A_{2g}(F) \rightarrow {}^3T_{1g}(P)(v_3)$ transitions, respectively, in an octahedral symmetry [29]. The v_2/v_1 value is 1.81 and it lies in the usual range (1.60-1.82) reported for the majority of octahedral Ni(II) coordination compounds [28]. Here the values of the spectral parameters are: $Dq = 946 \text{ cm}^{-1}$, $B' = 870 \text{ cm}^{-1}$, $\beta = B'/B = 0.84$, $\beta^0 = 16\%$ and $\text{CFSE} = -124.73 \text{ kJ mole}^{-1}$. The reduction of the Racah parameter from the free ion value (1030 cm^{-1}) to 870 cm^{-1} and the β^0 value (16%) are indicative of the covalent nature of the compound and the strong field nature of the ligand [14]. For a given ligand and given

stereochemistry, the covalent character of the corresponding Co(II) and Ni(II) coordination compounds is comparable since Co(II) and Ni(II) occupy the adjacent positions in the nephelauxetic metal ion series [i.e., Co(II) ~ Ni(II)]. In the present Co(II) and Ni(II) coordination compounds, the β^0 values are quite comparable: [Co(LH)(MeOH)₂]: 20%; [Ni(LH)(MeOH)₂]: 16%. For a given ligand and given stereochemistry, the spectrochemical series of metal ions on the basis of increasing $10Dq$ values is [14]: Ni(II) < Co(II). Our calculated $10Dq$ values indicate that the $10Dq$ values are in the expected order: Ni(II) < Co(II). The greater negative CFSE value ($-124.73 \text{ kJ mol}^{-1}$) for [Ni(LH)(MeOH)₂] in comparison to that [Co(LH)(MeOH)₂] ($\text{CFSE} = -96.13 \text{ kJ mol}^{-1}$) is as expected [29]. The coordination compound [FeCl₃(LH₃)] exhibits three bands at 13150, 16900 and 24750 cm^{-1} due to ${}^6A_{1g} \rightarrow {}^4T_{1g}(G)$, ${}^6A_{1g} \rightarrow {}^4T_{2g}(G)$ and ${}^6A_{1g} \rightarrow {}^4A_{1g}(G)$ transitions, respectively, in an octahedral environment [30].

Magnetic Measurements

The magnetic moments of [Co(LH)(MeOH)₂], [Ni(LH)(MeOH)₂] and [FeCl₃(LH₃)] are 4.78, 3.26 and 5.97 B.M., respectively. These values are in the normal ranges reported for magnetically diluted octahedral compounds of Co(II), Ni(II) and Fe(III) ions [31]. The coordination compounds of Zn(II) and MoO₂(VI) ions of **II** are diamagnetic, as expected.

Antibacterial Studies

The antibacterial activity of ligand (**II**) and its complexes was tested against bacteria, *E. Coli* (Gram negative) and *S. aureus* (Gram positive) by the disc diffusion method (Table 3).

Table 3. Antibacterial activity of **II** and its coordination compounds (zone of inhibition in mm)

Compound	<i>E. Coli</i> (Gram negative)	<i>S. Aureus</i> (Gram positive)
LH ₃ (II)	7	6
[Co(LH)(MeOH) ₂]	8	7
[Ni(LH)(MeOH) ₂]	7	10
[Zn(LH)]	10	12
[FeCl ₃ (LH ₃)]	8	9
[MoO ₂ (acac)(LH ₂)]	11	10

Stock solutions were prepared by dissolving the compounds in DMSO. Under aseptic conditions, plain sterilised discs were soaked in the solutions of the compounds overnight. Test culture was spread over the plates containing Mueller Hinton Agar

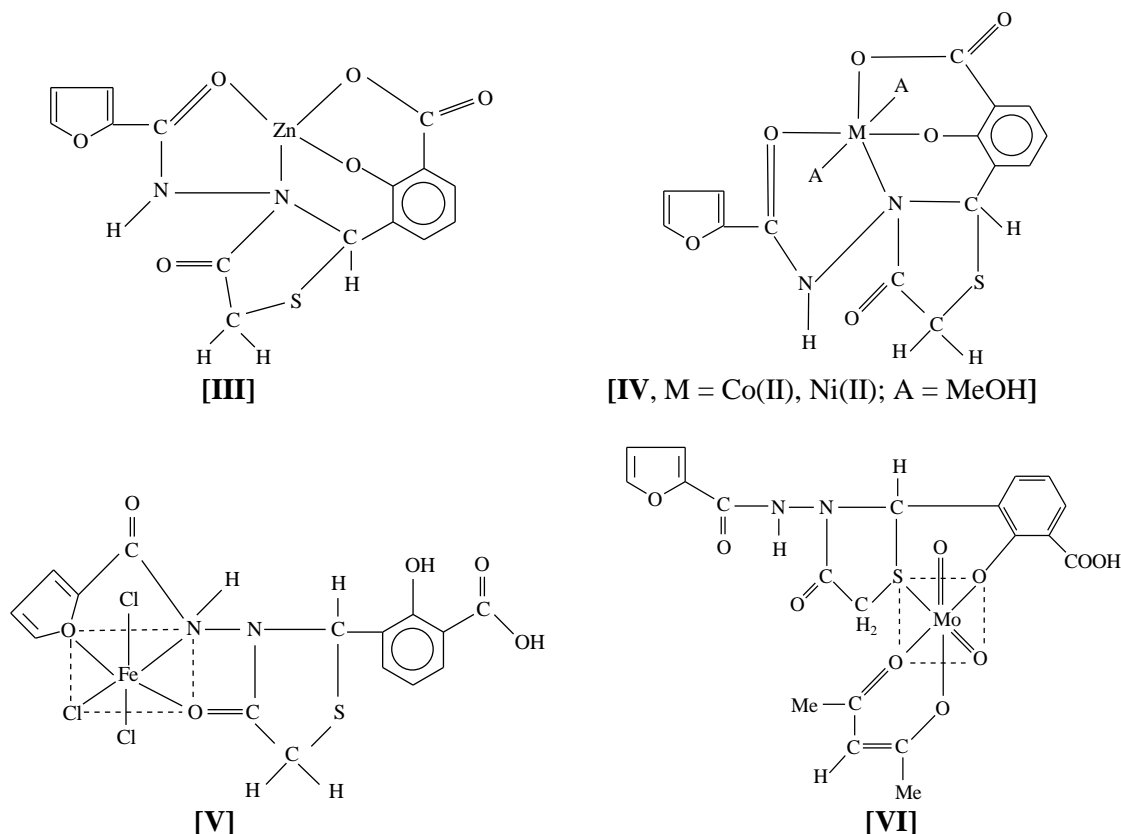


Fig. 2.

(MHA) using a sterile swab. Inoculated plates were dried for 30 minutes and discs were placed on the inoculated plates. The plates were left for 30 min at room temperature to allow diffusion. The plates were then incubated at 37 °C for 24 h for *E. Coli* and *S. aureus*. After incubation, the diameter of the zone of inhibition was noted for each disc.

Determination of Minimum Inhibitory Concentration (MIC)

The stock solutions of the compounds were prepared using distilled water as diluent. In a set of test tubes containing 2 mL of Mueller Hinton Broth, the compounds were serially diluted. 2 mL of the test culture was added to all tubes and the latter were incubated at 37°C for 24 h. Lack of turbidity was noted for the determination of MIC (Table 4).

Table 4. Minimum inhibitory concentration (MIC) of II and its coordination compounds ($\mu\text{g/ml}$)

Compound	<i>E. Coli</i> (Gram negative)	<i>S. Aureus</i> (Gram positive)
LH ₃ (II)	64	32
[Co(LH)(MeOH) ₂]	32	64
[Ni(LH)(MeOH) ₂]	64	64
[Zn(LH)]	64	32
[FeCl ₃ (LH ₃)]	32	32
[MoO ₂ (acac)(LH ₂)]	32	64

CONCLUSIONS

From the ongoing discussion it may be stated that **II** behaves as a monobasic bidentate OS donor ligand in [MoO₂(acac)(LH₂)], neutral tridentate ONO donor ligand in [FeCl₃(LH₃)] and dibasic tetradentate OONO donor ligand in [M(LH)(MeOH)₂] [where M = Co(II), Ni(II)] and [Zn(LH)]. Thus, on the basis of analytical, molecular weight, spectral and magnetic studies, we propose a tetrahedral structure, **III** for [Zn(LH)] and an octahedral structure, **IV** for [M(LH)(MeOH)₂] [where M = Co(II), Ni(II); A = MeOH], **V** for [FeCl₃(LH₃)] and **VI** for [MoO₂(acac)(LH₂)] as shown in Figure-2.

The newly synthesized compounds represent a class of coordination compounds of thiazolidinone and prove themselves as potential compounds in terms of coordination chemistry and biological activities.

REFERENCES

- 1.M. Pulici, F. Quartieri, *Tetrahedron Lett.*, **46**, 2387 (2005).
- 2.F. C. Brown, *Chem. Revs.*, **61**, 463 (1961).
- 3.M. Cacic, M. Molnar, B. Sarkanj, E. Has-Schön, V. Rajkovic, *Molecules*, **15**, 6795 (2010).
- 4.H. H. Parekh, K. A. Parikh, A.R. Parikh, *Journal of Sciences*, Islamic Republic of Iran, **15** (2), 143 (2004).

5. S. P. Shrivastava, N. Seelam, R. Rai, *E-Journal of Chemistry*, **9** (2), 825 (2012).
6. T. M. Bhagat, D. K. Swamy, S. G. Badne, S. V. Kuberkar, *Rasayan J. Chem.*, **4**(1), 24 (2011).
7. M. R. Shiradkar, M. Ghodake, K. G. Bothara, S. V. Bhandari, A. Nikalje, K. C. Akula, N. C. Desai, P. J. Burange, *ARKIVOC*, **XIV**, 58 (2007).
8. A. Verma, S.H. Saraf, *Eur. J. Med. Chem.*, **43**, 897 (2008).
9. J. R. Anaconda, J. Estacio, *Trans. Metal Chem.*, **31**(2), 227 (2006).
10. R. K. Patel, *Asian J. Chem.*, **13**, 89 (2001).
11. E. Subasi, A. Ercag, S. Sert, O. S. Senturk, *Synth. React. Inorg. Met.-org. and Nano-Met. Chem.*, **36**, 705 (2006).
12. D. Kumar, A. Kumar, *E-Journal of Chemistry*, **9**(4), 2532 (2012).
13. F. G. Mann, B. C. Saunders, *Practical Organic Chemistry*, London: Longmans, 1961, p. 435.
14. R. L. Dutta, A. Syamal, *Elements of Magnetochemistry*, 2nd Edn., New Delhi: Affiliated East West Press Pvt. Ltd., 1993.
15. D. Kumar, P. K. Gupta, A. Syamal, *Indian J. Chem.*, **41A**, 2494 (2002).
16. P. V. Patel, K. R. Desai, *Orient. J. Chem.*, **18**, 311 (2002).
17. D. C. Dash, A. Mahapatra, R. K. Mahapatra, S. Ghosh, P. Naik, *Indian J. Chem.*, **47A**, 1009 (2008).
18. P. J. Bahad, N. S. Bhave, A. S. Aswar, *J. Indian Chem. Soc.*, **77**, 363 (2000).
19. R. U. Roy, K. R. Desai, *Int. J. Chem. Sci.*, **3**, 529 (2005).
20. A. Syamal, M. R. Maurya, *Trans. Met. Chem.*, **11**, 235 (1986).
21. J. R. Anaconda, I. Osorio, *Trans. Met. Chem.*, **33**, 517 (2008).
22. Y. Y. Kharitanov, L. M. Zaitsev, G. S. Bochkarev, O. P. Evastafeva, *Russ. J. Inorg. Chem.*, **7**, 1617 (1964).
23. D. Kumar, A. Kumar, J. Sharma, *Journal of Chemistry*, Article ID 870325, (2013).
24. D. Kumar, A. Syamal, A. Kumar, A. Gupta, D. Dass, *Oriental J. Chem.*, **25** (4), 871 (2009).
25. J. R. Ferraro, *Low Frequency Vibrations of Inorganic and Coord Compds*, Plenum Press, New York, 1971.
26. B. J. K. Nag, S. Pal, C. Sinha, *Trans. Met. Chem.*, **30**, 523 (2005).
27. D. Kumar, A. Syamal, A. Gupta, M. Rani, P. K. Gupta, *J. Indian Chem. Soc.*, **87**, 1185 (2010).
28. A. Syamal, M. M. Singh, *Reactive Polymers*, **24**, 27 (1994).
29. J. E. Huheey, *Inorganic Chemistry, Principles of Structure and Reactivity*, 3rd Edn., New York: Harper & Row Publishers, 1983, p.374.
30. A. B. P. Lever, *Inorganic Electronic Spectroscopy*, 2nd Edn., Elsevier, Amsterdam, 1984, and references therein.
31. F. A. Cotton, G. Wilkinson, C. A. Murillo, M. Bochmann, *Advanced Inorganic Chemistry*, 6th Edn., New York: John Wiley, 1999.

ФИЗИКОХИМИЧНИ И АНТИБАКТЕРИАЛНИ ИЗСЛЕДВАНИЯ ВЪРХУ КООРДИНАЦИОННИ СЪЕДИНЕНИЯ С N-(2-КАРБАМОИЛ)-С-(3'-КАРБОКСИ-2'- ХИДРОКСИФЕНИЛ) ТИАЗОЛИДИН-4-ОН

Д. Кумар¹, Д. Дас², А. Кумар^{3*}

¹ Департамент по химия, Национален технологичен университет, Курукиетра, Харияна, Индия

² Департамент по химия, Инженерно-технологичен институт „Шри Кришан“, Курукиетра, Харияна, Индия

³ Департамент по химия, Колеж по технология и управление в Харияна, Кайтал, Харияна, Индия

Получена на 26 март, 2014 г.; коригирана на 31 юли 2014 г.

(Резюме)

Еквимоларната смес от 3-формил-салицилова киселина и хидразида на фуриевата киселина, разтворени в метанол образува Шифова база (I). Последната претърпява циклизация и образува N-(2-карбамоил-фураил)-С-(3'-карбокси-2'-хидроксифенил) тиазолидин-4-он, LH₃ (II) при реакцията с меркаптооцетна киселина в сух бензен. Разтворът на II в метанол реагира с йоните Co(II), Ni(II), Zn(II), Fe(III) и MoO₂(VI) и се образуват координационни съединения от типа [M(LH)(MeOH)₂] [където M = Co(II), Ni(II)], [Zn(LH)], [FeCl₃(LH₃)] и [MoO₂(асас)(LH₂)] (тук асасН = pentane-2,4-dione). Координационните съединения са охарактеризирани на базата на елементарен анализ, моларна проводимост, молекулно тегло, спектрални методи (IR, отражение, NMR) и измервания на магнитния susceptibilitet. Всички координационни съединения не са електролити ($\Lambda_m = 2.8-11.7 \text{ Ohm cm}^2 \text{ mol}^{-1}$) в DMF. II се отнася като монобазичен бидендатен OS донорен лиганд в [MoO₂(асас)(LH₂)], неутрален тридендатен ONO донорен лиганд в [FeCl₃(LH₃)], и дибазичен тетрадендатен OONO донорен лиганд в [M(LH)(MeOH)₂] [където M = Co(II), Ni(II)] и [Zn(LH)]. Всички съединения са мономери в дифенил. Абсолютното координационно число на Zn(II)-йоните е 4, а тези на Co(II), Ni(II), Fe(III) и MoO₂(VI) са 6. Предлага се тетраедрична структура на [Zn(LH)] и октаедрична структура за останалите съединения. Лигандът (II) и неговите съединения показват антибактериални свойства спрямо *E. Coli* (Грам-отрицателни) и *S. aureus* (Грам-положителни).

Azo-azomethine ligands with N₂O₂ donor atom sets and their binuclear UO₂(II) complexes: synthesis, characterization and biological activity

F. A. Saad¹, A. M. Khedr^{1, 2*}

¹ Chemistry Department, College of Applied Sciences, Umm Al-Qura University, Makkah, Saudi Arabia

² Chemistry Department, Faculty of Science, Tanta University, Tanta, Egypt

Received September 2, 2014, Revised November 5, 2014

Two azo-azomethine ligands with N₂O₂ donor atom sets and their binuclear UO₂(II)-complexes were synthesized for therapeutic uses. The ligands were derived from the condensation of 4-(4-hydroxy-3-formyl-1-ylazo)-N-pyrimidin-2-yl-benzenesulfonamide with ethylenediamine and 1,6-hexanediamine. The prepared ligands and their bi-homonuclear uranyl complexes were characterized by thermal analyses (TGA & conventional method), vibrational, electronic, ¹H NMR, and mass spectra as well as by different physicochemical techniques. The active coordination centers in the ligands and the geometrical arrangement of the complexes were investigated using the spectral data. Molar conductance measurements in DMSO solution denoted that the complexes are non-electrolytes. The investigated complexes and ligands were screened *in vitro* for their antimicrobial activity against fungi (*Aspergillus flavus* and *Candida albicans*), gram-positive bacteria (*Staphylococcus aureus*) and gram-negative bacteria (*Escherichia coli*). It was observed that the complexes are more potent fungicides and bactericides than the ligands.

Keywords: N₂O₂ azo-azomethine ligands, binuclear UO₂(II)-complexes, biological activity

INTRODUCTION

Azo-azomethine compounds and their metal complexes have found interesting utilities which arise from the importance of such compounds in biological and industrial applications [1, 2], but little work dealt with such subjects [3-5]. Also, sulfa compounds were the first drugs found to act selectively and could be used systematically as preventive and therapeutic agents against different diseases in humans [6]. The vast commercial success of these medicinal agents has made the chemistry of sulfa compounds a major area of research [7]. Sulfur ligands are wide-spread among coordination compounds and are important components of biologically active transition metal complexes [8, 9]. Metal complexes with heterocyclic unsaturated ligands are also of great interest in inorganic and organometallic chemistry, especially due to their unique electrical and magnetic properties [10, 11]. Also, metal complexes containing two or more metal ions per molecule find wide application in biological systems, catalysis, and material science [12–16], beside their peculiar spectroscopic and magnetic properties [17–21]. Complex formation between metal ions and sulfa compounds, combining antibacterial activity of sulfa derivatives and

antimicrobial activity of the metal ions, constitutes an important field of research due to their pronounced antimicrobial and fungicidal activities [22–25]. On the other hand, uranium is a symbolic element as it is the last natural element and it is the most common element of actinides. So, it is imperative to look into the structure and biological activity of new bi-homonuclear uranyl complexes with sulfa azo-azomethine ligands, in a continuation of our research work in designing new ligands and complexes [26-31]. The active coordination centers in the ligands and the geometrical arrangement of the complexes will be investigated using the analytical and spectral data.

EXPERIMENTAL

All reagents and solvents used in the present work were reagent grade provided from Merck, Aldrich or Sigma and were used as received.

Synthesis of azo-azomethine ligands

The ligands under interest were prepared according to the following procedures. 4-(4-hydroxy-3-formyl-1-ylazo)-N-pyrimidin-2-yl-benzenesulfonamide was synthesized according to the well-known published procedure [32]. A suspension of 4-amino-N-pyrimidin-2-yl-benzenesulfonamide (2.50 g, 10 mmol) in hydrochloric acid (18 mL) and water (8 mL) was heated to 70°C until complete dissolution. The clear solution was poured into ice water and was

* To whom all correspondence should be sent:
E-mail: abkhedr2010@yahoo.com

diazotized below 5°C with sodium nitrite (1.4 g, 20 mmol) dissolved in water (10 mL). The cold diazonium solution was added in the course of 30 min at 0°C to a solution of salicylaldehyde (1.07 mL, 10 mmol) in water (20 mL) containing sodium hydroxide (1.6 g) and sodium carbonate (3.7 g). During the addition process, the solution was vigorously stirred. The product was collected by vacuum filtration and was washed with NaCl solution (25 mL, 10%). Coupling of the diazonium reagent to salicylaldehyde occurred at the *para* position to the hydroxyl group. The azo compound was re-crystallized several times from ethanol.

Schiff base ligands (HL^1 and HL^2) were prepared using a method previously reported in the literature [33]. For each ligand, a mixture of 10 mmol of 4-(4-hydroxy-3-formyl-1-ylazo)-N-pyrimidin-2-yl-benzenesulfonamide (3.83 g) and ethylenediamine (0.60 g) or 1,6-hexanediamine (1.16 g) was dissolved in absolute ethanol (50 mL) with a few drops of glacial acetic acid as a catalyst. The resulting mixture was stirred under reflux for 10–12 h. The product was vacuum-filtered and washed with a small amount of hot ethanol. The various synthetic reactions are summarized in figure 1.

Synthesis of the metal complexes

Complexes of $UO_2(II)$ were synthesized by the reflux-precipitation method. Hot ethanolic solutions of the ligand (1 mmol in 50 mL of ethanol) and uranyl acetate dihydrate [2 mmol in 50 mL of water-ethanol mixture (50%, V/V)] were mixed. The resulting mixture was refluxed on a water bath for 8–10 h. The complexes which precipitated during the reaction were filtered off and washed several times with hot ethanol, then dried in vacuum over anhydrous calcium chloride. The yield of the reaction was found to be 78%–81%. Purities of the complexes were checked by TLC and melting point constancy.

Analytical and physical measurements

The metal contents in the complexes were determined gravimetrically following a standard procedure [34]. A weighed quantity of the complex (0.4–0.5 g) was treated with a few drops of conc. H_2SO_4 and 1 mL of conc. HNO_3 . It was heated till the organic matter decomposed and sulfur trioxide fumes came out. The same process was repeated three to four times to decompose the complex completely. Then, it was dissolved in water and the resulting solution was used for determining the metal ion. Uranium was precipitated as ammonium

diuranate, followed by ignition to its respective oxide.

The nature and contents of water molecules and acetate groups attached to the central metal ion were determined by conventional thermal decomposition studies. Complexes **1** and **2** were heated at five temperatures (100°C , 200°C , 300°C , 500°C and 1000°C) in a muffle furnace for 40–50 min. The resulting weights were measured. The weight loss at 100°C corresponds to the loss of lattice water from the complexes. The weight loss at 200°C corresponds to the loss of coordinated water. The weight loss at 300°C can be attributed to the removal of acetate groups. On heating at 500°C , the weight indicates loss of parts of the ligand. The weight of the pyrolysis product after heating at 1000°C corresponds to the formation of metal oxide as a final product [35]. Conductance measurements were performed for 10^{-3} mol L^{-1} solution in DMSO at room temperature using a Jenway (model 4070) conductance meter. Matrix Assisted Laser Desorption/Ionization Time-of-Flight (MALDI-TOF) mass spectra were recorded on a BRUKER Auto flex II LRF20 spectrometer using dithranol as a matrix. Fourier transformation infrared (FT-IR) spectra of the free ligands and their UO_2 -complexes in KBr pellets were measured using a FT-IR Bruker Tensor 27 spectrophotometer (Germany), within the range $4000\text{--}400\text{ cm}^{-1}$ (Central Laboratory, Tanta University, Egypt). UV/Vis spectra were measured on a Shimadzu 240 UV-Visible spectrophotometer in DMF solutions. The magnetic moments were measured at room temperature using the Gouy's method using a magnetic susceptibility balance (Johnson Matthey, Wayne, PA, 19087 USA) at 60 Hz. A Bruker DMX 750 (500MHz) spectrometer was used for obtaining ^1H NMR spectra, employing $DMSO-d_6$ as the solvent and TMS as the internal standard. Chemical shifts of ^1H NMR were expressed in parts per million (ppm, δ units), and coupling constant was expressed in units of Hertz (Hz). Thermal gravimetric analysis (TGA) of the complexes was performed on a Shimadzu TG-50 thermal analyzer from ambient temperature up to 800°C with a heating rate of $10^\circ\text{C}/\text{min}$ in nitrogen atmosphere.

Biological activity: antifungal and antibacterial screening

In vitro studies of the antifungal and antibacterial activities of the investigated ligands and complexes against *A. flavus*, *C. albicans*, *E. coli*, and *S. aureus* were carried out using the modified Kirby–Bauer disc diffusion method [36] at the micro-analytical unit of Cairo University. Briefly, 100 μL of the test fungi/bacteria were

grown in 10 mL of fresh media until they reached 10^5 cells mL^{-1} for fungi and 10^8 cells mL^{-1} for bacteria [37]. Hundred microliters of microbial suspension was spread onto agar plates corresponding to the broth in which they were maintained. Isolated colonies of each organism were selected from the primary agar plates and tested for susceptibility by the disc diffusion method [38]. From the many media available, NCCLS recommends Mueller–Hinton agar since it results in good batch-to-batch reproducibility. The disc diffusion method for filamentous fungi was tested using the approved standard method (M38-A) developed by the NCCLS [39] for evaluating the susceptibilities of filamentous fungi to antifungal agents. The disc diffusion method for yeasts was developed using the approved standard method (M44-P) by the NCCLS [40]. Plates were inoculated with filamentous fungi, *A. flavus*, at $25^\circ C$ for 48 h; Gram (+) bacteria, *S. aureus*, and Gram (-) bacteria, *E. coli*. They were incubated at $35\text{--}37^\circ C$ for 24–48 h. Yeast *C. albicans* was incubated at $30^\circ C$ for 24–48 h. Then the diameters of the inhibition zones were measured in millimeters [41]. Standard discs of tetracycline (antibacterial agent) and amphotericin B (antifungal agent) served as positive controls for antimicrobial activity; filter discs impregnated with 10 mL of

solvent (distilled water, DMSO) were used as negative controls. The agar used was Mueller–Hinton agar that was rigorously tested for composition and pH. Further, the depth of the agar in the plate is a factor to be considered in the disc diffusion method. This method is well-documented and standard zones of inhibition were determined for susceptible and resistant values. Blank paper discs (Schleicher & Schuell, Spain) with a diameter of 8.0 mm were impregnated with 10 mL of the tested concentration of the stock solutions. When a filter paper disc impregnated with a tested chemical is placed on agar the chemical will diffuse from the disc into the agar. This diffusion will place the chemical in the agar only around the disc. The solubility of the chemical and its molecular size will determine the size of the area of chemical infiltration around the disc. When an organism is placed on the agar it will not grow in the area around the disc if it is susceptible to the chemical. This area of no growth around the disc is known as a “zone of inhibition” or “clear zone”. For the disc diffusion, the zone diameters were measured with slipping calipers of the National Committee for Clinical Laboratory Standards. Agar-based methods such as disc diffusion can be good alternatives because they are simpler and faster than broth-based methods [42].

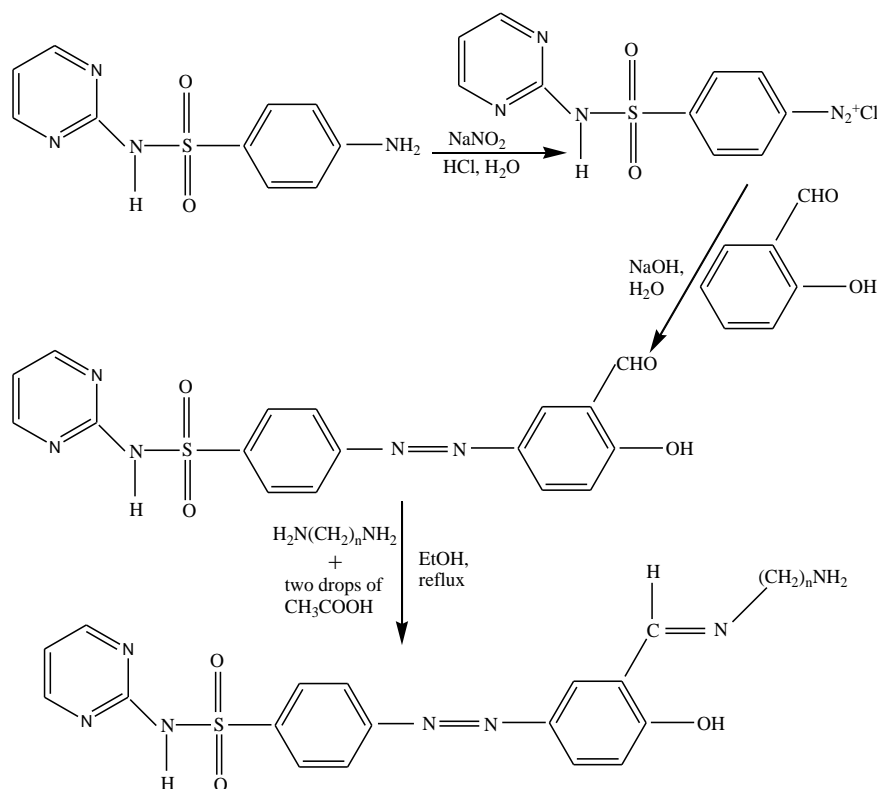


Fig. 1. Preparation of the azo-azomethine ligands [HL^1 ($n=2$) and HL^2 ($n=6$)].

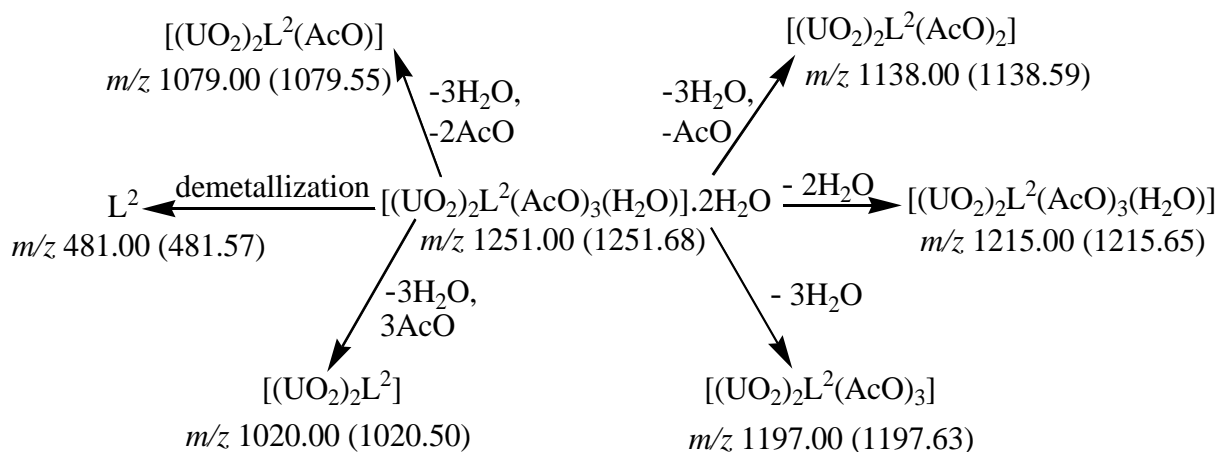


Fig. 2. Fragmentation pathways of [(UO₂)₂L²(AcO)₃(H₂O)]·2H₂O (**2**).

Table 1. Analytical and physical data of HL¹, HL² and their UO₂(II)-complexes^a (**1** and **2**).

Molecular formula (Empirical formula)	Mol. Wt. (Cal. Mol. Wt.)	Color (Δ _m)	Analytical data			
			Found % (Calcd.)			
			% Hydrated H ₂ O	% Coordinated H ₂ O	% AcO ⁻	% M
HL ¹ (C ₁₉ H ₁₉ N ₇ O ₃ S)	425.00 (425.46)	Yellow (—)	—	—	—	—
[(UO ₂) ₂ L ¹ (AcO) ₃ (H ₂ O)]·H ₂ O (C ₂₅ H ₃₁ N ₇ O ₁₅ SU ₂) (1)	1177.00 (1177.68)	Brown (6.32)	1.48 (1.53)	1.50 (1.53)	14.88 (15.04)	40.31 (40.42)
HL ² (C ₂₃ H ₂₇ N ₇ O ₃ S)	481.00 (481.57)	Yellow (—)	—	—	—	—
[(UO ₂) ₂ L ² (AcO) ₃ (H ₂ O)]·2H ₂ O (C ₂₉ H ₄₁ N ₇ O ₁₆ SU ₂) (2)	1251.00 (1251.68)	<i>F.</i> brown (6.12)	2.83 (2.88)	1.39 (1.44)	13.93 (14.15)	37.98 (38.03)

^a The yield of the synthesized compounds was 78-81%.

The synthesized complexes decompose without melting above 275 °C.

Mol. Wt. is the molecular weight obtained from mass spectra.

Δ_m is the molar conductance measured in Ohm⁻¹ cm² mol⁻¹.

RESULTS AND DISCUSSION

The ligands (HL¹ and HL²) and their UO₂(II)-complexes were formulated from the analytical, spectral and molar conductance data which supported the suggested formulae (Table 1). The complexes are highly colored and insoluble in water and common organic solvents such as methanol, ethanol, acetone, ether, CHCl₃, CCl₄ and benzene but moderately soluble in highly coordinating solvents such as DMSO and DMF. They are non-hygroscopic and highly stable under normal conditions. The low molar conductance values for the complexes in DMSO indicate them to be non-electrolytes in nature [42].

TOF-mass spectra

The constitutions and purities of the prepared ligands and their UO₂(II)-complexes are confirmed by MALDI-TOF mass spectrometry using dithranol as a matrix. The ligand spectra displayed accurate

molecular ion peaks at m/z 425 and 481 for HL¹ and HL², respectively, matched with the theoretical values. The mass spectra of [(UO₂)₂L¹(AcO)₃(H₂O)]·H₂O and [(UO₂)₂L²(AcO)₃(H₂O)]·2H₂O showed peaks at m/z 1177 and 1251, respectively, corresponding to the molecular weight of the parent ion [ML]⁺. A further confirmation for the molecular structure of the investigated complexes comes from the appearance of other peaks due to successive degradation of the target compound to various fragments [25]. For example, the mass spectrum of complex **1** displayed peaks at m/z 1177, 1159, 1141, 1082, 1023 and 964 corresponding to [(UO₂)₂L¹(AcO)₃(H₂O)]·H₂O (the molecular weight of the complex cation), [(UO₂)₂L¹(AcO)₃(H₂O)] (loss of the hydrated water molecule), [(UO₂)₂L¹(AcO)₃] (loss of two water molecules) [(UO₂)₂L¹(AcO)₂] (loss of two water

Table 2. Assignment of the IR spectral bands (cm⁻¹) of HL¹, HL² and their UO₂(II)-complexes **1** and **2**.

No	v(OH) [v(NH)]	v(NH ₂) [v(CH _{arom})]	v(CH=N _{arom}) [v(CH=N _{azom})]	v(N=N) [v(S=O)]	v _{as} (OCO) [v _s (OCO)]	v(SO ₂ N)	v _{as} (UO ₂) [v _s (C-S)]	v(M-O) [v(M-N)]
HL ¹	3425 [3357]	3260 [3039]	1650 [1584]	1411 [1263]	— [—]	1326, 1156	— [686]	— [—]
1	3425 [3357]	3260 [3042]	1624 [1582]	1410 [1262]	1519 [1476]	1326, 1156	843 [681]	664 [421]
HL ²	3425 [3356]	3259 [3039]	1652 [1583]	1409 [1262]	— [—]	1326, 1156	— [685]	— [—]
2	3425 [3357]	3262 [3042]	1621 [1581]	1409 [1263]	1495 [1442]	1326, 1157	844 [684]	639 [421]

molecules and one acetate group), [(UO₂)₂L¹(AcO)] (loss of two water molecules and two acetate groups), and [(UO₂)₂L¹] (loss of two water molecules and three acetate groups). Also, UO₂(II)-complexes **1** and **2** decompose *via* abstraction of the ligand, which gives rise to molecular ion peaks attributable to [L]⁺ (figure 2). This is a common behavior for metal ion complexes containing different ligands (ML) which decompose during spray ionization through cleavage of the metal-ligand bond [44]. This is good evidence confirming the proposed structures of the investigated complexes.

Vibrational (FT-IR) spectra and mode of bonding

Previous studies on metal complexes of Schiff base derivatives of sulfa-drugs indicated that metal ions are bonded to the ligand either through the Schiff base or the sulfonamide part for mononuclear complexes, while for binuclear ones both centers contribute [45]. In order to study the binding mode of HL¹ and HL² to the uranyl ion in the complexes, FT-IR spectra of the free ligands were compared with the spectra of the complexes. On examining the infrared spectra of the UO₂(II) chelates in comparison to the corresponding free ligands, the following observations can be made (Table 2);

1. IR spectra of HL¹ and HL² displayed strong sharp bands at 3425 cm⁻¹ assignable to v(OH).
2. IR spectra of complexes **1** and **2** displayed broad bands at 3425 cm⁻¹, which can be assigned to v(OH) of water associated with complexes. The presence of water renders it difficult to confirm the deprotonation of the OH groups on complex formation from the stretching vibration [46].

3. Stretching vibration bands at 1584, 1582 due to aliphatic v(CH=N) and at 1650 and 1624 cm⁻¹ corresponding to aromatic v(CH=N) in the spectra of HL¹ and HL², respectively, were found to be invariable shifts in the spectra of complexes **1** and **2** indicating the coordination of the aromatic and aliphatic azomethine nitrogens to the metal ion in chelate formation [47].
4. In the IR spectra of HL¹ and HL², sharp bands appeared at 1326 and 1156 cm⁻¹ due to v_{as}(SO₂N) and v_s(SO₂N), respectively. These bands slightly shifted to higher or lower frequencies upon coordination to UO₂(II) [47].
5. In the uranyl complexes **1** and **2**, the bands which are observed within the 1519-1495 and 1476-1442 cm⁻¹ ranges attributed to v_{as}(OCO) and v_s(OCO) of the acetate group, respectively, indicate monodentate coordination of this group [$\Delta(\text{OCO}) = v_{\text{as}}(\text{OCO}) - v_{\text{s}}(\text{OCO}) < 100 \text{ cm}^{-1}$] [48].
6. The medium intensity bands appeared around 3357, 3260, 3040, 2939, 1410, 1262 and 685 cm⁻¹ can be assigned to v(NH₂), v(NH), v(CH-aromatic), v(CH₂), v(N=N), v(S=O), and v(C-S), respectively.

This is supported by the appearance of two new bands at 664–639 cm⁻¹ and at 420 cm⁻¹ due to v(M–O) and v(M–N) [22], respectively. Also, the uranyl complexes **1** and **2** show a strong IR band near 843 cm⁻¹ assigned to v_{as}(UO₂) [49]. The assignment of bands of diagnostic importance in the IR spectra of the free ligands and metal complexes under study is collected in Table 2.

From these observations and the previous studies [24, 25, 45, 46], the mode of bonding in UO₂(II)-complexes **1** and **2** can be represented (figure 3).

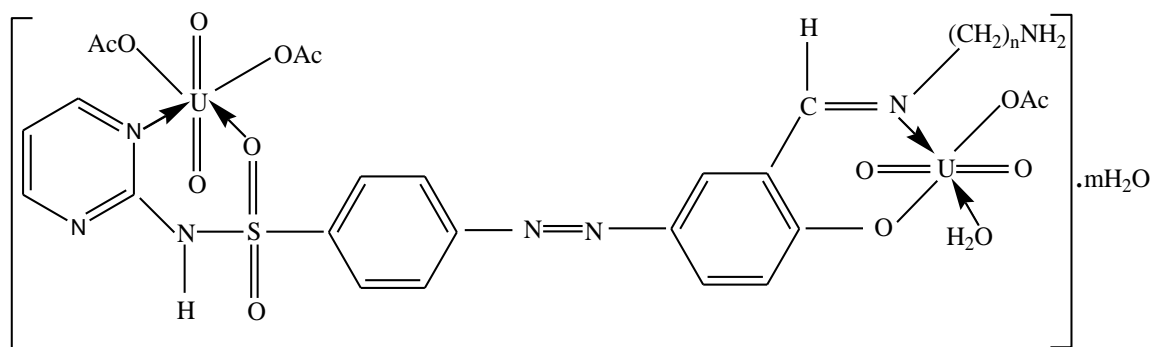


Fig. 3. Representative structures of binuclear UO₂(II)-complexes **1** and **2**, where n=2 and m=1 for complex **1** while n=6 and m=2 for complex **2**.

Table 3. Electronic and ¹H NMR spectral data of HL¹, HL² and their UO₂(II)-complexes **1** and **2**.

No	Electronic spectra (λ _{max} , nm)	¹ H NMR spectra						
		δ _{OH}	δ _{CH-N}	δ _{Ar-H}	δ _{NH}	δ _{NH₂}	CH ₃ -protons (CH ₃ COO)	δ _{H₂O}
HL ¹	290, 376, 452	11.31	8.47	7.61-6.99	9.55	8.98	—	—
1	293, 405, 481	—	8.49	7.82-7.00	9.56	9.00	3.37	2.51
HL ²	295, 372, 460	11.25	8.48	7.63-6.56	9.56	9.00	—	—
2	305, 380, 479	—	8.49	7.82-7.00	9.58	9.01	3.39	2.50

Table 4. Thermogravimetric analysis of UO₂(II)-complexes **1** and **2**.

Compound	% Loss in weight found (calcd.)	Temperature range (°C)	Assignment (thermal process)
[(UO ₂) ₂ L ¹ (AcO) ₃ (H ₂ O)]·H ₂ O (1)	1.61 (1.53)	50-100	Loss of hydrated H ₂ O.
[(UO ₂) ₂ L ¹ (AcO) ₃ (H ₂ O)]	1.48 (1.53)	120-175	Removal of coordinated H ₂ O.
[(UO ₂) ₂ L ¹ (AcO) ₃]	14.67 (15.04)	230-295	Elimination of coordinated acetate groups.
[(UO ₂) ₂ L ¹]	33.21 (33.33)	305-1000	Complete decomposition of the complex and formation of metal oxide as a final product.
[(UO ₂) ₂ L ² (AcO) ₃ (H ₂ O)]·2H ₂ O (2)	2.11 (2.88)	60-90	Loss of hydrated H ₂ O.
[(UO ₂) ₂ L ² (AcO) ₃ (H ₂ O)]	1.83 (1.44)	136-180	Removal of coordinated H ₂ O.
[(UO ₂) ₂ L ² (AcO) ₃]	14.24 (14.15)	220-275	Elimination of coordinated acetate groups.
[(UO ₂) ₂ L ²]	35.64 (35.83)	307-1000	Complete decomposition of the complex and formation of metal oxide as a final product.

Table 5. Antimicrobial activities of HL¹, HL² and their UO₂(II)-complexes **1** and **2**.

Compound	Inhibition zone diameter (mm mg ⁻¹ sample)			
	<i>E. coli</i> (G ⁻)	<i>S. aureus</i> (G ⁺)	<i>A. flavus</i> (Fungus)	<i>C. albicans</i> (Fungus)
Control: DMSO	0.0	0.0	0.0	0.0
Tetracycline (Antibacterial agent)	33.0	30.0	—	—
Amphotericin B (Antifungal agent)	—	—	20.0	20.0
HL ¹	13.0	14.0	0.0	0.0
Complex 1	15.0	15.0	0.0	0.0
HL ²	13.0	15.0	0.0	0.0
Complex 2	18.0	18.0	11.0	0.0

UV-Vis spectra and magnetic moment measurements

The electronic spectral data of the ligands and their $UO_2(II)$ complexes in DMF solution are presented in Table 3. HL^1 and HL^2 displayed mainly three bands; the first band appeared within the 290-295 nm range due to the low energy $\pi \rightarrow \pi^*$ transition corresponding to ${}^1L_b \leftarrow {}^1A$ state of the phenyl ring, while the second band appeared within the 372-376 nm range due to the $n \rightarrow \pi^*$ transition. The third band appeared in the 452-460 nm range which can be assigned to charge transfer (CT) transitions within the whole molecule [50]. The $UO_2(II)$ -complexes mainly showed a weak band near 480 nm and a highly intense band in the range 293-305 nm which are attributed to ${}^1\Sigma_g^+ \rightarrow {}^3\Pi_u$ transitions and charge transfer being overlapped with $\pi \rightarrow \pi^*$ transition, respectively [51]. It may be noted that the band occurring in the 380-405 nm range is due to the uranyl moiety because of apical oxygen $\rightarrow f^0(U)$ transition being merged with the ligand band due to $n \rightarrow \pi^*$ transition as evident from broadness and intensity [52]. $UO_2(II)$ complexes **1** and **2** show diamagnetic properties, as expected [53].

1H NMR spectra

In order to determine the center of chelation and replaceable hydrogen upon complex formation, 1H NMR spectra of the free ligands were studied and compared with the spectra of their $UO_2(II)$ -complexes (Table 3). The signals at 11.31 and 11.25 ppm due to δ_{OH} in the spectra of HL^1 and HL^2 disappeared in the 1H NMR spectra of the complexes denoting that complex formation occurs *via* deprotonation of the OH group [54]. The azomethine proton ($-\text{CH}=\text{N}-$) appeared as a singlet at 8.47 and 8.48 ppm in the free ligands has downfield shifts upon complex formation, supporting participation of the azomethine nitrogen in coordination to $UO_2(II)$ ion [9]. The signals at 7.63–6.56, 9.56–9.55, and 9.00–8.98 ppm due to δ_{Ar} , δ_{NH} and δ_{NH_2} in the free ligand spectra have downfield shifts in the spectra of the complexes due to increased conjugation on coordination, supporting the coordination of the ligands to $UO_2(II)$ ion. The downfield shift of these signals is due to deshielding by $UO_2(II)$ [55]. The 1H NMR spectra of $UO_2(II)$ -complexes displayed two new signals at 2.50-2.51 and 3.37-3.39 ppm for water and CH_3 from acetate, respectively [24]. Thus, the 1H NMR results support the IR inferences.

Thermal analysis

Thermal analysis was used to confirm the molecular structure of the complexes. Also, the thermal stability, properties, nature of intermediates and final products of the thermal decomposition of coordination compounds can be obtained from thermal analysis [56]. From the TGA curves, the mass loss can be calculated for the different decomposition steps and compared with those theoretically calculated for the suggested formula based on analytical and spectral results, as well as molar conductance measurements. TGA indicates the formation of a metal oxide as the end product from which the metal content could be calculated and compared with that obtained from analytical data. The investigated complexes **1** and **2** were subjected to TGA to throw more light on their molecular structures. The obtained results and the thermal decomposition patterns are presented in Table 4. From the tabulated results it can be concluded that the thermal decomposition of the complexes takes place in four steps. The lattice water molecules were volatilized within the temperature range of 50–100°C while the coordinated water molecules were removed within the range of 120–180°C. The number of water molecules was determined from the percentage weight losses at these steps. The removal of coordinated acetate groups was observed within the 220–295°C range [11]. The complete decomposition of the organic ligands occurred at temperatures higher than 305°C. The final product was the metal oxide. The metal content was also determined from the percentage weight of the remaining oxide, which was also used to calculate the molecular weight of the investigated complexes. The values determined were concordant with those obtained from the mass spectral studies.

In-vitro antimicrobial assay

It was reported that the biological and medicinal potency of coordination compounds has been established by antitumor, antiviral, and antimalarial activities, related to the ability of the metal ion to form complexes with ligands containing nitrogen and oxygen donors [57]. The *in vitro* anti-microbial activities of the investigated ligands and complexes were tested against *A. flavus*, *C. albicans*, *E. coli*, and *S. aureus* by the modified Kirby–Bauer disc diffusion method [37]. Standard drugs tetracycline and amphotericin B were also tested for their antibacterial and antifungal activities at the same concentrations and conditions. The complexes had significant antimicrobial activities against the tested

organisms compared with the free ligands (Table 5). Complexes **1** and **2** exhibited high activity against different types of the tested bacteria. Complex **2** displayed moderate activity against *A. flavus*, whereas complex **1** and free ligands are inactive against it. Ligands and complexes are inactive against *C. albicans*. Compared with tetracycline and amphotericin B, the complexes were less active. The data prove the potential of complexes **1** and **2** as broad-spectrum antibacterial agents. Also, complex **2** can be used as an effective antifungal agent against multicellular fungi. It is well known that the activity of any compound is a complex combination of steric, electronic, and pharmacokinetic factors. The action of the compounds may involve the formation of a hydrogen bond through $-N=C$ of the chelate or the ligand with the active centers of the cell constituents resulting in interference with normal cell process [58]. The microbototoxicity of the compounds may be ascribed to the metal ions being more susceptible toward the bacterial cells than the ligands [59]. The improved activities of the metal complexes as compared to the ligand can be explained on the basis of the chelation theory [60]. This theory explains that a decrease in the polarizability of the metal could enhance the lipophilicity of the complexes, which leads to a breakdown of the permeability of the cells, resulting in interference with normal cell processes [61]. This indicates that the chelation tends to make the Schiff bases act as more powerful and potent antimicrobial agents, thus inhibiting the growth of bacteria and fungi more than the parent Schiff bases [62, 63]. Therefore, it is claimed that the process of chelation dominantly affects the biological behavior of the compounds that are potent against microbial and fungal strains. *E. coli* was selected as the backbone of Gram negative bacteria whereas *S. aureus* was selected to represent Gram positive bacteria. Also, *A. flavus* was selected as a higher fungus which represents multicellular fungi whereas *C. albicans* represents the unicellular fungi; they represent a broad spectrum of test organisms. So, the obtained data prove the usefulness of $UO_2(II)$ -complexes as broad-spectrum antimicrobial agents.

CONCLUSION

Two azo-azomethine ligands and their bi-homonuclear uranyl complexes were prepared and characterized. Analytical data, molar conductance measurements, magnetic susceptibility, TOF-mass, IR, UV-Vis, and 1H NMR spectral studies suggest octahedral geometry of the complexes. The ligands

coordinate to the metal ions *via* the nitrogen atom of the pyrimidine ring, the oxygen atom of the sulfonamide group, the azomethine-N, and the oxygen atom of OH group in two chelation centers. Conductance data reveal that the complexes are non-electrolytes. The thermal data confirmed the suggested formula based on spectral results. The synthesized complexes were active against bacteria (*E. coli* and *S. aureus*) and fungi (*A. flavus*), thus giving a new thrust of these compounds in the field of metallo-drugs (bio-inorganic chemistry). Also, metal complexes of such type are of interest especially due to their potential as biocides and nematocides with unique electrical and magnetic properties [64].

REFERENCES

1. S. Bitmez, K. Sayin, B. Avar, M. Kose, A. Kayraldiz, M. Kurtoglu, *J. Mol. Struct.*, **1076**, 213 (2014).
2. K. Hart, N.C. Oforika, A.O. James, *Am. J. Sci. Ind. Res.*, **5**, 60 (2014).
3. N. Kurtoglu, *J. Serb. Chem. Soc.* **74**, 917 (2009).
4. M. Erfantalab, H. Khanmohammadi H., *Spectrochim. Acta A*, **125**, 345 (2014).
5. N.A. El-Wakiel, A.M. Khedr, R.A. Mansour, *Chinese J. Chem.*, **28**, 463 (2010).
6. Th. Nogrady, *Medicinal Chemistry*, 2nd Edn., Oxford University Press, New York, 1988.
7. T. Johnson, I.A. Khan, M.A. Avery, J. Grant, S.R. Meshnick, *Antimicrob. Agents Chemother.*, **42**, 1454 (1998).
8. C-Y. Wu, L-H. Chen, W-S. Hwang, H-S. Chen, C-H. Hung, *J. Organomet. Chem.*, **689**, 2192 (2004).
9. A.M. Khedr, N.A. El-Wakiel, S. Jadon, V. Kumar, *J. Coord. Chem.*, **64**, 851 (2011).
10. W. Nkoana, D. Nyoni, P. Chellan, T. Stringer, D. Taylor, P.J. Smith, A.T. Hutton, G.S. Smith, *J. Organomet. Chem.*, **752**, 67 (2014).
11. A.M. Khedr, M. Gaber, H.A. Diab, *J. Coord. Chem.*, **65**, 1672 (2012).
12. J. Malina, N.P. Farrell, V. Brabec, *Inorg. Chem.*, **53**, 1662 (2014).
13. P. Chellan, K.M. Land, A. Shokar, A. Au, S.H. An, D. Taylor, P.J. Smith, T. Riedel, P.J. Dyson, K. Chibale, G.S. Smith, *Dalton Trans.*, **43**, 513 (2014).
14. A.M. Khedr, H.M. Marwani, *Int. J. Electrochem. Sci.*, **7**, 10074 (2012).
15. H. Sato, K. Morimoto, Y. Mori, Y. Shinagawa, T. Kitazawa, A. Yamagishi, *Dalton Trans.*, **42**, 7579 (2013).
16. M-T Zhang, Z. Chen, P. Kang, T.J. Meyer, *J. Am. Chem. Soc.* **135**, 2048 (2013).
17. T.M. Ismail, A.M. Khedr, S.M. Abu-El-Wafa, R.M. Issa, *J. Coord. Chem.*, **57**, 1179 (2004).
18. N. Büyükkidan, M. Bülbül, R. Kasimoğullari, B. Büyükkidan B, *J. Enzyme. Inhib. Med. Chem.* **28**, 311 (2013).
19. R.M. Issa, A.M. Khedr, A. Tawfik, *Synth. React. Inorg. Met.-Org. Chem.*, **34**, 1087 (2004).

20. H. Sato, A. Yamagishi, *Int. J. Mol. Sci.*, **14**, 964 (2013).
21. R.R. Gagne, C.L. Spiro, T.G. Smith, C.A. Hamann, V.R. Thies, A.K. Shiemke, *J. Am. Chem. Soc.*, **103**, 4073 (1981).
22. C.M. Sharaby, G.G. Mohamed, M.M. Omar, *Spectrochim. Acta A.*, **66**, 935 (2007).
23. R.C. Maurya, S. Rajput, *J. Mol. Struct.*, **794**, 24 (2006).
24. R.M. Issa, S.A. Azim; A.M. Khedr, D.F. Draz, *J. Coord. Chem.*, **62**, 1859 (2009).
25. A.M. Khedr, D.F. Draz, *J. Coord. Chem.*, **63**, 1418 (2010).
26. S. Al-Ashqer, K.S. Abou-Melha, G.A.A. Al-Hazmi, F.A. Saad, N.M. El-Metwaly, *Spectrochim. Acta*, **132**, 751 (2014).
27. J.C. Knight, M. Wuest, F.A. Saad, M. Wang, D.W. Chapman, H.-S. Jans, S.E. Lapi, B.M. Kariuki, A.J. Amoroso,
28. F.A. Saad, J.C. Knight, B.M. Kariuki, A.J. Amoroso, *Dalton Trans.*, **42**, 14826 (2013).
29. F.A. Saad, N.J. Buurma, A.J. Amoroso, J.C. Knight, B.M. Kariuki, *Dalton Trans.*, **41**, 4608 (2012).
30. F.A. Saad, *Spectrochim. Acta A* **128**, 386 (2014).
31. G.A.A. Al-Hazmi, A.A. El-Zahhar, K.S. Abou-Melha, F.A. Saad, M.H. Abdel-Rhman, A.M. Khedr, N.M. El-Metwaly, *J. Coord. Chem.*, **68**, 993 (2015).
32. R. Botros, Azomethine dyes derived from an o-hydroxy aromatic aldehyde and a 2-aminopyridine, *US Patent* 4051119 (1977).
33. Z. Rezvani, M. A. Ghanea, K. Nejati, S. A. Baghaei, *Polyhedron*, **28**, 2913 (2009).
34. A.I.A Vogel, *Hand Book of Quantitative Inorganic Analysis*, 2nd Edn., Longman, London 1966.
35. A.P. Mishra, R.K. Mishra, S.P. Shrivastava, *J. Serb. Chem. Soc.*, **74**, 523 (2009).
36. A.W. Bauer, W.M. Kirby, C. Sherris, M. Turck, *Am. J. Clin. Path.*, **45**, 493 (1966).
37. M.A. Pfaller, L. Burmeister, M.S. Bartlett, M.G. J. *Clin. Microbiol.*, **26**, 1437 (1988).
38. National Committee for Clinical Laboratory Standards. *Performance Antimicrobial Susceptibility of Flavobacteria*, Vol. 41 (1997).
39. National Committee for Clinical Laboratory Standards. Reference Method for Broth Dilution Antifungal Susceptibility Testing of Conidium-forming Filamentous Fungi: Proposed Standard M38-A, NCCLS, Wayne, PA, USA, 2002.
40. National Committee for Clinical Laboratory Standards. Method for Antifungal Disk Diffusion Susceptibility Testing of Yeast: Proposed Guideline M44-P, NCCLS, Wayne, PA, USA 2003.
41. National Committee for Clinical Laboratory Standards. Methods for Dilution Antimicrobial Susceptibility Tests for Bacteria that Grow Aerobically. Approved standard M7-A3, NCCLS, Villanova, PA, 1993.
42. L.D. Liebowitz, H.R. Ashbee, E.G. Evans, Y. Chong, N. Mallatova, M. Zaidi, D. Gibbs, *Diagn. Microbiol. Infect. Dis.*, **40**, 27 (2001).
43. E. Tas, M. Aslanoglu, A. Kilic, O. Kaplan, H. Temel, *J. Chem. Res-(s)*, **4**, 242 (2006).
44. B.K. Singh, P. Mishra, B.S. Garg, *Transit. Met. Chem.*, **32**, 603 (2007).
45. K.Y. El-Baradie, M. Gaber, *Chem. Pap.*, **57**, 317 (2003).
46. G.G. Mohamed, M.A.M. Gad-Elkareem, *Spectrochim. Acta A*, **68**, 1382 (2007).
47. R.K. Agarwal, H. Agarwal, *Synth. React. Inorg. Met.-Org. Chem.*, **26**, 1163 (1996).
48. K. Nakamoto, *Infrared and Raman Spectra of Inorganic and Coordination Compounds*, Wiley Interscience Publication, Jhon Willey & Sons Inc., New York, 1986.
49. S.I. Mostafa, *Transit. Met. Chem.*, **23**, 397 (1998).
50. A. Cukuravali, I. Yilmaz, S. Kirbag, *Transit. Met. Chem.*, **31**, 207 (2006).
51. R. Chandra, *Synth. React. Inorg. Met.-Org. Chem.*, **20**, 645 (1990).
52. D.C. Dash, A. Mahapatra, P. Naik, R.K. Mohapatra, S.K. Naik, *J. Korean Chem. Soc.*, **55**, 412 (2011).
53. A.S. El-Tabl, F.A. El-Saied, A.N. Al-Hakimi, *Transit. Met. Chem.*, **32**, 689 (2007).
54. S.M. Abdallah, M.A. Zayed, G.G. Mohamed, *Arabian J. Chem.*, **3**, 103 (2010).
55. F.A. Hart, J.E. Newbery, D. Shaw, *Chem. Commun. (London)*, **1**, 45 (1967).
56. M. Badea, A. Emandi, D. Marinescu, E. Cristurean, R. Olar, A. Braileanu, P. Budrugaec, E. Segal, *J. Therm. Anal. Calorim.*, **72**, 525 (2003).
57. R.V. Singh, S.C. Joshi, A. Gajraj, P. Nagpal, *Appl. Organomet. Chem.*, **16**, 713 (2002).
58. A.M. Khedr, S. Jadon, V. Kumar, *J. Coord. Chem.*, **64**, 1351 (2011).
59. M.A. Phaniband, S.D. Dhumwad, *Transit. Met. Chem.*, **32**, 1117 (2007).
60. K.N. Thimmaiah, W.D. Lloyd, G.T. Chandruppa, *Inorg. Chim. Acta*, **106**, 81 (1985).
61. C.H. Collins, P.M. Lyne, *Microbiological Methods*, Butterworth, London, 1976.
62. A. Kulkarni, P.G. Avaji, G.B. Bagihalli, S.A. Patil, P.S. Badami, *J. Coord. Chem.*, **62**, 481 (2009).
63. S. Malik, S. Ghosh, L. Mitu, *J. Serb. Chem. Soc.*, **76**, 1387 (2011).
64. M. Jain, S. Gaur, V.P. Singh, R.V. Singh, *Appl. Organomet. Chem.*, **18**, 73 (2004).

ГРУПИ ОТ АЗО-АЗОМЕТИНОВИ ЛИГАНДИ С N_2O_2 –ДОНОРИ И ТЕХНИТЕ
ДВУЯДРЕНИ КОМПЛЕКСИ С $UO_2(II)$: СИНТЕЗА, ОХАРАКТЕРИЗИРАНЕ И
БИОЛОГИЧНА АКТИВНОСТ

Ф.А. Саад¹, А.М. Хедр^{1,2*}

¹ Департамент по химия, Колеж по приложни науки, Университет „Ум-ал-Ура“, Макка, Саудитска Арабия

² Департамент по химия, Научен факултет, Университет в Танта, Египет

Получена на 2 септември, 2014 г., коригерана на 5 ноември, 2014 г.

(Резюме)

Синтезирани са две азо-азометинови лиганди с донор от N_2O_2 и техните двуядрени комплекси с $UO_2(II)$ за терапевтични цели. Лигандите са получени чрез кондензация на 4-(4-хидрокси-3-формил-1-илазо)-N-пиримидин-2-ил-бензенсулфонамид с етилендиамин и 1,6-хександиамин. Получените лиганди и техните двеномядрени уранилови комплекси са характеризирани с термични анализи (TGA и конвенционален метод), вибрационни, електронни, 1H NMR и маспектри, както и чрез различни физикохимични техники. Активните координационни центрове в лигандите и геометричното разположение на комплексите са изследвани с помощта на спектрални данни. Измервания на моларната проводимостта в разтвор на DMSO показва, че комплексите са не-електролити. Изследваните комплекси и лиганди бяха скринирани *ин витро* за тяхната антимикуробна активност срещу гъби (*Aspergillus flavus* and *Candida albicans*), грам-положителни бактерии (*Staphylococcus aureus*) и грам-отрицателни бактерии (*Escherichia coli*). Установено е, че комплексите са по-мощни фунгициди и бактерициди, отколкото лигандите.

Multicomponent reactions of diethyl oxalate: synthesis of pyrrole derivatives in water

F. Sheikholeslami-Farahani*

Department of Chemistry, Firoozkooh Branch, Islamic Azad University, Firoozkooh, Iran

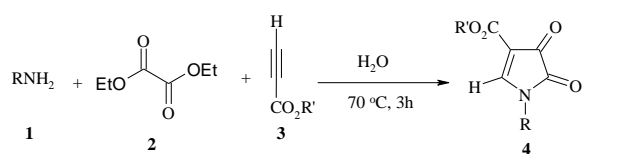
Received February 13, 2014; Revised July 21, 2014

An expert tactic for the preparation of 1H-pyrrole derivatives *via* the reaction between primary amines, alkyl propiolates and diethyl oxalate is described. Particularly, valuable features of this method include high yields of products, short reaction time, and straightforward and convenient procedure. Herein, the synthesis of substituted 1H-pyrroles was reported based on the three-component reaction of diethyl oxalate.

Keywords: Pyrrole, Alkyl propiolate, Oxalyl chloride, Primary amines, Water

INTRODUCTION

At the beginning of the new century, a move in importance in chemistry is obvious with the aim to extend environmentally gentle routes for the synthesis of numerous materials [1]. Green chemistry approaches hold out momentous potential not only for reduction of byproducts and waste produced, and lowering of energy costs but also in the development of new methodologies toward previously unobtainable materials, using existing technologies [2, 3]. More than a few biologically active synthetic compounds have five membered nitrogen containing heterocycles in their structures [4]. Among them, pyrroles are heterocycles of great importance because of their presence in frequent natural products similar to heme, chlorophyll, vitamin B12, and various cytochrome enzymes [5]. Some of the recently isolated pyrrole containing marine natural products have been found to display significant cytotoxicity and function as multidrug resistant (MDR) reversal agents [6]. Many of these biologically active compounds have appeared as chemotherapeutic agents. Also, polysubstituted pyrroles are molecular structures having immense importance in material science [7]. They have also been employed as antioxidants [8], antibacterial [9, 10] ionotropic [11, 12] antitumor [13], anti-inflammatory [14, 15] and antifungal agents [16]. Continuing our efforts directed towards the straightforward preparation of biologically active target molecules through multicomponent reactions, we performed the synthesis of some 1H-pyrrole derivatives *via* a three-component reaction of diethyl oxalate at 70 °C in water (Scheme 1).



1,3,4	R	R'	Yield (%) of 4
a	Bn	Me	85
b	4-MeC ₆ H ₄ CH ₂	Me	80
c	n-Bu	Me	87
d	Et	Et	85
e	^t Bu	Et	80

Scheme 1. Synthesis of compound 4

EXPERIMENTAL

Apparatus and analysis

Melting points were taken on a Kofler hot stage apparatus and are uncorrected. ¹H, ¹³C and ³¹P NMR spectra were obtained with a Bruker FT-500 spectrometer in CDCl₃, and tetramethylsilane (TMS) was used as an internal standard or 85% H₃PO₄ as external standard. Mass spectra were recorded with a Finnigan Mat TSQ-70 spectrometer. Infrared (IR) spectra were acquired on a Nicolet Magna 550-FT spectrometer. Elemental analyses were carried out with a Perkin-Elmer model 240-C apparatus. The results of elemental analyses (C, H, N) were within ±0.4 % of the calculated values. Acetylenic ester, phenacyl bromide, its derivatives and triphenylphosphine were obtained from Fluka and were used without further purification.

General procedure for the preparation of compounds 4a-e: To a stirred mixture of primary amine 1 (2 mmol) and alkyl propiolate 5 (2 mmol) in water (5 mL) diethyl oxalate 2 (2 mmol) was added at 70 °C. The reaction mixture was stirred for 3 h. After completion of the reaction [TLC (AcOEt/hexane 1:6) monitoring], the reaction mixture was purified by flash column chromatography on silica gel (Merck

* To whom all correspondence should be sent:
E-mail: sheikholeslami@yahoo.com

230–400 mesh) using n-hexane–EtOAc as eluent to afford the pure compounds **4**.

Methyl-1-benzyl-4,5-dioxo-4,5-dihydro-1H-pyrrole-3-carboxylate (4a). White powder; 172–174 °C, yield 0.44 g (85%) IR (KBr) ($\nu_{\max}/\text{cm}^{-1}$) = 1738, 1730, 1728, 1675, 1467, 1325 cm^{-1} . MS: m/z (%) = 245 (M^+ , 15), 214 (70), 91 (96), 77 (64), 31 (100). Anal. Calcd (%) for $C_{13}H_{11}NO_4$ (245.23): C, 63.67; H, 4.52; N, 5.71. Found: C, 63.75; H, 4.63; N, 5.82. ^1H NMR (500.1 MHz, CDCl_3): δ = 3.75 (3 H, s, MeO), 4.84 (1 H, d, 2J = 11.7 Hz, CH), 5.15 (1 H, d, 2J = 11.7 Hz, CH), 7.12 (2 H, d, 3J = 7.4 Hz, 2 CH), 7.45 (1 H, t, 3J = 7.8 Hz, CH), 7.68 (2 H, t, 3J = 7.4 Hz, 2 CH), 8.65 (1 H, s, CH) ppm. ^{13}C NMR (125.7 MHz, CDCl_3): δ = 47.8 (NCH₂), 52.2 (MeO), 112.2 (C), 128.5 (CH), 129.4 (2 CH), 129.8 (2 CH), 137.5 (C), 147.5 (CH), 162.4 (C=O), 163.5 (C=O), 165.7 (C=O) ppm.

Methyl-1-(4-methylbenzyl)-4,5-dioxo-4,5-dihydro-1H-pyrrole-3-carboxylate (4b). White powder, 164–166 °C, yield 0.49 g (80%). IR (KBr) ($\nu_{\max}/\text{cm}^{-1}$) = 1740, 1737, 1732, 1695, 1672, 1447, 1254, 1175 cm^{-1} . MS: m/z (%) = 259 (M^+ , 10), 153 (65), 105 (100), 77 (64), 31 (100). Anal. Calcd (%) for $C_{14}H_{13}NO_4$ (259.26): C, 64.86; H, 5.05; N, 5.40. Found: C, 64.92; H, 5.14; N, 5.53. ^1H NMR (500.1 MHz, CDCl_3): δ = 2.30 (3 H, s, Me), 3.84 (3 H, s, MeO), 4.75 (1 H, d, 2J = 12.4 Hz, CH), 5.23 (1 H, d, 2J = 12.4 Hz, CH), 7.24 (2 H, d, 3J = 7.9 Hz, CH), 7.32 (2 H, d, 3J = 7.9 Hz, 2 CH), 8.74 (1 H, s, CH) ppm. ^{13}C NMR (125.7 MHz, CDCl_3): δ = 20.7 (Me), 46.4 (NCH₂), 52.3 (MeO), 111.4 (C), 128.5 (2 CH), 128.7 (2 CH), 130.2 (C), 133.5 (C), 161.4 (C=O), 162.3 (C=O), 165.4 (C=O) ppm.

Methyl-1-(butyl)-4,5-dioxo-4,5-dihydro-1H-pyrrole-3-carboxylate (4c). White powder; 145–147 °C, yield: 0.63 g (87%). IR (KBr) ($\nu_{\max}/\text{cm}^{-1}$) = 1742, 1740, 1735, 1694, 1425, 1324, 1236 cm^{-1} . Anal. Calcd (%) for $C_{10}H_{13}NO_4$ (211.22): C, 56.86; H, 6.20; N, 6.63. Found: C, 56.92; H, 6.34; N, 6.73. ^1H NMR (500.1 MHz, CDCl_3): δ = 0.92 (3 H, t, 3J = 7.2 Hz, CH₃), 1.27 (2 H, m, CH₂), 1.43 (2 H, m, CH₂), 3.74 (3 H, s, MeO), 3.82–3.93 (2 H, m, NCH₂), 8.84 (1 H, s, CH) ppm. ^{13}C NMR (125.7 MHz, CDCl_3): δ = 13.4 (CH₃), 18.7 (CH₂), 28.6 (CH₂), 42.5 (NCH₂), 109.4 (C), 147.3 (CH), 161.2 (C=O), 162.5 (C=O), 164.2 (C=O) ppm.

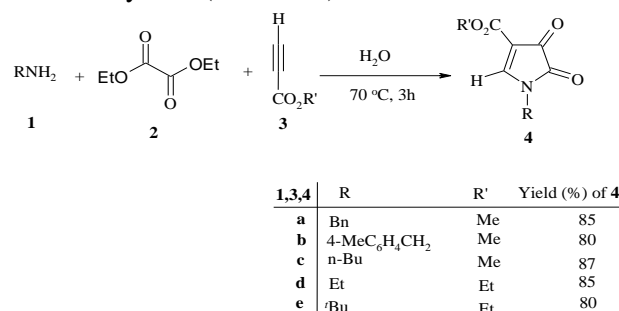
Ethyl-1-(ethyl)-4,5-dioxo-4,5-dihydro-1H-pyrrole-3-carboxylate (4d). White powder; 152–154 °C (decomp.); yield 0.35 g (85%). IR (KBr) ($\nu_{\max}/\text{cm}^{-1}$) = 1738, 1735, 1728, 1425, 1229 cm^{-1} . Anal. Calcd (%) for $C_9H_{11}NO_4$ (197.19): C, 54.82;

H, 5.62; N, 7.10. Found: C, 54.93; H, 5.73; N, 7.18. ^1H NMR (500.1 MHz, CDCl_3): δ = 1.28 (3 H, t, 3J = 7.4 Hz, CH₃), 1.36 (3 H, t, 3J = 7.5 Hz, CH₃), 3.68–3.82 (2 H, m, NCH₂), 4.25 (2 H, q, 3J = 7.5 Hz, CH₂O), 8.74 (1 H, s, CH) ppm. ^{13}C NMR (125.7 MHz, CDCl_3): δ = 13.4 (CH₃), 13.8 (CH₃), 38.4 (NCH₂), 61.4 (CH₂O), 110.4 (C), 146.2 (CH), 161.5 (C=O), 162.3 (C=O), 164.7 (C=O) ppm.

Ethyl-1-(tert-butyl)-4,5-dioxo-4,5-dihydro-1H-pyrrole-3-carboxylate (4e). White powder; 148–150 °C, yield 0.43 g (80%). IR (KBr) ($\nu_{\max}/\text{cm}^{-1}$) = 1745, 1740, 1738, 1462, 1430, 1347, 1232 cm^{-1} . Anal. Calcd (%) for $C_{11}H_{15}NO_4$ (225.24): C, 58.66; H, 6.71; N, 6.22. Found: C, 58.75; H, 6.82; N, 6.34. ^1H NMR (500.1 MHz, CDCl_3): δ = 1.34 (3 H, t, 3J = 7.4 Hz, CH₃), 1.48 (9 H, s, Me₃C), 4.23 (2 H, q, 3J = 7.4 Hz, CH₂O), 8.23 (1 H, s, CH) ppm. ^{13}C NMR (125.7 MHz, CDCl_3): δ = 13.7 (CH₃), 26.5 (Me₃C), 48.6 (NC), 61.4 (CH₂O), 110.7 (C), 139.8 (CH), 162.9 (C=O), 163.4 (C=O), 165.7 (C=O) ppm.

RESULTS AND DISCUSSION

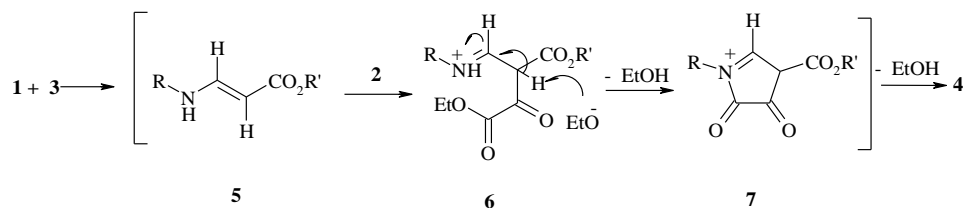
Three-component reactions between primary amine **1** and diethyl oxalate **2** with alkyl propiolates **3** at 70 °C in water produce 1H-pyrrole derivatives **4** in excellent yields (Scheme 1).



Scheme 1. Synthesis of compounds **4**

The structures of compounds **4a–e** were determined on the basis of their IR, ^1H NMR and ^{13}C NMR spectra. The mass spectra of these compounds show molecular ion peaks at the appropriate m/z values. Also, the ^1H NMR spectrum of **4a** exhibits two singlets at δ = 3.75 and 8.65 ppm for methoxy and methine protons, respectively. Two doublets at δ = 4.84 (d, 2J = 11.7 Hz) and 5.15 (d, 2J = 11.7 Hz) for CH₂ protons are registered along with signals for aromatic moiety.

On the basis of the well established chemistry of amine nucleophiles it is reasonable to assume that pyrrole derivatives **4** results from the initial addition



Scheme 2. Proposed mechanism for synthesis of **4**

of primary amines to alkyl propiolate and subsequent attack of the intermediate **5** to compound **2** producing the intermediate **6**. Intramolecular nucleophilic attack of the nitrogen to the carbonyl group in compound **6** generates compound **7** that by elimination of EtOH produces **4** (Scheme 2).

CONCLUSION

In conclusion, we reported a novel method involving primary amines and alkyl propiolates in the presence of diethyl oxalate for the synthesis of 1H-pyrrole derivatives. The advantages of our work are that the reaction is performed in water, without using a catalyst.

Acknowledgment: This research is supported by the Islamic Azad University, Firoozkooh Branch.

REFERENCES

1. P. Anastas, T. Williamson, *Green Chemistry, Frontiers in Benign Chemical Synthesis and Procedures*; Oxford Science Publications: New York, 1998.
2. G. W. V. Cave, C. L. Raston, J. L. Scott, *Chem. Commun.* 2159 (2001).
3. Z. Hossaini, F. Rostami-Charati, R. Hajinasiri, H. Jafaryan, M. Shahraki *Journal of Heterocyclic Chemistry*, **49**, 402 (2012).
4. D. Lednicer, L. A. Mitscher, In *Organic Chemistry of Drug Synthesis*; Wiley Interscience: New York, **1**, 226 (1977).
5. R. J. Sundberg, In *Comprehensive Heterocyclic Chemistry*; A. Katritzky, C. W. Rees, E. F. V. Scriven, Eds.; Pergamon: Oxford, **2**, 119 (1996).
6. H. Tao, I. Hwang, D. L. Boger, *Bioorg. Med. Chem. Lett.*, **14**, 5979 (2004).
7. (a) M. Baumgarten, N. Tyutyulkov, *Chem. Eur. J.* 1998, **4**, 987-989. (b) G. A. Pagani, *Heterocycles*, **37**, 2069 (1994).
8. J. Lehuède, B. Fauconneau, L. Barrier, M. Ourakow, A. Piriou, J. M. Vierfond, *Eur. J. Med. Chem.* **34**, 991 (1999).
9. R. W. Burli, D. McMinn, J. A. Kaizerman, W. Hu, Y. Ge, Q. Pack, V. Jiang, M. Gross, M. Garcia, R. Tanaka, H. E. Moser, *Bioorg. Med. Chem. Lett.* **14**, 1253 (2004).
10. R. W. Burli, P. Jones, D. McMinn, Q. Le, J. X. Duan, J. A. Kaizerman, S. Difuntorum, H. E. Moser, *Bioorg. Med. Chem. Lett.* **14**, 1259 (2004).
11. R. Jonas, M. Klockow, I. Lues, H. Pruecher, H. J. Schliep, H. Wurziger, *Eur. J. Med. Chem.* **28**, 129-140 (1993).
12. W. Von der Saal, J. P. Hoelck, W. Kampe, A. Mertens, B. *J. Med. Chem.* **32**, 1481-1491(1989).
13. W. A. Denny, G.W. Rewcastle, B. C. Baguley, *J. Med. Chem.* **33**, 814 (1990).
14. E. Toja, D. Selva, P. Schiatti, *J. Med. Chem.* **27**, 610 (1984).
15. V. J. Demopoulos, E. J. Rekka, *J. Pharm. Sci.* **84**,79 (1995).
16. M. Del Poeta, W. A. Schell, C. C. Dykstra, S. Jones, R. R. Tidwell, A. Czarny, M. Bajic, M. Bajic, A. Kumar, D. Boykin, J. R. Perfect, *Antimicrob. Agents Chemother.* **42**, 2495 (1998).

МНОГОКОМПОНЕНТНИ РЕАКЦИИ НА ДИЕТИЛ ОКСАЛАТ: СИНТЕЗА НА ПИРОЛОВИ ПРОИЗВОДНИ ВЪВ ВОДА

Ф. Шейкнолеслами-Фарахани

Катедра по химия, клон Фирузкух, Ислямски университет "Азад", Фирузкух, Иран

Постъпила на 13 февруари 2014 г.; коригирана на 21 юли, 2014 г.

(Резюме)

Описана е експертна тактика за получаване на 1Н-пирол производни чрез реакция между първични амини, алкилни пропиолати и диетил оксалат. Особено ценните характеристики на този метод включват високи добиви на продукти, кратко реакционно време, ясна и удобна процедура. В тази работа е описана синтеза на заместени 1Н-пироли на базата на трикомпонентна реакция на диетил оксалат

N-methyl imidazole or ammonium thiocyanate promoted synthesis of substituted pyrroles: Multicomponent reaction of alkyl propiolates in water

F. Sheikholeslami-Farahani*

Department of Chemistry, Firoozkooh Branch, Islamic Azad University, Firoozkooh, Iran

Received February 13, 2014; Revised August 25, 2014

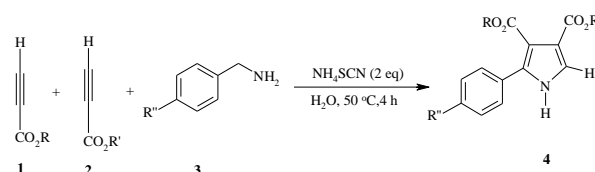
A novel, convenient, and efficient approach to the synthesis of substituted pyrroles is reported based on a three-component reaction. The reaction of primary amines with electron deficient acetylenic compounds in the presence of N-methylimidazole or ammonium thiocyanate in water lead to the formation of pyrroles in good yield.

Keywords: Water, Primary amine, N-methylimidazol, pyrroles, Three-component reaction, Green Chemistry.

INTRODUCTION

At the beginning of the new century, a move in importance in chemistry is obvious with the longing to extend environmentally gentle routes to a numerous of materials [1]. Green chemistry approaches hold out momentous potential not only for reduction of byproducts, a reduction in the waste produced, and lowering of energy costs but also in the development of new methodologies toward previously unobtainable materials, using existing technologies [2]. Of all of the existing areas of chemistry, medicinal and pharmaceutical chemistry, with their traditionally large volume of waste/product ratio, are maybe the most developed for greening [3]. Multicomponent reactions (MCRs) have been commonly employed by synthetic chemists as a too easy means to produce molecular diversity from bifunctional substrates that react successively in a intramolecular way [4]. Five membered, nitrogen-containing heterocycles are main building blocks in a broad number of biologically active compounds [5]. Among them, pyrroles are heterocycles of enormous importance because of their presence in several natural products like heme, chlorophyll, vitamin B₁₂, and various cytochrome enzymes [6]. Some of the recently isolated pyrrole-containing marine natural products have been set up to display considerable cytotoxicity and function as multidrug resistant reversal agents [7]. Many of these biologically active compounds have appeared as chemotherapeutic agents. In addition, substituted pyrroles are molecular skeleton having enormous importance in material science [8]. They have been also used as antioxidants, antibacterial, ionotropic,

antitumor, anti inflammatory and antifungal agents [9-14]. There are many methods for the synthesis of pyrroles [15-24]. As part of our current studies on the development of new routes in heterocyclic synthesis, we report an efficient synthesis of pyrrole derivatives **4** in good yield (Scheme 1).



1, 2, 3, 4	R	R'	R''	Yield (%) of 4
a	Me	Me	H	75
b	Me	Et	Me	87
c	Et	Me	MeO	70
d	Et	Et	Me	75

Scheme 1. Reaction of propiolate with benzyl amine in the presence of ammonium thiocyanate.

EXPERIMENTAL

Apparatus and analysis

All chemicals used in this work were purchased from Fluka (Buchs, Switzerland) and were used without further purification. Melting points were measured on an Electrothermal 9100 apparatus. Elemental analyses for C, H, and N were performed using a Heraeus CHN-O-Rapid analyzer. Mass spectra were recorded on a FINNIGAN-MAT 8430 spectrometer operating at an ionization potential of 70 eV. IR spectra were measured on a Shimadzu IR-460 spectrometer. ¹H and ¹³C NMR spectra were measured with a BRUKER DRX-500 AVANCE spectrometer at 500.1 and 125.8 MHz, respectively. ¹H, ¹³C, spectra were obtained for solutions in CDCl₃ using TMS as the internal standard or 85% H₃PO₄ as the external standard.

General procedure for preparation of compounds

4: To a stirred mixture of amine **3** (2 mmol) and acetylenic ester **2** (2 mmol) in water (5 mL) was

* To whom all correspondence should be sent:
E-mail: sheikholeslami@yahoo.com

added mixture of NH₄SCN (2 mmol) and acetylenic ester **1** (2 mmol) in water at 50 °C. After completion of the reaction (4 h; TLC (AcOEt/hexane 1:5) monitoring), the residue was extracted by AcOEt and washed by cold diethyl ether to give pure product.

General procedure for preparation of compounds 16: To a stirred mixture of alkyl propiolate **13** (2 mmol) and primary amine **14** (2 mmol) in water (5 mL) was added mixture of alkyl propiolate **15** and *N*-methylimidazole (5 mol%) in water (5 mL). The reaction mixture was then stirred for 1.5 h at 50 °C. After completion of the reaction [1.5 h; TLC (AcOEt/hexane 1:4) monitoring], the solid residue was filtered and washed by cold diethyl ether to give pure product **16**.

Dimethyl-2-phenyl-1H-pyrrole-3,4-dicarboxylate (4a): Yellow oil; yield: 0.39 g (75%). IR (KBr) ($\nu_{\max}/\text{cm}^{-1}$): 1725, 1634, 1487. ¹H NMR (500.1 MHz, CDCl₃): δ = 3.75 (3 H, s, MeO), 3.82 (3 H, s, MeO), 6.87 (1 H, s, CH), 7.12 (2 H, d, ³*J* = 7.5 Hz, CH), 7.42 (3 H, m, CH), 9.32 (1 H, br s, NH) ppm. ¹³C NMR (125.7 MHz, CDCl₃): δ = 51.2 (MeO), 51.8 (MeO), 112.4 (C), 125.8 (CH), 127.5 (2 CH), 128.4 (C), 128.7 (2 CH), 129.2 (CH), 132.0 (C), 143.4 (C), 162.4 (C=O), 163.8 (C=O) ppm. MS: *m/z* (%) = 259 (M⁺, 10), 228 (46), 91 (58), 77 (87), 31 (100). Anal. Calc. for C₁₄H₁₃NO₄ (259.26): C, 64.86; H, 5.05; N, 5.40; Found: C, 64.92; H, 5.14; N, 5.52.

4-ethyl-3-methyl-2-(4-methylphenyl)-1H-pyrrole-3,4-dicarboxylate (4b): Pale yellow oil; yield: 0.49 g (87%). IR (KBr) ($\nu_{\max}/\text{cm}^{-1}$): 1727, 1654, 1587, 1465. ¹H NMR (500.1 MHz, CDCl₃): δ = 1.24 (3 H, t, ³*J* = 7.4 Hz, CH₃), 2.42 (3 H, s, Me), 3.85 (3 H, s, MeO), 4.18 (2 H, q, ³*J* = 7.4 Hz, CH₂O), 7.12 (1 H, s, CH), 7.22 (2 H, d, ³*J* = 7.8 Hz, 2 CH), 7.38 (2 H, d, ³*J* = 7.8 Hz, 2 CH), 9.28 (1 H, br s, NH) ppm. ¹³C NMR (125.7 MHz, CDCl₃): δ = 13.8 (CH₃), 22.5 (Me), 52.7 (MeO), 61.4 (CH₂O), 115.2 (C), 125.4 (CH), 126.5 (2 C), 129.4 (C), 130.4 (2 CH), 131.2 (2 CH), 144.7 (C), 162.3 (C=O), 163.8 (C=O) ppm. MS: *m/z* (%) = 287 (M⁺, 15), 256 (45), 242 (58), 105 (100), 77 (86), 31 (100). Anal. Calc. for C₁₆H₁₇NO₄ (287.31): C, 66.89; H, 5.96; N, 4.88; Found: C, 66.93; H, 6.04; N, 4.92.

3-ethyl-4-methyl-2-(4-methoxyphenyl)-1H-pyrrole-3,4-dicarboxylate (4c): Yellow oil; yield: 0.42 g (70%). IR (KBr) ($\nu_{\max}/\text{cm}^{-1}$): 1724, 1627, 1545, 1462, 1335, 1275. ¹H NMR (500.1 MHz, CDCl₃): δ = 1.35 (3 H, t, ³*J* = 7.4 Hz, CH₃), 3.75 (3 H, s, MeO), 3.94 (3 H, s, MeO), 4.32 (2 H, t, ³*J* = 7.5 Hz, CH₂O), 6.94 (1 H, s, CH), 7.12 (2 H, d, ³*J* = 7.8 Hz, CH), 7.46 (2 H, d, ³*J* = 7.8 Hz, CH), 9.24 (1

H, br s, NH) ppm. ¹³C NMR (125.7 MHz, CDCl₃): δ = 14.2 (CH₃), 51.6 (MeO), 55.6 (MeO), 62.4 (CH₂O), 114.7 (2 CH), 115.2 (CH), 120.4 (C), 123.6 (C), 130.2 (C), 131.5 (2 CH), 141.7 (C), 160.2 (C), 161.7 (C=O), 164.5 (C=O) ppm. MS: *m/z* (%) = 303 (M⁺, 8), 272 (65), 182 (54), 121 (100), 77 (65), 31 (100). Anal. Calc. for C₁₆H₁₇NO₅ (303.31): C, 63.36; H, 5.65; N, 4.62; Found: C, 63.43; H, 5.74; N, 4.73.

Diethyl-2-(4-methylphenyl)-1H-pyrrole-3,4-tricarboxylate (4d): Yellow oil; yield: 0.45 g (75%). IR (KBr) ($\nu_{\max}/\text{cm}^{-1}$): 1728, 1637, 1587, 1465, 1346, 1237. ¹H NMR (500.1 MHz, CDCl₃): δ = 1.27 (3 H, t, ³*J* = 7.2 Hz, CH₃), 1.35 (3 H, t, ³*J* = 7.5 Hz, CH₃), 2.38 (3 H, s, Me), 4.22 (2 H, q, ³*J* = 7.4 Hz, CH₂O), 4.37 (2 H, q, ³*J* = 7.5 Hz, CH₂O), 6.97 (1 H, s, CH), 7.26 (2 H, d, ³*J* = 7.5 Hz, 2 CH), 7.43 (2 H, d, ³*J* = 7.6 Hz, 2 CH), 9.23 (1 H, br s, NH) ppm. ¹³C NMR (125.7 MHz, CDCl₃): δ = 13.4 (Me), 13.8 (Me), 20.4 (Me), 61.4 (CH₂O), 61.8 (CH₂O), 116.4 (CH), 121.8 (C), 128.3 (C), 129.5 (2 CH), 130.2 (2 CH), 140.6 (C), 144.8 (C), 160.2 (C), 161.4 (C=O), 162.5 (C=O) ppm. MS: *m/z* (%) = 301 (M⁺, 10), 196 (85), 105 (100), 77 (44), 45 (87). Anal. Calc. for C₁₇H₁₉NO₄ (301.34): C, 67.76; H, 6.35; N, 4.65; Found: C, 67.83; H, 6.42; N, 4.74.

Dimethyl-1-methyl-1H-pyrrole-3,4-dicarboxylate (16a): Pale yellow powder, m.p. 173-175 °C, Yield: 0.36 g (92%) IR (KBr): 1735, 1729, 1587, 1435, 1295, 1126 cm⁻¹. ¹H NMR: 3.58 (3 H, s, NMe), 3.78 (6 H, s, 2 MeO), 6.92 (2 H, s, 2 CH) ppm. ¹³C NMR: 35.8 (NMe), 51.8 (2 MeO), 137.2 (2 C), 138.3 (2 CH), 165.4 (2 C=O) ppm. EI-MS: 197 (M⁺, 15), 135 (85), 79 (64), 31 (100). Anal. Calcd for C₉H₁₁NO₄ (197.19): C 54.82, H 5.62, N 7.10; Found: C 54.93, H 5.74, N 7.22.

Dimethyl-1-ethyl-1H-pyrrole-3,4-dicarboxylate (16b): Yellow powder, m.p. 167-169 °C, Yield: 0.37 g (87%). IR (KBr): 1730, 1727, 1562, 1454, 12876 cm⁻¹. ¹H NMR: 1.23 (3 H, t, ³*J* = 7.4 Hz, Me), 3.58 (2 H, q, ³*J* = 7.4 Hz, NCH₂), 3.82 (6 H, s, 2 MeO), 6.87 (2 H, s, 2 CH) ppm. ¹³C NMR: 14.2 (Me), 48.3 (NCH₂), 52.4 (2 MeO), 137.5 (2 C), 139.0 (2 CH), 166.2 (2 C=O) ppm. EI-MS: 211 (M⁺, 10), 121 (76), 79 (58), 45 (100). Anal. Calcd for C₁₀H₁₃NO₄ (211.22): C 56.86, H 6.20, N 6.63; Found: C 56.74, H 6.14, N 6.52.

Dimethyl-1-butyl-1H-pyrrole-3,4-dicarboxylate (16c): Pale yellow powder, m.p. 178-180 °C, Yield: 0.41 g (85%) IR (KBr): 1728, 1725, 1545, 1378, 1268, 1226 cm⁻¹. ¹H NMR: 0.92 (3 H, t, ³*J* = 7.3 Hz, Me), 1.27 (2 H, m, CH₂), 1.52 (2 H, m, CH₂), 3.62 (2 H, t, ³*J* = 7.3 Hz, NCH₂), 3.75 (6 H, s, 2 MeO), 6.86 (2 H, s, 2 CH) ppm. ¹³C NMR: 13.2 (Me), 18.6 (CH₂), 32.4 (CH₂), 52.2 (2 MeO), 53.3 (NCH₂), 135.4 (2 C), 137.6 (2 CH), 167.0 (2 C=O) ppm. EI-MS: 239 (M⁺,

15), 208 (88), 31(100). Anal. Calcd for C₁₂H₁₇NO₄ (239.27): C 60.24, H 7.16, N 5.85; Found: C 60.33, H 7.25, N 5.92.

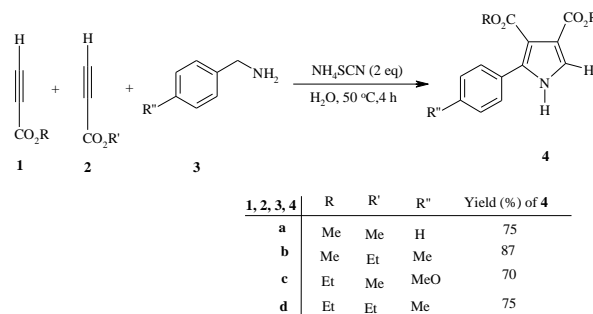
3-Ethyl-4-methyl-1-methyl-1*H*-pyrrole-3,4-dicarboxylate (16d): Yellow powder, m.p. 154-156 °C, Yield: 0.34 g (80%) IR (KBr): 1735, 1730, 1587, 1345, 1347, 1252 cm⁻¹. ¹H NMR: 1.22 (3 H, t, ³J = 7.2 Hz, Me), 3.64 (3 H, s, NMe), 3.78 (3 H, s, MeO), 4.28 (2 H, q, ³J = 7.2 Hz, CH₂O), 7.12 (1 H, s, CH), 7.22 (1 H, s, CH) ppm. ¹³C NMR: 13.7 (Me), 37.3 (NMe), 61.6 (CH₂O), 134.5 (C), 135.8 (CH), 136.4 (CH), 137.2 (C), 164.5 (C=O), 167.4 (C=O) ppm. EI-MS: 211 (M⁺, 15), 180 (68), 45 (87), 31 (100). Anal. Calcd for C₁₀H₁₃NO₄ (211.22): C 56.86, H 6.20, N 6.63; Found: C 56.93, H 6.33, N 5.6.72.

Dimethyl- 1-(4-methylbenzyl)-1*H*-pyrrole-3,4-dicarboxylate (16e). Yellow powder, m.p. 185-187 °C, Yield: 0.45 g (78%) IR (KBr): 1737, 1734, 1687, 1597, 1465, 1254 cm⁻¹. ¹H NMR: 2.38 (Me), 3.62 (3 H, s, NCH₂), 3.75 (3 H, s, MeO), 3.78 (3 H, s, MeO), 6.74 (1 H, s, CH), 6.85 (1 H, s, CH), 7.29 (2 H, d, ³J = 7.6 Hz, 2 CH), 7.36 (2 H, d, ³J = 7.6 Hz, CH) ppm. ¹³C NMR: 21.4 (Me), 51.2 (MeO), 52.3 (MeO), 61.7 (NCH₂), 127.6 (2 CH), 128.5 (2 CH), 132.4 (C), 134.5 (C), 134.6 (CH), 135.8 (CH), 136.2 (C), 137.4 (C), 167.3 (C=O), 169.5 (C=O) ppm. EI-MS: 287 (M⁺, 10), 181 (87), 105 (100), 77 (46), 31(100). Anal. Calcd for C₁₆H₁₇NO₄ (287.31): C 66.89, H 5.96, N 4.88; Found: C 66.95, H 6.07, N 4.97.

3-Ethyl-4-methyl-1-(4-methoxybenzyl)-1*H*-pyrrole-3,4-dicarboxylate (16f). Yellow powder, m.p. 182-184 °C, Yield: 0.53 g (83%) IR (KBr): 1733, 1728, 1694, 1587, 1486, 1375 cm⁻¹. ¹H NMR: 1.27 (3 H, t, ³J = 7.4 Hz, Me), 3.68 (3 H, s, NCH₂), 3.75 (3 H, s, MeO), 3.82 (3 H, s, MeO), 4.32 (2 H, q, ³J = 7.4 Hz, CH₂O), 6.65 (1 H, s, CH), 6.74 (1 H, s, CH), 7.15 (2 H, d, ³J = 7.5 Hz, 2 CH), 7.23 (2 H, d, ³J = 7.5 Hz, CH) ppm. ¹³C NMR: 14.2 (Me), 52.3 (MeO), 55.4 (MeO), 61.4 (CH₂O), 62.4 (NCH₂), 114.2 (2 CH), 132.4 (2 CH), 132.8 (C), 134.3 (CH), 134.8 (CH), 135.2 (C), 136.5 (C), 158.7 (C), 165.3 (C=O), 167.2 (C=O) ppm. EI-MS: 317 (M⁺, 10), 286 (88), 272 (82), 196 (68), 121 (100). Anal. Calcd for C₁₇H₁₉NO₅ (317.34): C 64.34, H 6.03, N 4.41; Found: C 64.42, H 6.15, N 4.52.

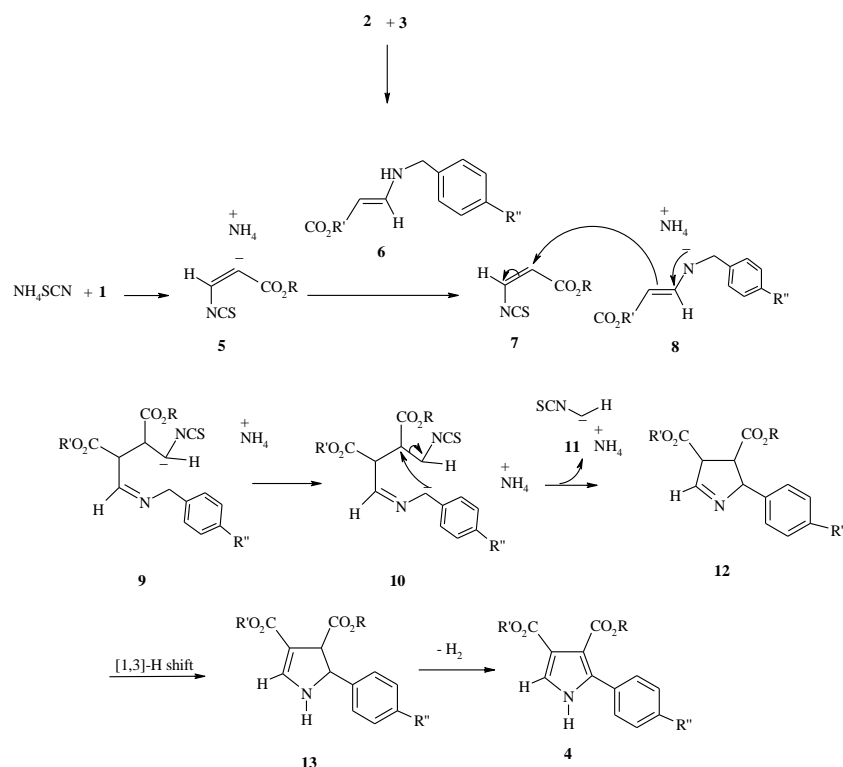
RESULTS AND DISCUSSION

The reaction of propiolates **1**, **2** with benzyl amines **3** in the presence of ammonium thiocyanate produce pyrrole derivatives **4** in excellent yield (Scheme 1). In these reactions the order of adding reagent is important. In compound **4b**, ammonium thiocyanate was mixed with methyl propiolate **1** for 1 h at 50 °C and added to mixture of amine and ethyl propiolate **2** that mixed for 1 h at 50 °C, but in compound **4c** is reverse, ammonium thiocyanate was mixed with ethyl propiolate **1** for 1 h at 50 °C and added to mixture of amine and methyl propiolate **2** that mixed for 1 h at 50 °C. The two component reaction of amine and propiolates is in the mixture of reaction but very low yield (10%). These reactions were not performed with aliphatic primary amines. Although there are many articles for the synthesis of pyrroles [15-20], the number of methods for synthesis of substituted pyrroles caused by benzylic oxidative cyclization, is restricted [25].



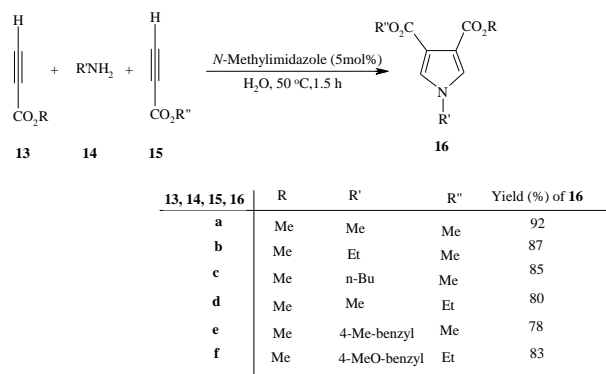
Scheme 1. Reaction of propiolate and benzyl amine in the presence of ammonium thiocyanate.

The structures of compounds **4** were assigned by IR, ¹H NMR, ¹³C NMR and mass spectral data. For example, the ¹H NMR spectrum of **4a** exhibited two singlets for two methoxy protons at (δ 3.75 and 3.82 ppm) and one singlet for methin protons at (δ 6.87 ppm). The ¹³C NMR spectrum of **4a** exhibited carbonyl resonance at 162.4 and 163.8 ppm which further confirmed the proposed structure. Probably, the first event includes protonation of the zwitterionic intermediate **5** formed from NH₄SCN and **1**, by the enaminoester intermediate **6** generated *in situ* from the primary amine **3** and acetylenic ester **2** to produce intermediates **7** and **8**. Then, nucleophilic attack of the conjugate base **8** on intermediate **7** leads to adduct **9**, which undergoes intramolecular protontransfer reactions to afford **10**. Intermediate **10** undergoes intramolecular cyclization by elimination of salt **11** to generate the dihydropyrrol derivative **12**, which is converted to desired product **4** by [1,3]-H shift and air oxidation (Scheme 2).



Scheme 2. Proposed mechanism for the synthesis of compound **4**.

Under similar conditions, the reaction of propiolates **13**, **15** and primary amines **14** in the presence of *N*-methyl imidazole produced pyrrole derivatives **16** in excellent yield (Scheme 3).



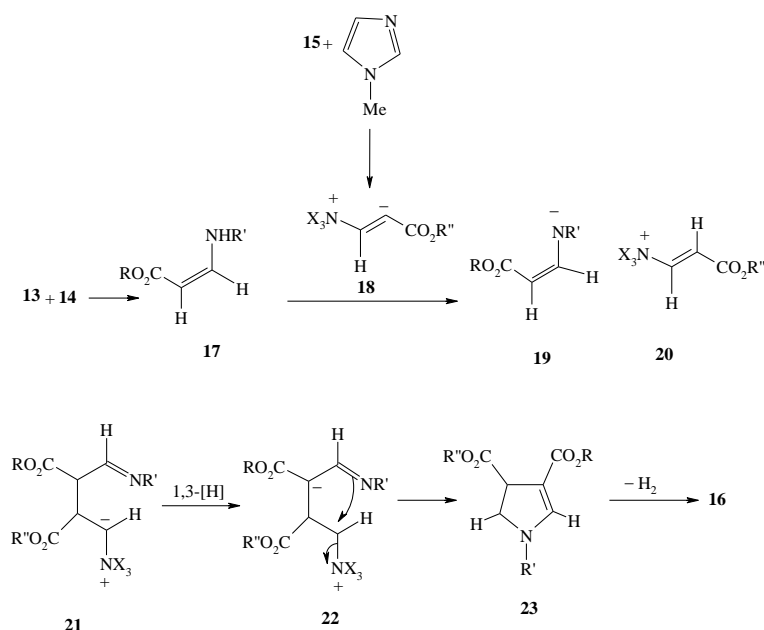
Scheme 3. Reaction of propiolate and primary amines in the presence of *N*-methyl imidazole.

The structures of compounds **16** were assigned by IR, ^1H NMR, ^{13}C NMR and mass spectral data. For example, the ^1H NMR spectrum of **16a** exhibited one singlet for two methoxy protons at (δ 3.78 ppm), one singlet for NMe protons at (δ 3.58 ppm) and one singlet for two methin groups at (δ 6.92 ppm). The ^{13}C NMR spectrum of **16a** exhibited 9 distinct resonances which further confirmed the proposed structure. The IR spectrum of **16a** displayed characteristic C=O bands. The mass spectra of **16a** displayed the molecular ion peak at the appropriate m/z. Presumably, the

zwitterionic intermediate **18**, formed from *N*-methylimidazole (X_3N) and alkyl propiolate **15**, is protonated by the enaminone **17**, generated *in situ* from primary amine **14** and alkylpropiolate **13**, to produce intermediates **19** and **20** (Scheme 4). Nucleophilic attack of the conjugate base **19** to intermediate **20** leads to adduct **21**, which undergoes two proton shifts to afford new zwitterionic intermediate **22**. Finally, intramolecular cyclization of intermediate **22** affords compound **23** by elimination of *N*-methyl imidazole, which is converted into **16** by elimination of hydrogen molecule (Scheme 4).

CONCLUSION

In summary, we report a reaction involving alkyl propiolates and primary amines in the presence of catalytic amount of *N*-methylimidazole at 50 °C in water which affords a new route to the synthesis of functionalized pyrroles. Also, these reactions were performed with alkyl propiolates and benzylamine in the presence of ammonium thiocyanate which afforded pyrrole derivatives. The present procedure has the advantage that not only is the reaction performed under neutral conditions, but the reactants can be mixed without any prior activation or modification.



Scheme 4. Proposed mechanism for the synthesis of compound 16.

Acknowledgment: This research is supported by the Islamic Azad University, Firoozkooh Branch.

REFERENCES

- P. Anastas, T. Williamson, Green Chemistry, Frontiers in Benign Chemical Synthesis and Procedures; Oxford Science Publications: New York, 1998.
- G. W. V. Cave, C. L. Raston, J. L. Scott, *Chem. Commun.*, 2159 (2001).
- R. A. Sheldon, *Chem. Ind.* 12-15(1997).
- J. Zhu, H. Bienayme, Wiley, VCH Verlag, Weinheim, 2005.
- M. Torok, M. Abid, S. C. Mhadgut, B. Torok, *Biochemistry* **45**, 5377 (2006).
- R. Sundberg, J. In Comprehensive Heterocyclic Chemistry; A. Katritzky, C. W. Rees, E. F. V. Scriven, Eds; Pergamon: Oxford, **2**, 119 (1996).
- H. Tao, I. Hwang, D. L. Boger, *Bioorg. Med. Chem. Lett.* **14**, 5979 (2004).
- M. Baumgarten, N. Tyutyulkov. *Eur. Chem. J.* **4**, 987 (1998).
- J. Lehuède, B. Fauconneau, L. Barrier, M. Ourakow, A. Piriou, J. M. Vierfond, *Eur. J. Med. Chem.* **34**, 991 (1999).
- R. W. Burli, P. Jones, D. McMinn, Q. Le, J. X. Duan, J. A. Kaizerman, S. Difuntorum, H. E. Moser, *Bioorg. Med. Chem. Lett.* **14**, 1259 (2004).
- R. Jonas, M. Klockow, I. Lues, H. Pruecher, H. J. Schliep, H. Wurziger, *Eur. J. Med. Chem.* **28**, 129 (1993).
- W. A. Denny, G. W. Rewcastle, B. C. Baguley, *J. Med. Chem.* **33**, 814 (1990).
- V. J. Demopoulos, E. Rekka, *J. Pharm. Sci.* **84**, 79 (1995).
- M. Del Poeta, W. A. Schell, C. C. Dykstra, S. Jones, R. R. Tidwell, A. Czarny, M. Bajic, A. Kumar, D. Boykin, J. R. Perfect, *Antimicrob. Agents Chemother.* **42**, 2495 (1998).
- A. F. Khlebnikov, M. V. Golovkina, M. S. Novikov, Yufit, D. S. *Org. Lett.* **14**, 3768 (2012).
- B. Das, G. C. Reddy, P. Balasubramanyan, B. Veeranjanyulu, *Synthesis* 1625-1628(2010).
- W. Liu, H. Jiang, L. Huang, *Org. Lett.* **12**, 312 (2010).
- M. S. T. Morin, B. A. Arndtsen, *Org. Lett.* **12**, 4916 (2010).
- A. Herath, N. D. P. Cosford, *Org. Lett.* **12**, 5182 (2010).
- D. Ciez, *Org. Lett.* **11**, 4282-4285(2009).
- B. L. Li, H. C. Hu, L. P. Mo, Z. H. Zhang, *RSC Adv.* **4**, 12929 (2014).
- F. P. Ma, P. H. Li, B. L. Li, L. P. Mo, N. Liu, H. J. Kang, Y. N. Liu, Z. H. Zhang, *Appl. Catal. A Gen.* **457**, 34 (2013).
- B. L. Li, M. Zhang, H. C. Hu, X. Du, Z. H. Zhang, *New J. Chem.* **38**, 2435 (2014).
- V. Estevez, M. Villacampa, J. C. Menendez, *Chem. Soc. Rev.*, **43**, 4633 (2014).
- D. Hong, Y. Zhu, Y. Li, X. Lin, P. Lu, Y. Wang, *Org. Lett.* **13**, 4668 (2011).

**N-МЕТИЛИМИДАЗОЛ ИЛИ АМОНИЕВ ТИОЦИАНАТ ПРОМОТИРАНА СИНТЕЗА НА
ЗАМЕСТЕНИ ПИРОЛИ: МНОГОКОМПОНЕНТНА РЕАКЦИЯ НА АЛКИЛ ПРОПИОЛАТИ
ВЪВ ВОДА**

Ф. Шеикнолеслами-Фарахани

Катедра по химия, клон Фирузкух, Ислямски университет "Азад", Фирузкух, Иран

Постъпила на 13 февруари 2014 г.; коригирана на 25 август, 2014 г.

(Резюме)

Докладва се нов, удобен и ефикасен подход към синтеза на заместени пироли, на базата на трикомпонентна реакция. Реакцията на първични амини с електрон дефицитни ацетиленови съединения в присъствието на N-метилимидазол или амониев тиоцианат във вода води до образуването на пироли с добър добив.

Rapid dehydrogenation of 3,4-dihydropyrimidin-2(1H)-ones using 1,4-bis(triphenylphosphonium)-2-butene peroxodisulfate and microwave heating

M. Gorjizadeh^{1*}, M. Afshari¹

¹Department of Chemistry, Shoushtar Branch, Islamic Azad University, Shoushtar Iran

Received January 13, 2014; Revised March 16, 2014

Efficient oxidative dehydrogenation of 3,4-dihydropyrimidin-2(1H)-ones to pyrimidin-2(1H)-ones was achieved using 1,4-bis(triphenylphosphonium)-2-butene peroxodisulfate as an oxidant under microwave irradiation. Chemoselective oxidation of 3,4-dihydropyrimidine in the presence of other oxidizable functional groups such as sulfide, alkyl, aldehyde was also achieved by this reagent.

Keywords: 3,4-dihydropyrimidin-2(1H)-ones; pyrimidin-2(1H)-ones; 1,4-bis(triphenylphosphonium)-2-butene peroxodisulfate; microwave irradiation; dehydrogenation.

INTRODUCTION

Microwave radiation provides an alternative to conventional heating, as it utilizes the ability of liquids or solids to transform electromagnetic energy into heat. The use of microwave irradiation has introduced several new concepts in chemistry. Absorption and transmission of the energy is completely different from the conventional mode of heating. The microwave technology has been applied to a number of useful research and development processes such as polymer technology, organic synthesis, application to waste treatment, drug release/targeting, ceramic and alkane decomposition [1-6].

3,4-dihydropyrimidin-2(1H)-ones (DHPMs) are a class of heterocyclic compounds which have a wide range of biological activities in medicinal chemistry including antifungal [7], antiviral [8], anti-inflammatory [9], and antioxidative properties [10]. These compounds can be easily prepared from ethyl acetoacetate, aromatic aldehyde and urea [11]. Therefore, dehydrogenation of DHPMs by an oxidizing agent should provide an efficient method for the preparation of pyrimidine derivatives.

In this paper, we describe an eco-friendly new method that utilizes 1,4-bis(triphenylphosphonium)-2-butene peroxodisulfate as an efficient reagent for the oxidation of various types of 3,4-dihydropyrimidin-2(1H)-ones under microwave irradiation conditions.

Peroxodisulfate ion is an excellent and versatile oxidant used mostly for the oxidation of compounds in aqueous solution [12]. In spite of the

great convenience of using $K_2S_2O_8$, $Na_2S_2O_8$ or $(NH_4)_2S_2O_8$ and their relatively high oxidation potential, many oxidations by peroxodisulfate do not proceed at a convenient rate. The decomposition of the peroxodisulfate ion requires strong mineral acids and heavy metal ions as catalysts, as well as protic and polar solvents; so the modification of $K_2S_2O_8$, $Na_2S_2O_8$ or $(NH_4)_2S_2O_8$ has attracted a great deal of attention [13].

EXPERIMENTAL

All products are known and were identified by comparison of their physical data, 1H NMR and ^{13}C NMR spectra with those of authentic samples [14–16]. 1H NMR and ^{13}C NMR spectra were taken on a 400 MHz Bruker spectrometer. The microwave reactions were carried out in a Milestone MW apparatus model MicroSynth (2500 W) equipped with a condenser. 1,4-Bis(triphenylphosphonium)-2-butene peroxodisulfate (BTPBPDS) was prepared as described in our previous paper [13] and other chemicals were purchased from Merck, Darmstadt, Germany. The purity determination of the products and reaction monitoring were accomplished by TLC on polygram SILG/UV 254 plates.

General Procedure for the Oxidation of 3,4-Dihydropyrimidin-2(1H)-ones

A mixture of 3,4-dihydropyrimidin-2(1H)-one (DHPMs) (1.0 mmol), and 1,4-bis(triphenylphosphonium)-2-butene peroxodisulfate (1 mmol) in acetonitrile and water (4:1.5 ml) was magnetically stirred and heated at 140°C by microwave radiation under reflux conditions for the time shown in Table 1. After completion of the

* To whom all correspondence should be sent:
E-mail: m.gorjizadeh@iau-shoushtar.ac.ir

reaction, cold water (5 ml) was added and the mixture was extracted with diethyl ether. The combined organic layers were dried over MgSO₄. The solvent was concentrated *in vacuo*; the resulting product was recrystallized from n-hexane/ethyl acetate to give the desired product (Table 1).

Table 1. Oxidation of 3,4-dihydropyrimidines with BTPBPDS in CH₃CN under microwave irradiation

Product	R	Time (Sec)	Yield ^a (%)
2a	C ₆ H ₅	120	87
2b	4-Cl-C ₆ H ₄	120	92
2c	4-Me-C ₆ H ₄	90	88
2d	4-OMe-C ₆ H ₄	60	85
2e	4-NO ₂ -C ₆ H ₄	150	80
2f	3-NO ₂ -C ₆ H ₄	190	88
2g	3-Br-C ₆ H ₄	120	88
2h	2,4-Cl ₂ -C ₆ H ₃	150	86
2i	2-Cl-C ₆ H ₄	180	85
2j	2-Furyl	120	92
2k	n-C ₃ H ₇	90	82
2l	C ₆ H ₁₁	120	87

^a Isolated yield

Spectral data of pyrimidin-2(1H)-ones

Ethyl-6-methyl-4-phenylpyrimidin-2(1H)-one-5-carboxylate (2a): M.p.: 132-133°C. ¹H-NMR (400MHz, CDCl₃): δ= 0.78 (t, 3H), 2.49 (s, 3H), 3.88 (q, 2H), 7.35 (t, 2H), 7.45-7.48 (m, 3H), 11.71 (s, 1H). ¹³C-NMR (100MHz, CDCl₃): δ=13.8 (CH₃), 18.6 (CH₃), 61.0 (CH₂), 108.5 (C), 128.01 (CH), 128.72 (CH), 130.7 (CH), 138.1 (C), 158.5 (C), 162.5 (C), 164.7 (C), 165.9 (C).

Ethyl-6-methyl-4-(4-chlorophenyl)pyrimidin-2(1H)-one-5-carboxylate (2b): M.p.: 184-185 °C. ¹H-NMR (400MHz, CDCl₃): δ= 0.89 (t, 3H), 2.58 (s, 3H), 3.96 (q, 2H), 7.42 (d, 2H), 7.59 (d, 2H), 12.01 (s, 1H). ¹³C-NMR (100MHz, CDCl₃): δ=13.9 (CH₃), 19.1 (CH₃), 61.2 (CH₂), 108.9 (C), 127.8 (CH), 128.9 (CH), 135.9 (C), 137.2 (C), 158.7 (C), 162.8 (C), 165.2 (C), 166.50 (C).

Ethyl-6-methyl-4-(4-methylphenyl)pyrimidin-2(1H)-one-5-carboxylate (2c): M.p.: 139-140 °C. ¹H-NMR (400MHz, CDCl₃): δ= 0.84 (t, 3H), 2.46 (s, 3H), 2.52 (s, 3H), 3.98 (q, 2H), 7.14 (d, 2H), 7.55 (d, 2H), 11.87 (brd s, 1H). ¹³C-NMR (100MHz, CDCl₃): δ=13.8 (CH₃), 19.0 (CH₃), 21.3 (CH₃), 61.5 (CH₂), 108.2 (C), 127.1 (CH), 128.9 (CH), 129.2 (C), 140.8 (C), 158.2 (C), 161.9 (C), 164.4 (C), 166.8 (C).

Ethyl-6-methyl-4-(4-methoxyphenyl)pyrimidin-2(1H)-one-5-carboxylate (2d): M.p.: 152°C. ¹H-NMR (400MHz, CDCl₃): δ= 0.82 (t, 3H), 2.48 (s, 3H), 2.61 (s, 3H), 3.85 (q, 2H), 6.87 (d, 2H), 7.12 (d, 2H), 10.17 (s, 1H). ¹³C-NMR (100MHz,

CDCl₃): δ=13.8 (CH₃), 19.5 (CH₃), 55.2(CH₃), 61.5 (CH₂), 108.2 (C), 110.8 (CH), 124.01 (CH), 127.3 (C), 158.2 (C), 159.1 (C), 162.5 (C), 164.5 (C), 167.1 (C).

Ethyl 6-methyl-4-(4-nitrophenyl)pyrimidin-2(1H)-one-5-carboxylate(2e): Mp: 154-155°C. ¹H-NMR (400MHz, CDCl₃): δ=1.05 (t, 3H), 2.68 (s, 3H), 4.15 (q, 2H), 7.57 (d, 2H), 7.64 (d, 2H), 12.89 (s, 1H). ¹³C-NMR (100MHz, CDCl₃): δ=13.8 (CH₃), 18.7 (CH₃), 61.3 (CH₂), 108.1 (C), 125.0 (CH), 127.6 (CH), 143.1 (C), 149.2 (C), 158.4 (C), 162.6 (C), 164.7 (C), 166.1 (C).

Ethyl-6-methyl-4-(3-nitrophenyl)pyrimidin-2(1H)-one-5-carboxylate (2f): M.p.: 167-168°C. ¹H-NMR (400MHz, CDCl₃): δ= 1.01 (t, 3H), 2.64 (s, 3H), 4.01 (q, 2H), 7.84 (m, 2H), 8.21 (d, 1H), 8.35 (s, 1H), 12.79 (brd s, 1H). ¹³C-NMR (100MHz, CDCl₃): δ=13.9 (CH₃), 18.1 (CH₃), 61.0 (CH₂), 107.8 (C), 122.3 (CH), 125.4 (CH), 130.72 (CH), 131.9 (C), 134.2(CH), 149.1 (C), 158.7 (C), 163.0 (C), 164.7 (C), 169.1 (C).

Ethyl-6-methyl-4-(3-bromophenyl)pyrimidin-2(1H)-one-5-carboxylate (2g): M.p.: 107-108°C. ¹H-NMR (400MHz, CDCl₃): δ= 0.93 (t, 3H), 2.58 (s, 3H), 3.99 (q, 2H), 7.37 (t, 1H), 7.59-7.67 (m, 3H), 12.03 (s, 1H). ¹³C-NMR (100MHz, CDCl₃): δ=13.8 (CH₃), 18.4 (CH₃), 61.1 (CH₂), 107.5 (C), 124.1 (C), 126.9 (CH), 130.2 (CH), 132.3 (CH), 133.2 (CH), 134.6 (C), 158.8 (C), 162.8 (C), 164.7 (C), 166.1 (C).

Ethyl-6-methyl-4-(2,4-dichlorophenyl)pyrimidin-2(1H)-one-5-carboxylate (2h): M.p.: 197-198°C. ¹H-NMR (400MHz, CDCl₃): δ= 0.95 (t, 3H), 2.59 (s, 3H), 4.00 (q, 2H), 7.35 (d, 1H), 7.49 (d, 1H), 7.59 (s, 1H), 12.11 (brd s, 1H). ¹³C-NMR (100MHz, CDCl₃): δ=13.8 (CH₃), 18.2 (CH₃), 61.0 (CH₂), 108.7 (C), 127.9 (CH), 130.1 (CH), 131.5 (CH), 132.9 (C), 134.7(C), 136.9(C), 159.2 (C), 163.2 (C), 164.7 (C), 169.1 (C).

Ethyl-6-methyl-4-(2-chlorophenyl)pyrimidin-2(1H)-one-5-carboxylate (2i): M.p.: 181-183°C. ¹H-NMR (400MHz, CDCl₃): δ= 0.75 (t, 3H), 2.50 (s, 3H), 3.82 (q, 2H), 7.37-7.39 (m, 4H), 11.61 (brd s, 1H). ¹³C-NMR (100MHz, CDCl₃): δ=13.8 (CH₃), 18.6 (CH₃), 61.0 (CH₂), 109.0 (C), 126.9 (CH), 128.8 (CH), 129.7 (CH), 130.7 (CH), 132.1 (C), 138.7 (C), 159.7 (C), 162.5 (C), 164.6 (C), 169.8 (C).

Ethyl-6-methyl-4-(2-furyl)-pyrimidin-2(1H)-one-5-carboxylate (2j): M.p.: 99-101°C. ¹H-NMR (400MHz, CDCl₃): δ= 0.85 (t, 3H), 2.58 (s, 3H), 3.90 (q, 2H), 6.71 (t, 1H), 7.33 (d, 1H), 7.48 (d, 1H), 11.33 (brd s, 1H). ¹³C-NMR (100MHz, CDCl₃): δ=13.4 (CH₃), 17.3 (CH₃), 61.1 (CH₂),

107.1 (C), 112.6 (CH), 114.2 (CH), 142.4 (CH), 144.5 (C), 158.5 (C), 161.3 (C), 162.0 (C), 163.1 (C).

Ethyl-6-methyl-4-propyl-pyrimidin-2(1H)-one-5-carboxylate (2k): M.p.: 106-109°C. ¹H-NMR (400MHz, CDCl₃): δ= 0.78 (t, 3H), 0.87 (t, 3H), 1.35 (m, 2H), 2.38 (t, 2H), 2.51 (s, 3H), 3.80 (q, 2H), 11.81 (brd s, 1H). ¹³C-NMR (100MHz, CDCl₃): δ=13.1 (CH₃), 13.8 (CH₃), 17.4 (CH₃), 22.45(CH₂), 28.63(CH₂), 60.1 (CH₂), 109.5 (C), 158.9 (C), 162.5 (C), 163.8 (C), 171.1 (C).

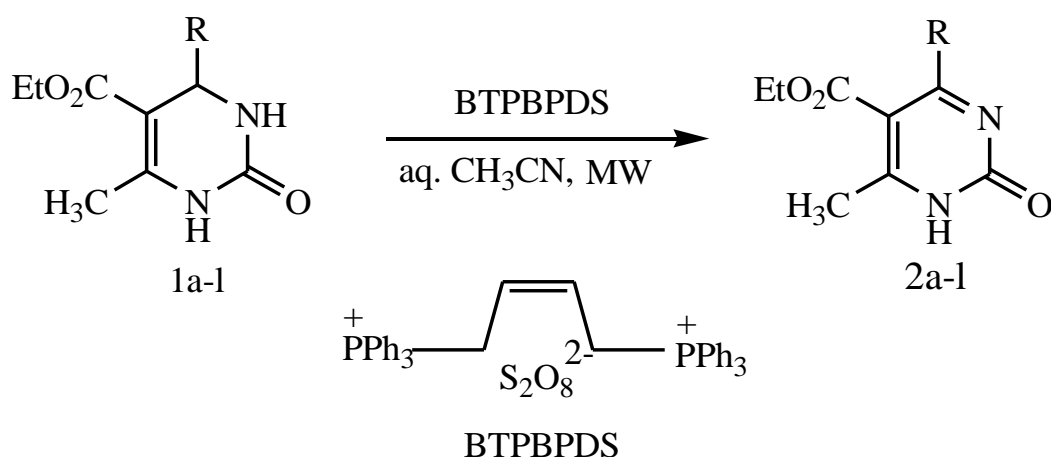
Ethyl-6-methyl-4-cyclohexyl-pyrimidin-2(1H)-one-5-carboxylate (2l): M.p.: 99-101°C. ¹H-NMR (400MHz, CDCl₃): δ= 0.79 (t, 3H), 1.11-1.17 (m, 2H), 1.42-1.47 (m, 4H), 1.68-1.75 (m, 4H), 2.49 (s, 3H), 3.82 (q, 2H), 10.87 (brd s, 1H). ¹³C-NMR (100MHz, CDCl₃): δ=13.5 (CH₃), 17.5 (CH₃), 25.4 (CH₂), 26.1 (CH₂), 29.8 (CH₂), 30.7 (CH), 61.1 (CH₂), 109.3 (C), 158.9 (C), 162.4 (C), 164.1 (C), 177.3 (C).

RESULTS AND DISCUSSION

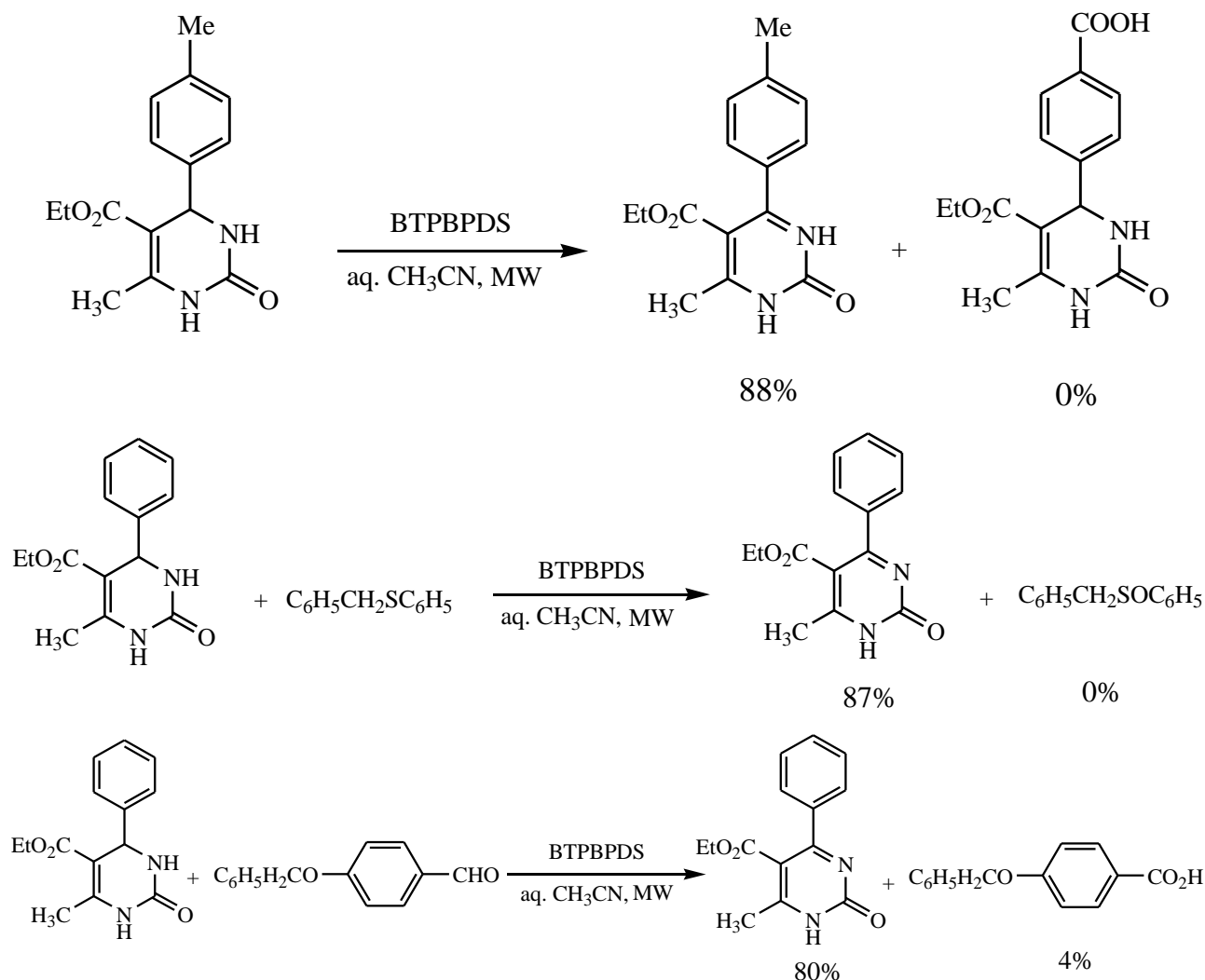
1,4-bis(triphenylphosphonium)-2-butene peroxodisulfate (BTPBPDS) was readily prepared by adding an aqueous solution of potassium peroxodisulfate to a solution of 1,4-bis(triphenylphosphonium)-2-butene dichloride in water. It is a very stable white solid which can be stored for months without losing its activity. It is soluble in acetonitrile, methanol, dichloromethane,

chloroform and ethyl acetate and slightly soluble in CCl₄ and diethyl ether.

In order to explore the availability of 1,4-bis(triphenylphosphonium)-2-butene peroxodisulfate as an oxidant under microwave irradiation, oxidation of ethyl-6-methyl-4-phenylpyrimidin-2(1H)-one-5-carboxylate (1a) was selected as a model reaction. The optimal reaction conditions including reactant ratio, reaction time, kind of solvent and microwave power were investigated. It was found that at a ratio of DHPMs to BTPBPDS of 1:1, solvent acetonitrile and microwave power of 400 W (determined by the power adjustor of the microwave oven), the reaction gave the highest yield within 120 sec. It is noteworthy that the presence of water was necessary for the reaction since no reaction of 1a in dry acetonitrile took place. Using similar conditions, a series of 3,4-dihydropyrimidin-2(1H)-ones (1a-l) were synthesized in high yield (Scheme 1). The protocol is suitable for dehydrogenation of aryl, alkyl and heterocyclic substituted DHPMs. Various aryl substituted pyrimidin-2(1H)-ones could be easily synthesized by this method. Different substituents (4-MeO, 4-Me, 4-NO₂, 4-Cl, 3-NO₂, 3-Br, 2-Cl and 2,4-Cl₂) on the aryl rings had no significant effect on the reaction conditions and the reaction yield. Alkyl groups, such as propyl and cyclohexyl substituted pyrimidines could also be readily prepared by this route (1k, 1l).



Scheme 1. Oxidation of 3,4-dihydropyrimidin-2(1H)-ones using BTPBPDS under microwave irradiation



Scheme 2. Chemoselective oxidation of 3,4-dihydropyrimidin-2(1H)-ones in the presence of BTPBPDS

In addition, ethyl 4-(2-furyl)-6-methylpyrimidin-2(1H)-one-5-carboxylate (2j) could also be synthesized by this approach (1j). In order to establish the general applicability of the method, we have performed several competitive oxidation reactions, the results of which are shown in Scheme 2. As can be seen, interesting chemoselective oxidation of 3,4-dihydropyrimidin-2(1H)-ones in the presence of other oxidizable functional groups such as sulfide, alkyl, and aldehyde groups, is achieved using this reagent system. To the best of our knowledge, such selectivities have not been reported previously in oxidation of dihydropyrimidines.

The dehydrogenation mechanism may involve oxidation of the water by sulfate anion radicals to form hydroxyl radicals, which are further converted by hydrogen abstraction from the 4-position to form dihydropyrimidonyl radicals. This can eliminate the other hydrogen atom to form the corresponding pyrimidinone.

CONCLUSION

In conclusion, this method provides an excellent approach for the safe, rapid, inexpensive and simple synthesis of medicinally important pyrimidin-2(1H)-ones in a single step.

Acknowledgment: We are grateful to the Islamic Azad University Shoushtar Branch for support of this work.

REFERENCES

1. K. Babak, N. Kian, *Heterocycles*, 60, 2287 (2003).
2. X-P. Ouyang, C-L. Liu, Y-X. Pang, X-O. Qiu, *Chin. Chem. Lett.*, 24, 1091 (2013).
3. S. Miyazaki, C. Yokouchi, M. Takada, *Chem. Pharm. Bull. Jpn.*, 37, 208 (1989).
4. M. Y. Tse, M. C. Depew, J. K. S. Wan, *Res. Chem. Intermed.*, 13, 221 (1990).
5. V. Santagada, E. Perissutti, G. Liendo, *Curr. Med. Chem.*, 9, 1251 (2002).
6. I. Polshettiwar, M. N. Nadagouda, R. S. Varma, *Aust. J. Chem.*, 62, 16 (2009).

7. M. Ashok, B. S. Holla, N. S. Kumari, *Eur. J. Med. Chem.*, 42, 380 (2007).
8. E. W. Hurst, R. Hull, *J. Med. Pharm. Chem.*, 3, 215 (1961).
9. S. S. Bahekar, D. B. Shinde, *Bioorg. Med. Chem. Lett.*, 14, 1733 (2004).
10. A. M. Magerramov, M. M. Kurbanova, R. T. Abdinbekova, I. A. Rzaeva, V. M. Farzaliev, M. A. Allakhverdiev, *Russ. J. Appl. Chem.*, 79, 787 (2006).
11. (a) J. C. Legeay, J. J. VandenEynde, J. P. Bazureau, *Tetrahedron Lett.* 48, 1063 (2007). (b) D. M. Pore, U. V. Desai, T. S. Thopate, P. P. Wadgaonkar, *Aust. J. Chem.*, 60, 435 (2007). (c) G. Karimipour, T. Mousavinejad, *Bulg. Chem. Commun.*, 45, 55 (2013).
12. D. A. House, *Chem. Rev.*, 62, 185 (1962).
13. (a) M. Gorjizadeh, M. Abdollahi-Alibeik, *Chin. Chem. Lett.*, 22, 61 (2011). (b) Y. H. Kim, M. Y. Park, S. G. Yang, *Phosphorus, Sulfur and Silicon*, 180, 1235 (2005). (c) R. Badri, M. Gorjizadeh, *Synth. Commun.*, 42, 2058 (2012). (d) R. Badri, M. Gorjizadeh, *Synth. Commun.*, 39, 4239 (2009).
14. H. R. Memarian, A. Farhadi, *Ultrasonics Sonochem.*, 15, 1015 (2008).
15. N. N. Karade, S. V. Gampawar, J. M. Kondre, G. B. Tiwari, *Tetrahedron Lett.*, 49, 6698 (2008).
16. M. Gorjizadeh, *Bull. Korean. Chem. Soc.*, 34, 1751 (2013).

БЪРЗО ДЕХИДРОГЕНИРАНЕ НА 3,4-ДИХИДРОПИРИМИДИН-2(1H)-ОНИ, ИЗПОЛЗВАЙКИ 1,4- БИС-(ТРИФЕНИЛФОСФОНИЕВ)-2-БУТЕН ПЕРОКСОСУЛФАТ И МИКРОВЪЛНОВО НАГРЯВАНЕ

М. Горджизаде^{1*}, М. Афшари¹,

¹Департамент по химия, Клон Шушар, Ислямски университет "Азад", Иран

Постъпила на 13 януари 2014 г.; коригирана на 16 март, 2014 г.

(Резюме)

Постигнато е ефективно окислително дехидрогениране на 3,4-дихидропиримидин-2(1H)-они с използването на 1,4- бис-(трифенилфосфониев)-2-бутен пероксосулфат като окислител при микровълново нагряване. Постигнато е и селективно окисление в присъствие на други окисляеми функционални групи, като сулфиди, алдехидни и алкилови с този реагент.

Electrodeposition of Ni-Co alloy on chemically oxidized Al

K. Ignatova^{1*}, Y. Marcheva²

¹ University of Chemical Technology and Metallurgy (UCTM) Sofia

² Technical University (TU) Sofia

Received September 19, 2013, Revised March 25, 2015

The kinetics of deposition of Co, Ni, and Ni-Co from low-acid citrate electrolyte on Cu and on chemically oxidized Al is compared. It is found that the formation of Ni-Co alloy on the Al cathode is hampered to a greater extent in comparison with the Cu electrode. In both cases (Cu and Al electrodes) "anomalous" co-deposition of Co and Ni is registered especially in an electrolyte with higher content of Ni. In case of deposition on Al cathode in stationary potentiostatic mode (cpm), the content of Co in the Ni-Co alloy is by 10 wt% higher than that in case of deposition of Ni-Co on Cu cathode. The Ni-Co alloy deposited on Al may be characterized as island-style coating, with spheroidal shape of the crystals (10-17 μm). The application of pulse potential mode (ppm) of deposition on the Al cathode leads to increased structural homogeneity and higher extent of filling the surface with crystals of Ni-Co alloy. The effect of the application of pulse potential mode, however, is strongly reduced when the extent of pulse filling at a given frequency is reduced.

Keywords: electrodeposition, chemically oxidized aluminum, pulse mode

INTRODUCTION

The interest in the industrial use of aluminum and aluminum alloys is related to the combination of factors such as low cost, light weight and good corrosion resistance [1]. A particularly important feature when using aluminum in aqueous solutions is the formation of oxide film on its surface that leads to passivation. The preparation of aluminum based micrometric and sub-micrometric materials is in the focus of a number of scientific research papers [2,3,6,7].

The application of metallic micro- and nano-particles on aluminum substantially changes its physical properties and behavior due to the increased unfolded surface area that determines its application in such important areas as catalysis [4]. An important issue is the "prevention" of nano-particles from agglomeration into larger structures [5]. Electrochemical methods are widely applied for preparation of micro- and nanostructured materials on oxidized aluminum [6,7]. The oxidation of aluminum itself can be carried out by either chemical or electrochemical means. The electrochemical method is preferred in the technology for manufacture of the so called "nanoneedles" that are formed in purposely created pores of predetermined size in aluminum foil [7]. This method is known as "electrochemical templating" and is used for preparation of nanoneedles of Ag [8], Au [9], Cd [10] and even

conductive polymers [11,12]. There is also evidence for application of non-electrochemical methods, e.g. pulsed laser deposition, for preparation of such materials [13].

This paper summarizes the results of the examination of the deposition kinetics of Co, Ni, and Ni-Co and the morphology of Ni-Co alloy from low-acid citrate electrolyte on Cu and on chemically oxidized Al in constant and in pulse potential mode.

EXPERIMENTAL

Oxidation of aluminum

The chosen procedure for preparation of the Al samples for galvanization involves chemical oxidation. The rectangular Al samples have dimensions 4 cm \times 1.5 cm and thickness of 0.5 mm. Prior to galvanization, the samples undergo the following sequence of operations:

(1) Chemical (alkaline) degreasing for 5-10 min in a solution composed of 30 g/l $\text{Na}_3\text{PO}_4 \cdot 12 \text{H}_2\text{O}$; 30 g/l Na_2CO_3 ; and 30 g/l Na_2SiO_3 at a temperature of 60-70°C.

(2) Washing in warm water ($t = 50-60^\circ\text{C}$) and cold water for 1-2 min.

(3) Chemical etching in 100 g/l NaOH for 0.5-1 min at $t = 50-60^\circ\text{C}$ followed by washing according to (2).

(4) Lightening in 0.6 M HNO_3 for 20-30 sec at $t = 18-25^\circ\text{C}$ and washing according to (2).

(5) Chemical oxidation for 5-7 min in a solution of 20 g/l Na_2CO_3 , 15 g/l $\text{Na}_2\text{Cr}_2\text{O}_7$, and 2.5 g/l NaOH, ($t = 80-100^\circ\text{C}$), followed by washing according to (2).

* To whom all correspondence should be sent:
E-mail: katya59ignatova@gmail.com

(6) Immersion for 4-5 min in a hydrochloric acid solution of 0,05 M Pd ($t = 40-50^{\circ}\text{C}$) to improve the conductivity of the oxidized surface, followed by washing according to (2).

After carrying out the above sequence of operations, the Al samples are ready for use as electrodes, as well as for taking of the polarization dependencies, and for deposition of Ni-Co alloys on their surface.

Experimental conditions

A conventional three-electrode cell (with total volume of 150 dm^3) provided with platinum foil counter electrode and saturated calomel electrode (SCE) as comparative electrode was used. All potentials were quoted with respect to SCE ($E_{\text{SCE}} = 0.241\text{ V}$). The kinetics of deposition is examined using electrodes of chemically oxidized aluminum or pure copper foil. The copper electrode is disc-shaped, with surface area of 1 cm^2 soldered in epoxy resin. The preparation of the copper cathodes involves etching in a special solution, washing in distilled water, and drying.

The examination is carried out in low-acid citrate electrolyte solutions with two ratios of the concentrations of Ni (as $\text{NiSO}_4 \cdot 2\text{H}_2\text{O}$) and Co (as $\text{CoSO}_4 \cdot 7\text{H}_2\text{O}$): Ni/Co=3 (electrolyte I), and Ni/Co=1 (electrolyte II). The concentration of Ni is constant (0.3 M) and the background additives are 0.485 M H_3BO_3 and 0.2 M $\text{Na}_3\text{C}_6\text{H}_5\text{O}_7 \cdot \text{H}_2\text{O}$ ($\text{Na}_3\text{citrate}$). The pH=5.5 of the electrolyte is controlled through addition of NaOH or citric acid.

The deposition kinetics of Ni-Co alloys is examined in constant potential mode using a Wenking electrochemical analysis system (Germany) at a scanning rate $v=30\text{ mV s}^{-1}$. The pulse electrodeposition of the coatings was carried out using rectangular potentiostatic pulses generated by a pulse generator connected to the input of a potentiostat especially designed for the purpose. In turn, the potentiostat is connected to the three-electrode cell. The average values of potential \bar{E} and current \bar{I} were measured using a digital voltmeter with high input resistance and ammeter, respectively, and the amplitude values of the potential E_p were measured using an oscilloscope. The relation between the value of average polarization ($\Delta\bar{E}$) and that of amplitude polarization (ΔE_p) in potentiostatic rectangular pulse conditions

is $\Delta\bar{E} = \theta \cdot \Delta E_p$, where $\theta = \frac{\tau_p}{\tau_p + \tau_z}$ is pulse filling,

τ_p is pulse time, and τ_z is interval between the pulses. At a pulse frequency of 500 Hz

($f = \frac{1}{T}$, Hz where $T = \tau_p + \tau_z$), and pulse fillings θ in the range from 0.2 to 0.5, the dependencies $\Delta\bar{E} - I_{\text{av}}$ and $\Delta E_p - I_{\text{av}}$ were calculated.

The morphology and the elemental content were examined using scanning electron microscopy (SEM) and energy dispersive spectroscopy (EDS), respectively, on a JEOL JEM 2100 instrument (Bulgarian Academy of Science, Institute of Optical Materials and Technologies).

RESULTS AND DISCUSSION

Kinetics of deposition of Co, Ni and Ni-Co

In order to verify the possibility for co-deposition of Ni and Co in alloy, their individual polarization dependencies were compared with the dependencies of their co-deposition in electrolyte I (Fig.1 a,b) and electrolyte II (Fig.2 a,b).

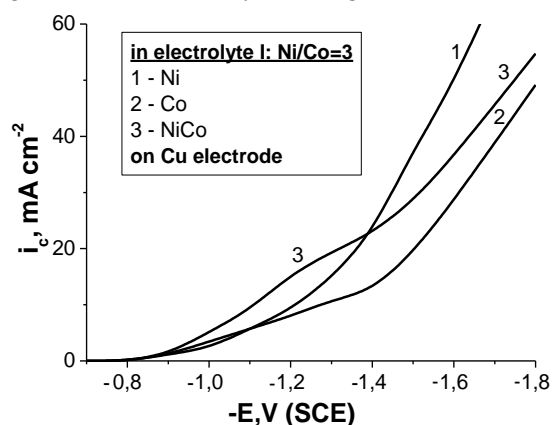


Fig. 1 a. Juxtaposition of the polarization dependencies of self-deposition in constant potential mode of: Ni (1); Co (2) and Ni-Co (3) on copper in electrolyte I ($v=30\text{ mV s}^{-1}$).

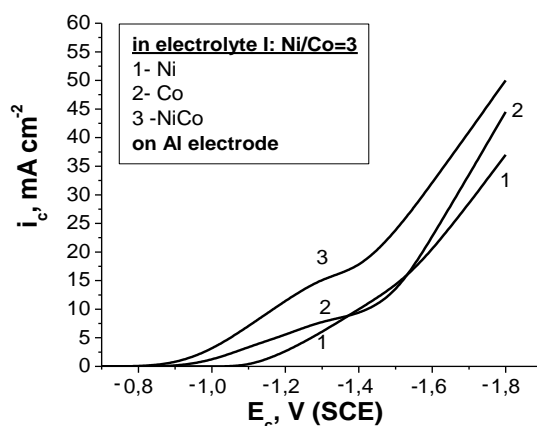


Fig. 1 b. Juxtaposition of the polarization dependencies of self-deposition in constant potential mode of oxidized aluminum in electrolyte I ($v=30\text{ mV s}^{-1}$).

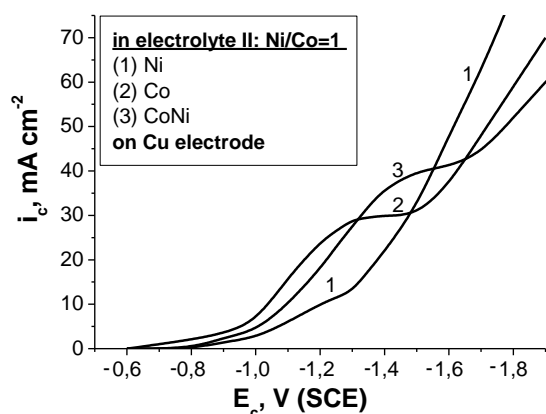


Fig. 2 a. Juxtaposition of the polarization dependencies of self-deposition in constant potential mode of Ni (1); Co (2) and Ni-Co (3) on copper in electrolyte II ($v=30 \text{ mV s}^{-1}$).

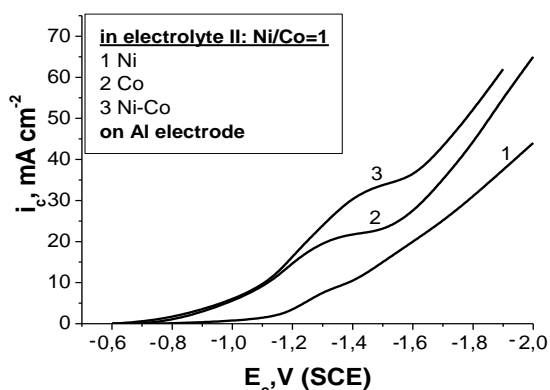


Fig. 2 b. Juxtaposition of the polarization dependencies of self-deposition in constant potential mode of Ni (1); Co (2) and Ni-Co (3) on oxidized aluminum in electrolyte II ($v=30 \text{ mV s}^{-1}$).

As is seen from Figs. 1 and 2, the course of the polarization dependencies in the deposition on oxidized aluminum cathode is identical with that on copper cathode but the current is much lower and the deposition always takes place at much higher polarization in the first case (on Al cathode). These regularities are reported by other researchers too, regardless of the method of oxidation [9].

As it is seen from the juxtaposition made, a much closer proximity of the curves of self-deposition of Ni and Co in the case of electrolyte I (Ni/Co=3) is observed (Fig.1 a,b), especially on Cu cathode. The co-deposition of the two metals in alloy is also possible in the case of oxidized Al cathode (Figs.1 b and 2 b) but the extent of approximation of their deposition potentials is lower. These results give reasons to suggest that the alloy formation on Al cathode will be inhibited to a higher extent in comparison with the case on Cu cathode. It follows from Figs. 1 and 2 that "anomalous" co-deposition takes place on both cathode metals in electrolyte II (Fig.2 a, b), and

only on the Al cathode in electrolyte I (Fig.1 b), which is typical for the metals from the iron group [14]. The "anomalous" co-deposition consists in preferential deposition of Co prior to Ni, in spite of the more positive standard electrode potential of Ni compared to Co ($E^\circ = -0.22 \text{ V}$ and $E^\circ = -0.27 \text{ V}$ vs NHE, respectively). The possible explanation of this phenomenon is the formation of oxides on the cathode [15] or adsorption and chemical processes associated with the complexes of the two metals (Co and Ni) [16].

Properties of the Ni-Co coatings

Chemical content

In Fig. 3 the data for the chemical content of Ni-Co coatings deposited on Cu cathode (curves 1, 2) or on oxidized Al cathode (curves 1*, 2*) in electrolyte I (curves 1, 1*) and electrolyte II (curves 2, 2*) are juxtaposed. As is seen from the results obtained on the Cu cathode, as the potential increases from -1.1 V to -1.5 V , the Co content in the alloy decreases by about 10 wt % in both electrolyte I and electrolyte II (Fig.3, curves 1 and 2).

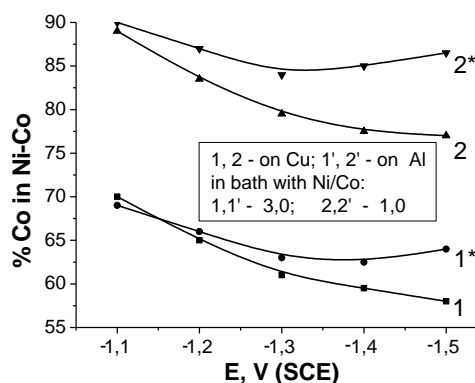


Fig. 3. Chemical content of Ni-Co coatings depending on the cathode potential on copper (1, 2) and on oxidized aluminum (1*, 2*) in electrolyte I (1, 1*) and electrolyte II (2, 2*) in constant potential mode.

However, in the case of oxidized aluminum cathode, the content of Co varies within 5 wt% with the variation of potential applied (Fig.3, curves 1* and 2*), as the dependencies run through a less pronounced minimum. The dependencies obtained can be explained with the different extent of approximation of deposition potentials. It was mentioned above that this extent is higher in the case of copper cathode. Therefore, when shifting from more positive to more negative potentials, the increase of Ni percentage in the Ni-Co alloy is much more easily achieved. In the case of oxidized Al, the same variation of potential from -1.1 V to -1.5 V results in a slight variation of Ni percentage.

With the increase of Co content in the solution, i.e. decrease of the ratio Ni/Co=3 (electrolyte I) to Ni/Co=1 (electrolyte II), its content in the alloy obviously increases (Fig. 3). In electrolyte I the content of Co is about 62 wt% on the copper cathode and about 69 wt% on the aluminum cathode; in electrolyte II the content of Co is about 80 wt% on the copper cathode and about 88 wt% on the aluminum cathode.

Morphology of the Ni-Co alloy

The scanning electron microscopy (SEM) images of Ni-Co alloy deposited on oxidized Al

cathodes in both constant and pulse potential modes are shown in Fig. 4 (a) and (b,c) for two values of pulse filling, $\theta = 0.5$ (b) and $\theta = 0.2$ (c), and frequency $f=500$ Hz. The SEM images in two magnifications are juxtaposed. As is seen, the Ni-Co alloy deposited on oxidized Al substrate at two current modes do not have the character of a coating that fills the surface. The coating obtained is island-type coating and the average size of the crystals of the Ni-Co alloy formed varies from 5 μm to 17 μm (Fig. 5).

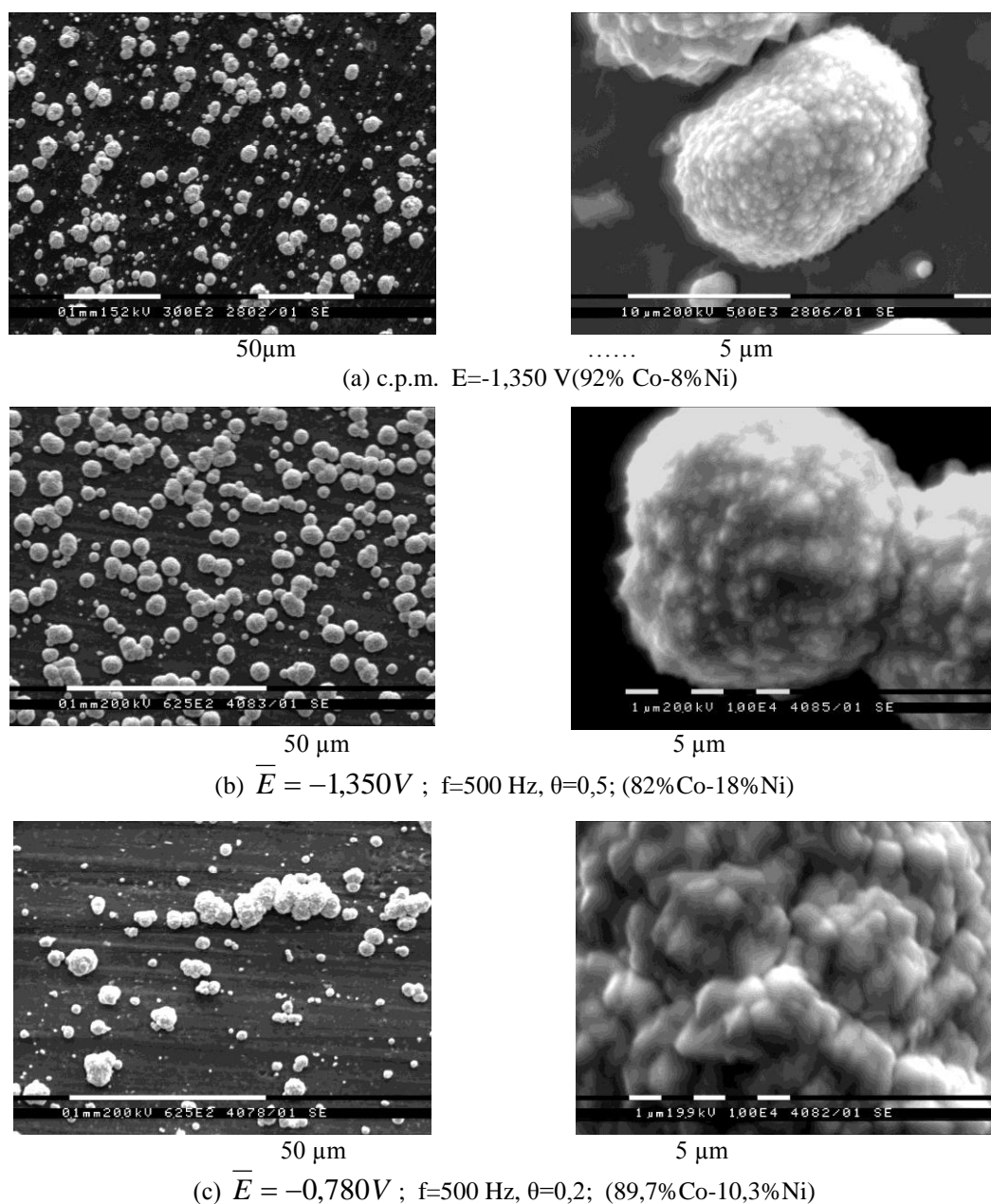


Fig. 4. SEM images and data for the chemical content of Ni-Co alloys deposited on oxidized Al in electrolyte II in constant potential mode (a), pulse potential mode at frequency 500 Hz at pulse filling $\theta=0.5$ (b) and $\theta=0.2$ (c) (E , resp. $\bar{E} = -1,350$ V (SCE)).

The SEM images evidence that the application of pulse potential mode with frequency of 500 Hz and pulse filling $\theta=0.5$ (Fig.4 b) leads to higher structural homogeneity of the alloy deposited on the surface of the Al cathode.

The density of filling the surface with spherical crystals increases in pulse mode compared to stationary mode (Fig. 4 a). At lower pulse filling $\theta=0.2$ (Fig.4 c), the formed crystals have rather irregular than spherical shape. The data from the chemical analysis of the alloys (Fig.4 a-c, under the photos) indicate that regardless of the more unfavorable conditions proven for co-deposition of the two metals on oxidized aluminum cathode compared to copper cathode (Fig. 2), in pulse mode, and especially at high pulse filling (Fig.4 b), the content of Ni in the alloy is 18 wt%.

The explanation for the high content of Ni is that when applying rectangular potential pulses to a certain average polarization $\overline{\Delta E}$ there is a much higher corresponding amplitude polarization $\Delta E_p = \overline{\Delta E}/\theta$: for example, when $\theta=0.5$ the amplitude polarization is twice higher. Thus, during the pulses there is a possibility to shift from lower polarizations corresponding to preferential deposition of Co, to polarizations corresponding to preferential deposition of Ni. With the decrease of pulse filling that effect should increase. At shorter duration of the pulses ($\theta=0.2$), the time for crystals generation and growth is negligible and during the longer pauses a certain blocking of the surface by products of adsorption and simultaneously emitted hydrogen gas is also possible. All the mentioned features make the above-described conditions less effective, not only for obtaining Ni-Co alloys enriched in Ni, but for the formation of morphologically uniform crystals too.

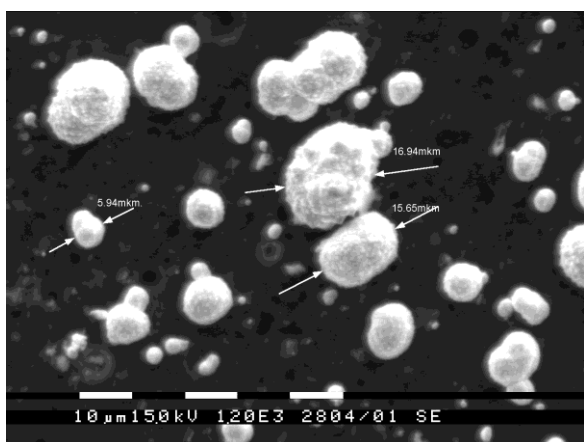


Fig. 5. SEM images of Ni-Co alloy from electrolyte II with designation of the size of crystals ($\overline{E} = -1,350$ V; $f=500$ Hz; $\theta=0.5$).

CONCLUSIONS

Based on the research carried out, we can conclude that the formation of Ni-Co alloy on aluminum cathode will be inhibited to a greater extent in comparison with that on copper cathode. On both Cu and Al cathodes “anomalous co-deposition” of Co and Ni is found, especially in an electrolyte with higher content of Ni. The Ni-Co alloy coating on aluminum can be characterized as island-style coating with spheroidal shape of the crystals (10-17 μm) and Ni content from 10 wt% to 18 wt% depending on the applied average potential and pulse filling at a ratio Ni/Co=1 (0.3 M Ni) in the electrolyte. The application of pulse potential mode (ppm) of deposition in an electrolyte of the same composition leads to increased structural homogeneity and higher extent of filling the surface with crystals of Ni-Co alloy.

REFERENCES

1. S. Zein, El. Abedin, F. Endres, *J. Applied Electrochem.*, **34**, 1071 (2004).
2. P. Grünberg, R. Sreinber, Y. Pang, M. Brodsky, H. Sowers, *Phys.Rev.Lett.*, **57**, 2442 (1986).
3. K. Bird, M. Schlesinger, *J. Electrochem. Soc.*, **142**, L64 (1995).
4. Peter. A. Cziraki, L. Pogany, Z. Kupay, Z. I. Bakonyi, M. Uhlemann, M. Herrich, B. Arnold, H. D. Bauer, K. Wetzig, *J. Electrochem. Soc.*, **148**, C168 (2001).
5. E. Budevski, G. Staikov, W. J. Lorenz, *Electrochemical Phase Formation and Growth*, VCH, Weinheim, 1996.
6. D. M. Kolb, *Electrochim. Acta*, **45**, 2387 (2000).
7. L. Cagnon, A. Gundel, T. Devolder, A. Morone, C. Chappert, J. E. Schmidt, P. Allongue, *Appl. Surf. Sci.*, **164**, 22 (2000).
8. W. Schindler, J. Kirschner, *Phys. Rev.*, **B55**, R1989 (1997)
9. W. Schindler, D. Hofmann, J. Kirschner, *J. Electrochem. Soc.*, **148**, C124 (2001).
10. T. Z. Fahidy, in: B.E. Conway et al. (Eds.), *Modern Aspects of Electrochemistry*, **32**, Kluwer Academic Publisher, New York, 1999, p.333
11. R. A. Tacke, L. J. Janssen, *J. Appl. Electrochem.*, **25**, 1 (1995).
12. J. M. D. Coey, G. Hinds, *J. Alloys Comp.*, **326**, 238 (2001).
13. J. P. Chopart, J. Douglade, P. Fricoteaux, A. Oliver, *Electrochim. Acta*, **36**, 459 (1991).
14. S. S. Belevskii, S. P. Yushchenko, A. I. Dikumar, *Surface Engineering and Applied Electrochemistry*, **48-1**, 97 (2012)
15. K. M. Yin, J.- H. Wei, J. R. Fu, B. N. Popov, S. N. Popov, R. E. White, *J. Appl. Electrochem.*, **25**, 543 (1995).
16. J. Horkans, *J. Electrochem. Soc.*, **128**, 45 (1981).

ЕЛЕКТРООТЛАГАНЕ НА Ni-Co СПЛАВ ВЪРХУ ХИМИЧЕСКИ ОКСИДИРАН Al

К. Игнатова¹, Й. Марчева²

¹*Химико-Технологичен и Металургичен университет (ХТМУ) София, кат. „Неорганични и електрохимични производства“*, ²*Технически Университет София, кат. „Химия“*

Постъпила на 19 септември 2013 г.; Коригирана на 5 март 2015 г.

(Резюме)

Съпоставена е кинетиката на отлагане на Co, Ni, и Ni-Co из слабокисел цитратен електролит върху електроди от Cu и химически оксидиран Al. Установено е, че отлагането върху алуминиев електрод е затруднено в по-голяма степен в сравнение с това върху меден електрод. И върху двата електрода (Cu и Al) се установява съотлагане на Co и Ni от „аномален“ тип, като то е по-характерно в електролит с по-високо съдържание на Ni. При отлагане в стационарен потенциостатичен режим (срт) върху електрод от алуминий съдържанието на кобалт в Ni-Co сплав е с около 10 % по-високо отколкото при отлагането му върху меден електрод. Ni-Co сплавно покритие върху алуминий може да бъде охарактеризирано като покритие от островен тип, кристалите на което са със сфероидна форма (10-17 μm). Прилагането на импулсен потенциостатичен режим (ррт) на отлагане върху алуминиев електрод води до нарастване на структурната еднородност и степента на запълване на повърхността с кристали от Ni-Co сплав. Ефектът от прилагането на импулсния режим силно отслабва с понижаване на степента на запълването на импулсите при дадена честота.

Combined theory of one- and two-electron bipolar and polar multicenter integrals of noninteger n Slater functions and Coulomb-Yukawa-like potentials with noninteger indices

I. I. Guseinov*

Department of Physics, Faculty of Arts and Sciences, Onsekiz Mart University, Çanakkale, Turkey

Received July 23, 2014, Revised October 22, 2014

By the use of one-range addition theorems suggested by the author, the combined theory for one- and two-electron multicenter integrals of χ -noninteger n Slater type orbitals (χ -NISTOs) and bipolar and polar noninteger Coulomb (C-NIBPs and C-NIPs) -Yukawa (Y-NIBPs and Y-NIPs)-like correlated potentials is presented. These multicenter integrals are expressed through the basic polar integrals of χ -integer n Slater type orbitals (χ -ISTOs) and Coulomb-Yukawa-like potentials with integer indices (C-IPs and Y-IPs). We note that the noninteger quantum number n is defined as n^* .

Key words: Exponential type orbitals, Addition theorems, Bipolar potentials, Multicenter integrals, Self-frictional quantum numbers **PACS:** 31.10.+z; 31.15.-p

INTRODUCTION

It is well known that the main problem in the accurate electronic structure calculations arises in the evaluation of the multicenter integrals which confirms that other theories are needed instead [1, 2]. The arguments of a new theory for multicenter integrals developed in this work are based on a completely different point of view, namely, making use of the bipolar potentials (see [3-5] and refs. quoted therein). The aim of this work is to evaluate the multicenter integrals with χ -NISTOs and C-NIBPs, C-NIPs, Y-NIBPs and Y-NIPs potentials. The obtained formulas are especially useful in the accurate calculation of electronic structure properties for atoms and molecules when a χ -NISTOs basis set and explicitly correlated methods are used in the linear combination of atomic orbitals – molecular orbitals (LCAO-MO) approximation [6].

DEFINITION AND BASIC FORMULAS

The χ -NISTOs, C-NIPs (for $\eta = 0$) and Y-NIPs (for $\eta > 0$) used in this work are defined as follows:

$$\chi_{n^*l_m}(\zeta, \vec{r}) = R_{n^*}(\zeta, r) S_{l_m}(\theta, \varphi) \quad (1)$$

$$O_{u^*v}(\eta, \vec{r}) = O_{u^*v}(\eta, r) S_{l_m}(\theta, \varphi), \quad (2)$$

where

$$R_{n^*}(\zeta, r) = \frac{(2\zeta)^{n^*+1/2}}{[\Gamma(2n^*+1)]^{1/2}} r^{n^*-1} e^{-\zeta r} \quad (3)$$

$$O_{u^*v}(\eta, r) = \left(\frac{4\pi}{2\nu+1} \right)^{1/2} r^{u^*-1} e^{-\eta r} \quad (4)$$

Here, $S_{l_m}(\theta, \varphi)$ are the complex (for $S_{l_m} = Y_{l_m}$) or real spherical harmonics defined as

$$S_{l_m}(\theta, \varphi) = P_{l|m}(\cos\theta) \Phi_m(\varphi), \quad (5)$$

where $P_{l|m}$ are the normalized Legendre functions and for complex spherical harmonics

$$\Phi_m(\varphi) = \frac{1}{\sqrt{2\pi}} e^{im\varphi}, \quad (6)$$

for real spherical harmonics

$$\Phi_m(\varphi) = \frac{1}{\sqrt{\pi(1+\delta_{m0})}} \begin{cases} \cos|m|\varphi & \text{for } m \geq 0 \\ \sin|m|\varphi & \text{for } m < 0. \end{cases} \quad (7)$$

Our definition of phases for the complex spherical harmonics ($Y_{l_m}^* = Y_{l-m}$) [7] differs from the Condon-Shortley phases [8] by the sign factor $(-1)^m$.

All of the one- and two-electron multicenter integrals examined in this work can be defined by the following combined formulas:

* To whom all correspondence should be sent:
E-mail: isguseinov@yahoo.com

$$U_{p_1^* p_1'^* k^*}^{ij,acb;eh}(\zeta_1, \zeta_1'; \eta) = \int \chi_{p_1^*}^*(\zeta_1, \vec{r}_{a1}) O_{k^*}^i(\eta, \vec{r}_{b1} - \vec{R}_{eh}) \left(-\frac{1}{2} \nabla_1^2\right)^j \chi_{p_1'^*}(\zeta_1', \vec{r}_{c1}) d^3 \vec{r}_1 \quad (8)$$

$$I_{p_1^* p_1'^* p_2^* p_2'^* k^*}^{ac,bd;eh}(\zeta_1, \zeta_1'; \zeta_2, \zeta_2'; \eta) = \iint \chi_{p_1^*}^*(\zeta_1, \vec{r}_{a1}) \chi_{p_1'^*}(\zeta_1', \vec{r}_{c1}) \chi_{p_2^*}(\zeta_2, \vec{r}_{b2}) \times \chi_{p_2'^*}^*(\zeta_2', \vec{r}_{d2}) O_{k^*}(\eta, \vec{r}_{21} - \vec{R}_{eh}) d^3 \vec{r}_1 d^3 \vec{r}_2, \quad (9)$$

where $p_i^* = n_i^* l_i m_i$, $p_i'^* = n_i'^* l_i' m_i'$, $k^* = u^* v s$, $\zeta_i > 0$, $\zeta_i' > 0$ and $\eta \geq 0$. Here, the values $ij = 00$, $ij = 01$ and $ij = 10$ in Eq. (8) correspond to the overlap, kinetic energy and nuclear attraction integrals,

$$S_{p_1^* p_1'^*}(\zeta_1, \zeta_1'; \vec{R}_{ac}) = U_{p_1^* p_1'^*}^{00,ac}(\zeta_1, \zeta_1') = \int \chi_{p_1^*}^*(\zeta_1, \vec{r}_{a1}) \chi_{p_1'^*}(\zeta_1', \vec{r}_{c1}) d^3 \vec{r}_1 \quad (10)$$

$$K_{p_1^* p_1'^*}(\zeta_1, \zeta_1'; \vec{R}_{ac}) = U_{p_1^* p_1'^*}^{01,ac}(\zeta_1, \zeta_1') = \int \chi_{p_1^*}^*(\zeta_1, \vec{r}_{a1}) \left(-\frac{1}{2} \nabla_1^2\right) \chi_{p_1'^*}(\zeta_1', \vec{r}_{c1}) d^3 \vec{r}_1 = -\frac{1}{2} \zeta_1'^2 \left\{ S_{n_1^* l_1 m_1, n_1'^* l_1' m_1'}(\zeta_1, \zeta_1'; \vec{R}_{ac}) - 4n_1'^* \left[\frac{\Gamma(2n_1'^* - 1)}{\Gamma(2n_1'^* + 1)} \right]^{\frac{1}{2}} S_{n_1^* l_1 m_1, n_1'^* - 1 l_1' m_1'}(\zeta_1, \zeta_1'; \vec{R}_{ac}) + 4(n_1'^* + l_1') (n_1'^* - l_1' - 1) \left[\frac{\Gamma(2n_1'^* - 3)}{\Gamma(2n_1'^* + 1)} \right]^{\frac{1}{2}} \times S_{n_1^* l_1 m_1, n_1'^* - 2 l_1' m_1'}(\zeta_1, \zeta_1'; \vec{R}_{ac}) \right\} \quad (11)$$

$$U_{p_1^* p_1'^* k^*}^{acb;eh}(\zeta_1, \zeta_1'; \eta) = U_{p_1^* p_1'^* k^*}^{10,acb;eh}(\zeta_1, \zeta_1'; \eta) = \int \chi_{p_1^*}^*(\zeta_1, \vec{r}_{a1}) \chi_{p_1'^*}(\zeta_1', \vec{r}_{c1}) \times O_{k^*}(\eta, \vec{r}_{b1} - \vec{R}_{eh}) d^3 \vec{r}_1. \quad (12)$$

As we see, Eqs. (9) and (12) are the bipolar (for $R_{eh} \neq 0$) and polar (for $R_{eh} = 0$) nuclear attraction (see Fig. 1) and two-electron (see Fig. 2) multicenter integrals, respectively.

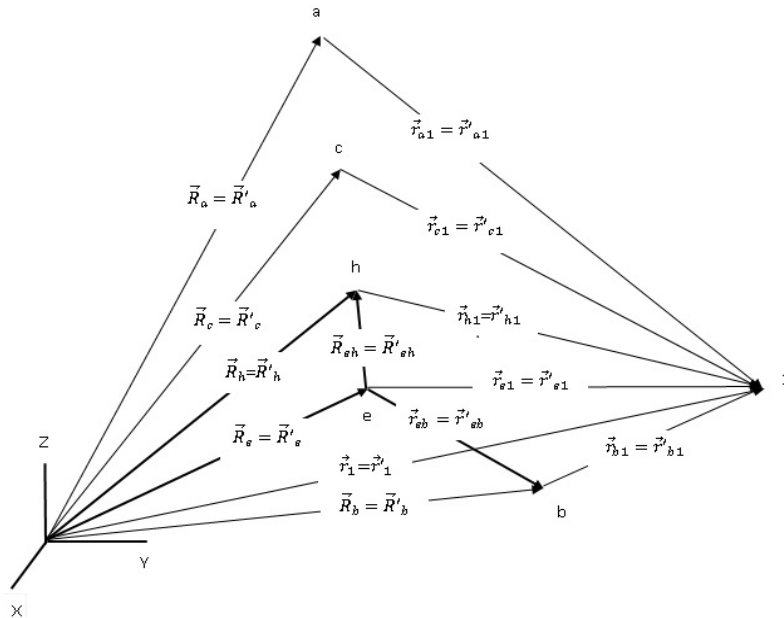


Fig. 1. Geometry of one-electron bipolar ($\vec{R}_{eh} \neq 0$) and polar ($\vec{R}_{eh} = 0$) molecule.

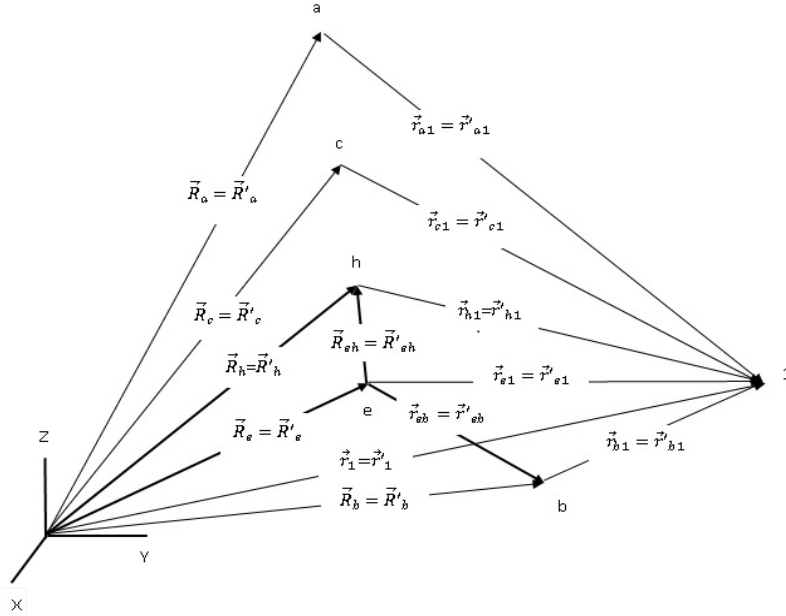


Fig. 2. Geometry of two-electron bipolar ($\vec{R}_{eh} \neq 0$) and polar ($\vec{R}_{eh} = 0$) molecule.

EVALUATION OF BIPOLAR AND POLAR MULTICENTER INTEGRALS

To evaluate the multicenter integrals (9) and (12) we use the formulas in standard convention for the two-center one-range addition theorems for χ -NISTOs in terms of χ -ISTOs in the following form [9, 10]:

$$\chi_{p^*}(\zeta, \vec{r} - \vec{R}_{ab}) = \sum_{\mu=1}^{\infty} \sum_{\nu=0}^{\mu-1} \sum_{\sigma=-\nu}^{\nu} \Omega_{qp^*}^{(\alpha^*)}(\zeta, \zeta; \vec{R}_{ab}) \times \sum_{\mu'=\nu+1}^{\mu} \tilde{\omega}_{\mu\mu'}^{(\alpha^*)\nu} \chi_{q'}(\zeta, \vec{r}), \tag{13}$$

where $\vec{r} = \vec{r}_a$, $\vec{r}_b = \vec{r}_a - \vec{R}_{ab} = \vec{r} - \vec{R}_{ab}$, $\vec{R}_{ab} = \vec{R}_b - \vec{R}_a$, $p^* = n^*lm$, $q = \mu\nu\sigma$ and $q' = \mu'\nu\sigma$. The expansion coefficients occurring in Eq. (13) are defined as follows:

$$\Omega_{qp^*}^{(\alpha^*)}(\zeta, \zeta; \vec{R}_{ab}) = (2\mu)^{\alpha^*} \sum_{u=l+1}^{\infty} \omega_{un^*}^{(\alpha^*)l} \times \sum_{n=\nu+1}^{\mu} \tilde{\omega}_{\mu n}^{(\alpha^*)\nu} \sum_{n'=l+1}^u \tilde{\omega}_{un'}^{(\alpha^*)l} S_{n\nu\sigma, n'lm}^{(\alpha^*)}(\zeta, \zeta; \vec{R}_{ab}) \tag{14}$$

$$\omega_{un^*}^{(\alpha^*)l} = \frac{\Gamma(u - n^*)\Gamma(n^* + l - \alpha^* + 2)}{\Gamma(l + 1 - n^*)} \times \left[\frac{(2u)^{\alpha^*}}{(u - (l + 1))! \Gamma(2n^* + 1) \Gamma(q_u^* + 1)} \right]^{1/2} \tag{15}$$

$$\tilde{\omega}_{\mu n}^{(\alpha^*)\nu} = \left[\frac{(2n)! \Gamma(q_{\mu}^* + 1)}{(2\mu)^{\alpha^*} (\mu - (\nu + 1))!} \right]^{1/2} \tilde{a}_{\mu n}^{\alpha^*\nu} \tag{16}$$

$$S_{n\nu\sigma, n'lm}^{(\alpha^*)}(\zeta, \zeta; \vec{R}_{ab}) = \int \frac{1}{(2\zeta r_a)^{\alpha^*}} \times \chi_{n\nu\sigma}^*(\zeta, \vec{r}_a) \chi_{n'lm}(\zeta, \vec{r}_b) d^3\vec{r}. \tag{17}$$

Here, $p_l^* = 2l + 2 - \alpha^*$, $q_u^* = u + l + 1 - \alpha^*$, $p_{\nu}^* = 2\nu + 2 - \alpha^*$, $q_{\mu}^* = \mu + \nu + 1 - \alpha^*$ and

$$\tilde{a}_{\mu n}^{\alpha^*\nu} = \frac{(-[\mu - (\nu + 1)])_{n-(\nu+1)}}{\Gamma(p_{\nu}^* + 1) (p_{\nu}^* + 1)_{n-(\nu+1)} (n - (\nu + 1))!} \tag{18}$$

$S_{n\nu\sigma, n'lm}^{(\alpha^*)}(\zeta, \zeta; \vec{R}_{ab})$ are the modified overlap integrals (MOIs) with χ -ISTOs in molecular coordinate system; $(-[\mu - (\nu + 1)])_{n-(\nu+1)}$ and $(p_{\nu}^* + 1)_{n-(\nu+1)}$ are the Pochhammer symbols. See Refs.[10,11] for the evaluation of MOIs which contain the integer ($\alpha^* = \alpha$, $-\infty < \alpha \leq 2$) or noninteger ($\alpha^* \neq \alpha$, $-\infty < \alpha^* < 3$) self-frictional quantum number.

To transform the bipolar potential in multicenter integrals (9) and (12) to the polar case we use the following relations:

$$\vec{r}_{a1} = \vec{r}_1 - \vec{R}_a = \vec{r}'_1 - \vec{R}_{ha}, \vec{r}_{c1} = \vec{r}_1 - \vec{R}_c = \vec{r}'_1 - \vec{R}_{hc}, \vec{r}_{b1} = \vec{r}_1 - \vec{R}_b = \vec{r}'_1 - \vec{R}_{hb} \tag{19}$$

$$\vec{r}'_1 = \vec{r}_{a1} + \vec{R}_{ha} = \vec{r}_{c1} + \vec{R}_{hc} = \vec{r}_{b1} + \vec{R}_{hb} \quad (20)$$

$$\begin{aligned} \vec{r}'_{b2} &= \vec{r}_2 - \vec{R}_b = \vec{r}'_2 - \vec{R}_{hb}, \vec{r}'_{d2} = \vec{r}_2 - \vec{R}_d \\ &= \vec{r}'_2 - \vec{R}_{hd} \end{aligned} \quad (21)$$

$$\vec{r}'_2 = \vec{r}_{b2} + \vec{R}_{hb} = \vec{r}_{d2} + \vec{R}_{hd} \quad (22)$$

and

$$\begin{aligned} \vec{r}'_{21} - \vec{R}_{eh} &= (\vec{r}_1 - \vec{R}_h) - (\vec{r}_2 - \vec{R}_e) \\ &= \vec{r}'_1 - \vec{r}'_2 = \vec{r}'_{21} \end{aligned} \quad (23)$$

$$\vec{r}'_1 = \vec{r}_1 - \vec{R}_h, \vec{r}'_2 = \vec{r}_2 - \vec{R}_e. \quad (24)$$

Then, we obtain:

$$\begin{aligned} U_{p_1^* p_1^*, k^*}^{acb;eh}(\zeta_1, \zeta'_1; \eta) &= \int \chi_{p_1^*}^*(\zeta_1, \vec{r}'_1 - \vec{R}_{ha}) \\ &\times \chi_{p_1^*}(\zeta'_1, \vec{r}'_1 - \vec{R}_{hc}) O_{k^*}(\eta, \vec{r}'_{b1}) d^3 \vec{r}'_1 \end{aligned} \quad (25)$$

$$\begin{aligned} I_{p_1^* p_1^*, p_2^* p_2^*, k^*}^{ac,bd;eh}(\zeta_1, \zeta'_1; \zeta_2, \zeta'_2; \eta) &= \\ \iint \chi_{p_1^*}^*(\zeta_1, \vec{r}'_1 - \vec{R}_{ha}) \chi_{p_1^*}(\zeta'_1, \vec{r}'_1 - \vec{R}_{hc}) \\ &\times \chi_{p_2^*}(\zeta_2, \vec{r}'_2 - \vec{R}_{eb}) \chi_{p_2^*}^*(\zeta'_2, \vec{r}'_2 - \vec{R}_{ed}) \\ &\times O_{k^*}(\eta, \vec{r}'_{21}) d^3 \vec{r}'_1 d^3 \vec{r}'_2. \end{aligned} \quad (26)$$

Taking into account Eq.(13) in (25) and (26) we obtain for one- and two-electron bipolar multicenter integrals the following series of expansion relations:

$$\begin{aligned} U_{p_1^* p_1^*, k^*}^{acb;eh}(\zeta_1, \zeta'_1; \eta) &= \\ &= \sum_{\kappa_1=1}^{\infty} \sum_{\nu_1=0}^{\kappa_1-1} \sum_{s_1=-\nu_1}^{\nu_1} \sum_{\kappa'_1=\nu_1+1}^{\kappa_1} \tilde{\omega}_{\kappa_1 \kappa'_1}^{(\alpha^*) \nu_1} \Omega_{\delta_1 p_1^*}^{(\alpha^*)}(\zeta_1, \zeta_1; \vec{R}_{ha}) \\ &\times \sum_{\gamma'_1=1}^{\infty} \sum_{\nu'_1=0}^{\gamma'_1-1} \sum_{s'_1=-\nu'_1}^{\nu'_1} \sum_{\gamma''_1=\nu'_1+1}^{\gamma'_1} \tilde{\omega}_{\gamma'_1 \gamma''_1}^{(\alpha^*) \nu'_1} \Omega_{\varepsilon'_1 p_1^*}^{(\alpha^*)}(\zeta'_1, \zeta'_1; \vec{R}_{hc}) \\ &J_{\delta'_1 \varepsilon'_1; k^*}^b(\zeta_1, \zeta'_1; \eta) \end{aligned} \quad (27)$$

$$\begin{aligned} I_{p_1^* p_1^*, p_2^* p_2^*, k^*}^{ac,bd;eh}(\zeta_1, \zeta'_1; \zeta_2, \zeta'_2; \eta) &= \\ &= \sum_{\kappa_1=1}^{\infty} \sum_{\nu_1=0}^{\kappa_1-1} \sum_{s_1=-\nu_1}^{\nu_1} \sum_{\kappa'_1=\nu_1+1}^{\kappa_1} \tilde{\omega}_{\kappa_1 \kappa'_1}^{(\alpha^*) \nu_1} \Omega_{\delta_1 p_1^*}^{(\alpha^*)}(\zeta_1, \zeta_1; \vec{R}_{ha}) \\ &\times \sum_{\gamma'_1=1}^{\infty} \sum_{\nu'_1=0}^{\gamma'_1-1} \sum_{s'_1=-\nu'_1}^{\nu'_1} \sum_{\gamma''_1=\nu'_1+1}^{\gamma'_1} \tilde{\omega}_{\gamma'_1 \gamma''_1}^{(\alpha^*) \nu'_1} \Omega_{\varepsilon'_1 p_1^*}^{(\alpha^*)}(\zeta'_1, \zeta'_1; \vec{R}_{hc}) \\ &\times \sum_{\kappa_2=1}^{\infty} \sum_{\nu_2=0}^{\kappa_2-1} \sum_{s_2=-\nu_2}^{\nu_2} \sum_{\kappa'_2=\nu_2+1}^{\kappa_2} \tilde{\omega}_{\kappa_2 \kappa'_2}^{(\alpha^*) \nu_2} \Omega_{\delta_2 p_2^*}^{(\alpha^*)}(\zeta_2, \zeta_2; \vec{R}_{eb}) \\ &\times \sum_{\gamma'_2=1}^{\infty} \sum_{\nu'_2=0}^{\gamma'_2-1} \sum_{s'_2=-\nu'_2}^{\nu'_2} \sum_{\gamma''_2=\nu'_2+1}^{\gamma'_2} \tilde{\omega}_{\gamma'_2 \gamma''_2}^{(\alpha^*) \nu'_2} \Omega_{\varepsilon'_2 p_2^*}^{(\alpha^*)}(\zeta'_2, \zeta'_2; \vec{R}_{ed}) \\ &\times J_{\delta'_1 \varepsilon'_1, \delta'_2 \varepsilon'_2; k^*}^b(\zeta_1, \zeta'_1; \zeta_2, \zeta'_2; \eta), \end{aligned} \quad (28)$$

where $\delta_i = \kappa_i \nu_i s_i$, $\delta'_i = \kappa'_i \nu'_i s'_i$, $\varepsilon_i = \gamma'_i \nu'_i s'_i$ and $\varepsilon''_i = \gamma''_i \nu''_i s''_i$. Here, $J_{\delta'_1 \varepsilon'_1; k^*}^b(\zeta_1, \zeta'_1; \eta)$ and $J_{\delta'_1 \varepsilon'_1, \delta'_2 \varepsilon'_2; k^*}^b(\zeta_1, \zeta'_1; \zeta_2, \zeta'_2; \eta)$ are the polar integrals defined as

$$\begin{aligned} J_{\delta'_1 \varepsilon'_1; k^*}^b(\zeta_1, \zeta'_1; \eta) &= \int \chi_{\delta'_1}^*(\zeta_1, \vec{r}'_1) \\ &\times \chi_{\varepsilon'_1}(\zeta'_1, \vec{r}'_1) O_{k^*}(\eta, \vec{r}'_{b1}) d^3 \vec{r}'_1 \quad (29) \\ J_{\delta'_1 \varepsilon'_1, \delta'_2 \varepsilon'_2; k^*}^b(\zeta_1, \zeta'_1; \zeta_2, \zeta'_2; \eta) &= \iint \chi_{\delta'_1}^*(\zeta_1, \vec{r}'_1) \\ &\times \chi_{\varepsilon'_1}(\zeta'_1, \vec{r}'_1) \chi_{\delta'_2}(\zeta_2, \vec{r}'_2) \chi_{\varepsilon'_2}^*(\zeta'_2, \vec{r}'_2) \\ &\times O_{k^*}(\eta, \vec{r}'_{21}) d^3 \vec{r}'_1 d^3 \vec{r}'_2 \end{aligned} \quad (30)$$

Now we use in Eqs. (29) and (30) the following one-center one-range addition theorems for χ -NISTOs charge density [7, 12]:

$$\begin{aligned} \chi_{\delta'_i}(\zeta_i, \vec{r}'_i) \chi_{\varepsilon''_i}(\zeta'_i, \vec{r}'_i) &= \frac{1}{\sqrt{4\pi}} \\ &\times \sum_{L_i=|\nu_i-\nu'_i|}^{\nu_i+\nu'_i} \sum_{M_i=-L_i}^{L_i} W_{\delta'_i \varepsilon''_i; P_i}(\zeta_i, \zeta'_i; Z_i) \chi_{p_i}(Z_i, \vec{r}'_i). \end{aligned} \quad (31)$$

The charge density expansion coefficients occurring in (31) are determined by

$$\begin{aligned} W_{\delta'_i \varepsilon''_i; P_i}(\zeta_i, \zeta'_i; Z_i) &= \frac{Z_i^{3/2}}{2^{N_i}} \left[\frac{2L_i+1}{2} \frac{(2N_i)!}{(2\kappa'_i)! (2\gamma''_i)!} \right]^{1/2} \\ C^{L_i|M_i}(\nu_i s_i, \nu'_i s'_i) A_{s_i s'_i}^{M_i} (1+t_i)^{\kappa_i+1/2} (1-t_i)^{\gamma''_i+1/2}, \end{aligned} \quad (32)$$

where $P_i = N_i L_i M_i$, $N_i = \kappa_i + \gamma_i'' - 1$,

$$Z_i = \zeta_i + \zeta_i', \quad t_i = \frac{\zeta_i - \zeta_i'}{\zeta_i + \zeta_i'}; \quad C^{L_i|M_i|}(\nu_i s_i, \nu_i' s_i')$$

and $A_{s_i s_i'}^{M_i}$ are the generalized Gaunt and Kronecker delta coefficients, respectively [7]. The substitution of (31) into Eqs. (29) and (30) gives:

$$\begin{aligned} & J_{\delta_1' \varepsilon_1''; k^*}^b(\zeta_1, \zeta_1'; \eta) \\ &= \sum_{L_1=|\nu_1-\nu_1'|}^{\nu_1+\nu_1'} \sum_{M_1=-L_1}^{L_1} W_{\delta_1' \varepsilon_1''; P_1}(\zeta_1, \zeta_1'; Z_1) \\ & \times J_{P_1; k^*}^b(Z_1; \eta) \end{aligned} \quad (33)$$

$$\begin{aligned} & J_{\delta_1' \varepsilon_1'', \delta_2' \varepsilon_2''; k^*}^b(\zeta_1, \zeta_1'; \zeta_2, \zeta_2'; \eta) \\ &= \sum_{L_1=|\nu_1-\nu_1'|}^{\nu_1+\nu_1'} \sum_{M_1=-L_1}^{L_1} W_{\delta_1' \varepsilon_2''; P_1}(\zeta_1, \zeta_1'; Z_1) \\ & \times \sum_{L_2=|\nu_2-\nu_2'|}^{\nu_2+\nu_2'} \sum_{M_2=-L_2}^{L_2} W_{\delta_2' \varepsilon_2''; P_2}(\zeta_2, \zeta_2'; Z_2) \\ & \times J_{P_1 P_2; k^*}^b(Z_1, Z_2; \eta). \end{aligned} \quad (34)$$

Here, the quantities

$$\begin{aligned} & J_{P_1; k^*}^b(Z_1; \eta) \\ &= \frac{1}{\sqrt{4\pi}} \int \chi_{P_1}^*(Z_1, \bar{r}_1') O_{k^*}(\eta, \bar{r}_{b1}') d^3 \bar{r}_1' \end{aligned} \quad (35)$$

$$\begin{aligned} & J_{P_1 P_2; k^*}^b(Z_1, Z_2; \eta) = \frac{1}{4\pi} \iint \chi_{P_1}^*(Z_1, \bar{r}_1') \\ & \times O_{k^*}(\eta, \bar{r}_{21}') \chi_{P_2}(Z_2, \bar{r}_2') d^3 \bar{r}_1' d^3 \bar{r}_2' \end{aligned} \quad (36)$$

are the one- and two-electron basic polar integrals of χ -ISTOs and Coulomb-Yukawa-like potential with noninteger indices, respectively.

As can be seen from the obtained formulas, the one- and two-electron bipolar multicenter integrals with the use of two-center one-range addition theorems for χ -NISTOs are expressed through the basic polar integrals of χ -ISTOs and Coulomb-Yukawa-like potential with noninteger indices.

The basic integrals (35) and (36) can be calculated by the use of Laguerre power series of functions with noninteger indices which can be established with the help of $L^{(p_i^*)}$ -generalized and $L^{(\alpha^*)}$ -modified Laguerre polynomials ($L^{(p_i^*)}$ -

GLPs and $L^{(\alpha^*)}$ -MLPs), respectively (see Ref. [9]). For the construction of Laguerre power series, we use the potential $O_{u^* \nu s}$ occurring in Eqs. (35) and (36) in the following form

$$O_{u^* \nu s}(\eta, \vec{r}) = O_{u \nu s}(\eta, \vec{r}) r^{\eta^*}, \quad (37)$$

where $u^* = u + \eta^*$, $0 < \eta^* < 1$ and u is the integer part of u^* . Then we obtain:

for $L^{(p_i^*)}$ -GLPs

$$r^{\eta^*} = \sum_{\mu=\nu+1}^{\infty} \sum_{\mu'=\nu+1}^{\mu} \tilde{Y}_{\mu\mu', \eta^*}^{(p_\nu^*) \nu} r^{\mu'-(\nu+1)} \quad (38)$$

for $L^{(\alpha^*)}$ -MLPs

$$r^{\eta^*} = \sum_{\mu=\nu+1}^{\infty} \sum_{\mu'=\nu+1}^{\mu} \tilde{Y}_{\mu\mu', \eta^*}^{(\alpha^*) \nu} r^{\mu'-1}, \quad (39)$$

where

$$\begin{aligned} & Y_{\mu\mu', \eta^*}^{(p_\nu^*) \nu} = \tilde{a}_{\mu\mu'}^{(p_\nu^*) \nu} \\ & \times \sum_{\mu'=\nu+1}^{\mu} \tilde{a}_{\mu\mu'}^{(p_\nu^*) \nu} \frac{\Gamma(q_\mu^* + 1) \Gamma(\mu'' + p_\nu^* + \eta^* - \nu)}{[\mu - (\nu + 1)]!} \end{aligned} \quad (40)$$

$$\begin{aligned} & \tilde{Y}_{\mu\mu', \eta^*}^{(\alpha^*) \nu} = \tilde{a}_{\mu\mu'}^{(\alpha^*) \nu} \\ & \times \sum_{\mu'=\nu+1}^{\mu} \tilde{a}_{\mu\mu'}^{(\alpha^*) \nu} \frac{\Gamma(q_\mu^* + 1) \Gamma(\mu'' - \alpha^* + \eta^* + 2)}{[\mu - (\nu + 1)]!}. \end{aligned} \quad (41)$$

Using Eqs.(38) and (39), we obtain for the one-center one-range addition theorems of O-NIPs based on the use of Laguerre power series the following relations:

$$\begin{aligned} & O_{u^* \nu s}(\eta, \vec{r}) \\ &= \sum_{\mu=\nu+1}^{\infty} \sum_{\mu'=u}^{\mu+u-(\nu+1)} \tilde{Y}_{\mu\mu'-u+\nu+1, \eta^*}^{(p_\nu^*) \nu} O_{\mu' \nu s}(\eta, \vec{r}) \end{aligned} \quad (42)$$

$$\begin{aligned} & O_{u^* \nu s}(\eta, \vec{r}) \\ &= \sum_{\mu=\nu+1}^{\infty} \sum_{\mu'=u+\nu}^{\mu+u-1} \tilde{Y}_{\mu\mu'-u+1, \eta^*}^{(\alpha^*) \nu} O_{\mu' \nu s}(\eta, \vec{r}). \end{aligned} \quad (43)$$

The substitution of Eqs.(42) and (43) into (35) and (36) gives for the basic polar integrals the following series expansions:

$$J_{P_1;k^*}^b(Z_1; \eta, \vec{R}'_{hb}) = \sum_{\mu=v+1}^{\infty} \sum_{\mu'=u}^{\mu+u-(v+1)} \tilde{Y}_{\mu\mu'-u+v+1, \eta^*}^{(P_v)^v} J_{P_1;k'}^b(Z_1; \eta, \vec{R}'_{hb}) \quad (44)$$

$$J_{P_1P_2;k^*}^b(Z_1, Z_2; \eta) = \sum_{\mu=v+1}^{\infty} \sum_{\mu'=u+v}^{\mu+u-1} \tilde{Y}_{\mu\mu'-u+1, \eta^*}^{(\alpha^*)^v} J_{P_1P_2;k'}^b(Z_1, Z_2; \eta), \quad (45)$$

where $J_{P_1;k^*}^b(Z_1, \eta; \vec{R}'_{hb}) \equiv J_{P_1;k^*}^b(Z_1, \eta)$,

$$J_{P_1;k'}^b(Z_1, \eta; \vec{R}'_{hb}) = J_{P_1;k'}^b(Z_1, \eta), \quad k' = \mu' \nu s \text{ and}$$

$$J_{P_1;k'}^b(Z_1, \eta; \vec{R}'_{hb}) = \frac{1}{\sqrt{4\pi}} \int \chi_{P_1}^*(Z_1, \vec{r}'_1) O_{k'}(\eta, \vec{r}'_{b1}) d^3 \vec{r}'_1 = A_{\mu'\nu}(\eta) S_{P_1k'}(Z_1, \eta; \vec{R}'_{hb}) \quad (46)$$

$$J_{P_1P_2;k'}^b(Z_1, Z_2; \eta) = \frac{1}{4\pi} \iint \chi_{P_1}^*(Z_1, \vec{r}'_1) \times O_{k'}(\eta, \vec{r}'_{21}) \chi_{P_2}(Z_2, \vec{r}'_2) d^3 \vec{r}'_1 d^3 \vec{r}'_2 = A_{\mu'\nu}(\eta) \times \frac{1}{4\pi} \int S_{P_1k'}(Z_1, \eta; \vec{r}'_{h2}) \chi_{P_2}(Z_2, \vec{r}'_{h2}) d^3 \vec{r}'_{h2} \quad (47)$$

The quantities $S_{P_1k'}$ occurring in Eqs. (46) and (47) are the overlap integrals over χ -ISTOs and $A_{\mu'\nu}(\eta)$ coefficients defined as, respectively:

$$S_{P_1k'}(Z_1, \eta; \vec{R}'_{hb}) = \int \chi_{P_1}^*(Z_1, \vec{r}'_{h1}) \chi_{k'}(\eta, \vec{r}'_{b1}) d^3 \vec{r}'_1, \quad (48)$$

Table 1. The computational results of basic integral $J_{P_1;k'}^b(Z_1, \eta; \vec{R}'_{hb})$.

N_1	L_1	M_1	Z_1	μ'	ν	s	η	R'_{hb}	θ'_{hb}	ϕ'_{hb}	Eq.(46)
1	0	0	4.1	2	1	1	1	1	108	288	0.0384304419337282709
3	0	0	9	2	0	0	3	2.3	90	180	0.001100902598119918
4	1	1	7.6	3	2	0	3.4	1.4	60	180	0.0011283910967783675
8	7	1	8.5	6	1	0	5.3	2.2	30	108	9.760836563464515 $E - 07$
9	4	1	9.6	7	3	1	6.3	1.8	120	72	-9.12773014368389 $E - 06$
9	8	8	2.5	8	6	6	1.5	1.1	30	60	-2.095067822209997817
10	6	6	3.4	9	7	7	2.3	2.9	108	120	0.677010199846579
11	7	6	8.7	8	6	6	3.5	2.1	150	108	0.0016434196671959369
12	10	10	6.1	14	8	5	7.8	2.5	108	60	-0.0000107171243862096
13	11	8	7.8	10	9	8	5.5	1.9	122	72	0.00007592144328909598
15	13	12	6.6	14	12	12	3.7	2.6	150	60	0.13030800995209336587
20	15	15	8.9	18	17	16	7.5	5.1	36	75	8.800413162432983 $E - 10$

$$A_{\mu'\nu}(\eta) = \left[\frac{(2\mu')!}{(2\nu+1)(2\eta)^{2\mu'+1}} \right]^{1/2}. \quad (49)$$

It should be noted that the two-electron integrals of χ -ISTOs occurring in Eq. (47) have been studied in our previous papers [7, 16].

CONCLUSION

It is shown that the one-range addition theorems for χ -NISTOs, C-NIPs and Y-NIPs, based on the use of $L^{(P_i^*)}$ -GLPs) and $L^{(\alpha^*)}$ -MLPs, are useful tools for the unified treatment of one- and two-electron bipolar and polar multicenter integrals when χ -NISTOs basis sets and Coulomb-Yukawa-like potentials with noninteger indices are employed in electronic structure calculations. The obtained formulas can be used for the evaluation of these integrals with arbitrary values of principal and self-frictional quantum numbers, screening constants and location of orbitals and parameters of potentials. On the basis of Eq. (46), we constructed a program for the computation of $J_{P_1;k'}^b(Z_1, \eta; \vec{R}'_{hb})$ using Mathematica 7.0 international mathematical software. The computational results are given in Table 1. It can be seen from Table 1 that the calculation results are stable for high values of quantum numbers. It is especially useful for accurate evaluation of the multicenter multielectron molecular integrals [10]. The presented theory is especially useful in the study of different electronic structure problems dealing with atoms, molecules and solids.

REFERENCES

1. I. N. Levine, Quantum Chemistry, Prentice Hall, New York, 2000.
2. I. P. Grant, Relativistic Quantum Theory of Atoms and Molecules, Springer and Business Media, New York, 2007.
3. B. C. Carlson and G. S. Rushbrooke, *Proc. Cambridge Phil. Soc.*, **46**, 626 (1950).
4. R. J. Buehler, J. O. Hirschfelder, *Phys. Rev.*, **83**, 628 (1951); 14985 (1952).
5. H. J. Silverstone, *Advan. Quant. Chem.*, **68**, 3 (2013).
6. C. C. J. Roothaan, *Rev. Mod. Phys.*, **23**, 69 (1951).
7. I. I. Guseinov, *J. Phys. B: At. Mol. Phys.*, **3** 1399 (1970).
8. E. U. Condon, G. H. Shortley The Theory of Atomic Spectra, Cambridge University Press, Cambridge, 1970.
9. I. I. Guseinov, *Bull. Chem. Soc. Jpn.*, **85**, 1306 (2012).
10. I. I. Guseinov, *Few-Body Syst.*, **54**, 1773 (2013).
11. I. I. Guseinov, *J. Math. Chem.*, **49** 1011 (2011).
12. I. I. Guseinov, N. Seckin Gorgun, N. Zaim, *Chin. Phys. B*, **19** 043101 (2010).
13. I. I. Guseinov, *Bull. Korean Chem. Soc.*, **30** 1539 (2009).
14. I. I. Guseinov, B. A. Mamedov, *Bull. Chem. Soc. Jpn.*, **83** 1047 (2010).
15. I. I. Guseinov, *J. Iran. Chem. Soc.*, **8** 643 (2011).
16. I. I. Guseinov, B. A. Mamedov, *Theor. Chem. Acc.*, **108** 21 (2002).

КОМБИНИРАНА ТЕОРИЯ НА ЕДНО- И ДВУ-ЕЛЕКТРОННИ БИ-ПОЛЯРНИ ИНТЕГРАЛИ ОТ НЕЦЕЛИ n - SLATER'ОВИ ФУНКЦИИ И COULOMB-YUKAWA-ПОДОБНИ ПОТЕНЦИАЛИ С ДРОБНИ ИНДЕКСИ

И. И. Гусеинов*

Департамент по физика, Факултет за изкуство и наука, Университет „18 март“, Чанаккале, Турция

Постъпила на 23 юли, 2014 г., коригирана на 22 октомври, 2014 г.

(Резюме)

Представена е комбинирана теория за едно- и дву-електронни многоцентрични интегралите от χ -нецели n – орбитали от Slater'ов тип (χ -NISTOs) и на биполярни и полярни нецели кулонови (C-NIBPs и C-NIPs) - Юкава (Y-NIBPs и Y-NIPs)-подобните потенциали. Тези многоцентрични интегралите се представят чрез базични полярни интегралите от χ -цели n – орбитали от Slater'ов тип (χ -ISTOs) и Coulomb-Yukawa-подобни потенциали с цели индекси (C-IPs и Y-IPs). Отбелязано е че не-целите квантови числа n се дефинират с n^* .

Effect of zinc dimethacrylate on compatibilization and reinforcement of peroxide dynamically cured PP/EPDM TPVs

L. Cao^{1,2}, X. Jiang^{1,2}, J. Ding^{3,*}, Y. Chen^{1,2,*}

¹The Key Laboratory of Polymer Processing Engineering, Ministry of Education, China(South China University of Technology), Guangzhou, 510640, China

²School of Mechanical and Automotive Engineering, South China University of Technology, Guangzhou, 510640, China

³College of Material Science and Engineering, South China University of Technology, Guangzhou 510640, China

Received July 23, 2014, Revised October 22, 2014

Thermoplastic vulcanizates (TPVs) based on polypropylene (PP)/ethylene–propylene–diene (EPDM) with a ratio of 40/60 (w/w) were *in situ* compatibilized by zinc dimethacrylate (ZDMA) *via* peroxide induced dynamic vulcanization. The effects of dynamic vulcanization and ZDMA on the compatibility between PP and EPDM phases and the mechanical properties of PP/EPDM TPVs were investigated. The incorporation of ZDMA improved the melt viscosity of the resultant TPVs. Dynamic mechanical analysis (DMA) demonstrated that the increase in ZDMA concentration improved the compatibility between EPDM and PP phases. Scanning electron microscopy (SEM) results showed that the incorporation of ZDMA reduced the size of crosslinked rubber particles. Differential scanning calorimetry (DSC) was conducted to investigate the crystallization behavior and the results indicated that the addition of ZDMA promoted the nucleation process of PP, but a higher ZDMA concentration showed a negative effect on the crystallinity of the PP component. Furthermore, it was found that the mechanical properties of the TPVs were significantly improved by ZDMA. Particularly, with about 18 wt % ZDMA in the PP/EPDM TPV, the tensile strength and elongation at break increased from 7.7MPa and 250% to 13.4MPa and 410%, respectively.

Key words: reinforcement; thermoplastic vulcanizates; compatibility; dynamic vulcanization; mechanical properties

INTRODUCTION

Thermoplastic vulcanizates (TPVs) are an important family of thermoplastic elastomers (TPE) since their introduction in 1970s [1]. They are prepared by melt mixing of thermoplastic and rubber in the presence of a curing agent. TPVs are blends where the rubber component is *in situ* crosslinked during melt mixing with thermoplastics at a certain temperature, using a curing agent. The way to prepare TPVs is called dynamic vulcanization [2-4]. The crosslinking of the rubber component causes a variation of the rubber/plastic viscosity ratio, which results in a change of phase morphology [5, 6]. TPVs combine the elasticity and mechanical properties of traditional rubber vulcanizates with the processing characteristics of thermoplastics [7]. Therefore, TPVs can be processed by injection, extrusion, compression, etc., which improves the productivity and reduces costs. TPVs have experienced a rapid development due to their good mechanical properties and processability.

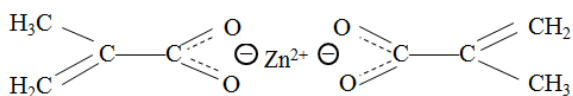
Among the different kinds of TPVs, PP/EPDM TPVs have received considerable attention because of their low cost and general availability in household, automobiles, appliances, construction industry and so on [8-11]. However, as PP and

EPDM are not thermodynamically miscible, it is necessary to improve the compatibility between PP and EPDM phases. There are only a few studies carried out in this field. A. Mirzadeh [12] *et al.* investigated the effects of various dispersion levels of nanoclay on the crosslinking reaction of PP/EPDM TPV. They found that nanoclay affects the crosslinking reaction through its barrier effect which increases the local concentration of curing agent, and dynamic vulcanization improved dispersion and intercalation of nanoclay. De Risi [13] *et al.* introduced zinc dimethacrylate (ZDMA) into peroxide dynamically vulcanized PP/EPDM TPV and found that more peroxide free radicals reacted with the radicals on the ZDMA molecule which limited chain fragmentation of the PP. They paid attention to the importance of ZDMA in minimizing the chain fragmentation rather than the potential improvement of interface adhesion and improved mechanical properties of the TPVs.

In recent years, it was found that some types of rubbers can be reinforced by a high loading of ZDMA (chemical structure is shown below) improving crosslink densities. On the other hand, ZDMA can also form polymerized ZDMA (PZDMA) which dispersed in the matrix or grafted onto rubber chains to enhance the crosslink network in the presence of peroxide free radicals [14-16].

* To whom all correspondence should be sent:
E-mail: cyk@scut.edu.cn; jpding@scut.edu.cn

Therefore, it may be a feasible way to prepare PP/EPDM/ZDMA TPVs *via* peroxide induced dynamic vulcanization to enhance the interface adhesion and the mechanical properties in order to extend their application.



In our previous works we found that the incorporation of ZDMA into PP/EPDM blend *via* peroxide-induced dynamic vulcanization largely improved the toughness of PP-rich blends due to the *in situ* reactive compatibilization of ZDMA [17-19]. We also found that ZDMA showed excellent reinforcement on EPDM-rich TPVs with various PP/EPDM ratios [20, 21]. However, the effect of ZDMA concentrations on the mechanical properties of EPDM-rich PP/EPDM TPV has been not studied yet. In this paper, we fixed the PP/EPDM ratio at 40/60 and prepared TPVs in the presence of ZDMA. The effect of ZDMA concentrations on the processing was evaluated by the torque of mixing. The morphology, dynamic mechanical properties, crystallization behavior, and mechanical properties of the resultant TPVs were studied in detail.

EXPERIMENTAL

Materials

Polypropylene (PP, HP500N, MFI=12g/10 min (210°C, 2.16 kg)) was purchased from CNOOC & Shell Petrochemicals Company Limited., China. Ethylene-propylene-diene monomer (EPDM4045, density=0.87g/cm³, 56% ethylene content, M_L (1+4, 100°C) = 40, 7.5% the third monomer: (5-ethylidene-2-norbornene) was obtained from Jilin Chemical Co., China. ZDMA was purchased from Xian Organic Chemical Technology Plant (Shanxi, China). Dicumyl peroxide (DCP) was obtained from Sinopharm Chemical Reagent Co. Ltd., China.

Compositions and Preparation of TPVs

Three weight ratios of EPDM/ZDMA were employed in this study: 100/10, 100/20 and 100/30 (w/w) [18]. Dynamically vulcanized PP/EPDM/ZDMA TPVs were prepared with a PP/EPDM weight ratio of 40/60 (w/w). The weight ratio of DCP was maintained constant relative to the amount of EPDM. The compositions in terms of the weight ratios of components for PP/EPDM/ZDMA TPVs are presented in Table 1.

Two-step processing method was employed to prepare the PP/EPDM/ZDMA TPVs, in which EPDM and ZDMA were mixed to get rubber compounds, and then the rubber compounds were

blended with PP melt. The detailed process can be found in our previous reports [20, 21].

Table 1. Formulations of the prepared samples (weight ratio)

Coding	PP	EPDM	ZDMA	DCP
B46	40	60	0	0
TZ46-0	40	60	0	0.6
TZ46-1	40	60	6	0.6
TZ46-2	40	60	12	0.6
TZ46-3	40	60	18	0.6

Dynamic Mechanical Analysis

Dynamic mechanical behavior of the samples was investigated using a dynamic mechanical analyzer (DMA 242C NETZSCH, Germany) in tensile mode at 10Hz with a heating rate of 3°C/min in the temperature range of -100 to 80°C.

Morphology Analysis

Nova NanoSEM 430 (FEI Company, Holland) was used to investigate the phase morphology of the samples. Before morphological observation, the cryogenically fractured surface of the specimens was pre-treated as follows: etching by boiling cyclohexane to remove non-crosslinked EPDM phase or etching by boiling xylene to remove PP and non-crosslinked EPDM phase.

Differential scanning calorimetry (DSC)

The crystallization behavior of the blends was studied by means of DSC (NETZSCH DSC 204 F1, Germany). In the tests, samples of about 5 mg were heated to 200°C with a rate of 10°C/min in nitrogen atmosphere and held at 200°C for 5 min to eliminate the thermal history. Afterward, the samples were cooled to 20°C with a rate of 20°C/min, let at 20°C for about 3 min, and then heated again to 200°C with a rate of 10°C/min. The degree of crystallinity (X_c%) was calculated according to Eq. (1):

$$X_c = \Delta H_c / (\Delta H_o * \phi) \times 100\% \quad (1)$$

where ΔH_c is the heat fusion of PP during crystallization, $\Delta H_o = 209$ J/g, represents the heat fusion of 100% isotactic PP and ϕ is the mass fraction of PP in the composites.

Mechanical properties

Standard tests of tensile and tear strength were conducted on a Computerized Tensile Strength Tester (UT-2080, U-CAN Dynatex Inc, Taiwan) at room temperature according to ISO 37-2005 and ISO 34-2004, respectively. All tests were repeated at least 5 times, and the results were averaged.

RESULTS AND DISCUSSION

Torques during dynamic vulcanization

Fig. 1 shows the torque curves *versus* mixing time for all samples. The first and second peaks correspond to the loading and melting of PP and EPDM (or EPDM/ZDMA compound), respectively. After EPDM is completely melted, the torque reaches a rather constant value, indicating the complete melting of PP and the full homogenization of the blends. The torque of the blends abruptly increases when DCP is added to the melt. This is related to the drastic changes in the viscosity and elasticity of the EPDM phase due to crosslinking. After passing through a maximum, the torque decreases until reaching a new constant value at the end of mixing. The decrease in torque is partly due to the deagglomeration of the physical networks formed by the crosslinked rubber droplets. Considering the strong reduction of torque, we believe that the DCP still induces the degradation of PP even in presence of ZDMA. However, note that for the PP/EPDM TPV (TZ46-0), the final stable torque is lower than that of PP/EPDM blend (B46), which indicates that degradation of PP occurs in the presence of peroxide free radicals. While for all the PP/EPDM/ZDMA TPVs, the final stable torques are higher than those before adding DCP, indicating that ZDMA limits the chain fragmentation of PP by consuming the free radicals, and thus the final stable torque shows an increase with increasing ZDMA concentrations, as expected.

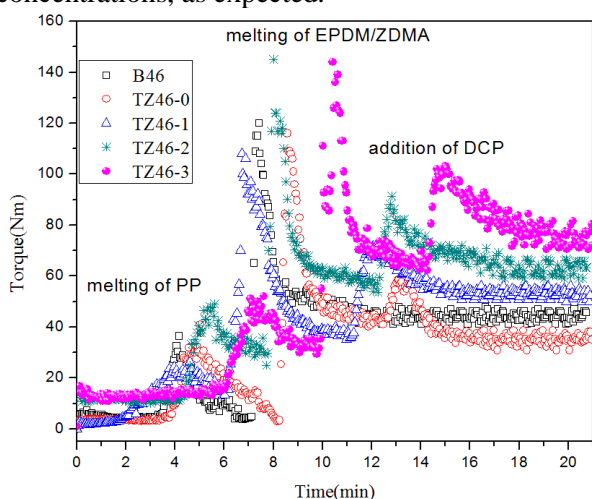


Fig. 1. Torques *versus* mixing time for all specimens.

DMA Analysis

Fig. 2a shows the effect of temperature on the storage modulus (E'). Each specimen shows a two-step decrease of E' value at temperatures ranging between $-70\sim-30^\circ\text{C}$ and $-20\sim40^\circ\text{C}$, which

corresponds to the glass transition of the EPDM phase and PP phase, respectively.

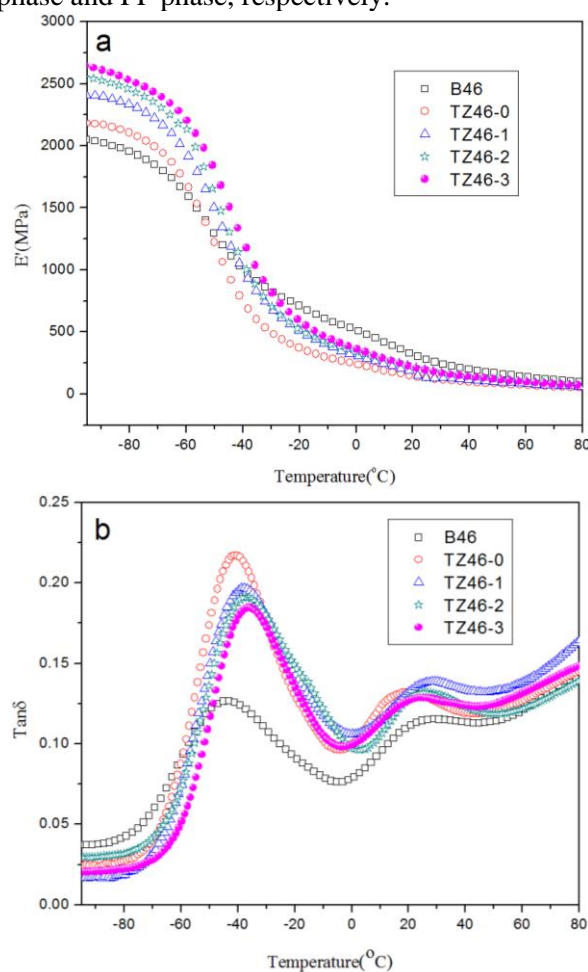


Fig. 2. Storage modulus (a) and loss tangent (b) *versus* temperature for all specimens.

It can be seen that TZ46-0 shows a higher E' value in the glass region than B46, which may result from the crosslinking of EPDM during dynamic vulcanization. Incorporation of ZDMA further improves the E' value showing an increase with increasing ZDMA concentrations below the glass transition temperature. The *in situ* polymerization of ZDMA can form homopolymer particles (h-PZDMA) and graft products (g-PZDMA). The h-PZDMA particles dispersed in the EPDM phase strongly reinforce the rubber droplets [19], contributing to the increased E' . The *in situ* compatibilization of ZDMA occurs at the interfacial layer between the PP and EPDM phases through the reaction between the double bonds of ZDMA and the free radicals generated in both EPDM and PP chains, forming graft products which improve the interface adhesion between PP phase and reinforced EPDM phase [18]. However, note that the E' of the B46 shows a higher value than other TPVs at temperatures above -30°C because E' is mainly contributed by the PP phase.

Fig. 2b shows the temperature dependence of $\tan \delta$. The strong one at around -37°C corresponds to the glass transition of the EPDM phase and the weak one at around 22°C is related to the glass transition of the PP phase. It is clearly seen that dynamic vulcanization apparently improves the Tg of EPDM phase due to the crosslinking of EPDM restricting the mobility of rubber chains. Moreover, Tg of the EPDM phase increases from -41.3°C to -38.3°C with a ZDMA concentration of 10 wt% relative to the amount of EPDM. The increasing ZDMA concentration further increases the Tg of EPDM phase, which can be well explained by the resultant denser rubber network restricting the mobility of rubber chains. In addition, B46 shows higher $\tan \delta$ values than TPVs in the lower temperature range due to the entanglement of EPDM chains under dynamic vulcanization, which makes it more difficult to move.

Morphology Analysis

Fig. 3 shows the morphology of the cryogenically fractured surface for PP/EPDM blend (B46), PP/EPDM TPV (TZ46-0) and PP/EPDM/ZDMA TPV (TZ46-2). Fig. 3a shows a typical cryogenically fractured surface without any plastic deformation signs for PP/EPDM blend, implying the poor compatibility between the two phases. As for the TPVs (Figs. 3b and c), the cryogenically fractured surface becomes rough, indicating improved compatibility between PP and the rubber phase. For TZ46-0 (Fig. 3b), a large number of random fringes formed during the cryogenic fracture process and a relative flat surface with light plastic deformation of the ligaments are observed. While, as shown in Fig. 3c, there are numerous fringes on the cryogenically fractured surface of PP/EPDM/ZDMA TPV, which means that the material undergoes a lighter brittle failure process compared with PP/EPDM TPV. This implies a good *in situ* reactive compatibilization effect of ZDMA on the TPVs. In order to further observe the phase morphology, we used boiling cyclohexane and boiling xylene to etch the cryogenically fractured surface of the simple blends and TPVs, respectively. Fig. 4a shows that PP and EPDM formed a co-continuous phase in the PP/EPDM blend in which the large holes represent EPDM phase. However, for the TPVs (TZ46-0, TZ46-2 and TZ46-3), numerous particles are observed. Since PP and non-crosslinked EPDM phases were removed by boiling xylene, the particles left shown in Figs. 4b, c and d are crosslinked EPDM phase. This phenomenon indicates that dynamic vulcanization changes the phase structure from co-continuous phase into "sea-island" structure (PP as

continuous phase and EPDM as dispersed phase). Moreover, it can be clearly seen that incorporation of ZDMA reduces the size of rubber particles, and the increase of ZDMA concentration further reduces the particle size (Figs. 4c and d).

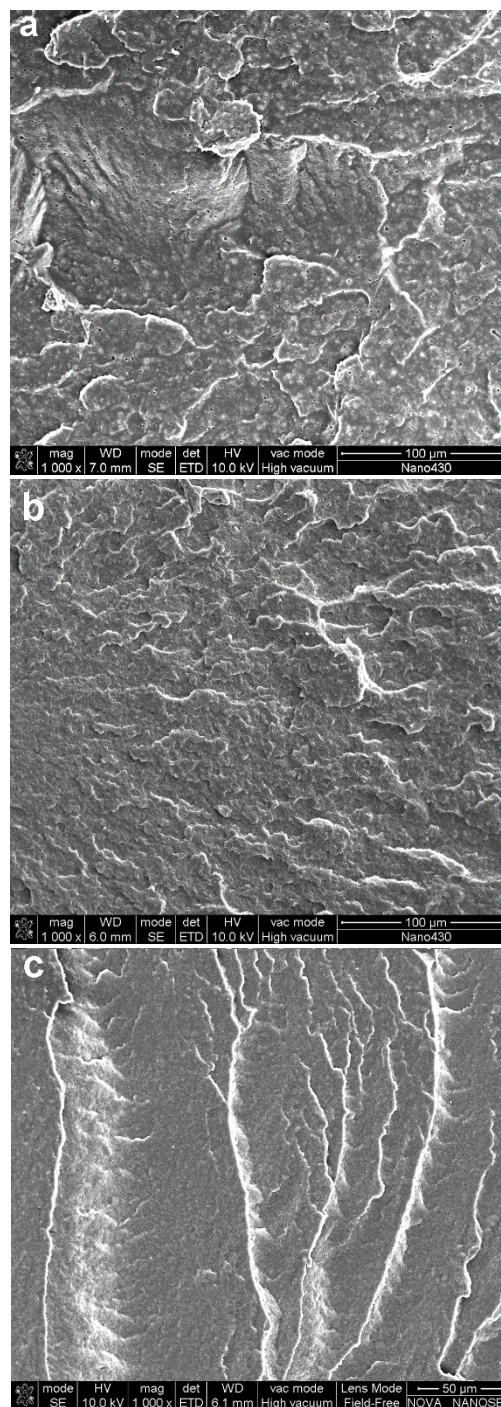


Fig. 3. SEM image for the cryogenically fractured surface of the TPVs: (a) B46; (b) TZ46-0; (c) TZ46-2.

It has been reported that the dispersion of EPDM during melt mixing with PP mainly depends on the viscosity difference between PP and EPDM [22]. When a curing agent is added, the viscosity of the rubber phase raises abruptly as dynamic

vulcanization, the viscosity difference between EPDM and PP increased. At this time, the effect of shear on the morphology of the blends may be dominant and the intense shear results in the dispersion of EPDM particles.

Afterwards, the viscosity difference between EPDM and PP plays the critical role, leading to the EPDM particles being immobilized by crosslinking and breaking down into small droplets under the applied shear field [23]. Since the ZDMA largely promoted the crosslinking process and the crosslink density of EPDM phase in the presence of peroxide free radicals, this leads to the immobilization of the rubber particles and therefore breaking down into smaller sizes. In addition, the size reduction also enlarges the contact area which may be beneficial for the interface interaction between PP and EPDM phases.

Crystallization behavior

Fig. 5 shows the DSC curves of all TPVs during non-isothermal crystallization. It can be seen that all PP/EPDM/ZDMA TPVs show a higher crystallization peak temperature (T_c) than PP/EPDM TPV, and T_c increases with increasing ZDMA concentrations. The effects of dynamic vulcanization and ZDMA concentration on T_c , onset crystallization temperature (T_o) and crystallinity (X_c) of the TPVs are summarized in Table 2. PP/EPDM/ZDMA TPVs show higher T_o and T_c values than those of PP/EPDM TPV, which indicates that the addition of ZDMA promotes the nucleation process of PP, leading to an increased crystallization rate and improved crystallization temperature. For PP/EPDM/ZDMA TPVs it can be seen that both T_o and T_c increase with increasing ZDMA concentrations. However, higher ZDMA concentration seems to have a negative effect on X_c of the PP phase. Note that T_o and T_c of TZ46-1 and TZ46-3 increase from 118.4°C to 121.3°C and 110.3°C to 112.5°C, respectively, while X_c decreases from 48.10% of TZ46-1 to 45.31% of TZ46-3. Here, the possible explanation of this crystallization behaviour is given below: The formation of polymerized ZDMA (PZDMA) in peroxide free radicals has been verified, it may have formed homopolymer (h-PZDMA particles) or grafted onto polymer chains to form graft products (g-PZDMA) [19].

Therefore, the h-PZDMA particles may serve as nucleating agents for the crystallization of PP phase, thus promoting the crystallization process of the PP component. On the other hand, *in situ* compatibilization of ZDMA occurs at the interfacial layer between PP and EPDM through the reaction

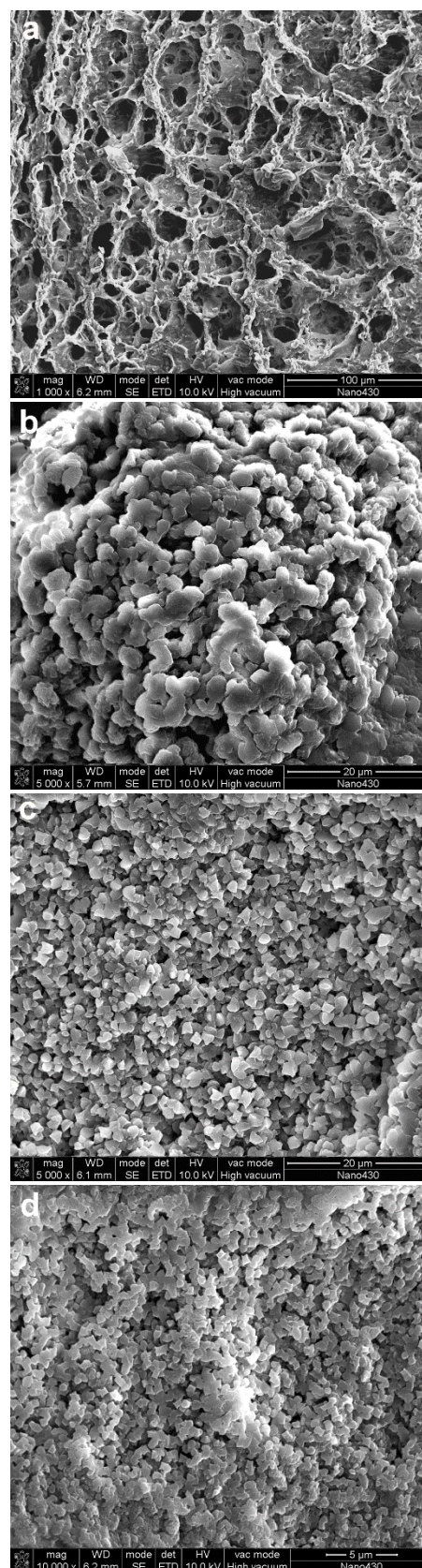


Fig. 4. SEM image for the etched cryogenically fractured surface: (a) B46 (cyclohexane-etched); (b) TZ46-0 (xylene-etched); (c) TZ46-2 (xylene-etched); (d) TZ46-3 (xylene-etched).

between the double bonds of ZDMA and the free radicals generated in both EPDM and PP chains, restricting the rearrangement of PP molecular segments during the crystallization process [17]. This leads to the decreased X_c at a higher ZDMA concentration.

Stress-strain behavior of PP/EPDM/ZDMA TPVs

Mechanical properties

To better understand the influence of ZDMA on the peroxide cured PP/EPDM TPVs, the mechanical properties for all specimens are summarized in Table 3. Representative stress-strain

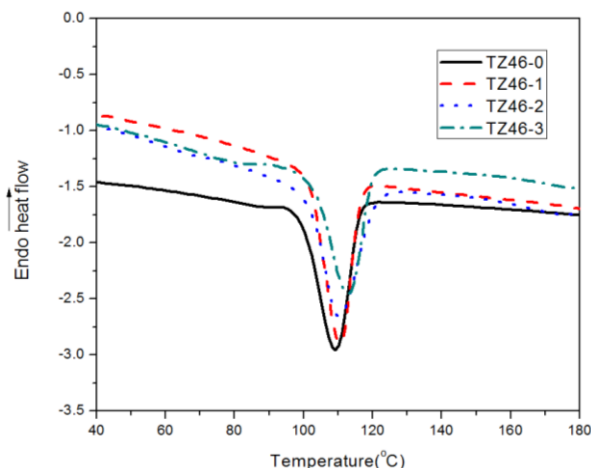


Fig. 5. DSC thermograms of the TPVs during non-isothermal crystallization

Table 2. Crystallization parameters for all specimens.

Sample	ΔH_c (J/g)	X_c (%)	T_c (°C)	T_o (°C)
B46	40.86	48.88	108.2	114.9
TZ46-0	36.26	43.63	109.5	116.6
TZ46-1	37.72	48.10	110.3	118.4
TZ46-2	35.06	47.22	110.9	119.2
TZ46-3	31.94	45.31	112.5	121.3

curves of the TPVs are shown in Fig. 6. The PP/EPDM/ZDMA TPVs display good combination of stress and strain properties: a rapid increase in tensile stress can be observed at the initial tensile and then the stress increases gradually with the larger extension of strain. All stress-strain curves show the representative elastomer character of soft and tough. Compared with the stress-strain curves of PP/EPDM blend and PP/EPDM TPV, improved tensile strength and elongation at break can be observed, due to the crosslinking of the rubber phase. The incorporation of ZDMA further improves tensile strength and elongation at break. For example, TZ46-1 exhibits tensile strength and elongation at break of about 11.8MPa and 421%, which is much higher than

7.7MPa and 250% of TZ46-0, indicating the strong reinforcing effect of ZDMA [24]. The improved mechanical properties indicate the good interaction between the ZDMA reinforced EPDM phase and the PP phase. Meanwhile, the higher crosslink density of EPDM also contributes to the improved mechanical properties.

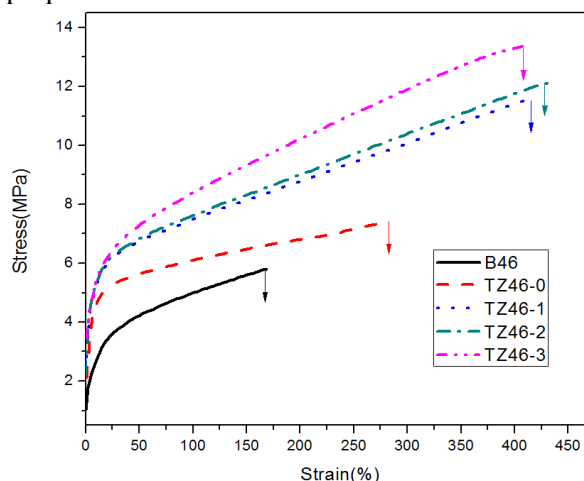


Fig. 6. Stress-strain behavior of all specimens.

Obviously, dynamic vulcanization improved the mechanical properties of the PP/EPDM blend. Incorporation of ZDMA largely improved the mechanical properties of the PP/EPDM TPVs. Especially, tensile strength and tear strength increased from 7.7MPa and 46.9kN/m to 11.8MPa and 72.3kN/m, respectively, with only 6wt% ZDMA added to the composites. This is attributed to the improved compatibility between EPDM and PP phases and the reinforced EPDM phase by ZDMA mentioned above.

In addition, ZDMA has caused a reduction of EPDM particles, as shown in the SEM images (Fig. 4), which may also contribute to the improved mechanical properties. Further increase in ZDMA concentration leads to an increased tensile strength, tear strength and tensile set at 100% elongation. The elongation at break reached maximum for ZDMA concentration of about 12wt%. The improved mechanical properties indicate that ZDMA is not only an effective *in situ* reactive compatibilizer for peroxide curing PP/EPDM TPVs, but also a strong reinforcing filler.

The effect of DCP concentration on the mechanical properties of PP/EPDM/ZDMA TPV (40/60, ZDMA concentration is 20wt% of EPDM) is also studied and shown in Fig. 7. It is clearly seen that both tensile strength and elongation at break increase with the increase of DCP concentration, which may be caused by the improved crosslink density of the rubber phase. However, further

Table 3. Mechanical properties of all specimens

Samples	B46	TZ46-0	TZ46-1	TZ46-2	TZ46-3
Tensile strength (MPa)	5.8	7.7	11.8	12.4	13.4
tensile set at 100% elongation (MPa)	5.0	6.0	7.5	7.9	8.3
Tear strength (kN/m)	42.0	46.9	72.3	77.1	86.2
Elongation at break (%)	168	250	421	439	410

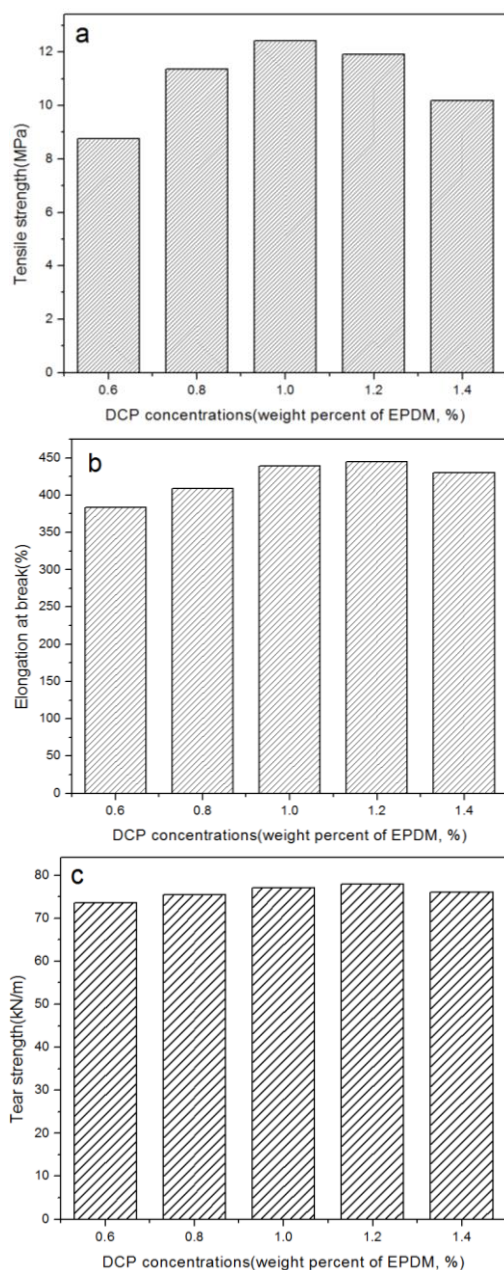


Fig. 7. Effect of DCP concentration on the mechanical properties of PP/EPDM/ZDMA TPV (40/60, ZDMA concentration is 20wt% of EPDM).

strength, which reaches a maximum value when DCP concentration is 1% of EPDM. This is due to the fact that high DCP concentration induced more serious decomposition of PP component. Elongation at break (Fig. 7b) shows the same tendency. Fig. 7c

shows that DCP concentration has little influence on the tear strength. From Fig. 7 it can be concluded that PP/EPDM TPV reaches better overall performance when the DCP concentration is 1% of EPDM

CONCLUSION

This work shows that ZDMA can function as an effective compatibilizer and, simultaneously, as a very strong reinforcing agent for PP/EPDM TPVs. The reinforced TPVs based on a PP/EPDM ratio of 40/60 displayed better overall performance when DCP concentration is 1 wt% of the EPDM component. The mechanical properties increased with increasing ZDMA concentrations. Particularly, the tensile strength and elongation at break increased from 7.7MPa and 250% to 13.4MPa and 410%, respectively, with about 18%wt ZDMA. Incorporation of ZDMA resulted in size reduction of the crosslinked EPDM particles and improved compatibility between the PP and EPDM phase, which contributed to the enhanced mechanical properties. In addition, incorporation of ZDMA promoted the crystallization process of PP but had a negative effect on its crystallinity.

REFERENCES

1. A. Y. Coran, B. Das, R. P. Patel, *US Patent*, **4**, 130 (1978).
2. R. R. Babu, N. K. Singha, K. Naskar, *J. Appl. Polym. Sci.*, **117**, 1578 (2010).
3. H. Mirzazadeh, A. A. Katbab, *Polym. Adv. Technol.*, **17**, 975 (2006).
4. Z. B. Wang, X. K. Cheng, J. Zhao, *Mater. Chem. Phys.*, **126**, 272 (2011).
5. A. Bouilloux, B. Eranst, A. Lobbrecht, R. Muller, *Polymer*, **38**, 4775 (1997).
6. U. Sundararaj, C. W. Macoko, C. K. Shih, *Polym. Eeg. Sci.*, **36**, 1759 (1996).
7. M. D. Ellul, A. H. Tsou, W. Hu, *Polymer*, **45**, 3351 (2004).
8. C. F. Antunes, M. V. Duin, A. V. Machado, *Mater. Chem. Phys.*, **133**, 410 (2012).
9. K. C. Dao, *J. Appl. Polym. Sci.*, **27**, 4799 (1982).
10. K. Naskar, *Rubber. Chem. Technol.*, **80**, 504 (2007)
11. K. Naskar, D. Kokot, J. W. M. Noordermeer, *Polym. Degrad. Stab.*, **85**, 831 (2004).
12. A. Mirzadeh, P. G. Lafleur, M. R. Kamal, C. Dubois, *Polym. Eng. & Sci.*, **52**, 1099 (2012).
13. F.R. de Risi, J.W.M. Noordermeer, *Rubber Chem. Technol.*, **80**, 83 (2007).

14. Y. K. Chen, C. H. Xu, *Polym. Composite.*, **32** 1505 (2011).
15. Z. L. Peng, X. Liang, Y. X. Zhang, Y. Zhang, *J. Appl. Polym. Sci.*, **84**, 339 (2002).
16. Y. L. Lu, M. Tian, H. Geng, L. Zhang, *Eur. Polym. J.*, **41**, 589 (2005).
17. Y. K. Chen, C. H. Xu, L. M. Cao, Y. P. Wang, X. D. Cao, *Polym. Test.*, **31**, 728 (2012).
18. Y. K. Chen, C. H. Xu, L. M. Cao, X. D. Cao, *Mater. Chem. Phys.*, **138**, 63 (2013).
19. Y. K. Chen, C. H. Xu, L. Y. P. Wang, *Polym. Eng. Sci.*, **53**, 27 (2013).
20. L. M. Cao, X. D. Cao, X. J. Jiang, C. H. Xu, Y. K. Chen, *Polym. Composite.*, **34**, 1357 (2013).
21. Y. K. Chen, C. H. Xu, X. Q. Liang, L. M. Cao, *J. Phys. Chem. B.*, **117**, 10619 (2013).
22. A. Katbab, H. Nazockdast, S. Bazgir, *J. Appl. Polym. Sci.*, **75**, 1127 (2000).
23. A. F. Antunes, M. V. Duin, A. V. Machado, *Polym. Test.*, **30**, 907 (2011).
24. Y. K. Chen, C. H. Xu, Y. P. Wang, *J. Rein. Plast. Compos.*, **31**, 705 (2012).

ЕФЕКТ НА ЦИНКОВИЯ ДИМЕТАКРИЛАТ ВЪРХУ СЪВМЕСТИМОСТТА И ЯКОСТТА НА ТЕРМОПЛАСТИЧНИ ПОЛИМЕРИ ОТ ПОЛИПРОПИЛЕН И ЕТИЛЕН-ПРОПИЛЕН ДИЕН, ПОЛУЧЕНИ ЧРЕЗ ПЕРОКСИД-ИНИЦИИРАНА ВУЛКАНИЗАЦИЯ

Л. Цао^{1,2}, К. Джианг^{1,2}, Дж. Динг^{3*}, Ю. Чен^{1,2*}

¹Лаборатория по преработка на полимери, Министерство на образованието (Югозападен технологичен университет), Гуанчжоу, Китай

²Училище за машинно и автомобилно инженерство, Югозападен технологичен университет, Гуанчжоу, Китай

³Колеж по материалознание и инженерство, Югозападен технологичен университет, Гуанчжоу, Китай

Постъпила на 8 април, 2014 г., коригирана на 8 септември, 2014 г.

(Резюме)

Термопластичните вулканизати (TPVs), основани на полипропилен (PP)/етилен-пропилен-диен (EPDM) с тегловно съотношение 40/60 са обработени *in situ* с цинков диметакрилат (ZDMA) чрез динамична вулканизация, индуцирана от пероксид. Изследвани са ефектите на динамичната вулканизация и ZDMA върху съвместимостта между фазите на PP и EPDM и механичните свойства на термопластичните вулканизати PP/EPDM. Включването на ZDMA подобрява вискозитета на стопилката на резултантните TPV. Динамичният механичен анализ (DMA) показва, че нарастването на конценмтрацията на ZDMA подобрява съвместимостта между фазите на EPDM и PP. Сканиращата електрон-микроскопия показва, че включването на ZDMA намалява размера на напречно-свързаните гумени частици. Диференциалната сканираща калориметрия е използвана за изследване на кристалинните отнасяния. Резултатите показват, че добавянето на ZDMA промотира зародишообразуването на PP, но по-високите концентрации показват отрицателен ефект върху кристалинността на PP-компонентата. Освен това е намерено, че механичните свойства на TPVs значително се подобряват от ZDMA. Добавянето на около 18 % (об.) ZDMA в термопластичните вулканизати от PP/EPDM води до повишаване на якостта спрямо усукване и удължаване на скъсване съответно от 7.7MPa и 250% до 13.4MPa и 410%, съответно.

Controlled aggregation of gold nanoparticles in a di-ureasil matrix. Optical and micro indentation investigation

M. P. Slavova^{1,2*}, G. I. Zamfirova³, V. I. Boev¹, V. T. Gaydarov⁴, L.K. Yotova¹, M.J.M. Gomes⁵, C. J. R. Silva⁶

¹ Institute of Electrochemistry and Energy Systems, Bulgarian Academy of Sciences, Sofia, BULGARIA

² Department of Biotechnology, University of Chemical Technology and Metallurgy, Sofia, BULGARIA

³ Department of Machine Elements and Chemistry, University of Transport., Sofia, BULGARIA

⁴ Department of Electrical Engineering and Physics, University of Transport., Sofia, BULGARIA

⁵ Centre of Physics, University of Minho, Braga, PORTUGAL

⁶ Centre of Chemistry, University of Minho, Braga, PORTUGAL

Received June 19, 2014, Accepted August 13, 2014

Nanocomposite materials with an organic-inorganic urea-silicate (di-ureasil) based matrix containing gold nanoparticles (NPs) were synthesized and characterized by optical (UV/Vis) spectroscopy and indentation measurement. The urea silicate gels were obtained by reaction between silicon alkoxyde modified by isocyanate group and polyethylene glycol oligomer with amine terminal groups in presence of catalyst. The latter ensures the successful incorporation of citrate-stabilized gold NPs in the matrix. It is shown that using a convenient destabilizing agent (AgNO₃) and governing the preparative conditions, the aggregation degree of gold NPs can be controlled. The developed synthesis procedure significantly simplifies the preparative procedure of gold/urea silicate nanocomposites, compared to the procedure using gold NPs, preliminary covered with silica shells. Mechanical properties of the prepared sample were characterised using depth sensing indentation methods (DSI) and an idea about the type of aggregation structures was suggested.

Keywords: Nanocomposite; Di-ureasil matrix; Gold nanoparticles; Nanoparticles aggregation; Sol-gel

INTRODUCTION

Producing nanocomposite functional materials for optical applications has attracted much attention in the last decade. Among different optical functionalities, metal NPs offer a great potential for applications in nonlinear optical devices, such as ultrafast optical switches and filters, and for uses as catalysts or sensors. The transfer of NPs into solid substrates while retaining the characteristic properties of single particles, i.e., preventing aggregation, is an important technological task which has to be solved in manufacturing practice.

The matrix itself must satisfy a number of requirements such as a high optical transparency in the visible range, mechanical, and chemical stability. Sol-gel process provides a straightforward and versatile fabrication method for the production of a large number of transparent glassy-like substances. The advantages of this process are low processing temperature, high purity of precursors, good uniformity, reproducibility of the composition and processability. Highly transparent hybrid organic-inorganic structures, where organic and

inorganic components are bonded through strong chemical bonds, were prepared by this method. Typical representatives of the covalently linked organic-inorganic materials are the so-called urea silicates or di-ureasils. Optically clear and elastic organic-inorganic di-ureasil nanocomposites containing gold NPs, stabilized by uniform silica shell were produced by mixing preformed NPs colloidal dispersions with urea silicate neat monomer prior to sol-gel transition. The silica shell was used to maintain the colloidal stability during the processes of hydrolysis and condensation [1].

Recently, we have established a procedure, allowing us to embed gold NPs, stabilized by pure electrostatic forces, thus avoiding the stage of covering the NPs with protected silica shells. This approach simplifies the manufacturing of the metal-doped urea silicates as the growth of silica shells around the metal NPs is a delicate and rather time consuming operation. Furthermore, the use of a convenient destabilizing agent (AgNO₃) permitted us to control the aggregation degree of gold NPs. In that way we can produce gold/ureasilicate nanocomposites with different absorption profiles, as the formation of large aggregates causes irreversible changes in their optical properties.

* To whom all correspondence should be sent:
E-mail: mslavova@bas.bg

In this work we present the preparation procedure of di-ureasil nanocomposites with embedded citrate-stabilized gold NPs. The reliable preservation of the nanoparticles in the matrix is confirmed by optical absorption measurements and indentation characteristics. It is shown that metal NPs, embedded in the ureasilicate matrix could be fixed at different aggregation stages by controlling the concentration of the aggregation agent in the reaction medium.

EXPERIMENTAL

Materials

O,O-bis(2-aminopropyl)-polypropylene glycol-block-polyethylene glycol-block-polypropylene glycol-500 (Jeffamine ED-600, Fluka) was dried under dynamic vacuum before use. 3-Isocyanate propyl-3-ethoxysilane (ICPTES, Aldrich), tetrachloroauric acid (Aldrich), 3-sodium citrate dihydrate (Aldrich), absolute ethanol (Riedel-de Haën), citric acid monohydrate (Merck) were used as received. Distilled water with a resistance around 18 MS/cm was used for the preparation of dilute aqueous solutions.

Preparation of samples

Urea-silicate neat monomer was prepared by mixing 0.936 mmol Jeffamine ED-600 and 1.870 mmol of ICPTES under stirring. Spherical gold NPs (15 nm) were prepared by boiling 5×10^{-4} M HAuCl₄ aqueous solution in the presence of 1.6×10^{-3} M sodium citrate aqueous solution, for 15 min [2]. Later, citric acid in ethanol solution, served as a catalyst for the sol-gel process, citric-stabilized Au colloid solution, and aggregation agent (AgNO₃ aqueous solution) were added to the liquid monomer. Table 1 shows the amount of AgNO₃ used for the preparation of the samples.

The mixtures were transferred to polystyrene cuvettes and dried in an oven at 40°C for 48 h. Finally, transparent, free of cracks samples with a base of 21 mm² and height of 7 mm were obtained. A photograph of the samples is presented in Fig. 1.



Fig. 1. Au/urea silicate samples with different degree of Au NPs aggregation.

Depth-sensing indentation method

The method known as either depth-sensing indentation (DSI) or instrumented indentation testing (IIT) is based on the experimental measured indentation curves (relationship between the test force and indentation depth) (ISO 14577-1).

The following micro indentation characteristics were determined (ISO 14577-1) [3]:

$$\text{Dynamic hardness: } HMV = a F/h^2, (1)$$

where (F) is the value of the instant load in a loading and unloading testing regime, ($a = 3.8584$) is a constant which depends on the shape of the indenter and (h) is the indentation depth. This characteristic reveals how the material responds to total deformation during the indentation test including plastic, elastic and viscoelastic deformation components.

– Martens hardness was determined from the slope of the increasing force/indentation depth curve in the 50% ÷ 90% P interval and characterises the material resistance against the penetration (P is the maximum applied load):

$$HM_s = 1/(26.43 \text{ m}^2), (2)$$

This characteristic has similar physical sense as dynamic hardness, but characterises the material properties at the maximum indentation depth at constant load.

– Indentation hardness is a measure for the material resistance to permanent deformation.

$$Hit = P/24.50h_c^2, (3)$$

where (h_c) is the so called “contact depth” which means the imprint depth when there is a contact between the indenter and the surface of the test piece.

– Microhardness profiles are dependences of Vickers hardness on the applied load (P), or on the penetration depth (h), respectively.

$$HV=f(P); HV=f(h), (4)$$

– Indentation Elastic Modulus calculated from the unloading part of the dependence by using the equation:

$$1/E_r = (1 - \nu_s^2)/E_{it} + (1 - \nu_i^2)/E_i, (5)$$

where (E_r) is the experimental converted elastic modulus based on indentation contact, (ν_s) is the Poisson ratio of specimen, whereas (E_i) and (ν_i) are the Young's modulus and Poisson's ratio for the indenter, respectively.

– Indentation creep which is a relative change in the indentation depth at constant test force:

$$Cit = (h_2 - h_1)/h_1 \quad (F = \text{const.}), (6)$$

where (h_1) and (h_2) are indentation depths at the beginning and the end of the creep measurement [4].

The tests were provided on the dynamic ultra microhardness tester DUH-211S. All measurements were performed at room temperature and the test regime was: loading with a constant loading speed of 0.2926 mN/s till 3 mN, then holding this load for 1 min and then unloading. For viscoelastic materials the relationship between load and depth of penetration is not linearly dependent. That is, for a given load the resulting depth of penetration may depend upon the rate of load application, as well as on the magnitude of the load itself. Ten measurements were made for each sample.

RESULTS AND DISCUSSION

The optical properties of a colloidal dispersion of spherical particles with a radius R can be described by Mie theory, who first explained the origin of the red color of gold colloids [5]. In a dilute colloidal solution containing N particles per unit volume (cm^3), the measured absorbance over the path length d is:

$$A = \log_{10} \frac{I_0}{I(d)} = \frac{NC_{ext}d}{2.303}, \quad (7)$$

where C_{ext} is the extinction cross-section of a single particle, d is path length and I_0 and $I(d)$ are incoming and transmitted light intensities. For a spherical particle with radius R , much smaller than the wavelength of light only the dipole oscillation contributes significantly to the extinction cross-section (dipole approximation) and C_{ext} can be written as the following relationship [6]

$$C_{ext} = \frac{24\pi^2 R^3 \epsilon_m^{3/2}}{\lambda} \frac{\epsilon''}{(\epsilon' + 2\epsilon_m)^2 + \epsilon''^2}, \quad (8)$$

where ϵ' and ϵ'' are the real and imaginary part of the wavelength dependent dielectric function and ϵ_m is the dielectric function of the medium.

Fig. 2 presents the experimental absorption spectrum of the initial aqueous solution of citrate-stabilized gold NPs with an average size of 15 nm, the experimental spectrum of the solid di-ureasil monolith doped with gold NPs, prepared without addition of the aggregation agent (sample 1) and the theoretical spectrum, calculated for the sample 1. The former one is based on eq. 2 utilizing the real and imaginary parts of the dielectric function for bulk gold [7].

There is an expected shift in the position of the plasmon peak obtained for the sample 1 (situated at 529 nm) with respect to the initial colloidal solution in water (located at 519 nm). This is due to a refractive index increase when changing the dispersion medium from ethanol ($n = 1.33$) to di-ureasil ($n = 1.508$) The plasmon peak position

obtained for sample 1 is in coincidence with the calculated one obtained by using the data for dielectric constant of Johnson and Christy and refractive index of the urea silicate matrix (1.508). It is obvious that the optical response of the prepared nanocomposite resembles that of the starting colloid in the range of plasmon band.

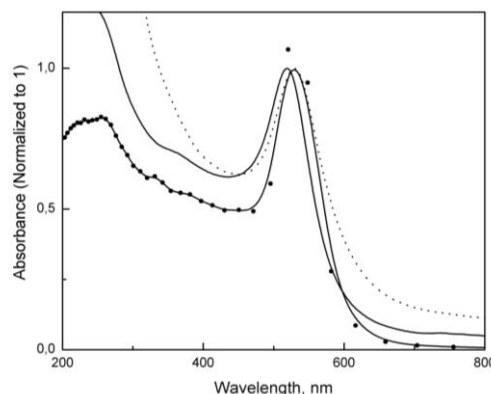


Fig. 2. Experimental absorption spectrum of the initial gold colloid in water (—), experimental absorption spectrum of sample 1 (.....) and calculated absorption spectrum of sample 1 (-•-•-). The calculated spectrum is B-spline connected.

Absorption spectra of the samples containing gold NPs with different degree of aggregation are presented in Fig. 3. Numbers over the curves correspond to the samples designation, presented in the Table 1.

Table 1. Amount of AgNO_3 used for the samples preparation.

Samples designation	Molar content of AgNO_3 , added to the reaction mixture [nmol]
1	—
2	88.5
3	111
4	150
5	177

It is seen from Fig. 2 that with increase of AgNO_3 concentration the first plasmon maximum at about 520 nm is broadening and the second maximum at ~700 nm appears and is getting more pronounced. It is clear that gold NPs, embedded in the matrix, undergo changes in color upon the process of aggregation due to the coupling interactions between the surface plasmon fields of the particles [8]. Appearance of longitudinal mode can be explained by formation of dimers and aggregates of higher order, which do not have spherical symmetry and can be roughly represented by equivalent ellipsoids.

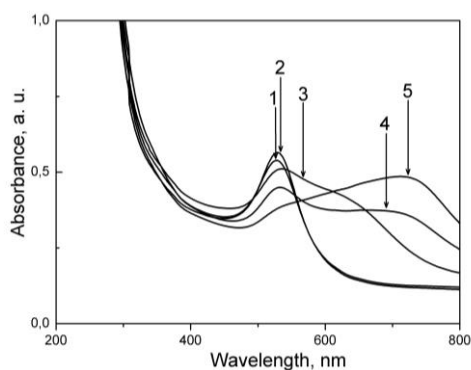


Fig. 3. Absorption spectra of the urea silicate nanocomposites with different degree of NPs aggregation.

Fig. 4 presents the indentation curves (Load – Indentation depth) for all samples. It can be seen that the curves of the loading and unloading are substantially parallel, which means that the samples are extremely elastic.

Fig. 5 shows the generalized arithmetic average of measured indentation characteristics for the studied samples. The lines between the points are only for visual facilitation of the trends.

From Figs. 5 a) and b) it becomes clear that the microindentation parameters change on adding AgNO_3 . The first portion decreases HMV, HMs and indentation elastic modulus E_{it} , while micro hardness characteristics H_{it} and HV^* increase. Taking into account that HMV and HMs characterize the total resistance against the penetration and H_{it} and HV^* – the resistance only against plastic deformation it could be concluded that resistance against elastic deformation decreases or the sample becomes more elastic. The next additions of AgNO_3 lead to improving all studied characteristics (Fig. 5a), b) and c) till 150 nmol (sample 4). Knowing that the quantity of the gold NPs is the same for all samples, the changes in mechanical properties could be attributed only to arising of different aggregation structures as a consequence of AgNO_3 addition. There are many publications dealing with the type of aggregation structures of gold NPs according to the type and quantity of aggregation agent: filamentary, racemose or cross-linked structures [9-11]. Moreover, the gold particles keep their individuality in the aggregates. We suppose that in our case the first portion of AgNO_3 partially destroys the stabilizing layer on the gold particles leading to the formation of loose cross-linked structure of gold particles. Obviously, the electrostatic forces between the particles are strong enough to improve the elasticity of the sample. Further AgNO_3 addition results in a more complete

destruction of the charged surface layer and more complete multilateral linking between the particles, making the cross-linked structure denser. Mechanical properties are improved. At a concentration of destabilizing agent higher than that in sample 4, the aggregation processes are so pronounced that the cross-linked structure is torn and regrouped in a denser cluster or racemose structure. The racemose formations so obtained do not have so much resistance as the cross-linked structure and microindentation characteristics decrease.

Addition of AgNO_3 has practically no influence on the creep processes (Fig.5 d). Ground for such interpretation of the micromechanical results gives us the research and TEM micrographs of aggregates of gold nanoparticles published in [10] (Fig. 6) and [11] (Fig. 7 b) for 500 seconds of electron-beam exposure inside a TEM liquid cell at 200 kV. Scale bar: 200 nm.

It can be assumed that the aggregation process starts in a small volume with a higher local concentration of AgNO_3 solution, just after its addition. When the solution is homogenized, the global concentration of AgNO_3 drops and the aggregation stops. More dilute solution of AgNO_3 results in a smaller degree of aggregation. Simultaneously, the viscosity of the urea silicate monomer rapidly increases within a short period of time, fixing the formed aggregates in the urea silicate gel.

CONCLUSIONS

Gold NPs stabilized by pure electrostatic forces were successfully introduced in the urea silicate matrix, avoiding the stage of covering the NPs with protected silica shells and a highly transparent monolith was obtained.

Using a common gold colloidal solution containing particles with unique size and shape and governing the preparative conditions, di-ureasil nanocomposites containing gold NPs aggregates were produced. The arrested aggregation of gold NPs was previously achieved in gelatin films [8]. However, this was obtained for the first time in highly transparent monolith samples.

Micromechanical characteristics change according to the type of aggregation structure. We suppose that the improvement of elastic indentation modulus and resistance against total and plastic deformation is due to the cross-linked structure formed by the gold NPs.

When the metal nanoparticles form racemose structures the mechanical properties slightly decrease.

This approach could be a promising way for the development of flexible filters with desired absorption profile and improved mechanical

properties on the basis of immobilized metal fractal aggregates.

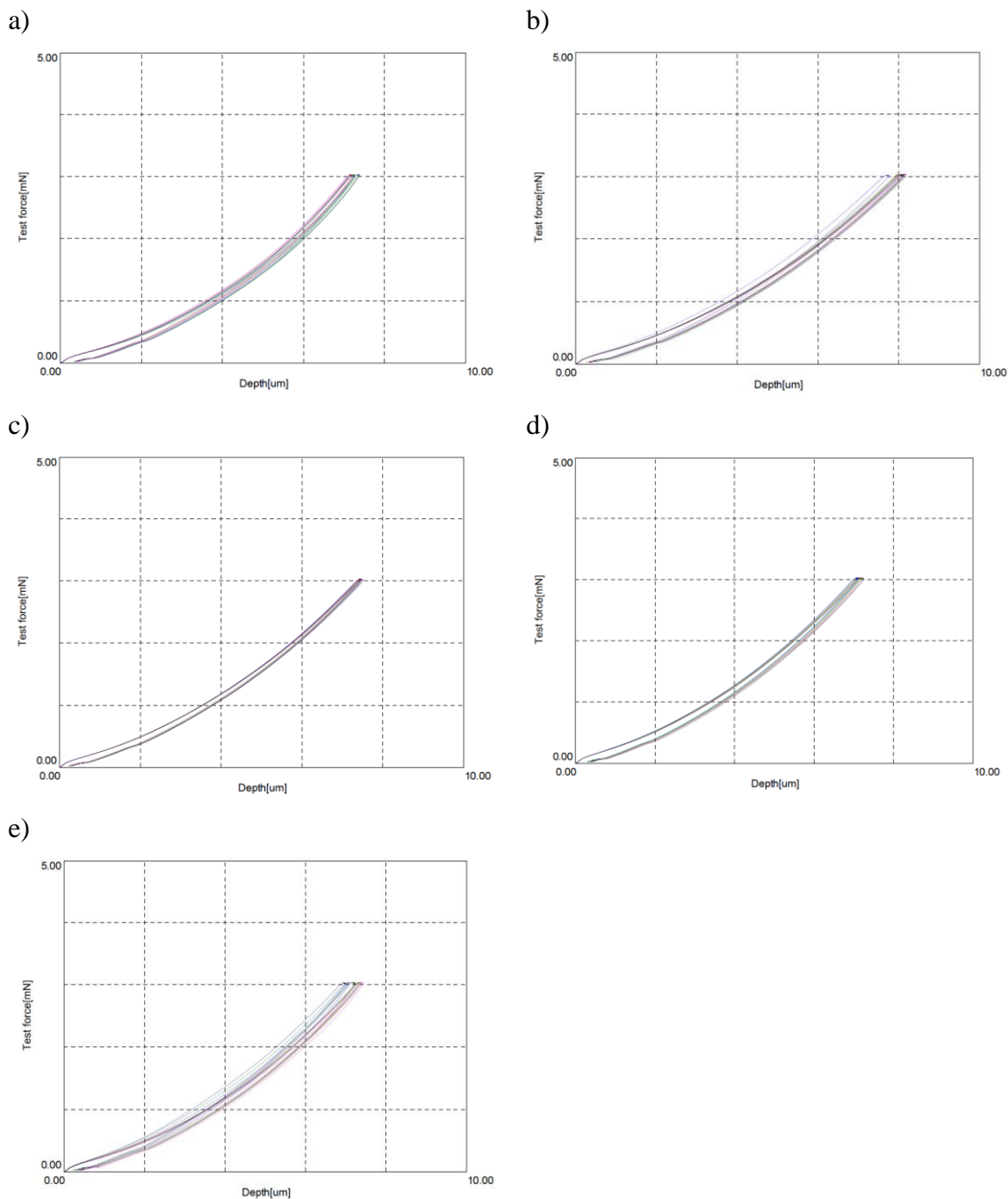


Fig. 4. Load/unload displacement curves: a) sample 1; b) sample 2; c) sample 3; d) sample 4; e) sample 5

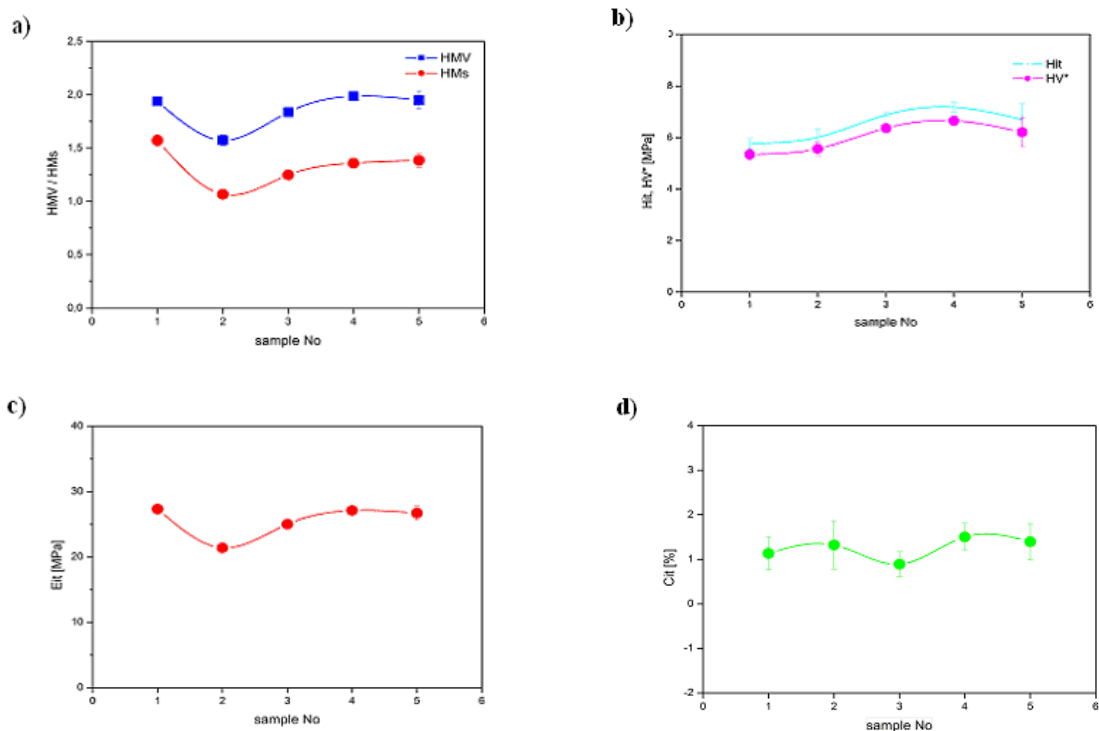


Fig. 5. a) Dynamic microhardness and Martens microhardness; b) Indentation microhardness and Vickers hardness; c) Indentation Elastic Modulus; d) Indentation creep

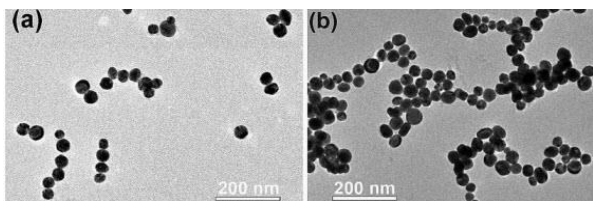


Fig. 6. Cetyl-3-methylammonium-ion-coated gold nanoparticles before (a) and after aggregation

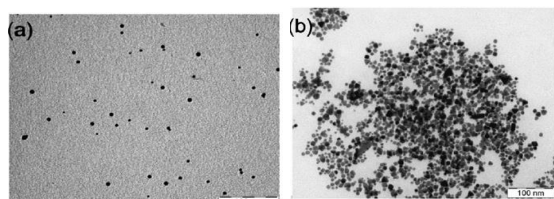


Fig. 7. TEM micrographs of I (a) and II (b) gold NPs samples used for the synthesis of nanocomposites, scale bar: 100 nm

REFERENCES

1. V. I. Boev, J Pérez-Juste, I Pastoriza-Santos, CJR Silva, MJM Gomes, LM Liz-Marzán, *Langmuir*, **20**, 10268 (2004).
2. J. Turkevich, P. C. Stevenson, J. Hiller, *Discuss. Farad. Soc.* **11**, 55 (1951).
3. *ISO/FDIS 14577-1:2013(E)*.
4. G. Zamfirova, V. Gaydarov, *Proc. 8th Intern. Congress "Machines, Technologies, Materials" Varna, Bulgaria, 2011*, p 73.
5. G. Mie, *Ann. Phys.*, **25**, 329 (1908).
6. P. Mulvaney, *Langmuir*. **12**, 788 (1996).
7. P. B. Johnson, R. W. Christy, *Phys. Chem. B*, **6**, 4370 (1972).
8. M. Quinten, D. Schoenauer, U. Kreibig, *Z. Phys. D*, **26**, 239 (1989).
9. J. Turkevich, G. Garton, P. C. Stevenson, *J. Colloid Sci. Suppl.*, **9**, 26 (1954).
10. Y. Liu, X. M. Lin, Y. Sun, T. Rajh, *J. Am. Chem. Soc.*, **135**, 3764 (2013).
11. I. Pardinás-Blanco, C. E. Hoppe, M. A. Lopez-Quintela, J. Rivas, *J. Non-Cryst. Sol.*, **353**, 826 (2007).

КОНТРОЛИРАНО АГРЕГИРАНЕ НА ЗЛАТНИ НАНОЧАСТИЦИ В ДИУРЕАСИЛАТНА МАТРИЦА. ОПТИЧНО И МИКРОИДЕНТАЦИОННО ИЗСЛЕДВАНЕ

М. П. Славова^{1,2*}, Г. И. Замфирова³, В. И. Боев¹, В. Т. Гайдаров⁴,
Л. К. Йотова², М. Д. М. Гомес⁵, К. Д. Р. Силва⁶

¹ *Институт по електрохимия и енергийни системи, Българска академия на науките, София, България*

² *Катедра биотехнологии, Химикотехнологичен и металургичен университет, София, България*

³ *Катедра машинни елементи, материалознание и химия, Висше транспортно училище, София, България*

⁴ *Катедра електротехника и физика, Висше транспортно училище, София, България*

⁵ *Център по физика, Университет Миньо, Португалия*

⁶ *Център по химия, Университет Миньо, Португалия*

Получена на 19.07. 2014, Приета на 13.08.2014

(Резюме)

Нанокompatитни материали с органично-неорганична карбамид-силикатна матрица (ди-уреасили), съдържаща златни наночастици (НП), са синтезирани и характеризирани с оптична (UV/ Vis) спектроскопия и индентационни измервания. Силикатните урея гелове са получени чрез реакция между силициев алкоксид модифициран с изоцианатна група и олигомер полиетилен гликол с аминни крайни групи в присъствие на катализатор. Последният гарантира успешното включване на цитрат стабилизирани златни НП в матрицата. Показано е, че степента на агрегация на златните НП може да се контролира с помощта на подходящ дестабилизиращ агент (AgNO_3) и промяна в условията на получаване.

Разработената процедура за синтез значително опростява подготвителна процедура на златото/ урея силикатни нанокompatити, в сравнение с процедурата за използване на предварителна покрити с кварцови черупки златни НП. Механичните свойства на приготвената проба са охарактеризирани с помощта на измерване на дълбочинно проникващ индентационен метод (DSI) и е направено предположение за вида на агрегационните структури.

Comparative investigation of the feasibility of bacterial biofilms formation on the surface of the hybrid material UREASIL

R. T. Gergova¹, M. P. Slavova^{2,3*}, V. I. Boev², M. S. Mourdjeva⁴, L. K. Yotova¹, R. T. Georgieva-Nikolova⁵

¹Department of Medical Microbiology, Faculty of Medicine, Medical University of Sofia, Sofia, Bulgaria

²Department of Biotechnology, University of Chemical Technology and Metallurgy, Sofia, Bulgaria

³Institute of Electrochemistry and Energy Systems, Bulgarian Academy of Sciences, Sofia, Bulgaria

⁴Institute of Biology and Immunology of Reproduction, Bulgarian Academy of Sciences, Sofia, Bulgaria

⁵Department of Chemistry and Biochemistry, Faculty of Medicine, Medical University of Sofia, Sofia, Bulgaria

Received June 19, 2014, Accepted August 19, 2014

The purpose of this study is to determine the possibility of biofilm formation from different bacterial strains on the UREASIL surface as compared with the formation of biofilms on glass surface.

Seven gram-positive and eight gram-negative bacterial strains were used in this study. The feasibility of microbial biofilm formation on the surface of the new material UREASIL and on the surface of glass (control samples) was detected by three methods: determination of the number of alive bacterial cells in the biofilms; determination of the protein content in the biofilms by a modified Lowry method; confocal laser scanning microscopy for detection/visualization of the biofilms.

The structure of UREASIL was more unfavorable for adhesion and breeding than that of the glass, but problematic species with strong production of capsule substance or slime, such as *Klebsiella pneumoniae* and *Pseudomonas aeruginosa* formed thick biofilms after 48 h cultivation on UREASIL, which were detected by three methods: confocal fluorescence microscopy, modified Lowry method and counting the number of surviving bacteria that colonized the surface of the glass and the UREASIL.

Key words: UREASIL, ureasilicate, biofilm formation

INTRODUCTION

Biofilm is the microbial lifestyle in natural and manmade environments. The initial microbial adhesion to surfaces is a complex process dependent on the non-specific interactions between bacteria and the surface, including van der Waals interactions, electrostatic forces, Lewis acid-base and hydrophobic interactions, the latter being the strongest of all long-range non-covalent forces [1]. After initial attachment, the accumulation step in biofilm formation depends on the bacterial proliferation, exopolysaccharide matrix production and intercellular adhesion [2]. The cells in the microbial biofilm demonstrate many changes in their metabolism: a higher biochemical activity by producing more new enzymes and metabolic adaptation mechanisms to a new variant of growth display. The biofilm formations present a higher level of resistance to all physical and chemical factors in comparison to their planktonic forms. Many genetic mechanisms of the cells play a role for the adaptation to the biofilm, a wide range of

characteristics provide a number of advantages over planktonic bacteria [3-5].

The dynamically developing industry constantly needs new products which satisfy different specific requirements. Very often the growth of biofilm formations is around a foreign body in patients, around medical implants and can progress to development of an infection. It has been estimated that the subjects from bacterial biofilms are generally about 1000-fold less susceptible to the effects of commonly used antimicrobial agents than their analogous planktonic cells and are highly resistant to the phagocytosis of the immune system phagocytes. In addition, the various attacks of the antimicrobial immunity are neutralized by the same formation. That is a reason for the development of chronic infections mediated by biofilms and it is a problem for their eradication [3,6,7].

In search of promising new materials we turned to ureasils: sol-gel materials. Sol-gel process is one of the most versatile methods for the preparation of organic-inorganic hybrid materials due to the low temperature of synthesis [8]. The incorporation of inorganic materials into organic matrices ensures physical rigidity, photophysical and thermal stability of the obtained hybrid materials [9]. It is

* To whom all correspondence should be sent:
E-mail: mslavova@bas.bg

widely used for preparation of glassy matrices for optical applications. However, flexibility of pure inorganic glasses obtained by the sol-gel method is limited and they are often susceptible to cracking during a drying stage. Including organic polymers in an inorganic silica framework makes the final material more flexible [10]. This approach was used for the synthesis of new organic-inorganic materials based on polyether chains covalently linked to a silica framework by urea bridges, referred to as ureasilicates or ureasils [11]. These materials were initially used as a host matrix for highly luminescent europium salts [12-15], ionic conductive lithium salts [16,17], magnetic nanoparticles (NPs) [18,19] and organic dyes [20]. Recently, it was demonstrated that optical functionalities, such as semiconductor [21-24] or metal [25] NPs, can be successfully incorporated into ureasilicates, which makes them promising materials for fabrication of non-linear optically active devices.

Ureasilicates are obtained by hydrolysis and condensation of a ureasilicate precursor prepared by reaction between a silicon ethoxide modified by isocyanate group (referred to as ICPTES) and a polyoxyalkyleneamine (referred to as Jeffamine) [26].

The purpose of this study is to determine the possibility of biofilm formation from different bacterial strains on the surface of the new hybrid material UREASIL in comparison with biofilm formation on other materials. This is done to investigate possible biomedical application of UREASIL.

MATERIALS AND METHODS

UREASIL

O,O-bis(2-aminopropyl)-polypropylene glycol-block-polyethylene glycol-block-polypropylene glycol-500 (Jeffamine ED-600, Fluka) was dried under dynamic vacuum before use. 3-Isocyanate propyltriethoxysilane (ICPTES, Aldrich), tetrachloroauric acid (Aldrich), trisodium citrate dihydrate (Aldrich), absolute ethanol (Riedel-de Haën), citric acid monohydrate (Merck) were used as received. Distilled water with a resistance around 18 MS/cm was used for the preparation of dilute aqueous solutions.

Microbial strains: Seven gram-positive and eight gram-negative strains were used for the experiments in this study. Two control strains from American type culture collection *Staphylococcus aureus* MSSA (ATCC29213) and *Escherichia coli* (ATCC25922) and the following clinical isolates

from patients, more of them multidrug resistant (MDR) were used: *Enterococcus faecalis* (n=3), *Staphylococcus aureus* MRSA (n=3), *Moraxella catarrhalis* BRO+ (n=1), *Escherichia coli* ESBL (n=1), *Klebsiella pneumoniae* ESBL (n=1), *Enterobacter aerogenes* MDR (n=1), *Morganella morganii* MDR (n=1), *Pseudomonas aeruginosa* MDR (n=1), *Acinetobacter baumannii* MDR (n=1), *Stenotrophomonas maltophilia* (n=1). The strains were stored in skim milk at -70°C. Before laboratory testing they were three times subcultivated, reproduced and after that they were used in the experiments.

Chemical materials: Na₂CO₃, NaOH, Na tartrate and CuSO₄ with chemical purity; 2N Folin-Ciocalteu reagent.

EXPERIMENTAL PROCEDURE

Synthesis of the ureasilicate monoliths

The synthesis of the ureasilicate monoliths included several steps. At the first step stoichiometric amounts of Jeffamine and ICPTES (1:2;R=2.0) were mixed in a glass vessel under stirring at 200 rpm for 10 min, so that the rapid uncatalyzed reaction between amino and isocyanate groups forming polyurea linkages took place [11]. The obtained material will be referred to hereafter as a conventional ureasilicate precursor. At the second step an additional amount of ICPTES was introduced in order to adjust the desired molar ratio between ICPTES and Jeffamine in the final mixture. Ethanol was used as a homogenizing agent and was added 5 min later. The third step consisted of the catalyzed hydrolysis/condensation of the mixture by addition of ammonia or citric acid aqueous solution. The mixture was stirred for 10 min more and poured into a polystyrene cell, covered with Parafilm[®], which was pin-holed after gelation at room temperature. The gelation time varied from 1 h to 3 days depending on the catalyst used and the R value. During the final step the cell with the resulting gel was kept in an oven at 40°C for two weeks, which assured completion of hydrolysis/condensation reactions and evaporation of residual liquids. This drying process led to sample shrinkage of about 30% of total volume [26].

Counting CFU/ml of surviving bacteria

The bacterial strains were grown on a Brain heart infusion (BHI) agar (Oxoid microbiology products, Cambridge, UK) at 35°C overnight. The suspension of each of them was prepared in BHI broth (Oxoid microbiology products, Cambridge,

UK) with bacterial density of at least $1.5-2 \times 10^8$ colony-forming units (CFU/ml). It was inoculated with 100 μ l of a pure microbial culture on the UREASIL fragments in a 96-well polystyrene microtiter plate (Nunc) and on the wells without Ureasil and was incubated at 35°C for 48 h. After the incubation the infected broth from the wells was aspirated under sterile conditions and the samples were washed with 200 μ l of PBS. Using serial 10-fold dilution and counting the value of CFU/ml on the BHI agar, the number of living bacterial cells and the concentration of biofilm were determined. The controls used were: three controls of UREASIL with sterile PBS, sterile broth and sterile water; and the same controls on the wells without UREASIL.

Modified Lowry method

The protein content was measured using a modified Lowry method [27]. The principle behind the Lowry method of determining protein concentrations [28] lies in the reactivity of the peptide nitrogens with copper [II] ions under alkaline conditions and the subsequent reduction of the Folin-Ciocalteu phosphomolybdic phosphotungstic acid to heteropolymolybdenum blue by the copper-catalyzed oxidation of aromatic acids.

10 μ l of the sample washings were diluted to 1 ml with distilled water. First, reagent A: 2% Na_2CO_3 in 0,1N NaOH, reagent B: 1% $\text{CuSO}_4 \cdot 5\text{H}_2\text{O}$ and reagent C: 2% sodium tartrate, were prepared. Reagent D was prepared by mixing reagents B and C in the ratio 1:1. Reagent D was prepared just prior to use. Thereafter 5 ml of mixed reagents A and D in a ratio of 1:50 were added and stirred for 140 min. Then 0.5 ml of 1N Folin-Ciocalteu reagent (phosphomolybdotungstate) were added. After 45 min the absorbance was measured at 750

nm against a control containing the same components without the microbial culture. The amount of protein was determined by the standard. As a reference a solution of bovine serum albumin was used.

Confocal laser scanning microscopy:

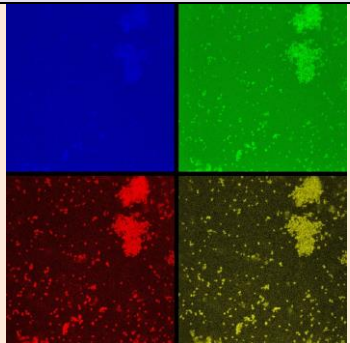
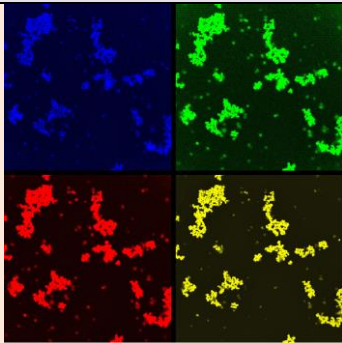
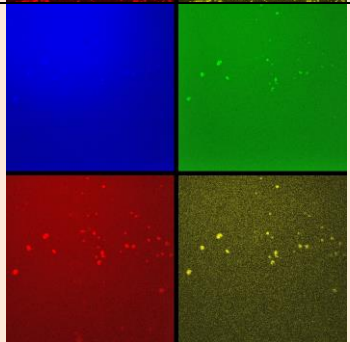
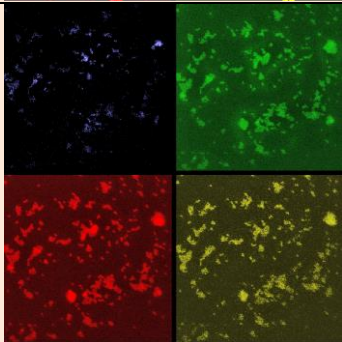
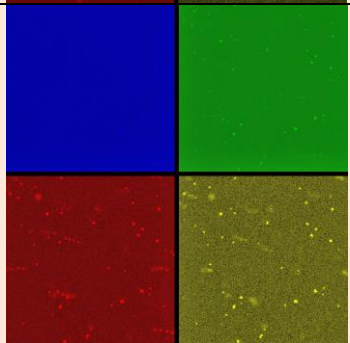
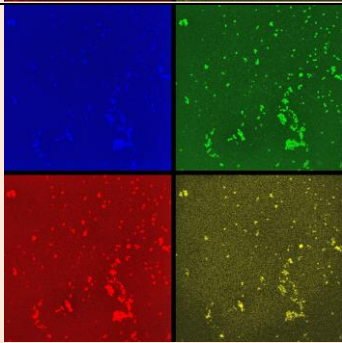
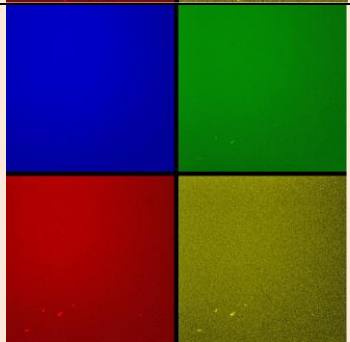
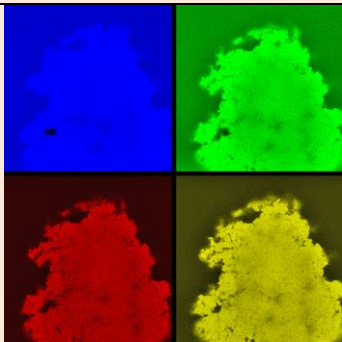
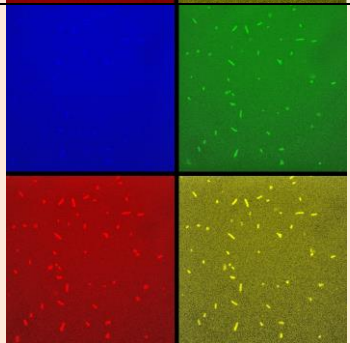
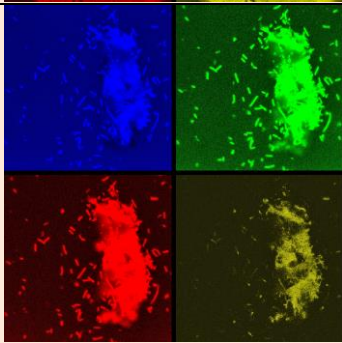
Confocal laser scanning microscopy is an important method for the study of biofilm structure. This is a non-destructive and non-invasive method [29]. Confocal laser scanning microscopy allows the detection and localization of the biofilm on the hybrid material UREASIL.

Glass coverslips covered with the hybrid material UREASIL and control glass coverslips were placed in a 6-well plate with BHI broth (Oxoid microbiology products, Cambridge, UK) and inoculated with 100 μ l of a pure microbial culture. After 48 h incubation at 35°C for forming a biofilm the culture media was removed and the biofilms were fixed in 2.5% GA in PBS at 8°C for 24 h. The fixed biofilms were rinsed 5 times with PBS before staining with 0.1% (w/v) acridine orange (AO) (Sigma Chemical Co., St. Louis, MO, USA) in PBS at room temperature for 5 min. AO is a membrane permeant nucleic acid stain that intercalates dsDNA and binds to ssDNA, as well as to ssRNA through dye-base stacking to give a broad fluorescence spectrum when excited at 476 nm. The biofilms were rinsed again as described above and were mounted on glass slides using Fluoromount-G (SouthernBiotech, Birmingham, AL, USA). Images were taken using a confocal microscope Leica DM2500 (Leica Microsystems, Wetzlar, Germany).

After immobilization, the QCM-resonator was put into 1 mL distilled water.

Table 1. Microbial biofilm detected by counting surviving bacteria

Microbial species (number of strains)	Microbial number over UREASIL [cfu/ml]	Microbial number over glass [cfu/ml]
<i>Staphylococcus aureus</i> MSSA (ATCC29213)	7×10^000	3×100^000
<i>Staphylococcus aureus</i> MRSA (n=2)	8×100^000 ; $3 \times 1^000^000$	$6 \times 1^000^000$; $2 \times 10^000^000$
<i>Streptococcus intermedius</i> (n=2)	3×100^000 ; $2 \times 1^000^000$	9×100^000 ; $7 \times 1^000^000$
<i>Enterococcus faecalis</i> (n=3)	9×10^000 ; 4×100^000	$4 \times 10^000^000$; $1 \times 10^000^000$
<i>Moraxella catarrhalis</i> bro2+ (n=1)	8×1^000	5×10^000
<i>Escherichia coli</i> (ATCC25922)	5×10^000	3×100^000
<i>Escherichia coli</i> ESBL (n=1)	9×10^000	$2 \times 10^000^000$
<i>Klebsiella pneumoniae</i> ESBL (n=1)	5×100^000	$8 \times 100^000^000$
<i>Morganella morganii</i> MDR (n=1)	$6 \times 10^000^000$	$8 \times 100^000^000$
<i>Pseudomonas aeruginosa</i> (n=1)	$7 \times 10^000^000$	$8 \times 1^000^000^000$
<i>Acinetobacter baumannii</i>	5×100^000	$4 \times 100^000^000$
<i>Stenotrophomonas maltophilia</i> (n=1)	9×10^000	$7 \times 100^000^000$

Stain	A. UREASIL		B. Glass	
<i>Staphylococcus aureus</i> MRSA				
<i>Streptococcus intermedius</i>				
<i>Enterococcus faecalis</i>				
<i>Moraxella catarrhalis</i>				
<i>Escherichia coli</i> ESBL				

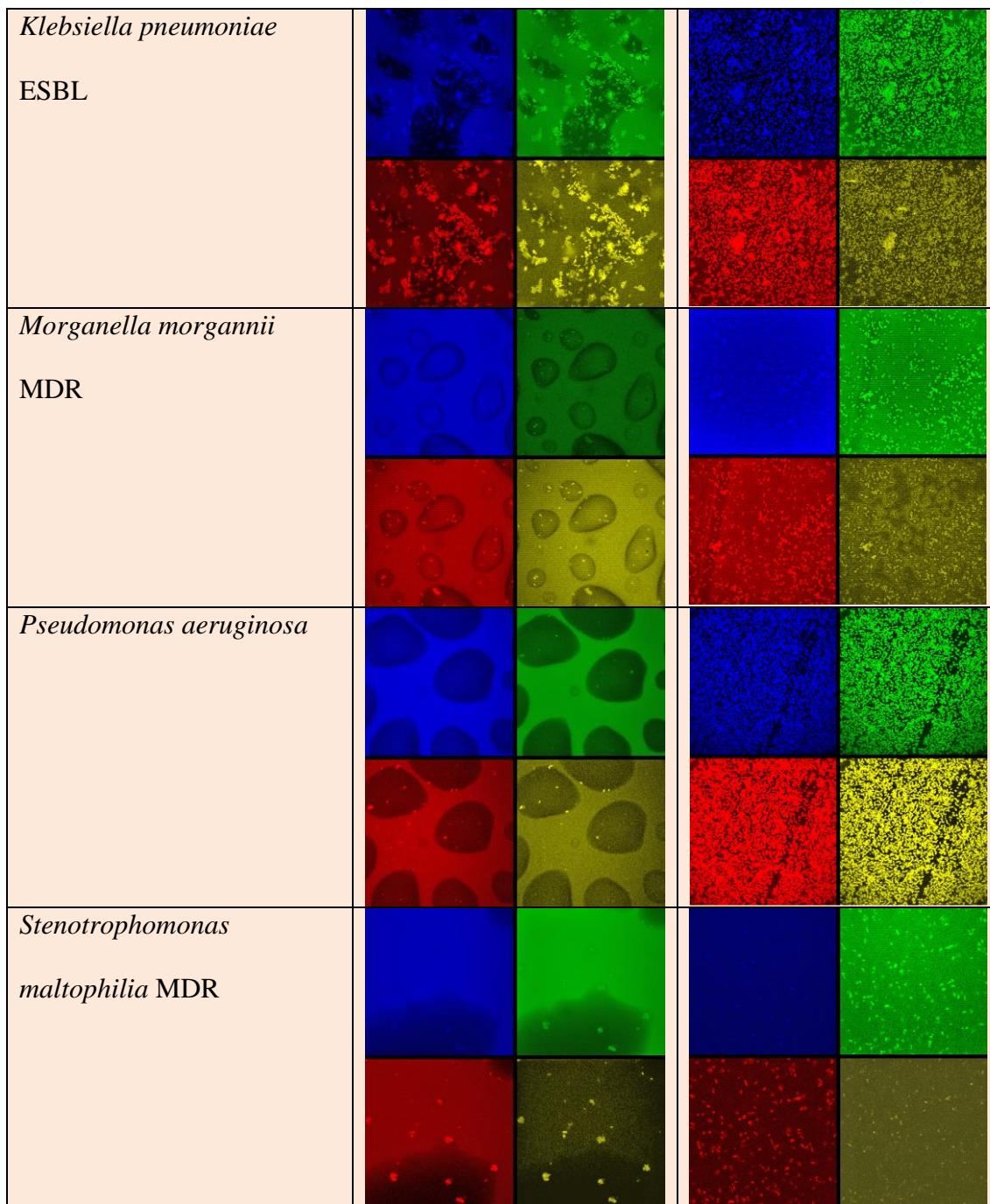


Fig. 1. Confocal fluorescence microscopy images:
A) biofilm formed on UREASIL, B) biofilm formed on glass.

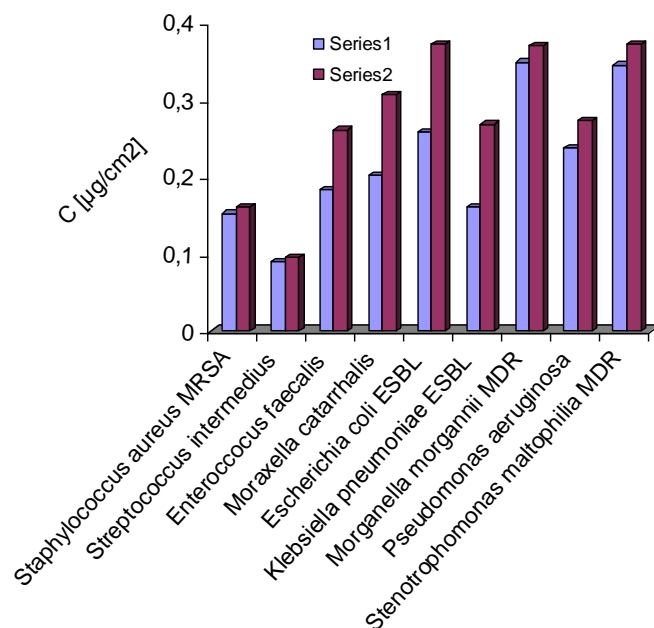


Fig. 2. Detection of microbial biofilm using a modified Lowry method for determination of protein quantity in washings: Series 1 - UREASIL; Series 2 - glass

RESULTS AND DISCUSSION

The formation of a biofilm after 48 h of incubation was evaluated by using the method of counting CFU/ml (Table 1) with the help of confocal laser scanning electron microscopy images (Fig. 1) and with a modified Lowry method for detection of the protein content in the studied samples (Table 2). The 48-h incubation period proved enough for the tested bacterial strains to build well-formed biofilms on the investigated areas (Fig. 1), a fact which corresponded with the results from other our previous research [30,31]. From the results given in Table 1 it can be concluded that, defined by the microbial number, the surviving bacteria colonizing the surface of the glass outnumber the surviving bacteria in the biofilm coating the ureasil. The difference is about 10 fold in staphylococci and moraxella and nearly 100 fold in enterococci, i.e. in Gram-positive and Gram-negative cocci. Only in *Streptococcus intermedius* the difference is less than 10. In Gram-negative rods and multidrug-resistant bacteria the difference in the number of surviving bacteria in the biofilm coating the glass is even higher – up to 1000 times more than ureasil. The differences shown in Table 1 and Fig. 1 between the various strains (ranging from 10 to 1000 times) depended on the capabilities of the particular bacteria involved with the different surface structures of the cell wall in their adhesion to surfaces and biofilm formation [3,5]. In conclusion, from the initial

results it can be argued that the structure of ureasil was more unfavorable for adhesion and breeding than that of the glass, but problematic species with strong production or overproduction of exopolysaccharide alginate, capsule substance or slime such as *Klebsiella pneumoniae*, *Morganella morganii*, *Pseudomonas aeruginosa* and other glucose non-fermenting bacteria: *Acinetobacter baumannii* and *Stenotrophomonas maltophilia* formed a thick biofilm after 48 h cultivation on ureasil. The biofilm formation from these bacteria is very strong and difficult to eliminate, because they have many surface biomolecules responsible for adhesion [5,30,31]. The formation of biofilm on the surface of a polystyrene plate, tested with *Pseudomonas aeruginosa*, showed results similar to those on the glass - a many times higher microbial number of this coating on the ureasil.

Sterile saline and broth cultivation without prior culturing microorganisms in them displayed no microbial growth.

The nine strains arbitrarily selected were quantified in the washings by the modified method of Lawry. The obtained results are shown in Fig. 2. The findings of this method confirm most of the results of the microbiological method. As a result of the studies it can be concluded that the number of surviving bacteria colonizing the surface of the hybrid material UREASIL is lower than that of the glass surface colony. These results are also confirmed by confocal microscopy, as can be seen in Fig. 1.

New strategies for prevention and treatment of clinically relevant bacterial biofilms are needed, because the biofilm-forming microbes are responsible for most of the chronic bacterial infections in humans and animals [3,5,30,31]. The results obtained support the conclusion that UREASIL is a material with good potential for biomedical applications.

This work explores the formation of a biofilm on the hybrid material UREASIL, as a first step in the study of the formation of a biofilm on a base material composite UREASIL with various types of nanoparticles. Further investigations regarding this theme are in progress.

REFERENCES

1. R Doyle *Microb. Infect.* **2**,391 (2000)
2. A Nostro, R Scaffaro, G Ginestra, M D'Arrigo, L Botta, A Marino, G Bisignano, *Appl. Microbiol. Biotechnol.*, **87**,729 (2010).
3. L Hall-Stoodley, J William, CP Stoodley *Nat. Rev. Microbiol.*, **2**, 95 (2004).
4. F Hayati, A Okada, Y Kitasako, J Tagami, K Matin, *Australn Dent. J.*, **56**, 40 (2011).
5. HL Usha, A Kaiwar, D Mehta. *Int. J. of Contempor. Dentistry*, **3**, 44 (2010).
6. N Dror, M Mandel, Z Hazan, G Lavie, *Sensors*, **9**, 2538 (2009).
7. ST Gunnel, B Gunnar, *Endodon Top*, **9**, 27 (2004).
8. T Angelova, N Rangelova, R Yuryev, N Georgieva, R Müller, *Sci. and Eng.*, **10**, 1016 (2012).
9. N Georgieva, R Bryaskova, N Lazarova, R Racheva, *Biotechnology Biotechnol. Equipment*, **27** (5), 4078 (2013).
10. C Sanchez, B Lebeau, F Chaput, JP Boilot *Adv. Mater.* **15**, 1969 (2003).
11. M Armand, C Poinsignon, JV Sanches, V de Zea Bermudez *U.S. Patent* 5283310 (1994).
12. LD Carlos, V de Zea Bermudez, RA S'a Ferreira *J. Non-Cryst. Solids*, **247**, 203 (1999).
13. LD Carlos, RA S'a Ferreira, V de Zea Bermudez, C Molina, LA Bueno, SJL Ribeiro *Phys. Rev. B*, **60**,10042 (1999).
14. LD Carlos, Y Messaddeq, HF Brito, RA S'a Ferreira, V de Zea Bermudez, SJL Ribeiro *Adv. Mater.*, **12**, 594 (2000).
15. RA S'a Ferreira, LD Carlos, RR Goncalves, SJL Ribeiro, V de Zea Bermudez, *Chem. Mater.*, **13**, 2991 (2001).
16. V de Zea Bermudez, L Alcacer, JL Acosta, E Morales, *Solid Stat Ionics*, **116**, 197 (1999).
17. SC Nunes, V de Zea Bermudez, D Ostrovskii, MM Silva, S Barros, MJ Smith, LD Carlos, J Rocha, E Morales, *J. Electrochem. Soc.*, **152**, A429 (2005).
18. NJO Silva, VS Amaral, LD Carlos, V de Zea Bermudez *J. Appl. Phys.*, **93**, 6978 (2003).
19. NJO Silva, VS Amaral, LD Carlos, V de Zea Bermudez *J. Magn. Mater.*, **272**, 1549 (2004).
20. E Stathatos, P Lianos *Langmuir* **16**, 8672 (2000)
21. VI Boev, CJR Silva, G Hungerford, MJM Gomes, *J. Sol-Gel Sci. Tech.*, **31**, 131 (2004).
22. VI Boev, A Soloviev, CJR Silva, MJM Gomes, *Sol Stat. Sci.* **8**, 50 (2006).
23. VI Boev, A Soloviev, B Rodriguez-Gonzalez, CJR Silva, MJM Gomes, *Mat. Lett.*, **60**, 3793 (2006).
24. JT Gonzalves, VI Boev, A Solovyev, CJR Silva, MJM Gomes, *Mat. Sci. Forum*, **514**, 1221 (2005).
25. VI Boev, J Perez-Juste, I Pastoriza-Santos, CJR Silva, MJM Gomes, L Liz, Marzan *Langmuir*, **20**, 10268 (2004).
26. VI Boev, A Soloviev, C Silva, M Gomes, D Barber, *J. Sol-Gel Sci. Techn.*, **41**, 223 (2007).
27. K Raunkjær, T Hvitved-Jacobsen, PH Nielsen *Water Res.* **28**, 251 (1994)
28. OH Lowry, NJ Rosebrough, AL Farr, RJ Randall *J. Biol. Chem.*, 193, 265 (1951)
29. LN Mueller, JFC de Brouwer, JS Almeida, LJ Stal, JB Xavier *BMC Ecology* **6**, 1 (2006)
30. RT Gergova, T Gueorgieva, I Angelov, V Mantareva, S Valkanov, I Mitov, S Dimitrov, *Proc. of SPIE* Vol. **8427** 842744-62012 (2012)
31. RT Gergova, T Gueorgieva, MS Dencheva-Garova, A Z Krasteva-Panova, V Kalchinov, I Mitov, J Kamenoff, *JICD*, in press, (2014).

СРАВНИТЕЛНО ИЗСЛЕДВАНЕ НА ВЪЗМОЖНОСТТА ЗА ОБРАЗУВАНЕ НА БАКТЕРИАЛНИ БИОФИЛМИ ВЪРХУ ПОВЪРХНОСТТА НА ХИБРИДЕН МАТЕРИАЛ UREASIL

Р. Т. Гергова¹, М. П. Славова^{2,3*}, В. И. Боев², М. С. Мурджева⁴,
Л. К. Йотова¹, Р. Т. Георгиева-Николова⁵

¹Катедра медицинска микробиология, Факултет по медицина, Медицински университет София, София, България

²Катедра биотехнологии, Химикотехнологичен и металургичен университет, София, България

³Институт по електрохимия и енергийни системи, Българска академия на науките, София, България

⁴Институт по биология и имунология на размножаването, Българска академия на науките, София, България

⁵Катедра химия и биохимия, Факултет по медицина, Медицински университет София, София, България

Получена на 19 юли, 2014 г., Приета на 19 август, 2014 г.

(Резюме)

Целта на това изследване е да се определи възможността за образуването на биофилм от различни бактериални щамове на повърхността на UREASIL в сравнение с образуването на биофилм върху стъклена повърхност.

Седем грам-положителни и осем грам-отрицателни бактериални щамове бяха използвани в експериментите в това проучване. Възможността за образуване на микробиален биофилм върху повърхността на новия материал UREASIL и на повърхността на стъклото (контролни проби) е установена по три метода: определяне на броя на живите бактериални клетки в биофилмите; определяне на белтъчното съдържание в биофилмите чрез използване на модифициран метод на Лоури; конфокална лазерно сканираща микроскопия за откриване и визуализация на биофилми.

Структурата на UREASIL е по-неблагоприятна за адхезия и размножаване от тази на стъклото, но проблемни видове със силно производство на капсулно вещество или слуз като *Klebsiella pneumoniae* и *Pseudomonas Aeruginosa* формират дебел биофилм след 48 часа култивиране върху UREASIL, който е открит и от трите метода: конфокална флуоресцентна микроскопия, модифициран метод на Лоури и чрез преброяване на броя на живите бактерии, които колонизират повърхността на стъклото и UREASIL.

Room temperature decomposition of hydrazine catalyzed by nickel oxide nanoparticles

F. Chekin*, S. Sadeghi

Department of Chemistry, Ayatollah Amoli Branch, Islamic Azad University, Amol, Iran

Received April 27, 2014, Revised September 1, 2014

In this work, we report a simple low-cost procedure to synthesize nickel oxide nanoparticles (NiO-NPs) by using sodium dodecyl sulphate (SDS) and gelatin as stabilizer. The synthesized NiO-NPs were characterized by transmission electron microscopy (TEM), powder X-ray diffraction (XRD), scanning electron microscopy (SEM) and UV-vis spectroscopy. The results showed that NiO nanoparticles with high crystallinity can be obtained using this simple method. The grain size measured by TEM was 16 nm in the presence of SDS, which agrees well with the XRD data. SDS plays an important role in the formation of the NiO nanoparticles. Further, the NiO nanoparticles were used as a solid-phase catalyst for the decomposition of hydrazine hydrate at room temperature. The decomposition process was monitored by UV-vis analysis. The present study showed that the nanoparticles were not poisoned after their repeated use in decomposition of hydrazine. It was found that hydrazine was catalytically decomposed to hydrogen and nitrogen gases by the resultant nickel oxide nanoparticles. The decomposition rate at 25 °C was 9.1 nmol/(min mg of NiO-NPs).

Keywords: nickel oxide nanoparticles, sodium dodecyl sulphate, hydrazine, gelatin, catalyst.

INTRODUCTION

Nowadays, synthesis and study of materials consisting of nanometer-sized particles are the subjects of intense research. Reduction of the particle size to the nanometer scale leads to a quantitative change in physical and chemical properties [1-3]. Nanoparticles in crystalline as well as in amorphous phase have important applications in magnetic recording, solar energy transformation, magnetic fluids, electronics, and chemical catalysis [4-12].

Nickel nanoparticles have attracted much attention because of their use in catalysis, medical diagnostics and magnetic applications. A number of techniques have been used for the preparation of nickel nanomaterials, such as chemical vapor deposition (CVD) [13], wet chemical method [14], laser-driven aerosol [15], hydrothermal method [16], and microemulsion [17].

Over the years, attempts have been made to prepare, stabilize and isolate homogeneously dispersed nanoparticles with and without capping agents [18,19]. Upon agglomeration, these particles lose their nanosizes and corresponding properties. In the last few years, extensive structural, kinetic and thermodynamic studies have been performed to explore the fundamental understanding of surfactant-water systems including the effect of

additives on micellization [20, 21]. However, there are still conflicting opinions on some aspects, particularly regarding factors controlling the synthesis and stabilization of nanoparticles in aqueous surfactant solutions. Therefore, it is quite difficult to scale up a general method for nanoparticles synthesis using surfactants, because numerous parameters with different influences enter into consideration, while studying a particular system.

Surfactants are amphiphilic in nature. They have two ends with different polarities, and form aggregates, such as micelles, where the hydrophobic tails form the core of the aggregate and the hydrophilic heads are in contact with the surrounding liquid. Surfactants can serve as a capping or protecting agent for nanoparticles against external forces [22,23]. The kinetics and morphology of nanomaterials can be either accelerated or changed, depending on the nature of the reducing agents and the surfactant. The surfactants not only provide favorable sites for the growth of the particle assemblies but also influence the formation process, as well as the chemical properties of the particulate guests, thus unfolding novel chemistries [24].

Hydrazine (N₂H₄) is widely used as (i) a high-energy propellant in rockets and spacecrafts by the military and aerospace industries; (ii) a powerful reducing agent for zero-emission fuel cells [25,26].

* To whom all correspondence should be sent:
E-mail: fchekin@yahoo.com
Tel.: +98 121 2517000; Fax: +98 121 2517043

Electro-oxidation of N_2H_4 is the basis of an established fuel cell, due to its high capacity and lack of contamination. However, N_2H_4 is toxic and can be readily absorbed by oral, dermal or inhalation routes of exposure [27]. It is therefore obvious that reliable and sensitive analytical methods for the determination of N_2H_4 are needed.

Here, we report the synthesis of nickel oxide nanoparticles using an anionic surfactant and gelatin. The nickel oxide nanoparticles were characterized by UV-vis, SEM, XRD and TEM methods. Nickel oxide nanoparticles were applied as a catalyst in the decomposition reaction of hydrazine.

EXPERIMENTAL

Gelatin from bovine skin, hydrazine hydrate, nickel chloride and sodium dodecyl sulphate (SDS) were purchased from Aldrich. All solutions were prepared using redistilled water. Other reagents were of analytical grade and were purchased from Aldrich or Merck and were used as received without further purification.

All spectroscopic experiments were performed on a UV-vis absorbance spectrophotometer (Shimadzu, Kyoto, Japan). All experiments were carried out at room temperature. TEM images were recorded using a LEO-Libra 120 transmission electron microscope. Hitachi S-3500N scanning electron microscope (SEM) was used for surface image measurements. The crystallization and purity of the synthesized samples were characterized by X-ray diffraction.

5 g of gelatin was dissolved in 100 mL of deionized water and was stirred at 60 °C for 30 min to achieve a clear gelatin solution. 10 mL of SDS surfactant solution (2 M) and 10 mL of nickel chloride solution (1 M) were added to the above solution under continuous stirring, after which the container was placed in a water bath. The temperature of the water bath was fixed at 80 °C. The stirring was continued for 3 h. The final product was placed in a furnace at a temperature of 500 °C for 8 h to obtain NiO nanoparticles. The yield of NiO nanoparticles calculated by weighing the produced NiO nanoparticles was found to be 81 and 85% for NiO nanoparticles synthesized in absence and presence of SDS, respectively.

RESULTS AND DISCUSSION

Fig. 1 shows the XRD pattern of the NiO-NPs prepared using gelatin in absence and presence of SDS. The dominant peaks for NiO-NPs were identified at about $2\theta = 37, 43, 62, 75$ and 79 ; they were indexed as (111), (200), (220), (311), and

(222), respectively, according to JCPDS reference number 078-0643.

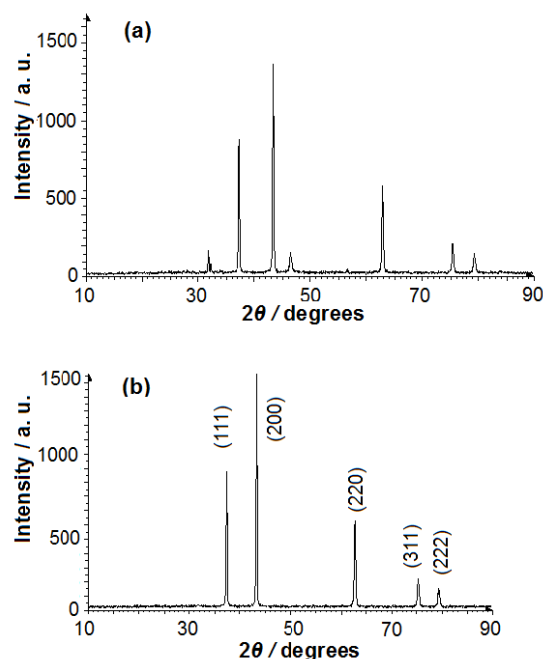


Fig. 1. XRD patterns of NiO-NPs synthesized in absence (a) and presence of SDS (b).

The average particle size of pure NiO-NPs was derived from the high intensity diffraction peak in Fig. 1, using Debye Scherrer's formula: $D = K\lambda / \beta \cos\theta$, where D is the crystallite size, K the Scherrer constant usually taken as 0.89, λ is the wavelength of the X-ray radiation (0.15418 nm for Cu K α), and β is the full width half maximum of the diffraction peak measured at 2θ (β for 43 value of 2θ is 0.61 and 0.45 for NiO-NPs powder synthesized in presence and absence of SDS, respectively). The average crystallite size of NiO-NPs synthesized in presence and absence of SDS was found to be approximately 14 and 19 nm, respectively. It is clear from the crystalline sizes that the SDS plays a major role in the synthesis of NiO nanoparticles and most probably controls the growth of nanoparticles by preventing their agglomeration. SDS (with negative charge) adsorbs Ni^{+2} ions *via* electrostatic force and prevents nanoparticles to get aggregated *via* coulombic repulsion and steric hindrance.

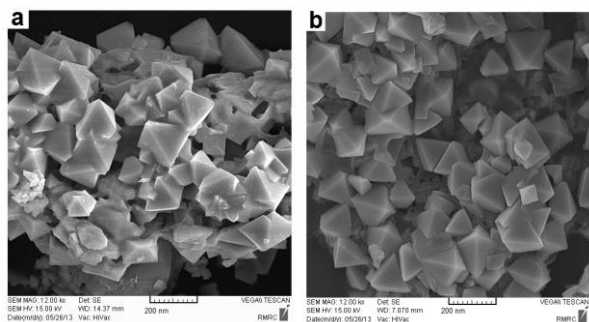


Fig. 2. SEM images of NiO-NPs synthesized in absence (a) and presence of SDS (b)

Fig. 2 shows the SEM images of the NiO nanoparticles synthesized using gelatin in presence and absence of SDS. It can be seen from the SEM image that the products are trigonal-shaped. The presence of SDS decreased the average size of the synthesized NiO particles (Fig. 2b) and the particles were uniform while without SDS, some particles were amorphous-shaped and had high size distribution (Fig. 2a).

EDAX results (Fig. 3) confirmed the presence of Ni and O elements in nanoparticles synthesized using gelatin in absence and presence of SDS.

Fig. 4 shows the TEM images and size histograms of the NiO nanoparticles synthesized using gelatin in presence and absence of SDS. According to the TEM analysis data and the size distribution plots, the small size of particles is generated by SDS surfactant. The obtained particle sizes from the TEM were in good agreement with those calculated from XRD analysis.

The optical absorption of suspended NiO nanoparticles was measured in the 200–600 nm wavelength range. Prior to the measurements of UV–vis absorption, the powder samples (2 mg/mL) were uniformly and gently dispersed in methanol solvent.

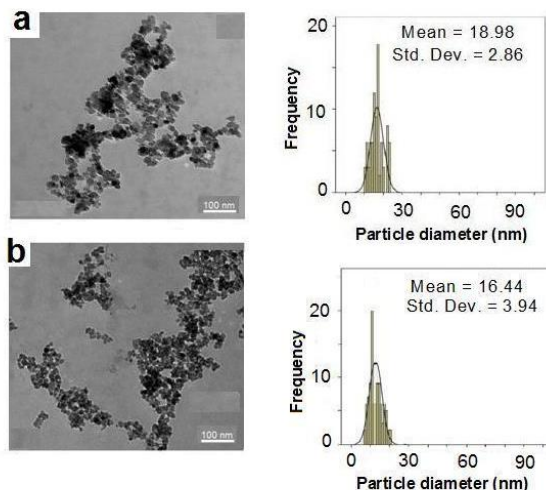


Fig. 4. TEM images and histograms of NiO-NPs synthesized in absence (a) and presence of SDS (b).

The UV–vis absorption spectra of the NiO nanoparticles at room temperature are depicted in Fig. 5.

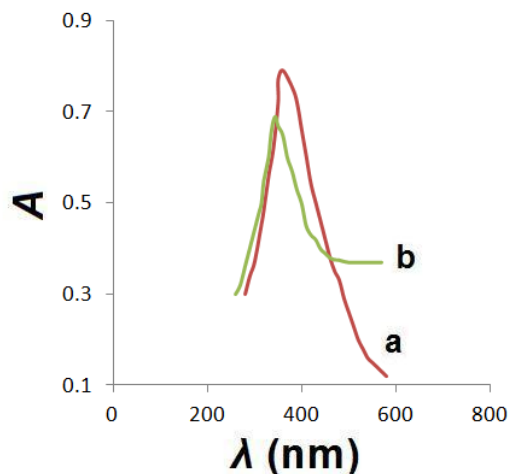


Fig. 5. UV-Vis patterns of NiO-NPs synthesized in absence (a) and presence of SDS (b).

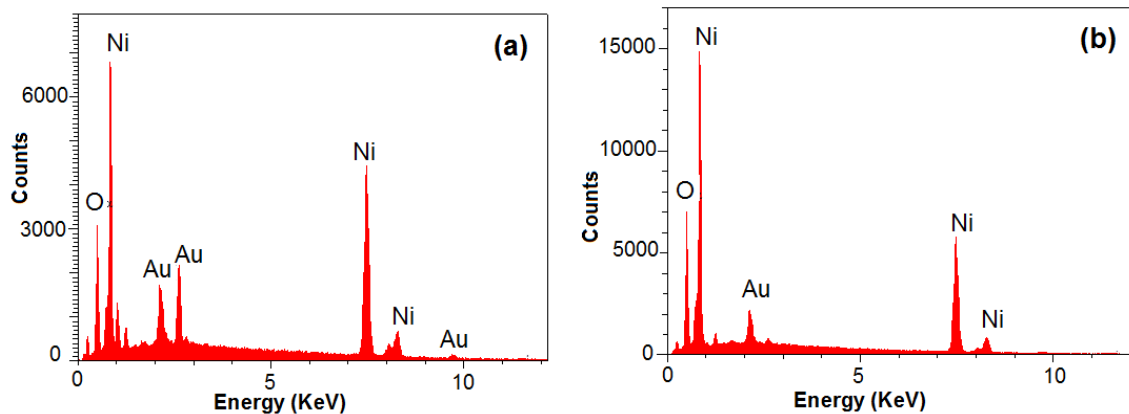


Fig. 3. EDAX images of NiO-NPs synthesized in absence (a) and presence of SDS (b).

Table 1. Compared parameters of NiO-NPs synthesized using different methods.

Method	Agent	Particle size (nm)	Synthesis temperature (°C)	Reference
Chemical	Sodium borohydride	20-40	500	[29]
Spray pyrolysis	Silica matrix	55	500	[30]
Soft-templating	Poly(propylene oxide)- poly(ethylene oxide)	31	400	[31]
Microemulsion	Tween 80	100-160	-	[32]
Sol-gel	SDS	16	500	This work

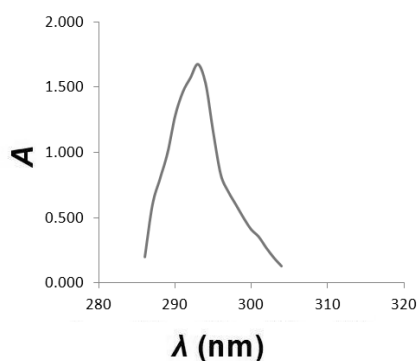
The band position of NiO prepared in absence of SDS (curve a) at around 370 nm corresponds to NiO nanoparticles. SDS (curve b) causes a shift of the band to almost 360 nm. This blue shift indicates the quantum confinement property of nanoparticles. In the quantum confinement range, the band gap of the particle increases which results in a shift of the absorption edge to lower wavelength, as the particle size decreases.

The band gap energy (E) was calculated according to the literature report [28] using the following equation:

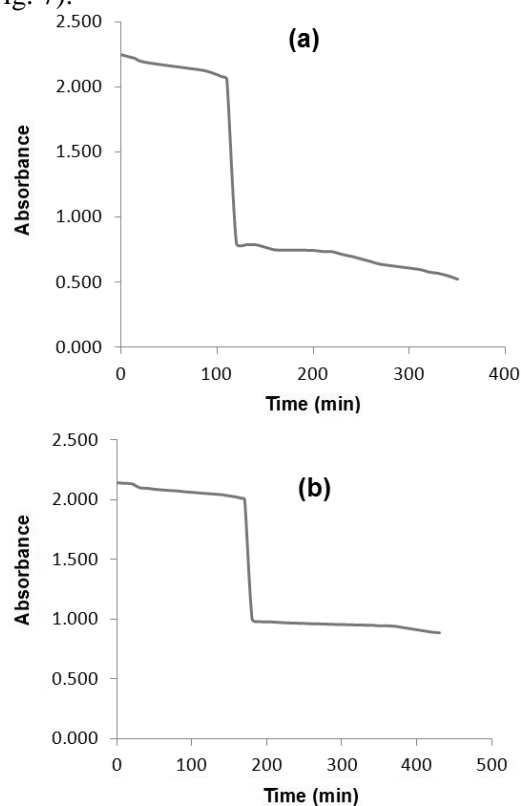
$$\text{Band gap energy } (E) = hc/\lambda \quad (1)$$

where h is the Plank's constant, 6.626×10^{-34} J s, c is the speed of light, 3.0×10^8 m/s; λ is the wavelength (nm). According to this equation, the band gap of NiO-NPs synthesized without surfactant is 3.4 eV and the band gap of synthesized NiO-NPs using SDS is 3.6 eV. These results confirm that when the size is smaller, the band gap will be larger.

The proposed method for synthesis of NiO nanoparticles was compared with those reported in the literature, as given in Table 1 [29-32]. As can be seen from Table 1, the present method is comparable with those reported in the literature. The catalytic decomposition reaction of hydrazine hydrate was studied in the presence of nickel oxide nanoparticles in aqueous medium. An aqueous solution of hydrazine (pH 7.00) has an adsorption peak at 293 nm (Fig. 6).

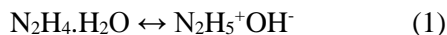
**Fig. 6.** UV-Vis pattern of 0.25 mM hydrazine in aqueous solution.

In a set of experiments, 2 mg of nickel oxide nanoparticles was added to a hydrazine aqueous solution (0.25 mM, 5 mL), and the reaction temperature was maintained at 25 °C. The intensity of hydrazine in presence of nickel oxide nanoparticles keeps on decreasing with time (Fig. 7).

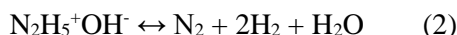
**Fig. 7** Plot of absorbance vs. time for the decomposition of hydrazine in presence of NiO-NPs as catalyst; conditions: (a) 0.25 mM hydrazine (5 ml) and (b) 0.25 mM hydrazine plus NiO-NPs (2 mg), at 25 °C.

There is no considerable change in intensity of the absorption peak in hydrazine solution without nickel oxide nanoparticles (not shown), indicating that its concentration in the reaction mixture remains almost constant and no decomposition reaction takes place in the absence of NiO nanoparticles as a catalyst. This study shows that nanoparticles have large active surface area for the decomposition reaction. For the evaluation of the catalytic rate of hydrazine decomposition reaction,

pseudo-first-order kinetics with respect to hydrazine can be used. The role of metal nanoparticles is very important in redox reactions. Hydrazine hydrate is readily soluble in water; since N_2H_4 is basic, the chemically active free ion is normally represented as $N_2H_5^+$ [33]:



Accordingly, it was clearly shown that hydrazine could be catalytically decomposed into hydrogen and nitrogen by nickel nanoparticles. The decomposition reaction is [34]:



The decomposition process involves chemisorption of hydrazinium ions onto the NiO nanoparticles surface, and interfacial electron transfer released by the hydrazinium ion [35].

As shown in Fig. 7, hydrazine decomposition rate in presence of NiO-NPs synthesized using SDS is high as compared to those synthesized without SDS. These results confirm that when the particle size is smaller, the active surface area for decomposition reaction is larger and the catalytic rate of hydrazine decomposition reaction increases. From the linear relationship between the amount of hydrazine decomposed and reaction time, the decomposition rate of hydrazine in presence of NiO-NPs synthesized in presence and absence of SDS was estimated to be 9.1 and 4.2 nmol/(min mg of NiO-NPs), respectively.

The NiO nanocatalyst was found functional after completion of the decomposition process. The particles were separated from the reaction mixture, washed with deionized water and vacuum-dried. These particles were reused at least 3 times for the same decomposition reaction. Every time, nearly the same reaction time was observed. So we concluded that the NiO nanoparticles were not poisoned.

CONCLUSIONS

Nickel oxide nanoparticles were synthesized from nickel chloride using gelatin in presence of SDS. The resultant nanoparticles were characterized by XRD, TEM, SEM and UV-Vis spectroscopy. The XRD results showed a pure nickel oxide crystalline phase with crystallite size about 14 nm, which agrees well with the TEM results. The catalytic decomposition reaction of hydrazine hydrate was studied in the presence of nickel oxide nanoparticles in aqueous medium. It was observed that hydrazine was catalytically decomposed into hydrogen and nitrogen gases by nickel oxide nanoparticles. The decomposition rate

at 25 °C was estimated to be 9.1 nmol/(min mg of NiO-NPs).

REFERENCES

1. S. A. Majetich, Y. Jin, *Science*, **284**, 470 (1999).
2. A. J. Zarur, J. Y. Ying, *Nature*, **403**, 65 (2000).
3. Y. Xia, P. Yang, Y. Sun, Y. Wu, B. Mayers, B. Gates, Y. Yin, F. Kim, H. Yan, *Adv. Mater.*, **15**, 353 (2003).
4. T. Prozorov, G. Kataby, R. Prozorov, A. Gedanken, *Thin Solid Films*, **340**, 189 (1999).
5. J. H. Lee, B. E. Park, Y. M. Lee, S. H. Hwang, W. B. Ko, *Current Applied Physics*, **9**, 152 (2009).
6. C. Wang, Y. Hu, C. M. Lieber, S. Sun, *J. Am. Chem. Soc.*, **130**, 8902 (2009).
7. C. S. Levin, J. Kundu, A. Barhoumi, N. J. Halas, *Analyt.*, **134**, 1745 (2009).
8. N. H. Kim, S. J. Lee, M. Moskovits, *Nano Lett.*, **10**, 4181 (2010).
9. M. P. Murray-Methot, M. Ratel, J. F. Masson, *J. Phys. Chem. C*, **114**, 8268 (2010).
10. G. Li, J. Zhai, D. Li, X. Fang, H. Jiang, Q. Dong, E. Wang, *J. Mater. Chem.*, **20**, 9215 (2010).
11. M. P. Pileni, *Adv. Funct. Mater.*, **11**, 323 (2001).
12. S. Sun, C. B. Murray, D. Weller, L. Folks, A. Moser, *Science*, **287**, 1989 (2000).
13. V. B. Vladimir, N. M. Valentin, V. G. Nikolay, *Chem. Vap. Deposition.*, **11**, 368 (2005).
14. Q. Zhen-ping, G. Hong-xia, L. Dong-sheng, Sh. Xue-ping, *J. Func. Mater. Devices*, **10**, 95 (2004).
15. H. E. Yuan-qing, L. I. Xue-geng, M. T. Swihart, *Chem. Mater.*, **17**, 1017 (2005).
16. L. Zhao-ping, L. Shu, Y. You, P. Sheng, H. Zhao-kang, Q. Yi-tai, *Adv. Mater.*, **15**, 1946 (2003).
17. L. Yun-jun, L. Wei-ping, W. Xian-ni, *West Leacher*, **2**, 20 (2002).
18. Z. Khan, O. Bashir, J. I. Hussain, S. Kumar, R. Ahmad, *Colloids Surf. B: Biointerfaces*, **98**, 85 (2012).
19. W. Wang, B. Gu, L. Liang, *J. Colloid Interf. Sci.*, **313**, 169 (2007).
20. S. Hosseini, W. R. Wan Daud, M. Badii, A. A. Hassan Kadhum, A. B. Mohammad, *Bull. Mater. Sci.*, **34**, 759 (2011).
21. Q. A. Drmosh, M. A. Gondal, Z. H. Yamani, T. A. Saleh, *Applied Surface Science*, **256**, 4661 (2010).
22. S. K. Mehta, S. Kumar, S. Chaudhary, K. K. Bhasin, *Nanoscale Res. Lett.*, **4**, 1197 (2009).
23. B. Tah, P. Pal, M. Mahato, G. B. Talapatra, *J. Phys. Chem. B*, **115**, 8493 (2011).
24. Sh. G. Dixit, A. R. Mahadeshwar, S. K. Haram, *Colloids and Surfaces A: Physicochemical and Engineering Aspects*, **133**, 69 (1998).
25. B. K. Jena, C. R. Raj, *J. Phys. Chem. C*, **111**, 6228 (2007).
26. Y. He, J. Zheng, Q. Sheng, *Microchim Acta*, **177**, 479 (2012).
27. B. Fang, R. X. Shen, W. Zhang, G. F. Wang, C. H. Zhang, *Microchim Acta*, **165**, 231 (2009).
28. M. Hoffman, S. Martin, W. Choi, D. Bahnemann, *Chem. Rev.*, **95**, 69 (1995).

29. Zh. You-xian, F. Wen-jie, A. Xue-qin, *Trans. Nonferrous Met. Soc. China*, **18**, 212 (2008).
30. H. S. Kim, Ch. S. Kim, S. G. Kim, *J. Non-Crystalline Solids*, **352**, 2204 (2006).
31. J. Choma, K. Jedynak, M. Marszewski, M. Jaroniec, *Applied Surface Science*, **258**, 3763 (2012).
32. A. T. Shah, M. I. Din, et al., *Colloids and Surfaces A: Physicochem. Eng. Aspects*, **405**, 19 (2012).
33. M. L. Singla, A. Negi, V. Mahajan, K. C. Singh, D. V. S. Jain, *Applied Catalysis A: General*, **323**, 51 (2007).
34. A. Salimi, R. Hallaj, S. Soltanian, *Biophysical Chemistry*, **130**, 122 (2007).
35. S. H. Wu, D. H. Chen, *J. Colloid & Interf. Sci.*, **259**, 282 (2003).

РАЗГРАЖДАНЕ НА ХИДРАЗИН, КАТАЛИЗИРАНО ОТ НАНО-ЧАСТИЦИ ОТ НИКЕЛОВ ОКСИД ПРИ СТАЙНА ТЕМПЕРАТУРА

Ф. Чекин *, С. Садеги

Департамент по химия, Ислямски университет „Азад“, Клон “Аятолах Амоли“, Амол, Иран

Постъпила на 27 април, 2014 г., коригирана на 1 септември, 2014 г.

(Резюме)

В тази работа се съобщава за прост и евтин метод за синтезата на нано-частици никелов оксид (NiO-NPs) използвайки натриев доцецил-сулфат (SDS) и желатин като стабилизатор. Синтезираните NiO-NPs са оарактеризирани с трансмисионна електрон-микроскопия (TEM), прахова рентгенова дифракция (XRD), сканираща електрон-микроскопия (SEM) и UV-vis спектроскопия. Резултатите показват, че по този прост метод са получени NiO-наночастици с висока кристалинност. Размерът на зърната, определени с TEM е 16 nm в присъствие на, което се съгласува добре с XRD-данните. SDS има важно значение за формиране на NiO-наночастиците. Тези частици са използвани като твърдо-фазен катализатор при разлагането на хидразин при стайна температура. Процесът на разлагане е наблюдаван чрез UV-vis анализ. Изследването показва, че наночастиците не се отравят при многократна употреба при разлагането на хидразин. Намерено е, че хидразинът се разлага на газообразни водород и азот. Скоростта на разлагане при 25 °C е 9.1 nmol/(min mg of NiO-NPs).

Effects of the industrial pollution on glutathione s-transferase in the liver of rainbow trout

R. Farzad¹, D. N. Inanlou¹, R. A. Cohan², M. Ghorbani^{2*}

¹Department of Research and Development, Research and Production Complex, Pasteur Institute of Iran, Tehran, Iran

²Department of Virology, Pasteur Institute of Iran, Tehran, Iran

Received May 17, 2014, Revised September 9, 2014

Glutathione S-transferase (GST) isozymes are widely distributed in nature and found in many organisms including microbes, insects, plants, fish, birds and mammals (Sherratt and Hayes). These enzymes show various activities toward different types of reactions, mostly by dissociation of the reduced glutathione (GSH) from the binding compound (Mannervik 1985). Fish are some of the species in the industrial world that are exposed to increasing level of polluted water. To investigate the effects of pollution on glutathione S-transferase activity we exposed rainbow trout to industrial pollution for a period of 4-6 weeks. Exposure to pollutants such as phenol, ammonia, mercuric chloride, cadmium chloride and mixture of agricultural anti parasitic agents significantly increased glutathione S-transferase activity with a sharp decrease of reduced glutathione (GSH) profile. By increasing the pH to 8.0 and the water temperature to 18°C, the GST activity also increased. We concluded that GST acts as a strong defense mechanism against environmental stresses by detoxifying industrial pollutants and some natural phenomena that reduce the water quality.

Key words: Glutathione S-transferase, rainbow trout, detoxification, toxicology.

INTRODUCTION

One of the important enzyme families that are involved in transformation of endogenous and xenobiotic compounds is glutathione S-transferase (GSTs) (1-2). These enzymes play a major role in detoxication by conjugating the tri-peptide glutathione (GSH) to electrophilic substrates produced during the oxidative stress and participate in the intracellular binding and transport of lipophilic compounds (3).

It is assumed that one of the major mechanisms of survival in a polluted water source is due to the detoxication of xenobiotics; and both GSH and glutathione-S-transferase are mainly responsible for this task (4-5). It is also suggested that glutathione can bind electrophilic carbon atoms or atoms such as cadmium, zinc, lead and mercury (6), as well as ammonia (7).

GSTs and their activity have been extensively characterized in rats, mice, and humans (8). Based on the protein sequence, substrate specificity and immunological activity of GSTs, they have been classified into different forms such as Alpha, Mu, Pi (9) and Theta (10) classes that are mainly located in the cytosole. Although there is no specific classification for GSTs in fish, they have been

studied and characterized in a few species and it is suggested that GSTs activity in fish is similar to that in mammals (11-12).

It is reported that the major GST isoform in the liver of rainbow trout is pi (13) which is the same as the predominant class in human brain (14). Pi function is to detoxify toxic substrates that are carried by the fish blood (13) or cerebrospinal fluid in human brain (15).

The enzyme has only recently been described in some fresh waterfish (16) and there are little reports available on the involvement of this enzyme in detoxication of industrial pollutants in fresh water fish. The present study on the profiles of reduced glutathione and glutathione-S transferase in the liver of a rainbow trout may reveal a probable mechanism of detoxification in fish.

MATERIALS AND METHODS

In this study, 90 rainbow trouts weighing 50-150 g and between 10 and 20 cm in length were obtained from a regional trout farm (Karaj, Iran) and acclimatized in aerated glass tanks (60 × 40 × 100) containing 200 liter de-chlorinated water and maintained at 13°C with pH 7.5 for 72 hours prior to the experiment. All experiments were performed according to the IACUC standard protocols. All chemical compounds were purchased from Sigma Company (Canada).

* To whom all correspondence should be sent:
E-mail: mghorbani@irimc.org

The water quality in the fish farm was evaluated prior to the experiments using a Tytronics Sentinel analyzer (Galvanic Applied Sciences Inc., Canada). The composition of the water was as follows:

Component	PPM
Ammonia	1
Copper	0.12
Chloride	22
Dissolved oxygen	0.05
Mercury	No detectable
Phenol	18
Sulphide	18
Total hardness	105
Total solids	420

Fishes were divided into 6 groups of 15, including a control group, and exposed to non-lethal concentrations of ammonia (60 ppm), CdCl₂ (160 ppm), HgCl₂ (0.16 ppm) and phenol (22 ppm) for 2 days. A mixture of all toxins including phenol (6 ppm), CdCl₂ (60 ppm), ammonia (20 ppm) and HgCl₂ (0.08 ppm) was added to the fish tank containing the sixth group. After the exposure, fishes were transferred to toxicant free fresh water (with the same quality as before) and kept for 30 days. Group one was elected as the control group and maintained under identical conditions. Five fish from each tank were sampled immediately after 2 days of exposure and on days 15 and 30 after exposure.

Preparation of hepatocytes

Hepatocytes were collected according to the general method described by MelgarRiol et al. (17). Fish were anaesthetized by exposure to 3-aminobenzoic acid ethyl ester (Sigma, Canada) for a few minutes. Fish were then placed on a cutting board and a ventral incision was made along the medial line. The portal vein was cleaned from the surrounding tissues and cannulated by placing a ligature around the vein 1-2 cm away from the liver. The liver was then perfused using a peristaltic pump at a flow rate of 10 ml per min for 20 min to clear all the blood using a calcium-free solution containing 11.76 mM Hepes, 160.8 mM NaCl, 3.15 mM KCl, 0.5 mM EDTA and 0.33 mM Na₂HPO₄, pH 7.65, while the heart was cut to avoid high pressure in the system. The perfusion buffer was then replaced with a collagenase solution containing 6.67 mM CaCl₂ and 0.5 mg collagenase for 20 min, at a flow rate of 5 ml. The liver was then removed and the gall bladder was dissected carefully. The liver was then smashed against a sterile wire mesh strainer (100-µm) and washed with cold PBS. The cells were collected in a sterile

falcon tube and centrifuged at 1500×g for 3 min. The supernatant was decanted and the cell pellet washed in 15 ml EMDM medium and centrifuged as before. The supernatant was removed and the pellet was re-suspended in 25 ml EMDM, and cell viability was evaluated by the trypan blue exclusion test (18).

Isolation of GSTs

Hepatocytes were homogenized followed by sonication for 2 min and cytosolic fractions were collected after centrifugation at 100000×g for 20 min (19). The cytosol was then dialyzed against 10 mM potassium phosphate buffer pH 6.5. The dialyzed cytosol containing approximately 105 units of GST activity towards 1-chloro-2, 4-dinitrobenzene (CDNB) (Sigma, Canada) was used in previously packed CM-cellulose column (1.7 × 25 cm) (Sigma, USA), equilibrated in the cold room with 1 liter of equilibration buffer (10 mM potassium phosphate buffer, pH 6.5) at a flow rate of 42 ml/h. The column was washed at a flow rate of 37.5 ml/h with 500 ml of the equilibration buffer until no absorption was detected at 280 nm wavelength. After a few washings, the GSTs were eluted from the CM-cellulose column with a linear KCl gradient of 200 ml potassium phosphate buffer (10 mM, pH 6.5) and 200 ml of the same buffer containing 50 mM KCl. The fractions of about 2.5 ml were collected during the gradient elution with a flow rate of 35 ml/h. The protein profile of chromatography was determined by measuring the absorbance of fractions at 344 nm. The GSTs activities were then determined using CDBN as substrate and expressed as pg GSH/mg liver protein.

The result was expressed in terms of aa/min/mg protein. The liver protein was determined by the method of Lowry et al. (20) using bovine serum albumin (Sigma, Canada) as the standard.

Determination of liver GST activity

CDNB was used as a substrate to determine the GSTs activities through formation of thioether and detection at 344 nm. The CDBN reaction mixture included 100mM potassium phosphate, 1 mM CDBN and 1 mM GSH. The cytosolic proteins were diluted 1/50 in 20mM potassium phosphate buffer at pH 7.4 and stored at 25°C prior to addition to the reaction mixture. The result was expressed in terms of nmoles/min/mg protein. The optical densities were determined at every 5 seconds for 100 seconds.

Table 1. Reduced glutathione level in the liver of rainbow trout during and after exposure to non-lethal concentrations of ammonia, cadmium chloride, mercuric chloride, phenol and a mixture of toxicants. The significance is shown as $p < 0.05$.

Toxicants	Glutathione level (pg GSH/mg liver protein)		
	Days of Toxicant exposure	Days after exposure	
	2 Days	15 Days	30 Days
Control	110.32 ± 5.2	122.85 ± 8.8	132.64 ± 5.5
Ammonia	124.99 ± 7.3*	111.81 ± 12.2	126.02 ± 11
Cadmium chloride (CdCl ₂)	74.71 ± 5.7*	128.99 ± 17	112.99 ± 7.3
Mercuric chloride (HgCl ₂)	82.92 ± 8.3*	117.99 ± 13	124.99 ± 9.2
Phenol	69.69 ± 7.3*	125.99 ± 6.3	120.99 ± 9.3
Mixture of toxicants	61.99 ± 6.7*	114.99 ± 10.6	128.99 ± 13.2

Statistical analysis

Results are presented as mean ± SEM. Statistical analysis used Instat software for analysis of variance followed by a Student-Newman-Keuls post hoc test. Significant differences were assessed at $P < 0.05$.

RESULTS

Glutathione

All toxicants used in this study reduced the GSH content in the liver during the 2 days exposure which returned to the normal level after transferring the fish to fresh water (Table 1).

Glutathion-S-Transferase activity

Fish intoxication with ammonia increased the level of glutathione S-transferase activity which was concomitant with the reduction of GSH level in the liver (Fig 1, Table 1). The enzyme activity declined sharply after transferring fish to fresh water (Fig 1).

Fish exposed to Cadmium Chloride also exhibited a significant enhancement of glutathione S-transferase activity in the liver which was declined on day 15 and returned to normal level on day 30 after exposure (Fig 2).

Treatment of rainbow trout with mercury (HgCl₂) induced a similar response as compared to other toxicants. However, it showed only a slight decrease on days 15 and 30 after exposure and was still significantly above the normal level (Fig 3).

Treated fish with phenol, exhibited a significant increase in GST activation on day 2 of exposure up to 2.5 times higher than the control group, whereas, the level of GSH returned to below normal level on day 15 and 30 of exposure (Fig 4).

The mixture of toxicants caused the activation of glutathione S-transferase to the maximum level (Fig 5). Again, like other toxicants, the level of enzyme activity returned to almost basal level in this group of fish.

DISCUSSION

It has been reported that glutathione S-transferase enzyme (GSTs) in the liver of animals is able to detoxify poisons in the blood flow (21). It appears that GSTs can bind to a large number of compounds. GSTs can be resolved into their ionic isozymes by ion-exchange columns depending on their ionic properties (21).

GSTs can appear in an organism in multiple forms. The establishment of such multiplicity has been discovered by chromatography and electrophoresis as well as by measuring the activity of the isozymes using CDNB as the electrophilic substrate (22).

In a number of studies of glutathione S-transferases, glutathione affinity chromatography has been extensively used (23). It has been shown that GST specific activity towards CDNB in freshly isolated hepatocytes was significantly higher as compared to the GST activity in cell culture (24).

The GST ligands are nucleophilic centers and intend to attack electrophilic compounds. Such compounds will be considered as the substrate for GST enzyme. Due to the large reactivity of these compounds to interact with GST enzyme system and the wide catalytic capability of GST enzyme, it appears that GSTs are involved with detoxication of both xenobiotics and normal constituents of food which are converted to less reactive compounds (24).

It has also been suggested that GSH may be involved in the protection of liver against a number of toxic compounds (25).

GSH depletion from liver could activate xenobiotics circulation which in turn increases hepatotoxic action. Meanwhile, hepatic toxicity of certain xenobiotics would be decreased by elevation of the GSH concentration in the liver (26).

In an industrial environment and due to the availability of excessive amount of toxicants such as cobalt and lead, glutathione depletion from the

liver of mice may occur, suggesting that the GST peroxidase is inhibited and resulted in the elevation of liver GSH levels due to the antioxidant properties of cobalt (27).

It seems that physiological and xenobiotic stimulations may activate the liver functions by increasing the levels of hepatic glutathione in both mammals and fish. There are many compounds such as acrolein and acrylonitrile that cause elevation of glutathione during the incubation of hepatocytes (28).

Purification of cytosolic GSTs from sheep lung has shown that metal ions such as Ni²⁺, Cd²⁺, Ba²⁺, Mn²⁺, Co²⁺, Cu²⁺, Pb²⁺ and Zn²⁺ inhibit the activity of GSTs. Glutathione-S-transferase activity has also been detected in the cytosolic fractions of tissue homogenates, especially in rat brain and liver, as well as avian brain homogenate (29).

It has been suggested that the release of glutathione from fish liver will increase the toxicity of several compounds and glutathione-S-transferase activity in fish that is similar to that in rat (30).

It is assumed that both glutathione and glutathione-S-transferase play an important role in the detoxification mechanism in both fish and mammals. In this study, we demonstrated that the decrease of glutathione is associated with the enhancement of glutathione-S-transferase activity.

We suggest that exposure to xenobiotics and toxins in many organisms causes the induction of glutathione that helps the organism to adapt itself to the changes in the environment and resist against acute pollution, as well as reducing the harmful effects of the toxicants. In the mean time, the isolated rainbow trout hepatocytes appear to be an ideal approach to analyze the effect of toxicants on the activity of glutathione-S-transferase. Since all GST subunits are not acting the same there are needs for comparative experiments to investigate the effects of different toxicants on various glutathione subunits.

REFERENCES

1. B. Coles, B. Ketterer, *Biochem Mol Biol.*, **25**, 47 (1990).
2. A. M. Gulick, W. E. Fahl, *ProcNatAcadSci U S A.*, **92**, 8140 (1995).
3. J. D. Hayes, *Free Radic Res.*, **22**, 193 (1995).
4. K. Johanning, G. Hancock, B. Escher, A. Adekola, M. J. Bernhard, C. Cowan-Ellsberry, J. Domoradzki, S. Dyer, C. Eickhoff, M. Embry, S. Erhardt, P. Fitzsimmons, M. Halder, J. Hill, D. Holden, R. Johnson, S. Rutishauser, H. Segner, I. Schultz, J. Nichols, *CurrProtocToxicol.*, **14**, 28 (2012).
5. R. M. Yu, P. K. Ng, T. Tan, D. L. Chu, R. S. Wu, R. Y. Kong, *Aquat. Toxicol.*, **90**, 235 (2008).
6. J. Doull, C. D. Klaassen, M. O. Amdur, *Toxicology: the Basic Science of Poisons*, Macmillan, New York, 1980, p. 60.
7. S. Chatterjee, S. Bhattacharya, *Toxicol. Lett.*, **17** 329 (1983).
8. C. B. Pickett, A. Y. Lu, *Ann. Rev. Biochem.*, **58**, 743 (1989).
9. B. Mannervik, P. Alin, C. Guthenberg, H. Jensson, M. K. Tahir, M. Warholm, H. Jörnvall, *ProcNatAcadSci U S A.*, **82**, 7202 (1985).
10. D. J. Meyer, B. Coles, S. E. Pemble, K. S. Gilmore, G. M. Fraser, B. Ketterer, *Biochem. J.*, **274**, 409 (1991).
11. E. P. Gallagher, P. L. Stapleton, D. H. Slone, D. Schlenk, D. L. Eaton, *Aquat. Toxicol.*, **34**, 135 (1996).
12. S. G. George, In: *Aquatic Toxicology: Molecular, Biochemical and Cellular Perspectives*. CRC Press, Boca Raton, FL, 1994, p. 37.
13. B. Hu, L. Deng, C. Wen, X. Yang, P. Pei, Y. Xie, S. Luo, *Fish Shellfish Immunol.*, **32**, 51 (2012).
14. S. L. Stareevie, A. Muruganandam, B. Mutus, B. S. Zielinski, *Chem. Senses*, **18** 57 (1993).
15. P. J. Carder, R. Hume, A. A. Fryer, R. C. Strange, J. Lander, J. E. Bell, *Neuropathol. Appl. Neurobiol.*, **16** 293 (1990).
16. C. L. Kirstein, R. Coopersmith, R. J. Bridges, M. Leon, *Brain Res.*, **543**, 341 (1991).
17. M. J. MelgarRiol, M. C. N'ovoValinas, M. A. GarcíaFernández, M. PérezLópez, *Comparative Biochemistry and Physiology Part C*, **128**, 227 (2001).
18. H. O. Jauregui, N. T. Hayner, J. L. Driscoll, R. W. Holland, M. Lipsky, P. M. Galletti, *In Vitro*, **12**, 1100 (1981).
19. W. H. Habig, M. J. Pabst, W. B. Jakoby, *J. Biol. Chem.*, **249**, 7130 (1974).
20. O. H. Lowry, N. J. Rosebrough, A. L. Farr, R. J. Randall, *J. Biol. Chem.*, **193**, 265 (1951).
21. W. B. Jakoby, *Adv. Enzymol.*, **46**, 383 (1978).
22. J. M. Goodrich, N. Basu, *In Vitro*, **26**, 630 (2012).
23. M. Trute, B. Gallis, C. Doneanu, S. Shaffer, D. Goodlett, E. Gallagher, *Aquat. Toxicol.*, **81**, 126 (2007).
24. M. Pesonen, T. Andersson, *Aquat. Toxicol.*, **37**, 253 (1997).
25. S. Taya, C. Punvittayagul, W. Inboot, S. Fukushima, R. Wongpoomchai, *Asian Pac J Cancer Prev.*, **15**, 2825 (2014).
26. S. Chatterjee, S. Bhattacharya, *Toxicol. Lett.*, **22**, 187 (1984).
27. R. R. Dalvi, T. J. Robbins, *J. Environ. Pathol. Toxicol.*, **1**, 601 (1978).
28. A. Zitting, T. Heinonen, *Toxicology*, **17**, 333 (1980).
29. A. A. Fryer, R. Hume, R. C. Strange, *Biochim. Biophys. Acta*, **883**, 448 (1986).
30. R. Dixit., H. Mukhtar, P. K. Seth, C.R. Krishnamurti, *Biochem. Pharmacol.*, **30**, 1739 (1981).

ЕФЕКТИ НА ПРОМИШЛЕНОТО ЗАМЪРСЯВАНЕ ВЪРХУ ГЛУТАТИОН S-ТРАНСФЕРАЗАТА В ЧЕРНИЯ РОБ НА ДЪГОВАТА ПЪСТЪРВА

Р. Фарзад¹, Д. Н. Инанлу¹, Р. А. Коан², М. Горбани^{2*}

¹*Департамент за изследване и развитие, Изследователско-производствен комплекс, Ирански Пастъор-институт, Техеран, Иран*

²*Департамент по вирусология, Ирански Пастъор-институт, Техеран, Иран*

Постъпила на 17 май, 2014 г., коригирана на 9 септември, 2014 г.

(Резюме)

Глутатион-S-трансферазните (GST) изозими са широко разпространени в природата и са намерени в много организми като микроби, насекоми, растения, риби, птици и бозайници (Sherratt и Hayes). Тези ензими показват разнообразна активност спрямо различни типове реакции, главно чрез дисоциацията на редуцирания глутатион (GSH) от свързващите съединения (Mannervik, 1985). Рибите са сред видовете, най-изложени на замърсените води в промишлено-развитото общество. За изучаването на тези ефекти беше използвана дъговата пъстърва като тестов вид при експозиции от 4 до 6 седмици. Експозицията към замърсители като фенол, амоняк, меркури-хлорид, кадмиев хлорид и смес от земеделски и паразитни агенти значително повишава активността на глутатион-S-трансферазата с рязко понижаване на профила на редуцирания глутатион (GSH). Активността на GST се повишава при рН 8.0 и температура на водата 18°C. Беше установено, че GST действа като силен защитен механизъм срещу екологичните стресове, като обезврежда промишлените замърсители и някои естествени фактори, влошаващи качеството на водите.

Numerical study of the non-linear radiation heat transfer problem for the flow of a second-grade fluid

A. Mushtaq¹, M. Mustafa^{2,*}, T. Hayat^{3,4}, A. Alsaedi⁴

¹ *Research Centre for Modeling and Simulation (RCMS), National University of Sciences and Technology (NUST), Islamabad 44000, Pakistan*

² *School of Natural Sciences (SNS), National University of Sciences and Technology (NUST), Islamabad 44000, Pakistan*

³ *Department of Mathematics, Quaid-I-Azam University 45320, Islamabad 44000, Pakistan*

⁴ *Department of Mathematics, Faculty of Science, King Abdulaziz University, P. O. Box 80257, Jeddah 21589, Saudi Arabia*

Received March 26, 2014, Revised July 11, 2014

Radiation effects in the two-dimensional flow of an electrically conducting second-grade fluid are examined. Non-linear radiative heat flux is considered in the formulation of the energy equation. Viscous dissipation effects are retained. The developed nonlinear differential systems are solved numerically using the shooting method with a fourth-fifth order Runge-Kutta integration procedure. The solutions are validated with the built-in numerical solver `bvp4c` of the software MATLAB. The dimensionless expressions of skin friction coefficient and rate of heat transfer at the sheet are evaluated and discussed.

Keywords: Thermal radiation; Second-grade fluid; Heat transfer; Shooting method; Non-linear Rosseland approximation

INTRODUCTION

The study of viscoelastic boundary layer flows due to the movement of inextensible surfaces is important in many manufacturing processes. A number of technical processes concerning polymers involve the cooling of continuous strips or filaments by drawing them through a quiescent fluid. The thin polymer sheet constitutes a continuously moving surface with a non-uniform velocity through an ambient fluid. In these cases the properties of the final product depend to a great extent on the rate of cooling, which is governed by the structure of the boundary layer near the moving strip. Due to the entrainment of the ambient fluid, this boundary layer is different from that in the Blasius [1] flow past a fixed flat plate. Crane [2] was probably the first to discover the flow due to a stretching surface in an otherwise ambient fluid. Since then many authors have studied various aspects of this problem such as the effects of surfaces mass transfer, magnetic field, arbitrary stretching velocity, variable wall temperature or heat flux (Gupta and Gupta [3], Chakrabarti and Gupta [4], Grubka and Bobba [5], Banks [6], Chen and Char [7], Ali [8], Pop and Na [9], Magyari and Keller [10], Liao and Pop [11], Kumari and Nath

[12], Hayat *et al.* [13-15], Mustafa *et al.* [16,17], Zheng *et al.* [18-20], Liu *et al.* [21], etc. The thermal radiation effect in such flow configurations is prominent in nuclear power plants, satellites and space vehicles, in combustion appliances such as fires, furnaces, IC engines, ship compressors, solar radiation buildings, etc. Influence of thermal radiation on the steady incompressible flow of a viscoelastic fluid with constant suction has been discussed by Raptis and Perdakis [22]. Sedeek [23] and Raptis *et al.* [24] examined the thermal radiation effect on the boundary layer flow of an electrically conducting viscous fluid. Bataller [25] examined the radiation effects in the Blasius flow of a viscous fluid. Elbeshbeshy and Emam [26] discussed the thermal radiation effects on the unsteady flow due to a stretching sheet immersed in a porous medium. Homotopic solutions for a unsteady mixed convection flow of a Jeffrey fluid with thermal radiation have been provided by Hayat and Mustafa [27]. Motsumi and Makinde [28] investigated the radiation effects on the incompressible flow of a nanofluid with viscous dissipation. Flow and heat transfer of a MHD viscous fluid over an unsteady stretching surface with radiation heat flux are examined by Zheng *et al.* [29]. In another paper, Zheng *et al.* [30] discussed the buoyancy lift effects on the mixed flow and radiation heat transfer of a micropolar fluid towards a vertical permeable plate.

* To whom all correspondence should be sent:
E-mail: meraj_mm@hotmail.com

Recently the flow analysis of non-Newtonian fluids has received remarkable attention due to its relevance in various processes such as plastic manufacture, performance of lubricants, application of paints, polymer processing, food processing and movement of biological fluids. In particular, the boundary layer flow of a second-grade fluid is widely discussed. Numerical investigation of the mass transfer effects in the flow of an electrically conducting second-grade fluid has been performed by Cortell [31]. Mixed convection flow of a second-grade fluid past a vertical flat surface with variable surface temperature has been investigated by Mushtaq et al. [32]. Hayat et al. [33] examined the effects of thermal radiation and viscous dissipation in the Blasius flow of a second-grade fluid. Three-dimensional boundary layer flow analysis of a second-grade fluid has been addressed by Nazar and Latip [34]. Exact solutions for the hydro-magnetic flow and heat transfer in a second-grade fluid with heat generation/absorption have been obtained by Abel et al. [35]. Nazar et al. [36] discussed the Stokes second problem for a second-grade fluid. Jamil et al. [37] examined the flow of a second-grade fluid due to constantly accelerated shear stresses. Homotopic solutions for a squeezing flow of a second-grade fluid between parallel disks have been computed by Hayat et al. [38]. Perturbation analysis for a flow of modified second-grade fluid over a porous plate has been performed by Pakdermili et al. [39]. Steady laminar boundary layer flow of a second-grade fluid in the presence of thermophoresis effects has been examined by Olajuwon [40].

In some recent papers the heat transfer characteristics have been investigated using non-linear Rosseland approximation for thermal radiation (see Pantokratoras and Fang [41], Mushtaq et al. [42], Cortell [43] and Mushtaq et al. [44]). The present work deals with the influence of non-linear thermal radiation on the flow of an electrically conducting second-grade fluid due to a stretching sheet. The developed mathematical problems were solved for the numerical solution through a shooting method. It is important to point out that computation of either analytic or numerical solutions of the classical Navier–Stokes equations (characterizing complex flow mechanics) [45–48] is often handy for the researchers. Graphs showing the behavior of various parameters are sketched and analyzed.

PROBLEM FORMULATION

We consider the steady flow of an incompressible second-grade fluid over a stretching

sheet situated at $y = 0$. Let $U_w = ax$ be the velocity of the stretching sheet where $a > 0$ is constant. A uniform transverse magnetic field of strength B_0 is applied normal to the flow. The induced magnetic field is neglected under the assumption of small magnetic Reynolds' number. The boundary layer equations governing the steady two-dimensional stagnation-point flow of second-grade fluid are [31–33]:

$$\frac{\partial u}{\partial x} + \frac{\partial v}{\partial y} = 0, \tag{1}$$

$$u \frac{\partial u}{\partial x} + v \frac{\partial v}{\partial y} = \nu \frac{\partial^2 u}{\partial y^2} - \frac{\sigma B_0^2}{\rho} u + \frac{\alpha_1}{\rho} \left(\frac{\partial u}{\partial x} \frac{\partial^2 u}{\partial y^2} + u \frac{\partial^3 u}{\partial x \partial y^2} + v \frac{\partial^3 u}{\partial y^3} + \frac{\partial u}{\partial y} \frac{\partial^2 v}{\partial y^2} \right), \tag{2}$$

where ν is the kinematic viscosity, σ is the electrical conductivity of the fluid, B_0 is uniform magnetic field along the y -axis, $\alpha_1 (\geq 0)$ is the material fluid parameter of the second-grade fluid, u and v are the velocity components in x - and y -directions, respectively. The boundary conditions in the present problem are

$$u = U_w(x) = ax, \quad v = 0 \quad \text{at } y = 0, \\ u \rightarrow 0 \quad \text{as } y \rightarrow \infty. \tag{3}$$

Introducing the following variables

$$\eta = \sqrt{\frac{a}{\nu}} y, \quad u = axf'(\eta), \quad v = -\sqrt{\nu a} f(\eta). \tag{4}$$

Eq. (1) is identically satisfied and Eqs. (2) and (3) become

$$f''' + ff'' - f'^2 - Mf' + \beta(2f'f''' - ff^{iv} - f''^2) = 0 \tag{5}$$

$$f(0) = 0, \quad f'(0) = 1, \quad f'(+\infty) \rightarrow 0, \tag{6}$$

where $M = \sigma B_0^2 / \rho a$ is the magnetic parameter and $\beta = \alpha_1 a / \rho \nu$ is viscoelastic parameter. It interesting to note that Eq. (5) subjected to the boundary conditions (6) admits a closed form exact solution of the following form (see Cortell [31]).

$$f(\eta) = \frac{1 - e^{-b\eta}}{b}; \quad b = \sqrt{\frac{1 + M}{1 + \beta}}. \tag{7}$$

Heat transfer analysis

Under usual boundary layer assumptions, the energy equation in the presence of thermal radiation and viscous dissipation effects is given by

$$u \frac{\partial T}{\partial x} + v \frac{\partial T}{\partial y} = \alpha \frac{\partial^2 T}{\partial y^2} + \frac{\nu}{C_p} \left(\frac{\partial u}{\partial y} \right)^2 - \frac{1}{\rho C_p} \left(\frac{\partial q_r}{\partial y} \right) + \frac{\alpha_1}{\rho C_p} \left(u \frac{\partial u}{\partial y} \frac{\partial^2 u}{\partial x \partial y} + v \frac{\partial u}{\partial y} \frac{\partial^2 u}{\partial y^2} \right), \tag{8}$$

where T is the temperature, α is the thermal diffusivity, C_p is the specific heat at constant pressure and q_r is the radiative heat flux. Using the

Rosseland approximation for thermal radiation and applying to optically thick media, the radiative heat flux in Eq. (8) is given by [49]

$$q_r = -\frac{4\sigma^* \partial T^4}{3k^* \partial y} = -\frac{16\sigma^* T^3}{3k^*} \frac{\partial T}{\partial y}, \quad (9)$$

where σ^* and κ^* are the Stefan-Boltzman constant and the mean absorption coefficient, respectively. Now (8) can be expressed as

$$u \frac{\partial T}{\partial x} + v \frac{\partial T}{\partial y} = \frac{\partial}{\partial y} \left[\left(\alpha + \frac{16\sigma^* T^3}{3\rho C_p k^*} \right) \frac{\partial T}{\partial y} \right] + \frac{v}{C_p} \left(\frac{\partial u}{\partial y} \right)^2 + \frac{\alpha_1}{\rho C_p} \left(u \frac{\partial u}{\partial y} \frac{\partial^2 u}{\partial x \partial y} + v \frac{\partial u}{\partial y} \frac{\partial^2 u}{\partial y^2} \right). \quad (10)$$

It is worth mentioning here that in the previous studies on thermal radiation (see [22-30] and various references therein), T^4 in Eq. (9) was expanded about the ambient temperature T_∞ . However in the subsequent subsection this was avoided.

Constant wall temperature (CWT)

The relevant boundary conditions in this situation are

$$T = T_w \text{ at } y = 0; \quad T \rightarrow T_\infty \text{ as } y \rightarrow \infty, \quad (11)$$

with $T_w > T_\infty$ and T_w and T_∞ are the sheet's temperature and the ambient fluid's temperature, respectively. Defining the non-dimensional temperature $\theta(\eta) = (T - T_\infty)/(T_w - T_\infty)$ and also $T = T_\infty(1 + (\theta_w - 1)\theta)$ with $\theta_w = T_w/T_\infty$ (temperature ratio parameter), the first term on the right hand side of Eq. (10) can be written as $\alpha \partial / \partial y [\partial T / \partial y (1 + R_d(1 + (\theta_w - 1)\theta)^3)]$, where $R_d = 16\sigma^* T_\infty^3 / 3k\kappa^*$ denotes the radiation parameter for the CWT case, and $R_d = 0$ provides no thermal radiation effect. The latter expression can be further reduced to:

$$\frac{\alpha(T_w - T_\infty)}{Pr} [(1 + R_d(1 + (\theta_w - 1)\theta)^3)\theta']', \quad (12)$$

where $Pr = \nu/\alpha$ is the Prandtl number. Eq. (14) takes the following form

$$[(1 + R_d(1 + (\theta_w - 1)\theta)^3)\theta']' = -Pr \left(f\theta' + E_c^* [f''^2 + \beta (f'f''^2 - ff''f''')] \right), \quad (13)$$

with boundary conditions

$$\theta(0) = 1, \quad \theta(+\infty) \rightarrow 0, \quad (14)$$

where $E_c^* = U_w^2/C_p(T_w - T_\infty)$ is the local Eckert number. We notice that x- coordinate could not be eliminated from the energy equation. Thus we look for the availability of local similarity solutions. Using Eq. (7), (13) becomes

$$[(1 + R_d(1 + (\theta_w - 1)\theta)^3)\theta']' = -Pr \left[\left(\frac{1 - e^{-b\eta}}{b} \right) \theta' + E_c^* b^2 (1 + \beta) e^{-2b\eta} \right]. \quad (15)$$

The heat transfer rate at the sheet is defined as

$$q_w = -k \left(\frac{\partial T}{\partial y} \right)_{y=0} + (q_r)_w = -k(T_w - T_\infty) \sqrt{\frac{\alpha}{\nu}} [1 + R_d \theta_w^3] \theta'(0), \quad (16)$$

and with the help of the local Nusselt number $Nu_x = xq_w/k(T_w - T_\infty)$, one obtains

$$\frac{Nu_x}{\sqrt{Re_x}} = -[1 + R_d \theta_w^3] \theta'(0). \quad (17)$$

Prescribed surface temperature (PST)

The boundary conditions in this case are

$$T = T_w = T_\infty + cx^2 \text{ at } y = 0; \quad T \rightarrow T_\infty \text{ as } y \rightarrow \infty, \quad (18)$$

where $c > 0$ is a constant and Eq. (10) reduces to $(1 + R_d)\theta''$

$$= -Pr \left[\begin{array}{c} f\theta' - 2f'\theta \\ + E_c [f''^2 + \beta (f'f''^2 - ff''f''')] \end{array} \right], \quad (19)$$

with the boundary conditions (18). Here $E_c = \alpha^2/cC_p$ is the constant Eckert number. Using Eq. (7), (19) becomes

$$(1 + R_d)\theta'' = -Pr \left[\left(\frac{1 - e^{-b\eta}}{b} \right) \theta' - 2\theta e^{-b\eta} \right] + E_c b^2 (1 + \beta) e^{-2b\eta}. \quad (20)$$

Here the heat transfer rate at the sheet becomes

$$q_w = -k \left(\frac{\partial T}{\partial y} \right)_{y=0} + (q_r)_w = -kcx^2 \sqrt{\frac{\alpha}{\nu}} [1 + R_d] \theta'(0), \quad (21)$$

and using the definition of reduced Nusselt number one obtains

$$\frac{Nu_x}{\sqrt{Re_x}} = -[1 + R_d] \theta'(0). \quad (22)$$

Numerical Method

We have solved Eqs. (15) and (20) with the boundary conditions (14) by the shooting method using fourth-fifth order Runge-Kutta integration technique. The governing equations are reduced to a system of first order equations with boundary conditions (14) as

CWT case

$$\begin{cases} \frac{d\theta}{d\eta} = P; \\ \frac{dP}{d\eta} = \frac{\left[-Pr \left(\frac{1-e^{-b\eta}}{b} \right) P + E_c^* b^2 (1+\beta) e^{-2b\eta} \right]}{1 + R_d (1 + (\theta_w - 1)\theta)^3}, \end{cases} \quad (23)$$

PST case

$$\begin{cases} \frac{d\theta}{d\eta} = P; \\ \frac{dP}{d\eta} = \frac{\left[Pr \left(2\theta e^{-b\eta} - \left(\frac{1-e^{-b\eta}}{b} \right) P \right) \right]}{1 + R_d}, \end{cases} \quad (24)$$

with boundary conditions

$$\theta(0) = 1, \quad \theta(\infty) \rightarrow 0. \quad (25)$$

In order to integrate Eqs. (23) and (24) we require a value for $P(0)$ i.e $\theta'(0)$, however no such value is given at the boundary. Due to this reason, suitable values of $P(0)$ are guessed and then integration is carried out. The values of $P(0)$ are iteratively obtained such that solutions satisfy the boundary condition at large η with an error less than 10^{-7} .

NUMERICAL RESULTS AND DISCUSSION

This section discusses the behavior of embedded physical parameters on the dimensionless velocity and temperature functions. Influence of magnetic parameter M on the velocity is depicted in Fig. 1(a). It is noticed that increasing magnetic field strength restricts the flow and consequently thins the momentum boundary layer. Fig. 1(b) indicates an increase in the velocity and the boundary layer thickness when the viscoelastic effects strengthen.

Fig. 2 is plotted to perceive the effects of radiation parameter on the temperature θ . The results are given for both CWT and PST cases. In contrast to the linear radiation heat transfer problem, even a minor variation in the radiation parameter greatly influences the temperature and the thermal boundary layer thickness. The increase in temperature distribution with the radiation parameter is significant in the CWT case when compared with the PST case.

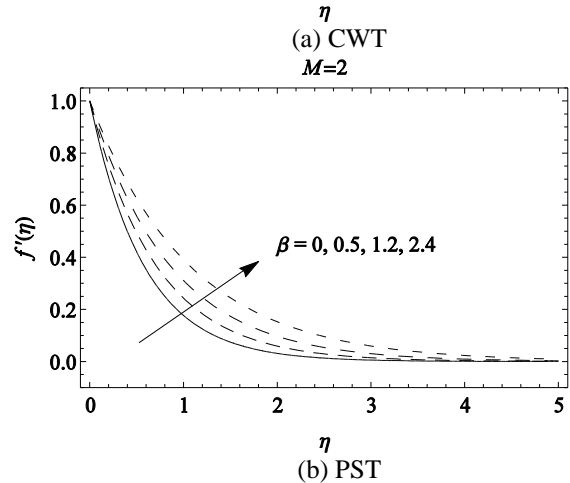
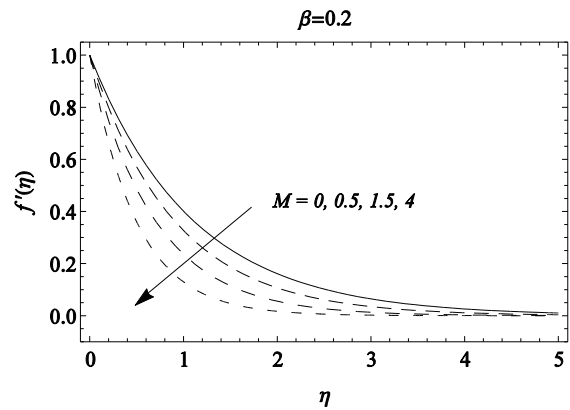


Fig.1. Velocity field f' for different values of magnetic parameter M and viscoelastic parameter β .

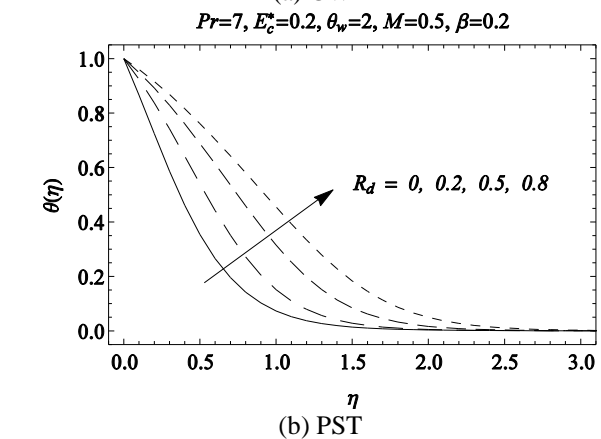
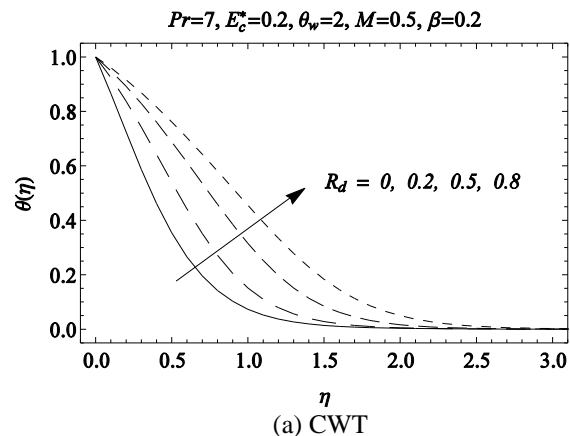


Fig. 2. Temperature profiles for different values of the radiation parameter R_d .

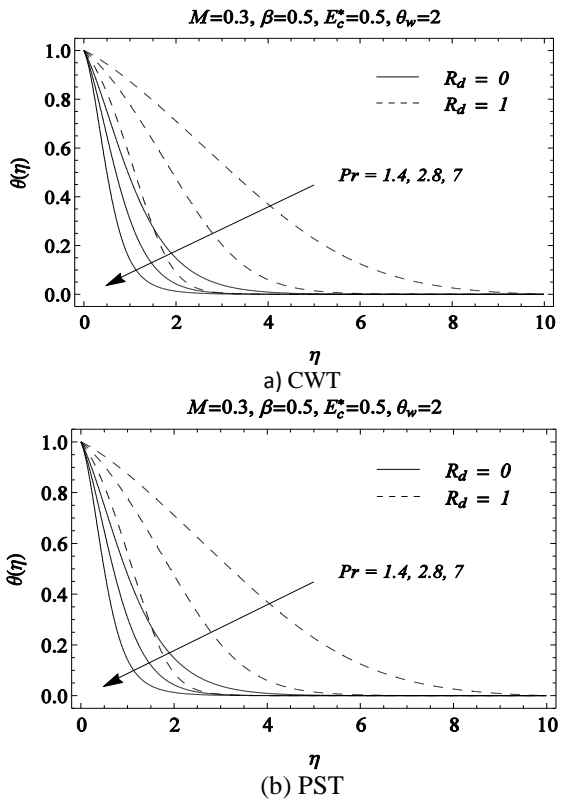


Fig. 3. Temperature profiles for different values of Pr

The effect of Prandtl number Pr on the temperature is shown in Fig. 3.

Increase in Pr may be regarded as a decrease in the thermal diffusivity and consequently a thinner thermal boundary layer is expected for a greater Pr . Specifically $Pr = 0.72, 1, 7$ corresponds to air, electrolyte solution such as mixture of salt and water and water, respectively. We observed that the profiles get closer to the boundary as Pr increases indicating a diminution in the thermal boundary layer thickness. We also noticed that temperature profiles show large deviation with the variation of Pr for a sufficiently strong thermal radiation effect ($R_d = 1$).

The influence of Eckert number Ec on the temperature for both CWT and PST cases is observed in Fig. 4. Here the profiles are computed with and without thermal radiation effects. When $R_d = 0$ the temperature θ first increases to a maximum value and then smoothly descends to zero value as $\eta \rightarrow \infty$. Moreover, the temperature θ is an increasing function of Ec .

Fig. 5 illustrates the behavior of second-grade fluid parameter β on the thermal boundary layer. In accordance with Abel et al. [39], the temperature θ is a decreasing function of β . In other words, the fluid becomes colder as normal stress differences

are increased. Numerical values of the dimensionless heat transfer rate at the sheet for

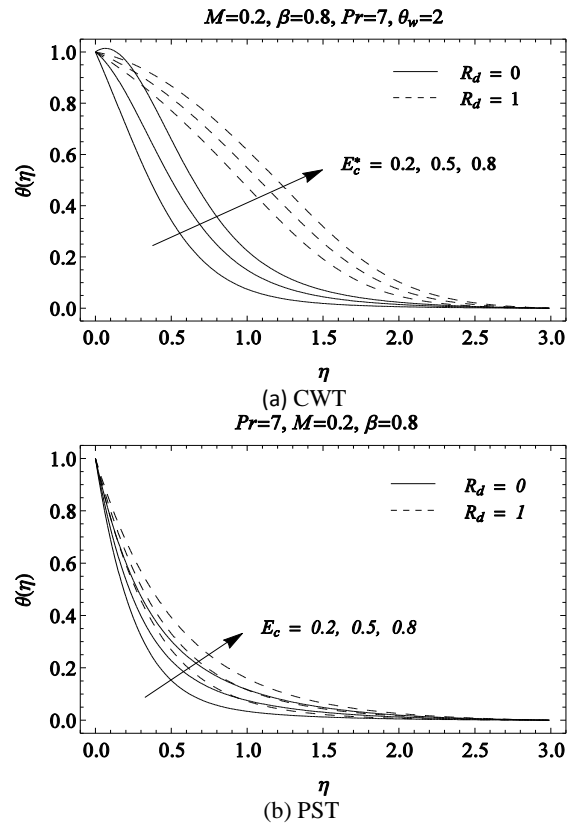


Fig. 4: Temperature profiles for different values of the Eckert number.

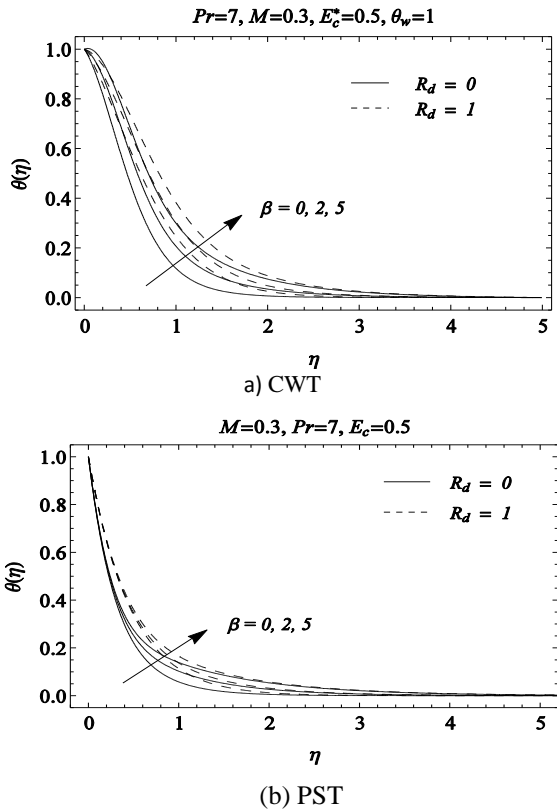


Fig. 5. Temperature profiles for different values of the viscoelastic parameter β .

various parametric values are provided in tables 1 and 2.

The results are presented with and without thermal radiation effects. The results are also compared with those obtained through the built-in numerical solver *bvp4c* of the software MATLAB and found in an excellent agreement. The Nusselt number ($-\theta'(0)$) is positive for all values of the parameters. This is because the fluid is colder than the solid wall and heat, therefore, flows from the stretching sheet to the fluid. Regardless of the values of other parameters the magnitude of the local Nusselt number is larger in the absence of thermal radiation effects ($R_d = 0$). The magnitude of the local Nusselt number is an increasing function of the second-grade fluid parameter. However, it slightly decreases as the magnetic field effects intensify. We have earlier observed in the graphical results that profiles become increasingly

steeper when Pr is increased. The Nusselt number, being proportional to the initial slope, increases with an increase in Pr . That's why the wall heat transfer rates are larger in the case of liquids when compared with gases such as air, hydrogen, etc. Moreover, the behavior of the Eckert number E_c on the dimensionless heat transfer rate is similar to that of Pr in a qualitative sense.

CONCLUSIONS

Thermal radiation effects on the flow of an electrically conducting second-grade fluid are investigated. Heat transfer analysis data were considered for two different heating processes, namely, (i) a sheet with a constant wall temperature (CWT) and (ii) a sheet with the prescribed surface temperature (PST). The temperature function in the

Table 1. Heat transfer rate at the wall $\theta'(0)$ in the CWT case for various parametric values

Pr	θ_w	E_c^*	M	β	R_d	$f''(0)$	$\theta'(0)$			
							bvp4c	Shooting		
7	2	0.2	0	0	1	-1	-0.37106	-0.37106		
					0	-1.45808	-1.45806			
			0.5	1	-0.81649	-0.38379	-0.38380			
				0	-1.44118	-1.44116				
			0.5	1	1	-0.86602	-0.34539	-0.34539		
				0	-1.20864	-1.20863				
		1.5	1	1	-0.77459	-0.34809	-0.34809			
			0	-1.18001	-1.17999					
		1.5	2	1	-0.91287	-0.27540	-0.27540			
			0	-0.75827	-0.75826					
		0.72	1	0.2	0.5	0.5	1	-1	-0.22543	-0.22544
							0	-0.36975	-0.36975	
1.5	1				-1.2909	-0.16740	-0.16740			
0.5	3			1	-0.79056	0.01436	0.01436			
				0	1.20696	1.20698				
				0	-0.28331	-0.28332				

Table 2. Heat transfer rate at the wall $\theta'(0)$ in the PST case for various parametric values

Pr	E_c	M	β	R_d	$f''(0)$	$\theta'(0)$			
						bvp4c	Shooting		
7	0.2	0	0	1	-1	-2.56119	-2.56120		
					0	-3.69545	-3.69550		
			0.5	1	-0.81649	-2.59471	-2.59472		
				0	-3.72385	-3.72381			
			0.5	1	1	-0.86602	-2.49538	-2.49542	
				0	-3.57175	-3.57177			
		1.5	1	1	-0.77459	-2.50739	-2.50744		
			0	-3.58013	-3.58019				
		0	1.5	2	1	-0.91287	-2.75488	-2.75489	
						0	-3.99382	-3.99388	
		0.72	0.5	0.25	1	1	-0.79056	-2.78670	-2.78673
							0	-4.02502	-4.02509
0.72	0.5	0.5	2	1	-0.70710	-0.64036	-0.640370		
					0	-0.96354	-0.96354		
					0	-0.63373	-0.63374		
				0	-0.93594	-0.93596			

radiation term of the energy equation is not further expanded by Taylors' series about the ambient temperature in the CWT case. The key points of the present study can be summarized as follows:

1. The presence of magnetic field creates a bulk known as Lorentz force which opposes the fluid velocity and, as a consequence, boundary layer thins as the strength of magnetic field increases. Moreover, the temperature θ is an increasing function of the magnetic parameter M . On the other hand, the magnitude of velocity and the boundary layer thickness are increasing functions of the second-grade fluid parameter β .

2. Temperature θ , being a strong function of the radiation parameter in the CWT case, appreciably increases in the CWT case when compared with the PST case.

3. A significant reduction in the temperature function is observed when the Prandtl number Pr is increased for sufficiently stronger thermal radiation effect. This outcome is similar in both CWT and PST cases. Moreover, the rate of heat transfer at the sheet enhances when Pr is increased.

4. The magnitude of Nusselt number $\theta'(0)$ increases with an increase in the viscoelastic effects and magnetic field strength.

5. The present work for the case of Newtonian fluid can be recovered by setting $\beta = 0$.

REFERENCES

1. H. Blasius, *Z. Math. Phys.*, **56**, 1 (1908).
2. L. J. Crane, *J. Appl. Math. Phys. (ZAMP)*, **21**, 645 (1970).
3. P. S. Gupta, A. S. Gupta, *J. Chem. Eng.*, **55**, 744 (1977).
4. A. Chakrabarti, A. S. Gupta, *Quart. Appl. Math.*, **37**, 73 (1979).
5. L. J. Grupka, K. M. Bobba, *ASME J. Heat Transfer*, **107**, 248 (1985).
6. W. H. H. Banks, *J. Méc. Theor. Appl.*, **2**, 375 (1983).
7. C. K. Chen, M. I. Char, *J. Math. Anal. Appl.*, **135**, 568 (1988).
8. M. E. Ali, *Int. J. Heat Mass Transfer*, **16**, 280 (1995).
9. I. Pop, T. Y. Na, *Mech. Res. Comm.*, **25** 263 (1998).
10. E. Magyari, B. Keller, *Eur. J. Mech. B-Fluids*, **19**, 109 (2000).
11. S. J. Liao, I. Pop, *Int. J. Heat Mass Transf.*, **47** 75 (2004).
12. M. Kumari, G. Nath, *Commun. Nonlinear Sci. Numer. Simulat.*, **14**, 3339 (2009).
13. T. Hayat, M. Mustafa, M. Sajid, *Z. Naturforsch.*, **64** 827 (2009).
14. T. Hayat, M. Mustafa, S. Asghar, *Nonlinear Anal.: Real World Applications*, **11**, 3186 (2010).
15. T. Hayat, M. Mustafa, A. A. Hendi, *Appl. Math. Mech.*, **32**, 167 (2011).
16. M. Mustafa, T. Hayat and A. A. Hendi, *ASMEJ. Appl. Mech.*, **79**, 1 (2012).
17. M. Mustafa, T. Hayat, S. Obaidat, *Z. Naturforsch.*, **67a**, 70 (2012).
18. L. Zheng, J. Niu, X. Zhang and Y. Gao, *Math. Comp. Mod.*, **56**, 133 (2012).
19. L. Zheng, X. Jin, X. Zhang, J. Zhang, *Acta Mechan. Sini.*, **29**, 667 (2013).
20. L. Zheng, N. Liu, X. Zhang, *J. Heat Transf.*, **135**, 031705 (2013).
21. I. C. Liu, H. H. Wang and Y. F. Peng, *Chem. Eng. Comm.*, **200** 253 (2013).
22. A. Raptis and C. Perdikis, *ZAMP*, **78**, 277 (1998).
23. M. A. Seddeek, *Int. J. Heat Mass Transfer*, **45**, 931 (2002).
24. A. Raptis, C. Perdikis, H. S. Takhar, *Appl. Math. Comput.*, **153**, 645 (2004).
25. R. C. Bataller, *Appl. Math. Comput.*, **198**, 333 (2008).
26. E. M. A. Elbeshbeshy, T. G. Emam, *Therm. Sci.*, **15**, 477 (2011).
27. T. Hayat, M. Mustafa, *Zeitschrift für Naturforschung*, **65a**, 711 (2010).
28. T. G. Motsumi, O. D. Makinde, *Phys. Scr.*, **86**, doi:10.1088/0031 8949/86/04/045003 (2012).
29. L. Zheng, L. Wang, X. Zhang, L. Ma, *Chem. Eng. Comm.*, **199**, 1 (2012).
30. L. Zheng, N. Liu, J. Niu, X. Zhang, *J. Porous Media*, **16**, 575 (2013).
31. R. Cortell, *Chem. Eng. Process.*, **46**, 721 (2007).
32. M. Mushtaq, S. Asghar, M. A. Hossain, *Heat Mass Transf.*, **43**, 1049 (2007).
33. T. Hayat, M. Mustafa, M. Sajid, *Z. Naturforsch.*, **64a**, 827 (2009).
34. R. Nazar, N. A. Latip, *Eur. J. Sci. Res.*, **29**, 509 (2009).
35. M. S. Abel, N. Mahesha and S. B. Malipatil, *Chem. Eng. Comm.*, **198**, 191 (2010).
36. M. Nazar, C. Fetecau, D. Vieru, C. Fetecau, *Nonlinear Anal.: Real World Applications*, **11**, 584 (2010).
37. M. Jamil, A. Rauf, C. Fetecau and N. A. Khan, *Commun. Nonlinear Sci. Numer. Simulat.*, **16**, 1959- (2011).
38. T. Hayat, A. Yousaf, M. Mustafa, S. Obaidat, *Int. J. Num. Meth. Fluids*, **69**, 399 (2012),.
39. M. Pakdermili, T. Hayat, M. Yurusoy, S. Abbasbandy, S. Asghar, *Nonlinear Anal. RWA*, **12**, 1774 (2011).
40. B. I. Olajuwon, *Int. Comm. Heat Mass Transf.*, **38**, 377 (2011).
41. A. Pantokratoras, T. Fang, *Physic. Scrip.*, **87**, 015703 (2013).
42. A. Mushtaq, M. Mustafa, T. Hayat, A. Alsaedi, *J. Aerosp. Engg.*, **27**, DOI: 10.1061/(ASCE)AS.1943-5525.0000361, (2014).
43. R. Cortell, *J. King Saud University-Science*, **26** (2014) doi.org/10.1016/j.jksus.2013.08.004.
44. A. Mushtaq, M. Mustafa, T. Hayat, A. Alsaedi, *J. Taiwan Inst. Chem. Eng.*, **45**, 1176 (2014).

45. M. M. Rashidi, S. A. Mohimani Pour, T. Hayat, S. Obaidat, *Comp. Fluids*, **54**, 1 (2012).
46. M. M. Rashidi, M. T. Rastegari, M. Asadia, O. Anwar Bég, *Chem. Eng. Comm.*, **199**, 231 (2012).
47. O. A. Beg, M. M. Rashidi, T. A. Beg, M. Asadi, *J. Mech. Med. Bio.*, **12**, 1250051 (2012).
48. M. M. Rashidi, S. Abelman, N. FreidooniMehri, *Int. J. Heat Mass Transfer*, **62**, 515 (2013).
49. S. Rosseland, *Astrophysik und Atomtheoretische Grundlagen*, Springer, Berlin, 1931.

ЧИСЛЕНО ИЗСЛЕДВАНЕ НА НЕЛИНЕЙНИ ПРОБЛЕМИ НА РАДИАЦИОННОТО ТОПЛОПРЕНАСЯНЕ ПРИ ТЕЧЕНИЕТО НА ФЛУИДИ ОТ ВТОРА СТЕПЕН

А. Мушак¹, М. Мустафа^{2,*}, Т. Хаят^{3,4}, А. Алсаеди⁴

¹ Изследователски център по моделиране и симулиране, Национален научно-технологичен университет, Исламабад, Пакистан

² Училища по естествени науки, Национален научно-технологичен университет, Исламабад, Пакистан

³ Департамент по математика, Университет „Куаид-И-Азам“, Исламабад, Пакистан

⁴ Департамент по математика, Научен факултет, Университет „Крал Абдул Азиз“, Джеда, Саудитска Арабия

Постъпила на 26 март, 2014 г., коригирана на 11 юли, 2014 г.

(Резюме)

Изучени са ефектите на радиационното топлопренасяне в двумерно течение в електропроводяща течност от втора степен. Нелинейният радиационен топлинен поток се отчита при формулирането на уравнението за енергията. Ефектите на вискозна дисипация на енергията са взети под внимание. Системата от нелинейни диференциални уравнения е решена числено по метода на прострелването с интеграционна процедура по Рунге-Кута от четвърта степен. Решенията са проверени с вградена числена процедура bvp4c от софтуера MATLAB. Пресметнати са коефициента на триене и скоростта на топлопренасяне.

BULGARIAN CHEMICAL COMMUNICATIONS

Instructions about Preparation of Manuscripts

General remarks: Manuscripts are submitted in English by e-mail or by mail (in duplicate). The text must be typed double-spaced, on A4 format paper using Times New Roman font size 12, normal character spacing. The manuscript should not exceed 15 pages (about 3500 words), including photographs, tables, drawings, formulae, etc. Authors are requested to use margins of 3 cm on all sides. For mail submission hard copies, made by a clearly legible duplication process, are requested. Manuscripts should be subdivided into labelled sections, e.g. **Introduction, Experimental, Results and Discussion**, etc.

The title page comprises headline, author's names and affiliations, abstract and key words.

Attention is drawn to the following:

a) **The title** of the manuscript should reflect concisely the purpose and findings of the work. Abbreviations, symbols, chemical formulas, references and footnotes should be avoided. If indispensable, abbreviations and formulas should be given in parentheses immediately after the respective full form.

b) **The author's** first and middle name initials, and family name in full should be given, followed by the address (or addresses) of the contributing laboratory (laboratories). **The affiliation** of the author(s) should be listed in detail (no abbreviations!). The author to whom correspondence and/or inquiries should be sent should be indicated by asterisk (*).

The abstract should be self-explanatory and intelligible without any references to the text and containing not more than 250 words. It should be followed by key words (not more than six).

References should be numbered sequentially in the order, in which they are cited in the text. The numbers in the text should be enclosed in brackets [2], [5, 6], [9–12], etc., set on the text line. References, typed with double spacing, are to be listed in numerical order on a separate sheet. All references are to be given in Latin letters. The names of the authors are given without inversion. Titles of journals must be abbreviated according to Chemical Abstracts and given in italics, the volume is typed in bold, the initial page is given and the year in parentheses. Attention is drawn to the following conventions:

a) The names of all authors of a certain publications should be given. The use of “*et al.*” in

the list of references is not acceptable.

b) Only the initials of the first and middle names should be given.

In the manuscripts, the reference to author(s) of cited works should be made without giving initials, e.g. “Bush and Smith [7] pioneered...”. If the reference carries the names of three or more authors it should be quoted as “Bush *et al.* [7]”, if Bush is the first author, or as “Bush and co-workers [7]”, if Bush is the senior author.

Footnotes should be reduced to a minimum. Each footnote should be typed double-spaced at the bottom of the page, on which its subject is first mentioned.

Tables are numbered with Arabic numerals on the left-hand top. Each table should be referred to in the text. Column headings should be as short as possible but they must define units unambiguously. The units are to be separated from the preceding symbols by a comma or brackets.

Note: The following format should be used when figures, equations, etc. are referred to the text (followed by the respective numbers): Fig., Eqns., Table, Scheme.

Schemes and figures. Each manuscript (hard copy) should contain or be accompanied by the respective illustrative material as well as by the respective figure captions in a separate file (sheet). As far as presentation of units is concerned, SI units are to be used. However, some non-SI units are also acceptable, such as °C, ml, l, etc.

The author(s) name(s), the title of the manuscript, the number of drawings, photographs, diagrams, etc., should be written in black pencil on the back of the illustrative material (hard copies) in accordance with the list enclosed. Avoid using more than 6 (12 for reviews, respectively) figures in the manuscript. Since most of the illustrative materials are to be presented as 8-cm wide pictures, attention should be paid that all axis titles, numerals, legend(s) and texts are legible.

The authors are asked to submit **the final text** (after the manuscript has been accepted for publication) in electronic form either by e-mail or mail on a 3.5” diskette (CD) using a PC Word-processor. The main text, list of references, tables and figure captions should be saved in separate files (as *.rtf or *.doc) with clearly identifiable file names. It is essential that the name and version of

the word-processing program and the format of the text files is clearly indicated. It is recommended that the pictures are presented in *.tif, *.jpg, *.cdr or *.bmp format, the equations are written using "Equation Editor" and chemical reaction schemes are written using ISIS Draw or ChemDraw programme.

The authors are required to submit the final text with a list of three individuals and their e-mail addresses that can be considered by the Editors as potential reviewers. Please, note that the reviewers should be outside the authors' own institution or organization. The Editorial Board of the journal is not obliged to accept these proposals.

EXAMPLES FOR PRESENTATION OF REFERENCES

REFERENCES

1. D. S. Newsome, *Catal. Rev.–Sci. Eng.*, **21**, 275 (1980).
2. C.-H. Lin, C.-Y. Hsu, *J. Chem. Soc. Chem. Commun.*, 1479 (1992).
3. R. G. Parr, W. Yang, *Density Functional Theory of Atoms and Molecules*, Oxford Univ. Press, New York, 1989.
4. V. Ponec, G. C. Bond, *Catalysis by Metals and Alloys* (Stud. Surf. Sci. Catal., vol. 95), Elsevier, Amsterdam, 1995.
5. G. Kadinov, S. Todorova, A. Palazov, in: *New Frontiers in Catalysis* (Proc. 10th Int. Congr. Catal., Budapest, 1992), L. Guzzi, F. Solymosi, P. Tetenyi (eds.), Akademiai Kiado, Budapest, 1993, Part C, p. 2817.
6. G. L. C. Maire, F. Garin, in: *Catalysis. Science and Technology*, J. R. Anderson, M. Boudart (eds), vol. 6, Springer-Verlag, Berlin, 1984, p. 161.
7. D. Pocknell, *GB Patent 2 207 355* (1949).
8. G. Angelov, PhD Thesis, UCTM, Sofia, 2001.
9. JCPDS International Center for Diffraction Data, Power Diffraction File, Swarthmore, PA, 1991.
10. *CA* **127**, 184 762q (1998).
11. P. Hou, H. Wise, *J. Catal.*, in press.
12. M. Sinev, private communication.
13. <http://www.chemweb.com/alchem/articles/1051611477211.html>.

CONTENTS

<i>M. S. Odabas, J. Radusiene, B. Karpaviciene, N. Camas</i> , Prediction model of the effect of light intensity on phenolic contents in <i>hypericum triquetrifolium turra</i>	467
<i>R. B. Mladenova, N. D. Yordanov</i> , EPR study of free radicals in pasta products	472
<i>A. Sankiewicz, A. Tokarzewicz, E. Gorodkiewicz</i> , Regeneration of surface plasmon resonance chips for multiple use	477
<i>D. D. Stoyanova, D. R. Mehandjiev</i> , Phase formation and catalytic activity of Cu-Co-spinel catalyst deposited on Al/Si/Mg – support	483
<i>H. Ahmari, S. Zeinali Heris</i> , Numerical analysis of mass and momentum transfer in co-axial cylinders with rotating inner cylinder	491
<i>B. Baghernejad</i> , Nano-TiO ₂ : An efficient and useful catalyst for the synthesis of 3-cyano-2(1 <i>H</i>)-pyridone derivatives.....	497
<i>N. Goel, S. Kumar, S. Bawa</i> , NaBH ₄ /I ₂ mediated one-pot synthesis of 4-(substituted-anilinomethyl-3-(6-methoxy-2-naphthyl)-1-phenyl-1 <i>H</i> -pyrazoles and their antimicrobial screening	502
<i>A. Fallah Shojaei, F. Golriz</i> , High photocatalytic activity in nitrate reduction by using Pt/ZnO nanoparticles in the presence of formic acid as hole scavenger	509
<i>I. Kraicheva, B. L. Shivachev, R. P. Nikolova, A. Bogomilova, I. Tsacheva, E. Vodenicharova, K. Troev</i> , Crystal structure of <i>p</i> -[<i>N</i> -methyl(diethoxyphosphonyl)-(4-dimethylaminophenyl)]toluidine – a potential cytotoxic agent	515
<i>D. Vladikova, Z. Stoyanov, A. Chesnaud, A. Thorel, M. Viviani, A. Barbucci, Ch. Nicoletta, A. Bertei, G. Raikova, P. Carpanese, M. Krapchanska</i> , Reversibility in monolithic dual membrane fuel cell	519
<i>E. Sakin, E. D. Sakin</i> , Relationships between particle size distribution and organic carbon of soil horizons in the Southeast area of Turkey	526
<i>I. Ivanov, L. Vezekov, D. Danalev</i> , Design and synthesis of potential inhibitors of multienzyme systems included in Alzheimer's disease	531
<i>R. S. Perić, Z. M. Karastojković, Z. M. Kovačević, M. B. Mirić, D. M. Gusković</i> , Changes of hardness and electrical conductivity of white gold alloy Au-Ag-Cu after aging treating	535
<i>F. Sadri, A. Ramazani, A. Massoudi, M. Khoobi, S. W. Joo</i> , Magnetic CuFe ₂ O ₄ nanoparticles as an efficient catalyst for the oxidation of alcohols to carbonyl compounds in the presence of oxone as an oxidant.....	539
<i>M. Malekshahi Byranvand, S. Shahbazi, A. Nemati Kharat, S. Afshar</i> , Application of mechanochemical method as a new route for synthesis of β -phase AgI nanoparticles	547
<i>A. Arami, B. Karami, S. Khodabakhshi</i> , A green synthetic route to some supramolecules using molybdate sulfuric acid (MSA) as a highly efficient heterogeneous catalyst	552
<i>B. Vafakish, M. Barari, E. Jafari</i> , Sunflower seed oil polymerization by ion exchange resins: acidic heterogeneous catalysis	558
<i>P. Ebrahimi, M. Mohammad Esmaeili, S. Ganji, A. Sattarian, H. Sabouri</i> , Cyanogenic glucoside determination in <i>Sorghum Halepense</i> (L.) Pers. leaves at the different growth stages	565
<i>R. G. Sotomayor, D. R. Delgado, F. Martínez</i> , Preferential solvation of naproxen and piroxicam in ethanol + water mixtures	571
<i>Z. Heidarneshad, M. Vahedpou¹, S. Ahmad Razavizadeh</i> , A theoretical DFT study on the stability of imidazopyridine and its derivatives considering the solvent effects and NBO analysis	578
<i>S. M. Stankov, A. Momchilov, I. Abrahams, I. Popov, T. Stankulov, A. Trifonova</i> , Synthesis and characterization of Si and Mg substituted lithium vanadium(III) phosphate	587
<i>E. D. Raczynska</i> , Geometric and energetic consequences of prototropy for neutral and ionized 4-aminopyrimidine in water solution	594
<i>M. A. Bodaghifard, N. Ahadi</i> , One-pot synthesis of tetrahydrobenzo[<i>b</i>]pyran and dihydropyrano[<i>c</i>]chromene derivatives using ammonium Alum in green media.....	603
<i>M. Vosoughi, F. Mohebbali, A. Pesaran Seied Bonakdar, H. Ardeshiri Lordegani, A. R. Massah</i> , ZSM-5-SO ₃ H as an efficient catalyst for the one-pot synthesis of 2,4,5-trisubstituted and 1,2,4,5- tetrasubstituted imidazoles under solvent-free conditions	607
<i>F. I. Sapundzhi, T. A. Dzimbova, N. S. Pencheva, P.B. Milanov</i> , Exploring the interactions of enkephalin and dalargin analogues with the μ -opioid receptor	613
<i>V. Parthasarathy, V. Dhanalakshmi, R. Anbarasan</i> , Synthesis, characterization and melt functionalization of high density poly (ethylene) with zinc salt	619
<i>A. Ahmadi</i> , Synthesis and anti-inflammatory evaluation of novel piperazine derivatives of mefenamic acid	626
<i>S. Joohari, M. Monajjemi</i> , NMR and NBO study of vinblastine as a biological inhibitor	631
<i>D. Kumar, D. Dass, A. Kumar</i> , Physico-chemical and antibacterial studies on the coordination compounds of N-(2-carbamoylfuranyl)-C-(3'-carboxy-2'-hydroxyphenyl) thiazolidin-4-one	647
<i>F. A. Saad, A. M. Khedr</i> , Azo-azomethine ligands with N ₂ O ₂ donor atom sets and their binuclear UO ₂ (II) complexes: synthesis, characterization and biological activity	654
	735

<i>F. Sheikholeslami-Farahani</i> , Multicomponent reactions of diethyl oxalate: synthesis of pyrrole derivatives in water	664
<i>F. Sheikholeslami-Farahani</i> , N-methyl imidazole or ammonium thiocyanate promoted synthesis of substituted pyrroles: Multicomponent reaction of alkyl propiolates in water	667
<i>M. Gorjizadeh, M. Afshari</i> , Rapid dehydrogenation of 3,4-dihydropyrimidin-2(1 <i>H</i>)-ones using 1,4-bis(triphenylphosphonium)-2-butene peroxodisulfate and microwave heating	673
<i>K. Ignatova, Y. Marcheva</i> , Electrodeposition of Ni-Co alloy on chemically oxidized Al	678
<i>I. I. Guseinov</i> , Combined theory of one- and two-electron bipolar and polar multicenter integrals of noninteger <i>n</i> Slater functions and Coulomb-Yukawa-like potentials with noninteger	684
<i>L. Cao, X. Jiang, J. Ding, Y. Chen</i> , Effect of zinc dimethacrylate on compatibilization and reinforcement of peroxide dynamically cured PP/EPDM TPVs	691
<i>M. P. Slavova, G. I. Zamfirova, V. I. Boev, V. T. Gaydarov, L.K. Yotova, M. J. M. Gomes, C. J. R. Silva</i> , Controlled aggregation of gold nanoparticles in a di-ureasil matrix. Optical and micro indentation investigation	699
<i>R. T. Gergova, M. P. Slavova, V. I. Boev, M. S. Mourdjeva, L. K. Yotova, R. T. Georgieva-Nikolova</i> , Comparative investigation of the feasibility of bacterial biofilms formation on the surface of the hybrid material UREASIL	706
<i>F. Chekin, S. Sadeghi</i> , Room temperature decomposition of hydrazine catalyzed by nickel oxide nanoparticles ...	714
<i>R. Farzad, D. N. Inanlou, R. A. Cohan, M. Ghorbani</i> , Effects of the industrial pollution on glutathione s-transferase in the liver of rainbow trout	720
<i>A. Mushtaq, M. Mustafa, T. Hayat, A. Alsaedi</i> , Numerical study of the non-linear radiation heat transfer problem for the flow of a second-grade fluid	725
INSTRUCTIONS TO THE AUTHORS	733

СЪДЪРЖАНИЕ

<i>М. С. Одабаши, Дж. Радусиене, Б. Карнавичиене, Н. Камаши, Модел, предсказващ ефекта на интензивността на светлината върху фенолното съдържание в <i>hypericum triquetrifolium</i> turra</i>	471
<i>Р. Б. Младенова, Н. Д. Йорданов, EPR изследване на свободните радикали в макаронени изделия</i>	476
<i>А. Санкиевич, А. Токажевич, Е. Городкевич, Регенерация на чипове с повърхостен резонанс за многократно употреба</i>	482
<i>Д. Д. Стоянова, Д. Р. Механджиев, Фазообразуване и каталитична активност на Cu – Co шпинелен катализатор нанесен върху Al/Si/Mg – носител</i>	490
<i>Х. Ахмари, С. Зейнали Херис, Числен анализ на преноса на маса и енергия при коаксиални цилиндри при въртящ се вътрешен цилиндри</i>	496
<i>Б. Багернеджад, Нано-TiO₂: ефективен и полезен катализатор за синтеза на 3-циано-2 (1H) -пиридонови производни</i>	501
<i>Н. Гоел, С. Кумар, С. Бава, Едностадийна синтеза на 4- (заместен-анилинометил-3- (6-метокси-2-нафтил) -1-фенил-1H-пиразоли посредством NaBH₄ / I₂ и тяхната антимикробна оценка</i>	508
<i>А. Фалах Шоджаеи, Ф. Голриц, Висока фотокаталитична активност на наночастици от Pt/ZnO при редуцията на нитрати в присъствие на мравчена киселина като донор на електрони</i>	514
<i>И. Крайчева, Б. Л. Шивачев, Р. П. Николова, А. Богомилова, И. Цачева, Е. Воденичарова, К. Троев, Кристална структура на р-[N-метил(диетоксифосфонил)-(4-диметиламинофенил)]толуидин-потенциален цитотоксичен агент</i>	518
<i>Д. Владикова, З. Стойнов, А. Чесно, А. Торел, М. Вивиани, А. Барбучи, К. Николела, А. Бертей, Г. Райкова, П. Карпанезе, М. Кръпчанска, Обратимост в двойно мембранна горивна клетка</i>	525
<i>Е. Сакин, Е. Д. Сакин, Взаимовръзки между разпределението на частици по размери и органичния въглерод в почвени хоризони в югоизточна Турция</i>	530
<i>Ив. Иванов, Л. Везенков, Д. Даналев, Дизайн и синтез на потенциални инхибитори на мултиензимни системи участващи при болестта на Алцхаймера</i>	534
<i>Р. С. Перич, З. М. Карастойкович, З. М. Ковачевич, М. Б. Мирич, Д. М. Гускович, Промени в твърдостта и електропроводимостта на сплавта „бяло злато“ (Au-Ag-Cu) след стареене чрез термично третиране</i>	538
<i>Ф. Садри, А. Рамазани, А. Масуди, М. Кхуби, С. У. Джу, Магнитни наночастици от CuFe₂O₄ като ефективен катализатор за окисляването на алкохоли до карбонилни съединения в присъствие на оксон като окислител</i>	546
<i>М. Малекшани Биранванд, С. Шахбази, А. Н. Кхарат, С. Афишар, Приложение на механохимични методи като нов път за синтезата на β-фазови наночастици от AgI</i>	551
<i>А. Арами, Б. Карами, С. Ходабахши, “Зелен” синтетичен път към някои супра-молекули с използването на молибдат-сярна киселина (MSA) като високо-ефективен катализатор</i>	557
<i>Б. Вакафиш, М. Барари, Е. Джафари, Полимеризация на слънчогледово масло с йонообменна смола: киселинен хетерогенен катализ</i>	564
<i>П. Ебрахими, М. Мохамед Есмаели, С. Ганджи, А. Сатарян, Х. Сабури, Определяне на цианогенни глюкозиди в листата на <i>Sorghum halepense</i> (L.) Pers. в различни етапи на развитие</i>	570
<i>Р. Г. Сотомайор, Д. Р. Делгадо, Ф. Мартинес, Нови, прости и валидирани UV-спектрофотометрични методи за определяне на пиридоксин хидрохлорид в разтвори и препарати</i>	577
<i>З. Хейдарнежад, Ф. Хейдарнежад, С. Ахмед Резавизаде, Теоретично DFT-изследване на стабилността на имидазопиридин и негови производни при отчитане на ефекта на разтворителя и NBO-анализ</i> ...	586
<i>С. М. Станков, А. Момчилов, И. Абрахамс, И. Попов, Т. Станкулов, А. Трифонова, Синтез и охарактеризиране на литиево ванадиев фосфат, дотиран със силиций и магнезий</i>	593
<i>Е. Д. Рачинска, Геометрични и енергийни следствия от прототропията на неутрален и йонизиран 4-аминопиримидин във водни разтвори</i>	602
<i>М. А. Бодагифард, Н. Ахади, Едностадийна синтеза на тетрахидробензо[b]пиранови и дихидропирано [c]хроменови производни с амониев алум в „зелена“ среда</i>	606
<i>М. Восуги, Ф. Мохебали, А.П.С. Бонакдар, Х.А. Лордегани, А.Р. Масах, ZSM-5-SO₃H като ефикасен катализатор за едно-стадийната синтеза на 2,4,5-три-заместени и 1,2,4,5- тетра-заместени имидазоли в отсъствие на разтворител</i>	612
<i>Ф. И. Сапунджи, Т. А. Дзимбова, Н. С. Пенчева, П. Б. Миланов, Изследване на взаимодействията на енкефалинови и даларгинови аналози с μ-опиоиден рецептор</i>	618
<i>В. Партасаратхи, Ж. Дханалакшми, Р. Анбаразан, Синтеза, охарактеризиране и функционализиране в стопилка на полиетилен висока плътност с цинкова сол</i>	625
<i>А. Ахмади, Синтеза и противо-възпалително действие на нови производни на пиперазина на мефенаминовата киселина</i>	630
	737

<i>С. Джохари, М. Монайеми</i> , NMR и NBO-изследване на винбластин като биологичен инхибитор	646
<i>Д. Кумар, Д. Дас, А. Кумар</i> , Физикохимични и антибактериални изследвания върху координационни съединения с N-(2-карбамоил)-С-(3'-карбокси-2'-хидроксифенил) тиазолидин-4-он	653
<i>Ф.А. Саад, А.М. Хедр</i> , Групи от азо-азометинови лиганди с N ₂ O ₂ –донори и техните двудрени комплекси с UO ₂ (II): синтеза, охарактеризиране и биологична активност	663
<i>Ф. Шейкнолеслами-Фарахани</i> , Многокомпонентни реакции на диетил оксалат: Синтеза на пиролови производни във вода	666
<i>Ф. Шейкнолеслами-Фарахани</i> , N-метилимидазол или амониев тиоцианат промотирана синтеза на заместени пироли: многокомпонентна реакция на алкил пропиолати във вода	672
<i>М. Горджизаде, М. Афиари</i> , Бързо дехидрогениране на 3,4-дихидропиримидин-2(1H)-они, използвайки 1,4- бис-(трифенилфосфониев)-2-бутен пероксосулфат и микровълново нагряване	677
<i>К. Игнатова, Й. Марчева</i> , Електроотлагане на Ni-Co сплав върху химически оксидиран Al	683
<i>И. И. Гусинов</i> , Комбинирана теория на едно- и дву-електронни би-полярни интегрални от нецели p-Slater'ови функции и Coulomb-Yukawa-подобни потенциали с дробни индекси	690
<i>Л. Цао, К. Джианг, Дж. Динг, Ю. Чен</i> , Ефект на цинковия диметакрилат върху съвместимостта и якостта на термопластични полимери от полипропилен и етилен-пропилен диен, получени чрез пероксид-иницирана вулканизация	698
<i>М. П. Славова, Г. И. Замфирова, В. И. Боев, В. Т. Гайдаров, Л. К. Йотова, М. Д. М. Гомес, К. Д. Р. Силва</i> , Контролирано агрегиране на златни наночастици в диуреасилатна матрица. Оптично и микроидентационно изследване	705
<i>Р. Т. Гергова, М. П. Славова, В. И. Боев, М. С. Мурджева, Л. К. Йотова, Р. Т. Георгиева-Николова</i> , Сравнително изследване на възможността за образуване на бактериални биофилми върху повърхността на хибриден материал UREASIL	713
<i>Ф. Чекин, С. Садеги</i> , Разграждане на хидразин, катализирано от нано-частици от никелов оксид при стайна температура	719
<i>Р. Фарзад, Д. Н. Инанлу, Р. А. Коан, М. Горбани</i> , Ефекти на промишленото замърсяване върху глутатион s-трансферазата в черния роб на дъговата пъстърва	724
<i>А. Муцак, М. Мустафа, Т. Хаят, А. Алсаеди</i> , Числено изследване на нелинейни проблеми на радиационното топлопренасяне при течението на флуиди от втора степен	732
ИНСТРУКЦИЯ ЗА АВТОРИТЕ	733